A MULTIDISCIPLINARY ASSESSMENT OF HYALOCLASTITE DEPOSITS IN PETROLEUM SYSTEMS USING FIELD STUDIES, DRILL CORE, BOREHOLE IMAGE AND WIRE-LINE LOG DATASETS

WATTON, TIMOTHY,JAMES

A MULTIDISCIPLINARY ASSESSMENT OF HYALOCLASTITE DEPOSITS IN PETROLEUM SYSTEMS USING FIELD STUDIES, DRILL CORE, BOREHOLE IMAGE AND WIRE-LINE LOG DATASETS

TIMOTHY JAMES WATTON

A THESIS ACCEPTED FOR THE DEGREE OF DOCTOR OF PHILOSOPHY

DEPARTMENT OF EARTH SCIENCES

DURHAM UNIVERSITY

2013

THESIS ABSTRACT

This thesis aims to document hyaloclastite deposits in different depositional environments from field outcrops in Iceland to characterise lithofacies heterogeneity enabling comparison to subsurface datasets. Field hyaloclastite datasets from Stóri-Núpur (subaerial-marine transition) and Hjörleifshöfði (an emergent Surtseyan volcano) are used to support the interpretation of hyaloclastite and associated volcanic deposits in core, borehole image logs and wire-line log datasets from Hawaii (Hawaiian Scientific Drilling Project II – HSDP II borehole) and the Faroe-Shetland Basin (LOPRA1/1A well and the Rosebank field).

This study provides additional constraints on lava delta formation in predominantly basaltic systems where hyaloclastite depositional profiles reflect localised extrusion pathways and syn-sediment reworking which control 3D lithofacies architecture. Furthermore this thesis documents the evolution of Hjörleifshöfði using field mapping and major/trace element geochemistry. Hjörleifshöfði can split into five phases of deposition charting the submarine to emergent building of the volcano, unique as it also records a phase of silicic volcanism (Sólheimar Ignimbrite) which dates late stage volcanism to no earlier than 12,383 C14 years BP.

Petrophysical and petrographic observations suggest hyaloclastite deposits are unique in terms of their velocity/density and P and S wave relationships due to palagonite formation, basalt clast support, phenocryst and zeolite component amongst others which impacts on depth conversion and the calculation of reflection coefficients. Wire-line log response gamma-ray (GR), resistivity (RES), P-wave sonic velocity (Vp) is also closely linked to the dominant interstitial secondary minerals and phenocryst components of sideromelane glass.

Borehole image log analysis of mixed volcanic and volcaniclastic rocks allows the accurate characterisation of distinct internal lava flow features, contact relationships and joint networks enabling better characterisation of volcanic sequences in the subsurface via careful comparison with field examples.

Field, core and wire-line log data is combined to form a multidisciplinary assessment of hyaloclastite deposits in the subsurface suggesting that the complexity and scaling issues in hyaloclastite rocks is generally overlooked which may impact on future petroleum exploration in volcanic basins.

STATEMENT OF COPYRIGHT

ACKNOWLEGDEMENTS

Firstly, I would like to thank all of my supervisors, Dougal Jerram, Richard Brown, Thor Thordarson, Nic DePaola and Richard Davies who have been there for a least part of the project! They have all contributed greatly to discussion fieldwork and generally correcting my "unique" writing style.

DONG Energy E and P, UK Ltd. are thanked for funding and helping conceive the project. Their hands off approach, yet constant support has enabled the science to be pursued fully. In particular I thank Mike Smith and Alywn Ross for giving my confidence in the project and for letting me publish and include work completed as part of an internship in 2010.

Chevron North Sea, Ltd, Statoil, UK. Ltd., OMV, UK Ltd. And particularly Sarah Lumbard are thanked for allowing FMI data to be published and presented in this thesis.

Steve Cannon formally at DONG Energy E and P, UK limited is particularly thanked for reading several chapters and introducing me to the world of petrophysics. Without Steve's guidance a lot of this project would not be possible.

Support in the field was provided by a number of people, Thor Thordarson, Catherine Nelson, Kirstie Wright, Dougal Jerram and especially Clayton Grove. Clayton accompanied me on all my trips and constantly questioned my interpretations as well as providing expert off road driving skills and some seriously pink shorts!

Nick Schofield, Brian Bell, Dave Jolley, David Brown, Catherine Nelson and Simon Passey have at some point been involved with the Volcanic Margins Research Consortium. Ideas shared and explored at these meetings have fueled a lot of research in this project and their comments on presentations have been greatly beneficial.

I would like to thank Kate Dobson for kindly running a hyaloclastite core plug on the Manchester X-ray CT imaging facility, Breno Waichel for use of the handheld gamma ray device, Mike DaSilva at the AHMN for access of the HSDP II core and Chris Nodling for running and prep of the XRF samples.

I would like to apologize to everyone in the open plan area for the messiest desk ever seen in the department!

I would like to thank all the admin staff especially Paula Elliot who has helped sort out expenses and field trip booking throughout the project as was a helping deal with a difficult situation in Namibia.

BJ, Baker, Grove, Clarky, Damby, Natrass, Tolan, Reynolds and all the PhD students in Earth Sciences are thanked for constant banter, work related chat over beer and discussion which had made the project a lot more fun.

Finally, I would like to thank my family and soon to be wife Lou who has had to put up with 4 months of constant moaning about writing my thesis. Without them I could not imagine undertaking this project and they have supported me throughout.

CONTENTS

LIST OF FIGURES AND TABLES

1

CHAPTER FIGURES

1. Introduction

1.1 Project Outline

This thesis aims to assess the potential roles that hyaloclastite deposits and associated volcaniclastic rocks play within petroleum systems by using field, laboratory and well logging techniques to provide new volcanological data for subsurface applications. This chapter summarizes the motivation, aims and structure of the project, the approaches used (field-based and core, wire-line and image log). Data for this thesis has been obtained from a number of different localities including Iceland (field studies), Hawaii (drill core) and the Rosebank Field, Faroe-Shetland Basin, UKCS (drill core, wire-line log and bore hole imaging). The details of each locality are summarized in the introduction to each chapter, however, a brief summary of the geology in each setting is provided here. The general structure of the thesis is based upon three papers, one published and two accepted. These are provided in the appendix for each corresponding chapter in support of the thesis.

1.2 Project Motivation – Field Based Approach

The transition from a predominantly siliclastic to a volcanic-dominated system in volcanic margin settings is generally poorly understood. In many examples, this transition 'zone' is characterised by sequences, sometimes hundred's of meters thick, of fragmented volcanic rocks that have been erupted into water/wet environments and are loosely termed hyaloclastite deposits. These deposits and their associations form the focus of this study.

Submarine hyaloclastite deposits can form thick (>1 km), complex sequences during the onset of large igneous provinces (e.g. Planke et al., 2000; Ross et al., 2005; Jerram et al., 2009; Wright et al., 2012) and can mask petroleum plays (Jegen et al., 2009; Davison et al., 2010; Ellefsen et al., 2010). Only a few field studies of submarine hyaloclastite deposits exist (Fuller, 1931a; Jones, 1970; Jones and Nelson, 1970; Bluck, 1980; Bishop, 1985; Larsen and Pedersen, 1990; Porębski and Gradziński, 1990; Schmincke et al., 1997; Pedersen et al., 1998; Skilling, 2002; Behncke, 2004; Smellie et al., 2006; Tucker and Scott, 2009). Most field-based approaches have generally focussed on settings where subaerial lavas entered into a

marine or lacustrine environment or where hyaloclastite deposits formed as a by-product of emergent volcanism, with only limited effort made to compare the differences of both of the environments. This is often because lateral 3D exposure is commonly limited meaning only cross sections are available for study (e.g. Jones and Nelson, 1970; Porębski and Gradziński, 1990). The results of these studies have been scaled-up when interpreting thick remotely imaged offshore hyaloclastite sequences but the field implications of construing such an idea has not been discussed (Kiørboe, 1997; Wright et al., 2012). The term hyaloclastite has been used to describe a range of different volcaniclastic products and the nomenclature developed to describe these is complex, making comparisons sometimes difficult (this is addressed specifically in chapter 2). However, in this thesis hyaloclastite is defined as a breccia derived from passive fragmentation processes with a limited active component and does not involve reworking processes. It comprises of mainly sideromelane glass, basalt fragments, clay phases and zeolites. In the case of reworking the term reworked hyaloclastite should be used to note a second phase of deposition. However in core where field relationships are unclear and reworking cannot be conclusively attributed a non-genetic use of the term hyaloclastite in this thesis refers to deposits composed of >90% quenched sideromelane glass (with limited vesicularity) as a matrix component to encompass hyaloclastite deposits that have been locally reworked (such as in the HSDP II core, see chapter 6). In this thesis volcaniclastic rocks refer to rocks that contain a mixed volcanic lithoclast component.

This thesis specifically focuses on submarine hyaloclastite examples where ice confinement has not modified the deposits, although similarities with these ice-affected systems are discussed. Skilling, (2002) indicated that future work was needed to characterize hyaloclastite successions in terms of their internal complexity. Therefore this study aims to better characterise the variety facies and facies associations found in ‘hyaloclastite’ deposits in the field; to understand differences in hyaloclastites formed in different settings; and to compare onshore with offshore data in order to identify key variations in such sequences (see section 1.3).

1.2.1 Assessment of Hyaloclastite Lithofacies Complexity on Small- to Large-Scales

Excellent exposures of hyaloclastite sequences in southern Iceland, at Stóri-Núpur and Hjörleifshöfði, were selected (see chapter 4 for details) in order to study sub-outcrop to outcrop-scale lithofacies variation in hyaloclastite deposits in different settings and to compare to published work. Variations in the environment of deposition can control small-scale and large-scale hyaloclastite lithofacies volcaniclastic lithofacies heterogeneity (Fig. 1.1). In order to better understand hyaloclastite deposits in the subsurface (i.e. those imaged in seismic surveys) this heterogeneity needs to be better understood. Moreover, from a volcanological framework, the key differences between sub-aerial to sub-marine and sub-marine to sub-aerial hyaloclastite producing systems can be systematically characterised augmenting previous studies of such systems.

Existing studies of hyaloclastite deposits either compare the large scale-lithostratigraphic framework or general seismic lithofacies associations of hyaloclastite deposits (e.g. Pedersen et al., 2002; Jerram et al., 2009; Wright et al., 2012). In this thesis, several studies of large-scale hyaloclastite sequences on Iceland are described and considered in terms of their overall volcanic lithofacies framework. Comparison is made between them and subsurface data on very large scale offshore hyaloclastite deposits recorded from the Faroe-Shetland Basin and Hawaii (Chapter 8).

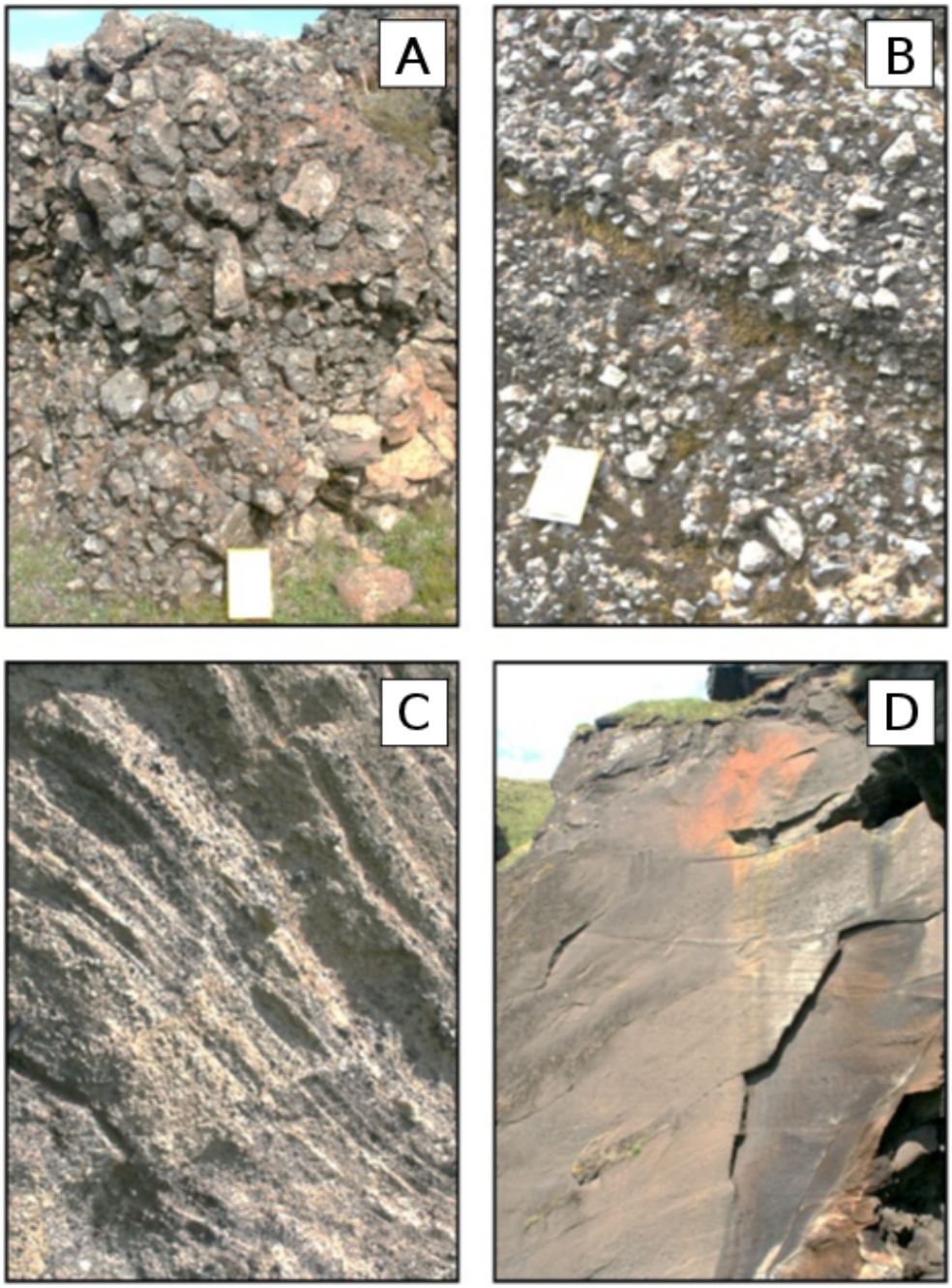

Figure 1.1. Variations in hyaloclastite lithofacies from Iceland. A) A blocky hyaloclastite breccia (Stóri-Núpur) B) Aligned clast, reworked hyaloclastite breccias, (Stóri-Núpur) C) Imbricated pebble reworked hyaloclastite breccias, field of view 2 m (Hjörleifshöfði) D) Large cross bed sets in reworked hyaloclastite breccias field of view 20 m (Hjörleifshöfði).

1.3 Project Motivation – Core and Well Log based Approaches

The ability to accurately interpret volcanic deposits in the subsurface from remote datasets has increased dramatically following recent studies that have enabled a more precise characterization of volcanic packages in offshore wire-line log datasets (Planke, 1994; Delius et al., 1995; Delius et al., 1998; Bücker et al., 1998; Planke and Cambray, 1998; Brewer et al., 1999; Delius et al., 2003; Helm-Clark et al., 2004; Bartetzko et al., 2005; Nelson et al., 2009). However, many unanswered questions remain such as the variability in petrophysical response of hyaloclastite deposits (chapter 6) and the identification of mixed siliciclastic and volcaniclastic rocks (chapter 7).

1.3.1 Direct Core to Petrophysical Observations

The EU 5th Framework SIMBA (ENK6-CT-2000-00075) in Nelson, (2010) indicate that there is still a huge variety in the density and p-wave velocity (Vp) values of volcanic rocks (e.g. Single, 2004) (Fig. 1.2). A direct comparison of drill core to the petrophysical properties of volcanic rocks (especially hyaloclastite deposits) is still lacking. Currently, Vp data sets of hyaloclastite deposits are based solely upon the LOPRA1/1A well (cf. Nelson et al., 2009). In this thesis, uses the 3 km-long Hawaiian Scientific Drilling Project (HSDP) Phase II core (cf. Stopler et al., 2009) to make a detailed comparative study of recovered petrophysical logs with core data. This has enabled a more accurate characterization of hyaloclastite lithofacies in the subsurface.

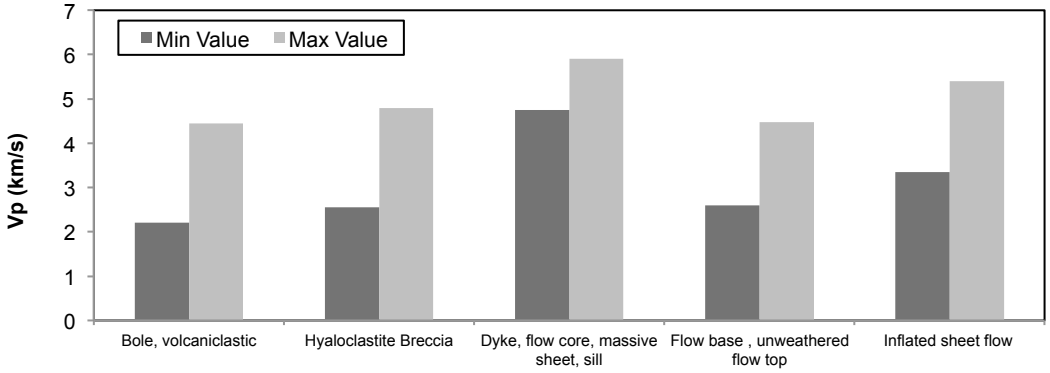

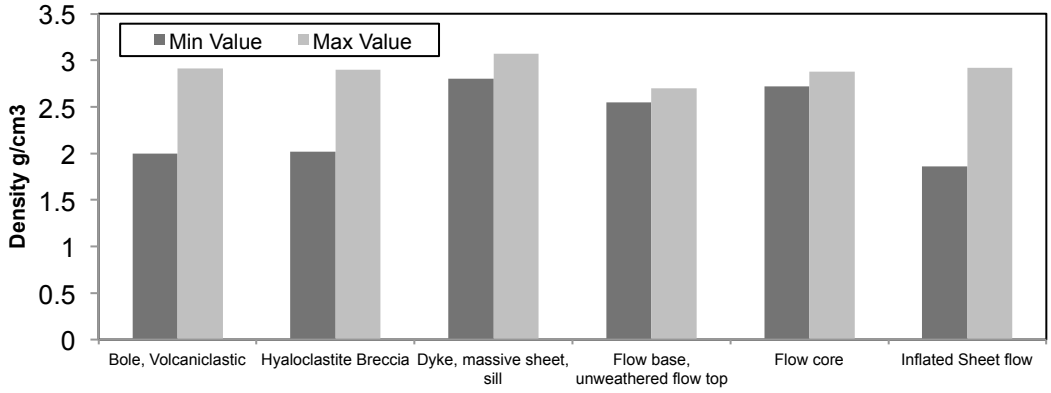

Figure 1.2. Max and Min Vp and density distributions for different volcanic units based upon the SIMBA data base from SIMBA; Single, 2004 and Nelson, 2010 unpublished theses. The recorded variation in Vp response is in hyaloclastite deposits in the SIMBA project 2 km/s where as LOPRA 1/1A variation is c. 0.2 km/s (Data provided in the appendix for this chapter).

1.3.2 Comparison of Hyaloclastite Systems to Core and Wire-line Log Datasets

The limited availability of drill core through hyaloclastite deposits and the wide variability in hyaloclastite deposits means currently only limited data exists to compare density to velocity responses, let alone lithofacies-specific examples (cf. Moore, 2001). Characterization of density/Vp relationships is a useful predictive tool if, for example, density is not recorded or material has not been cored (common in petroleum exploration wells). In this thesis, HSDP phase II core measurements, including density and velocity relationships, are compared to known methods of density determination from Vp. This is an essential first step in obtaining a better understanding of the acoustic properties of hyaloclastite deposits, which may aid seismic imaging by enabling recognition of the causes of seismic reflectors (chapter 6).

1.3.3 Integration of Field and Remote Approaches to Large Scale Volcanic Facies Variation: Assessing the Petroleum Potential of Volcanic Systems

Hyaloclastite deposits are often scaled-up into the subsurface from field examples of relatively thin hyaloclastite and volcaniclastic successions (see Kiørboe, 1997; Wright et al., 2012, who base models on Jones and Nelson, 1970). However in the subsurface, for example in the North Atlantic Igneous Province (NAIP), hyaloclastite deposits can be >1 km thick and extend for > 20 km laterally in 2D

seismic lines—significantly bigger than all studied onshore hyaloclastite deposits. Presently, there have been no drill penetrations of prograding foresets in large offshore hyaloclastite deposits. To encompass hyaloclastite deposits on these scales in field examples involves not only the study of the hyaloclastite deposits but also the supplying lava flow field. Therefore a large range of lithofacies types which include, tabular and compound lava flows, fluvial volcaniclastic deposits, hyaloclastite deposits and products of lava water interaction, such as, peperites, rootless cones and two-tiered columnar joints which are dependant on lava effusion pathways and may also incorporate an established fluvial or lacustrine sediments (Fig. 1.3). The Árnes district in the Sutherland region in southern Iceland allows a comparison of the large-scale lithofacies relationships over a scale similar to seismic surveys (chapter 8).

1.3.4 Identification of Volcanic Lithofacies Variation (including hyaloclastite deposits) in the Subsurface

Formation Micro Image logs (FMI) (chapter 2; 7) provide a virtual image of the borehole wall and once calibrated to core and other datasets they allow accurate lithofacies characterization of volcanic successions that can aid well log interpretation (Ekstrom et al., 1987). This technique allows the assessment of borehole data down to a centimetre-scale. Chapter 7 also outlines methods for the calibration of FMI logs where core may not be present and provides a useful reference tool for the analysis of volcanic rocks. This study uses datasets derived from the Rosebank Field, Faroe Shetland Basin, United Kingdom Continental Shelf (UKCS).

1.4 Geological Settings

The following section provides an overview geological history of each of the main study areas presented in the thesis. The introductory section of each chapter expands on each overview to provide more specific information regarding each locality. This section aims to inform the reader of the regional context of the project and not provide a definitive geological history, which is outside the scope of the project. Further information the author suggests consulting references cited in this section.

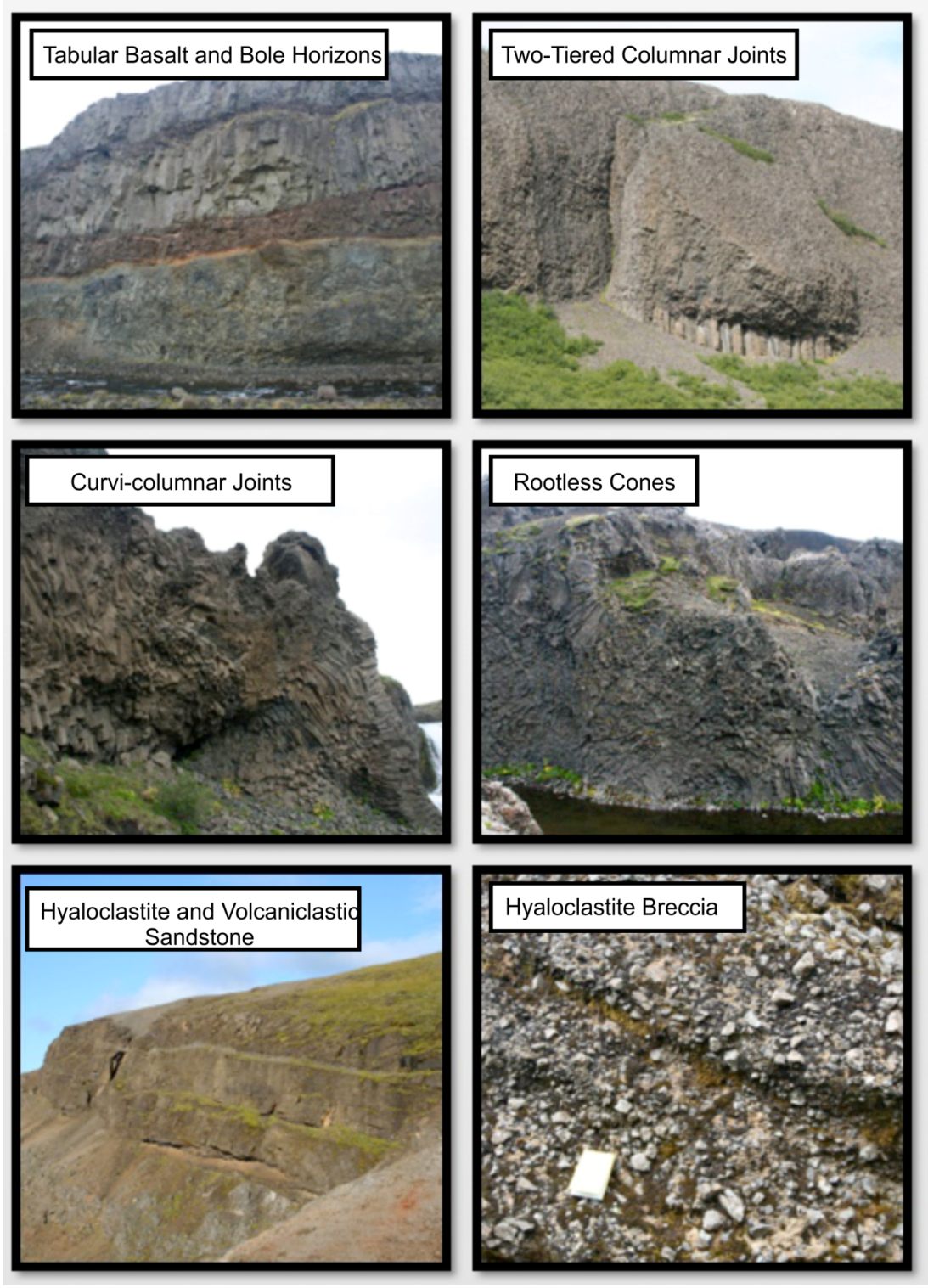

Figure 1.3. Lithofacies variation in large-scale hyaloclastite sequences form onshore examples in Iceland. All of these lithofacies and facies relationships are likely to exist when comparing hyaloclastite deposits and associated lava flow fields at seismic scales.

1.4.1 Overview Iceland

Iceland is a 3 km high, 350,000 km^2 island that lies on the junction between two plate margin structures, the Mid-Atlantic Ridge and the Greenland-Iceland-Faroe Ridge (Fig. 1.4, Gudmundsson, 2000; Thordarson and Larsen, 2007 and references therein). The crust beneath Iceland is between 10–40 km thick, has been buoyed by the Iceland mantle plume for the last 65 Ma, and is the last remaining part of the North Atlantic Igneous Province (NAIP) that is still active (Vink, 1984; White et al., 1995; Wolfe et al., 1997; Saunders et al., 1997). Approximately 30% of the Iceland structure lies above sea level with the remainder forming a 50–200 km shelf (Thordarson and Larsen, 2007). The oldest rocks exposed on Iceland are 14–16 Ma old, although construction of the island is thought to have begun around 24 Ma ago (Moorbath et al., 1968; Watkins and Walker, 1977; Saemundsson, 1978; Kristjansson, 1982).

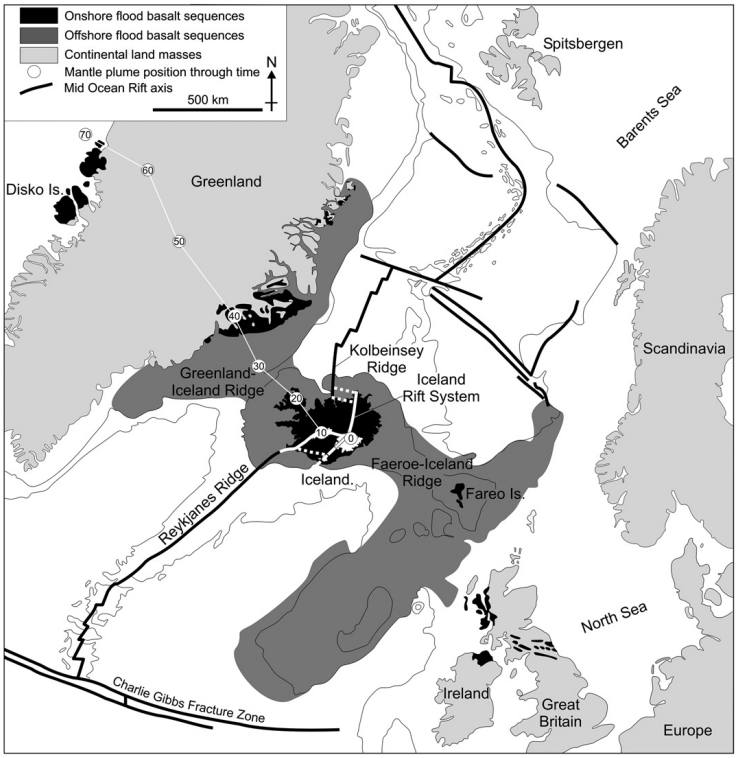

Figure 1.4. Overview of volcanic exposure on Iceland, the migration of the Iceland mantle plume and the extent of the North Atlantic Igneous Province (NAIP), which also includes the volcanic rocks within the Faroe-Shetland Basin (FSB). Shown on the figure is the geometry of the Icelandic rift zone consisting of two spreading centres separated by a seismically active zone in trans tensional regime (From Thordarson and Larsen, 2007).

Iceland can be divided into a number of active volcanic zones that were established from the interaction between rifting and plume interaction (Bjornsson, 1985). The main focus of magmatism occurs along the axial zone and is typified by tholeiitic affinities divided into the Western Volcanic Zone (WVZ) and the North Volcanic Zone (NVZ), which are linked by the Mid-Iceland Belt (Thordarson and Larsen, 2007). The WVZ is linked to the Mid-Atlantic Ridge via the Reykjanes Peninsula whereas the NVZ continues north and joins the Tjörnes Fracture Zone. The Eastern Volcanic Zone (EVZ) is a spur that is propagating off the southern tip of the NVZ and is characterized by mildly alkalic magmatism (Gudmundsson, 1995). The South Iceland Seismic Zone (SISZ), which acts as a transform offset (Hackman et al., 1990) separates the EVZ and WVZ. In this thesis the main study areas lie within the SISZ and southern tip of the EVZ.

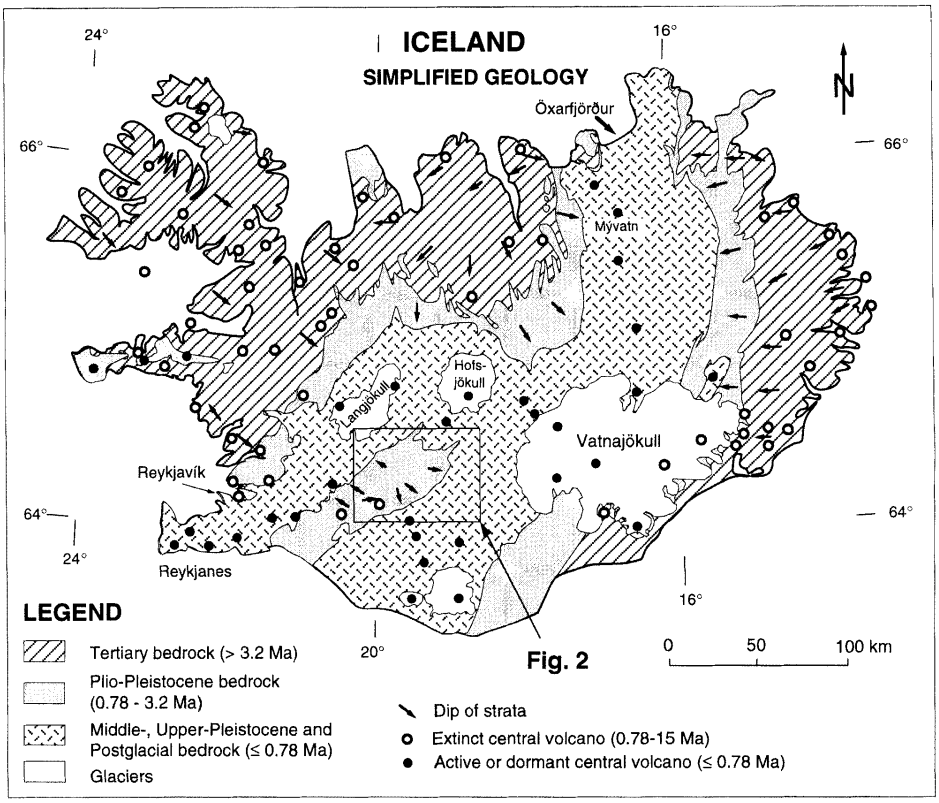

Figure 1.5. A simplified geological map of Iceland with relative ages and general dip directions indicating basement structure. The Hreppar formation (0.78-3.2 Ma) is contained within the highlighted box (From Kristjánsson et al., 1998).

1.4.2 An Overview of the Sutherland District, South-Central Iceland, Hréppar Formation - Stóri-Núpur

The Hréppar formation is a decade old term that has been applied to a succession of rocks that lie within the SISZ in the Sutherland district of central Iceland (Fig. 1.5). The succession is composed of interbedded volcaniclastic, hyaloclastite and siliciclastic rocks that were laid down <3 Ma ago (Kristjánsson et al., 1998). Several studies have noted a broad, shallowly dipping (4-6°) anticline in the Hréppar formation, which trends NE-SW, parallel to the existing Thórsárdulur Valley (Saemundsson, 1967, 1970; Einarsson, 1967; Kristjánsson et al., 1998). The anticline is considered a result of subsidence in the two flanking volcanic zones (WVZ/EVZ, Saemundsson, 1974) with the central core thought to be the remnants of a crustal fragment left in place from continued eastward movement of the active spreading zone during the last 3 Ma (Kristjánsson et al., 1998).

Volcanism in the Thórsárdulur Valley is generally poorly understood. Two extinct volcanic centres lie near or in the valley area, Stóra-Laxá and Thórsárdulur. Stóra-Laxá is one of only a few igneous complexes which host intrusions of > 20 m thickness (Fridleifsson, 1976). Thórsárdulur, which is younger, has only been described in terms of its products' lateral extent (Kristjánsson et al., 1998).

The stratigraphy of Hreppar Formation has been determined by regional geological mapping and K/Ar dating (summarized in Kristjánsson et al., 1998). Most data concerning geochronology and stratigraphy is linked to various geothermal exploration programs and is sourced from Iceland National Energy Authority reports (in native Icelandic). The gross lithostratigraphy north of Búfell is summarized in a detailed chronostratgraphic framework (Kristjánsson et al., 1998, also see fig. 8.1, chapter 8). Lithologically the Hréppar formation consists of inter-glacial lavas, hyaloclastite and volcaniclastic sediments punctuated by periods of glacial activity. The Stóri-Núpur lava delta lies at the southern end of the Hréppar formation and has not been previously studied.

1.4.3 Eastern Volcanic Zone (EVZ) - Hjörleifshöfði

The southern spur of the EVZ is also referred to as the Southern Transgressive Zone, in which silicic volcanic central volcanoes of Katla and Eyjafjallajökull are located (Fig. 1.6, Lacasse et al., 2007). Hjörleifshöfði is one of a

number of small volcanic mounds (that also includes Pétursey, Hafursey and Dryhólaey) that surround the Katla and Eyjafjallajökull volcanoes. The Mýrdalsjökull glacier mostly covers Katla and Eyjafjallajökull but Hjörleifshöfði lies isolated in the sandur plain to the south. The age of Hjörleifshöfði is unknown, however, palaeo-magnetic data indicate that it formed during the last magnetic reversal (c. 800Ka, Jarðfræikort Geological Mapping, 1:600,000 scale, 2009). This thesis aims to determine the origin and evolution of Hjörleifshöfði for the first time.

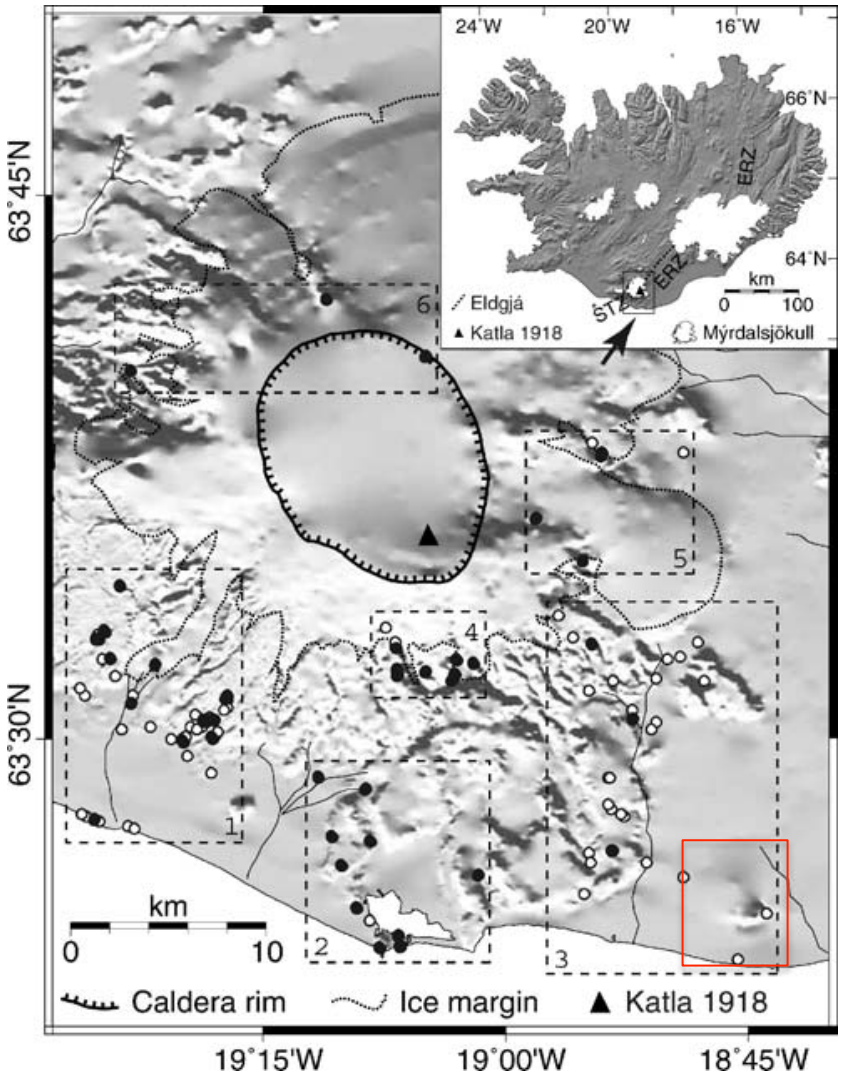

Figure 1.6. A overview topographic map showing the southern tip of the EVZ highlighting the Katla caldera (dashed line) presently covered by the Mýrdalsjökull glacier. Hjörleifshöfði lies on the far southeast of the map within the Katla 1918 field (red box, From Lacasse et al., 2007).

1.4.4 Overview of Hawaii

The Hawaiian island and submarine seamount archipelago consists of eight main islands and numerous small atolls. The archipelago is part of the much larger Emperor island chain that crosses the Pacific plate (Clague and Jarrard, 1973). The timing of the initiation of the diversion is much debated, although current estimates from radiometric dating place it at 50 Ma (Sharp and Clague, 2006 and references therein).

The Hawaiian Island chain is thought to lie on a static mantle plume upon which the Pacific plate moves across (c. 40° south Moore and Clague, 1992). The plume is the subject of much debate and is not covered here, but has been imaged by seismic tomography as a vertical pillar of lower density material that originates at the at the core mantle boundary (Zhao, 2001). Hawaii is the newest of the Hawaiian Islands and of the Hawaiian-Emperor chain.

The island of Hawaii is the largest of the Hawaiian island chain and has grown at a rate of 0.02 km^2/yr for the past 600 ka. It consists of seven tholeiitic shield volcanoes, Mahukona, Kohala, Mauna Kea, Hualalai, Mauna Loa, Kilauea, and Loihi (Moore and Clague, 1992). The Hawaiian Scientific Drilling Project (HSDP), summarized in chapter 6, was drilled on the island of Hawaii at Hilo and charts the evolution of the Mauna Kea Volcano (Fig. 1.7).

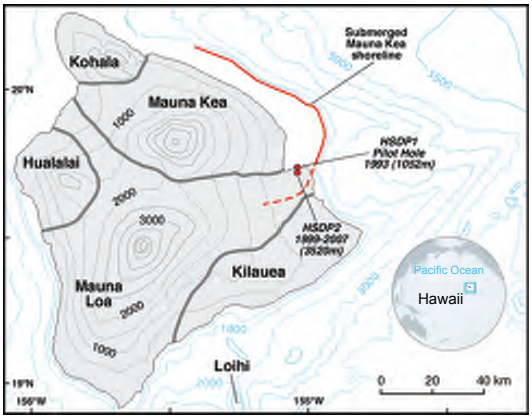

Figure 1.7. The principal volcanoes that make up the Island of Hawaii and the boundary of the submarine stage of Mauna Kea. The HSDP II core samples both the the Mauna Loa and Mauna Kea volcanoes. From Stopler et al., 2009.

1.4.5 Overview Faroe-Shetland Basin

The Faroe-Shetland Basin (FSB) is a product of rifting during the continental separation that opened the North Atlantic Ocean between Greenland and NW Europe and of the impingement of the Iceland hotspot at the base of the lithosphere during the Mesozoic to early Cenozoic (Richie et al., 1996; England et al., 2005; Passey and Bell, 2007). The geology and structure of the FSB is complex (Dóre, 1999; Dean et al., 1999). Three main extensional events are of particular importance in the region; the Caledonian orogeny in the Silurian, a Mesozoic-Early Cenozoic rifting phase that lead to the deposition of a thick Jurassic-Paleocene sedimentary rocks, the opening of the Atlantic and the accumulation of huge volumes of basalt lava and associated volcaniclastic sediments. Three compressional events in the Eocene, Oligocene and Miocene caused major basin inversion (Sørenson, 2003). The main structural elements of the FSB are summarized in Figure 1.8 which include major inversion structures such at the Corona Ridge (Rosebank field location) and much debated NW-SE transfer lineaments thought to control sediment deposition in the basin however, many are unclear (Moy and Imber, 2009 and references therein).

The main phase of volcanism in the FSB occurred during the Palaeocene between 62-54 Ma ago (cf. Richie and Hitchen, 1996; Hansen et al., 2009; Wright et al., 2012). It was characterized by emplacement of basalt lava flows, sills, hyaloclastite lava deltas and long-lived silicic volcanic centres (e.g. Richie and Hitchen, 1996; Passey and Bell, 2007; Thomson and Schofield, 2008; Hansen et al., 2011; Wright et al., 2012). Volcanism in the FSB has been tentatively linked back to the Faroe Islands through tracing of seismically resolvable packages (Kiørboe, 1999). Volcanism in the NW margin of the FSB is represented by the Faroe Lava Group that comprises > 6 km succession of basaltic volcaniclastic and laterally extensive formation of subaerial basalt rocks (Ellis et al., 2002; Passey and Jolley, 2008).

This thesis investigates volcanic lithofacies variations in the Rosebank field. The Rosebank field lies on the Corona Ridge, a broad anticline that is a result of Palaeocene inversion in the UK sector (Dean et al., 1999). The structure is penetrated by five wells that cored a mix of sedimentary rocks and lavas attributed to the Flett formation. The stratigraphy and data recovery in the field is summarized in Chapter 7.

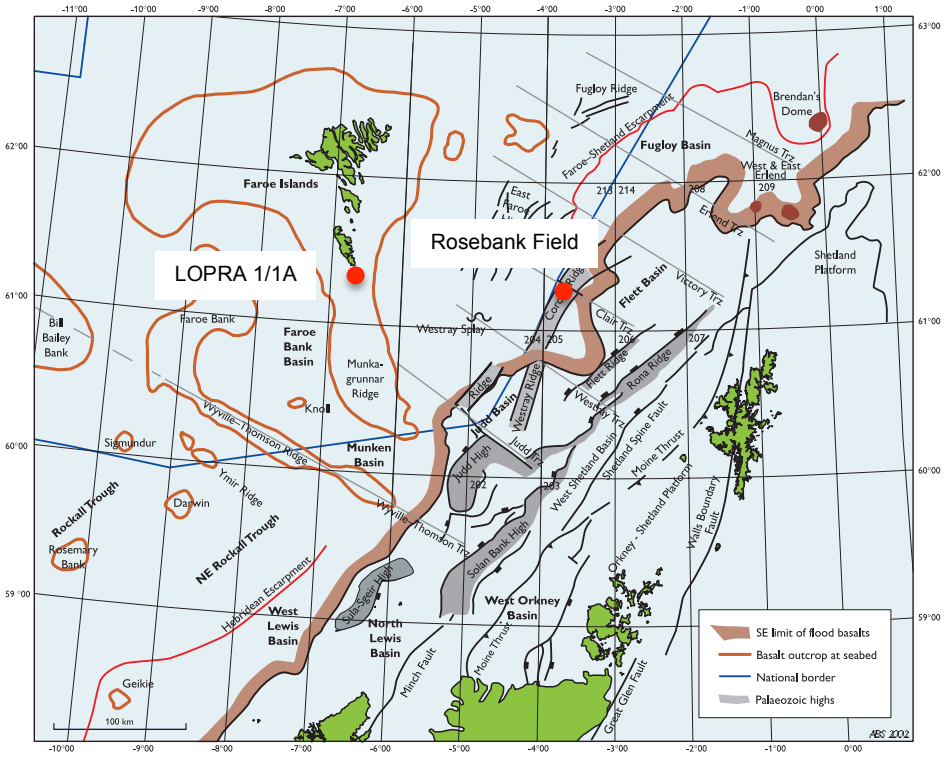

Figure 1.8. The main structural elements and extent of the basalt within the Faroe-Shetland Basin. The Rosebank Field lies on the Corona Ridge directly between the Faroe and Shetland Islands with the LOPRA 1/1A well also used in this study marked for reference (modified from Søresen, 2003).

1.5 Summary of Aims and Generalised Approach

The aims of this thesis is to identify complexities in hyaloclastite deposits, understand their depositional settings and the controls on architecture, and apply this knowledge to subsurface examples via assessment of remote datasets. The specific objectives of the project are to:

- Provide a systematic understanding of the definition and classification of hyaloclastites;
- Accurately characterize hyaloclastite in a variety of environmental settings;
- Determine models of the formation of large scale (>10 km) volcanic lithofacies relationships which include hyaloclastite deposits;
- Describe the complex volcanic evolution of Hjörleifshöfði an emergent volcano;

- Compare hyaloclastite core to its petrophysical responses;
- Apply volcanological knowledge to subsurface applications and provide methods for accurate lithological identification where limited core is available.

1.6 Thesis Outline

Chapter 1: Introduction and overview geological history of study areas. Thesis aims and project motivation.

Chapter 2: Overview of analytical techniques used in the thesis.

Chapter 3: A review of hyaloclastite deposits that summarizes ideas on their genesis and past field studies.

Chapter 4: Field studies of hyaloclastite sequences comparing morphology, environmental setting, degree of reworking.

Chapter 5: A detailed analysis of lithofacies relations in emergent volcanic settings. Characterization of the geology and evolution of Hjörleifshöfði—an emergent Surtseyan volcano.

Chapter 6: An analysis of hyaloclastite deposits in the subsurface with specific examples from the Hawaiian Scientific Drilling Project (HSDP) Phase II core.

Chapter 7: Remote studies of volcanic lithofacies variation. Formation Micro Image (FMI) analysis of volcanic successions with examples from the Rosebank field.

Chapter 8: Discussion, conclusions and recommendations for future work. Discussion and documentation of the large-scale lithofacies variations in hyaloclastite systems using field and remotely studied examples, the use of PEF logs for correlation of volcanic packages and the reworking of pillow lava successions.

Appendices: Papers Published in support of the thesis; interpretations of borehole data, FMI image logs, EDX datasets, XRD datasets and additional field logs. This is provided on DVD that can be obtained from the author. A guide for use printed at the end of the thesis.

2

2. Analytical Techniques

Chapter Summary

This chapter provides background information on the analytical techniques used in the data chapters of this thesis. Techniques used in each chapter are tabulated below (Table 2.1). Principals of each technique are outlined in this chapter with specific information and results provided in the introductory section for each chapter.

Table 2.1

Chapter Number	Title	Techniques used
4	Field Studies of Hyaloclastite Deposits in Iceland	Field
5	The Geology and Evolution of the Hjörleifshöfði Outlier	Field, X-ray Fluorescence Spectroscopy (XRF)
6	Hyaloclastite Deposits in Wire-line Logs	Field (logging), Well Logs, Scanning Electron Microscopy and EDS
7	Bore Hole Imaging of Volcanic Successions using FMI; examples from the West of Shetland	Field, Well Logs, Borehole Imaging
8	Discussion; Conclusions and Future work	Field, Borehole Imaging, Well Logs, Scanning Electron Microscopy

Table 2.1. Key analytical techniques used in the development of each specific thesis chapter

2.1 Field Data Acquisition

Field-based datasets for this project have been sourced from volcanic rocks in Iceland, USA and Namibia over a total of 24 weeks. The location of each study has been provided in the introduction to each chapter or mentioned in the relevant section within the chapter text. Field characterization was not only carried out on hyaloclastite deposits but a wide range of volcanic deposits enabling accurate field examples to be compared to bore-hole image logs (Chapter 7 and 8).

a. ***Mapping*** – Geological mapping was carried out on base maps that were either aerial photographs or where resolution allowed topographic maps (US military source only available from from Landmælingar Islands in Iceland). This project has also extensively used mapping from Landmælingar Islands (Icelandic Land Survey- LMI [http://atlas.lmi.is/kortasja/]) as a constant reference tool for locality names. Geological base maps were then digitized using CorelDraw™.

b. ***Logging*** – Lithological logging of volcanic successions in the field was conducted on a centimeter scale. Logging encompasses the grain size classification for volcanic and sedimentary rocks calibrated for use on a single sheet using the Wentworth scale (Wentworth, 1922) and McPhie et al., (1993). The logging sheet created for this thesis is used in the book Field Guide to Igneous Rocks by Jerram and Petford, (2011) (Fig. 2.1). All logs are provided in the appendix. This project has opted for a lithofacies based approach to characterized deposits based upon composition, grain size and structure.

c. **Sampling** – Originally sampling was conducted for lithological characterization and thin section analysis. Additional sampling was made for rock property analysis but difficulties in core recovery meant that experiments could not be conducted (see future work in chapter 8 for more detail). Attempts were made to drill cores of hyaloclastite deposits in the field using a petrol powered rock drill, water-cooling and a 28 mm diamond-tipped bit. This failed because the differential torque at the drill bit between hard basalt clasts and soft interstitial clay and zeolite. Furthermore the presence of water-soluble clays (water was used as both a lubricant and for cooling) meant that basalt clasts become dislodged in the drill bore. Both 20 mm and 40 mm drill core bores were tested in the field but no cores could be successfully extracted. In an attempt to overcome this, large (~30 x 30 x 30 cm) orientated blocks were taken for drilling in the laboratory under more controlled conditions. However, while cores could be extracted more successfully in the laboratory, the drilling process induced micro-fractures which were not present in the original block and thus compromised rock property data (see X-ray-CT imaging, section 2.8).

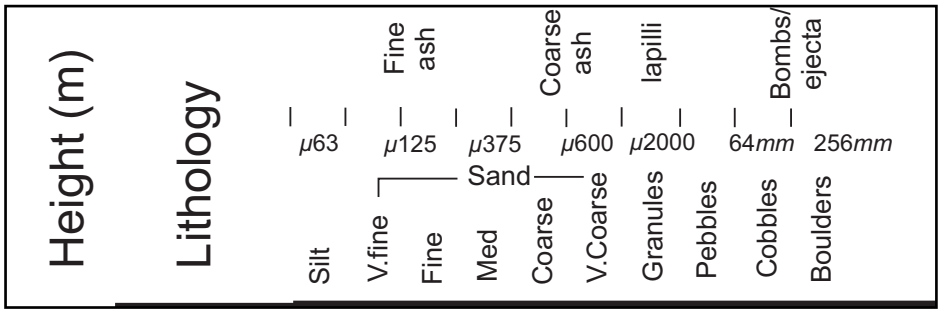

Figure 2.1 Calibrated sedimentary and volcanic grain size scale used in logging within this thesis from Wentworth, (1922) and McPhie et al., (1993).

2.2 Wire-line Log Principals

Well log data used in this project was collected using Dual Laterlog DLL, Spectral Gamma Ray SGR (with GR, K%, Th ppm and U ppm) and Compensated Sonic Tools. Core Tube Loggers controlled hole deviation. Geophysical log measurements for the HSDP II core were conducted by the University of Hawaii, GDZ Postdam (University of Aachen) and the University of Goettingen in 1999. Well log data for the Rosebank field was collected between 2005-2009 for Chevron North Sea Limited by Schlumberger and given to partners DONG Energy E and P Ltd., Statoil, UK Ltd. and OMV, UK Ltd. All log data is stored locally on the DONG database. This section summarizes the principles behind each of the well log tools used in this thesis. Well headers and location are provided in the introduction to each section.

Well log tools are attached to a cable (a 'string') and collectively are known as the sonde. Data can be recorded either during or after the drilling process. Heave compensation is required if the device is attached to a ship or a floating rig in order to minimize the influence of wave action (Desbrands, 1985). To maintain the quality and accuracy of a log constant calibration of the sonde is needed due to long cable lengths and changes in ambient pressure and temperature during data acquisition. Simple post processing can remove spikes in the data by averaging the two values that surround the data point. Representative wire-line responses for different volcanic

lithologies are provided in tables within chapter 6, 7 (also see Helm-Clarke et al., 2004; Boldreel, 2006; Nelson et al., 2009).

2.2.1 Gamma Ray and Photoelectric Absorption factor

In both localities a spectral gamma ray (SGR) tool was used to record formation (rock sequence) radioactivity, which can be used as a lithological identification tool. SGR tools measure the individual response of radioactive minerals to a gamma ray source (potassium 40, the uranium family and the thorium family), which vary widely in crustal rocks (Desbrands, 1985; Hearst and Nelson, 1985). The response occurs at different energy levels:

- potassium : Gamma ray energy 1.46 MeV
- thorium Series : Gamma ray energy 2.62 MeV
- urainium-Radium series : Gamma ray energy 1.76 MeV

The GR spectrum emitted by each element is recorded using counters linked to a crystal. When ionized by incoming particles the crystal emits visible light that is recorded by a photomultiplier. The intensity of the light is proportional to the energy of the ionizing particle (Hearst and Nelson, 1985). The photomultiplier then produces a pulse proportional to the energy detected so a pulse-height spectrum can be constructed that records the energy level as a series of peaks (Heath, 1964). This uses the principle of the photoelectric effect where the incident gamma ray equals the kinetic energy required for an atom to release its electron. This emits an X-ray equal to the binding that is characteristic of the medium. A selection of low energy gamma rays can be recovered as recorded by the ***photoelectric absorption factor,*** which is a useful for mineralogical characterization (Desbrands, 1985; Helm-Clarke et al., 2004). The probability of such an interaction over a set area is called the cross section and is expressed in centimetres. At higher energies, the gamma ray scatters through the formation (Compton scattering), which can be absorbed by the photoelectric interaction and creates noise in the spectrum. The larger the crystals or the more homogeneous the medium, the greater the accuracy of the GR logs. The GR log is calculated using algorithms to accurately quantify the total element amounts. This is dependent on several factors, which include the logging speed and the counter

efficiency. Potassium is calculated as a percentage value where as U and Th are recorded as concentrations (ppm) so:

$$\text{Total gamma ray or API} = 8 \times \text{Uranium ppm} + 4 \times \text{thorium ppm} + \text{potassium \%}. \quad (2.1)$$

2.2.2 Density

Density logs record the formation's bulk density, which is a function of mineral assemblages and the fluid enclosed in the pore space. Density logging is also performed using a gamma ray source. Formation density is calculated from the Compton scattered medium-energy gamma rays that return to the detector (the linear attention coefficient). The linear attention coefficient is proportional to the density of a material, which is a function of gamma ray energy and the number of electrons scattered via Compton scattering per volume area. Sondes are calibrated such that they count the number of backscattered gamma rays over a set distance from the emitter. The number of counts that reach the detector is related to the bulk density (see Hearst and Carlson, 1969; Gluyas and Swarbick, 2004). The ***photoelectric cross section*** can be defined as the photoelectric cross section multiplied by the formation density (Debrandes, 1985).

2.2.3 Neutron Porosity

Neutron logs use fast neutrons that collide with the nuclei of atoms and slow them down. They are used to calculate a proxy of porosity. After travelling a certain distance from a source, neutrons slow down as they travel through the formation. As neutrons begin to scatter elastically they reach lower energy levels emitting gamma rays that are recorded at a detector. Neutrons are typically emitted by a chemical source, such as americium or beryllium. The most common interaction is with hydrogen as the mechanics of elastic collision predict that the most energy is released where particles of equal mass meet. As hydrogen is fundamentally associated with the amount of water in the pore space of a rock, the measurement of the neutron population can be directly linked to the porosity of the medium or its interstitial fluids (Debrandes, 1985). However in rocks that contain a high percentage of water

bound clays, such as hyaloclastite deposits, actual porosity is difficult to calculate and so can be used as a proxy for volcanic components within the log. The number of counts recorded at the receiver then can be converted to formation porosity (see Wood et al., 1974).

2.2.4 Acoustic logging P and S wave

P and S wave measurements are recorded by propagating an acoustic pulse from a transmitter through rock to one or more receivers (Debrandes 1985). This is conducted using a borehole-compensated sonde that employs two or more transmitters used alternatively. These are averaged to provide an exact measurement. The velocity and attenuation of sound waves depend on many factors including density, porosity, saturation and fracture density (Hearst and Nelson 1985). The emitter generates a pulse in the form of sound waves. The disturbance propagates through the medium by elastic deformation. Compression waves (P waves) are the first arrivals and shear waves (S waves) are the second arrival.

P waves are propagated parallel to the direction of particle displacement in a substance that can resist compression. S waves travel perpendicular to the direction of particle displacement. Particles move in a lateral motion and drag neighboring particles that continue the propagation. The time between the transmission of the pulse and the reception of the first p-wave arrival is the one-way travel time for the transmitter and the receiver. Data is presented as sonic slowness (ΔT) (travel time per foot in the formation), which can be converted to velocity:

$$\Delta T = \frac{10^6}{v} \tag{2.2}$$

where ΔT is in micro seconds per foot and velocity is in feet per second.

2.2.5 Resistivity Logging

Resistivity measurements are based on the electrochemical differences between different rocks, which influence how strongly the material opposes the flow

of an electric current. The resistivity tool is useful as it can be used as a proxy for formation permeability as it measures how connectivity of the fluid in contact with the electric current. Conventional resistivity tools emit a current that travels radially out into the formation. A guard current is supplied externally to ensure the potential across all sections of the receiving electrode remains the same. Measurement of the current required to keep the potential equal is proportional to the resistivity of the layer. Both localities in this thesis use the Dual Laterlog tool which doubles the guard currents and emits different frequencies for each part of the sonde to record deep and shallow resistivity dependent on the field radii (Desbrands, 1985).

2.2.6 Borehole Image Logs – Formation Micro Imaging (FMI)

The Formation Micro Imager (FMI) is a qualitative, high-resolution, resistivity tool designed by Schlumberger, which produces comparative images of the sidewalls of a well bore (Ekstrom et al., 1987). The FMI tool obtains resistivity measurements from eight sensor pads placed upon four orthogonally positioned calliper arms that run along the borehole walls (Ekstrom et al., 1987; Siddiqui et al., 2004, Fig.2.2). Each pad contains an array of closely spaced microelectrodes that injects current into the formation. Much like conventional resistivity logging the potential of each pad is constantly maintained relative to the return electrode (Pensky, 1999). The current is modulated at each pad that allows a qualitative conductivity image of the borehole wall to be constructed (Cheung, 1999).

The data coverage is dependent on the pad spacing—typically 80–100 % of the hole is covered at resolutions of 5 mm or less (Pensky, 1999; Cheung, 1999). Processing of the FMI image yields a high-resolution vertical image of the borehole that is color-coded for resistivity values. Static and dynamic images can be produced depending on the methods used to average the downhole resistivity values—static images are produced for the entire well, whereas dynamic images are averaged every 2 m.

The FMI tool is susceptible to the condition of the borehole sides, such as cave-ins and mud losses. Recognized FMI artefacts in Rosebank datasets include “wiper-tip and reaming” events caused by scratching of the borehole during cleaning (Lofts and Bourke, 1999) or relate to the bit type used to drill basalt intervals.

Aggressive Tri-cone bits can cause striations on hard rocks leading to horizontal lamination in basalt intervals. However during logging of the Rosebank field these parameters were well controlled.

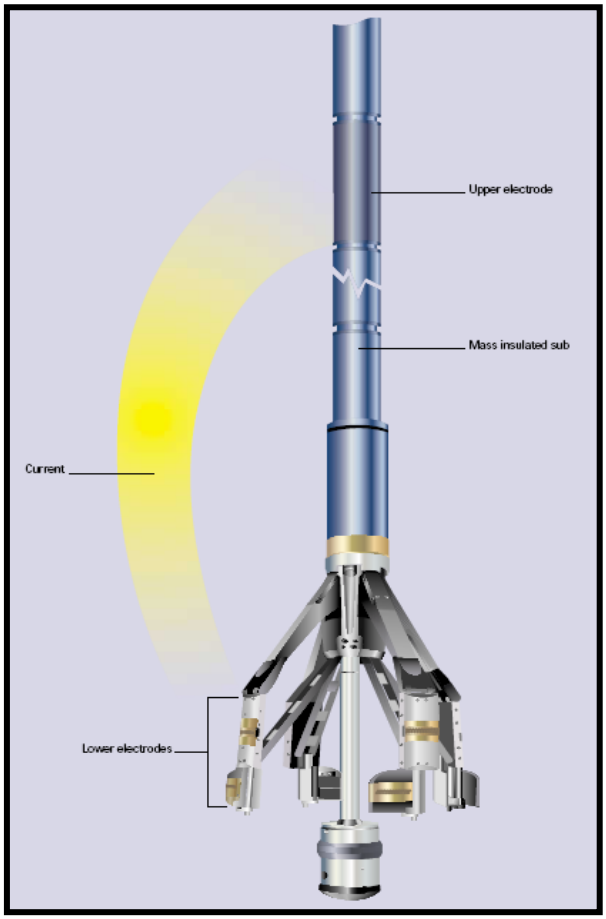

Figure 2.2 A 3D model of a FMI tool. Note the sensor pads on each arm (lower electrodes) and the following tool sonde (Mass insulated sub) for data recording (From Siddiqui et al., 2004).

2.2.7 Handheld Gamma-Ray Device

Spectral gamma ray data for outcrops in Namibia were acquired using a Radiation Inc. RS-230 BGO Super-Spec handheld device. The device uses a Bismuth Germanate source to record SGR components (as U ppm, Th ppm, and K %) at high precision much like a sonde on a conventional gamma ray well log tool. Handheld gamma ray tools are useful for characterizing formations quickly at outcrops and for comparison with sub surface examples characterized by well log tools (Fig. 2.3).

Figure 2.3. The author using a handheld gamma ray tool in Namibia. Acquisition usually takes 60 seconds and SGR data is displaced on a digital readout. Use of the tool was granted by Dr. Breno Waichel (UCSF, Brazil).

2.3 Core and Sidewall Core

Cored material obtained by using a special coring bit and a two sleeve barrel (Blackbourn, 1990). The bit, an annular cutting ring, is attached to the outer barrel that bears the load of the casing and drill string. The inner sleeve houses the cut core and is separated from the outer sleeve by drilling fluids. As the inner barrel remains stationary the core is undisturbed. The bit is fragile and the process is lengthy and typically only limited core is recovered during commercial well operations (Blackbourn, 1990).

Sidewall cores are a more cost-effective way of providing core data points over large intervals. Sidewall cores in the Rosebank field were recovered using a

percussion sidewall gun. Essentially a heavy steel bar is run down the hole on a cable that contains small explosives. A small core barrel is forced into the borehole wall from the explosion. The core barrel penetrates up to 4 cm into the wall and is held on two or more steel wires (Blackbourn, 1990). When the string is pulled up a sample is torn out of the borehole wall and brought to the surface. All core and sidewall core data used in the thesis is discussed in chapter 7.

2.4 Thin Section Preparation

All thin sections used in this thesis are polished thin sections. Thin section preparation was carried out in both the Durham University and University of Birmingham thin section laboratories. Polished thin sections were created for all thin sections in order for EDX analysis (see section 2.6.2). Polished thin sections were created from billets cut from rock samples in the saw facility. The sample was then trimmed to the standard thin section size (normal = 27 x 46 mm, large 51 x 71 mm) and then adhered to a glass slide. Usually excess material (contributing to the thickness of the sample) is trimmed using a fine diamond saw. The specimen was then ground to 20 μm thickness. All thin sections used in the SEM have also been carbon coated in the Physics Department in Durham University. Carbon coating is required to negate charging of the sample surface under electron bombardment from the SEM and has limited effect on the accuracy of element X-ray analysis. The coating of 20 nm thickness is formed when the samples are placed under vacuum and an electric current (~ 100 A) is passed through two small carbon rods with sharpened tips. Carbon evaporates at the tips and precipitates through out the chamber. A sensitive quartz oscillator device exposed to the coating is linked to a digital thickness read out. The process can be repeated until a desired thickness is reached without harming the sample.

2.5 Optical Microscopy

2.5.1 Imaging

Thin section images were acquired at the University of Birmingham, Earth Imaging Laboratory in the Earth Science Department. Images were acquired on a

standard petrological microscope (Ziess Axioscope) fitted with 2.5×, 5×, 10×, 20× objective lenses. Photomicrographs (at least 300 dpi) were taken using a Ziess Axiocam CCD sensor fitted to the camera mount controlled by software provided with the camera.

Large scans of standard sized thin sections were acquired on a conventional transparency slide scanner (Minolta Dimage). Standard thin section slides (27 × 46 mm) fit in the transparency holder for the image scanner. Computer software in the transparency setting controls the acquisition. Images were recorded at 300 dpi for image analysis. Large thin sections (51 × 75 mm) were acquired on a conventional flat bed scanner (Epson Perfection 4900 Photo), as they are larger than 35mm transparencies. Slide scanners were used as they provided additional control over the focal distance when acquiring an image from the sample (A detailed step-by-step methodology of this technique is outlined in Grove and Jerram, 2011).

2.5.2 Computer-Based Image Analysis

Detailed image analysis was carried out on the HSDP polished thin sections to characterize olivine content of the samples. The 300 dpi scans were first processes according to the workflow in figure 2.4a. Analysis was performed using the JPor program that measures the number of thresholded pixels and compares it to the total pixel count of the image—the outputted percentage is the total number of thresholded pixels as a proportion of the original image. The accuracy of this technique is comparable to point counting (Grove and Jerram, 2011). Additionally this allowed the percentage of olivine, zeolite, palagonite, porosity and glass to be recorded for each image (Fig. 2.4b). Percentages were calculated after the image was converted to an 8 bit paletted file (Pallets used for image analysis are provided in the appendix for chapter 6). The same pallet is used for the same process of each section. The pallet controls the threshold accuracy in the ImageJ program, which is used to calculate the overall percentage (following the method of Grove and Jerram, 2011). Once the initial processing was complete the methodology and macro plugin of Grove and Jerram (2011) was used to calculate the percentage of each element. This data was exported to Excel spread sheets (see appendix for chapter 6).

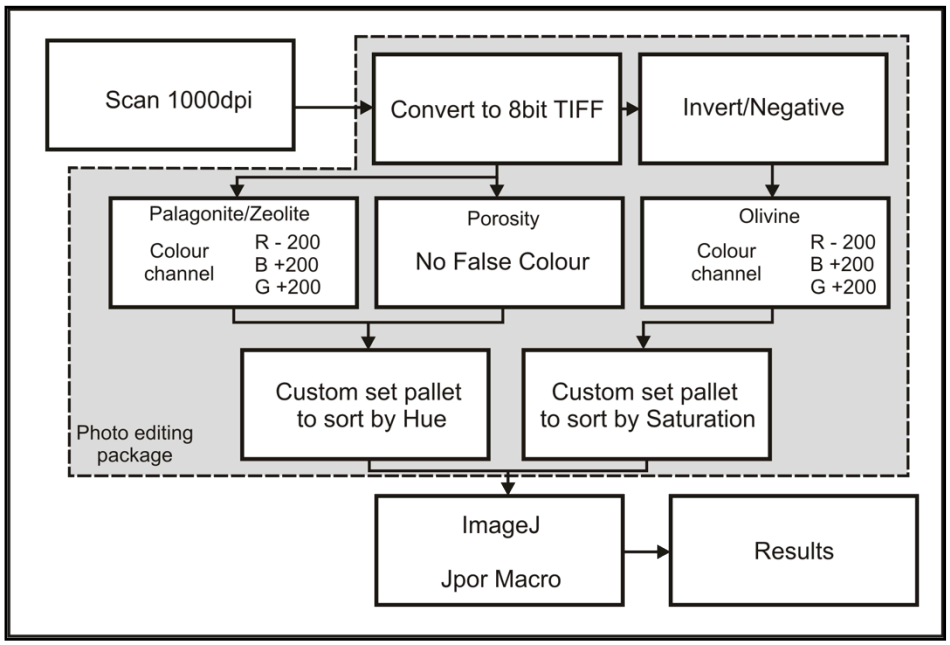

Figure 2.4a. Image processing approach using photo-editing software to convert scanned tiff images and determine mineralogy. Photo editing package in this case was Corel Photo Paint™ however freeware is available such as GIMP II [http://www.gimp.org/].

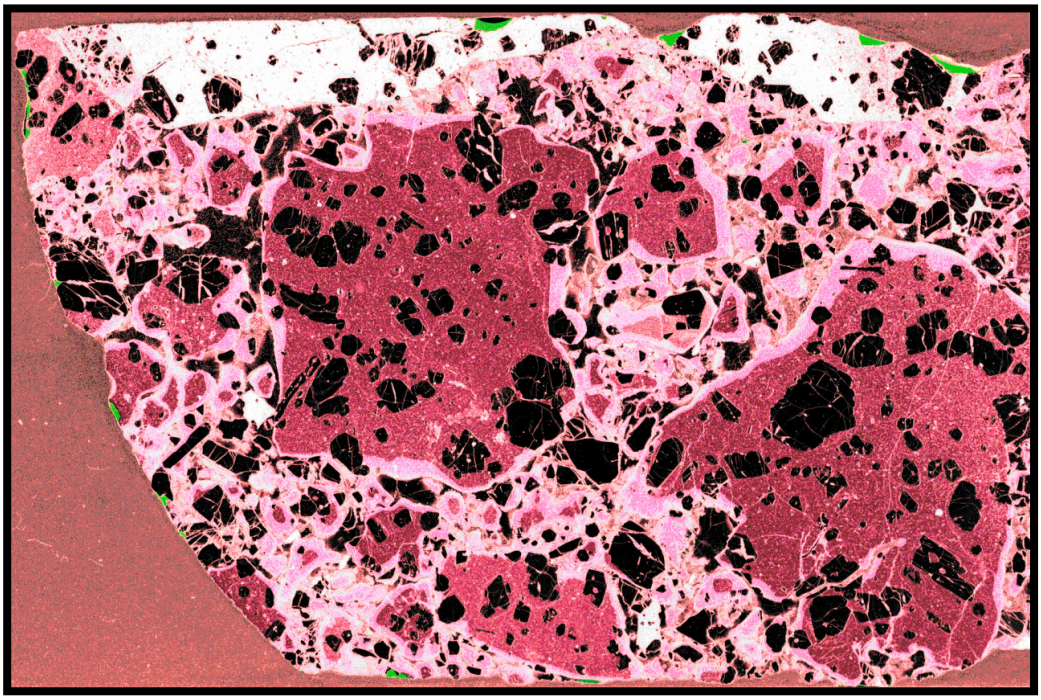

Figure 2.4b. A processed tiff false-coloured and paletted for olivine phenocryst abundance determination. All olivine phenocrysts appear black in the image which is easily threshold using the JPor macro of Grove and Jerram, (20011).

2.6 Scanning Electron Microscope (SEM) Acquisition

All samples in this thesis were analysed using a scanning electron microscope at the Durham University Scanning Electron Microscope (SEM) Facility using a Hitachi SU-70 FEG SEM. Calibrated EDX (Oxford Instruments INCA x-act LN_2-free analytical Silicon Drift Detector) major elemental analysis was conducted on 42 sites. In total 400 EDX mineral analyses were collected. This section summarizes the process of SEM image acquisition and EDX analysis.

2.6.1 SEM Imaging

A SEM produces a raster image by scanning an electron beam across a surface line by line. They comprise simply of a source of electrons (termed an electron gun), a means in order to focus them into a fine beam (a lens), a mechanism for sweeping the bean to create a raster, a device for recording electrons emitted by the sample and a image display system (Reed, 1996). The maximum magnification of the recorded image is proportional to the beam size, whereas the minimum magnification depends on the maximum angle at which the beam can be deflected without creating distortion.

Electrons are sourced at the electron gun that essentially heats up a filament to temperatures at which thermionic emission occurs. The filament acts a cathode and anode that has a small aperture to focus the beam. This is assisted with another electrode (the 'wehnelt', Reed, 1996). The filament and sample material dictates the strength of the vacuum needed to stop chemical degradation of apparatus, which can vary between 10^{-4} to 10^{-10} torr (1 torr $\approx$ 1 mbar $\approx 10^2$ pascals).

The electron source is focused using a magnetic field called the lens. The lens focuses the beam onto the sample. The lens strength needed is dependent on the working distance (the distance of the sample from the lens) and the accelerating voltage of the beam. The lens itself consists of several cylindrical pole pieces that focus the electrons passing through their centre like light passing through a optical lens. Magnetic lenses suffer from spherical aberrations that are controlled by the aperture (disk with a hole in), which limits the final beam width. Magnetic lenses also suffer from astigmatism that arises from imperfections in the magnetic field

controlling the electron beam. This leads to a haze or movement in the image (Reed 1996).

Specimens are mounted on a stage that consists of a metal disk, a screw and a mounting shoe. The shoe slots into a feeder arm which travels into the vacuum chamber. The shoe is mounted on an electronically controlled x-y-z stage mechanism.

The basic electron image is created in a similar way to the gamma ray tool as outlined above. Electrons hit the sample and are either backscattered or deflected towards, via a positive potential, a scintillator. The scintillator, when subjected to electrons, converts energy to light detected at the photomultiplier. Backscatter electrons in the case of the Durham SEM facility require a separate detector that is moved into the chamber when required.

There are two types of recorded image according to the type of electron detected:

Secondary electron – Secondary electron (SE) images are emitted from the very near surface of the sample. SE images are much like side-illuminated photographs. As the beam angle is tilted the SE yield increases and if a positive bias is placed upon SE detection to electron the direction-side protruding features become shaded. As the SEM was used only on thin sections in these thesis SE images are of limited use. However, they can help determine mineralogy in a similar way to how crystal relief is used in conventional microscopy (Fig. 2.5).

Backscatter electron – Backscatter electron images (BSE) are typically generated by samples with a smooth, polished surface. This is of particular use with polished thin sections. Backscattered electrons are high-energy electrons that rebound off the sample surface. The number of electrons that return to the detector are proportional to the mean atomic number of the sample material under the electron beam. As such, material with a high mean atomic number will produce more backscattered electrons than material with a low mean atomic number. Backscatter images can therefore be used to identify mineralogy (Fig. 2.5).

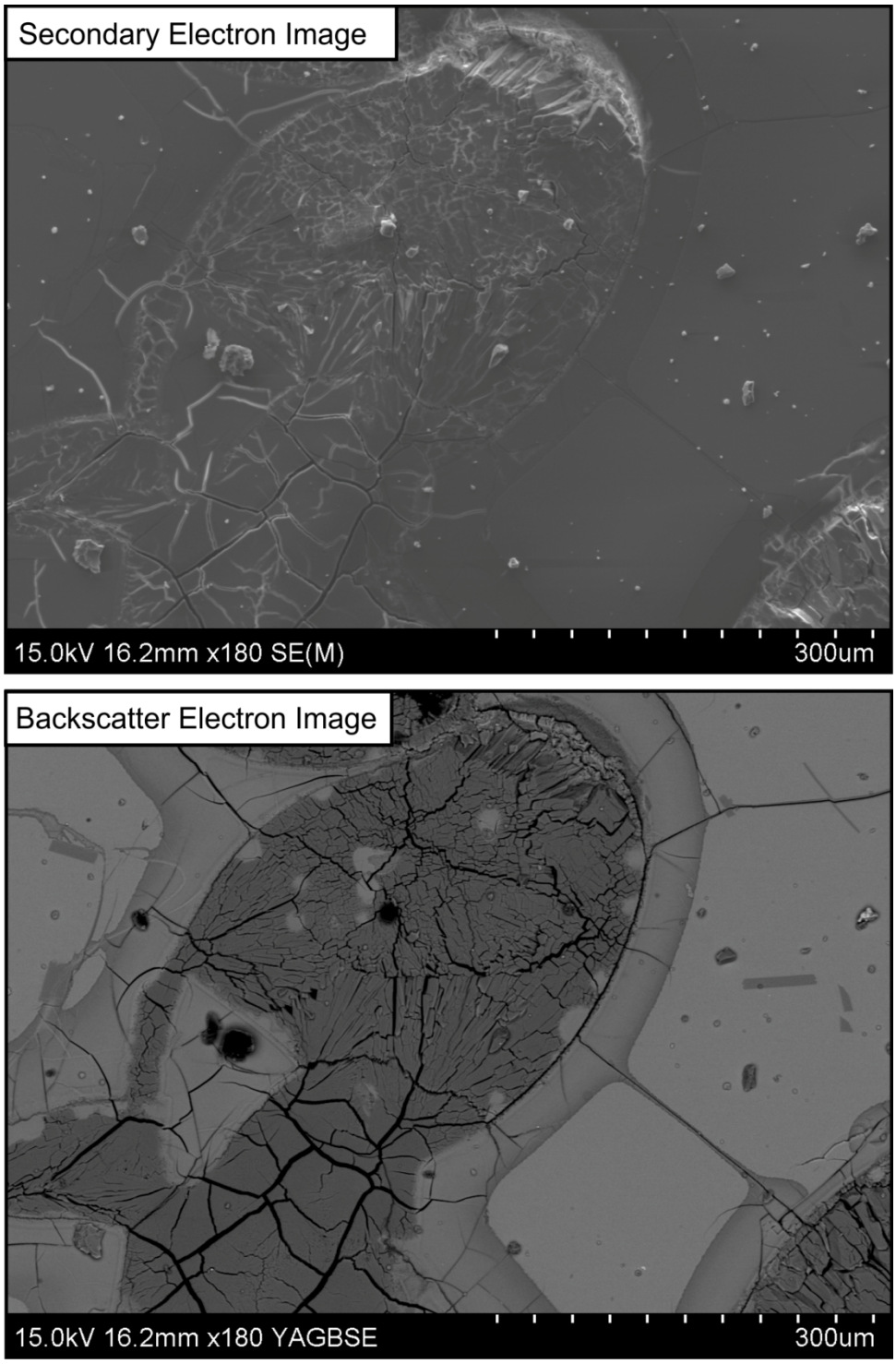

Figure 2.5. An example of a secondary electron (SE) image which is of limited use because the thin section is of uniform thickness. However, relief on minerals can be seen as bright lines. The backscatter image shows the variation in atomic number highlighting the petrology of the section. This section from the HSDP II core shows sieromelane glass, palagonite and interstitial pore-filling zeolite minerals (see chapter 6).

2.6.2 Quantative Geochemical Analysis Using Energy Dispersive X-ray Spectroscopy (EDX)

EDX is an analytical technique used in the chemical characterization of a sample using X-ray excitation. It can be used to identify elements and calculate their proportions. X-rays can be targeted at the entire sample, as a spot point, or a line transect using the Oxford instruments software (EDAX). The equipment consists of an X-ray detector, a pulse processor (which measures the electronic signals to determine energy levels) and a multiple channel analyser that interprets the X-ray data.

As each element has a different atomic number and energy level in its electron shell, X-rays are deflected off and received at the detector in different proportions for each shell of each element. For geological samples, this process records a spectra relating to each element that makes up a given sample (Fig. 2.6). Each spectra has peaks at characteristic energy levels that can be used to identify the element present. The longer the target is bombarded the more counts are recovered and the greater the accuracy of detection for this thesis a detection time of 60 seconds was used. Each time the equipment is used a cobalt sample is placed under the detector to calibrate the system.

To quantify results the Oxford Instruments EDAX software was used for all sites. The software applies corrections based upon several processes such as matrix correction (X-rays will penetrate the sample at different depths dependant on the atomic number) and ZAF corrections (where Z - Atomic Number, Absorption - A and Fluorescence – F are calculated separately using suitable physical models). Principally, when these corrections have been taken into account, the software measures the number of counts recorded in a given time frame. The number of counts is then recorded in a series of discrete measurements to form Gaussian distributions. Castaing, (1951) showed that the relative intensity of an X-ray line is approximately proportional to the mass concentration of the element concerned. Given this approximation, the apparent concentration (C) can be derived by:

$$C = \left[\frac{I_{sp}}{I_{st}}\right] C_{st} \qquad (2.3)$$

where I_{sp} and I_{st} are the intensities measured for the specimen and sample, respectively, and C_{st} is the concentration of the element in the standard. This data is then tabulated in the EDAX software (see appendix for chapter 6 for project datasets).

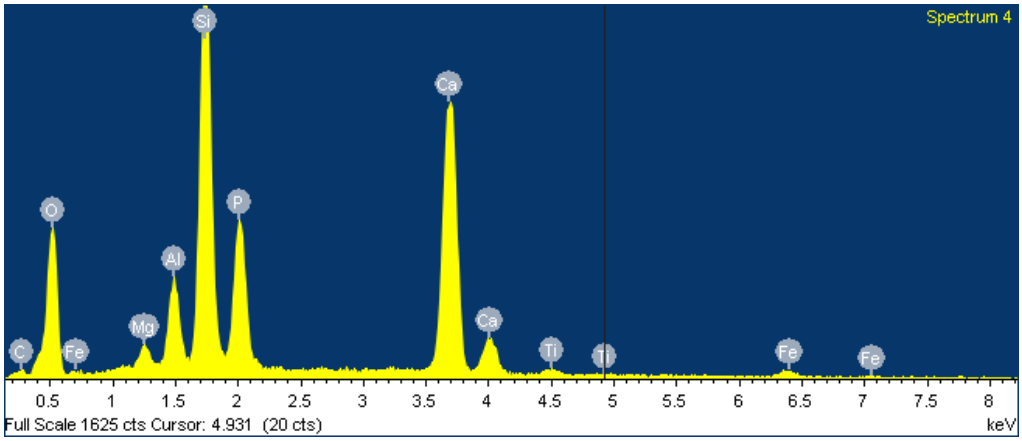

Figure 2.6. An example of a spot X-ray spectra showing energy level peaks for different shell numbers. The EDAX program has attributed these peaks to each element. Elements selected can be overridden if needed.

2.7 XRF Processing and Acquisition

XRF datasets were acquired at the University of Edinburgh. This section summarizes the methodology used to determine the major and trace element concentrations of samples from the Hjörleifshöfði outlier. All results are presented in chapter 5.

XRF measures the emission of characteristic fluorescent X-rays after bombardment with high energy X-rays. XRF works on similar principals to EDX techniques whereby high-energy radiation is sufficient to dislodge an inner electron that is replaced by an electron from its outer shell. Radiation is released because the binding energy of the outer electron is higher than that of the inner electron. The emitted radiation is of a lower energy level than the primary incident X-ray and hence is termed fluorescent radiation. As the energy level of the emitted photon is characteristic for each element then the abundance of the emitted radiation can be used to calculate the element abundance.

Major element concentrations were determined after fusion with a lithium borate flux containing La_2O_3 as a heavy absorber by a method similar to that of Norrish and Hutton, (1969). Rock powder was first dried at 110°C for 2 hours, and a nominal but precisely weighed 1 g aliquot was ignited at 1100°C for 20 minutes to determine loss-on-ignition (LOI). The residue was then mixed with Johnston-Matthey Spectroflux 105 in a sample/flux ratio of 1:5 based on the un-ignited sample mass and fused at 1100°C in Pt 5 % Au crucibles in a muffle furnace. After initial fusion the crucible and contents were re-weighed and any flux weight loss made up with extra flux. After a second fusion over a Meker burner, the mixture was thoroughly mixed by repeated swirling and cast onto a graphite mould and flattened into a thin disc using an aluminium plunger, both kept at 220°C, on a hot plate.

Trace element concentrations were determined on pressed powder pellets. Eight grams of powder were mixed with eight drops of a 2 % solution of poly-vinyl alcohol. The mixture was then backed and surrounded by a 0.5 mm thick aluminium cup and formed into a 40 mm diameter disc by pressing against an 40 mm diameter polished tungsten carbide disc at a load of 0.6 tonnes/cm^2.

The fused and pressed samples were analysed on a Phillips PW2404 automatic X-ray fluorescence spectrometer with an Rh-anode X-ray tube. Corrections for matrix effects on the intensities of major element lines were made using theoretical alpha coefficients calculated on-line using Phillips software. The coefficients were calculated to allow for the amount of extra flux replacing volatile components in the sample so that analytical totals should be 100 % less the measured LOI. The intensities of the longer wavelength lines (La, Ce, Nd, Cu, Ni, Co, Cr, V, Ba and Sc) were corrected for matrix effects by using alpha coefficients based on major element concentrations measured at the same time on the powder samples. Matrix corrections were applied to the intensities of the other trace element lines by using the count rate from the Rh-K alpha Compton scatter line as an internal standard. Line overlap corrections were applied using synthetic standards. The spectrometer was calibrated with a range of USGS and CRPG standards using values given by Govindaraju, (1994)

2.8 3D X-ray CT – Micro-fracture Development

Dr. Kate Dobson carried out 3D X-ray Computer tomography (CT) on one drilled sample at the University of Manchester X-ray imaging Facility. 3D X-ray CT allows the assessment of the validity of cored samples for rock property analysis. As noted above drilling either in the field or on large blocks of hyaloclastite material in the laboratory caused most samples to fracture and break. Other samples produced partial cores or had missing chips along the margins of the core. This make experiments using Hassler sleeves impossible. Only a few cores were successful and these samples were highly indurated with zeolite minerals, which enabled the sample to maintain coherency. However, small fractures were seen on the cores that were not present in the initial sample. Therefore an investigation was needed into how pervasive drilling-induced fractures were.

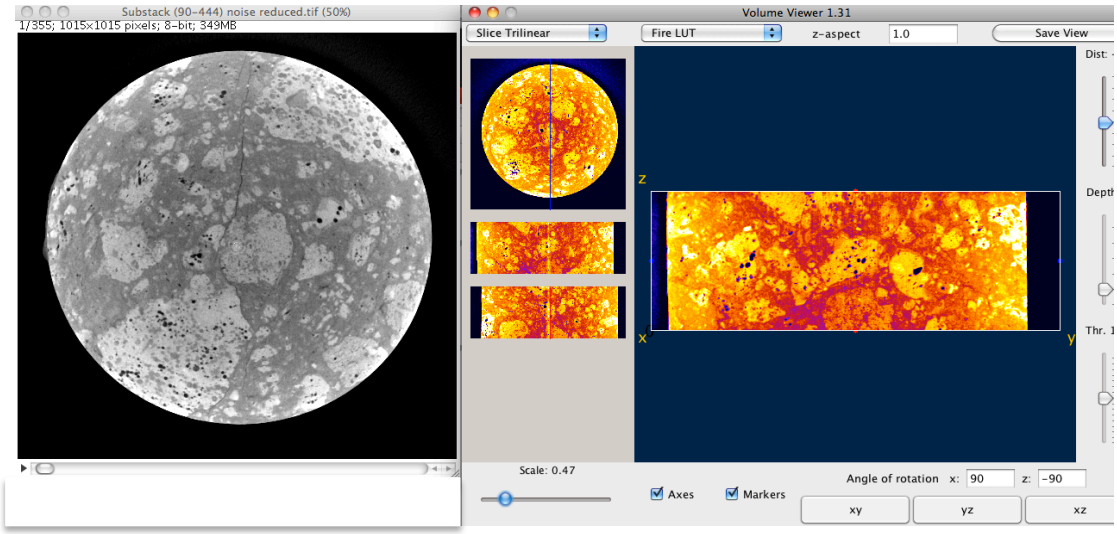

Figure 2.7 a. Left, stacked 2D slices showing X-ray images, grayscale corresponds to density (darkest colour has the lowest density). Right, processed stack (colours altered for viewing ease) within the 3D project tool where by the volume can be sliced in any direction to show fractures.

3D X-ray CT works on a similar principal to a 2D X-ray projection image. When an X-ray passes through material of varying density it is attenuated by different amounts. The remnant X-ray is exposed at an image receptor so the signal received is proportional to the density of the material. In X-ray CT tomography an

image is acquired at a number of angles and distances through 360 degrees. The projection images are then reconstructed using a mathematical algorithm to calculate a spatial map of the linear attenuation coefficient of each 2D axial slice. Each slice is composed of a number of voxels (3D pixels), which vary according to the size of the area of interest.

Post-processing of the 3D volume was conducted at Durham University. Only simple volume rendering was required to show micro-fractures. This was conducted in the ImageJ program. Once collected, the raw data needs to be processed into a number of 2D slices. Image J can then threshold each slide based upon the intensity of the grayscale image to highlight dense areas or voids. The core example contains 355 separate 2D slices, which can be combined into a stack and analysed in a 3D project (Fig. 2.7a and c). The 3D project tool can be used to slide and scroll through any images parallel or orthogonal to the stack. To assess 3D features an Image J plugin (Volume Viewer) can be used once the entire stack has been processed (thresholded) for the grayscale value desired (figure 2.7b).

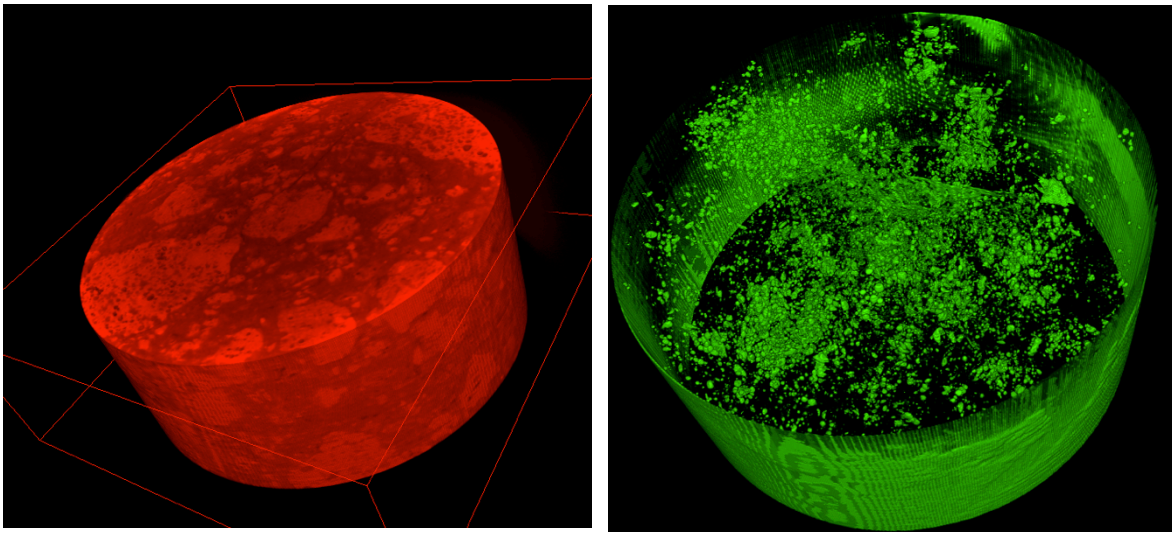

Figure. 2.7 b. Volume rendering of the hyaloclastite core plug. The red image shows a 3D view of the core plug with no thresholding applied. The green image is after thresholding has been applied to show void space e.g. porosity (in this case vesicles in basalt clasts) and fractures that appear as sheets. Generally Pore space is not corrected in this sample. The raw volume and stacked .tif's used to make this image are provided in the appendix for this chapter.

3D micro X-ray CT shows that even in coherent core examples micro fracture and clast torque features are present (Fig. 2.7c). As these features are induced by drilling and create 3D fracture networks they are likely to influence the permeability of the sample making measurements difficult. Therefore only limited rock property measurements could be conducted on hyaloclastite samples in this project.

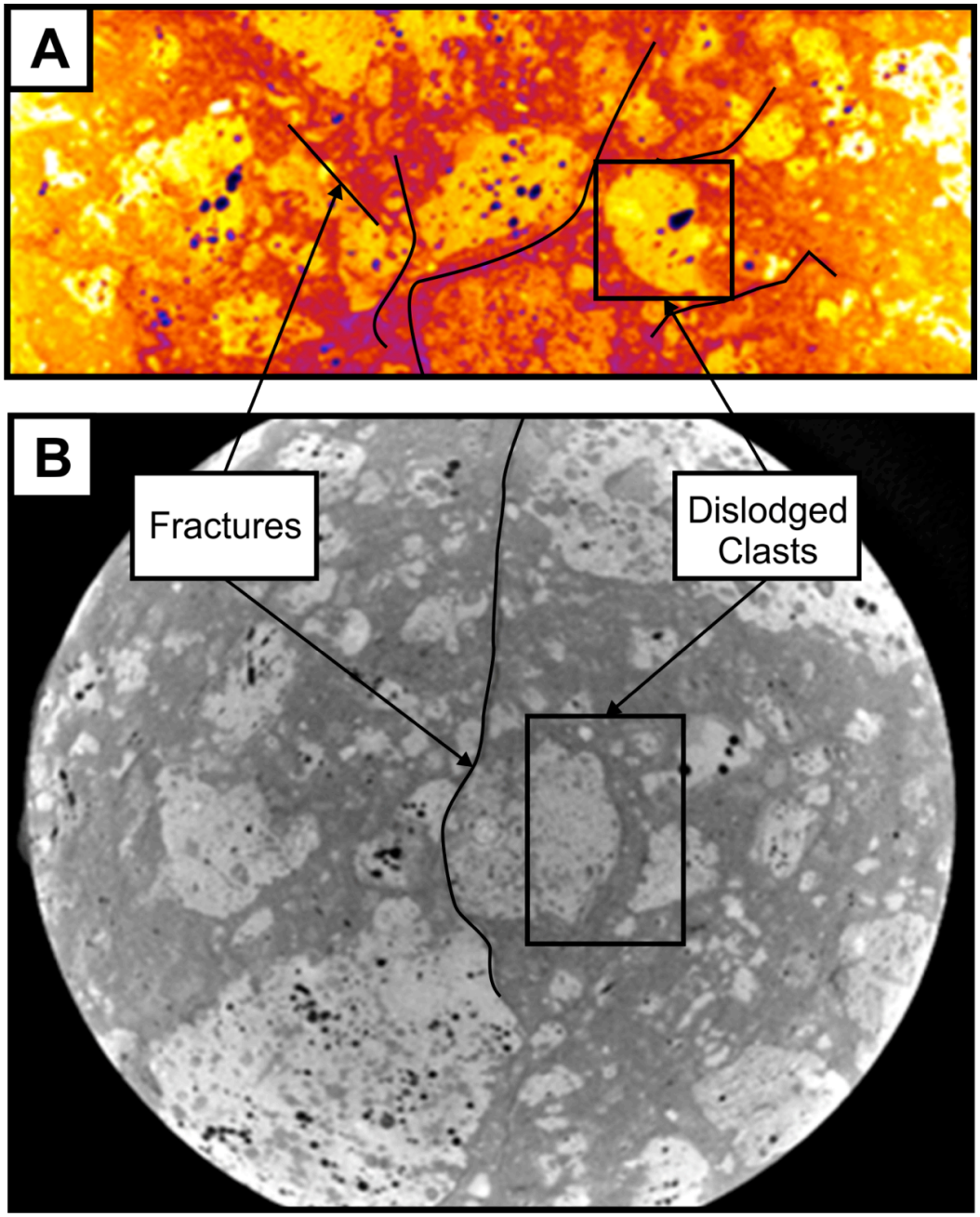

Figure. 2.7 c. Examples of drilling-induced phenomena showing torque clasts and associated voids (A) and pervasive fractures (B) that are present within cores.

3

3. A REVIEW OF HYALOCLASTITE DEPOSITS: FRAGMENTATION, DIAGENESIS AND DEPOSITIONAL MORPHOLOGY 45

CHAPTER FIGURES AND TABLES

3. A Review of Hyaloclastite Deposits: Fragmentation, Diagenesis and Depositional Morphology

Chapter Summary

The range of deposits and processes that form hyaloclastite deposits are very large and difficult to summarize in one place. This thesis focuses on basaltic submarine hyaloclastite deposits in unconfined settings (without the influence of ice). However this review also summarizes some of the principals of subglacial and more silicic hyaloclastite deposits providing references for further reading. Condensed below is a selection of literature that primarily focuses on basalt hyaloclastite deposits and the processes that govern their deposition and diagenesis. This chapter is intrinsically linked to chapter 4 that follows. Much of the discussion of chapter 4 borrows on ideas from this literature review and expands upon them in the context of new fieldwork. It is suggested that these chapters are read together.

3.1 Introduction: Volumetric Importance of Hyaloclastite Deposits

Hyaloclastite deposits form following quenching of lava with ice or water contact. Quenching and associated processes such as steam explosivity leads to the formation of breccias comprised of basaltic lithic clasts and sideromelane glass which rapidly alters to clays (palagonite and smectite) promoting the formation of zeolites (Commonly chabazite and phillipsite). Hyaloclastite deposits form in a wide range of environmental settings and a range of scales that are summarized here. The term hyaloclastite is discussed further in section 3.2.

The abundance and importance, in terms of basin formation of lava deltas and phreatomagmatic products, in predominantly mafic volcanic systems, is becoming increasingly recognised (e.g. Jerram and Widdowson, 2005; Ross et al., 2005; Manville et al., 2009). Volcaniclastic deposits include peperites (Jerram and Stollhofen, 2002; Petry et al., 2007; Waichal et al., 2007), pyroclastic rocks (Peate et

al., 2003; Ross et al., 2005), and suites of hydromagmatic rocks collectively termed hyaloclastite deposits (Ross et al., 2005).

Basalt-dominated volcaniclastic deposits constitute a significant portion (> 40 vol %) of the volcanic successions in Large Igneous Provinces (LIPs), seamounts and ocean island volcanoes (e.g., Hawaiian Islands, Canary Islands, NAIP, Schmincke, 1967; Schmincke et al., 1997; Staugiel and Schmincke, 1984; Seaman et al., 2000; Thordarson, 2004; Boldreel, 2006; Nelson et al., 2009). In many LIPs hyaloclastite deposits are an important early product of volcanism and can reach ≤ 1 km-thick in both oceanic (e.g. Greene et al., 2010) and continental settings (Jerram et al., 2009; Wright et al., 2012). In other LIP's they mark the emergence of oceanic plateaus (e.g. Thordarson, 2004; Manville et al., 2009, Fig. 3.1). Hyaloclastite deposits provide important information on the nature and onset of flood basalt volcanism as well as data on the evolution of basin-wide subsidence. Additionally hyaloclastite deposits generally form the initial basin component fill covering potential sedimentary successions that are targets for hydrocarbon exploration (e.g. White et al., 2003; Jerram et al., 2009; Wright et al., 2012).

The occurrence of hyaloclastite deposits in the North Atlantic Igneous Province (c. 65 Ma) (Jerram et al., 2009) and in borehole data (Schmincke, 1967; Moore, 2001; Walton and Schiffman, 2003; Walton et al., 2005; Boldreel, 2006; Passey and Bell, 2007; Schiffman et al., 2006; Garcia et al., 2007; Nelson et al., 2009) has highlighted a need for an understanding of the key potential down hole lithofacies relationships in hyaloclastite and associated volcanic rocks.

Skilling, (2002) demonstrated that englacial, lacustrine and marine hyaloclastite sequences display different lithofacies architectures. Subsequent work has emphasised that the initial depositional setting strongly controls the lithofacies relations, composition and characteristics of hyaloclastite deposits (Tucker and Scott, 2009). The large-scale processes acting within hyaloclastite deltas and methods of environmental discrimination have been considered by Skilling, (2002). However Skilling, (2002) indicted the breath of research into lava-delta deposits was lacking with small-scale lithofacies variations common and not well constrained (Schmincke et al., 1997). Furthering understanding these small-scale changes is tantamount to understanding the physical characteristics of lava deltas for exploratory purposes and constraining their depositional environment and their expression in the subsurface.

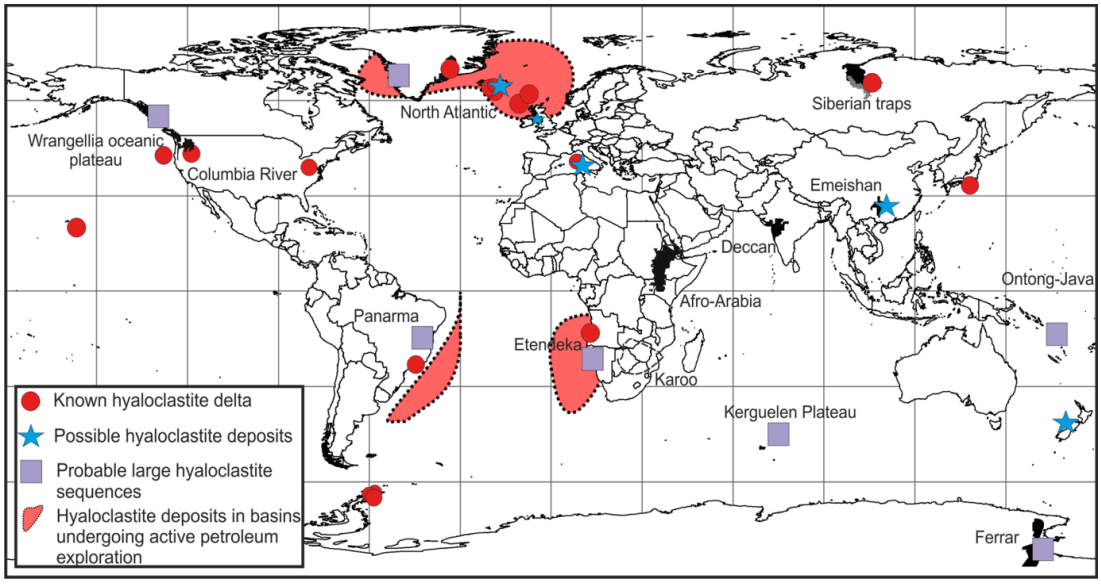

Figure 3.1. The distribution of known prograding hyaloclastite delta deposits, possible hyaloclastite delta deposits, probable large thicknesses of hyaloclastite (>1km) and large igneous provinces as adapted from Ross et al., (2005). (Location of hyaloclastite deposits from Fuller, 1931a/b; Jones and Nelson, 1970; Moore et al., 1973; Furnes and Fridelsson, 1974; Furnes and Sturt, 1976; Schmincke et al.,1978; Schmincke and Von Rad, 1979; Bluck, 1982; Long and Wood, 1986; Yamagishi, 1991; Porębski and Gradziński, 1990; Tribble, 1991; Pedersen et al., 1998; Tanner and Calvari, 1999; Moore, 2001; Skilling, 2003; Thompson, 2005; Smellie et al., 2008; Jerram et al., 2009; Tucker and Scott, 2009.Marked in pink are basins containing large sequences of hyaloclastite deposits undergoing active petroleum exploration.

3.2 Hyaloclastite Terminology and Definition

Hyaloclastite deposits are the products of lava-water or lava-ice interaction where quenching of hot lava or magma causes fragmentation and the production of glass (processes described in section 3.3). Hyaloclastite deposits are essentially breccias composed of sideromelane glass, lava fragments, which lithifies due to clay formation (palagonite and smectite), zeolites and calcite (cf. Fisher and Schimncke, 1984; Moore, 2001; Stroncik and Schmincke, 2002; Walton and Schiffman, 2003; Johnson and Smellie, 2007). The interaction of passive fragmentation and the active, explosive contribution of glass through phreatomagmatic processes are difficult to quantify in hyaloclastite deposits and therefore the term hyaloclastite has been used for a variety of fragmental rock types associated with the interaction of magma or

lava with water, including; the brecciated margins of intrusive rhyolite bodies (Hanson and Schweickert, 1982), quenched brecciated igneous rocks intruded into wet sediment (sensu. intrusive hyaloclastite, McPhie et al., 1993), inter-pillow matrix material (Silvestri, 1963; Moore et al.,1973; Furnes and Fridleifsson, 1974), talus slope breccia (Jones and Nelson, 1970; Moore et al.,1973; Tribble, 1991; Skilling, 2002), ice confined fragmented basalt ridges (cf. Gudmundsson et al., 1995; Schopka et al., 2006), water-quenched marginal breccias to rhyolitic edifices (Schutter et al.,1998) or subglacial flows (cf. Tuffen et al., 2002; Tuffen, 2007; McGarvie et al., 2007), associated with littoral cone formation (Clague and Moore, 1991; Jurado-Chichay and Rowland, 1995), the product of explosive volcanic eruptions (cf. Fisher and Schimcke, 1984; Palagonia and Vizzini, Sicily, Schmincke et al.,1997,) and distally-deposited fragmented volcanic material in deep water setting (Silvestri, 1963; Ollier et al., 1998; Wells et al., 2009) or those transported via fluvial processes (Tolan and Beeson, 1984). Therefore the term hyaloclastite includes deposits and rocks formed by both primary fragmentation processes (explosive and non-explosive), as well as those formed by syn-eruption, pre and post-lithification resedimentation and reworking (Carlise, 1963; Kokelaar, 1984; Tribble, 1991; Mattox and Mangan, 1997; Skilling, 2002; Umino et al., 2006; Stewart and McPhie, 2006).

As a result the term hyaloclastite is ill defined and should be restricted to passive fragmentation processes with a limited active component and does not involve reworking processes. In the case of reworking the term reworked hyaloclastite should be used to note a second phase of deposition. Therefore in this thesis the term hyaloclastite is used to describe rocks that generally form as a result of passive quench fragmentation of coherent lava with water with only mild phreatomagmatic/explosive interactions occurring periodically throughout the construction of the sequences (sensu. White, 2006). However in core where field relationships are unclear and reworking cannot be conclusively attributed a non-genetic use of the term hyaloclastite in this thesis refers to deposits composed of >90% quenched sideromelane glass (with limited vesicularity) as a matrix component to encompass hyaloclastite deposits that have been locally reworked (such as in the HSDP II core, see chapter 6). Chapter 4 summarizes the discrimination factors used to distinguish hyaloclastite deposits in the context of this

thesis. However, none of these parameters can be used individually therefore the identification of hyaloclastite deposits requires analysis from macro- to micro-scale textures.

3.3 Mechanisms of Lava Fragmentation

Hydro-volcanic fragmentation occurs during water-lava or water- ice contact. Field characterisation of hyaloclastite deposits themselves has identified a number of different potential methods of fragmentation (e.g. Lonsdale and Batiza, 1980; Jurado-Chichay and Roland, 1995; White, 1996; Skilling, 2002). Experimental investigations of fragmentation have led to a greater understanding in the mechanisms that govern quenching and the quench rates of volcanic glasses in submarine systems (Sheridan and Wolhetz, 1983; Wohletz, 1983; Wilding et al., 2000; Wilding et al., 1995; Wolhletz, 2002; Mastin et al., 2009). Laboratory-based observations have been linked to field and remote studies of hyaloclastite deposits in order to explain morphological variability and define the generation of brecciated material (Lonsdale and Batiza, 1980; Skilling, 2002). Non-explosive (passive) fragmentation is usually localized and generally occurs via rapid quenching with only limited vigorous hot lava/magma-water interaction. Explosive (active) fragmentation involves Molten Fuel Coolant Interaction (MCFI) occurs when hot magma (fuel) vigorously and often explosively interacts with water (coolant). The MFCI process drives hydro-magmatic fragmentation and is dependent on (1) the magma to water mass ratio, (2) the nature of the mixing between magma and water and (3) the volumetric expansion of the water (steam) (cf. Wohletz, 1986; White, 1996; Hooten and Ort, 2002; Wohletz, 2002). Specific types of MCFI processes can occur such as bulk interaction where mingling does not strictly occur leading to explosive activity (Kokelaar, 1983). Outlined below are examples of how fragmentation processes act to contribute material in a lava-fed hyaloclastite deposits by defining both processes and field expressions (Fig. 3.2 and summarized in Table 3.1).

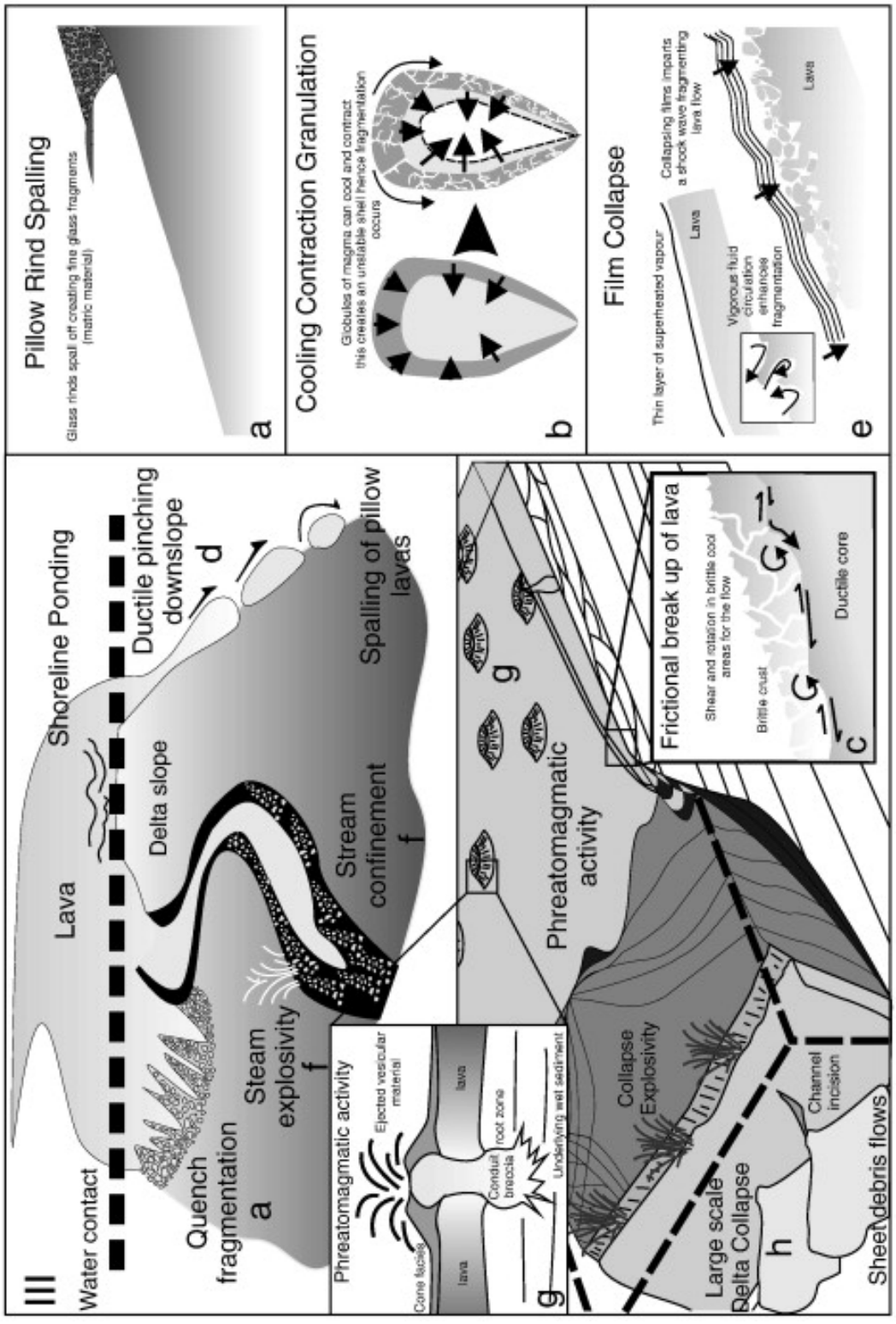

Figure 3.2. Methods of fragmentation in hyaloclastite deposits with deposition models adapted and summarized from Porębski and Gradziński, 1990 and Schmincke et al., 1997.

Table 3.1

Affinity	Fragmentation Type	Description	Key Locations	Key References
Passive Fragmentation Processes	***Quench Fragmentation and Cooling Contraction Granulation (Fig. 3.2 a+b)***	Occurs upon initial lava water contact lava quenches rapidly to form glass (sideromelane). Process susceptible to changes in lava viscosity, flow rate and distance from the source. Dissagration of pillow rinds or lava entering in discrete channels is the main source of quenched material. Material spalls from pillow rinds usually due to cooling contraction granulation. Cooling contraction occurs where steam explosively is suppressed. Cooling a droplet of magma causes a temperature gradient between its rim and the centre. Deformation in the outer layer initially is viscous but becomes rapidly becomes rigid. The inner layer will contract more hence fragmentation occurs.	Shoreface contact of lava Initial phases of emergent volcanism, Quenching of "Fire fountaining" during delta collapse.	Carlisle, 1963, Moore et al.,1973; Lonsdale and Baptiza, 1980; Fisher and Schminkce, 1984; Aalto, 1986; Kokelaar, 1986; Mattox and Mangan, 1997; Schmincke et al.,1997; Wilding et al.,2000; Head and Wilson, 2003.
	Frictional Break-up (Autobrecciation) (Fig. 3.2 c)	Shearing between the top of the lava and the water and is further exacerbated by internal flow. Viscous pāhoehoe or 'A'ā flows with a solidified crust become further fragmented through inflation. Also can occur between the quenched outer surface of pillow lavas as they prograde out in small lobes Fragmented material can be transferred downslope by gravity.	Common where littoral cone formation occurs, during pillow lava lobe formation.	Yamagishi, 1987; Self et al.,1998; Jurado-Chichay and Rowland, 1995.
	Ductile Pinching and Gravitational collapse (Fig. 3.2 d+h)	Gravity and angle of repose causes pillows to elongate, thin and subsequently detach created "spalled" pillows in a hyaloclastite matrix. Brittle fragmentation leads to mass wasting of clastic material down the delta front analogous to talus slopes.	Delta front at high to critical angles of repose.	Mattox and Mangan, 1997; Skilling, 2002; Sansone and Smith, 2006.
	Film Collapse (Fig. 3.2 e)	Drives initial magma fragmentation at shallow water depths. A fine film of super-heated vapour that surrounds the magma upon water contact (Leidenfrost film). Collapse of the vapour film imparts pressure waves on the lava producing blocky and splinter sized fragments. The amount of fragmentation varies in relation to viscosity of the lava and surface tension or the film.	Common when confinement occurs e.g. through narrow lava channels upon water entry. Seen during pillow lava formation as large bangs on video footage.	Mills, 1984; Kokelaar, 1986; Tribble, 1991; Skilling, 2002; Waichel et al., 2007.
Active Phreatomagmatic Processes	***Steam Confinement/ Contact Steam Fragmentation (Fig. 3.2 f)***	Violent explosive activity in a positive feedback mechanism develops where localized phreatomagmatic eruptions cause a chain reaction exploiting fractures. Progressive granulation can form vast sheets as the fragmentation process moves away from its source. Viscosity is thought to be a dominant control on the fragmentation process.	Shore face cone collapse, Lava ponding along coastline. Exploitation of fractures in pillow lavas.	Jones and Nelson, 1970; Furnes and Sturt, 1976; Moore et al.,1973; Lonsdale and Baptiza, 1980; Skilling, 2002; Head and Wilson, 2003.
	Littoral Cone / Rootless cone formation (Fig. 3.2 g)	Littorial cone formation can add material to the hyaloclastite delta actively (through lithic blasts and explosions) or passively through subsequent collapse. Erosion in the surf zone can cause the cone to collapse down the delta front. Post collapse, lava tubes exploit the now relic conduit to change the locus of lava entry.	Lava ponding along coastline	Jurado-Chichay and Rowland, 1995; Mattox and Mangan, 1997; Umino et al., 2006; Dickinson et al., 2009.

Table 3.1. A Summary of processes leading to clastic imput as hyaloclastite delta. See text for details.

3.3.1 Passive Fragmentation Processes

Quench Fragmentation

Quench fragmentation occurs when lava does not initially fragment upon contact with water and instead forms pillow lavas etc.. The "skin" of the pillow lava lobe quickly solidifies acting to insulate the flow. However the pillow rind quenches rapidly to form a glass. The quench process is sensitive to both the lava viscosity and the flow rate (Moore et al., 1973; Mattox and Mangan, 1997; Wilding et al., 2000). Similar fragmentation processes operate where lava enters water in discrete channels, forming lava tubes forming lava tubes (Moore et al., 1973; Lonsdale and Baptiza, 1980; Tribble, 1991; Mattox and Mangan, 1997). Disaggregation of pillow lava rinds either through cooling contraction granulation, frictional break up or suppressed steam confinement (Lonsdale and Batiza, 1980; Kokelaar, 1986) leads to abundant pillow rind fragments which can be a major constituent of hyaloclastite deposits (Carlisle, 1963; Moore et al., 1973; Lonsdale and Baptiza, 1980; Aalto, 1986). Additionally when lava is rapidly quenched (e.g., lava flowing off a small wave-cut platform) large amounts of brecciated material can be produced as droplets of lava are rapidly cooled (Moore et al., 1973). These processes operate in both subaerial to subaqueous and emergent settings.

Cooling contraction granulation

Cooling contraction granulation (CCG) occurs due to volume reduction during cooling. CCG can occur where steam explosively is suppressed and is characteristic of deeper marine settings where water pressure impacts on the efficiency of fragmentation (Kokelaar, 1986). Cooling of a droplet of magma in water causes a temperature gradient between its rim and its centre. Deformation in the outer layer of the magma droplet is initially viscous but rapidly becomes rigid (Head and Wilson, 2003). The inner layer will then contract as cooling progresses to the centre of the droplet leading to cracking on the now rigid surface of the droplet (Kokelaar, 1986; Head and Wilson, 2003).

Frictional break-up (Autobrecciation)

Frictional break-up occurs when lava flows within a body of water creating a well-defined lobe of material with a clearly defined crust. Internal flow through the still molten core creates shearing between the lava crust and surrounding water (Jurado-Chichay and Rowland, 1995). Dependent on the morphology of the flow either, pāhoehoe or ‘a‘ā the solidified crust can become more fragmented through inflation (Self et al., 1998). Fragmented material can then is transferred downslope by gravity or progressively disaggregated from the flow crust contributed to the pile of material forming a hyaloclastite deposit (Yamagishi, 1991). Within suberial to subaqueous systems this process may be common where littoral cone formation occurs (Jurado-Chichay and Rowland, 1995).

Ductile Pinching of the lava flow

Pinching of flows occurs on the surface of the talus slope created by hydrovolcanic processes. Gravity causes pillows to elongate, thin and detach developing “spalled” pillow lavas on foreset bedded units that are close to the critical angle of repose (Skilling, 2002). Spalled pillow lavas often roll down the talus slope and break up adding quenched material passively to the hyaloclastite pile. At near critical angles of repose fragmented material is deposited downslope by gravity and gravitation collapse processes. These processes can lead to the formation of small sediment plumes or mas wasting at the lava-fed delta front (Sansone et al., 1991; Sansone and Smith, 2006).

3.3.2 Explosive fragmentation

The processes of explosive interaction are intimately interlinked with each other but also passive fragmentation processes.

Film collapse

Film Collapse is thought to drive initial phreatomagmatic fragmentation at shallow water depths (Kokelaar, 1983). Upon contact with the water a fine film of super-heated vapour can develop on the magma surface (Mills, 1984; Kokelaar, 1986; Waichel et al., 2007). The degree of fragmentation depends on viscosity of the lava/ magma and surface tension of the vapour film and the sustained propagation on film collapse through magma-water mixing domains. Kokelaar (1983) termed this

contact-surface steam explosivity (cf. Wohletz, 1986). Collapse of the vapour film imparts pressure waves on the lava crust that results in fragmentation producing blocky and splinter shaped fragments (Kokelaar, 1986). Within the surf zone film collapse can be vigorous due to rapid invasion and expulsion of seawater (Moore et al., 1973; Mattox and Mangan, 1997) both creating and collapsing vapour films.

Stream confinement or contact steam fragmentation

Occurs at high rates of lava extrusion and where confinement occurs e.g., through narrow channels or lava tubes (Moore et al., 1973; Lonsdale and Baptiza 1980; Tribble, 1991; Kauahikaua et al., 1998; Head and Wilson, 2003). Lonsdale and Baptiza (1980) envisaged a positive feedback mechanism whereby a localised water infiltration caused a chain reaction as steam expanded which exploited any pre-existing fractures progressively granulating the lava to produce vast sheets of hyaloclastite deposits. Kokelaar (1986) termed this process bulk interaction. The viscosity of the lava is thought to be a dominant control on the fragmentation process (Jones and Nelson, 1970; Furnes and Sturt 1976).

Explosive lava-water interaction and littoral cone formation

In the submarine environments fragmented material from pseudocraters developed as a result of phreatomagmatic activity can contribute to the fragmented material (Head and Wilson, 2003) occurring due to enhanced steam confinement (Fröhlich et al., 1993; Jurado-Chichay et al., 1995; Umino et al., 2006). Littoral cones can form at the margins of a lava flow as they enter water. Littoral cones comprise of dense spatter and scoria derived from underlying lava flow produced by rapid degassing. Collapse of active lava tube acting as a supply conduit on wet hyaloclastite deposits or in a confined, wave undercut, water filed void caused by erosion can create strong explosions (Jurado-Chichay et al., 1995). Littorial cone formation can add material to the hyaloclastite delta actively (through lithic blasts and explosions) or passively through subsequent collapse (Jurado-Chichay et al., 1995). This has the potential to contribute highly vesicular material to the hyaloclastite deposit.

3.4 Hyaloclastite Depositional Settings

Most basaltic hyaloclastite deposits form in five general settings:

1) Where subaerial lavas flow subaerially and enter into the sea e.g., Iceland (e.g. Jones 1969; Watton et al., 2013), Antarctica (e.g. Jones and Nelson, 1970; Skilling, 2002) and Hawaii (e.g. Moore et al., 1973; Tribble, 1991; Mattox and Mangan, 1997).
2) During non explosive emergent volcanism (Schmincke and Von Rad, 1979; Yamagishi 1987, 1991; Schmincke et al., 1997; Tanner and Calvari, 1999; Watton et al., 2013) and where secondary sedimentation processes move this material downslope in deeper marine settings (Schmincke et al., 1967; Ollier et al., 1998).
3) Where lava flows into lakes (e.g. Fuller, 1931 a, b; Bishop, 1985; Emeleus and Gyopari, 1993; Pedersen et al., 1998; Godchaux and Bonnichsen, 2002; Tucker and Scott, 2009).
4) Where lava flows into rivers (e.g. Hamblin, 1994; Fenton et al., 2006)
5) In subglacial settings (e.g. Gudmundsson et al., 1997; Werner and Schmincke, 1999; Loughlin, 2002; Skilling, 2009; Smellie et al., 2011).

These five end-members have the ability to produce a variety of clastic products. Each type of environment results in hyaloclastite deposits with different morphologies and lithofacies relationships

3.4.1 Basaltic Hyaloclastite, Lava-Delta Formation

Most documented hyaloclastite deposits form lava deltas that resulted from the progradation of breccia sheets following lava ingress into the sea or lakes (Fuller 1931a; Jones and Nelson 1970; Moore et al., 1973; Fisher and Schmincke, 1984; Schmincke et al., 1997; Pedersen et al., 1998; Skilling, 2002; Shevais et al., 2005; Wells et al., 2009; Jerram et al., 2009; Wright et al., 2012; Stevenson et al., 2012). Good examples of hyaloclastite deltas include those in Antarctica, Japan and Sicily (Porębski and Gradzinski, 1990; Yamagashi, 1991; Schmincke et al., 1997) and offshore within the Møre, Vøring and Faroe-Shetland Basins (UK and Faroe Islands) (e.g. Planke et al., 2000; Thomson, 2005; Jerram et al., 2009; Wright et al., 2012).

Additionally palaeotopography can control the development of hyaloclastite foresets and significantly contribute to their lateral thickness variation. Lateral facies changes have been used to obtain information about regional changes in physical conditions during emplacement of hyaloclastite flows. Field relations suggest that the change from units dominated by lava to those dominated by hyaloclastite reflects a downslope, down current, proximal to distal lithofacies relationships and are summarized below.

3.4.2 Field Characterisation of Lava Deltas

The first field characterization of lava-delta morphology was made by Fuller, (1931a) following the initial discovery of pillow lava sequences by Russel, (1902) in the Columbia River Flood Basalt Group. Fuller, (1931a) recognised three distinct lithofacies, a foreset bedded hyaloclastite, a massive breccia and ellipsoidal (subsequently termed pillow lava) facies, which formed within lacustrine conditions. Fuller (1931a) hypothesised that the foreset bedding was caused by progradation of the fragmentation processes and hence the overlying lavas would be genetically related and that the upper lava sequences would periodically thin indicating a change in relative water levels). Elipsoidal lithofacies consisting of pillow lavas and empty lobes were considered to represent higher viscosity lava and hence did not extensively fragment. Massive breccia facies represented quenched lava tops that became autobrecciated with subsequent interflow of the basalt.

Jones, (1970) outlined the degree of heterogeneity in hyaloclastite deposits and pillow lava breccia for the first time. Jones, (1970) noticed that lava delta formation consists of a number of lithofacies types that may be related to emplacement or post emplacement processes. Several lithofacies types were identified, Tuffs- derived from hydrous fragmentation processes; Pillow and para-pillow lavas; which represent pāhoehoe and ‘a‘ā lavas flows under water; Flow-foot breccias- formed from the disaggradation of pillow lavas and subsequent collapse; Boulder breccias- products of the total fragmentation of ‘a‘ā lava flows. A characteristic pillow lava- tuff- sheet lava/flow-foot breccia sequence was recorded a number of localities and was thought to relate to phases of effusive and explosive volcanism during the emergence of volcanoes from shallow melt water lakes. This

study provides the basis for the study of the variety in hyaloclastite lithofacies within this thesis.

Jones & Nelson, (1970) demonstrated that the hyaloclastite pile produced would vary in relation to relative sea level change and hence record a series of sea level fluctuations in the passage zone—the junction between sheeted lava flows and the prograding hyaloclastite foreset bedded unit below. Jones & Nelson (1970) indicated that the passage zone marked the water level at time of effusion and has since been documented widely within Hawaii (e.g. Moore et al. 1973) and the James Ross Island Volcanic Group, Antarctica (Skilling, 2002, Troedson and Smellie 2002, Smellie et al., 2008). Jones and Nelson (1970) also recognised that hyaloclastite delta foreset deposits had a high average dip (commonly 30°) but the pillow breccia unit at the top of the foresets dipped less. The average angle of repose has also been recorded by a number of authors (Moore et al., 1973; Fornari et al., 1979; Porębski and Gradzinski 1990).

Furnes and Fridleifsson, (1974) demonstrated that in shallow water hyaloclastite lithofacies distribution was controlled by tidal range producing a stepped geometry. Furnes and Fridleifsson, (1974) recognised an asymmetric pattern where the passage zone itself, at low tide, would shallowly dip in the same direction as the foreset beds, but at high tide a much steeper dip would form. In time a zig-zag pattern would be produced charting changing tidal ranges during fragmentation on depositional of hyaloclastite material. Additionally, a long wavelength change in cyclicity was recorded over hundreds of meters in length thought to relate to spring tides. Subsequently Furnes and Sturt, (1976) developed a series of schematic cross-sections to describe the interplay between the sedimentation of hyaloclastite deposits and the prevailing tide. Lavas and hyaloclastite deposits could be interlayered depending on the relative importance of erosional dissection in to the passage zone thus creating complex lithofacies stacking patterns.

Where lava is supplied from a constricted channel, pāhoehoe lava flows can widen where the gradient decreases (Moore et al., 1973; Fornari et al., 1979). Widening acts to produce a large apron of material that aids quench fragmentation processes. However discrete channels can also occur. Furthermore, these processes do not necessarily lead to progradation instead as they lie on a significantly steep slope they will mantle any underlying topography as sheet like deposits. Lava flux

(the supply of material to the delta front) also initially controls the development of sheet lithofacies. At high flux rates sheet hyaloclastite deposits are likely to develop due to an increased rates of fragmentation (Carr and Jones, 2001).

Progradation of a hyaloclastite pile can also be facilitated by extensive lava tube and elongate pillow lava development, where pillows accumulate in the accommodation space to form clinoforms (Bishop, 1985).

Porębski and Gradziński (1990) produced a detailed interpretation on the development of a lava delta based upon field evidence from the Oberek Lava Delta, West Antarctica. Porębski and Gradziński (1990) envisaged that when a lava flow crosses the shoreline it undergoes quench fragmentation processes that range from non-explosive granulation to explosive fragmentation. The hydroclastic components therefore vary greatly and can be mixed with epiclastic detritus and slope flank talus leading to complex lithofacies arrangements. Each lithofacies could then be prescribed into a series of different growth phases/ lithofacies bundles.

Porębski and Gradziński, (1990) indicated that the development of lava deltas can be separated into a number of main growth phases/ lithofacies bundles. Initial debris flows (termed-laharic flows) are triggered by the collapse of the sediment slope forming basal petromict (multi-clast size) breccias. Porębski and Gradziński, (1990) thought that jigsaw-fit breccias lock together to maintain a high angle of slope. Subsequently, slower fed lava flows produces another phase of foreset dipping strata. Production of grain avalanches and flow slumps is common (Porębski and Gradziński, 1990) and form a discontinuous surface between the steeply dipping coarse breccias (Jones, 1970; Jones and Nelson, 1970; Yamagishi, 1991; Skilling, 2002). Finally small low-viscosity lava flows interact with basin sediments to produce thin tangential foresets at the front of the lava delta. The small lava streams are meant to quench more rapidly and hence produce a variety of fragments (Moore et al., 1973) as well as steam explosivity (Kokelaar, 1986). The changing sediment lithology over short distances could also enhance slope failure via creating planes of weakness (Porębski and Gradziński 1990, Skilling, 2002; Thompson et al., 2008). Porębski and Gradzinski, (1990) also recorded a prodelta sediment phase which forms toe sets (Fig. 3.2). Prodelta sedimentation is likely to be minimal due to small amounts of fine-grained sediment (Skilling, 2002) however fine sediment plumes can occur upon lava water contact (Sansone et al., 1991). Foresets with tangential bases

must have experienced some fluid turbulence and hence finer grained sedimentation (Porębski and Gradziński, 1990). The lack of finer grained material implies that most lava fed deltas prograde faster than there alluvial cousins (Schmincke et al., 1997; Skilling, 2002). Marine lava-delta sequences are likely to have rounded to sub rounded clasts and be laterally discontinuous due to coarse grain size and steep offshore bathymetry (Skilling, 2002)

The progradation of foreset bedded hyaloclastite units is facilitated by debris flows (Yamagishi, 1991). The top of hyaloclastite delta successions is dominated by hyaloclastite sheet flows and intercalated with sediments (termed the topset units). These structures are interpreted as a series of debris flows that prograde out into the basin. When the lava supply decreased significantly the process of cooling-contraction granulation becomes established and is enhanced by spalling of material due to mechanical movements after congealing (Yamagishi, 1987). The foreset bedded and topset hyaloclastites consist of stratified breccia beds and pseudo-pillows (elongate tube like structures displaying pillow like multiple rinds) dipping 20-30° displaying reverse grading consistent with a debris flow hypothesis (Yamagishi, 1991).

Relationships between the slope angle and the type of hyaoclastite deposit were noted by Schmidt and Schmincke, (2002). Studies of two lava delta systems in an uplifted and eroded volcanic pile in Porto Santo, Atlantic Ocean, revealed that on steep offshore slopes foreset breccias developed, whereas on gentle dipping platforms pillow lava and tube networks dominate. The angle of slope therefore promotes brecciation and subsequent progradation of a hyaloclastite pile (Jones and Nelson, 1970; Moore et al., 1973; Schmidt and Schmincke, 2002).

Skilling, (2002) provided the seminal study on the development of lava deltas. Skilling, (2002) noted that lava delta deposits were composed from a number of different processes relating to fragmentation and the remobilisation of material at or down the delta front. Most lava deltas had a relatively flat lying transition from lava into water with asymptotic foresets that prograded out into accommodation space. However, immediately apparent was the sometimes-complex association between supplying lava flows, clastic facies and hyaloclastite which were though to arise from lavas ploughing and pounding against other units and post emplacement slump collapse scarps displacing or reworking hyaloclastite material. Characteristic

depositional morphologies were formed dependant on environmental setting, in this case, submarine or subglacial examples. Marine examples are generally dominated by a planar passage zone with littoral sedimentation possible; tidal effects determining fluctuation in the passage zone (c.f. Furnes and Fridleifsson, 1974); and laterally extensive contemporaneous lobes of hyaloclastite breccia. Conversely subglacial deposits were controlled by water level changes controlled by changes in the glacial or melt water regime to produce collapse structure; drainage events removing fine material; steep margins where material could abut against ice at the margin to a melt water pool. Skilling, (2002) finally highlighted that more work was needed to link physical processes as recorded at active deltas to ancient examples in the rock record.

3.4.3 ‘A‘ā Lava Delta Formation

The recognition of processes acting in ‘a‘ā lava deltas has only just been realised. ‘A‘ā lava deltas unlike documented pāhoehoe equivalents have an ill-defined passage zone, a chaotic association between hyaloclastite (non water depth dependant) and coherent lava lobes and a lower foreset dip direction (c. 10-20°) (Smellie et al., 2013). ‘A‘ā lava flows also behave differently at the lava water interface, probably due to rheological properties or the rate of supply to the delta front, and flow into lakes sometimes with limited fragmentation (Stevenson et al., 2012; Watton et al., 2013). However as flow continues clinker breccias in the flow base and crust lead to small breakouts allowing water ingression leading to complete brecciation of the flow (Smellie et al., 2013). Therefore, ‘a‘ā lava deltas are generally more chaotic in terms of there lithofacies stacking patterns and further study is needed to constrain active depositional processes in there systems.

3.4.4 Controls on Lava Delta Formation

Hyaloclastite deposits form instantaneously in geological time with large deltas growing within a few weeks or months (Moore et al., 1973; Schmincke et al., 1997). Rapid lithofacies changes over few tens of meters are characteristic of shallow-water volcanic assemblages (Schmincke et al., 1997; Tucker and Scott, 2009). During the formation of hyaloclastite deposits constructional and mass-

wasting processes can occur simultaneously and work to control the growth and subsidence of the lava delta (Schmincke et al., 1997). Therefore in subaqueous settings the infilling therefore the first order controls on lava-delta deposition are, a shallowing of the basin from infilling, eustatic sea-level fluctuations, isostatic subsidence and uplift.

Subsequent second order processes such as the parameters of the lava (viscosity, volume, gas content and effusion rate), location, spacing and number of lava feeder streams, coastal topography and sinuosity, immediate off shore bathymetry, tidal range, coastal orientation with respect to orientation of primary wave/stream direction then create the discordance in lithofacies deposits (Furnes and Sturt, 1976; Porębski and Gradzinski, 1990; Tribble, 1991; Carr and Jones, 2001; Schmidt and Schmincke, 2002; Skilling, 2002)

Therefore the development of hyaloclastite deltas is dependent not only on basin conditions but also on the architecture and geometry of the flow and physical characteristics of the lava flow supplying the material. These processes control clinoform angle and are thought to be imaged in the subsurface.

3.4.5 Lava Deltas in the Subsurface

Lava –fed delta systems in the subsurface have been recognised in seismic surveys in the North Atlantic Igneous Province (~65 Ma) and off shore Australia (age unknown) (Symonds et al., 1998; Kiørboe, 1999; Planke, 2000; Berndt et al., 2001; Thompson, 2005; Calves et al., 2011; Spitzer et al., 2011; Wright et al., 2012; Holford et al., 2012). Lava fed deltas consist of high amplitude reflectors (topset units), prograding low-amplitude foreset-bedded units that dip towards the basin centre, and coherent high-amplitude reflectors interpreted as lava flows (see Wright et al., 2012)(Fig. 3.3). Foreset-bedded packages are interpreted as hyaloclastite deposits (lava deltas) and can reach up to 1 km thickness (Jerram et al., 2009). The only current 3D interpretations of lava deltas indicate they resemble large fans prograding out into the basin from multiple sources (Thompson, 2005) with the delta front is dominated by large curved fault scarps which may represent large scale collapse structures (e.g. Wright et al., 2012).

Lava delta morphology in the subsurface is thought to be controlled by relative sea level changes at the time of eruption effectively plotting sea level rise

and fall similar to sequence stratigraphic packages (Wright et al., 2012). This can aid palaeogeograpahic reconstruction and plot the evolution of large igneous province development in marine dominated successions.

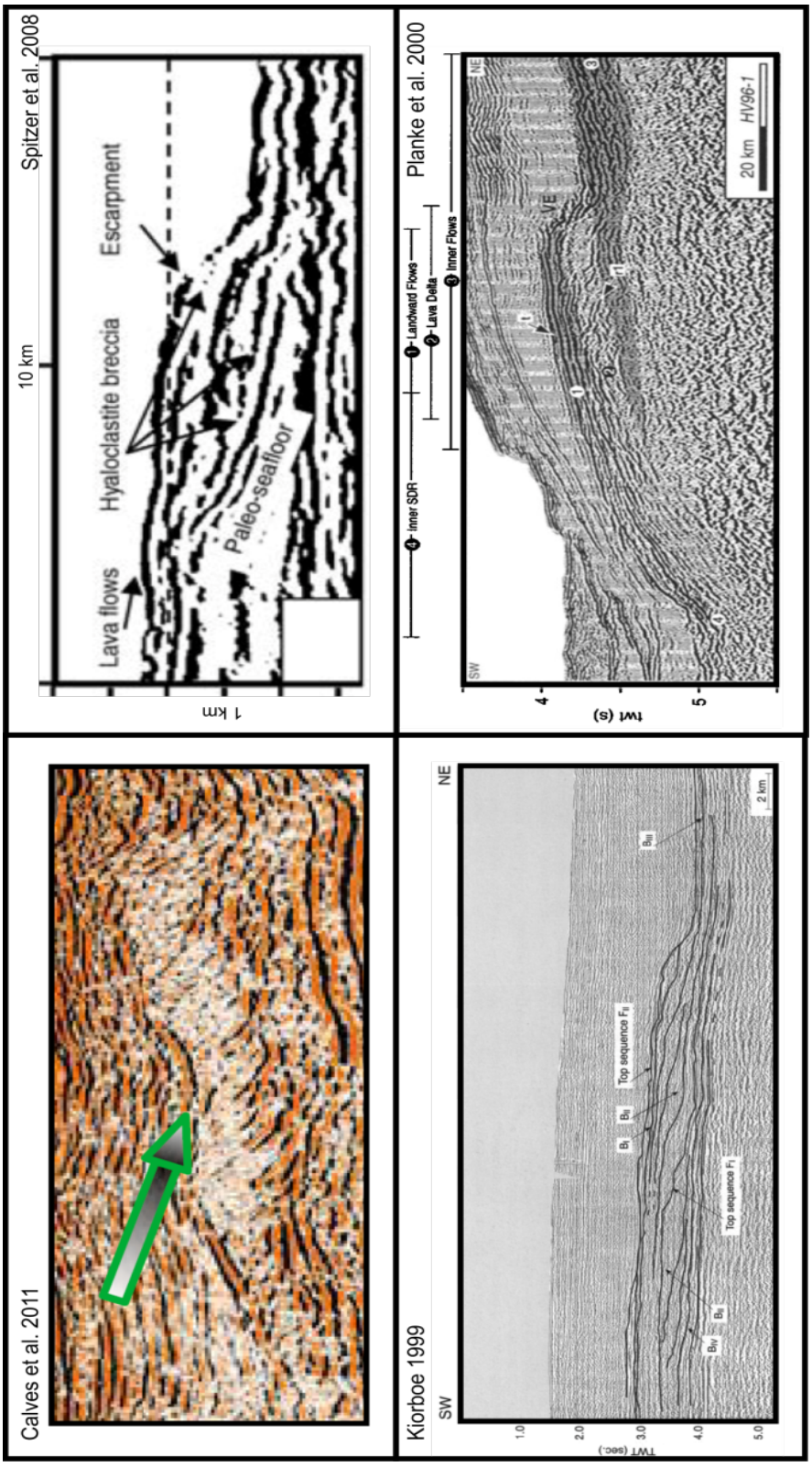

Figure 3.3. Examples Lava-fed deltas in the subsurface, examples from; Kiørboe 1999; Planke 2000; Calves et al., 2011; Spitzer et al., 2011. Each example shows a series of prograding reflectors determine to represent a lava delta consisting of a set of supplying lava flows and less defined prograding hyaloclastite deposits. A Detailed discussion of these systems is provided in chapter 8.

3.4.6 Comparison with Coarse-grained Siliciclastic Deltas.

Morphologically most hyaloclastite deposits are thought to compare well to Gilbert-style, high-energy, gravity-driven coarse-grained deltas (Porębski and Gradzinski, 1990; Ollier et al., 1998; Skilling 2002). Models of hyaloclastite deposition are often simplified as subsiding prograding clinoform packages (e.g. Schmincke et al., 1997 - Fig. 3.1). This approach is analogous to Jones and Nelson's (1970) model where relative sea level controls the height of the passage zone with the additional effects of subsidence. A comparison to siliciclastic systems is discussed in chapter 4 although the reader is asked to consult Skilling, 2002 for a more definitive overview.

3.4.7 Basaltic Submarine Hyaloclastite deposits (Seamounts and Surtseyan volcanism)

Large hyaloclastite and pillow lava piles are formed during the initial phases of submarine volcano and seamount growth or during Surtseyan eruptions (cf. Schmincke, 1967; Staugiel and Schimincke, 1984; Moore, 1985; Schmincke et al., 1997; Seaman et al., 2000; Behncke, 2004) or during sea floor eruptions such as axial spreading ridges (Fornari et al., 1979; Lonsdale and Baptiza, 1980; Bonatti and Harrison, 1988; Batiza and White, 2000; Dicknson et al., 2009). Near Hilo, Hawaii the hyaloclastite pile reaches c.1km thickness (Seaman et al., 2000 Moore, 2001; Katz and Cashman, 2003; Hawaiian Scientific Drilling Project Phase II). More detail on the products of hyaloclastite deposits and other volcanically derived products in surtseyan volcanism is provided in the introduction to chapter 5.

Hyaloclastite deposits in sea floor settings radially dip from a central fissure. As the volcanic pile builds Surtseyan style processes act to produce a volcanic pedestal. As volcanism become subaerial complex relationships between pillow lava, tuffs and hyaloclastite breccia deposits occur (e.g. Behncke, 2004). The production rate of hyaloclastite at ridges is probably also linked to the rate of spreading (Bonatti and Harisson, 2008). In most cases hyaloclastite and pillow lava make up prominent topographic features that contain abundant pillow lava lobes that turn into breccias sheets more distally to the site of eruption due to gravitational collapse and mass

wasting processes. Thick sequences of hyaloclastite deposits are likely to be derived from supressed phreatomagmatic eruptions leading to non-explosive fragmentation processes at depth forming large talus slopes stabilised by the precipitation of palagonite (Lonsdale and Batiza, 1980; Schiffman et al., 2005).

Examples of hyaloclastite deposits formed in these settings can be found deep into the geological record, such as spreading ridge pillow lava and hyaloclastite sequences of Mt. Kalnik (Triassic, Palinkas et al., 2008), metamorphosed hyaloclastite deposits of the Kamiskotia Volcanic Complex (Precambrian c. 2.9-3.5 Ga, Finamore et al., 2008; Hathaway et al., 2008), As parts of obducted opholotic slabs (Ballantrae ophiolite, SW Scotland, Ordovician, Bluck, 1982 or the Troodos Ophiolite Cyprus, Cretaceous, Boyle and Robertson, 1984) and the thick oceanic core complex at Kane Megamullion (Precambrian – 3.3-2.1 Ga, Dick et al., 2008).

3.4.8 Non-Progradational Hyaloclastite breccias

In shallow lakes dome-like formations of pillow lavas and hyaloclastite can spread over 2–3 km and well-characterized examples of these deposits exist in the Snake River Plain, U.S.A. (White, 1996; Godchaux and Bonnichsen, 2002). In low energy lacustrine environments and subglacial settings where the volume of water is limited lava can quickly become insulated from further quenching by its own carapace (Kokelaar, 1986; Lescinsky and Fink, 2000; Lodge and Lescinsky, 2009; Tucker and Scott, 2009). Large blocks of hyaloclastite can be incorporated into lava flows via internal shear or gravity collapse over short distances (Tucker and Scott, 2009). Thin lenses of hyaloclastite can occur in these deposits and have been attributed to explosive activity (Tucker and Scott, 2009).

In marine settings lava flows can actively flow into the sea to form mega-pillow complexes (Yamagishi, 1991; Bear and Cas, 2007). Mega-pillows develop due to relatively low magma discharge rates and limited water depths, which result in limited fragmentation. Instead the lava forms a series of lobes that are emplaced successively (on top of each other). Where discharge rates are high, deposits often are composed of fragmented sheet hyaloclastite lithofacies that contain remobilized hyaloclastite material similar to deposits at axial spreading ridges (Dickinson et al., 2009).

Submarine lavas flows can be extensive (up to 110 km length) and form in water depths of up to 5.5 km (Holcomb et al., 1988). Extensive lava flows have been imaged using sonar and bathymetric techniques in a number of settings in Hawaii (Holcomb et al., 1988), and Pico Island, Azores (Mitchell et al., 2008). Submarine lava flows have dendritic morphologies analogous to terrestrial lava tube networks (Mitchell et al., 2008).

At smaller scales invasive flows can produce pillow lava mounds and associated hyaloclastite material in water saturated sediments. This is common in the Columbia River Flood Basalt Group where lava flows into lacustrine sediments which insulates the flow. The flow forces the saturate sediment out of the way until water ingression occurs, either leading to pillow lava lobes or fragmentation to hyaloclastite breccia (e.g. Wells et al., 2009).

3.4.9 Basaltic Subglacial Volcanic Systems

Subglacial basaltic volcanism commonly results in pillow lava and hyaloclastite ridges up to 300 m in height (e.g., 1995 Gjálp eruption at Vanajökull, Gudmundsson et al., 1997; Schopka et al., 2006). Differences in ice thicknesses and styles of confinement lead to significant lithofacies variations (see Smellie and Skilling, 1994). In unconfined melt water lake settings, hyaloclastite morphologies can closely resemble those seen in Surtseyan settings where lavas cap an underlying hyaloclastite and pillow lava mound. Ice confinement at the margins of the volcanic pile can increase the steepness of volcanic material that progrades into a melt water lake (cf. Werner and Schmincke, 1999; Skilling, 2009; Smellie et al., 2011). However, the distinction between lacustrine and subglacial environments can be difficult (Loughlin, 2002). Where significantly deep melt-water lakes develop this allows similar (unconfined) depositional processes to produce large lava delta sequences (e.g. Pedersen et al., 1998; Smellie et al., 2011). Subglacial eruptions have also been used to reconstruct former ice thicknesses to aid palaeoenvironmental studies (Lesincsky and Fink 2000; Helgason and Duncan 2001; Dixon et al., 2002; Smellie et al., 2006; Tuffen et al., 2010; Owen et al., 2012).

The processes involved in the development of the hyaloclastite deposits are dictated in part by ice thickness and by the development of melt water, which

controls the hydrostatic pressure and the availability of water to the system (Smellie and Skilling, 1994; Smellie, 2000). Therefore subglacial deposits can be separated into two main types; eruptions beneath thin ice and eruptions beneath thick ice:

Thin Ice (Alpine style glaciers)

- *Stacked esker sequences* – Dominated by subglacial emplacement as ice is lifted and water flows from the vent. They comprise of melt water dispersed tephra, subaqueous lavas and hyaloclastite material deposited as thin ridges or sheets (Smellie and Skilling, 1994; Smellie, 2008).

Thick Ice such as Icecaps

- *Table mountains or Tuyas* – Where heat causing the ice to melt above a point source such as a shield volcano (Gudmundsson et al., 1997; Werner and Schmincke, 1997; Skilling, 2009) forming a volcanic cone surrounded by a melt water lake in which hyaloclastite deposits can form or prograde out into. Once emergent "typical" surtseyan processes can dominate.
- *Hyaloclastite Ridges or Tindars* – formed where ice confining does not fully melt causing confined ridges - fissure eruptions or mounds - point sources (Schopka et al., 2006). This can also occur where confining ice pressures are high possibly limiting explosive MCFI processes (Zimanowski and Buttner, 2003).
- *Lava fed delta systems* - They can occur in melt water lakes as the edifice become emergent lavas begin to form, covered in the lava delta section of the literature review (see Skilling, 1994, Werner and Schmincke, 1997; Smellie, 2001).

Resedimentation of material by fluvial processes or from the catastrophic release of melt water (jökulhlaups) can emplace widespread flood deposits (see Bjornsson, 2003), which can preferentially remove fine material. Density-modified grain flow deposits and high-density turbidites can be deposited (Skilling 1994, Smellie, 2001; Schopka et al., 2006). Ice confinement can control the depositional extent of material, allowing steeper angles of repose or, if the ice melts at a later stage, resedimentation (Werner and Schmincke, 1999; Skilling, 2009; Smellie et al.,

2011). The degree of fragmentation is in part dictated by highly variable pressure regimes, not just depth. This causes a great variety in fragmented products that can be again related to melt water drainage (Gudmundsson et al., 2004).

3.4.10 Silicic Hyaloclastite Deposits

Hyaloclastite deposits derived from the fragmentation of magmas and lavas of acidic to intermediate compositions form unique deposits and depositional styles that are quite different to those generated during from basaltic volcanism.

Commonly acid to intermediate deposits form small domes or mega pillow sequences accompanied by jigsaw-fit breccia (cf. Pichler, 1965; Yamagishi and Dimorth, 1984; Schutter et al., 1998 for submarine examples and Furnes et al., 1980; Tuffen et al., 2002; Tuffen, 2007; McGarvie et al., 2007; Owen et al., 2012) for subglacial acidic hyaloclastite deposits). Field studies of submarine acidic hyaloclastite deposits are rare. Yamagishi and Dimroth (1985) compared Archean and Miocene acidic hyaloclastite deposits. They described hyaloclastite deposits that consist of a feeder dyke that branched into lava lobes and lava pods. Many of the lava bodies grade into in-situ hyaloclastite breccias. Hyaloclastite deposits are a common accessory product during the formation of silicic dome deposits or the intrusion of silicic magma into water saturated sediments commonly forming a carapace around intrusions (Picher, 1963; Doyle and McPhie, 2000; Maeno and Taniguchi, 2006; Nemeth et al., 2008). A unique type of deposits of hyaloclastite origin can also occur where products of effusive silicic volcanism quench when entering water (cf. Stix, 1991).

Subglacial silicic volcanism is characterised by lower magma temperatures leading to less melt water production so little or no melt water accumulation (Hoskuldsson and Sparks, 1997). Two main types of volcanism are produced, explosive which occur at high effusion rates and intrusive, at low effusion rates where the cavity is dominated by hyaloclastite material (Tuffen et al., 2007). Commonly they form water-saturated breccias and intrusive peperitic lavas that can be redeposited by melt water removal.

3.4.11 Fluvial Hyaloclastite Deposits

Hyaloclastite deposits can form in river channels when lava flows into rivers. Characteristically, hyaloclastite dams form, which block or divert the rivers (Hamblin, 1994; Guilbaud et al., 2005). Four main types of lava dam have been recognised (Hamblin et al., 1994, Brossy, 2006):

1. Single flow dams are characterized by one lava flow and associated pillow lava breccias (up to 185 m thick and 138 km in length). These dams are thought to occur during rapid emplacement processes from large volume eruptions;
2. Massive dams contain thicker basalt lava and pillow lava sequences (up to 240 m thick), which occur where the lava becomes constrained in narrow valleys and effusion out paces the reestablishment of the river system;
3. Thin dams are up to 10 m thick and contain one small lava flow capped by fluvial sand or gravel where lava effusion rates are low;
4. Complex dams – Contain multiple lava flows and fluvially reworked inter beds which have been eroded the upper layer of lava flows;

Fluvial erosion can destabilise basalt and hyaloclastite dams (see Hamblin et al., 1994) and result in catastrophic flooding (cf. Tolan and Beeson, 1984; Fenton et al., 2006). Hyaloclastite deposits can be reworked as a component in a fluvial system and deposited downstream (Fenton et al., 2002).

3.5 Reworking Processes

3.5.1 Causes of Reworking

Resedimentation of hyaloclastite material can occur soon after deposition or after shallow burial (Fisher and Schmincke, 1984; Bergh and Sigvaldson, 1991; Mattox and Mangan, 1997; Ollier et al., 1998; Head and Wilson, 2003; Sohn et al., 2008). Hyaloclastite material that is deposited in unstable regimes (e.g., on volcanic flanks) is prone to remobilisation (Lonsdale and Baptiza, 1980; Sansone and Smith, 2006; Schiffman, et al., 2006; Thompson et al., 2008; Dickson et al., 2009) by

gravity-driven particulate mass flows (White, 1996; Schmincke et al., 1997). Conversely, hyaloclastites deposited in a tectonically inactive shallow water basin or lacustrine environment is less likely to be remobilised (except by wave undercutting which may lead to lava bench collapse, Mattox and Mangan, 1997).

In emergent settings hyaloclastite can occur in complex relationships with lava, tephra in a volcaniclastic apron (Busby-Spera and White, 1987; Sohn, 1995; White, 1996). This is due to the varying rates of extrusion, changing viscosity, explosive activity, proximity to source, resedimentation process and rate of subsidence (Schmincke et al., 1997). Emergent volcanoes' flanks are inherently unstable and prone to collapse (Lonsdale and Baptiza, 1980) and resedimentation is common. These processes can be enhanced by progressive emergence of the volcano where wave action can begin to destabilise the flank.

Foresets on lava deltas are close to the critical angle of repose (Moore et al., 1973, Lonsdale and Baptiza, 1980; Mattox and Mangan, 1997; Schmincke et al., 1997) therefore downslope resedimentation is common. Thus mass flow deposits (referred to by Porebeski and Gradzinski 1990 as, llaharic flows) are common at the toes of deltas (bottomsets). Bottomsets have been imaged by seismic reflection surveys on some large ancient hyaloclastite deltas (Planke et al., 2000). In lava deltas fine sediment can be remobilised into sediment plumes during the initial phases of delta formation (Sansone et al., 1991; Tribble 1991). This contributes to the fine-grained material in more distal parts of the delta (e.g. toeset units Porębski and Gradziński, 1990).

Gravity-driven processes lead to the formation of high-angle Gilbert style deltas (Porębski and Gradziński, 1990; Skilling, 2002). However where the water is shallow then lava-fed deltas have a chaotic distribution with little or no resedimentation (Skilling, 2002).

3.5.2 Delta Front Collapse

Delta front collapse is a primary driver of resedimentation in hyaloclastite deposits. Mattox and Mangan (1997) hypothesised that there two end members of delta front collapse; open mixing where by the lava tube catches up with the delta front leading to complete collapse of the delta front (tephra jetting occurs as MCFI processes become active at the water interface); combined mixing that leads to the

submergence of the delta front (littoral fountains and bubble bursts develop). These processes act in two ways: firstly, it creates a scarp that allows waves to impact on lava entering the sea (Mattox and Magan, 1997). This can enhance the fragmentation process and lead to increased delta development (Moore et al., 1973). Delta front collapse deposits reduce the slope angle and create a platform onto which lava can prograde (Fornari et al., 1979; Yamagishi, 1991). Coarse-grained breccias have been documented within field examples (Clague et al., 2002; Porębski and Gradziński, 1990).

Triggers for delta collapse can include: the saturation of sediment underlying the delta (Schiffman et al., 2006), the continued emplacement of lava flows (Mattox and Mangan 1997), rapid subsistence (Schmincke et al., 1997) and phreatomagmatic activity (Umino et al., 2006). Although not truly analogous to lava-fed deltas, Bergh and Sigvaladson (1991) showed that some hyaloclastite deposits display flow structures, for example; clast imbrication, aligned lava pods, crossbedding and normally graded beds that suggest that the sediment was remobilization through a degree of turbulent mixing or pulsing of hyaloclastite material entering the basin through periodic lava-water interaction by numerous turbidity currents and debris flows. These processes are likely to operate in large-scale hyaloclastite deposits seen at seismic scales (e.g. Fig. 3.3) and therefore defined below.

3.5.3 Debris/ Mass Flows

At abyssal depths hyaloclastite deposits can grade into epiclastic (post-lithification reworking of hyaloclastite) deposits (Portner et al., 2010) or at shallower water levels sheet breccias (Bear and Cas, 2007) and, at depth coalescence of multiple hyaloclastite bodies can led to complex facies relationships (Schmincke et al., 1979). In transitional submarine to sub aerial environments at shallower water depths Bergh and Sigvaldasson (1991) developed an emplacement model (standard depositional model) for resedimented hyaloclastite deposits during an eruption:

A) High lava effusion rates produce a low water/melt ratio and low efficiency of conversion of thermal energy to mechanical energy. This lead to a heterogeneous mass of quenched fragments. This moves downslope under gravity. This is analogous to early stage quench fragmentation processes.

B) The lava flow becomes increasingly fragmented with distance from the vents. The upper hyaloclastite mass and enclosed lava moves as a mass flow allowing lava lobes to align in the direction of transport. This creates basal petromict or polymict breccias (Porębski and Gradziński, 1990 and Clague et al., 2002) or bottom sets (Planke et al., 2000)

C) During the final phase of emplacement small-volume density slurrys are produced due to intermittent particle suspensions. These follow the each lava flow in rapid succession. Low-concentration turbulent flow and reworking by bottom currents can produce deposits at the end of the unit (prodelta sedimentation) and channel structures (Ollier et al., 1998)

Hyaloclastite-rich lithofacies that result from debris flows commonly display inverse grading as well as a positive correlation between bed thickness and maximum clast size (Gloppen and Steele, 1980). Many beds show inverse grading at the base and massive upper parts. Tanner and Calvari (1999) theorised that pillow basalt breccia represented a talus deposit similar to a fan toe deposit (Schmincke et al., 1997). This would produce the interfingering morphology between lava and hyaloclastite common in resedimented hyaloclastite deposits (Tanner and Calvari, 1999). Tractional sedimentation from turbidity currents submarine channelisation can produce large-scale sedimentary structures (Bergh and Sigvaldasson, 1991). Channelized flow has been recorded at abyssal depths, remobilising hyaloclastite material creating large talus cones from a point source (Ollier et al., 1998; Stow et al., 1998). Channelized flow, on smaller scales could occur at shallower water depths but has not yet been recorded. Therefore the development of submarine hyaloclastite sequences is highly complex and caused not only by primary fragmentation but also intrinsically linked to reworking processes (Skilling, 2002).

3.6 Towards More Complex Lithofacies Models.

Models of lithofacies associations in mafic volcanic deposits have become increasingly more detailed as new data sets and approaches become available (e.g. Self et al., 1998; Single and Jerram, 2004; Planke et al., 2000; Nelson et al., 2009). Some complex lithofacies models for hyaloclastite deposits exist and are linked to

primary and secondary fragmentation processes (e.g. Porębski and Gradzinski, 1990; Skilling, 2002). Both models show that hyaloclastite deposits are composed of material derived from both primary fragmentation and some degree of downslope reworking. A few questions remain unanswered such as the comparison between hyaloclastite deposits that form in different environmental settings. Complex internal lithofacies architectures in each of these examples develop due to variation in lava supply, reworking and final depositional processes and therefore need to be investigated and compared in order to compare hyaloclastite deposits in the subsurface (e.g. core, wire-line logs and seismic datasets).

3.7 Hyaloclastite Diagenesis

3.7.1 Palagonitization

Palagonitization occurs due to the relative instability of basaltic volcanic glass at atmospheric temperature and pressure, which promotes devitrication and clay formation (Stroncik and Schmincke, 2002). Understanding the rates and development of palagonite within hyaloclastite deposits is important as it can mask sedimentary structures, reduce porosity/permeability and affect density. In hyaloclastite deposits palagonite forms a rind around each of the sideromelane shards or along exposued fracture planes. Hay and Iijima, (1968) demonstrated that during burial sideromelane glass becomes hydrolysed to form palagonite at increasing depths: this significantly decreases the porosity. A number of studies in Hawaii have revealed that clay mineral precipitation in hyaloclastite deposits occurs progressively and is zoned into illite, smectite and palagonitite layers at increasing depths (Moore, 2001, Walton and Schiffman, 2003, Schiffman et al., 2006). Below the palagonite zone the porosity of the deposits is significantly reduced and the bulk density is at its highest (Schiffman et al., 2006). The process of palagonitization is still not fully understood and is thought to occur just after initial quenching has take place (Furnes 1976; Stroncik and Schmincke, 2002). Stroncik and Schiminkce, (2002) summarised that dissolution-precipitation are responsible for the transformation of sideromelane into palagonite. Diagenesis principally involves the alteration of sideromelane glass and generation of palagonite—a low-temperature brown, yellow or greenish alteration product (Hay and Ijima, 1968; Thorseth et al., 1991; Stroncik and Schmincke, 2001,

2002; Walton and Schiffman, 2003; Walton et al., 2005). The formation of palagonite occurs in two stages depending on the extent of the exchange process (Stroncik and Schmincke, 2002; Kruber et al., 2008). The first stage, gel palagonite, is generally depeleted in SiO_2, Al_2O_3, MgO, Ca_2O, Na_2O and K_2O and is enriched in TiO_2, FeO and H_2O in comparison to its parental glass. The second stage, fibrous palagonite is commonly associated with smectite and involves the uptake of SiO_2, Al_2O_3, MgO and the loss of TiO_2 and H_2O. However element loss or gain varies significantly on local environmental conditions (Crovisier et al., 2003).

Palagonite has a variety of morphologies and crystalline phases arsing due to a loss of the metal phases and silica which lead to distinct ageing steps (AGS) I and II where palagonite crystalizes due to the secondary precipitation of previously lost phases with the addition of Ti, Fe and K leading to radial fibrous structures. The type of palagonite precipitated may control aspects of rock properties such as ductility although its effect is largely unknown.

Stroncik and Schmincke, (2001) indicate the rate of palagonitization can be calculated according to Fick's law;

$$S = \sqrt{CT} \tag{3.1}$$

Where S is the thickness of the palagonite layer in μm, C is a constant but varies depending on the environmental setting and T is the duration of the process. C can range between 480 to 2,000 μm/10^3 years and depends on glass composition and water type whether meteoric or saline (Stroncik and Schmincke, 2002). Stroncik and Schmincke (2002) modified and added to Furnes' (1974) parameters indicating that the rate of palagonite precipitation is dependent on:

- Temperature;
- The structure of the primary material;
- The reactive surface area of the primary material;
- The structures of the precipitating secondary phases;
- The growth rates of the secondary phases;
- Time;

- Different fluid properties (e.g. pH, Eh, ionic strength and oxygen fugacity, which are, in turn, affected by other properties, e.g. porosity and permeability).

The process of palagonitization is particularly susceptible to temperature changes. At high temperatures (e.g., >120^{o} C) diffusion of chemical species leads to bypass of the palagonite process to form crystalline clay minerals (Jacoksson and Moore, 1986). However at temperatures <120 ^{o}C rate of palagonitization is proportional to increases in temperature. The relation between palgonite thicknesses and time varies; at the Mid-Atlantic Ridge palagonite growth is slower that that at Hawaiian, for example (Stroncik and Schmincke, 2002 after Hekinian and Hoffert, 1975 and Moore, 1966). Groundwater circulation and higher temperature regimes, as a result of igneous intrusion or hydrothermal activity, speed up the palagonitization process and produce thicker palagonite rinds (Walton and Schiffman, 2003). Clays will precipitate where flow becomes constricted and hence will be preferentially deposited in pore throats. This action can cut connectivity and significantly decrease permeability. The AGS I and AGS II (radial fibrous structures) then act to fill the enclosed voids created by the initial palagonite rim and create coherent fibres between grains.

3.7.2 Authigenic Mineral Growth

Authigenic mineral precipitation accompanies the palagonitzation process in hyaloclastite deposits.Palagonite formation is simultaneous with chabazite (zeolite) formation (Walton et al., 2005), so that the basic reaction is;

Sideromelane + components from pore water = palagonite + chabazite + components to the pore waters (3.2)

Therefore zeolites will precipitate in the pore spaces during burial and fluid circulation

Zeolites are microcrystalline aluminosilicates that have unique framework structures (IZA database of zeolite structures [www.iza-online.org/]). Most zeolites can contain a variety of cations in their porous structure (Alberti et al., 1997). The most common naturally occurring zeolites in volcanic rocks are chabazite, phillipsite,

analcime, clinoptilolite and natrolite. The type of precipitated zeolite, with some overlap, is strongly linked to temperature (Jørgensen, 2006). Accompanying zeolite precipitation are other hydrothermal minerals such as Ca-Silicates (e.g., gyrolite, Walton and Schiffman, 2003). Na, K and Ca ratios in phillipsite and chabazite, the two most common zeolite types in hyaloclastite deposits, have been shown to relate to the salinity of water in subglcial hyaloclastite examples (Johnson and Smellie, 2007).

In hyaloclastite deposits the ratio of authigenic minerals to palagonite is hypothesised to be 1:1 (Furnes, 1974). However this is not always the case as authigenic mineral precipitation is highly dependent on charged ground water circulation. Initially authigenic mineral precipitation reduces porosity. Palagonitization is limited by authigenic mineral precipitation blocking grain contact areas (Furnes, 1974). Therefore authigenic mineral precipitation reduces the amount of palagonite formation hence preserving "minus cement" porosity (i.e., porosity minus the volume of the interstitial material, Walton and Schiffman, 2003). In Hawaii higher temperature regimes (e.g., low-grade contact metamorphism zones) produce a distinctive group of hyaloclastite deposits that have enhanced minus cement porosity (Walton and Schiffman, 2003). Therefore the minus cement porosity in this case is:

$$\text{Minus cement porosity} = \theta - \text{interstitial mineralisation} \qquad (3.3)$$

Where θ is the actual porosity minus the pore lining and pore-filling cements (Walton and Schiffman, 2003). Contact metamorphosed samples display a distinctly higher minus cement porosity than samples from ambient conditions. This can be attributed to early stage mineralisation that helped the deposit resist initial compaction. Therefore, at least initially hyaloclastite deposits are controlled by crushing of the rock under compaction (Walton and Schiffman, 2003). However enhanced fluid circulation promoted by dyke intrusion can lead to the precipitation of authigenic minerals exceptions to these processes occur in high temperature hydrothermal systems, low grade metamorphism and metasomatic processes govern the mineral type. These processes are best summarized in Zierenberg et al., (1995) but lie outside the scope of this study. Hyaloclastite deposits and pillow breccias that

are rapidly exhumed or do not experience any hydrothermal fluid circulation can remain porous (Tolan pers. Comm., provided in appendix to this chapter). The mechanisms behind this are not fully understood however they can lead to non-saline aquifers at depth (Thomas et al., 1996).

3.8 Conclusions

This chapter reviews previous work involving the fragmentation, shallow level diagenesis and formation of a variety of hyaloclastite deposits throughout the geological record. As discussed above hyaloclastite deposits occur in a wide range of settings that include submarine, fluvial, subglacial and lacustrine examples. Parallels can be drawn between each of these settings but there are also significant differences. However studies that integrate more than one example from each setting are limited. Furthermore recognition of the complexity of hyaloclastite deposits in field outcrop examples and the scaling relationships between these examples and large scale examples in the subsurface is relatively unknown and discussed in subsequent chapters.

4

CHAPTER FIGURES AND TABLES

4. Field Studies of Hyaloclastite Deposits in Iceland

Chapter Summary

Analysis of the spatial lithofacies variability within lava-fed delta formations in southern Iceland has revealed complex three-dimensional volcanic architectures in hyaloclastite deposits in non-glacial settings. Two depositional environments are studied, (a) lava entering a marine embayment (Stóri-Núpur) and; (b) lava advancing into a body of water of the flanks of a Surtseyan cone (Hjörleifshöfði). Interaction between environmental factors such as shoreline geomorphology, water depth, wave energy levels, the nature of the lava transport system, lava supply rate all affect the resulting lava deltas creating complex lithofacies arrangements and stacking patterns. Recognised here are two types of hyaloclastite deltas. One of syn-sedimentary origin (Hjörleifshöfði) and one derived from primary fragmentation processes (Stóri-Núpur). Syn-sedimentary systems are dominated by destabilisation of the hyaloclastite pile leading to reworking downslope and share similarities to alluvial delta systems. Conversely in primary fragmented systems waxing and waning cycles in volcanic effusivity that act to control lithofacies variation.

4.1 Introduction

Current models of hyaloclastite deposits are relatively simple and focus on the large-scale structure, with limited information on internal lithofacies variations at small-scales and the 3D lithofacies variability. Improved definitions and a better understanding of hyaloclastite lithofacies types, particularly the detail within delta sequences, are therefore needed. This chapter describes two examples of basaltic hyaloclastite successions in Iceland. Detailed field documentation and geological mapping has allowed key hyaloclastite and lava lithofacies and lithofacies associations to be used to document the sequence of events and identify the emplacement processes. For this study two types of hyaloclastite deposits were identified: A) deposits formed distally from vents in a marine embayment at a coastal margin and; B) deposits formed as part of a Surtseyan volcanic system. A model for each case study is provided documenting the variations in 3D geometry and the

stacking of hyaloclastite lithofacies in relation to their environmental setting and parent lava flows. In light of these findings we discuss the application of siliciclastic terminology to lava-fed delta systems.

. The interaction of passive fragmentation and the active, explosive contribution of glass through phreatomagmatic processes are difficult to quantify in hyaloclastite deposits. Table 4.1 summarizes the discrimination factors used to distinguish hyaloclastite deposits. However, none of these parameters can be used individually and the identification of hyaloclastite deposits requires analysis from macro to micro scale textural analysis.

4.2 Outcrop Examples of Hyaloclastite Deposits – Southern Iceland

4.2.1 Geological Setting

Both examples of hyaloclastite deposits in this study are located in south central Iceland away from areas of current active volcanism. The first example is from the 2.8–1.1 Ma (ages determined from K-Ar and palaeomagnetic studies) Hreppar Formation (Kristjánsson et al., 1998); the lava delta sequence that is exposed at Núpsfjall above Stóri-Núpur in the Árnes district (Fig. 4.1 and see chapter 8). The second example is from a much younger (<800 Ka) Hjörleifshöfði promontory situated on Mýrdalssandur about 10 km east of the town of Vík in south central Iceland. The Stóri-Núpur formation represents hyaloclastite deposits formed when lava flowed into a shallow marine embayment well away from the source vents. Hjörleifshöfði is a remnant of an emergent Surtseyan volcano; subaqueous eruption and proximal lavas flowed into to the sea in an open-ocean environment.

Table 4.1

Discrimination Factors	Outline	Drawbacks	Key References
Vesicularity in matrix glass	Hyaloclastite deposits can have limited glass vesicularity representing passive quench related fragmentation and spalling of pillow lava rinds. Vesicular quench glass is a common product of phreatomagmatic ejecta quenching on contact with water. E.g. Surtseyan, phreatomagmatic driven deposits commonly have vesicle components of up to 30% (e.g. Figure 5.5. chapter 5).	Vesiculation is a separate process from the fragmentation. Actively vesiculating magma entering to the sea floor can form passively quench fragmented pile of hyaloclasts. However rapidly rising magma column which interact with external water to violently fragment the magma to form fundamentally blocky, non-vesicular pile of glassy pyroclasts. However in subglacial and other wet environments examples highly vesicular glass can form. Separation of dominant phreatomagmatic processes based solely on vesicularity of the sample can be very difficult.	McPhie et al., 1993; Cole et al., 2001; Schopka et al., 2006; Murtagh et al., 2011.
Textural Variation (Clast Sorting)	Clast sorting can occur due to gravity settling and variations in flow dynamics. In hyaloclastite deposits primary fragmented breccia often displays poor sorting. Remobilisation of this material even over short distances allows grain and clast sorting. This can be useful in determining hyaloclastite deposits of syn-sedimentary origin but not necessarily in helping finger print the mode of fragmentation.	Most hyaloclastite that have undergone sorting have undoubtedly undergone some sedimentary process. Therefore the origin of the clasts or glass component in such a deposit is likely to be a mixture of both phreatomagmatic and passive fragmentation.	Fisher and Schmincke 1984; McPhie et al., 1993.
Textural Variation (Clast Morphology)	Jigsaw fit highly angular clasts and spalled pillow lava rinds preserving convex quench surfaces can indicate passive autobrecciation and fragmentation. Separation of volcanic spatter when the host sediment itself is a glassy volcanic sandstone can be extremely difficult. However careful examination of the clasts (surface rope) and presence of volcanic bombs can help identify these deposits.	During delta front collapse mixing of clasts and lava fragments can occur leading to complex volcanic deposits displaying both hyaloclastite and phreatomagmatic affinities. However interlocking grains indicates limited movement from source and is a good indicator of passive fragmentation.	Moore et al., 1973; Honnorez and Kirst, 1975; McPhie et al. 1993; Skilling, 2009.
Bedform Geometry/ Three Dimensional Architecture	Common hyaloclastite bedform geometries are dependent on the environment that the hyaloclastite deposit originally formed. However hyaloclastite transition from capping lava flows or lateral pillow lava association can help determine passive or phreatomagmatic origin.	Hyaloclastite deposits can have a steep angle of repose due to interlocking grains and basalt clasts. However Porębski and Gradzinski, (1990) note that hyaloclastite deltas can have toe-set deposits at lower angles of repose which are clearly resedimented sorted deposits. Therefore each lithofacies highlighted in this chapter is termed primary (derived from passive or limited phreatomagmatic processes) or a syn-sediment (dominantly constituted from sedimentary processes (sensu. resedimented hyaloclastite by McPhie et al., 1993).	Porębski and Gradzinski, 1990; McPhie et al., 1993.
Glass Roundness	Glass roundness can be used as a proxy for reworking or a determining factor for the style of fragmentation. Sharp bubble walls at the edge of vesicular glass shards can be rounded off during reworking processes.	Due to sharp bubble walls at the edge of vesicular glass shards that can be rounded off during reworking processes fine grained phreatomagmatic deposits could be mistaken from those formed from passive quench fragmentation.	Honnerez and Kirst, 1975

Table 4.1. Discrimination of fragmentation methods involved in the classification of hyaloclastite deposits for this study.

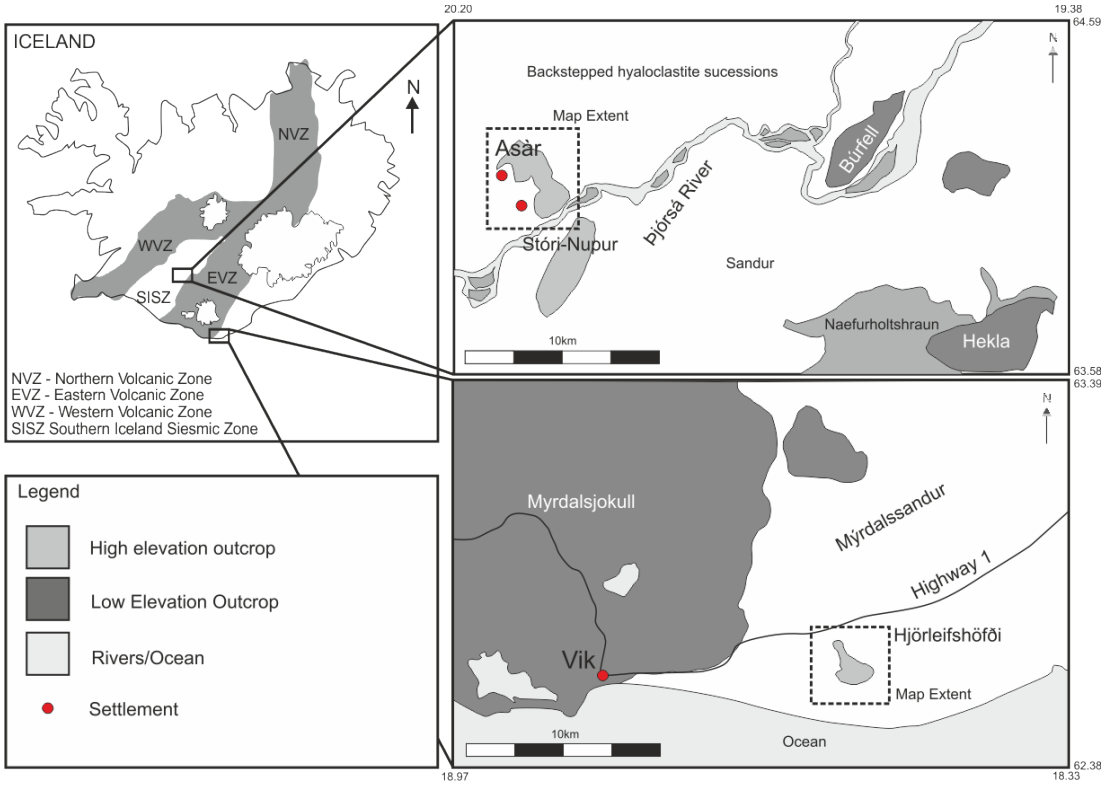

Figure 4.1. Study area location in Iceland. 1) The Stóri-Nupur to Ásàr hyaloclastite succession in the Hréppar region. 2) The Hjörleifshöfði outlier, South Iceland. Both are now located on the margin of active volcanic zones.

4.2.2 Lithofacies Descriptions

Each lithofacies description and interpretation is provided in Table 4.2. This manuscript has adopted a classicisation method used by McPhie et al., (1993) and Skilling (2009) whereby lithofacies are divided into coherent lavas flows and those of volcaniclastic origin. The volcaniclastic deposits were divided on the basis of grain size fine hyaloclastite=FH (<1/16 mm), hyaloclastite sandstone=HS (1/16-2 mm), granular hyaloclastite=GH (2-4 mm), hyaloclastite breccia=HB (4-64 mm), coarse hyaloclastite breccia=CBH (>64 mm). Volcanogenic lithofacies are limited in Stóri-Núpur however, VB=volcanic breccia and VS=volcaniclastic sandstone are noted at the top and base of Hjörleifshöfði. Fine grained unconsolidated deposits assumed to be of air fall origin are termed FA= Fine ash. Common bedforms are added as a suffix hence p=planar bedded, i=imbricated, c=channelized, cb=crossbedded and tcb=trough cross-bedded. Coherent lava flow facies=L are separated based upon characteristic fractures or jointing hence the prefix c=columnar jointed, ft=flow top breccia and ch=curvi-colunmar or hackly fracture. Pillow lava

dominated horizons=P and have the prefix i=isolated pillows and h=for a pillow dominated hyaloclastite succession. Each lithofacies highlighted in this chapter is termed primary (derived from passive or limited phreatomagmatic processes) or a syn-sediment (dominantly derived from sedimentary processes).

Table 4.2

Lithofacies code	Lithofacies	Locality	Characteristics	Example illustration	Interpretation	Primary or syn-sediment	Common associations
cL	Columnar jointed flow core	Stóri-Nupur/Hjörleifshöfði	Tholeiitic basalt. Large, regularly spaced, well developed columns 30–50 cm width. Finely crystalline. Phenocryst absent.	Fig. 4.6a	Core of the lava flow can form well developed columns where ponds. Limited water interaction (cf. Long and Wood, 1986).	Primary	cL
ftL	Flow top breccia	Stóri-Nupur/Hjörleifshöfði	Brecciated lava mainly flow crust into jigsaw fit clasts up to 2 m width. Partial rafting of larger blocks. Radial columns are present within larger slabs. Matrix material fine to medium glass with palagonite and zeolite cements. Pillow lavas are absent.	Fig. 4.6a	Result of lava cooling and downslope shearing of the flow top leading to brecciated layers. Detached blocks can move as gravity slides or be carried as part of the Pāhoehoe front. Glass quench surfaces and glass matrix material relate to cooling on water entry.	Primary	ftL, cL, and hP
chL	Curvi-columnar and hackly fractured basalt core	Stóri-Nupur/Hjörleifshöfði	Massive lava flows with crude columnar bases. Curvy columnar joints radiate from master joint sets. Progressively brecciated in contact with the volcaniclastic conglomerates near base of the succession at Stóri-Nupur. Where breiccated the matrix consists of medium to coarse sideromelane glass and a grain coating palagonite cement.	Fig. 4.6a	Joints sets follow the cooling front. Can be irregular appearance due to tide or wave interaction and localised pockets of phreatomagmatic activity.	Primary	ftL, cL, and hP
hP	Pillow lava and hyaloclastite breccia	Stóri-Nupur/Hjörleifshöfði	Pillow basalts and autobrecciated lavas. Pillows are elongate; 1–3 m width 0.5 m high with 20–30 cm quenched glass rinds. Pillows supported in a fine to medium grained sideromelane matrix with abundant zeolite pore space fill.	Fig. 4.3g	Lava quenching and forming pillow geometries through progressive flow. Pillows are large and elongate as act like small tongues or lava lobes penetrating into the water. Spalling of rind material leads to a fine hyaloclastite interstitial material.	Primary	ftL, cL, hP, and HBc
iP	Isolated pillow breccia	Stóri-Nupur/Hjörleifshöfði	Pillows isolated within uniform grained hyaloclastite material small percentage of lithic and basalt fragments. Pillow rinds are sometimes detached but can often still be joined to parent pillow. Pillow rounded usually 1:1 width to height ratio. Matrix is coarse grained with spalled pillow rinds in close proximity to their parent pillow lavas.	Fig. 4.3c	Spalling or sliding of pillows leads to separation from the main pillow flows. Pillows become engulfed by remobilised quenched glass rind material. Commonly forms a debris slurry of pillows and glass which moves down the delta front.	Syn-sediment	hP and iP
FA	Tephra and quench lapilli	Stóri-Nupur/Hjörleifshöfði	Thinly bedded discontinuous horizons. Extremely vesicular examples > 50% have well defined laminations and low angle cross-bedding structures. < 20% vesicle fragments form more isolated structures c. 2–3 m across. Material can be mixed in thin 10 cm trough cross-bedded intervals. Complete replacement of grains with palagonite and zeolites is common.	Fig. 4.6a	Periods of subaerial volcanism that created airborne suspensions of volcanic particles. > 50% vesicles interpreted to represent tephra intervals. < 20% material interpreted to be products of localised phreatomagmatic activity. Mixed intervals indicate some degree of marine shoaling or remobilisation of the material.	Primary	HBp, FA, hP, and cL (in Hjörleifshöfði)
HBp	Planar bedded hyaloclastite breccia	Stóri-Nupur/Hjörleifshöfði	Planar bedded to almost tangential beds from underlying volcaniclastic slope angle. Brecciated highly angular basalt clasts up to 40 cm. Partial matrix support > CBH. Matrix composed of coarse grained but moderately sorted sideromelane glass. Cemented mainly but palagonite. Some very rare rounded clasts of undetermined origin similar to those in underlying volcaniclastic apron.	Fig. 4.3f	Infilling material to a high slope angle to create and angle of repose possible for progradation of CBH. Initial fragmentation of the lava produces highly angular fragments. Some mixing of undetermined source suggests mobilisation and mixing of loose surface material.	Primary to syn-sediment	HBp and iP (in Stóri-Nupur) HBp, FA, hP, and cL (in Hjörleifshöfði)
CBH	Hyaloclastite breccia (dominate clast support)	Stóri-Nupur/Hjörleifshöfði	Thick beds (up to 4 m) of dominant clast supported breccia. Bimodal mixing of isolated larger clasts with a matrix of interlocking mosaic of small clasts (55 per 0.5 m^2) with adjoining faces (jigsaw fit). Can contain pods of HBi. Coarse poorly sorted matrix of sideromelane glass with palagonite rinds. Limited zeolite fill.	Fig. 4.3a	Originate from subaqueous lava that travelled down slope. Brecciation due to friction break up and initial quench fragmentation coupled with erosional processes. Some beds develop forest geometries where poor clast sorted facilitates steeper angles of repose due to clast interlocking.	Primary	CBH and HBi
HBi	Imbricated hyaloclastite breccia	Stóri-Nupur/Hjörleifshöfði	Lithology As CBH but has higher matrix to clast ratio (< 20 per 0.5 cm^2). Clasts are sorted into 10–50 cm imbricated layers. Common medium	Fig. 4.6h	Where autobrecciated material becomes mobilised downslope sorting of the material causes imbrication. Small bodies or 'pockets' of medium	Syn-sediment	CBH and HBI

Lithofacies code	Lithofacies	Locality	Characteristics	Example illustration	Interpretation	Primary or syn-sediment	Common associations
			grade sideromelane glass with palagonite rims. Zeolite component increasing.		grade material develop due to sorting.		
FHc–HSc/HBc	Hyaloclastite channel breccia and tuff-breccia	Stóri-Nupur/Hjörleifshöfði	Thin (0.3–1 m) channels of 2–3 m width. Fine grained sideromelane glass and basalt fragment in matrix. Form anastomosing packages which can be loosely traced in outcrop. Generally clast poor and matrix supported. Coarser material occurs in scours c.3 0–40 m width. Matrix material poorly sorted medium grained sideromelane glass. Zeolite component decreases in coarser scours where the glass increases to coarser grain. Occasionally very large channels (10–12 m width) of hyaloclastite breccia (min. clast size 1 m) occur near fault scarps (Hjörleifshöfði only).	Fig. 4.3b	Reworking of fine material between periods of volcanic quintessence. Surface run off/wave action leads to the mobilisation of fine suspension loads. In emergent settings erosional scour can develop due to destabilisation of the sediment pile causing small sediment plumes downslope. HBc represents very large sediment bypass events moving highly brecciated material to great depths down the sediment slope.	Syn-sediment	HBc, CBH, HBi, and iP
GHip	Imbricated planar crossbedded hyaloclastite breccia	Stóri-Nupur/Hjörleifshöfði	4–8 m thick imbricate cross bed sets. The beds grade and fine up from 50–80 cm to clast sizes c. 2–10 cm. Each 2–15 cm lamination form fining up cycles. In Stóri-Nupur it is forms small sheets up to 1 m thick. Matrix; medium to coarse grained sideromelane glass with some tephra (highly vesicular up to 1 cm diameter). The tephra is easily recognisable as has undergone rapid palagonitisation in comparison to the sideromelane glass.	Fig. 4.6c, e	High angle cross bedding could represent Gilbert style delta deposition. These features develop from large scale flank collapses of the hyaloclastite pile. This is supported by the presence of large scale slump structures.	Syn-sediment	GHip, CBH, and FHc–HSc
VStcb	Trough cross-bedded volcaniclastic sandstone/breccia	Hjörleifshöfði	VStcb overlies GHip after an underlose unconformity. Trough cross-bed sets are up to 1 m thickness. Matrix supported breccia sheets are associated with thinned finely bedded clast poor intervals. The clasts are composed solely from angular to subangular basalt. The faces of the clasts can be smoothed. The matrix is a mix of sideromelane glass, tephra and locally derived pyroclastic material. Palagonite cements the deposits and zeolite is an uncommon accessory in the pore space.	Fig. 4.6c	The unconformity between the structures suggests changing environmental conditions. The trough cross bedding represents more localised shore face reworking accompanied by the influx of new material and rounding of the basalt clasts. This suggests wave interaction, see Section 4.2.	Syn-sediment	VStcb
VB	Massive breccia	Hjörleifshöfði	Massively bedded (up to 10 m) matrix supported bimodal breccia unit. Contains very large boulders up to 80 cm. Clasts of ropey Pāhoehoe basalt fragments, highly vesicular blocks and tephra. Highly underlose contacts separates each of the beds. The matrix consists of broken fine grain sideromelane glass, palagonitised material, secondary calcite and zeolite.	Fig. 4.6d, f	Massive beds indicate initial debris flow deposits source from the flank of the initial volcano before the initial vent stage. They contain numerous incised channels which indicate sourcing from an effluent force.	Syn-sediment	VB

Table 4.2. Lithofacies description and interpretation for field examples.

4.2.3 Field Examples - Stóri-Nupur to Ásàr – Lava entry distal from Vent

The Hreppar formation is a 600 m thick late Pliocene (2.5 Myr) to early Pleistocene (1.0 Myr) volcanogenic succession consisting largely of subaerial basaltic lava flows as well as volcaniclastic rocks (Geirsdóttir et al., 1993). Volcaniclastic rocks in the Hreppar formation have been generated in glacial, submarine and subaerial environments. Volcanic lithofacies are largely composed of basaltic lavas and associated hyaloclastite deposits formed by local fissure eruptions

occasionally interrupted by silicic tephra deposits form nearby central volcanoes of Laxárdalur to the west and Thjórsárdalur to the east (Kristjánsson et al., 1998).

The Stóri-Núpur to Ásàr example is a ~3 km long exposed section through a hyaloclastite deposit. The hyaloclastite material lies on a wave cut platform consisting of an older polymict volcaniclastic conglomerate. Capping the sequence are younger subaerial lavas. Three large ~1 km wide lobes can be recognised in which each of the recorded facies lie (Fig. 4.2A). The overall dip of the unit is shallow (up to 25º but often less than 5º). Some of the lithofacies can be mapped but most are discontinuous over 200–400 m.

The hyaloclastite delta succession at Stóri-Núpur contains eleven lithofacies types (summarised and described in Fig. 4.2A, B, 4.3 and Table 4.2). The lava facies (lithofacies cL and chL) are representative of water-enhanced cooling regimes forming joint perpendicular to cooling surfaces (cf. Long and Wood, 1986). All thirteen logs for Stóri-Núpur can be viewed in the appendix for chapter 1.

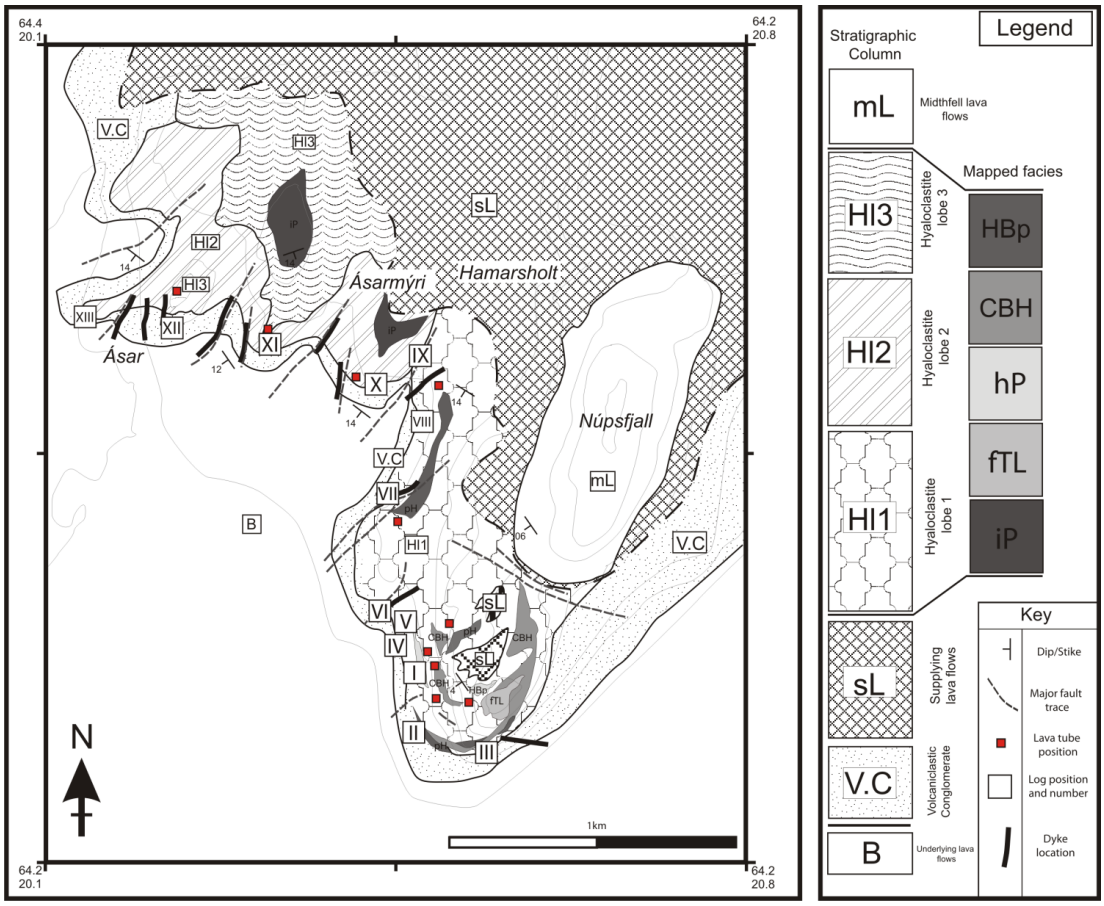

Figure 4.2A. Simplified geological map of the Stóri-Nupur Delta showing the three major lobes of fragmented material in which the individual lithofacies are located. Some of these lithofacies can be mapped (see map).Thirteen logs were made through the hyaloclastite succession each locations is highlighted on the map. Full detailed logs are provided in the appendix for this chapter.

The Stóri-Nupur to Ásàr succession lies on an eroded volcaniclastic conglomerate wave cut platform creating a high-angle break-in-slope (Fig. 4.2B and Fig. 4.3). The lowermost unit at Stóri-Nupur consists of a wedge of brecciated material with ill-defined planar beds (angular to subrounded clasts). These are often chaotically arranged into small lobes or poorly defined sheets 100–300 m in width (lithofacies HBp). The complex stacked hyaloclastite lithofacies within the Stóri-Nupur lava delta are cut by small 2-3 m wide reworked channels of fine-grained hyaloclastite glass (lithofacies FHc-HSc) and thicker clast-supported breccia sheets 2–10 m in thickness (lithofacies CBH). FHc-HSc often forms the base or a top of a sequence (Fig. 4.2B). However both confined (channels) and unconfined (sheets) are common at the same stratigraphic level.

HBp is overlain by autobrecciated "jigsaw" fit and more massive hackly-jointed lava flows (lithofacies ftL) that grade laterally (over 30-50 m) into clast-supported hyaloclastite breccias (lithofacies CBH) that dip at 35° (Fig. 4.2B, 4.3). The fragmentation front or "passage zone" height is highly variable across the succession but is exposed at the summit of Núpsfjall and near Hamarsholt (Fig. 4.2A). Pillow lava horizons occur sporadically throughout the sequence either in isolation (Fig. 4.3, iP) or as grouped bodies (10-15 m thick, hP, e.g. at Ásarmýri). Pillow breccias form thick beds grading upwards into boulder-dominated breccias (Fig. 2B and Fig.3). Between pillow successions imbrication of basalt clasts hints at reworking processes (HBi).

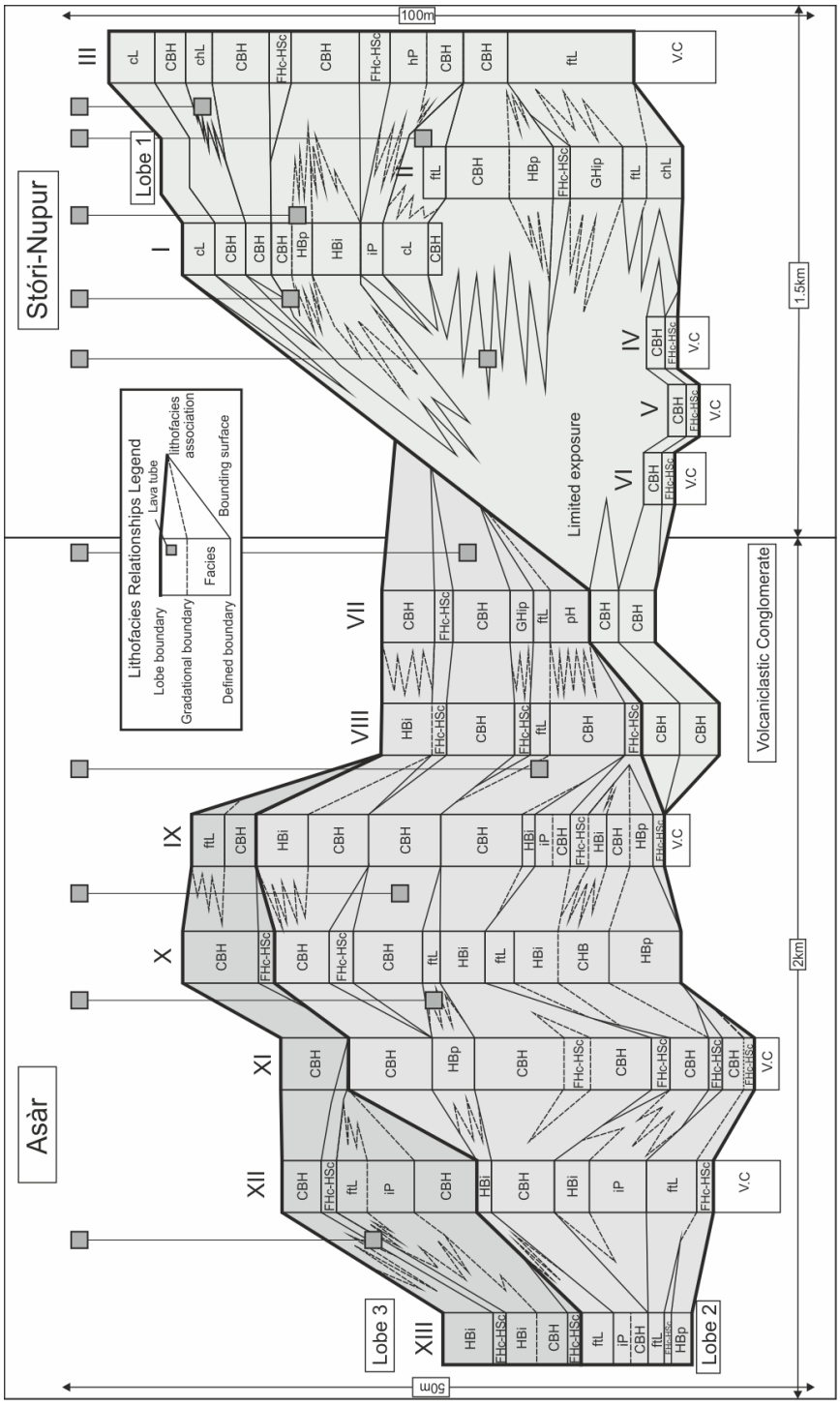

Figure. 4.2B A Fence diagram constructed from lithofacies correlation between logs. Each lithofacies identifier corresponds with table 4.2. Note that the dashed lines between lithoacies indicated linked lithofacies relationships, which are also highlighted in table 4.2. Lava tubes and there stratigraphic position are also highlighted and there position relates to the map in Fig. 4.2A . See text for a detailed explanation. Full detailed logs are provided in the appendix for chapter 4.

Within the large breccia piles, numerous dissected tube structures are observed along the delta front in outcrops below Núpsfjall (see Fig. 4.2A and B). They are unequally spaced (20–150 m) and occur at varying heights (50-150 m). In the absence of crosscutting relationships from HBc these tubes could have been active post-deposition of the hyaloclastite breccias that surrounds them. If lava tube activity had ceased remobilisation of the hyaloclastite breccia above the lava tube would have occurred. Around all lava tubes within lithofacies CBH there is a build-up of authigenic minerals within the hyaloclastite matrix indicating increased heat flow.

Imbrication within hyaloclastite breccia occurs in some foreset bundles usually where the angle of dip is greatest (20˚) (Fig. 4.2B, Fig. 4.3, HBi). Sand-grade hyaloclastite lenses (lithofacies FHc-HSc) occur in small channels c. 2–5 m in width along with more laterally continuous sheets that are 2–3 m thick and up to 10 m wide (Fig. 4.3). Preserved lava lobes associated with hyaloclastite deposition are observed in some vertical successions (Fig. 4.3e). Dykes cross-cut all beds above Stóri-Nupur and increase in frequency towards Ásàr. The cross-cutting relationships and the lack of diagenetic alteration (zeolite precipitation) in pore spaces suggest they formed post-lithification. Peperitic contacts within Stóri-Núpur are unusually absent.

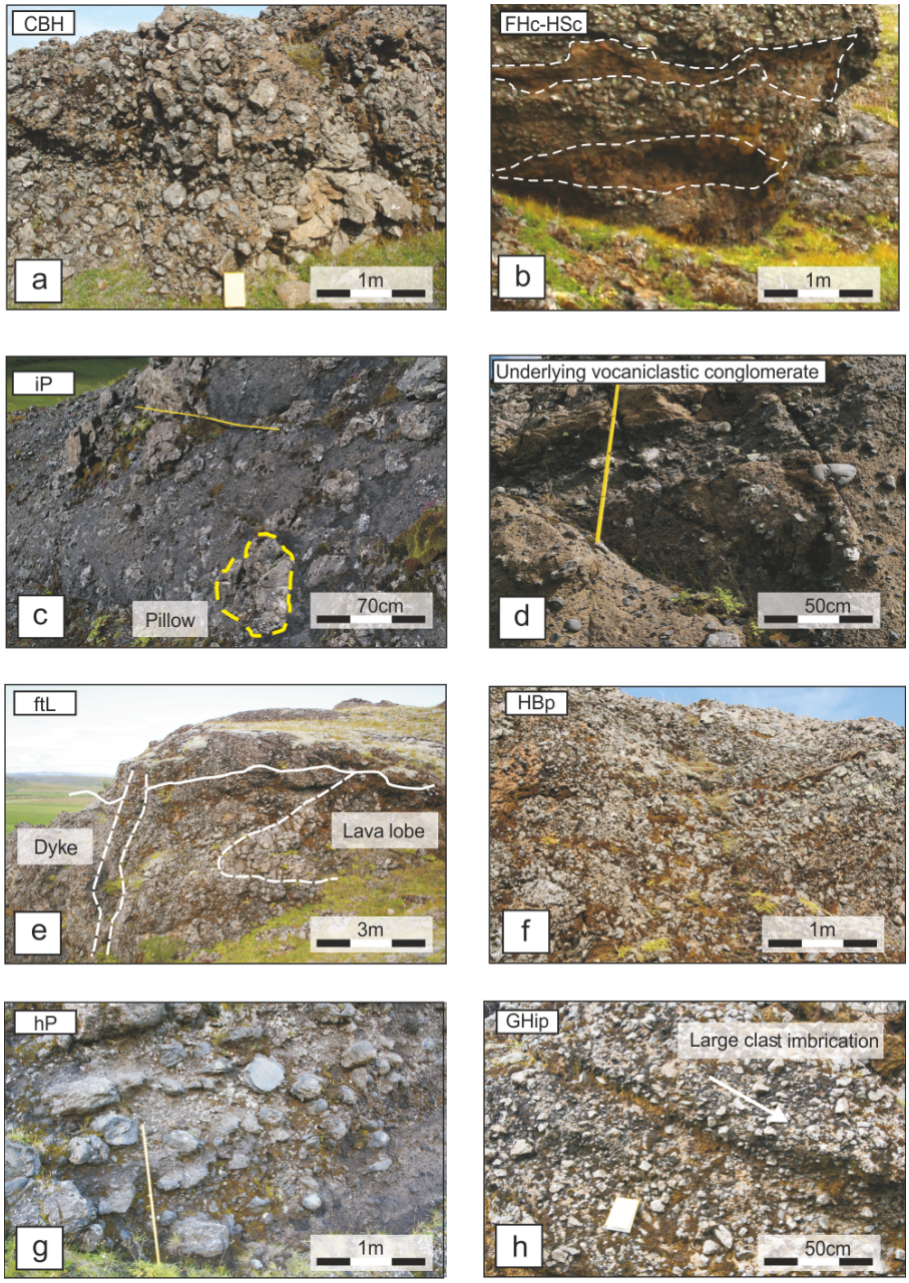

Figure. 4.3. Examples of key facies within the Stóri-Nupur lava delta, which correspond with logs in Fig.3B and table 4.2. a) A Clast supported hyaloclastite breccia with jig-saw fit clasts (CBH), b) Small discontinuous lenticular channels (FHc-HSc) between CBH horizons indicating cessation in active deposition. c) A pillow dominated succession with slight fabric from lobe 3. d) underlying the Stóri-Nupur deposit is a wave cut volcaniclastic conglomerate clearly identified by highly rounded clasts. e) A coherent lava lobe producing ftL breccia where large parts of the flow are rafting of the front of the lobe. A later dyke cuts the sequence. f) Moderate sorting in the HBp facies, g) hP facies dominated by pillows and pillow fragments, some pillows are highly rounded and could be spalled off the delta front. h) GHip in Stóri-Nupur is not as well developed as in Hjörleifshöfði, some clast alignment can be seen in this example.

4.2.4 Lithofacies correlation- Stóri-Nupur to Ásàr – Lava entry distal from Vent

Due to the high log density in Stóri-Nupur to Ásàr the internal lithofacies relationships in the hyaloclastite succession can be shown in a fence diagram (Fig. 2B and the appendix for this chapter). Three distinct lobes have been identified through geological mapping and aerial photography. Boundaries between units in lobes have been identified based upon log correlation and field relationships.

Clast-supported breccias (lithofacies CBH) and imbricated breccias (lithofacies HBi) of lobe 1 grade laterally into one another with HBi percentage increasing with increasing slope angle. Boundaries between lithofacies are separated by packages of FHc-HSc representing periods where active fragmentation has ceased within that part of the delta.

Flow-top rafted lithofacies (ftL), pillow lava hyaloclastite (HBp) and imbricated hyaloclastite (HBi) grade laterally into one another (lobe 2). Throughout lobe 2 there is a downslope increase in HBi away from CBH. Lobe 3 contains a total higher lava percentage with abundant ftL. The rafted ftL is laterally associated with lithofacies CBH and HBi as the slope angle and distance from the point of fragmentation is increased. A thick isolated pillow succession (iP) is commonly associated with CBH and HBi as again slope angle increases.

Lava tubes are shown to be associated with ftL and lava flows (lithofacies cL) whereas other times they are linked with lithofacies CBH. Lava tubes within CBH are observed in the field (Fig. 4.4). In these cases lava tubes are situated within breccia carapaces (see synthesis). The size of the lava tubes ranges from 0.5-2 m across and up to 1 m high. Within each lava tube there is evidence for multiple thin layers akin to pillow lava rinds laterally extensive about their surface. All the lava tubes in Stóri-Núpur are ovoid in cross section.

Figure. 4.4. A Lava tube at the passage zone within hyaloclastite breccia (Stóri-Núpur).

4.2.5 Field Examples – Hjörleifshöfði - Pre-emergent to Emergent Surtseyan Volcanism

Hjörleifshöfði is a small (~4 km^2) isolated Quaternary outlier in southern Iceland. It sits in a large sandur plain formed by glacier melt water outwash following late Holocene subglacial activity at Katla volcano. Aggradation of outwash sediments turned Hjörleifshöfði from an island into part of the mainland. Detailed field mapping, logging and sampling of Hjörleifshöfði has allowed the recognition of thirteen lithofacies (Fig. 4.5, Table 4.2). Five depositional phases (indicated on key and are expanded on in chapter 5). A preliminary summary of the geological history of Hjörleifshöfði is provided below.

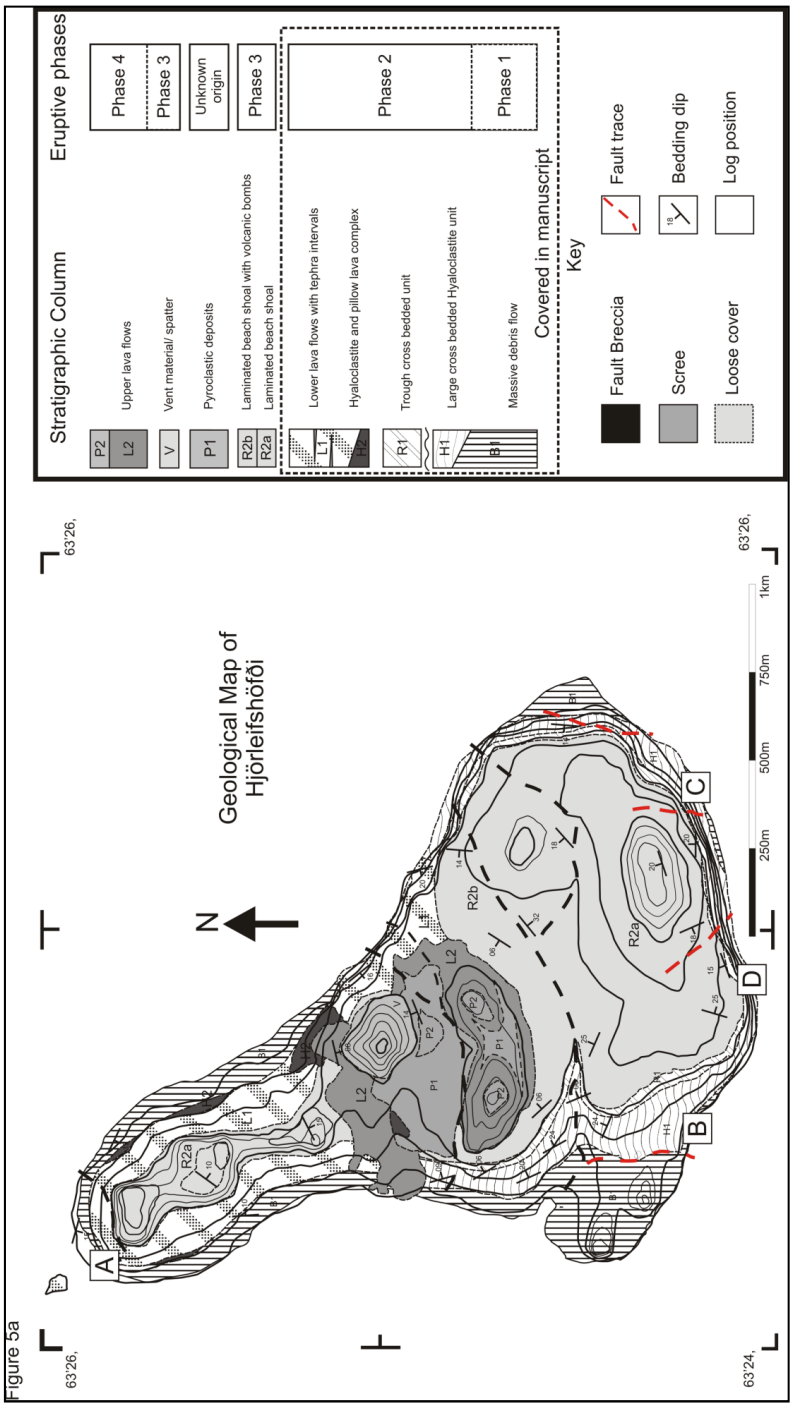

Figure 5a

Figure. 4.5. A simplified geological map of the Hjörleifshöfði outlier. The positions of the logs are indicated (and correspond with material provided in the appendix for this chapter) on the map as well as photographic examples in figure 6. Phases of construction of the edifice are referred to in the text.

Phase one documents the pre-emergent phase of Surtseyan volcanism and accompanying hyaloclastite material. Most large syn-sedimentary listric faults dissect the deposits of phase one and may have acted as pathways for magma intrusion in the shallow subsurface. Phase 2 involved continue emplacement of hyaloclastite material, reworking (beach shoaling) and the emplacement of subaerial and subaqueous lava flows, fine grained vesicular tephra, basaltic spatter and hyaloclastite breccias. This is the focus of the current manuscript and is clearly separated on the geological map (Fig. 4.5) The lower lava flows (mapped unit L1) thicken towards the north of the island suggesting lava was ponding in a large dammed crater separate from sea water influence however at the south of island abundant hyaloclastite material was been generated. This view is supported by the size and apparent displacement of the faulting on Hjörleifshöfði suggesting a much large edifice previously existed. As such the Surtseyan, hydromagmatic edifice that underlies Hjorliefshofdi is very poorly exposed. Subsequent subsidence created a shallow marine succession of reworked volcaniclastic material (Phase 3). A second phase of effusive basalt volcanism and associated pyroclastic material (fine grained, lithic-rich ignimbrites and thin (1-4m) accretionary lapilli tuff intervals) (Phase 4) cap the succession. However the affinity of the ignimbrite succession to Hjörleifshöfði is unknown. Inward dipping beds, the location of basaltic spatter and the distribution of ballistically emplaced volcanic bombs constrain the location of the vent.

Of the thirteen lithofacies are recognised in Hjörleifshöfði two are not seen at Stóri-Nupur (lithofacies VB, VStcb). However the relative volume of the syn-sedimentary to primary component varies considerably. The base of the sequence at Hjörleifshöfði is a massively bedded volcaniclastic debris flow containing abundant hyaloclastite material and hydromagmatic vesicular tephra (10–30 m thickness) (Fig. 4.6, lithofacies VB). The unit is matrix-supported and contains large clasts up to 1 m in diameter. A variety of clast types are present including pāhoehoe fragments and tephra shards supported in a matrix of rounded sideromelane shards. Channels up to 30 m wide are present within the massive volcaniclastic sequence containing large clasts up to 2 m in diameter (lithofacies HBc).

VB is overlain by foreset imbricated hyaloclastite lithofacies with large (5–10 m) cross bed sets and slump structures (Fig. 4.6, GHip). In Hjörleifshöfði the GHip

successions are considerably thicker (up to 70 m) and more abundant that in Stóri-Núpur. The hyaloclastite material is well-sorted with a coarse-grained matrix. The unit is distinctly imbricated and contains five crossbed sets (Fig. 4.6). The whole sequence exhibits slump structures normal to the direction of the crossbed propagation.

Overlying GHip is an unconformity that truncates the large crossbed sets. The overlying trough cross-bedded lithofacies (VStcb) is relatively thin (10-15 m) and well-sorted above the unconformity. There is a distinct onlap of the reworked volcaniclastic material onto the hyaloclastite successions. This could occur via uplift due to magma accumulation at depth or by reworking of the delta top by wave action. The lower cross bed sets (GHip) are truncated against the unconformity suggesting slumping took place prior to emergence.

The base of the lava flow facies consists of pillow breccias (pL) which grade laterally into more coherent lava flows. Overlying pL are coherent lava flows with small pockets of hyaloclastite material that could have resulted from localized quenching of the lava flow. Some degree of phreatomagmatic activity may have also contributed material creating very glass rich deposits (Tucker and Scott 2009) (Fig. 4.6). Spalled pillow lavas occur in a fine-grained massive to poorly laminated hyaloclastite layer at the base of the lava pile.

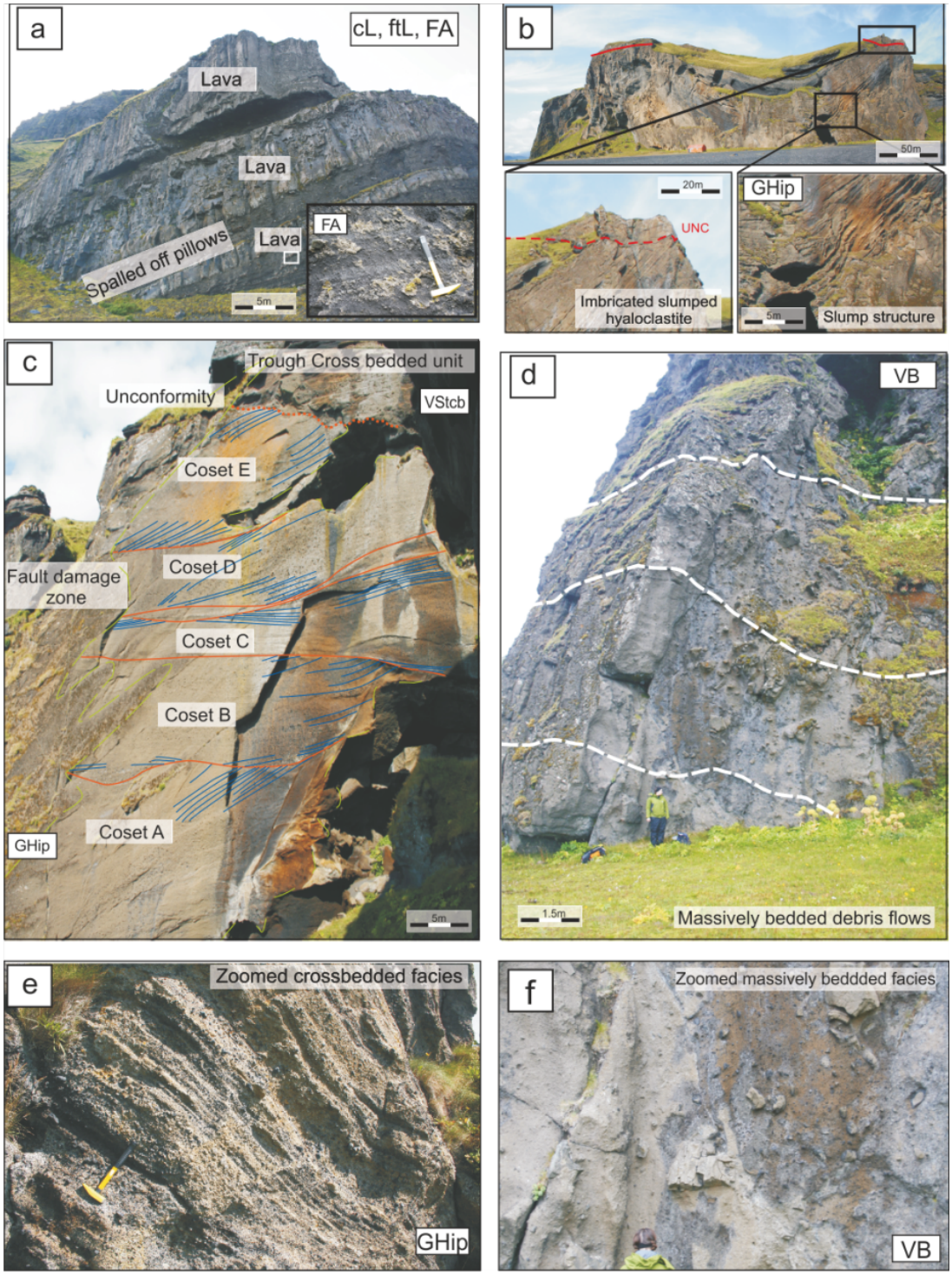

Figure. 4.6. Examples of key field examples from Hjörleifshöfði. Detailed lithofacies descriptions are in table 4.2 The lower lava sequence (L1) showing the interbedded tephra and localized pillow lava horizons between large tabular flows. b) Large slump structure in the hyaloclastite pile. c+e) Large scale crossbedding structures in the hyaloclastite pile (GHip). d+f) Underlying massive debris flow breccia containing a highly vesicular glass matrix (VB).

4.3 Discussion

A series of schematic models that describe the evolution of the Icelandic examples have been developed from the field relationships and lithofacies descriptions outlined above and in the accompanying table (Fig. 4.7). The evolution of each locality is significantly different and is reflected in the variation in lithofacies types. Each case study is controlled by the environmental setting or type of lava entry and is discussed below.

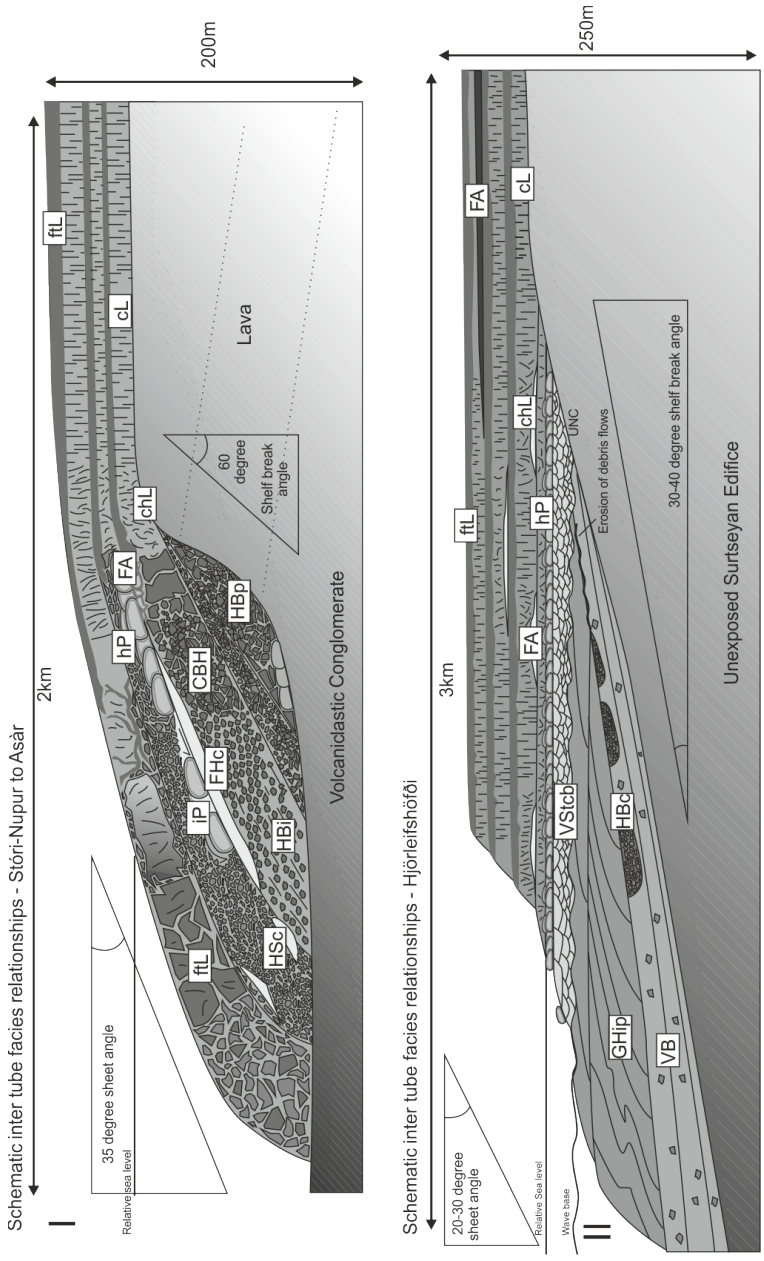

Figure. 4.7 Schematic representations of the lithofacies stacking patterns in Stóri-Nupur (I) and Hjörleifshöfði (II). All of the lithofacies correspond with a detailed description in table 4.2.

4.3.1 Stóri-Núpur to Ásàr

The hyaloclastite lithofacies at Stóri-Núpur either form small channels or unconfined forming breccia sheets. This reflects a variety of depositional processes. Crude foresets can be defined but are unlike the clear, regularly spaced pillow lava and hyaloclastite foresets observed elsewhere (e.g. Iblean Mountains, Sicily, Schimncke et al., 1997; Antarctica, Skilling, 2002). Instead, the Stóri-Núpur examples are closely associated with autobrecciated and "cube" jointed lava flows and are more analogous to thick sheets. Where the passage zone is observed the transition from lava to hyaloclastite is a gradational one rather than a sharp change as documented in examples from Greenland and Antarctica (Pedersen et al., 1998; Skilling, 2002).

Imbrication of hyaloclastite material records downslope mobilisation. This can occur due to spalling of fragmented material (e.g. Carlise, 1963; Schmincke et al., 1997) or through bench collapse (e.g. Mattox and Mangan, 1997). Isolated pillow lavas occur where ductile pinching processes operate at high angles of repose (Skilling, 2002). Periods of limited lava flux (supply to the fragmentation front), cessation of volcanism, bench collapse or selective switching off of lava supply due to migration in the point of fragmentation are denoted by small fine-grained lenticular hyaloclastite channels remobilising matrix material as fine suspension loads. These characteristics are manifested as cycles of Fhc-HSc to CBH cycles (Fig. 2b). Fhc-HSc to CBH cycles are important as the boundaries between these cycles marks breaks in larger eruptive cycles which form each hyaloclastite lobes.

When considering the lithofacies variations in hyaloclastite deposits it is important to realise how the outcrop exposure dissects a series of fragmented sets. What is clear from Stóri-Núpur is that the 3D lithofacies distribution is complex primarily due to the variable position of lava break-outs and the unequal failure of the delta front through cycles of bench collapses. A cross sectional view only represents a 2D view of the lithofacies variations at one point in the hyaloclastite delta. Subtle complexities in terms of smaller-scale lithofacies variation are often missed and the understanding of processes that are active in hyaloclastite deposits could be overlooked.

Stóri-Núpur has similarities with Hawaiian examples (Moore et al., 1973; Tribble, 1991). Both are dominated by autobrecciated lava flows which arise due to

rapid aggradation rates (e.g. in the case of the Mauna Ulu eruption covering an area of 470,000 m^2 in one year (Moore et al., 1973). This may indicate that the Stóri-Núpur Delta formed very rapidly (e.g. a few years). Like the Hawaiian examples, the Stóri-Núpur delta also contains abundant lava tubes. These can act to destabilise the delta (Mattox and Mangan, 1997) or change the locus of sedimentation. The field evidence presented here suggests that these lava tubes are active within hyaloclastite lobes surrounded by a breccia carapace. Enhanced zeolite growth in pore spaces surrounding the lava tube indicates higher temperature flushing of pore fluids. Coeval formation of lava tubes is suggested due to the rapid rate of palagonite formation within pore spaces that inhibit dominant zeolite growth away from the lava tubes. Interestingly lava tubes also exit at a variety of heights within the sequence within Stóri-Núpur (see Fig. 4.2B for relative position in sequence). Essentially the advancing lava in Stóri-Núpur is condensed into a lava tube system with a high discharge rate.

4.3.2 Hjörleifshöfði

In pre-emergent to emergent settings large subaqueous debris flows develop due to the collapse of the volcano flanks (Fornari et al., 1979; Londsdale and Baptiza 1980; Schmincke et al., 1997). These created thick (50m) underlying debris flow deposits (Fig 4.6 f, facies VB). The presence of pāhoehoe textures on large rafted blocks (Dmax-1m) suggests that at least some of this material was derived subaerially. Downslope remobilisation promotes channel development and transportation into deeper marine settings (Bergh and Sigvaldson 1991; Ollier et al., 1998; Maicher et al., 2000). At Hjörleifshöfði lithofacies VB likely represents the distally reworked portion of an earlier Surtseyan edifice (e.g. Cole et al., 2001). This is supported in part by the presence of vesicular glass indicating hydromagmatic fragmentation (Cole et al., 2001; Schopka et al., 2006).

In Hjörleifshöfði the overlying channelized hyaloclastite material (HBc) erodes into VB. Large crossbed sets are created as the material exits a submarine channel (GHip). In Hjörleifshöfði the imbricated hyaloclastite material is more clast-rich than the underlying debris flow deposits and contains abundant vesicle poor sideromelane and palagonite unlike the smectite rich debris flows (VB). The increased basalt clast abundance indicates there was an additional source of basalt

clasts. Unlike Stóri-Nupur GHip deposits are well developed indicating significant syn-sedimentary remobilisation of the hyaloclastite pile.

Lava could have been supplied via submarine flows down pre-existing channels fragmenting at depth them becoming distally reworked or from large-scale flank collapse, which remobilised fresh autobrecciated lava downslope (analogous to facies M1of White (1996), albeit with more abundant glass fragments). Simple fragmentation and progradation of the passage zone has been discounted due to the clast sorting and imbrication in very large crossbed sets indicating a sedimentary origin for this hyaloclastite deposit. Therefore the Hjörleifshöfði outlier consists of an older hyaloclastite fan to the south of the island and younger deposits associated with the central vent towards the west and north truncated by a relatively thin trough cross-bedded succession (VStcb). This truncation denotes the level of storm wave base. Material above the unconformity corresponds to material that was reworked by tidal processes or wave erosion. The overlying pillow lava lithofacies supports continual subsidence at this phase of development. The capping lava flows above the pillow lava sequence formed within a subaerial environment as indicated by oxidation of lava flow tops. Periodically the lava pile could have been subsiding as there are small pockets of hyaloclastite material between flows, which elsewhere have been attributed to low-volume shoreline explosive activity (Tucker and Scott, 2009).

In Surtseyan settings higher degrees of reworking occur due to the relative instability of a volcanoes flank. In general Hjörleifshöfði complies with Bergh and Sigvaldson's (1991) standard depositional model and White's (1996) model for a pre-emergent volcanic system. However, initial debris flows (VB) are subsequent replaced with vesicle poor glass rich, basalt clast dominated successions (GHip). Large cross bed sets (up to 5m) suggest dominant reworking of primary hyaloclastite deposits. During the deposition of the first hyaloclastite unit primary fragmentation must have been occurring in proximity to the area of deposition due to the high clast concentrations (GHip). For the secondary hyaloclastite unit (H2) fragmentation was sourced directly from younger lava flows (forming facies HBp). Therefore bedded hyaloclastite formation (GHip) at Hjörleifshöfði is controlled by uplift associated with shallow level intrusion, progressive building and destabilisation of the

hyaloclastite pile and flank failure rather than controlled small scale flow break out such as in Stóri-Nupur.

Morphologically the sequence at Hjörleifshöfði shares similarities to other hyaloclastite deposits within submarine to emergent Surtseyan systems (eg. The Iblean Mountains, Sicily, Schimncke et al 1997; Mussorgsky Peaks and Mount Greig, Antartica, Smellie and Hole 1997). All systems have complex lateral and vertical transitions into Surtseyan type deposits. This reflects the ill-defined line between phreatomagmatic and passive fragmentation. All deposits also have stratified tops that are indicative of reworking processes. Reworking maybe due to rapid subsidence (Schmincke et al., 1997) or wave erosion (see section 4.2). However Hjörleifshöfði has some major differences. There is no visible coherent pillow lava sequence underlying the main hyaloclastite section with only sporadic pillow lava sequences at the lower lava contact. This suggests that the Hjörleifshöfði succession was probably sourced from a combination of subaqueous building of the volcanic cone and local subaerial flows once the island was emergent.

A detailed understanding of the lithofacies differences could be a key to helping to determine between types in remotely studied examples. Where volcanic supply is maintained from underwater volcanism to emergent and into subaerial settings, sequences such as those at Hjörleifshöfði can grow to produce extensive lava fed delta systems. It is likely that in areas along the North Atlantic margin where large deltas are imaged (e.g. Jerram et al., 2009; Wright et al., 2012), the initial origins may have been as emergent volcanic systems. Sequences such as these could potentially be characterised by the nature of the sub-lava flow volcaniclastic sequence, such as that preserved in Hjörleifshöfði.

4.4 Synthesis

Within hyaloclastite delta settings the formation of initial debris flows creates a shallow basement angle that facilitates the progradation of foreset bedded units and creates the delta front (Fornari et al., 1979; Yamagishi, 1991; Mattox and Mangan, 1997). The initial debris flow may be controlled by variations in lava flux due to differing eruption styles (Carr and Jones, 2001) and lava viscosity (Furnes and Sturt, 1976). Basal debris flows are present in both examples from Iceland. However the

initial basalt debris flows act in different ways in each setting. In Stóri-Núpur they act as initial accommodation space filling of a steep shelf edge break in contrast to Hjörleifshöfði where a lower angle sediment bench is created allowing for further sediment to accumulate.

Initially the flow rate, cooling, crystallization and composition of the lava control the viscosity of the flow and affects the flow pathways once contact with water is made. Clinoform development can be significantly complicated by lava entry and lava tube development via bypass of the passage zone supplying material to points lower in the delta. The deposition of fragmented material can lead to different stacking patterns due to varying environmental parameters such as the local geomorphology, proximal accommodation space and wave influence.

The subsequent development of the delta is controlled mainly by gravity-driven processes (Skilling, 2002), which are modified shore face reworking (Furnes and Sturt, 1976), changes in relative sea level (Jones and Nelson, 1970) or by subsidence (Schiminkce et al., 1997) and delta front collapse (Mattox and Mangan 1997, Skilling, 2002). In emergent Surtseyan examples reworking and collapse is likely to be triggered by vent-centred uplift or growth and destabilisation of the sediment pile. For example sediment instability and vent uplift trigger slumping in Hjörleifshöfði. Hyaloclastite deposits on Hjörleifshöfði are therefore analogous to sedimentary deposits. Conversely in Stóri-Núpur either bench collapse (from wave erosion) or lava tube entry caused instability and a degree of downslope mobilisation created the complex 3D lithofacies heterogeneity.

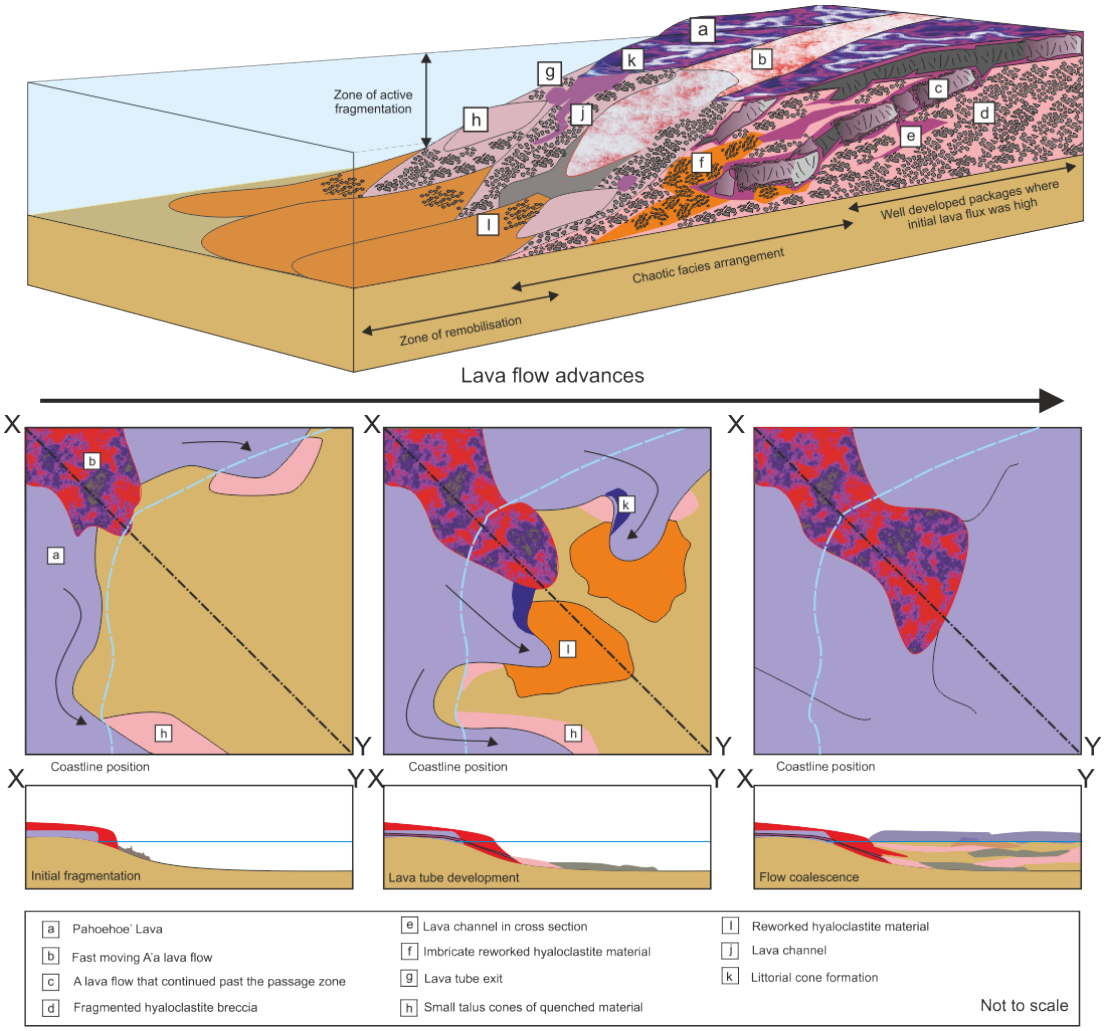

Figure. 4.8. Hyaloclastite development from localised break out and lava tube entry. This especially occurs in Stóri-Nupur not only creating the 3 large lobes present on the map but the chaotic lithofacies arrangement seen in the middle of these lobes where bedding dip directions are non-uniform. This is characteristic of primary fragmented hyaloclastite systems. In Hjörleifshöfði similar lithofacies arrangements are common in the upper sequence however waves (in the upper sequence) and syn-sedimentary reworking (in the lower sequence) act to create more uniform deposits. Note the wide zone of active fragmentation denoted by the exit of lava tubes, the development of lava channels and flow lobe entry. See text for details.

4.4.1 Passage Zone and Sea Level

The passage zone refers to a well-constrained zone of fragmentation located at palaeo-sea level height (e.g. Jones and Nelson, 1970; Porębski and Granzinski 1990; Schmincke et al., 1997; Skilling 2002; Wright et al., 2011). Fluctuations in the passage zone due to tidal changes (Furnes and Fridleifsson, 1976) and lava bench collapse through wave undercutting or lava tube destabilisation (Mattox and Mangan,

1997; Skilling, 2002, Smellie et., 2011). However the variation in passage zone height and position could also be due to changes in the locus if lava entry, the continued activity of lava tubes in the hyaloclastite pile and the type of lava flow morphology.

The development of the highly variable lithofacies relationships and in particular the chaotic 3D architecture of the Icelandic hyaloclastite examples may be explained through the processes of lava entry which in turn change the relative passage zone height (Fig. 4.8). As lava does not necessarily enter the water outright (due to cooling) it can turn and flow along the water's edge, tangentially to the axis of the main flow (Umino et al., 2006) (Fig. 4.8a and 4.9). A break-out from such a flow may subsequently act as an isolated channel or lava tube focusing fragmentation (Tribble, 1991). Once a channel system develops lava does not necessarily fragment in a well-defined zone and instead small pockets of fragmental material may be formed (Skilling, 2002; Tucker and Scott, 2009; Smellie et al., 2011). Instead large planar sheets do not develop but more localised lobes of material. Once the locus of lava entry has changed secondary "fans" of breccias develop until the top lava flows coalesce. In this situation the passage-zone shows a generalized relative sea level height however can highly variable laterally.

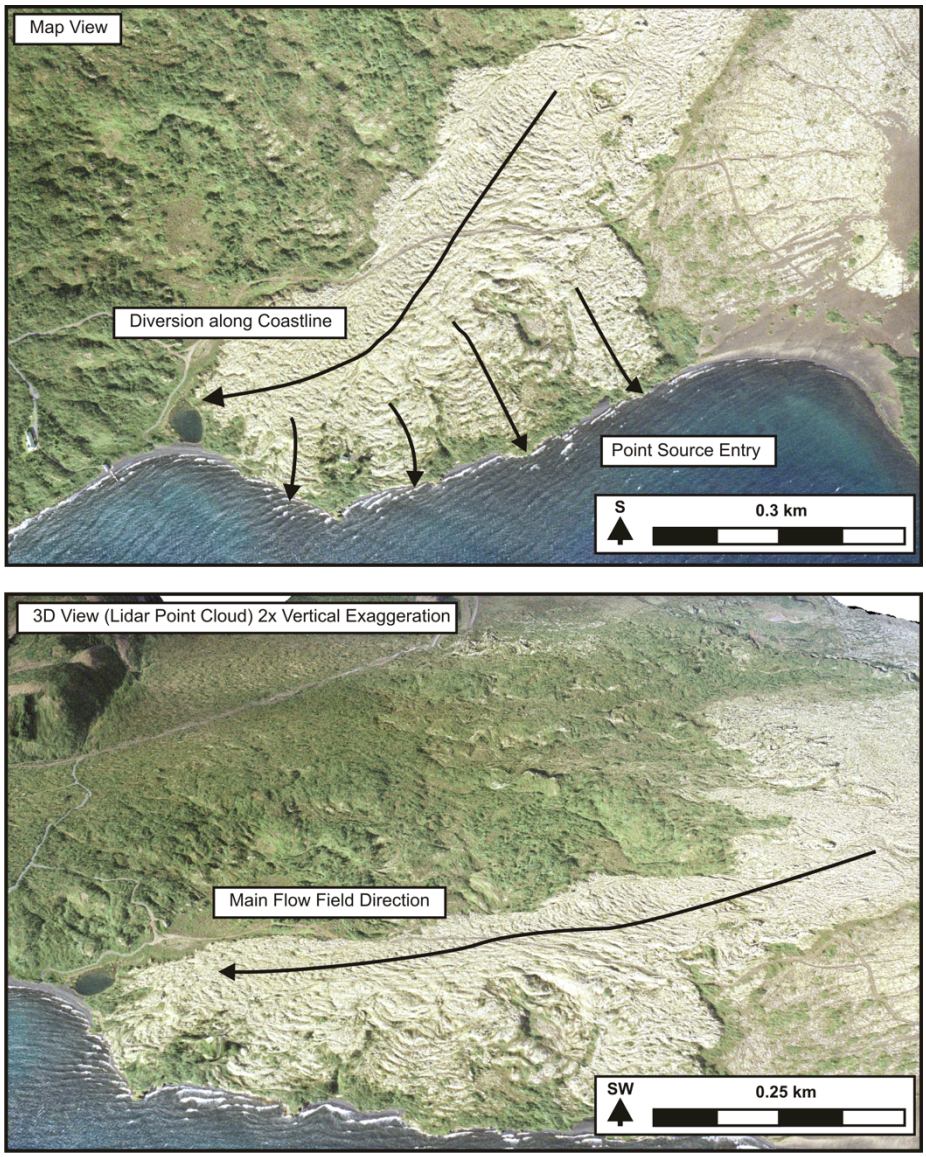

Figure 4.9. Examples from the Nesjrahraun of lava diversion at the point of lava entry. Lava therefore bypasses the shoreface and enters a series of point sources. Data from NERC Aerial Data base flight IPY-07-02.

Subsequent cooling of the lava flow promotes the formation of a lava tube network. This concentrates the flow into a number of point sources upon exit. Fragmentation is inhibited where lava tubes develop within the hyaloclastite deposit as they are surrounded in a breccia carapace. On exit from these structures hyaloclastite material can then form much below the water level at the time of eruption. The fragmentation level is therefore only indicative of the position of the

lava tube height and not the water level. Where pressure in the lava tube builds phreatomagmatism may occur creating littoral cones and bubble burst fragments due to the ingress of water (e.g. Jurado-Chichay and Roland, 1996). Alternatively the position or draining of these lava tubes promotes bench collapse that can be catastrophic (e.g. Mattox and Mangan, 1997) or piece meal collapses (USGS Hawaiian Volcano Observatory video footage) creating a relative displacement in the height of the passage zone.

The position of wave base, the susceptibility to wave action and the rate of progradation also affect the preservation of the passage zone. A planar passage zone can be produced in emergent settings due to constant collapse or reworking of the hyaloclastite material at wave base. The degree of wave action is reduced in sheltered bays and lava is more likely to enter water as a coherent flow or produce rafted flow breccias as seen in Stóri-Núpur. Interestingly the rapid addition of material to the hyaloclastite apron soon after a bench collapse is likely to create steps in the passage zone. This is a phenomenon, which is observed in all examples on both outcrop and seismic scale (e.g. Skilling, 2002; Wright et al., 2012). Therefore it can become difficult to separate a sea level induced change from one caused by wave reworking processes.

Changes in lava viscosity due to cooling and groundmass crystallization (Cashman et al., 1999) can lead to differences in flow morphology. On entry into water the type of flow morphology will either promote or inhibit fragmentation. Pāhoehoe flows may cool on entry and cause small breakouts that promote lava entry in channels or lava tubes. ‘A‘ā flows plough into the water creating an elongate tongue of lava (e.g. Smellie et al., 2011 and Stevenson et al., 2012). Lava flow morphology controls lava water entry especially at the water interface and can act to either destabilise the delta or act as an anchor for pāhoehoe coalesce (Fig. 4.8).

The processes outlined above mean that there is a ill-defined passage zones in Stóri-Núpur. In Hjörleifshöfði the interaction with waves has created a more uniform zone (see section 4.2). The passage zone in 3D is a complex mass of lava breakouts and lava tubes that can occur at different levels in the lava delta simultaneously (Fig. 4.8). This is unlike observations in Antarctica (e.g. Skilling 2002) where the passage zone is a near continuous horizontal surface. Stóri-Núpur may then reflect an end member in hyaloclastite development. In this case the competition of lava flux,

accommodation space and coastline sinuosity are key factors that control hyaloclastite delta morphology. Lava flux is defined as the relative volume reaching the delta front at any one time. For example, in flood basalt volcanism the fragmentation front develops rapidly and may prograde out into a basin due to the coalescence of pāhoehoe flows into larger inflated sheets (Self et al., 1998). In this case the lava/hyaloclastite contact as defined by the passage zone provides a good proxy for relative sea level as sheet-like fragmentation is more likely to occur (analogous to clinoform packages; Wright et al., 2012). Sheet-like hyaloclastite deposits develop in examples where accommodation space is limited, yet lava flux is high (e.g. Tucker and Scott, 2009). Hyaloclastite deposits formed at low lava fluxes, increased accommodation space, high slope angles and extreme coastline sinuosity (e.g. Iceland) form more chaotic deposits. We suggest that the use of the passage zone as a proxy for a palaeo-shoreline in areas like outlined above, can be compromised. However, at basin scales the passage zone may still be a relatively good indicator of available accommodation space.

4.4.2 Importance of Wave/Tidal Interaction

Wave interaction plays a critical role in the development of hyaloclastite systems. Undercutting of non-lithified hyaloclastite material can lead to collapse producing syn-sedimentary hyaloclastite deposits (Porębski and Gradzinski, 1990; Mattox and Mangan, 1997; Smellie and Hole, 1997). Tidal changes can also affect the position lava fragments due to tidal reach and the coherency of the passage zone due to long and short wave length cycles of rising and falling sea level (Furnes and Surt, 1976). Where wave interaction is limited such as in lacustrine settings pillow lava formation is common (e.g. the Columbia River Flood Basalts, USA, Fuller, 1931a; Wells et al., 2009). In remote studies (bathymetric reconstruction of Pico Island, Azores) the coherency of hyaloclastite deposits is questioned and surf related erosion of hyaloclastite material is an invoked mechanism for shelf sediment deposition (Mitchell et al., 2008). However preserved interbedded lava and hyaloclastite sequences on Mauana Loa, Hawaii (Lipman and Moore, 1996) and in the HSDP Phase II core (Seaman et al., 2000) suggest some hyaloclastite deposits can resist wave erosion. Rapid post depositional subsidence could also limit the

effect of wave action by “lowering” more coherent lava into the surf zone. Indeed rapid subsidence has been documented in hyaloclastite systems (Schmincke et al., 1997).

The examples of hyaloclastite deposits presented in this manuscript have contrasting depositional histories and lithofacies variation. In Stóri-Nupur the passage zone is ill-defined in it lateral three-dimension extent suggests that wave action is limited especially pre-lithification. In contrast at Hjörleifshöfði the passage zone is more planar although lava flows do still enter the water. In this case Hjörleifshöfði, as part of an exposed isolated volcanic island to strong wave interaction could have created a more planar passage zone (e.g. lithofacies VStcb).

4.4.3 Comparison to Alluvial Deltas

Lava-fed deltas are thought to be similar to coarse-grained steeply bedded Gilbert-type or Gilbert modified deltas (Skilling 2002; Wright et al., 2011). They are best compared with “type-A” feeder systems which contain a high percentage of bedload sediment (Postma, 1990; Skilling, 2002). One of the most important differences is that clasts in lava-fed deltas are not carried by an effluent force (e.g. a river) (Skilling, 2002). Lava-fed deltas can be analogous to subaqueous debris cones or talus cones (Skilling, 2002).

However this study shows that hyaloclastite delta deposits can form from dominant primary fragmentation (Stóri-Núpur) and dominant syn-sedimentary reworking (Hjörleifshöfði). Unlike source or meander switching in alluvial deltas that occurs over a number of years, source switching can occur quickly over weeks or months and possibly in one flow event, especially if the lava flow morphology changes or rapid inflation occurs. Consequently it may be better not to consider large hyaloclastite sequences in terms of alluvial processes, but instead as a function waxing and waning cycles in eruptive episodes whereby the recorded hyaloclastite unit is a product of not one lava flow but one depositional event supllied by a number of lava flows.

Lava flows do not enter the water as sheets and instead enter at a point source in low effusivity examples (e.g. Stóri-Núpur). Due to numerous breakouts, bypass of lava flows through the passage zone and rapid tube focusing at the delta front the creation of a uniform fan is difficult. The stacking of lava flows is also complicated

by the flow of material through lava tubes or the flow core and simple aggradation does not occur. Both processes complicate stacking patterns and/or promote slumping. As a result we might consider primary hyaloclastite deposits with limited reworking as being separate to alluvial deltas, especially when sequence aggradation processes are susceptible to eruptive episodes. However those deposits such as Hjörleifshöfði where dominated by syn-sedimentary reworking should be considered similar to their sedimentary counterparts.

4.5 Conclusions

Field data from Stóri-Núpur and Hjörleifshöfði provides additional constraints on lava delta formation in predominantly basaltic systems. Documented here are hyaloclastite deposits characterised by thick, laterally extensive successions with poor lithofacies correlation over large areas. Both examples show distinct hyaloclastite depositional profiles reflecting localised extrusion pathways and syn-sediment reworking controlling the 3D lithofacies architecture. Small lava breakouts, variations in lava flow morphology and lava tube development act to produce complex 3D lithofacies heterogeneities prior to any downslope remobilisation. However, if the lava flux is sufficiently high, pāhoehoe sheets can coalescence into a large inflated sheet and sheet-like fragmentation can promote clinoform development. Conversely, if lava flux is high yet the available accommodation space is limited then more sheet-like flows will develop. Additionally shoreline sinuosity acts to promote hyaloclastite lobe coalesce, which can happen over both small- and large-scales to complicate the 3D lithofacies architecture. In Surtseyan settings, reworking is promoted due to the inherent instability of the volcano flank leading to mass movement and slump structures. Distinction should be made between hyaloclastite deposits of syn-sedimentary deposition and those dominated by primary fragmentation and near shore deposition. Observations from Stóri-Núpur suggest only syn-sedimentary hyaloclastite systems can be compared to alluvial systems whereas primary hyaloclastite deposits are more susceptible to changes in eruptive episodes and lava supply.

5

5. THE GEOLOGY AND EVOLUTION OF THE HJÖRLEIFSHÖFÐI OUTLIER, ICELAND116

CHAPTER FIGURES AND TABLES

5. The Geology and Evolution of the Hjörleifshöfði Outlier, Iceland

Chapter Summary

Hjörleifshöfði is a small (~4 km^2) isolated Quaternary volcanic outlier in southern Iceland that provides an excellent exposure of a Surtseyan volcano. It sits in a large sandur plain formed by glacier melt water outwash from late Holocene subglacial activity at Katla volcano: Aggradation of outwash sediments turned Hjörleifshöfði from an island into part of the mainland. Detailed field mapping and sampling of Hjörleifshöfði has allowed the recognition of thirteen lithofacies and five depositional/reworking phases. Hjörleifshöfði now is what remains of a small slice of an earlier emergent island. Stage one represents the pre-emergent phase of Surtseyan volcanism and is characterized by submarine cone building and hyaloclastite deposition. Large syn-sedimentary listric faults dissect stage 1 deposits and are inferred to result from edifice collapse. Phase A involved cone building and continued emplacement of hyaloclastite material. Large faults probably denote the crater rim of a larger edifice. Phase AR involves reworking of material in sub to supralittoral conditions. Phase B occurs only to the north of large listric normal faults emplacing of subaerial lava flows, hyaloclastite and fine-grained vesicular tephra. Phase B lava flows thicken northwards suggesting ponding in a large dammed crater separated from the sea. Continued subsidence resulted in the deposition of a shallow marine succession of reworked volcaniclastic material (Phase C). A distinct red fine-grained, lithic-rich (with partially quenched fragments) ignimbrite succession fills topographic lows (in phase C). Phase D consists of a parasitc vent formation and localized lava emplacement with marine reworking of volcaniclastic material along the southern margin. A thin (~1 m) accretionary lapilli-bearing tuff layer caps the (Phase D) succession. Inward-dipping beds, the location of basaltic spatter and the distribution of ballistically emplaced bombs constrain the location of the vent that supplied the early and late lava flows. The deposits of each stage have been analyzed for major and trace elements to fingerprint the source of the basalt clasts in hyaloclastite material and the origin of silicic rocks, which share remarkably similar chemistry to the Sólhiemar Ignimbrite. This dates the last stage of effusive basalt

volcanism on Hjörleifshöfði to < 12,383 C14 years BP. Hjörleifshöfði provides an excellent exposure of a submarine to subaerial volcanic system, and is part of a series of small volcanic centers around the flanks of the Katla and Eyjafjallajökull volcanoes.

5.1 Introduction

The Hjörleifshöfði outlier is the remains of a small stranded volcanic island (4 km^2), in southern Iceland, composed of volcanic, pyroclastic and hydromagmatic rocks (including hyaloclastite) and volcaniclastic sediments (Fig. 5.1). It is one of a number of small volcanic mounds (Pétursey, Hafursey and Dryhólaey) that surround the Katla and Eyjafjallajökull volcanoes. Palaeo-magnetic studies indicate that it formed during the last magnetic reversal (c. 800 ka, Jarðfræikort Geological Mapping, 1:600,000 scale, 2009). Due to its proximity to the Katla volcano and ice cap, and due to limited age constraints Hjörleifshöfði was considered either a subglacial volcano (Hjaltadottir et al., 2008; Mountney et al., 2008; Russel et al., 2010) or a submarine volcano (Thordarson et al., 2008). The recognition of hyaloclastite deposits and surtseyan deposits along its southern margin supports the latter hypothesis that Hjörleifshöfði is the remnants of a submarine Surtseyan volcano although this will investigated further within this chapter (Watton et al., 2013).

Hjörleifshöfði provides superb and rare cross-sections through a submarine-subaerial volcano and therefore may be useful in helping to interpret submarine volcanoes and volcanic rocks that have been imaged solely using subsurface datasets (e.g., those offshore in the Faroe-Shetland Basin, e.g. Richie and Hitchen, 1996; Archer et al., 2005)

This chapter outlines the geology and volcanic evolution of Hjörleifshöfði in order to examine lateral and vertical variations in hyaloclastite deposits associated with Surtseyan volcanism and explores their relationships with other volcanic products. This chapter builds on models of the hyaloclastite systems outlined in Chapter 4.

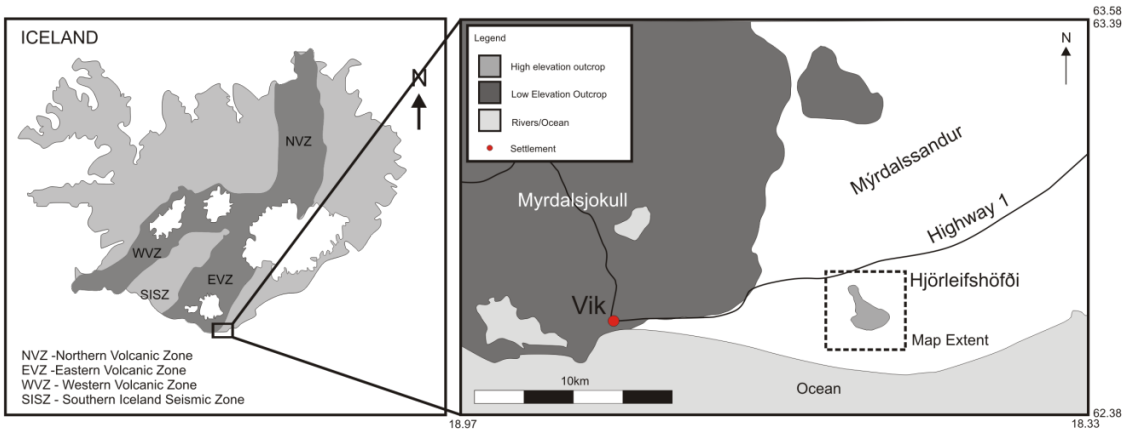

Figure 5.1. Location map of Hjörleifshöfði including outlined mapped field area as well as the position of the Mýrdalsjökull glacier and nearby town of Vík.

5.2 Surtseyan Volcanism

The eruptive mechanisms, volcanic products and morphology of Surtseyan volcanoes have been studied in some detail (cf. Thorarinsson, 1964, 1965, 1966, 1968; Moore, 1967; Waters and Fisher, 1971; Wohletz, 1983, 1986; Kokelaar 1983, 1986; Sohn 1994; Cas et al., 1989; Sohn and Chough, 1989, 1992, 1993; Skilling, 194; White, 1996; Zimanowski et al., 1997; Morrissey et al., 2000; White and Houghton, 2000; Cole et al., 2001; Sohn and Park, 2005; Stewart and McPhie, 2006; Sorrentino et al., 2011; Krajl, 2012; Mitchell et al., 2012; Sohn et al., 2012). Surtseyan edifices develop due to localized volcanic activity initiated in marine settings. Surtseyan edifices build from the sea floor and are initially dominated by pillow lavas (Cas et al., 1989). Subsequently. As they shoal cones of clastic material start to form until they become subaerial(Kokelaar, 1986). Surtseyan eruptions evolve as a series of monogenetic eruptions, often switching forming numerous satellite side vents (Thorarinsson, 1967; Jakobsson and Moore, 1982; Kokelaar and Durant, 1983; Maicher, 2003) that can be widely spaced in time (Verwoerd and Chevallier, 1987).

Once Surtseyan eruptions become emergent two characteristic and distinct eruption styles control the dispersal of tephra. Rooster tail events originate from multiple shallow explosions in the vent area where there is intermittent seawater access over timescales of seconds to minutes. Each explosion produces sub-horizontal jets reaching typical distances and heights of <1000 m (Thorarinsson,

1965; Cole et al., 2001, Nemeth et al., 2006, Vaugh and Webley, 2010). Continuous uprush events occur when the vent becomes isolated from seawater over longer periods of time (10s of minutes to hours) leading to more powerful, efficient expulsion of material. They occur due to explosions located deeper in the vent and produce high (up to 2 km) tephra eruption columns. Convective circulation means columns can reach 12 km in height (Thorarinsson et al., 1964). These processes lead to the formation of a tuff cone that typifies Surtseyan edifices (Mitchell et al., 2012).

Upon emergence, if water is blocked from the vent, lavas can accumulate at the base of lava fountains. If lava reaches the coastline it can passively fragment to hyaloclastite and form prograding hyaloclastite deltas that enlarge the volcanic edifice (e.g. Schmincke et al., 1997 and Watton et al., 2013). Intense wave erosion means that the preservation potential of the supra-wave base parts of Surtseyan volcanoes is low (Kokelaar et al., 1983). However this has been found out to relate to edifice size and magma storage depth within the edifice, which is hypothesised to control large-scale flank failure (Mitchell et al., 2012). Hyaloclastite can be deposited on the flanks of a Surtseyan edifice either from primary fragmentation of a lava flow (Schmincke et al., 1997) or as chaotic beds reworked by sedimentary processes (Watton et al., 2013).

Surtseyan volcanism is driven by explosive magma-water interaction—a physical processes somewhat analogous to Molten Fuel-Coolant Interaction (MCFI) in nuclear reactors (cf. Wohletz, 1986; White, 1996; Hooten and Ort, 2002; Wohletz, 2002). MCFI-type processes are thought to drive hydro-magmatic fragmentation and are dependent on the magma-to-water mass ratio, which can vary widely and rapidly during an eruption. Mechanisms that contribute to clastic particles in surtseyan deposits are discussed in Table 5.1. However other processes can also aid fragmentation such as magma velocity at the vent and volatile content. This leads to complex arrangements of deposits in time and space, which are further complicated by variations in the dispersal of tephra and lava due to interactions with the atmosphere and seawater. (e.g. Wohletz, 1986; Kokelaar, 1986; Morrissey et al., 2000; White and Houghton 2001; Mastin et al. 2009).

Table 5.1

Affinity	Fragmentation Type	Description	Key Locations	Key References
Passive Fragmentation Processes	***Quench Fragmentation***	Lava quenches rapidly to form glass (sideromelane). Quenching rate is susceptible to changes in lava viscosity, eruption rate and volatile content. This type of quenching occurs after material has been erupted hence is not a true MCFI. Disaggregation of pillow rinds or lava entering in discrete channels is the main source of quenched material.	Initial stages of emergent volcanism, Quenching of "Fire fountaining" upon water re-entry or pillow lava formation on the sea floor.	Carlisle, 1963, Moore et al., 1973; Lonsdale and Baptiza, 1980; Fisher and Schminkce, 1984; Aalto, 1986; Kokelaar, 1986; Wolhetz 1986; Mattox and Mangan, 1997; Schmincke et al., 1997; Wilding et al., 2000; Wolhetz 2002; Head and Wilson, 2003.
	Cooling Contraction Granulation	Cooling contraction occurs where steam explosively is suppressed. Cooling a droplet of magma causes a temperature gradient between its rim and the centre. Deformation in the outer layer initially is viscous but becomes rapidly becomes rigid. The inner layer will contract more hence fragmentation occurs.		
	Frictional Break-up (Autobrecciation)	Shearing between the top of lava flows upon water entry or a column of ejected material an sea water can cause break up. Viscous pāhoehoe or 'A'ā flows with a solidified crust become further fragmented through inflation. Also can occur between the quenched outer surface of pillow lavas as they prograde out in small lobes Fragmented material can be transferred downslope by gravity.	Where the Surtseyan volcano becomes emergenet and subaerial lava flows begin to develop.	Yamagishi, 1987; Self et al., 1998; Jurado-Chichay and Rowland, 1995.
	Ductile Pinching	Gravity and angle of repose causes pillows to elongate, thin and subsequently detach created "spalled" pillows in a hyaloclastite matrix	Edifice margin at high to critical angles of repose.	Mattox and Mangan 1997; Skilling, 2002.
Active Phreatomagmatic Processes(MCFI)	***Film Collapse***	Drives initial magma fragmentation at shallow water depths. A fine film of super-heated vapour that surrounds the magma upon water contact (Leidenfrost film). Collapse of the vapour film imparts pressure waves on the lava producing blocky and splinter sized fragments. The amount of fragmentation varies in relation to viscosity of the lava and surface tension or the film.	Common when confinement occurs e.g. through narrow lava channels upon water entry. Seen during pillow lava formation as large	Mills, 1984; Kokelaar, 1986; Morrisey et al., 2010; Skilling, 2002; Waichel et al., 2007.

			bangs on video footage.	
	Steam Confinement/ Contact Steam Fragmentation	Violent explosive activity in a positive feedback mechanism develops where localized phreatomagmatic eruptions cause a chain reaction exploiting fractures. Progressive granulation can form vast sheets as the fragmentation process moves away from its source. Viscosity is thought to be a dominant control on the fragmentation process.	Cone collapse, Lava ponding along coastline. Exploitation of fractures in pillow lavas.	Jones and Nelson, 1970; Furnes and Sturt, 1976; Moore et al., 1973; Lonsdale and Baptiza 1980; Skilling, 2002; Head and Wilson, 2003.
	Large Scale Flank Collapse	Flank collapse causes debris flows and subsequent resedimentation in deep marine settings. Collapse occurs due edifice size and position of underlying magma chamber. Collapse is also a function of the present clay mineral phases, high sedimentation rates and changing sea level.	On the flank of volcanic edifices for destabilisation of material	Bergh and Sigvaldason, 1991; White 1996, Yokose and Lipman, 2004; Ollier et al., 1998; Schiffman et al., 2006; Thompson et al., 2008; Mitchell, 2012.

Table 5.1. Mechanism of clastic material generation in surteyan volcanic systems

Fragmentation, eruption, transport and deposition process are interlinked and produce pyroclasts with a wide range of grain-sizes and vesicularities. Due to the wide variety of eruptive processes it can be difficult to discriminate fragmented material of hyaloclastite (passive disaggregation processes) from that of phreatomagmatic (active) fragmentation. Table 4.1 in Chapter 4 summarizes the parameters used to separate hyaloclastite and phreatomagmatic deposits in the Hjörleifshöfði exposure.

5.3 Methodology and Approach

Detailed 1:2500 scale geologic mapping and lithological logging of the Hjörleifshöfði rocks was carried out in the summer of 2010. Thirty-six samples were collected for XRF analysis. The samples represented each of the units in Hjörleifshöfði as well as clasts separated from the hyaloclastite material. Only large clasts were selected for separation, which allowed sawing so no matrix was analysed. Samples were then cleaned in ethanol and air dried before crushing. Crushing of the

samples for XRF analysis was performed in Durham University first using an anvil press then powdered in agate vials. Major and trace element analysis was carried out at the University of Edinburgh. Methodology of the XRF process has been provided by the University of Edinburgh and summarized in the analytical technique section (Chapter 2). Analytical detection error is provided in the appendices.

5.4 Outline of Geology and Introduction to Lithofacies

The Hjörleifshöfði volcano is broadly triangular in plan view (Fig. 5.2). Holocene subglacial volcanic activity at Katla volcano has added sediment to the existing coastline making Hjörleifshöfði now part of the Icelandic mainland. The 1912 jökulhlaup likely contributed most of this additional material. Erosional processes, potentially exacerbated by jökulhlaups, have created easily accessible and spectacular cliff sections. Limited vegetation means both lateral and vertical exposure is excellent. The southern end of the outcrop has good exposure with cliffs up to 160 m high. Small cliffs up to 40 m high surround the rest of the volcano. Gullies through the cliffs allow 3D sections through the stratigraphy.

The geology of Hjörleifshöfði has been split into five phases that represent four distinct depositional and one reworking event in the history of the volcano. (Table 5.2). Phase B and C are coeval to Phase AR but represent deposition on the northern and southern margin of the volcano respectively. The relationship between mapped units, lithofacies and phases are represented well in table 5.3 and figure 5.12. Mapped units (e.g. R1, Fig. 5.2), each unit is comprised of either one or a number of lithofacies (e.g. VStcb, Table 5.3) which correspond to a depositional phase (e.g. AR, Table 5.2).

Table 5.2

Units	*Dominant Rock Type*	*Depositional / Reworking Phase*
P2	Volcaniclastic	D
V, L2	Effusive	D
P1, R2a, R2b	Volcaniclastic	C Coeval to AR/C
L1, H2	Effusive / Breccia	B Coeval to AR/C
R1	Breccia	AR

B1,H1	Breccia	A

Table 5.2 Mapped units, dominant rock types and depositional / reworking events used to construct the description and interpretation of the Hjörleifshöfði volcano.

Geographically the succession on Hjörleifshöfði can be divided into north and south, separated by a large NE-SW trending fault (Fig. 5.2) The southern end of the outcrop is composed of volcanic breccias of phreatomagmatic and hyaloclastite origin (Phase A, Fig. 5.2). An undulose unconformity separates hyaloclastite from volcaniclastic sandstones and breccias (Phase AR). Phase B is missing at the southern end of the outcrop which instead sees the accumulation of pyroclastic material (Phase C, mapped unit P1). The top of the outcrop plateaus-out to elevation gains of < 30 m except for the central dome like structure, which is comprised of vent agglomerate and spatter (Phase D, mapped unit V). The dome-like structure is surrounded on both sides by lava flows relating to the vent (mapped unit L2), which are in turned capped by P2 phase deposits. The L2 lava flows cover much of the underlying stratigraphy on the western side of the outcrop, suggesting indicating a potentially significant time gap prior to their emplacement.

The northern end of the outcrop is underlain by volcanic breccias of Phase A but the greater thickness is composed of basaltic lava flows, which pinch out towards the south (Phase B, Cross section A to A^{I}). Phase C volcaniclastic deposits (mapped unit R2a/b) occur as a thin drape on the northern part of the outcrop and increase in thickness towards the south. Lava flows (mapped unit L2) of Phase D are not present in the north, but mapped unit P2 deposits cover the entire outcrop.

The deposits of each phase are summarized in the following section (5.4.1). Each phase is composed on a number of mapped units that, in turn is divided into a number of lithofacies (section 5.7.1, table 5.3).

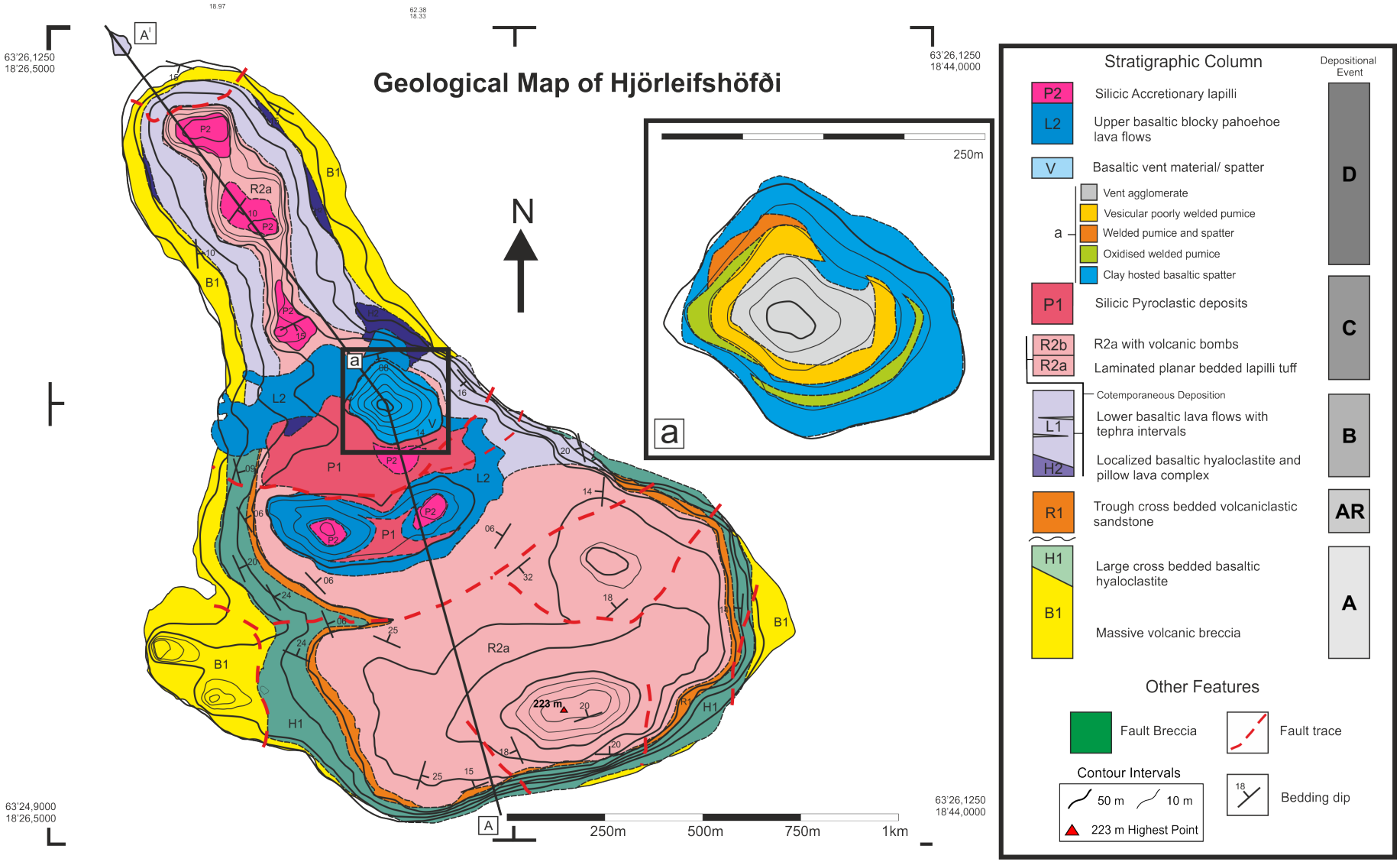
Geological Map of Hjörleifshöfði
63°26,1250
18°26,5000
63°26,1250
18°44,0000
63°24,9000
18°26,5000
63°26,1250
18°44,0000
N
250m
a
A
A'
P2
R2a
B1
L2
P1
V
H1
R1
223 m
250m
500m
750m
1km
Stratigraphic Column
Depositional Event
Silicic Accretionary lapilli
Upper basaltic blocky pahoehoe lava flows
Basaltic vent material/ spatter
Vent agglomerate
Vesicular poorly welded pumice
Welded pumice and spatter
Oxidised welded pumice
Clay hosted basaltic spatter
Silicic Pyroclastic deposits
R2a with volcanic bombs
Laminated planar bedded lapilli tuff
Cotemporaneous Deposition
Lower basaltic lava flows with tephra intervals
Localized basaltic hyaloclastite and pillow lava complex
Trough cross bedded volcaniclastic sandstone
Large cross bedded basaltic hyaloclastite
Massive volcanic breccia
D
C
B
AR
A
Other Features
Fault Breccia
Fault trace
Contour Intervals
50 m
10 m
223 m Highest Point
Bedding dip

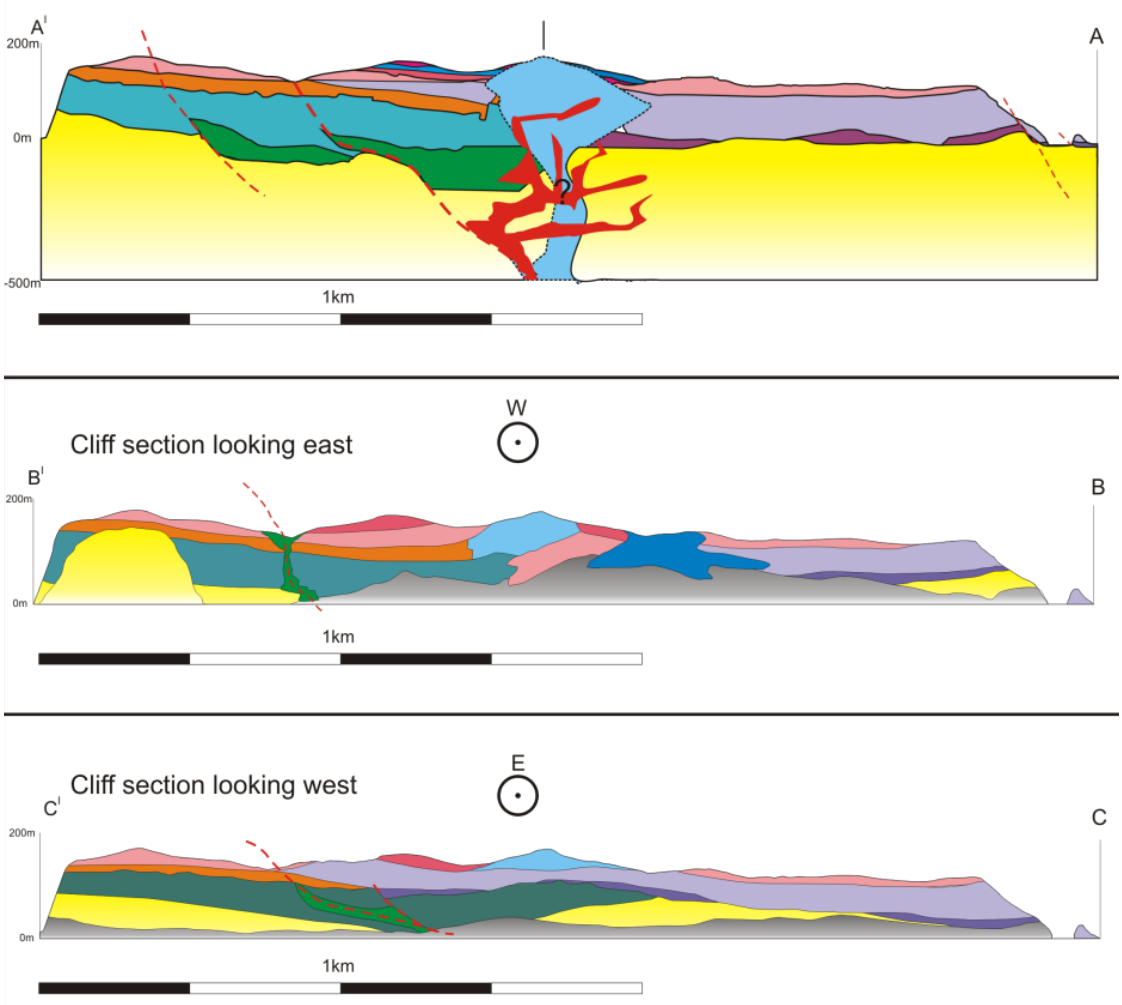

Fig.5.2 Geological map, cross section and cliff section views of the Hjörleifshöfði outcrop. Please see section 5.3 for details.

Each lithofacies is summarized in Table 5.3. This chapter has adopted a classification method used by McPhie et al., (1993), Skilling (2009) and in Chapter 4 whereby lithofacies are divided into coherent lava flows, volcaniclastic deposits, and pyroclastic deposits. Products of hydro-fragmentation are divided on the basis of grain size fine granular hyaloclastite=GH (2–4mm) and hyaloclastite breccia=HB (4–64 mm). Products of hydro-fragmentation are covered in detail in Chapter 4 and Watton et al. (2013). Volcano-sedimentary lithofacies are divided using sedimentary grain sizes VB=volcanic breccias, VS= volcaniclastic sandstone. Both hydro-fragmented and volcano-sedimentary deposits display clear evidence of sedimentary processes and so a sedimentary grain size terminology has been invoked. Units that contain high silica contents use the classification scheme adopted by McPhie et al

1993 for volcanogenic rocks where by fine grained unconsolidated deposits assumed to be of fallout origin are termed

Fourteen lithofacies can be recognised in eleven depositional units on Hjörleifshöfði. A summary of lithofacies descriptions and interpretation has been provided in Table 5.3. Lithofacies descriptions for the lower hyaloclastite and sequence have been modified and simplified from Watton et al. (2013). The reader is asked to refer to chapter 4 for aspects of hyaloclastite deposition and discussion.

Table 5.3

Code From paper	*Lithofacies*	*Description*	*Association*	*Mapped unit*	*Depositional Unit*	*Interpretation*	*Figure Number*
D	Intrusive	Intrusive dolerite composition dyke bodies cutting bedding within VB. Finely crystalline, phenocrysyt absent. Margins of the dyke quenched.	Intrusive into VB	Dykes	N/A	Geochemical affinity suggests relation to side vent formation indicating magma intrusion into crater rim.	**Fig. 5. 22**
VB	Massive matrix supported Breccia	Massively bedded (up to 10m) matrix supported bimodal breccia unit; boulders Dmax. 80 cm. Clasts components; ropey pahoehoe basalt fragments, highly vesicular basalt blocks and tephra. Bedding highly underlose matrix vesicular palagonitized glass, secondary calcite and zeolite.	VB/GHip /hP	B1	A	Phreatomagmatic cone build up from rooster tail events and subsequent downslope mass movement. Represents the distal portion of the the pre-existing edifice. Interbed zones contain numerous incised channels, which indicate sourcing from an effluent force.	**Fig. 5.3, 5.4 C & E, 5.5**
GHip	Imbricated hyaloclastite breccia	4–8m imbricate cross bed sets, fining up; 50–80 cm to c.2–10 cm clasts. Matrix well sorted medium to coarse grained sideromelane glass with some tephra (highly vesicular up to 1cm diameter). Tephra easily recognisable due to rapid palagonite formation and high vesicularity.	GHip/VB	H1	A	High angle cross bedding could represent high energy Gilbert style delta deposition from large scale flank collapses of a hyaloclastite pile. Supported by the presence slump structures (cf. Watton et al. 2013). Geochemically linked to L1 lavas.	**Fig. 5.3, 5.4 A, B, C, 5.5**
HBp	Massive Hyaloclastite	Massively bedded, localized, 2–3m thick lobes. angular clasts Dmax. 40 cm, partially matrix supported with a coarse but well sorted sideromelane matrix Closely associated with late sequence L1 lava flows.	HBp,tL	H2	B	Late stage lava water interaction as the L1 lava piles build and flows over saturated sediment of the dammed crater floor partially forming thin hyaloclastite deposits. In L2 lava hyaloclastite forms a the base of lava flows as it flows on to saturated Vstcb.	**Fig. 5.6 B**

VStcb	Cross stratified volcanic breccia	Clasts are composed solely from angular to subangular basalt. Clasts can be smoothed. The matrix is a mix of sideromelane glass, tephra and locally derived pyroclastic material. Palagonite cement zeolite usually absent. VStcb unconformably overlies GHip.	VStcb/VStb	R1	AR	Erosion unconformity, changing environmental conditions. Shore face reworking accompanied by the influx of new material leads to rounding of the basalt clasts. Likely deposited in a high energy shoreface environment	**Fig. 5.3, 5.6 E,**
VStb	Thinly bedded volcanic sandstone	Horizontally bedded matrix supported occasional basalt clasts. Matrix of fine to medium grained rounded volcanic (tephra and basalt) particles. R2a bomb sags are absent bomb sags present = R2b.	VStcb/VStb	R2a/ R2b	C	Marine shoaling of tephra fall and phreatomagmatically derived material, highly palagonitised. Bombs derived from side vent during final stage of effusive activity.	**Fig. 5.6 D&G**
vCA	Tephra	Planar or low angle cross-laminated, coarse grained, highly vesicular glassy fragments. Homogenous ground mass of glass fragment. Sharp bubble walls. High degrees of palagonite formation.	tl, hP	L2	B	Rooster tail events creating thin homogenous tephra interbeds in L1 lavas	**Fig. 5.12 D**
LTth	Thickly bedded tuff with clasts	Welded (upper), non-welded (lower) P1 interval. Fiamme streaked and elongate glass and vesicles. Basal unit contains clasts up to 6cm. Two main types of lithic, basalt fragments and welded silicic. Small quenched basalt lithics are more abundant at the base of the sequence. Inverse grading. Fiamme flattened in welded unit, lithics remain prominent. Gas escape pipes and assimilated clasts also present.	LTth	P1	C	Possible Ignimbrite flow with poor vertical sequence exposure. Quenching of small basalt lithics suggests water interaction especially at the flow base. Evidence of hot emhacement (gas escape pipes), Geochemically separate from vent and lavas, potential Sólhiemer Ignimbrite origin.	**Fig. 5.7, 5.8, 5.9, 5.10, 5.11**
aSP	Welded breccia with clay hosted material	Basalt clasts up to 30 cm; rope like marks, flattened and squashed. No matrix material.	aSP/lSP/ vA	V	C	Agglutinated basaltic spatter during subaerial vent phase.	**Map (a), Fig. 5.7**
lSP	Clay hosted breccia	Distal to side vent. Basalt clasts upto 30 cm, rope like textures, partial flattening, each clast surrounded by fine clay. Partial quenching of of clast surfaces.	aSP/lSP	C/ V	C	Vent spatter and solid ejecta on to saturated ground partial quenching and mixing with host sediment.	**Map (a)**
aLT	Rounded Lapilli tuff	Concentric rounded small lapilli fragments thin <50cm cover.	bL/aLT	P2	D	Last stage accretionary lapilli formed by nucleating particles in an ash column. Possibly linked to Katla eruptions.	**Fig. 5.12 C**

hP	Pillow Lava and Pillow lava breccia	Pillows, elongate; 1–3 m width by 0.5 m. 20–30 cm quenched glass rinds. Fine to medium grained sideromelane matrix with abundant zeolite pore space fill.	GHip, hP, tL	L1	A	Thick basal pillow lava partially preserved. Pillows are large and elongate as act like small tongues or lava lobes penetrating into the water. Spalling of rind material leads to a fine hyaloclastite interstitial material.	**Fig. 5.12 F**
tL	Lava	Tholeiitic basalt. Tabular basalt, clear core, crust, base relationships. Show columnar, curvi-columnar and hackley fracture.	hP/tL	L1	B	Earlier dammed crater filling subaerial flows. Joint set development from saturated sediment contact.	**Fig. 5.12 B & D**
bL	Blocky Lava	Core well developed with columnar joints. Flow crust breccaited into small blocks dmax. 30cm.	hP/tL	L2	D	Late stage flow originating from vent. Flows down existing stratigraphy	**Fig. 5.12 C**
vA	Agglomerate	Large boulders of agglutinated basalt clasts (5–30cm). Clear dolerite xenoliths (sharp boundaries).	bL/aLT	V	D	Vent agglomerate with xenoliths	**Fig. 5.12 A**

Table 5.3. Table of Lithofacies codes, descriptions, figures and stages for reference. FA= Fine ash <0.06mm. CA= Coarse ash 0.06–2 mm and LT= lapilli 2–64 mm. Basaltic ejected particles, SP = spatter with material >64mm are termed bombs and blocks accordingly. Common bedforms are added as a suffix hence p=planar bedded, i= imbricated, c=channelized, cb= crossbedded and tcb= trough cross-bedded, tb= thinly bedded, th=thickly bedded. Conversely for ease of identification direct effusive fragmented products have prefixes of v= vitricic, l= lithfied, a=agglutinated. Coherent lava flows have been split into mapped units and their internal structure is not commented on here but bL= blocky pahoehoe are separated from tL= tabular flows. Pillow lava dominated horizons=hP.

5.4.1 Depositional Phase A – Phreatomagmatic and Hyaloclastite Cone Building

The earliest preserved activity on Hjörleifshöfði is represented by a cone building phase (Phase A) which is composed of two dominant lithofacies volcanic breccia (VB) and Imbricated Granular Hyaloclastite (GHip). GHip in this chapter represents the hyaloclastite succession characterised in Chapter 4.

Description – Lithofacies VB – Volcaniclastic breccia lithofacies

Mapped unit B1 is characterised by volcaniclastic breccia (lithofacies VB, Fig 5.3 and 5.4) and is exposed at the southern margin of Hjörleifshöfði. The clasts in the breccia are composed of ropey pāhoehoe basalt, highly vesicular basalt, non vesicular basalt and vesicular tephra. Clasts range from 1-80 cm in diameter. The

matrix is composed of poorly sorted, medium- to coarse-grained, vesicular palagonitized glass, cemented with palagonite and smectite clays with porosity filled by secondary calcite and zeolites.

The unit dips 5–25° NW and thins from 150 m in the south to 40 m in the north (Fig. 5.3). Beds in the unit are generally massive at the base of the section, but become planar bedded higher in the deposit. Towards the base, some basalt clasts are imbricated giving transport directions towards the SW. Higher up, where the beds become more planar, sand wave bed forms are present. These have wavelengths of ~2 m and amplitudes of 0.2–0.5 m (Fig. 5.3). Lamination c. 4–40 cm between coarse and fine material also becomes common near the contact with the overlying hyaloclastite breccia (lithofacies GHip). Contacts between beds but are undulatory and scoured.

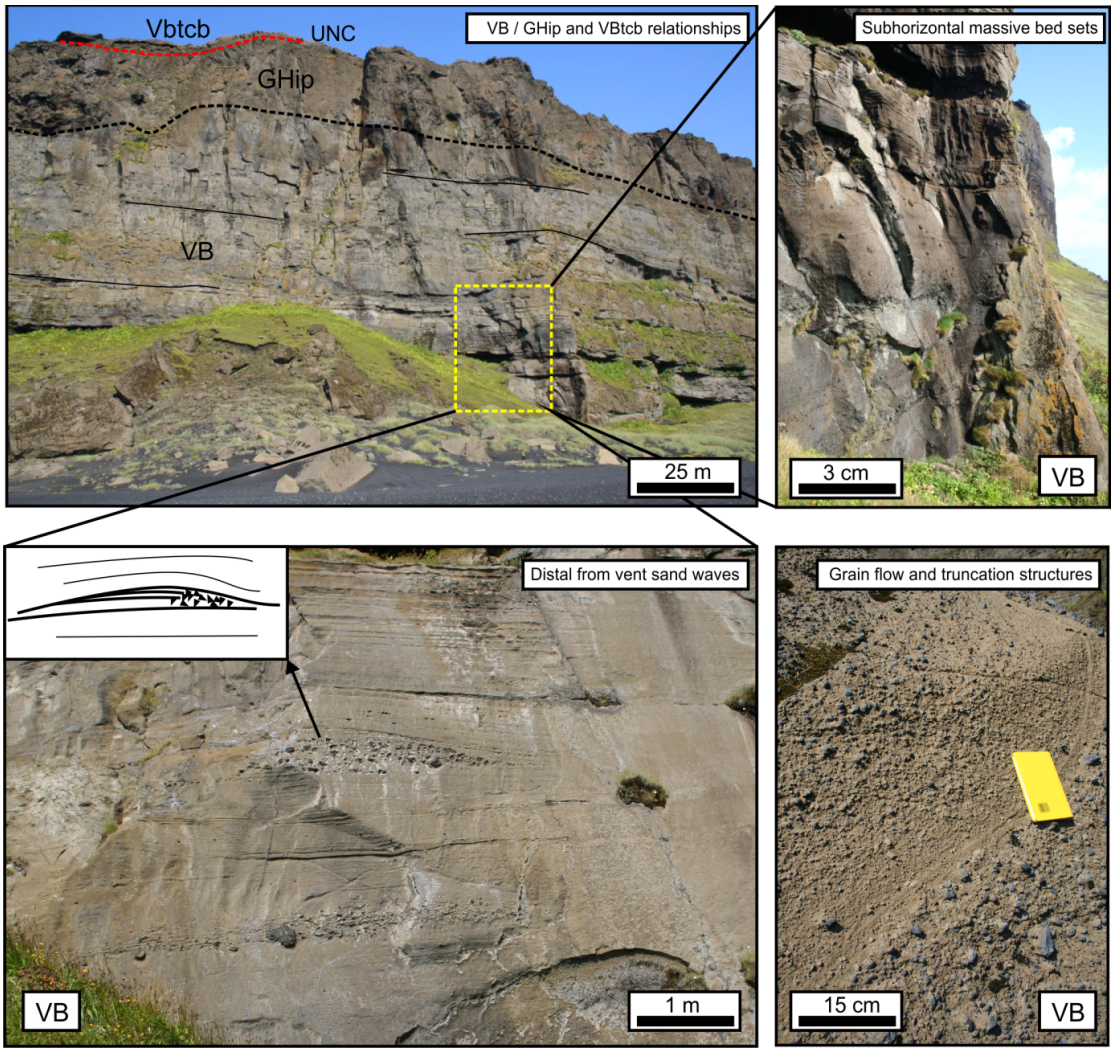

Figure 5.3. Mapped unit B1 exposure showing variation in lithofacies VB . Top left shows the relationships between mapped units, B1, H1 and R1, lithofacies VB, GHip and VBtcb in the far SE of Hjörleifshöfði. Note the undulose but non-erosive contact between VB and the overlying hyaloclastite succession (lithofacies GHip). Top right shows the generally internally massive but planar-bedded breccia and tuff material forming the phreatomagmatic cone. Bottom right shows small sand waves with coarse lags on the leeward side of the bedform. Bottom left shows grain flow fluid contacts between pulses of sediment.

Description – Lithofacies GHip – Hyaloclastite Breccia

Mapped Unit B1 passes upwards into Unit H1 that is composed of imbricated granular hyaloclastite (lithofacies GHip). Lithofacies GHip is composed of angular basalt clasts that vary in diameter from 2–80 cm. The matrix is composed of well-sorted medium to coarse-grained sideromelane glass with rare highly vesicular scoria up to 1cm diameter. Lithofacies GHip consists of 4–8 m thick imbricate cross sets that form fining-upward cycles (Fig 5.4A**).** Unit H1 outcrops on the southern end of Hjörleifshöfði (c. 30–90 m thickness), thins towards fault A and lies conformably above VB (Fig. 5.3).

Petrographical Comparison of lithofacies VB and GHip

Sideromelane clasts in lithofacies GHip are surrounded by palagonite (Fig. 5.5). Lithofacies GHip contains large pore spaces filled by palagonite, conversely lithofacies VB has a lot of inter-grain and grain edge porosity preserved from burst bubble walls on glass grains. The morphology of the glass shards and the ratio of glass-to-palagonite observed in thin-section are key discriminating factors between the two lithofacies. Glass in VB is solely composed of highly vesicular grains. In GHip the glass clasts are not vesicular and contain phenocrysts of olivine and plagioclase feldspar. Zeolites minerals are distributed throughout the sample, crystals are often broken potentially indicating transport This is unlike in many hyaloclastite examples from elsewhere where zeolite mineralisation usually fills in any secondary pore space left by the palagonitization process.

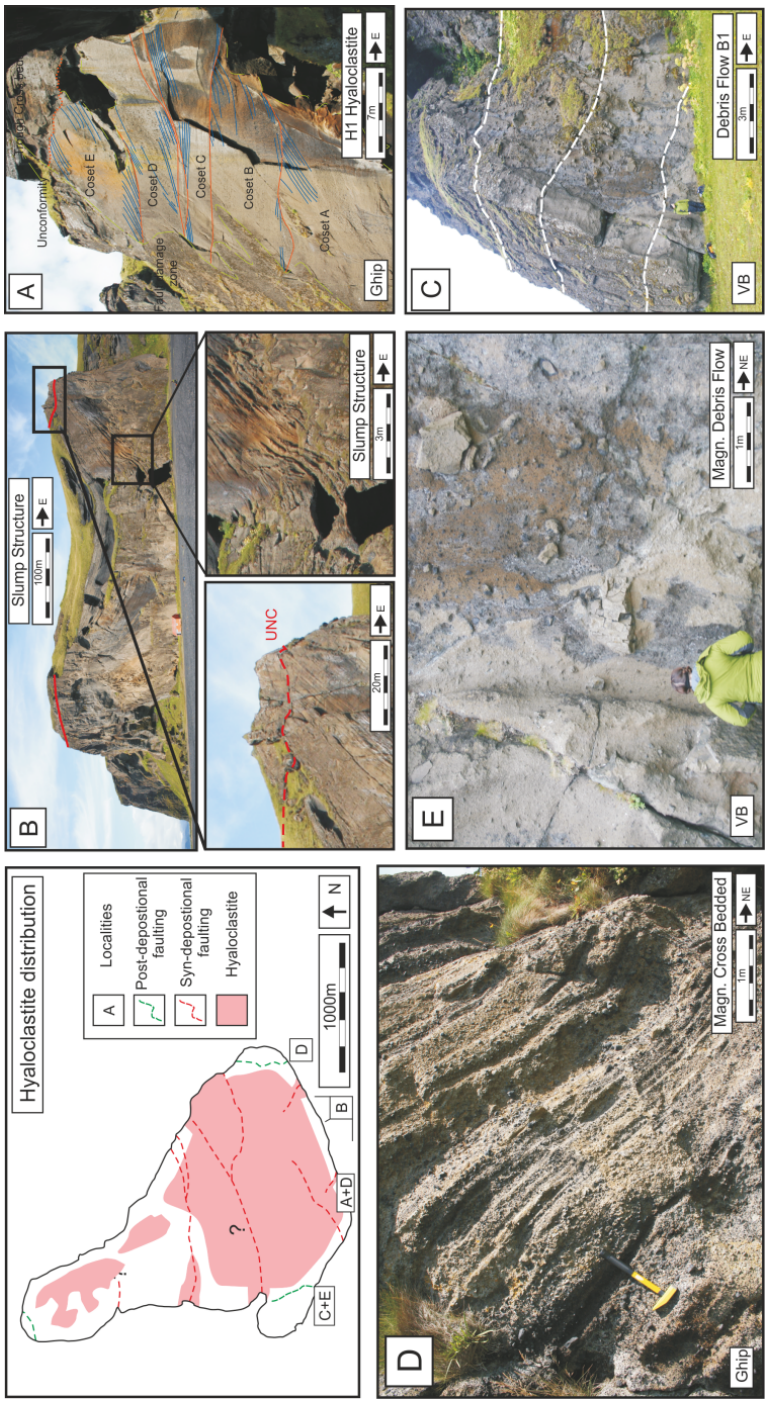

Figure 5.4. Example with locations of mapped unit H1 hyaloclastite exposures compared to mapped unit B1. Inset map shows the distribution of hyaloclastite material on Hjörleifshöfði. A and D show typical syn sedimentary hyaloclastite textures (lithofacies GHip) of large scale cross bedding after Watton et al. 2013. B shows the large-scale synformal feature bounded by type I damage zones and N/S trending normal faults. C and E are lithofacies VB. Note the textural (relative matrix amount and clast size distribution) as well as morphological (cross vs. planar bedding) between the two exposures.

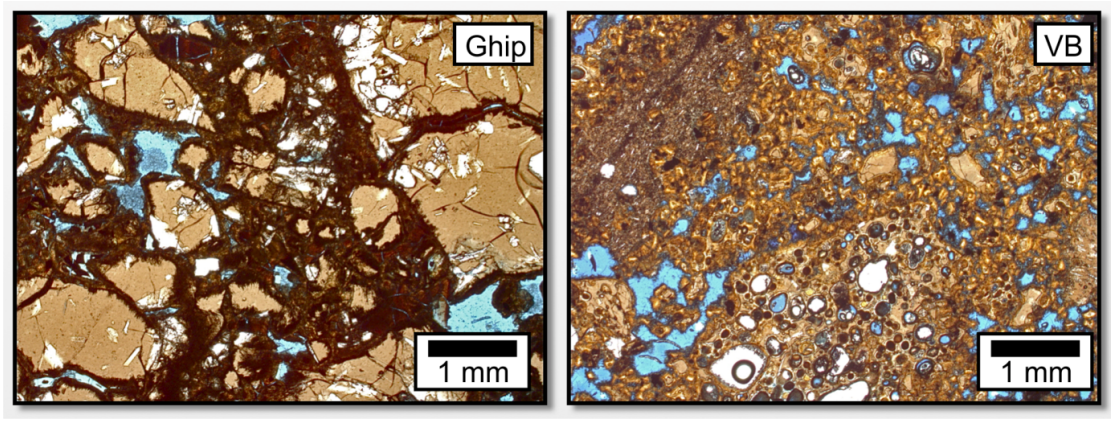

Figure 5.5. Thin section examples of lithofacies GHip and VB. Both are viewed in plane polarized light and have been blue stained for porosity. See section 5.3.1.1 for detailed description.

Interpretation – Lithofacies VB, – Phreatomagmatic Cone and Hyaloclastite Building

The characteristics of the lithofacies in Phase A such as a gradual fining-up through the unit B1 exposure, matrix support and the presence of internally massive thick planar beds suggest lithofacies VB represents submarine debris flow deposits (Brand and White, 2007). Highly vesicular glass grains dominate the matrix. Clast morphology, vesicularity and crystallinity indicate that this material was probably sourced from phreatomagmatic activity (cf. Sohn and Chough, 1993). The volcanic glass fragments share textural similarities with clasts within proximal surge deposits in tuff cones (e.g. Mattsson 2010). The coarse fraction is largely composed of crystalline basalt fragments. The presence of pāhoehoe clasts in addition to quenched pillow lava rinds indicates that the lithofacies was not sourced solely from phreatomagmatic eruptions but also contains a hyaloclastite (non-pyroclastic) component. This is consistent with emplacement by debris flows (Sohn and Chough, 1993; Brand and White, 2007). Sedimentary structures such as low-angle cross-stratification and sandwave bedforms (Fig 5.3) are also typical of deposits formed by turbulent, low particle concentration, that can result from a dilution of debris flow through the ingestion of water which lead to tuff cone formation (Fisher and Waters, 1970; Crowe and Fisher, 1973; Wright et al., 1980; Sohn and Chough, 1993; Cole et al., 2001).

In pre-emergent to emergent settings subaqueous debris flows can be initiated by collapse of the sections of a volcano's flanks (Fornari et al., 1979; Londsdale and Baptiza, 1980; Sohn and Chough, 1993; Schmincke et al., 1997). Initially thick sheet like debris slurries cascade down the volcano flank, occasionally concentrating and initiating channel development upon transportation into deeper marine settings (Bergh and Sigvaldson, 1991; Ollier et al., 1998; Maicher et al., 2000). Such deposits have been identified at a number of Surtseyan volcanoes (Sohn and Chough, 1993; Sohn, 1994; Cole et al., 2001; Sohn and Park, 2005; White, 2010; Sorrentino et al., 2011; Kraj, 2012).

Interpretation – Lithofacies GHip – Phreatomagmatic and Hyaloclastite Cone Building

Lithofacies GHip is a syn-sedimentary hyaloclastite deposit. The clasts show the typical features of quench and passive fragmentation of lava, such as limited vesiculation. The coarse fraction is composed solely of fragmented basalt and partially quenched clasts indicating hyaloclastite origin (Honnorez and Kirst, 1975; McPhie et al., 1993). The reader is asked to consult table 4.2, chapter 4 for the methodology used to separate phreatomagmatic clasts from those of hyaloclastite origin. In Surtseyan settings greater degrees of reworking occur due to the relative instability of the volcano flanks. Large cross-bedsets can form as material exits a submarine channel (e.g. Ollier et al., 1998). In Hjörleifshöfði the unit H1 has probably been sourced from flank collapses. The source of the hyaloclastite material is likely to be lava flows contemporaneous with phase B as indicated by geochemistry (section 5.5.2).

5.4.2 Reworking Phase AR – Emergence of the Volcanic Pile

Phase AR represents a period of reworking that led to the deposition of mapped unit R1, which unconformably overlies mapped unit H1 (Fig 5.4 B). Mapped unit R2 conformably overlies mapped unit R1. Two lithofacies characterize mapped units forming trough and planar-bedded volcaniclastic sandstones, lithofacies VStcb and VStb. Mapped unit R1 is only exposed on the southern flank of

Hjörleifshöfði whereas mapped unit R2 extends over much of the outcrop thinning towards the north.

Description- Lithofacies VStcb– Trough-cross bedded volcaniclastic sandstone; VStb and thinly bedded volcaniclastic sandstones

Trough cross-bedded volcaniclastic sandstone (lithofacies VStcb) of Unit Clasts are composed of moderately to well-sorted angular to subangular basalt clasts (2-10 cm diameter) that show evidence of abrasion; a The matrix is composed of medium- to very coarse-grained particles mainly sideromelane glass, highly vesicular pyroclasts and locally-derived silicic material. It is cemented by clay, typically palagonite. Trough cross-bedding occurs in sets c. 30 cm high. Foreset dips are omnidirectional. Mapped unit R1 forms packages up to 20 m thick. The unit dips 15–20° NW. Mapped unit R1 thins rapidly towards the northern end of the island and does not overly the unit L1 lava sequence at any point suggesting it was contemporaneous to mapped unit L1 emplacement (see section 5.5).

Unit Rs2a/b (Fig. 5.6) is mainly composed of thinly bedded volcaniclastic sandstone (lithofacies VStb) and forms the main drape of volcaniclastic cover over the southern half of the island (Fig. 5.6 A, D, E). The lithofacies is composed of well-sorted, fine- to medium-grained rounded pyroclasts and lava clasts. Coarser-grained layers are composed predominantly of basalt lava clasts. The lithofacies is planar laminated with laminations defined by alternations between coarser- and finer-grained layers (Fig. 5.6 D).

The presence of bomb sags in Unit R2b (Fig. 5.6 F, G) denote proximal deposition coeval with eruptions (Mapped unit V). The bombs have bread crust surface textures. Bomb sags increase in abundance towards the vent (mapped unit V, Fig. 5.2).

Mapped unit R2 reaches 12 m thick and conformably overlies mapped unit R1. Bedding dips are quaquaveral towards the vent structure mapped unit V (Fig. 5.2). Lithofacies VStb overlies and onlaps onto mapped unit L1 (basalt lava flows) in the northern part of the island.

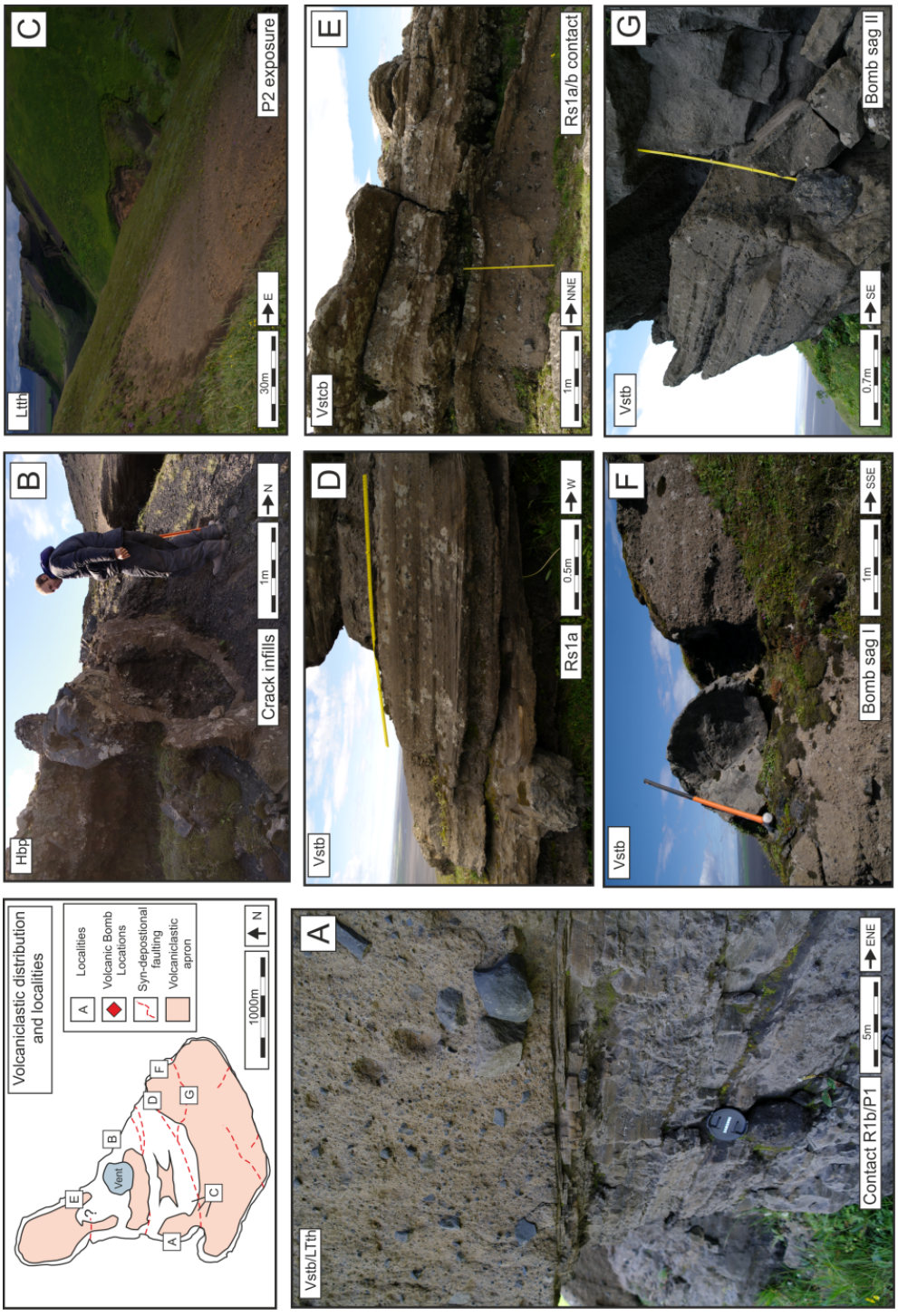

Figure 5.6. Example of outcrop exposure of mapped volcaniclastic units with location map (R1, R2a/b and P1/2). A) Contact between planar laminated lithofacies VStb (mapped unit R2a) and the reworked base of lithofacies LTth (Mapped unit P1). B) Crack infills of VStb (Mapped unit R2a) in lithofacies HBp (Mapped unit H2). C) Main exposure of mapped unit P2 showing poor vertical extent. D) Outcrop exposure of R2a (lithofacies VStb) showing planar lamination. E) Outcrop exposure of mapped unit R1 (lithofacies VStcb), note increased clast size in comparison

to lithofacies VStb. F/G) Volcanic bombs (localities on inset map) cutting laminations in lithofacies VStb.

Interpretation- Lithofacies VStcb, VStb – Erosion and marine shoaling of volcanic material throughout edifice subsidence

Mapped units R1 and R2 are composed of lithofacies VStcb and VStb and record the emergence of the volcanic system. Mapped unit R1 overlies an unconformity (Fig. 5.4B) that likely denotes the level of wave base. Material above the unconformity corresponds to material that was reworked by tidal processes as indicated by trough cross bedding with omnidirectional foreset bed geometries, the appearance of silicic material and increased sorting relative to lithofacies GHip.

Lithofacies VStcb is inferred to have been deposited in sublittoral conditions, whereas lithofacies VStb may represent eulittorial to supralittorial sedimentation in shallow water depths as inferred from the finer particle sizes, and the increased sorting and rounding of clasts (e.g. winnowing of fine-grained material was observed on Surtsey soon after emergence; Kokelaar and Durant, 1983).

The alternating coarse- and fine-grained layers within lithofacies VStb may represent the deposits of ongoing explosive eruptions which created small grain flows as clasts fell out on to an inclined substrate (e.g. Sohn and Chough, 1993). All of the above corresponds closely with observations of the emergence of Surtsyean edifices (Gutiérrez et al., 2006; Murphy et al., 2008).

Unit R2 extends over most of the outcrop in comparison to Unit R1 which is found only on the southern margin. This observation may indicate continued subsidence of the entire edifice through phase C allowing the accumulation and shoaling of pyroclastic material (mapped unit P1).

5.4.3 Depositional Phase B – Subaerial lava flow accumulation, Crater Damming

During emergence of the volcanic pile (phases AR and B) lava flows accumulated on the northern flanks. Phase B is recorded by unit H2 and Unit L1 lava flows, and is composed of four main lithofacies.

Description – Lithofacies HBp – Hyaloclastite pods,

This lithofacies comprises hyaloclastite breccia pods (HBp). . It consists of of clasts up to 40 cm from granule to medium grained sideromelane glass. Lithofacies HBp is characterized by localized, thin (2–3 m) lenticular beds that sometimes exhibit crude horizontal lamination and stratification. Cooling cracks within clasts HBp are sometimes filled by overlying volcanic sediments **(**Fig. 5.6 B**)**.

Compositionally lithofacies HBp is similar to lithofacies GHip (above) however its matrix is poorly-sorted. Occasionally spalled lava pillows are present. These are typically 50 cm in diameter and are roughly spherical. They and can traced into the tL lava flows of mapped unit L1.

Interpretation – Lithofacies HBp - Hyaloclastite pods, quenching in shallow water

Lithofacies HBp occurs in thin packages at the base of lithofacies tL lava flows (mapped unit L1). Spalled pillow lavas in lithofacies HBp suggest some degree of downslope remobilisation I infer that this lithofacies represents lava flows that quenched and fragmented in relatively shallow water within the flooded crater (analogous to shallow lacustrine environments, e.g. Tucker and Scott, 2009).

Description – Lithofacies tL, bL- Subaerial Lava Flows

Effusive subaerial tholeiitic basalt lava flows make up the upper third of the Hjörleifshöfði succession. They occur interbedded with lithofacies lT and HBp. The morphology, flow thickness and structure of basalt lava flows on Hjörleifshöfði are described in chapter 4, table 4.2. In this chapter we have grouped the lavas into tL (lavas that show tabular geometries with well developed core and crust relationships, Fig. 5.7B), and bL (lavas that have blocky structures dominated by fragments of lava flows formed through post emplacement processes). The geochemical affinities of the basalt units are further discussed in section 5.5.2.

Basalt lava flows outcrop on the north and northeast side forming high cliffs, some of the lava flow exposures are on recently down faulted blocks (Fig. 5.7 D). The lava flows dip 20^0 towards large listric bounding faults and strike normal to the curvature defined by the fault. Mapped unit L1 basalt lava flows form a ~50 m thick

sequence overlying the debris flow deposits of Unit B1 associated with faulting and onlap of Surtseyan cone deposits to the south of the volcano. and the lavas pass towards the south into hyaloclastite deposits once they build up to the maximum height of the Surtseyan cone deposits.

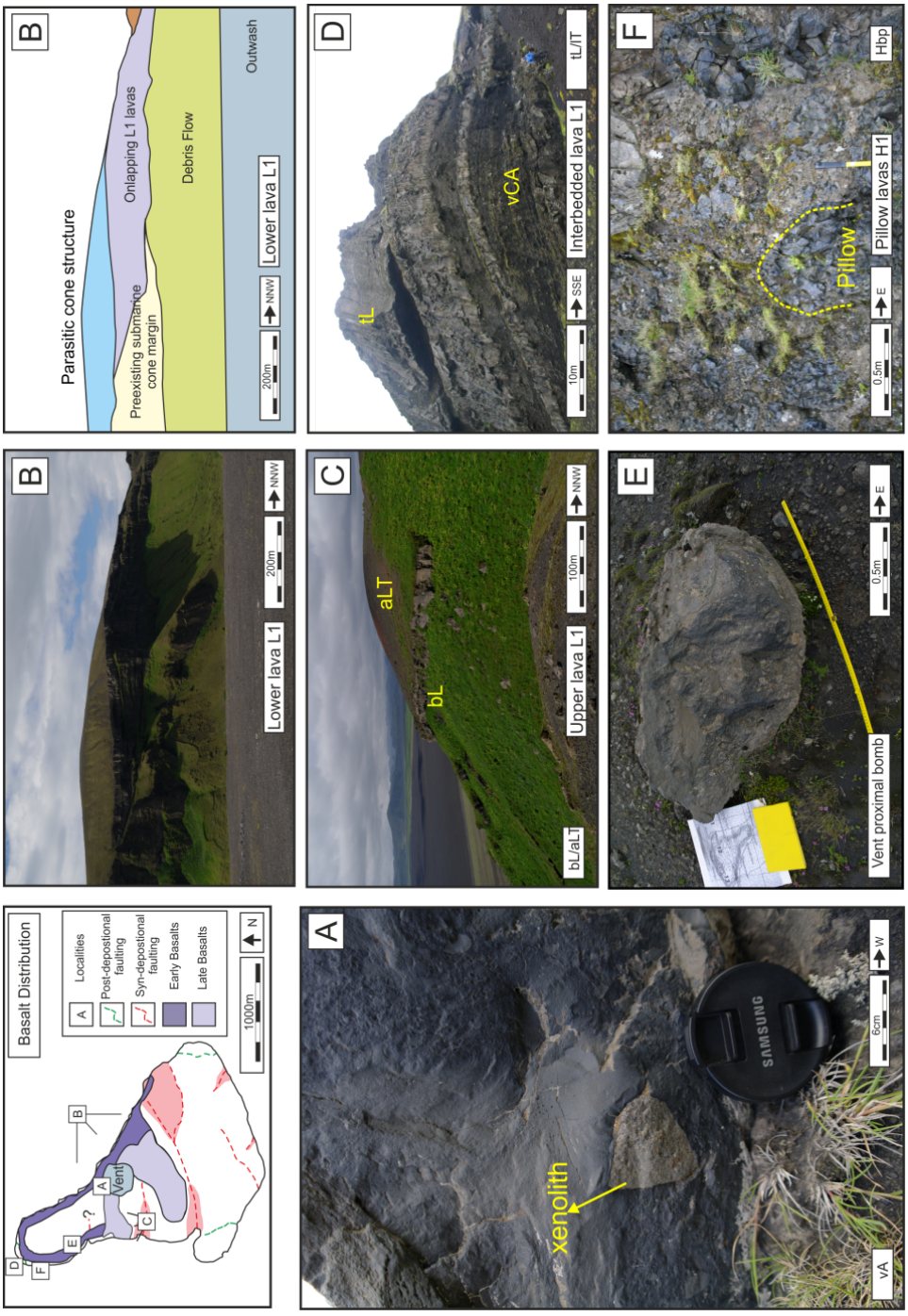

Figure. 5.7. Examples of effusive volcanic rocks on the Hjörleifshöfði volcano with location map. A) Vent agglomerate (lithofacies vA) containing dolerite xenolith of similar composition to dyke material. B) Mapped unit L1 lava flows onlapping the cone structure overlying mapped unit B1. Side vent highlighted on diagram. C) Exposure of mapped unit L2 lava with highlighted mapped unit P2 deposits. D) Mapped L1 lava succession with interbedded tephra horizons, possibly from continued phreatomagmatic activity. E) Vent proximal volcanic bomb in cone tephra (mapped unit R2b, lithofacies Vstb. F) Pillow lavas exposure above H1 succession.

Description Lithofacies – lT, - thinly bedded tuff

Thin beds of tuff (lT) occur interbedded with the tL lava flows. They are crudely horizontally stratified and composed entirely of highly vesicular, subangular to angular, coarse ash-grade basalt glass shards with cuspate bubble margins. Lithofacies lT forms beds that are discontinuous (broadly lenticular) in depressions in the suface of mapped unit L1 lava flows, up to 2 m thick that mimic the dip and strike direction of the overlying lava flows (Fig. 5.7D). Lithofacies lT infills fractures or cracks in crust of tL flows.

Interpretation – tL, lT – Effusive Basalt Volcanism

Two phases of effusive volcanism have occurred during the emergence of Hjörleifshöfði. The lower lava sequence (unit L1) occurs as a series of tabular lava flows that interact with water situated sediments to produce distinct curved columnar joints (Long and Wood 1986, also see Chapter 4). The lavas onlap an existing cone structure and overly slump scarp fault breccias and therefore represent a crater-filling phase. The interbedded tuffs probably record fallout from weak explosive eruptions (Thorarinsson, 1965; Cole et al., 2001, Brand and White 2007). Effusive volcanism that generated Unit L2 occurred during phase D.

5.4.4 Depositional Phase C – Silicic Volcanism, Ignimbrite

Mapped unit P1 overlies mapped unit R2 and outcrops in the central portion of the volcano. The ignimbrite has a non-welded base and a welded top (lithofacies LTth upper and lower).

Description – Lithofacies LTth – non-welded to welded lithic tuff

This lithofacies comprises variably welded lithic tuff. It is massive, planar bedded and low-angle cross-laminated, matrix-supported, and contains up to c.15 vol. % lithic lapilli. (Fig 5.8) becoming planar to very low angle cross-laminated (<5°) before becoming welded. The lithic lapilli are predominantly angular to sub-angular basalt lava clasts (up to 4 cm in diameter) c.70% of total lithics and subordinate vesicular pumice fragments (up to 10 cm in diameter). The the matrix is composed of glass shards highly glassy and is highly porous. Some lithic fragments at the base have have glass rinds and the matrix contains more clay. Large pore cavities (up to 5 cm width) are present at the base of lithofacies LTth but porosity increases into lithofacies LTth upper. Circular, 15–20 cm wide patches occur on the bedding surfaces of the ignimbrite. They are composed of slightly finer-grained clasts than the surrounding ignimbrite and were not observed in cross section (Fig. 5.9).

Bedding within the ignimbrite dips 15–20° NW (similar to mapped unit R2) although thedip direction is variable. Mapped unit P1 is approximately 10 m thick (average) and thickens into depressions in R2 topography. Characteristic field contacts in Fig. 5.6 A and Fig 5.8 show a planar contact with no visible truncation of lithofacies VStb bedding structures. The upper contact is generally covered by scree and is poorly exposed although is closely exposed to agglutinated spatter deposits (lithofacies aSP) derived from late stage basaltic activity.

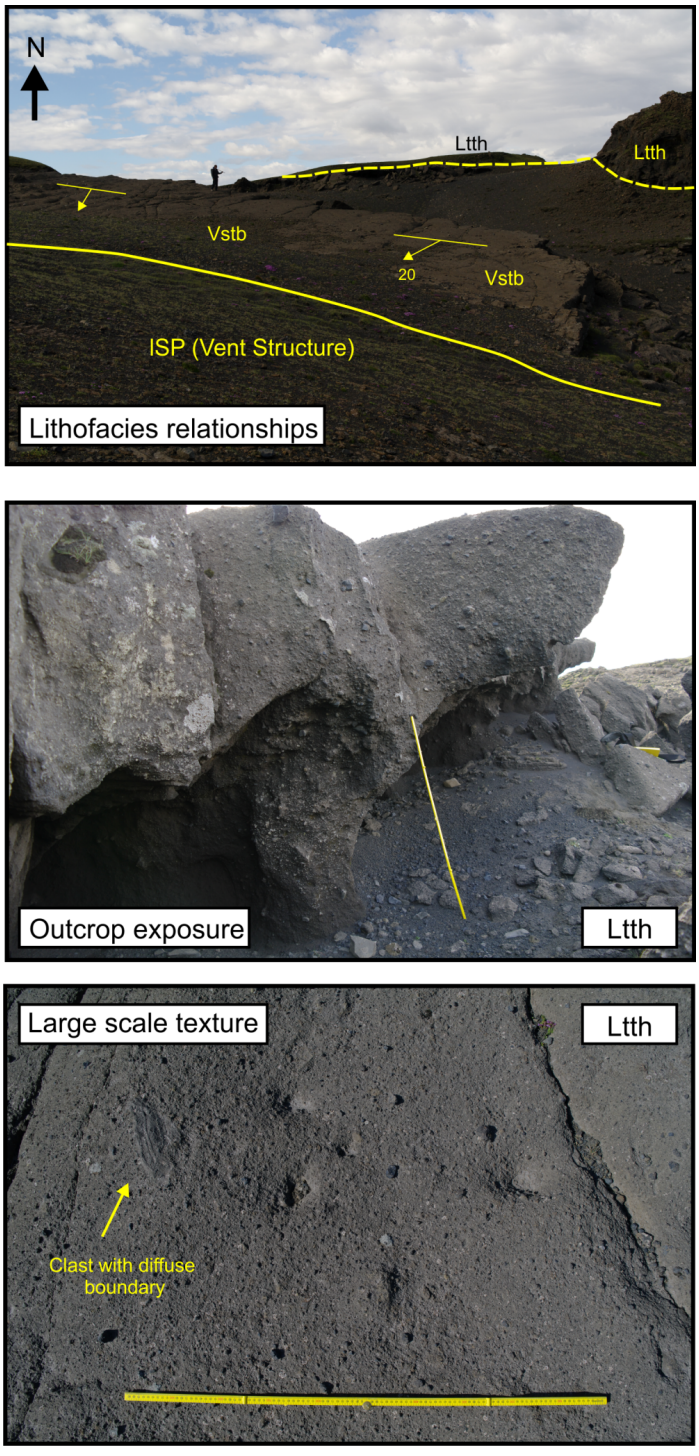

Figure 5.8 Contact exposure of mapped unit P1, lithofacies LTth at the lower part of mapped unit P1 overlying mapped unit R2 deposits. The uppermost diagram shows the planar bedding and dip of lithofacies tbVS. The lower two diagrams show the massive large scale texture of the base of mapped unit P1,lithofacies LTth, diffuse boundary clasts, large vesicles (up to 5 cm) and pumice fragments (light clasts).

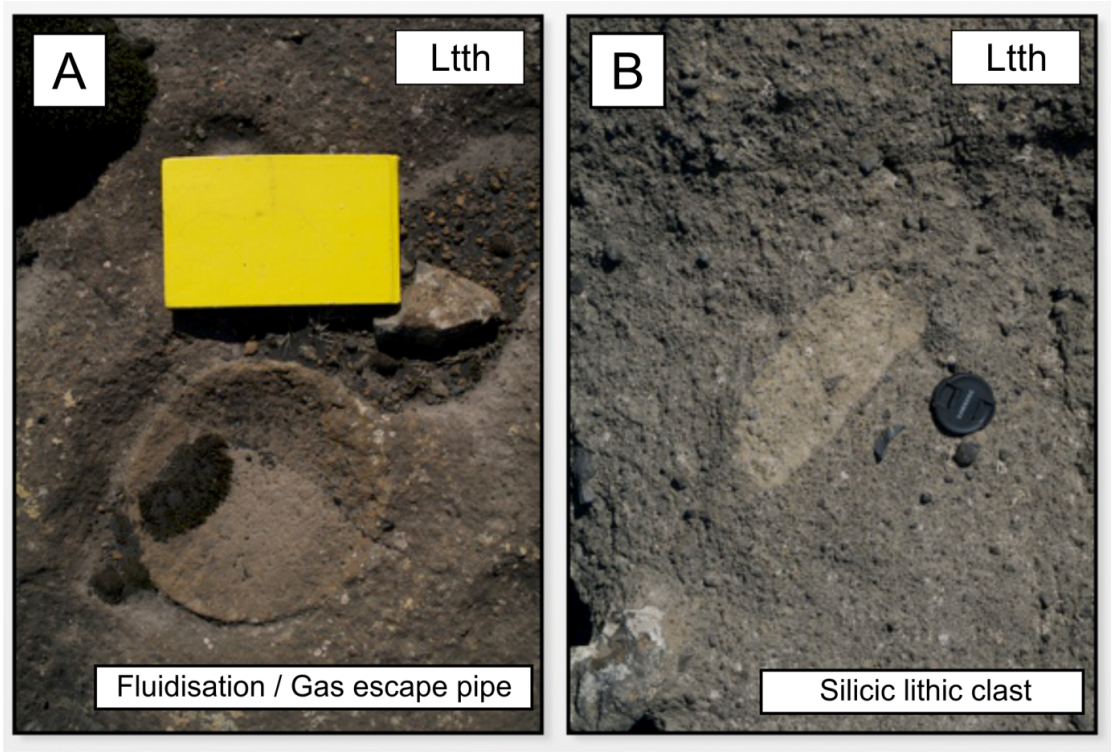

Figure. 5.9 Evidence of hot emplacement, A) Fumrole/ gas pipe structures (15 cm width), B) Silicic lithic clast within ignimbrite.. Fumrole pipes are located only on the top of bedding surfaces and can be observed in outcrop towards the far north of mapped unit P1 (see map Fig 5.2).

Lithofacies LTth is medium to coarse grained, dominated by glass shards, and contains rare flattened pumice clasts (fiamme), plagioclase and and quartz crystal fragments, and lithic clasts. Non-flattened pumice fragments are also present (e.g. Fig 5.11 D). There are two types of lithic clast, basaltic and vitric (clast type I, II respectively, Fig. 5.10 and 5.11). Basaltic clasts are microcrystalline and have partially quenched rinds. Vitric clasts are composed of densely welded red glass with quartz crystals. Both the vitric clasts and the fiamme can exhibit a preferred orientation in the matrix giving the rock a poorly developed eutaxitic texture. Glass shards are well preserved and exhibit a high inter granular porosity with limited clay alteration (Fig. 5.11 matrix). Porosity is lower in the lower parts of the ignimbrite due to the presence of pore-filling clay minerals. Crystals within the matrix include both whole crystals of plagioclase, and broken fragments of plagioclase and quartz. Highly vesicular pumice blocks up to 10 cm in diameter, occur in the upper parts of the ignimbrite. (Fig. 5.11).

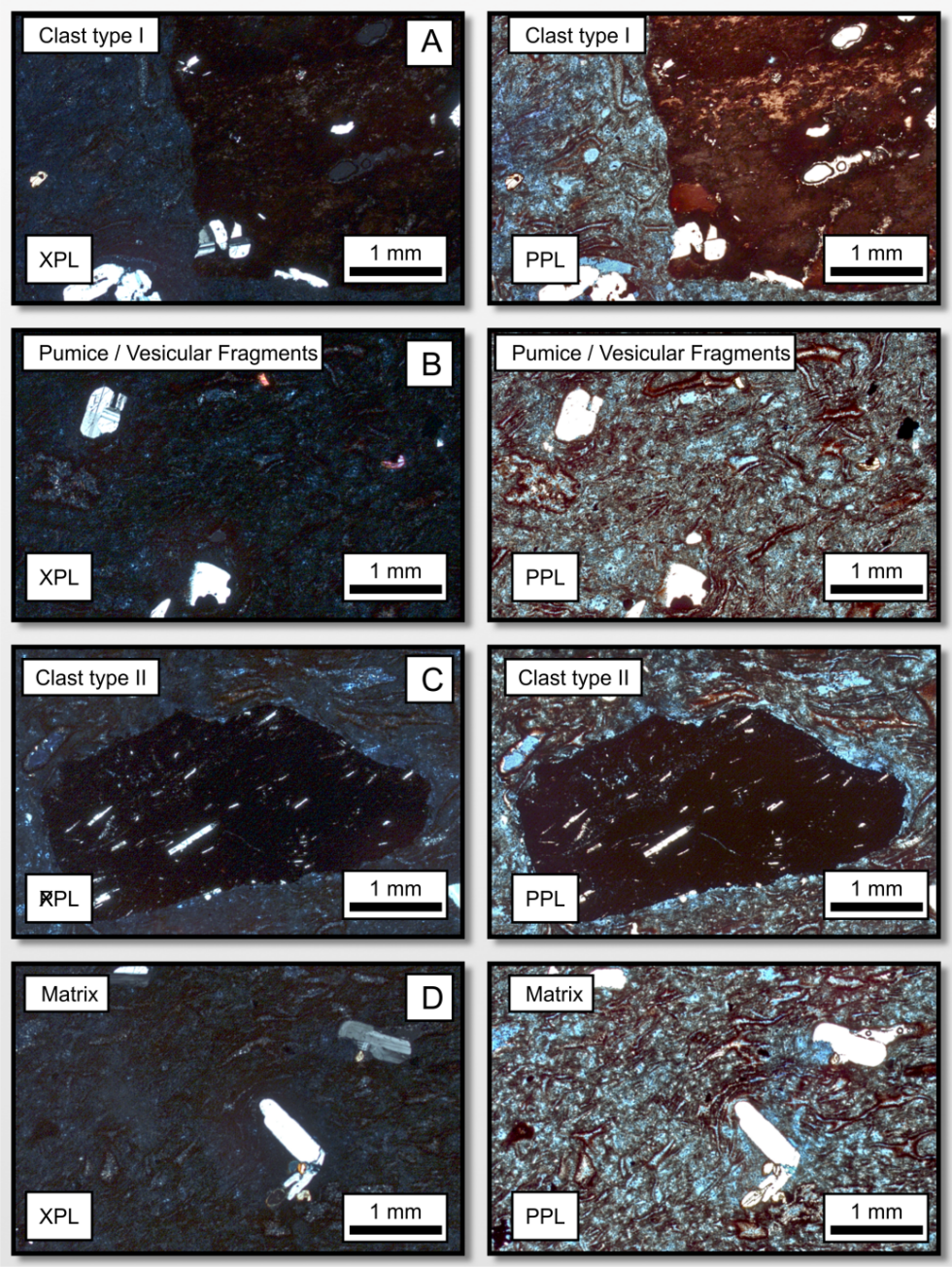

Figure. 5.10 Thin section examples of Mapped unit P1, lithofacies LTth lower, PPL – Plane Polarized Light, XPL – Cross Polarized Light. All thin sections have been stained blue for porosity. A) Clast type 1; densely welded vitric glass containing amorphous quartz and sub angular plagioclase phenocrysts. B) Clast type II are darker coloured containing microcrystalline acicular plagioclase laths, in some examples the margins can be quenched. Both clasts type are subrounded. C) Highly vesicular virtic fragments also occur in the matrix and may represent pumice clasts or fiamme. D) Matrix of vitric glass and phenocrysts of plagioclase, eutaxitic texture developed. In comparison to lithofacies LTth upper (Fig. 5. 13) there is more micro-porosity and less defined pore spaces due to the presence clays.

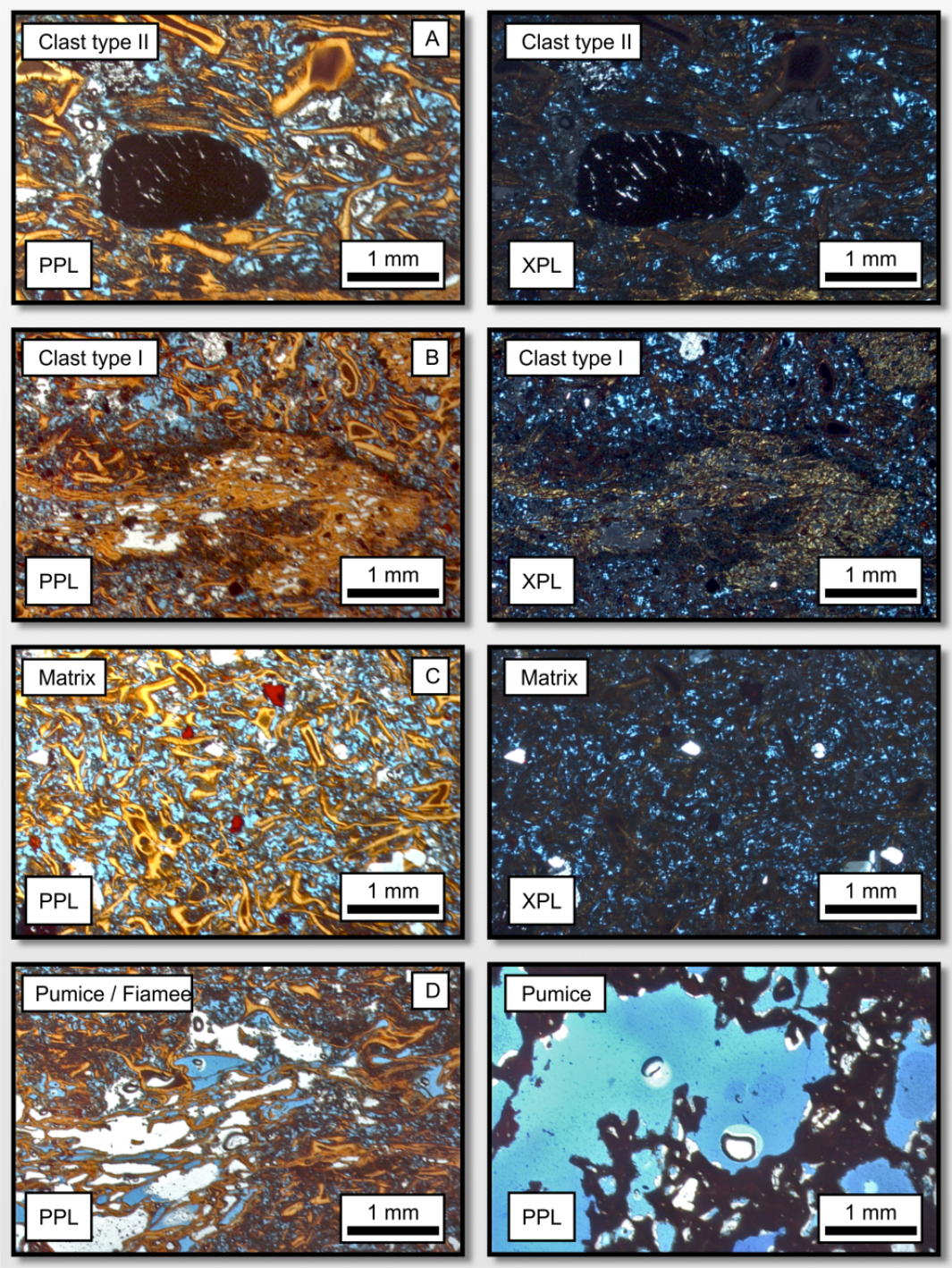

Figure. 5.11 Thin section examples of mapped unit P1 lithofacies LTth upper, PPL – Plane Polarized Light, XPL – Cross Polarized Light. All thin sections have been stained blue for porosity. A) Vitric clasts, subangular and contain more amorphous quartz than lithofacies LTth lower. B) Rounded mafic clasts with microcrystalline plagioclase feldspar. C+D) Highly vesicular fiamme and pumice fragments. E) Highly vesicular matrix, iron-weathering causing reddening in glass.

The overall exposure of unit P1 ignimbrite is generally poor with only partial parts of the succession exposed across the upper plateau of Hjörleifshöfði. A reconstructed cross-section is through the ignimbrite is given in figure 5.12. The ignimbrite is sandwiched between the deposits of phases AR and D and is accredited to phase C, but it may have been emplaced during late-stage effusive activity of phase B.

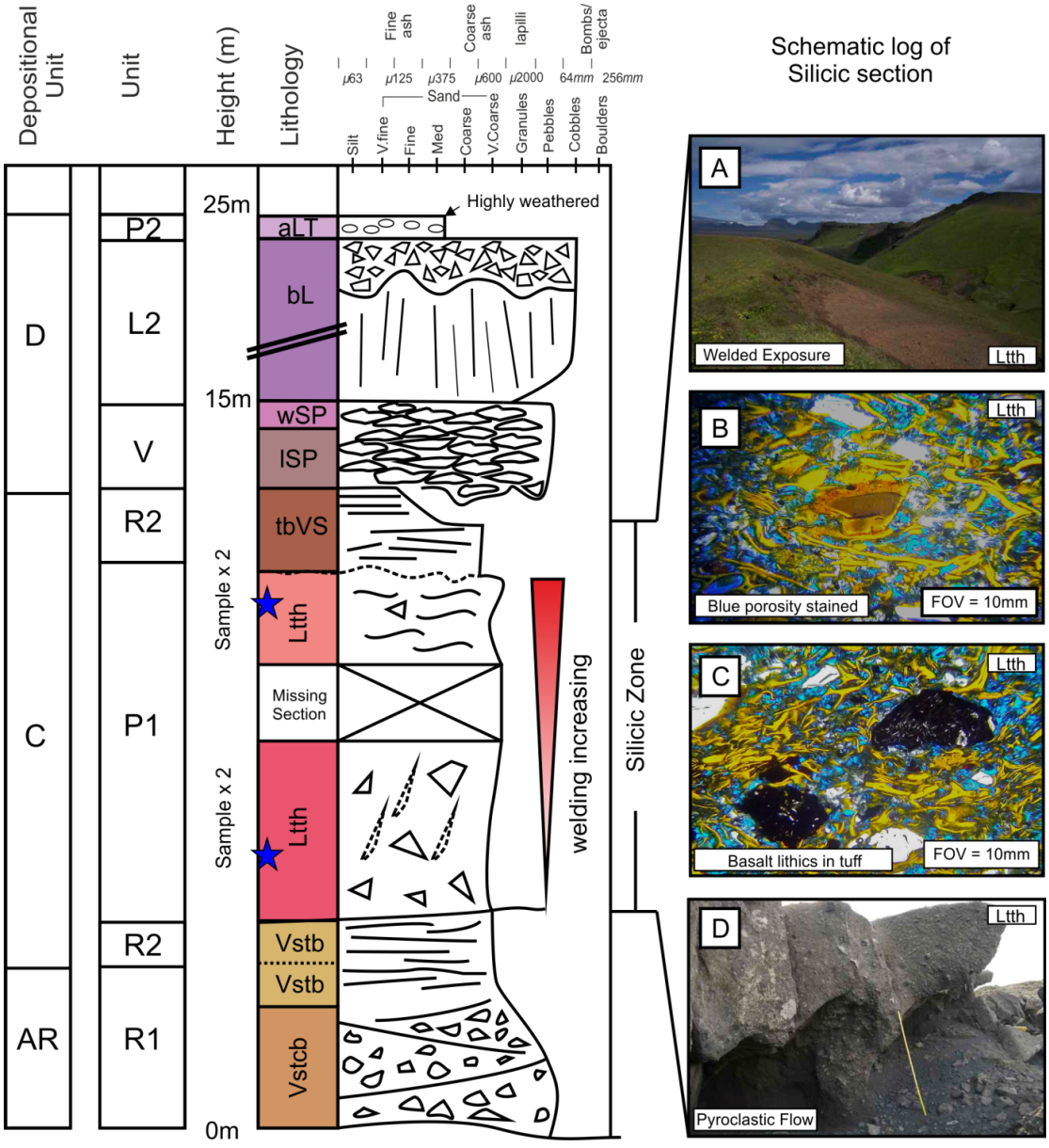

Figure. 5.12. Schematic Section of mapped unit P1 a poorly exposed high silica unit. Unit thickness average 10 m. Lithofacies LTth occurs interbedded in R2 deposits. A) Welding and porosity increase in upwards in P1, the upper lithofacies LTth is also reddened. B + C) show then section examples the vitric matrix of common lithic clast component of lithofacies LTth upper. D) Shows lithofacies LTth lower and massive bedding. See text for additional details.

Interpretation* – lithofacies LTth – *non-welded to welded lithic tuff

Unit P1 is interpreted as an ignimbrite due to its silicic composition, field relationships, welding and composition (abundant glass shards and pumice fragments) Ignimbrites can be sourced from pyroclastic flows or surges originating from explosive volcanism typical of intermediate to acidic magmatism. Pyroclastic flows and surges are dense solid-gas flows generated by either collapse of an eruption column or collapse of a lava dome or cryptodome (Branney and Kokelarr, 2002). Pyroclastic surge and flow deposits can be simplified to the term pyroclastic density current, which avoids specific implications of these terms (Freundt, 1999; Branney and Kokelarr, 2002) Because all other volcanic products on Hjörleifshöfði are basaltic the ignimbrite was likely sourced from a neighbouring volcanic centre (see section 5.5).

The lower part of the ignimbrite exhibits low angle cross-bedding, partially quenched clasts and in places its matrix is mixed with clay material. As lithofacies LTth upper has a high porosity and no inter-granular clay formation it suggests that the clay was externally sourced and not a post-depositional diagenetic effect. Lithofacies LTth lower may then represent a pyroclastic surge deposit that entered a shallow marine system, which promoted mixing, partial quenching and incorporated some shoaled clay material from lithofacies VStb (mapped unit R2) hypothesised by several authors (Reedman et al., 1987; Orton and Fritz, 1990; Cas and Wright, 1991; McPhie et al., 1993). Lithofacies LTth upper contains more vitirc fragments, no intergranular clay and a more pronounced eutaxtic texture which indicates a higher degree of welding (McPhie et al., 1993). Gas escape pipes also occur in lithofacies LTth upper indicating heat transfer post deposition (Branney and Kokelaar, 2002). Pyroclastic density currents often enter the sea and are documented by many authors (e.g. Self and Rampino, 1981; Sigurdsson et al., 1991). The process of deposition in a very shallow water environment could lead to mixing and stratification causing clay influx and bedding structures and a higher clast component (similar to block and ash flows Sparks et al., 1980). Lithofacies LTth upper represents subaerial accumulation due to high porosity and massive bedded indicating limited remobilisation of pyroclastic particles. Alternatively, welded ignimbrites the lower

parts are non-welded due to heat loss to the substrate. Later deposited parts (ignimbrites aggrade incrementally with time) and are insulated from the substrate and remain hotter for longer therefore it is not unusual for welding intensity to increase upwards. As such the clay content could still be a reflection of the initial temperature of the deposit causing early vapour phase alteration in the non-welded part of the deposit. Diagenesis then turns the vapour phase minerals into clays.

Both Lithofacies LTth upper and lower contain abundant basaltic lithic fragments. Lithofacies LTth upper shows limited mixing suggesting the basaltic lithic fragments are likely to be externally derived. This observation is consistent with partial quenching of basalt clasts in Lithofacies LTth lower and the proposed geochemical affinity of the silicic unit (see section 5.5).

5.4.5 Depositional Phase D – Return to Basaltic Volcanism, Parasitic Vent Formation

The last stage of volcanism on Hjörleifshöfði is characterized by a return to basaltic volcanism. A parasitic side vent is produced (mapped unit V) as well a second phase of subaerial effusive volcanism (mapped unit L2).

Description lithofacies -vA, lSP, aSP – Agglomerate, lithfied and agglutinated spatter

A dome-like structure composed of agglutinated spatter occurs on the on top of Hjörleifshöfði. It is250 m wide, 50 m high and has 11° slopes–(Fig. 5.2). The basaltic spatter and vesicular scoria fragments that show a variety in oxidation states (lithofacies lSP - lithified spatter (hosted in clay sediments) and lithofacies aSP – agglutinated spatter - , Fig. 5.2). Lithofacies lSP deposits are hosted in matrix of fine clay similar to lithofacies VStb (mapped unit R2). Clasts in both lithofacies lSP and aSP are composed mainly of basaltic spatter rags up to 30 cm in diameter. In lithofacies lSP the rags have well defined margins,, are elongated but not flattened, and have textures characteristic of emplacement as molten rags of magma. (similar to the volcanic bombs in lithofacies VStb). In Lithofacies aSP spatter clasts are characteristically squashed into “cow pie”-like structures are are agglutinated. Clasts in lithofacies aSP have no matrix and the degree of post-emplacement compaction

increasing towards the centre of the dome structure due to progressive increase in welding. The summit of the dome is scattered with large blocks of vent agglomerate (lithofacies vA).

Lithofacies vA is composed of agglutinated clasts of glassy, vesicular basalt and abundant, small dolerite lithic lithic lapilli and blocks up to 8 cm in diameter. Mapped unit V, lithofacies vA deposits have occasional microcrystalline plagioclase but are generally characterized by a glassy and highly vesicular groundmass. Unlike lithofacies tL, vA deposits are composed of a series of agglutinated clasts (clast boundaries shown on section Fig. 5.13) are likely to form by post compaction welding. Conversely mapped unit L1 lava flows, lithofacies tL in thin section is microcrystalline, glassy with occasional large plagioclase and pyroxene clusters (Fig. 5.13A). The mineralogy of both lithofacies tL and vA matches doleritic xenoliths found within aggulintaged clasts of lithofacies vA however, the xenoliths have an larger groundmass crystal size (1-2 mm) (Fig. 5.14). The margins of the xenolith can be partially assimilated into agglutinated clasts in lithofacies vA (Fig. 5.14).

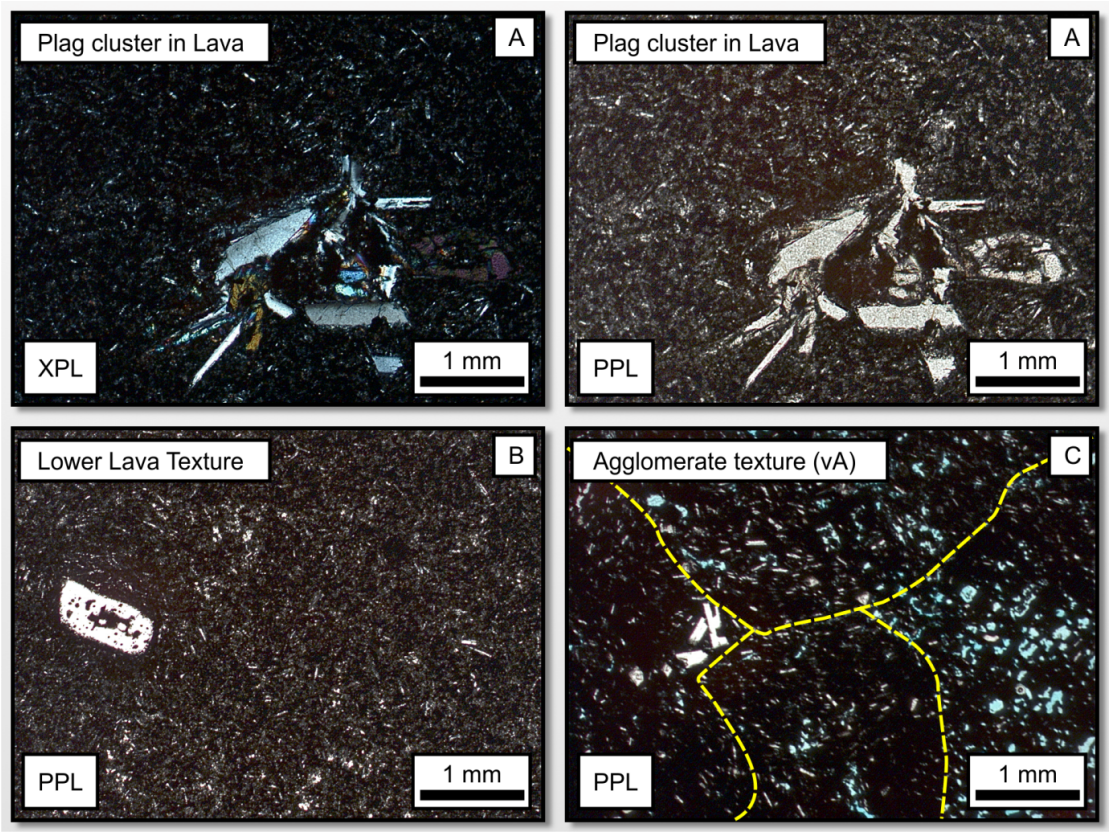

Figiure. 5.13. Thin section examples of Mapped unit L1 and V, lithofacies tL and vA respectively. All sections have been blue stained for porosity. A) Phenocryst cluster of plagioclase and olivine. Groundmass is finely crystalline. B + C) Comparison of mapped unit L1 and V textures. Lithofacies tl has a microcrystalline groundmass and poorly developed eutaxitic texture. Lithofacies vA is vesicular and is composed a series of agglutinated basalt clasts with small but well developed plagioclase phenocrysts.

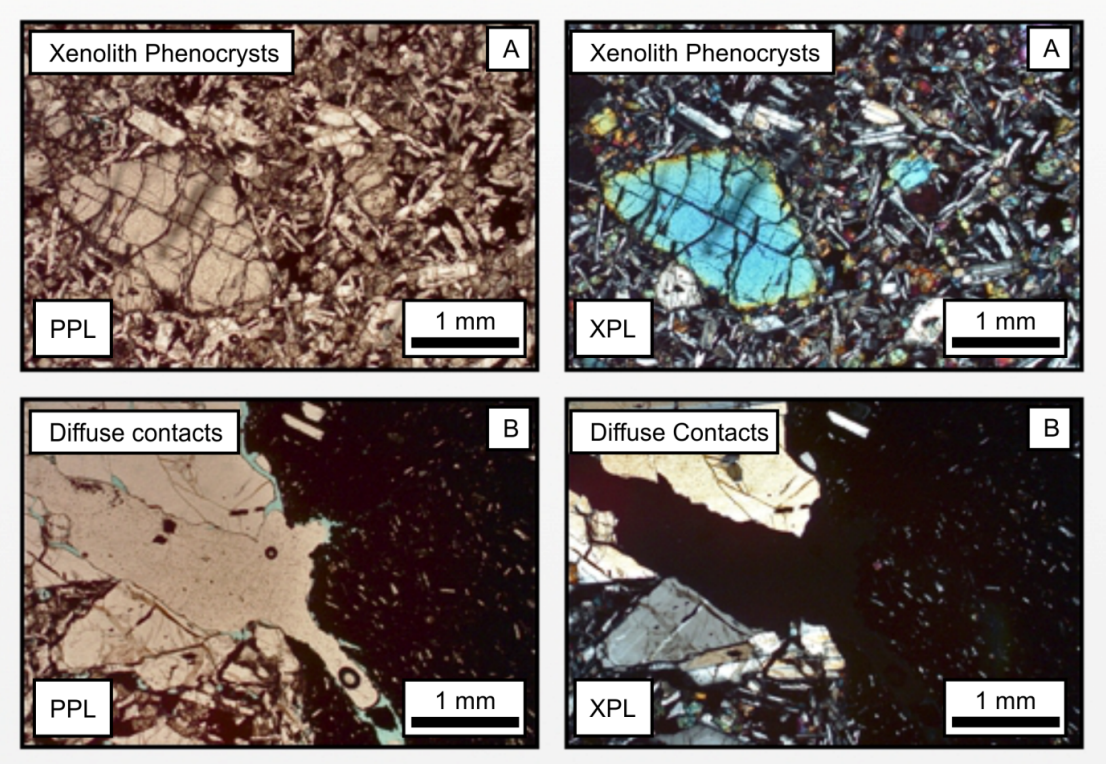

Figure. 5.14. Thin section example of lithofacies vA, xenoliths component. A) Dolerite texture, medium grained groundmass with large olivine phenocrysts. B) Margin of the xenoliths in places is sharp, however in some instances fluid, fluid textures can be observed.

Interpretation – Lithofacies vA, lSP, aSP - Parasitic vent formation and spatter onto saturated ground and late stage effusive basalt volcanism.

Lithofacies lSP and aSP contain clasts of basaltic material and scoria which share characteristics (such as bread crust surface texture and composition) with volcanic bombs in mapped unit R2. Away from the dome structure spatter rags are less agglutinated and hosted in a matrix of fine-grained clay. Clast become progressively agglutinated and flattened towards the dome structure suggesting vent proximal emplacement (via fire fountaining <100s m from vent). The dome structure

may therefore represent original bedding (therefore limited erosion) on of a vent. Additionally mapped unit L2 lava flows are traceable to this structure suggesting it was locally supplying late stage effusive activity.

Vent agglomerates (lithofacies aV) contain dolerite xenoliths with partial assimilation textures indicating hot emplacement temperatures. The vent itself has a composite structure consisting of mainly welded and non-welded basaltic spatter typical of subaerial fissure eruptions that probably formed the lava flow (mapped unit L2) during the course of eruption (Head and Wilson, 1989). The upper lava sequence (lithofacies bL, mapped unit L2) is the last recorded volcanic activity that fills in palaeo-topographic lows. It is blocky and in places cube jointed suggesting interaction with standing water perhaps as a result of continued subsidence of island creating thin hyaloclastite layers at the base of lava flows (Saemundsson, 1970).

Description – lithofacies aLT – thin bedded tuff

Mapped unit P2 is characterized by lithofacies aLT which is highly weathered and poorly exposed on the surface of the Unit L2 lava flows (Fig. 5.7 CThe lithofacies forms a 50 cm-thick, massive bed that drapes the underyling topography with a uniform thickness. The grains are fine grade, spherical (2-3 mm diameter) and highly oxidized. The Iron rich oxides cement the deposit. They are poorly lithified and easily broken with minimal force. The deposition of Lithofacies aLT deposition occurred as the final stage of recorded volcanic activity on Hjörleifshöfði.

Interpretation – lithofacies aLT – Air Fall Tephra

Lithofacies aLT presents a silicic ash fall deposit of unknown age. Spherical grains could be interpreted as accretionary lapilli developed in the atmosphere post eruption. Small ash grains adhere to water molecules and when agitated in an eruption column accrete extra material to form rounded concentrically layered particles (Gilbert and Lane, 1994). As this sample could not be tested due to intense weathering, its affinity cannot be determined; however its origin is likely to be similar to that of lithofacies LTth.

5.5 XRF Geochemical Analysis

XRF analysis was performed to support field interpretations, to classify hyaloclastite clasts, to aid edifice reconstruction and to identify and correlate the ignimbrite in the sequence. Thirty-six samples were collected to represent each of the units in Hjörleifshöfði, as well as clasts separated from the hyaloclastite deposits. Preparation methodology and analytical techniques are covered in section 5.1.3. Altered samples were excluded from the Alteration in five of the samples made them useless for correlation purposes. Altered samples were characterised by analysing fluid-mobile trace elements that allow the recognition of the palagonitisation (Pearce 1976; MacGeehan and MacLean, 1980; Rollinson 1993). This methodology has been outlined in detail in the appendix for this chapter.

5.5.1 Observations

Samples from submarine and subaerial units plot within error in the basalt field on a TAS (total alkali silica) plot (Le Maitre et al., 1984) (Fig. 5.15) and show a tholeiitic affinity (Fig. 5.16). The ignimbrite samples are rhyolitic in composition. Samples of mapped unit H1 hyaloclastite breccia and mapped unit L1 lavas plot in a small field. All major element concentrations for all samples plot within the broad Katla or Eyafjallajokull compositional fields (from Lacasse et al. 2006 and the GEOROC data base [georoc.mpch-mainz.gwdg.de/georoc/]). Samples of Mapped unit L2 basalt lava flows have highly evolved basaltic compositions, slightly lower magnesium number (Mg#), higher SiO_2 and K_2O and slightly lower TiO_2 values (Fig. 5.15). A dyke sample (HL4B) forms a less evolved outlier. Generally mapped unit H1 hyaloclastite clasts correlate with mapped unit L1 lava samples.

Ignimbrite samples have high silica values (69–72 wt %) and high total alkali contents (Fig 5.17 and 5.18). All samples are enriched in FeO for a given CaO value, which may be indicative of iron oxidation during weathering.

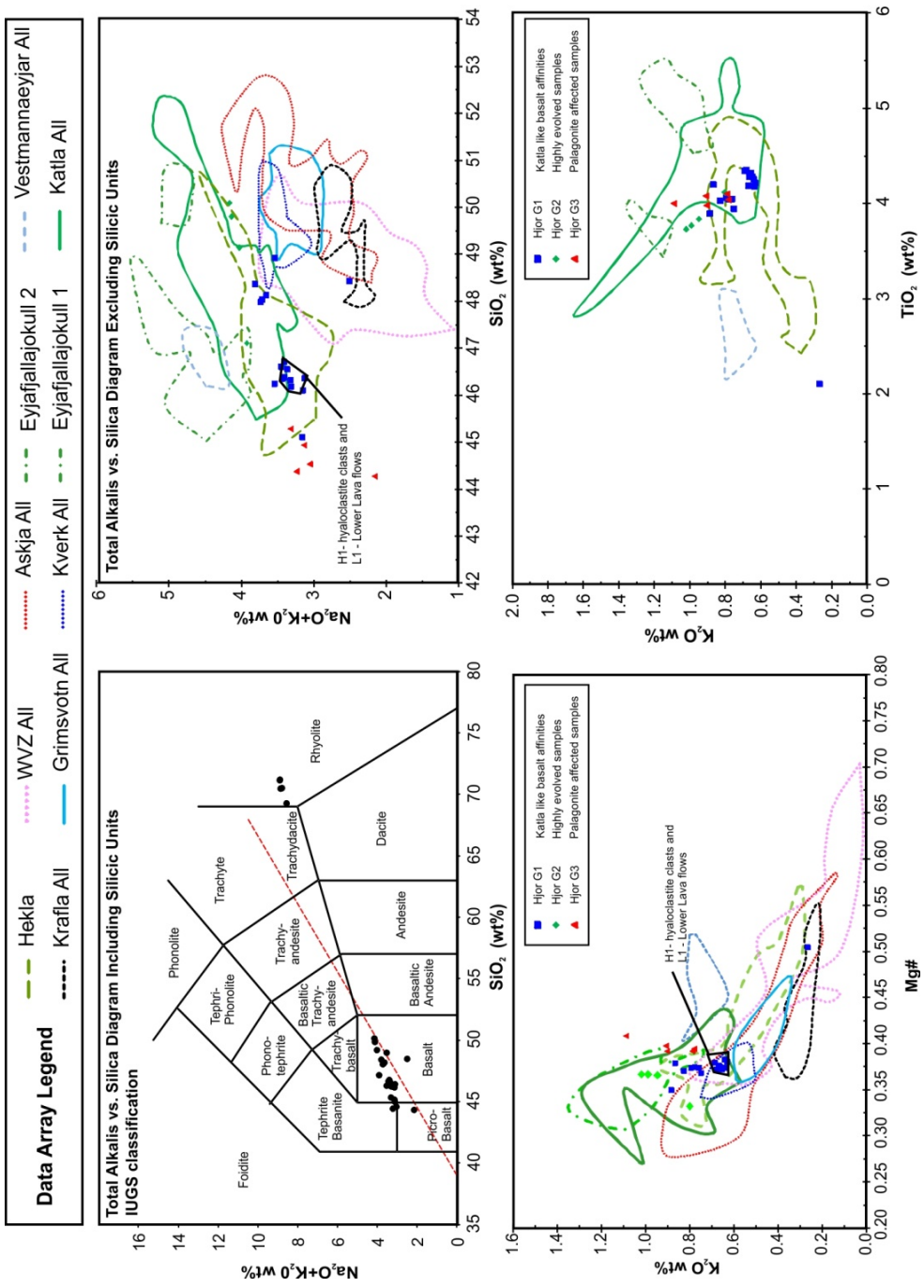

Figure. 5. 15. Geochemical discrimination diagrams for Hjörleifshöfði samples. Top left shows a TAS plot of all samples; all other examples contain low silica samples only. TAS plots confirms bimodal geochemical composition of samples. Silicic units plot in the rhyolite field. All other discrimination plots show only basalt examples. Fields show characteristic arrays for specific volcanoes and regions (data from Sinton et al. 2007; Lacasse et al. 2006 and GEOROC [georoc.mpch-mainz.gwdg.de/georoc/] data base). See text for details. WVZ = Western Volcanic Zone.

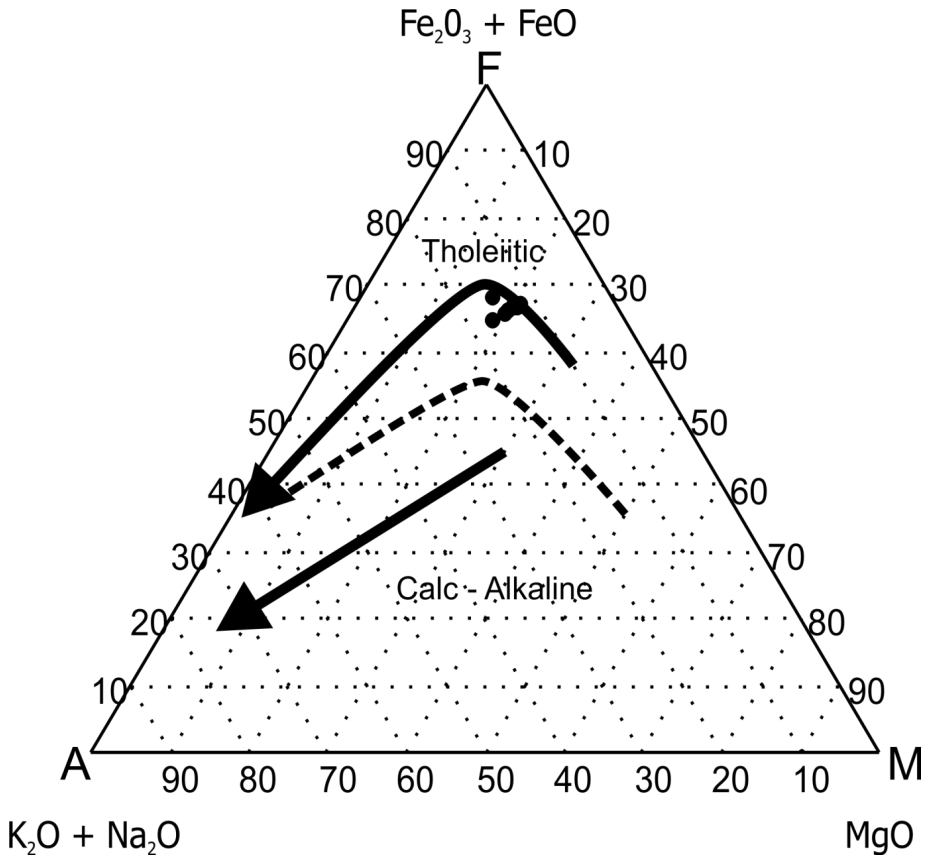

Figure. 5. 16. AFM ternary diagram showing tholeiitic affinity for basalt samples of the Hjörleifshöfði

In order to identify the ignimbrite at Hjörleifshöfði a normalized major and trace element comparison was made with the average values of representative samples from each potential source volcano (Fig. 5.18,data from Jonasson, 2007; Lacasse et al., 2007; Sinton et al., 2007; Martin and Sigmarsson, 2010 and the GEOROC data base). The lower part of figure 5.18 and 5.29 shows the closest matches to the Hjörleifshöfði ignimbrite samples Katla (Ka), Eyjafjajokull (Ey) and the Sólheimar Ignimbrite (SOL). The Sólheimar ignimbrite is a common widespread marker horizon in Southern Iceland (Tomlinson et al. 2012) and is a near-perfect match for the Hjörleifshöfði ignimbrite (Fig. 5.20; r^2 values close to 1).

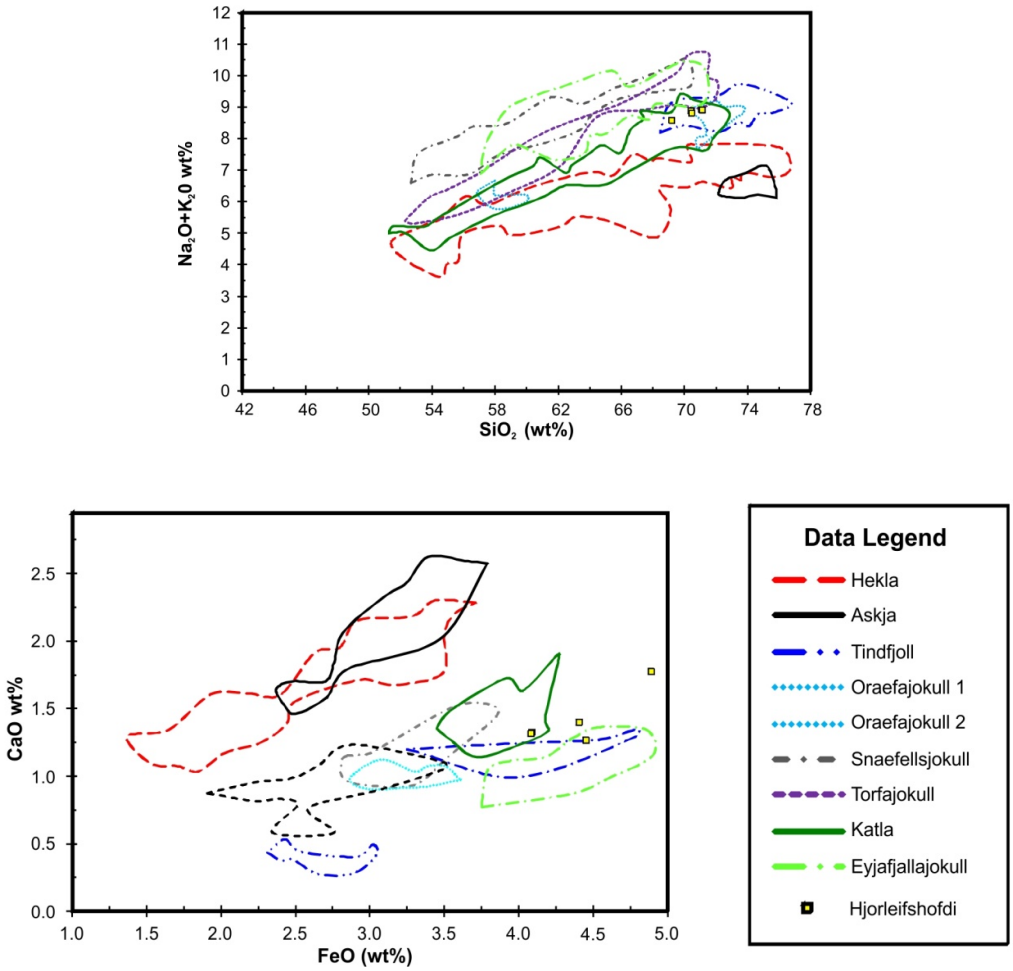

Figure. 5.17. Geochemical discrimination plots for silicic units only. See text for details (data from Sinton et al. Lacasse et al. 2006 and GEOROC data base).

5.5.2 Synthesis of Results

Affinity Basaltic Volcanism

Basalt lavas at Hjörleifshöfði show affinities with Katla and Eyafjallajokull samples. Mapped unit L1 lava flows plot in a field associated with mapped unit H1 hyaloclastite clast samples whereas mapped unit L2 lavas show more evolved compositions although form a evolutionary trend that does not deviate from mapped unit L1 flows. This suggests hyaloclastite clasts from mapped unit H1 are associated and probably contemporaneous with mapped unit L1 lava flows.

Affinity of Silicic Volcanism

The ignimbrite succession on is a close match to the Sólheimar ignimbrite exposed to the south of the Katla structure (The Solheimar ignimbrite is the source of the widespread Vedde Ash tephra marker horizon, Tomlinson et al., 2012). The outcrops on Hjörleifshöfði closely resemble the thickest Solheimar ignimbrite flow-unit (WPA_IC_KT03D) exposed 20 km west of Katla. Both outcrops have a characteristic basal breccia grading upwards into massive highly glassy welded matrix-supported flow-units. The ignimbrites at both outcrops contain two characteristic lithic clast types—rounded basalt clastsand densely welded ignimbrite clasts—with minor amounts of quartz crystals and clay mineralisation. I infer that the two ignimbrites are the same and thus the onset of side vent volcanism at Hjörleifshöfði can be estimated in C14 years at between 12,383–11,841 or 10,310 BP (Birks et al. 1996).

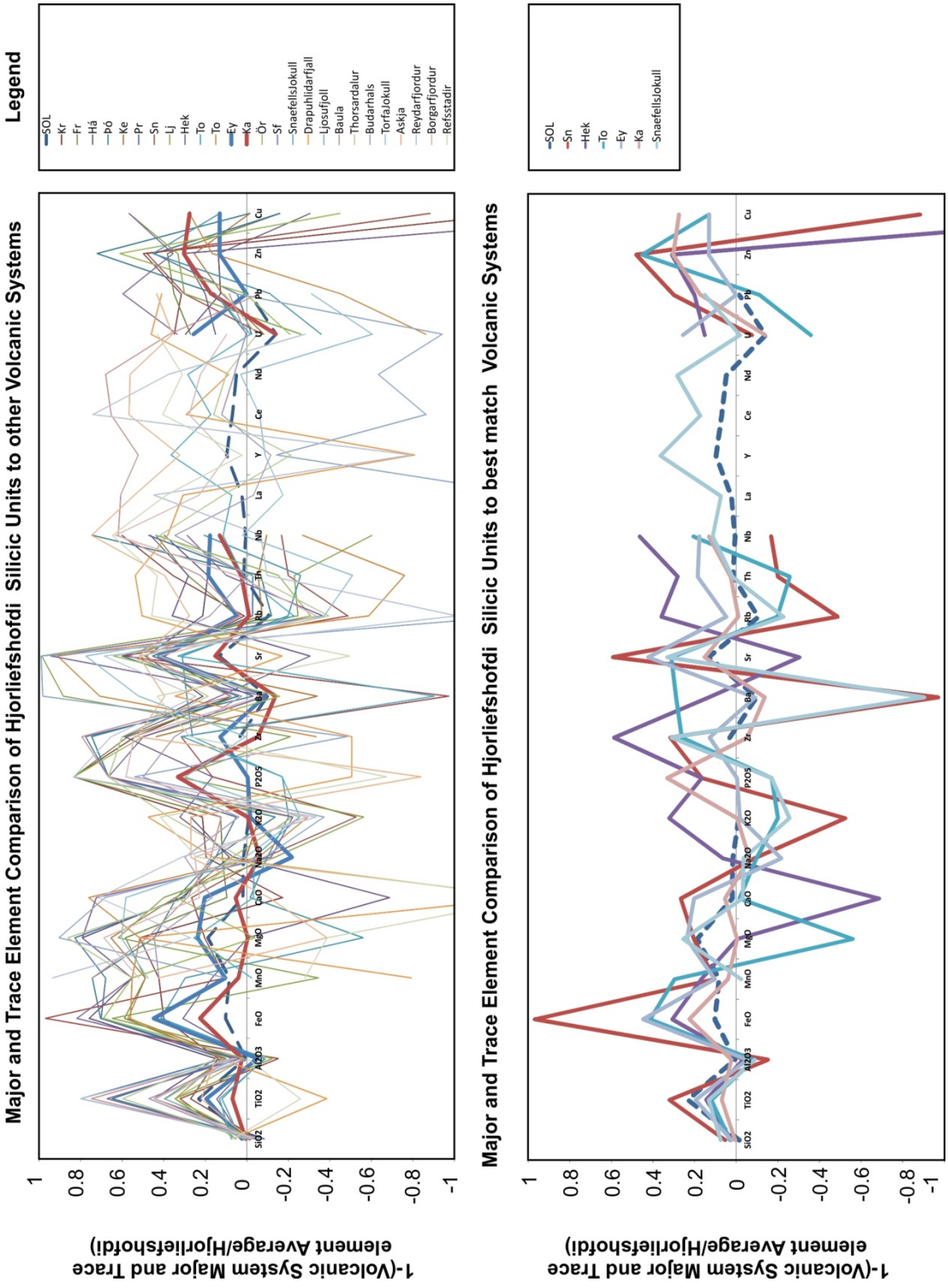

Figure. 5.18. Major and trace element normalized plots of average silicic Icelandic volcanic systems relative to Hjörleifshöfði. Upper diagram is for all local silicic systems in Iceland. The lower diagram shows the closest matches to the Hjörleifshöfði system. All data has been sourced from Jonasson, 2007; Martin and Sigmarsson, 2010; Tomilinson et al., 2012. Abbreviations listed in appendix for this chapter.

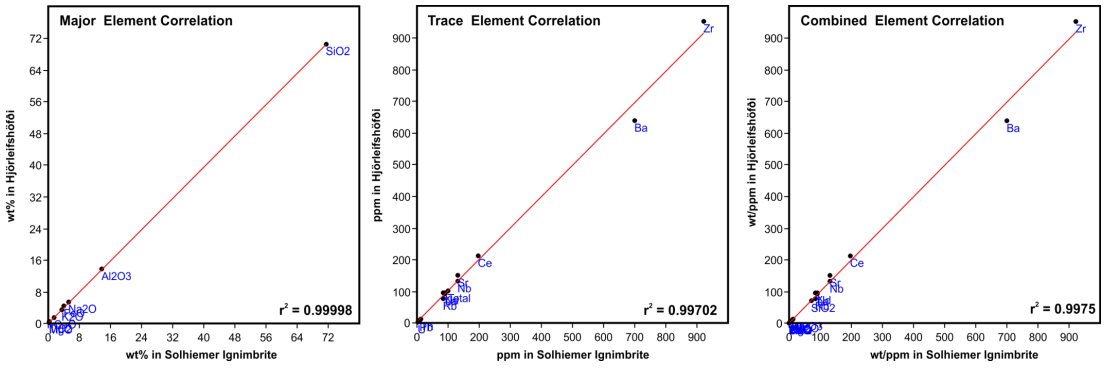

Figure 5.19. Major, Trace and Major + Trace element comparison plots. Y-axis, Hjörleifshöfði weight (wt) % and x-axis Sólheimar Ignimbrite. Regression coefficient is shown for each graph. See text for details.

5.6 Structural Geology

Description

Faults on Hjörleifshöfði can be divided into two main structural trends (1) major, low-angle normal faults that trend SW-NE and (2) minor, high-angle normal faults that trend E-W. The outcrop is dissected by three major listric faults with normal displacements that trend roughly SW-NE and dip 20–40°NW. In outcrop, the along-strike exposure is poor although strike-parallel exposure is good (Fig. 5.20 A and B respectively) SW-NE trending faults form partial arcs. The largest fault (in cross-section B) has an apparent displacement of ~100 m. The large fault cuts the Units B1 and H1 (see map Fig. 5.2). North-south-trending faults have much lower apparent displacements c. 10 m.

On the southern tip of the volcano a number of faults apparently promoted slumping within the deposits (Fig. 5.21). These faults are oriented N-S and dip 60–80° ENE and intersect the lower part of the sequence (Phase A, Table 5.4). Two types of fault damage zones are seen at Hjörleifshöfði. Type I damage zones are characteristic of N-S trending faults. Sedimentary structures have been homogenized in the sedimentary rocks surrounding the faults. These chaotic zones reach 40 m wide. The fault cores of type I damage zones are exposed high in the cliff making observation difficult. A large synform which plunges 10°, and has limbs that dip 35° is associated with Type 1 damage zones (Fig. 5.4B). In this synform bedding is folded, but does not show signs of soft-sediment deformation. However, numerous

small N-S trending faults with meter-scale displacements that are associated with this structure display no visible damage zones.

Type II damage zones are associated with NW-SE trending faults and are more complex. Damage zones are composed of domains of bedded material up to 5 m wide that are chaotically organized in a 10 m-wide zone. The rafts are supported in a fine-grained sandy matrix. Wedge-shaped accumulations (that can reach 40 m thickness) of highly brecciated massively bedded material with clasts up to boulder size have filled in the accommodation space created by extension and rotation of the fault-bounded blocks. (Fig. 5.20 D). The extent of the damage zone and the wedge of breccia are larger on the SE end of the faults thinning to the SW.

Dykes are exposure in cliff section at the southern end of Hjörleifshöfði. Dykes extend up to 60 m terminating in mapped unit R. Generally dykes are vertical to sub vertical trending N/S. Dyke width reaches up to 0.7 m and margins can be chilled. Vesicle bands occur parallel to the dyke margins. Surrounding the dykes are < 1 m thick indurated zones that extend up (Fig. 5.21 B^{I} and B^{II}) characterised by zeolite mineral precipitation in pore space.

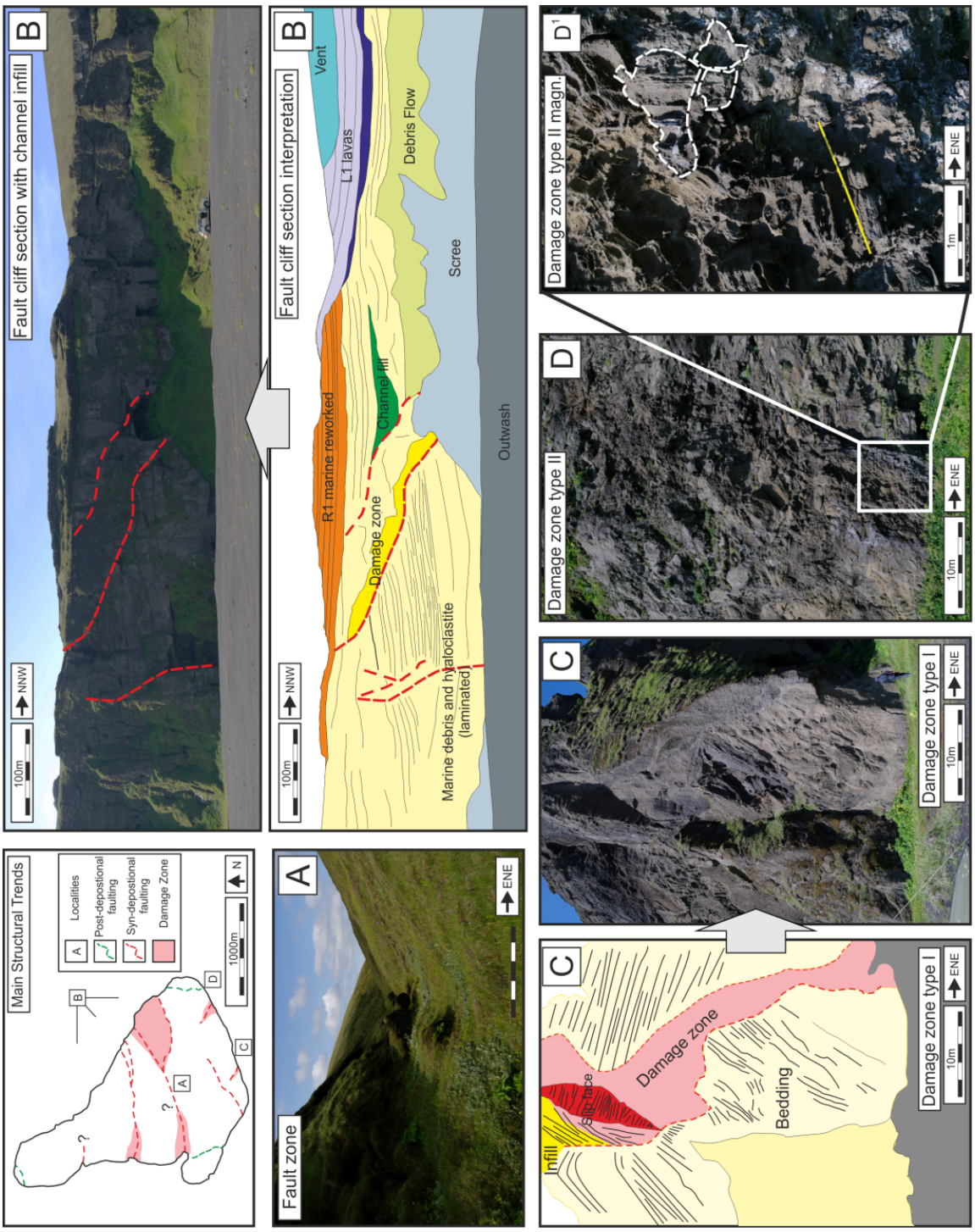

Figure. 5.20 Photos, locations and interpretation of faulting and damage zones on Hjörleifshöfði. A) Fault zone A on top of edifice looking W. Exposure is poor covered in vegetation. B) Fault Zone A looking E towards Hjörleifshöfði. Interpretation shows the distribution of faults and the relationship of each unit. C) and D) show the two types of damage zone which are describes in the section text.

Interpretation

The width and simple internal structure of type I damage zones suggest slip was accommodated over a small area (Caine et al., 1996). The fault bounding the synform structure (Figure 5.4) suggests that they may have promoted soft sediment deformation and slumping over wider areas soon after deposition. Low-angle small displacement normal faulting dissects the slumped deposits following type I damage zone formation. Dyke intruded the low angle faults—no dykes are associated with type II damage zones. Dykes also locally interact with small displacement normal faults that control magma intrusion pathways.

Type II damage zones are more complex and have poorly developed fault cores. Domains of material suggest a higher degree of sediment lithification prior to faulting (Caine et al., 1996). Type II features are associated with large-scale faulting inferring that they represent collapses of large sectors of the volcanic cone, following partial lithification soon after formation. Figure 5.22 compares the size of type II zone and fault lengths to those seen in other emergent or submarine volcanic edifices. The collapse structure in Rota-1, Southern Bank, Mariana Arc, (Fig. 5.22 A) is comparable in length, but the volume of displaced material far exceeds that observed on Hjörleifshöfði. Collapse structures observed on the flanks of Surtsey are smaller but are similar to type I damage zones. Structures such as these develop from small-scale collapse and channelization of the existing tuff cone (Jakobsson et al., 2009).

Curved listric faults with high apparent displacements are similar to fault scarps that bound volcanic craters (e.g. Surtsey) (e.g, Mahood and Hildreth 1986; Sohn, 1994; Solgevik et al., 2007; Sohn and Park, 2005; Sohn et al., 2012).

The scale of faulting at Hjörleifshöfði and the similarity to faulting seen in Surtseyan edifices in the Sea of Japan suggest that it the present outcrop of Hjörleifshöfði is part of a larger volcanic structure. The lava flows on the northern flank on Hjörleifshöfði have probably protected the outcrop from erosion.

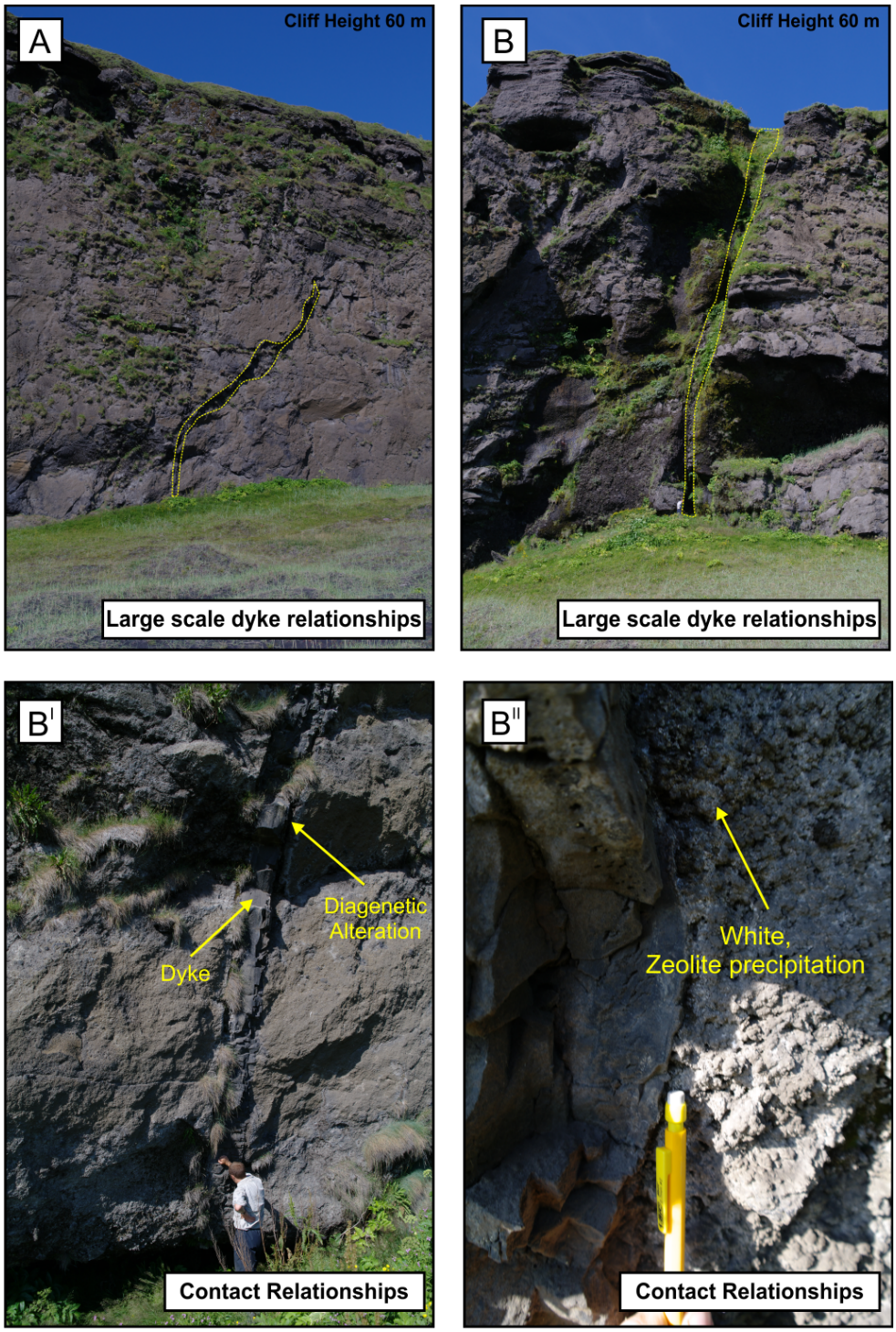

Figure 5.21 Dyke relationships on Hjörleifshöfði. Dykes can extend more than 60 m (A and B). Dykes can interact with small scale faulting with no apparent damage zones to produce lower dip angles (A). Otherwise they can clearly cut stratigraphy at high angles (B). BI and BII show the zone of induration and dyke margins. Precipitation of zeolite may indicate increased hydrothermal circulation post dyke emplacement.

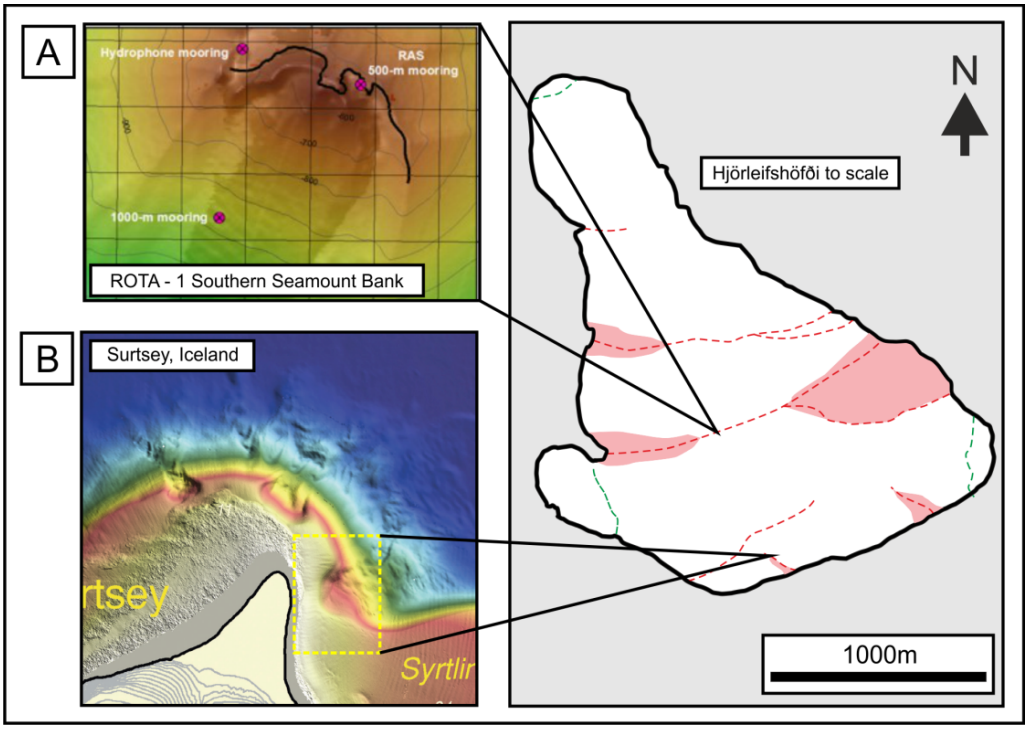

Figure 5.22. Comparison of fault zone extent on Hjörleifshöfði to bathymetrically recorded slump slides A) ROTA-1 Southern Bank, Mariana Arc adapted from Chadwick et al. 2012. B) Surtsey, Iceland adapted (slump height 200 m) from Jakobsson et al., 2009. All data is scaled and orientated to the outline of Hjörleifshöfði.

5.7 Edifice Reconstruction

The evidence outlined above suggests that Hjörleifshöfði is part of a much larger volcanic structure. The lower lava series (Mapped unit L1) thins rapidly and terminates toward fault A in cross section 2 (Fig. 5.2). If we assume that the lava flows a accumulated in a crater to the north of Hjörleifshöfði and to the south the lava flows fragmented to form the hyaloclastite deposits of H1 (as inferred from the similarities in geochemistry) then fault A could be considered a crater-bounding fault scarp near to the original crater rim (cf. Mahood and Hildreth, 1986; Sohn, 1994; Solgevik, et al. 2007; Sohn et al. 2012). If we consider the crater to be circular then the arc of fault A can be related to the diameter of the original crater by the equation (Fig. 5.23);

$$r = \frac{W^2}{8H} + \frac{H}{2} \quad (5.1)$$

where r is the radius of the circle, W is the width of the arc and H is the height of the arc measured from the geological map of Hjörleifshöfði in figure 5.2. If W = 1200m and H = 175 m then the radius r = ~1116.6 m. This gives a crater diameter of roughly 2000 m and, based upon cliff height, the total width of the subaqueous tuff cone to be ~ 7000 m. These dimensions are similar to those of other submarine volcanoes (Smith, 1988; Mitchell, 2001; Mitchell et al., 2002). Similar crater morphologies can be observed in bathymetric images of seamounts (Vailulu'u sea mount, American Samoa; NOAA bathymetric data [www.pmel.noaa.gov/vents/marianas_site.html]) where large craters develop from the subsidence and collapse of the vent structure (Fig. 5.24).

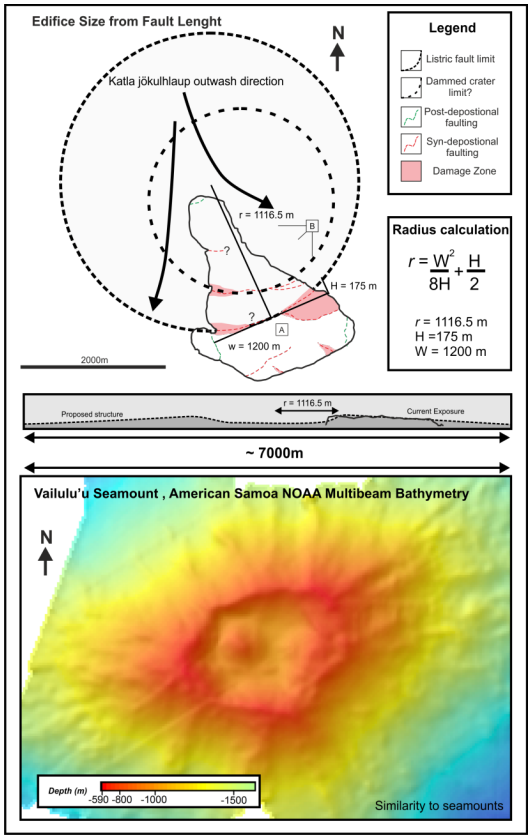

Figure. 5.23. Edifice size from fault arc calculations eq. 5.1. Calculations suggests the radius of the entire pre-existing structure cone was ~ 7km. Bathmetric data from the NOAA database [www.pmel.noaa.gov/vents/marianas_site.html]. See section 5.7.1.

5.7.1 Volcanic Evolution of Hjörleifshöfði

The evolution of Hjörleifshöfði can be divided into five main phases (Fig. 5.25 and 5.26). Each phase can be linked to relative water depth of the central vent and relative uplift or subsidence of the volcanic pile. Each stage is summarized below in figure 5.26.

Phase A

- Construction of the submarine tuff cone through submarine eruptions, basaltic fragmentation and thick debris flows (Mapped Unit B1, Lithofacies VB)
- Syn-sedimentary hyaloclastite deposition from distal reworking of fragmented products (Mapped unit H1, lithofacies GHip, also see chapter 4).
- Continued fragmentation of subaerial lava flows adding addition hyaloclastite material. Geochemical evidence may also suggest that mapped units L1 and H1 contemporaneous.
- Collapse of the cone margin leads to bounding listric fault producing a dammed crater to north and the submarine edifice flank to the south.

Phase AR

- Sub to supra littoral reworking of deposits (mapped unit R1) on Hjörleifshöfði implies that it was exposure to strong Atlantic weather systems producing large waves.
- Extensive fault breccias formation more centrally and on the north side of Hjörleifshöfði forming initial vent fill (e.g. Jakobsson and Moore, 1982; Moore, 1985).
- Continued Surtseyan activity leads to the accumulation and shoaling of basalt fragments and vesicular tephra in subaerial to littoral conditions.

Phase B

- Subaerial emplacement of mapped unit L1 lava flows is occurring at the same stratigraphic level AR phase reworking on the south side of the outcrop. .
- Tephra horizons (lithofacies lT) represent “rooster-tail” phases associated with continued submarine activity elsewhere on the structure.
- Subsidence of the volcanic pile allows water ingression and the spread of mapped unit R2a deposits on to mapped unit L1 lavas on the northern side of the island before phase C activity.

Phase C

- Pyroclastic density currents deposits ignimbrites in topographic lows and occur interbedded in mapped unit R2 deposits in a littoral shoreface environment.
- Mapped unit P1 petrographically and geochemically correlates well with the Sólheimar Ignimbrite suggesting that subsequent volcanism on Hjörleifshöfði is either (C14 years) at between 12,383–11,841 or 10,310 BP (Birks et al., 1996; Tomlinson et al., 2012).

Phase D

- A small subaerial fissure eruption creates a small side vent on the existing structure allowing the accumulation of vent proximal spatter and emplace volcanic bombs in still unlithified mapped unit R2.
- Vent agglomeratic deposits (lithofacies vA) accumulate at the apex of the dome structure on Hjörleifshöfði and contain xenoliths of dolerite material.
- Late stage effusive lava flows across mapped unit R2 continued damming of the crater and subsidence of initially deposited mapped unit R2 lithofacies.
- Localized hyaloclastite development on the eastern flank of the volcanoforming mapped unit H2, In cross-section the vent is flared near the surface presenting the conduit to vent transition (e.g. Keating et al., 2008).
- Late stage subsidence post emplacement likely controls current dip and dip direction. Most deposits dip radially towards the side vent structure

suggesting draining of the underlying magma reservoir (common feature of many volcanoes, e.g., Bonforte et al., 1998).

- Highly weathered beds containing accretionary lapilli are exposed on top of Unit L2 lava flows. The degree of weathering and poor exposure means geochemical analysis of their affinity would be impossible. These may be sourced from neighbouring volcanoes (e.g., Katla).

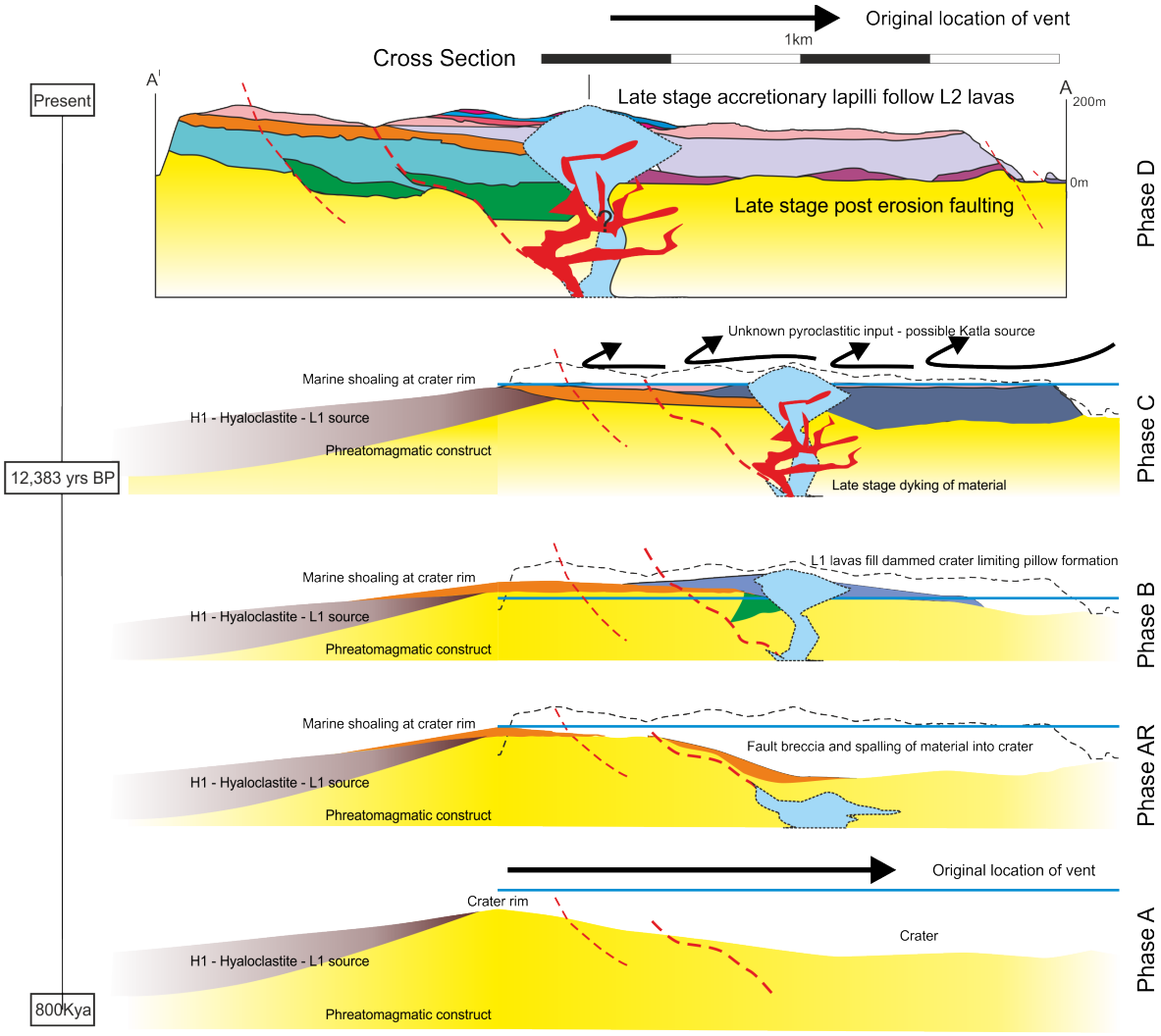

Figure 5.24. Cross section evolution summary of the Hjörleifshöfði volcano. Time scale refers to the best age estimate confirmed by palaeomagnetic data (Iceland Land Survey Mapping). Cross section only shows the southern extend of the larger underlying edifice. See section 5.7.2 for details.

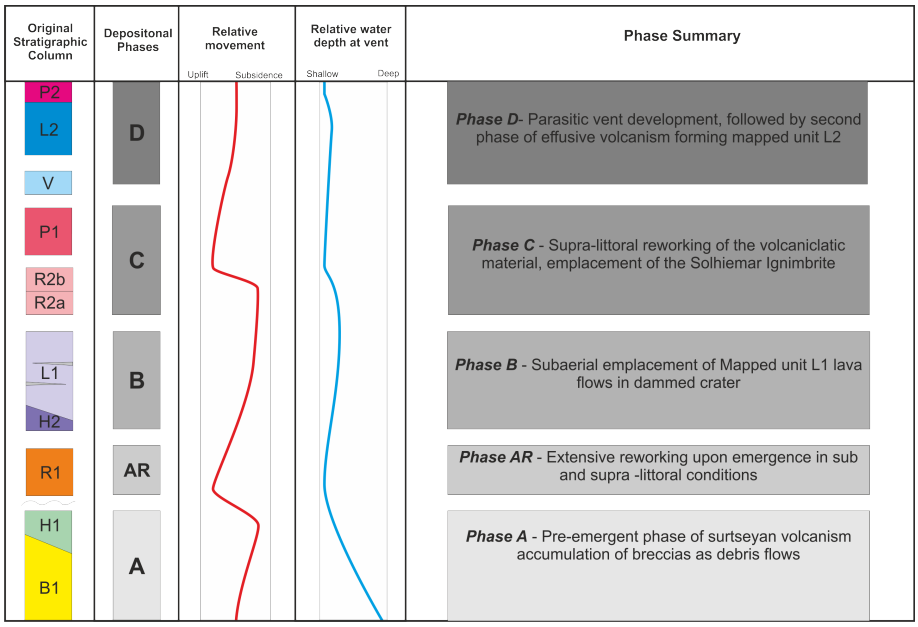

Figure. 5.25. Stage evolution summary table for the Hjörleifshöfði volcano. Relative movement refers to uplift (associated with edifice building and subterranean magma accumulation) and water depth indicates what the summit of Hjörleifshöfði experienced through each of the stages. See section 5.7.2 for details.

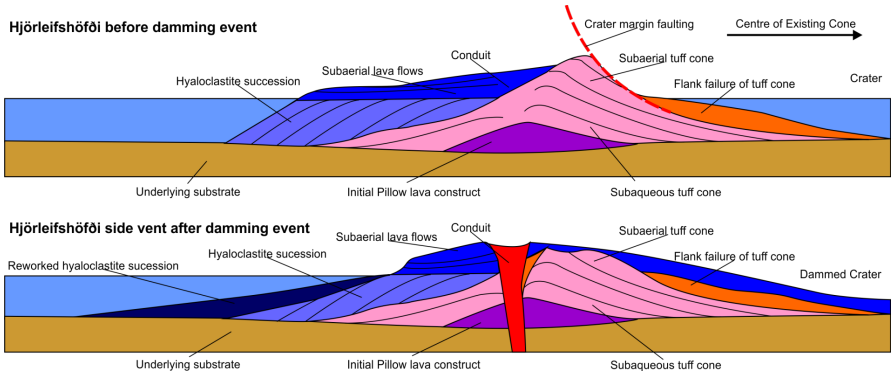

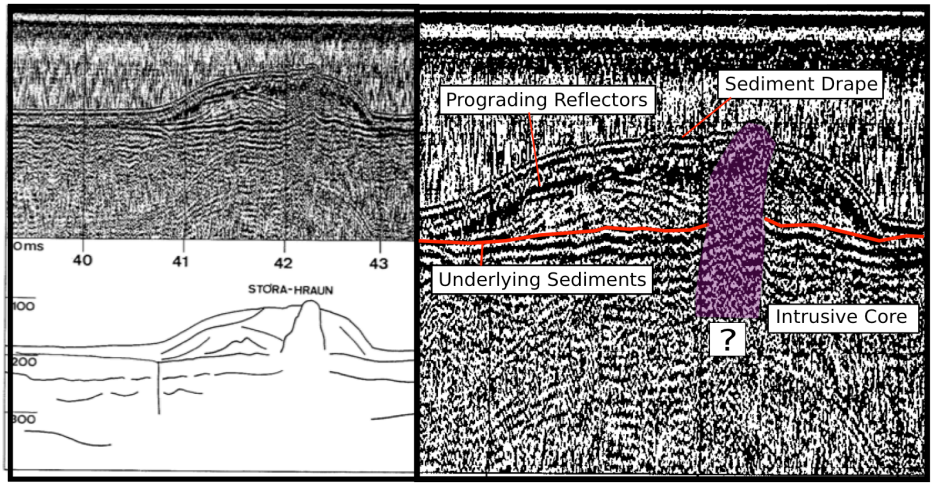

Figure. 5.26. A summary before and after diagram of the Hjörleifshöfði side vent during crater damming. Based upon Thordarson personal communication. Underneath the summary diagram is a 2D seismic reflection section of Stora-Hraun (see section 5.8). The profile has been interpreted simply for this chapter showing the main intrusive body. Stora-Hraun never became emergent however prograding reflectors potentially representing debris flow facies analogous to VB exist of the flank of the structure (Adapted from Thors and Jakobsson, 1982).

5.8 Comparison to Surtseyan Edifices

Hjörleifshöfði is likely to be a submarine volcano however similar morphologies are seen in Hlöðufell (Skilling, 2009) or Hruðfell (Werner and Schmincke, 1997) where large melt water lakes form around a previous volcanic edifice (e.g. Trodeson and Smellie, 2002) However the outcrop pattern; an asymmetrically distributed, large subaerial lava pile, distally derived subaqueous debris flow deposits, extensive Phase AR reworking and the timing of ignimbrite emplacement at the height of the late glacial maximum (Tardiglacial, Clark and Alvárez-Fernández, 2004) where melt water production was at its highest suggests against total ice confinement.

The deposits at Hjörleifshöfði share similarities with other hyaloclastite deposits within submarine to emergent Surtseyan volcanoes (e.g. Tuff cones of the Marion and Prince Edward Islands, Verwoerd and Chervallier, 1987; Waiareka-Deborah Volcanics, New Zealand, Cas et al., 1989; Ambrym Vocano, Vanuatu, Robin et al., 1993; Pahvant Butte, Utah, White, 1996; The Iblean Mountains, Sicily, Schmincke et al., 1997; Mussorgsky Peaks and Mount Greig, Antartica, Smellie and Hole, 1997; The Kangerluluk Sequence, Greenland, Mueller and Stendal, 2000; Cepelinhos, Azores, Cole et al., 2001; Jeju Island, Korea, Sohn et al., 2005 and Sohn et al., 2012; Sinker Butte, Idaho, Brand and White, 2007; Capaelas tuff cone, Azores, Solgevik et al., 2007, Chatham Islands, New Zealand, Sorrentino et al., 2011; Smerekovec, Solvenia, Kralj, 2012). All these volcanoes exhibit complex lateral and vertical transitions from a Surtseyan cone-building phase to effusive lava flows. All cone-building sequences have stratified tops, which are indicative of reworking processes.

The low angle normal faults with large displacements on Hjörleifshöfði are similar to crater-margin faults seen on the edges of other submarine to emergent volcanic edifices (Mahood and Hildreth, 1986; Sohn, 1994; Sohn, 1994; Sohn and Park, 2005; Solgevik et al., 2007; Jackobsson et al., 2009). On Hjörleifshöfði this leads to the north-south divide between subaerial lava flows and submarine or littoral marine volcaniclastic sediments either side of a crater-bounding fault. Crater lake filling lavas in late-stage Surtseyan eruptions elsewhere (e.g. Sinker Butte, Brand and White, 2007) are much thinner than those at Hjörleifshöfði suggesting that crater damming occurred early, but also that effusive subaerial activity was late enough to avoid lava water fragmentation processes before the vent sufficiently drained.

The Hjörleifshöfði phase A cone building deposits are similar to distal submarine debris flow deposits elsewhere (Cole et al., 2001), Mueller and Stendal, (2000), White, (2000), Sohn et al., (2005), Sorrentino et al. (2011). They are similar to those observed on Surtsey (Moore, 1985) albeit with distinct cross-bedding features suggesting a component of channelized flow (e.g, Ollier et al., 1998). This evidence suggests that the lower portion of the present Hjörleifshöfði edifice is a distal section of a larger submarine tuff cone.

Lateral migration of vents is common in small basaltic volcanoes (e.g. Thorarinsson, 1967; Houghton and Schmincke, 1989; Thordarson and Self, 1993, Houghton et al., 1999; Cole et al. 2001; Sohn et al., 2012). Additionally pulsing of volcanic activity for example, in the Jeju volcanic complex leads to small disconformities throughout the cone succession that are triggered by changes in the depth of fragmentation. Changes in the source of fragmentation can also occur due to filling of the vent with material or large-scale collapse of vent margins, which can redirect the magma supply (Sohn and Park, 2005, Befus et al., 2008, Sohn et al., 2012). Interestingly on Hjörleifshöfði side vent formation occurs following the emplacement of a pyroclastic flow from a neighbouring volcano, which may have acted to block or compromise an existing site of fragmentation, since eroded and shifted the locus of fragmentation to the nearest plane of weakness, in this case the crater bounding fault.

The presence of xenoliths in vent agglomerate is relatively unusual in Surtseyan eruptions. Fragments of the underlying strata usually occur in tuff cone deposits of Surtseyan volcanoes (e.g. Andrews, 2003; Maicher et al., 2000; Mattsson

et al. 2005) The parasitic vent at Hjörleifshöfði may represent the site of a small parasitic subaerial eruption, which fed the upper subaerial lava flow sequence (e.g. Sinker Butte, Brand and White, 2007).

The superb outcrops at Hjörleifshöfði volcano allows it to be compared to 2D seismic lines shot across the submarine section of Surtsey volcano (Thors and Jakobsson, 1982). The submarine section of Surtsey consists of a number of flanking vents. Stora-Hraun (the largest side vent) has a series of seaward-dipping reflectors, similar to hyaloclastite and submarine debris flow deposits (Fig. 5.26). A high-angle dome-like structure lies near the centre of both volcanoes possibly indicating the position of the vent. Stora-Hraun lies on flat lying reflectors. These structures are similar to those seen at Hjörleifshöfði such as a low angle initial debris flow deposits, prograding hyaloclastite lithofacies and continuous sediment drapes (Fig. 5.26).

These observations are useful for offshore petroleum exploration in volcanically active basins where Surseyan volcanoes or extensive submarine shield volcanoes are present (e.g. the North Atlantic igneous Province; Archer et al., 2005).

5.9 Conclusions

- Hjörleifshöfði is a well-exposed partially preserved Surtseyan volcano.
- The evolution of Hjörleifshöfði can be split into six phases of deposition charting the submarine to emergent building of the edifice and the development of a parasitic cone.
- Hjörleifshöfði is unique in the scientific literature as the edifice incorporates a phase of silicic volcanism attributed to an external source that can be used to help interpret its timing and origin as a non-ice confined submarine to subaerial volcano.
- Major and trace element geochemistry has proved useful in tying hyaloclastite deposits to parent lava flows and to recognising the source of the ignimbrite as the 12,383 C14 years BP Sólheimar Ignimbrite from Katla).

- As silicic pyroclastic rocks occur interbedded in the succession below the parasitic cone late volcanism occurred no earlier than 12,383 C14 years BP (during the last late glacial maximum, when sea level was at its highest). This is much better than previous estimates based on palaeomagnetic data of <800 thousand years BP.
- The extensive exposure of Hjörleifshöfði to Surtsey allows a comparison to be made to 2D seismic surveys revealing new information about parasitic side vents in the subsurface.

6

CHAPTER FIGURES AND TABLES

Figure. 6.49. C10 site 5 x 450 mag. YAGBSE (Backscatter) image of sulphide crystals surrounds to clay filled vesicle probably and early stage quench feature. 259

6. Hyaloclastite Deposits in Wire-line Logs

Chapter Summary

Offshore sequences of volcaniclastic rocks (such as hyaloclastite deposits) are poorly understood in terms of their rock properties and their response to burial. As petroleum exploration enters more volcanically influenced basins (e.g. volcanic rifted margins) worldwide, the understanding of volcanic rock properties becomes important both in terms of drilling and how the rocks themselves may behave as seals, reservoirs or permeability pathways. The Hawaiian Scientific Drilling Project (HSDP) Phase II in 2001 obtained a 3 km-long core of volcanic and volcaniclastic rocks that records the emergence of the largest of the Hawaiian Islands. Core recovery of 2945 m resulted in an unparalleled data set of volcanic and volcaniclastic rocks. This dataset provides one of the best available examples of hyaloclastite deposits and associated volcanic lithologies, to study the relationships between drill core and wire-line log data, lithofacies variation and burial diagenesis. Initially discussed are the results of previous density measurements in comparison to predicted velocity/density relationships in hyaloclastite deposits from the HSDP II core. Then using logging from field examples and time intervals from seismic sections, implications for depth conversion and seismic reflectivity in hyaloclastite deposits is discussed. However in order to characterise well log responses, further detailed logging, optical petrology and major element analysis of two sections at depths A) 1831–1870 and B) 2530–2597 m, are compared to recovered petrophysical logs. Both intervals show sub 1.5 km burial alteration and diagenesis. Deviation in petrophysical properties does not seem to correlate to changes in grain size or clast sorting, but instead correlates with alteration type (zeolite component) and bulk mineralogy (total olivine phenocryst % component). This dataset is important in helping to calibrate well log responses through hyaloclastite intervals in areas of active petroleum exploration such as the North Atlantic (e.g. West of Shetland, UK/Faroe Islands, Norwegian Margin) and South Atlantic margins (e.g. offshore Angola, Brazil).

6.1 Introduction

Hyaloclastite deposits are commonly interbedded with both lavas and sedimentary rocks, and in sedimentary basins thought to be good indicators of palaeo-sea levels (e.g. Jerram et al., 2009; Wright et al., 2012) and can mask potential subjacent hydrocarbon plays (the sub-basalt imaging problem, e.g. Maresh and White, 2005; Jegen et al., 2009; Davison et al., 2010; Ellefsen et al., 2010). This is a particular problem in volcanic rifted margins where early volcaniclastic sequences, thought to be predominantly hyaloclastite deposits, can be found in a variety of settings (e.g. Lava deltas in the West of Shetland, UK/Faroe and Norwegian margins (Planke et al., 2000; Jerram et al., 2009, Inner flow facies, Norwegian margin (Planke et al., 2000). A good understanding of the geometry and petrophysical properties of hyaloclastite sequences is therefore required to help understand their impact on the sub-basalt imaging problem and to aid successful hydrocarbon exploration in basins that contain large volumes of these poorly understood rock types..

Detailed petrophysical observations of hyaloclastite rocks in petroleum-bearing basins are limited. For example, there are only a few well penetrations of hyaloclastite in the ~1 km thickness that underlies most of the volcanic and sedimentary Palaeogene rocks in the Faroe-Shetland Basin (FSB), UKCS and Faroe Islands. The LOPRA-1/1A borehole (Faroe Islands) has provided a range of geophysical information on various volcanic rocks (cf. Boldreel, 2006; Christie et al., 2006; Nelson et al., 2009), but only a small interval (not publically released) was cored. Thus, no direct comparison of the petrophysical parameters of hyaloclastite rocks (obtained via wire-line logging) has been made with drill core over varying burial depths.

Commonly, it is assumed that hyaloclastite deposits have a relatively uniform p-sonic velocity (Vp) distribution and only limited gamma ray (GR) variation, based on the LOPRA-1/1A available data (Boldreel, 2006; Nelson et al., 2009). It is unclear if this can be extended to cover hyaloclastite deposits in general or if this is typical of a particular style of lithofacies present in the LOPRA-1/1A studied interval. Recent studies have identified significant lithofacies variations in onshore examples (Watton et al., 2013), which suggest a large potential range in rock properties for lithofacies invariably described under the classification of hyaloclastite. Most hyaloclastite

sequences contain a number of lithofacies that are distinguished by texture and grain-size and that formed due to variations in the efficiency of the lava fragmentation processes and due to varying degrees of downslope remobilization (e.g. Watton et al., 2013). Thus, hyaloclastite deposits can be highly variable in terms of clast density, particle size distribution, matrix proportion, alteration and crystal content (a function of lava composition) (see chapter 4 for detailed description of hyaloclastite terminology). The extent to which sub-surface hyaloclastite sequences may contain a range of different rock types with a range of petrophysical properties remains an unexplored key question.

This chapter combines detailed lithological logging of drill core taken from the ~3 km-deep Hawaiian Scientific Drilling Project Phase II (HSDP) with published and unpublished geophysical log data in order to constrain the petrographical and petrophysical variations of hyaloclastite deposits (data sourced from International Continental Drilling Project public data base [www.icdp-online.org/front_content.php?idcat=1119]). Core section runs were selected from intervals at similar depths to hyaloclastite rocks in volcanic-affected basins worldwide that are currently undergoing active petroleum exploration. Each core section has been compared to its petrophysical well log responses recorded during the coring of HSDP phase II. Implications of this study for hydrocarbon exploration is explored and discussed in chapter 8.

6.1.1 Hawaiian Scientific Drilling Project Phase II Context

The HSDP was set-up to investigate the causes of mantle plumes via drilling and sampling of a deep-cored interval in order to study chemical variation with depth (proxy for time, Stopler et al., 2009). HSDP drilling took place over two six-month periods from 1999–2001 and reached a depth of 3043 m at Hilo on the eastern flank of Hawaii. Core recovery was halted for 98 m where hole stability was low in unconsolidated hyaloclastite material (rotary drilled interval, Garcia et al., 2007). All geophysical log measurement was conducted by the University of Hawaii, GDZ Postdam (University of Aachen) and the University of Goettingen.

Aspects of HSDP II hyaloclastite deposits have been studied in some detail and published in subsequent reports/papers following the drilling. Figure 6.1

highlights the lower 2 km-thick submarine section as recorded by Moore, (2001), Walton and Schiffman, (2003), Stolper et al., (2004), Walton et al., (2005), Schiffman et al., (2006). The major zones of alteration, geochemical variation, weight percentage of water absorbed (effective porosity) and density identified by extensive sampling programs are indicated along this section. Four distinct geochemical zones and types have been recognized in the hyaloclastite deposits and lava samples based upon MgO normalized SiO_2, SiO_2, Zr/Nb values and H_2O content (Seaman et al., 2004; Rhodes and Vollinger, 2004). High SiO_2 refers to samples with > 50 wt % silica, degassed samples (H_2O < 0.21 % and S < 0.04), partially degassed (H_2O < 0.21-0.09 % > S > 0.04 %) and undegassed (H_2O > 0.45 % and SiO2 > 0.09 %) (Stopler et al., 2004). The amount of degassing refers to pressures encountered during formation, degassed samples lost water at pressures similar to atmospheric whereas undegassed samples did not experience less than 40-50 bars (Stopler et al., 2004).

Glasses in hyaloclastite deposits can be divided into four discrete zones (Fig. 6.1). Zone 1, 1079-c.1950 m, high SiO_2 degassed; Zone 2 c.1950-2233 m, decreasing SiO_2, degassed; Zone 3, 223-2481 m, low-SiO_2, undegassed; Zone 4, 2481-3043 m, high- SiO_2, undegassed (Stopler et al., 2004). Lava types are also divided into four separate types, Type 1 lavas are typified by high SiO_2 and Zr/Nb values (affinity similar to Mauna Kea; Type 2, low SiO_2 high Zr/Nb, above 850 m; Type 3 low SiO_2 and Zr/Nb (affinities similar to Loihi; Type 4, high SiO_2 and low Zr/Nb below 1974 m (Rhodes and Vollinger, 2004).

Variation in SiO_2 and H_2O is thought to arise from the different source magmas interacting with the underlying peridotite to generate high SiO_2 olivine-rich melts (Seaman et al., 2001; Seaman et al., 2004; Stolper et al., 2004). Periodic switches in sourcing lead to olivine-phyric and olivine-poor lava flows which is thought to reflect small changes in source component and melt production superimposed by shallow melt segregation (Rhodes and Vollinger, 2004).

Both Moore (2001) and Walton et al. (2003) recognized that the diagenesis of the HSDP II hyaloclastite was strongly depth-dependent. Following burial, increasing temperatures promoted the break down of glass and the growth of palagonite, which reduced the effective porosity of the deposits at depths greater than 1800 m. Zeolite precipitation was associated with palagonite and smectite growth

during element exchange in the palagonisation process (e.g. Walton et al., 2005). Two low-temperature zeolites occur in HSDP II— chabazite and phillipsite. Associated zeolite minerals are Ca-silicate phases (e.g., gyrolite,Walton and Schiffman, 2003). Variations in the abundance and type of zeolite minerals may reflect changes in the meteoric-saline water interface during burial, however, this is yet to be fully characterised. It should be noted that zeolites are a common mineral phase in the low temperature diagenesis of basaltic lithologies (e.g. Jørgenson, 2006), and are found throughout the flood basalt provinces worldwide.

Buysch et al., (2000) and Pechnig et al., (2000) characterized the entire subaerial and submarine well-log succession using a combination of gamma-ray (GR) and deep resistivity logs (RES). They recognized eight major well log units (Fig. 6.1a) and were able to differentiate lava flows, hyaloclastites and sediment (volcaniclastic) horizons. Three hyaloclastite units occur at depths greater than 1800 m. Log unit (LU) 4 below 1820 m corresponds to more strongly lithified hyaloclastite, in which consolidation and precipitation have created higher resistivity values. Hyaloclastite successions at greater depths are interbedded with pillow lavas (Units 5, 7, 8, 9, Fig. 6.1b).

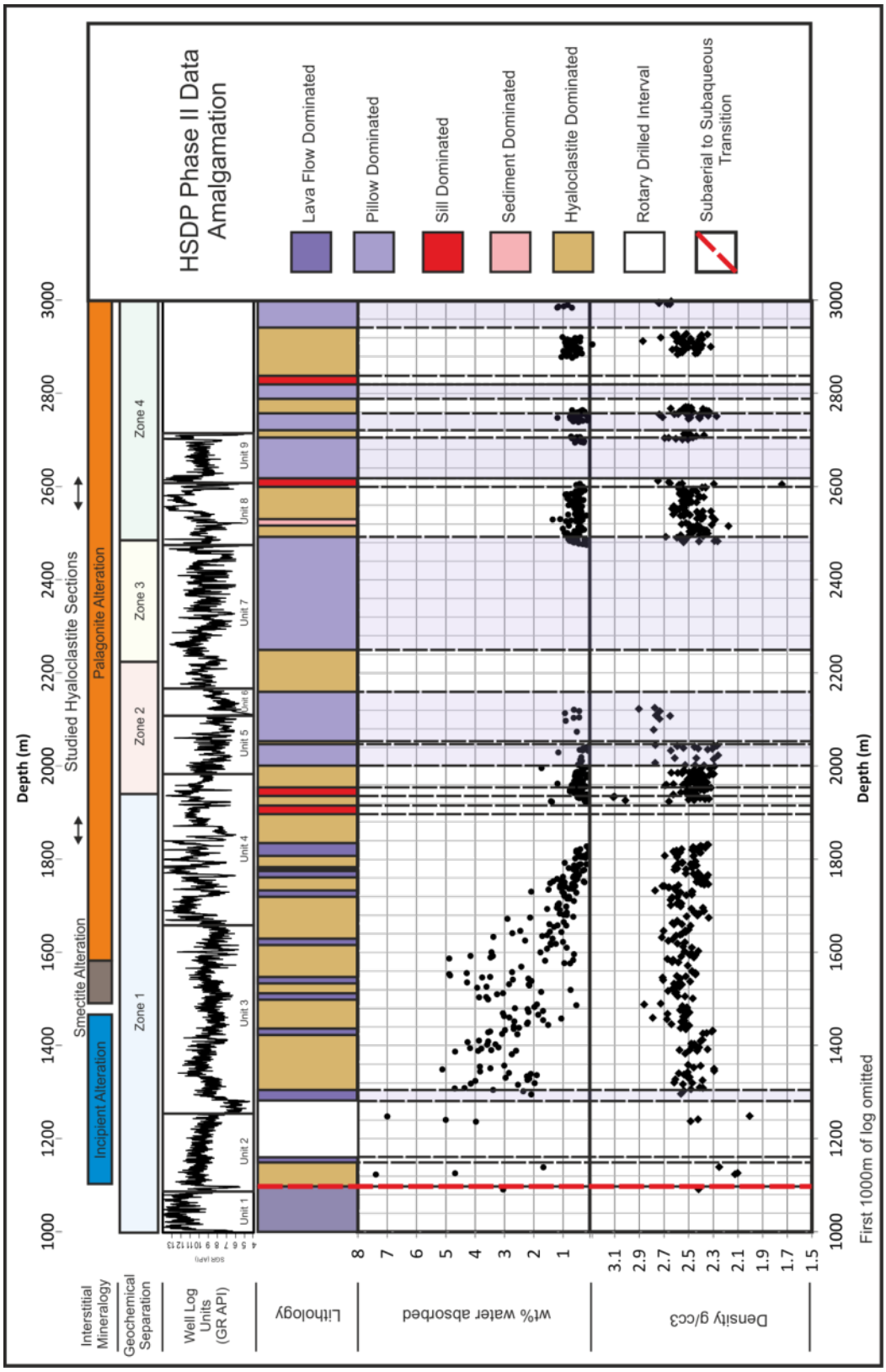

Figure 6.1a. Overview of previous HSDP phase II data. Long-wave length log changes reflect changes in lava geochemistry (SiO_2). Effective porosity (weight % of H_2O absorbed) is reduced rapidly during early burial diagenesis. See section 6.1.2 for details.

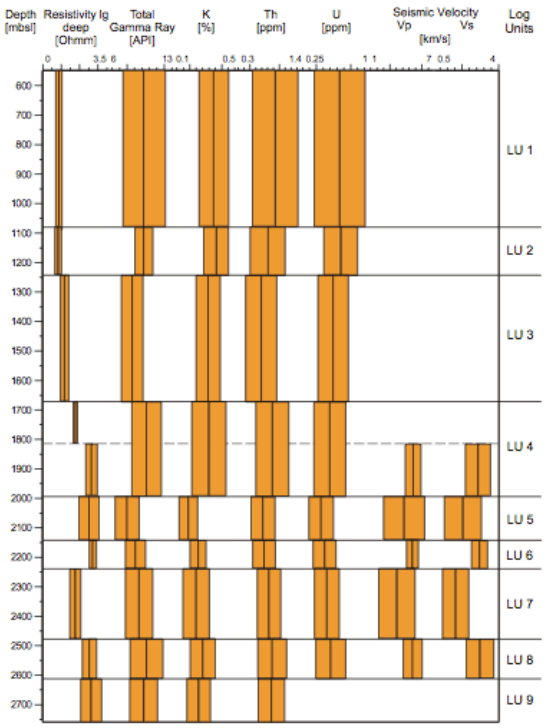

Figure. 6.1b Down-hole log separation of entire HSDP II with mean and outlier values. Note 8 units characterize the submarine section of the core (below 1089 m) (from Pechnig et al., 2000). Available as public data on the ICDP database [http://www.icdp-online.org/upload/pdf/hawaii/agu2000_poster_renate2.pdf].

6.2 Density Prediction Using P-wave (Vp) Velocity in HSDP II

The response of hyaloclastite deposits in conventional wire-line log parameters has only been tested in a limited capacity. Current datasets such as the LOPRA 1/1A borehole indicate that hyaloclasite deposits have near uniform Vp values (c. 5.1 km/s) (Boldreel, 2006; Nelson et al., 2009). Considered here are hyaloclastite deposits from the HSDP phase II dataset as recorded from conventional wire-line logging tools (outlined in chapter 2). This chapter tests the hypothesis that all hyaloclastite deposits will show a relatively uniform velocity analogous to those intersected in the LOPRA 1/1A borehole (e.g. Boldreel, 2006; Nelson et al., 2009).

Where direct density data are not available, geophysicists use an empirical relationship between sonic p-wave velocity (Vp) and density (ρ) to determine synthetic seismic wavelets for seismic reflection correlation (Lindseth, 1979). However, only limited laboratory measurements of density in hyaloclastite deposits are available to validate or disprove the empirical relationships that predict density

from Vp. The HSDP II dataset is important in this regard because it contains over 300 lab measurements of saturated density in hyaloclastite deposits (e.g. Moore, 2001). Down hole calibrated velocity logs overlap with 72 % (234) of these samples. This section reviews the accuracy of conventional siliciclastic modelling techniques in comparison to laboratory-based grain density data used to calibrate (Vp) and (ρ) in hyaloclastite deposits for the first time.

Grain density in the HSDP II core was calculated in Moore, (2001) using an emersion technique. The weights of the 324 hyaloclastite samples (from > 1800 m depth) were measured during and after emersion in water to determine the porosity of each sample. The grain density is calculated by:

$$\rho_g = \frac{Wa}{(Wa - Ww)} \tag{6.1}$$

and saturated density;

$$\rho_s = \frac{Was}{(Was - Ww)} \tag{6.2}$$

where ρg and ρs are grain and saturated density, Wa and Was are measured weight in air and measured weight in air after towel drying and Ww is the weight of a sample while submerged in water. This data can be plotted against wire-line-derived Vp values at the same depth intervals to give a Vp vs. density plot. This data set can be compared directly to empirically or regression-derived density values, to test the accuracy and cross correlation of such data in hyaloclastite deposits Histograms showing the results of Vp and density from the HSDP II samples are presented in Figure 6.2a and 6.2b. The bin size for each histogram is the same. It is apparent there is a spread in both datasets, however, there is a wider spread in recorded density values than there is in Vp response. This observation indicates that hyaloclastite variation may be more pronounced than the LOPRA 1/1A dataset leads us to believe.

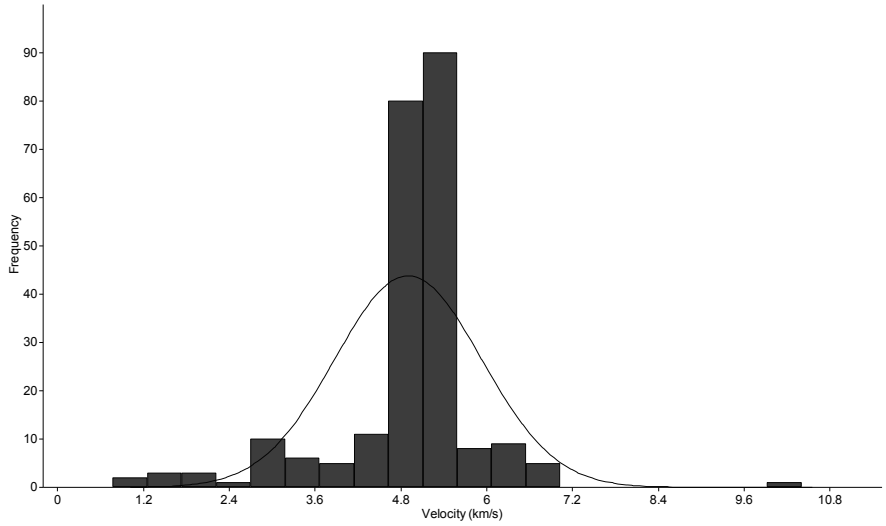

Figure 6.2a. Velocity Histogram for Moore 2001 hyaloclastite samples from the HSDP II core. Sample measurement of Vp is derived from log responses. Bin number = 15.

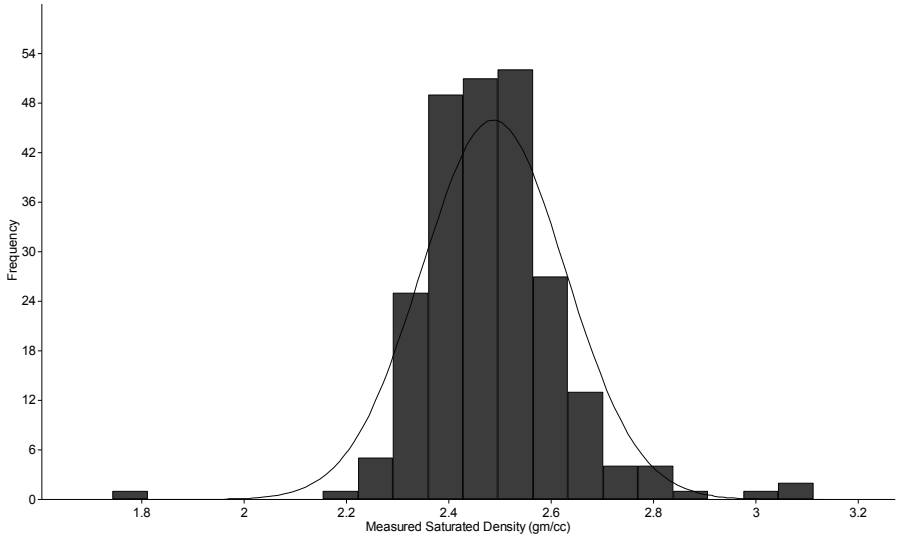

Figure. 6.2b. Density Histogram for Moore 2001 hyaloclastite samples. Sample measured using emersion technique outlined in section 6.2. Bin number = 15. (gm/cc = grams per cubic centimetre = g/cm^3)

6.2.1 Nafe-Drake Curve (Ludwig et al., 1970 after Brocher, 2005)

The Nafe-Drake relation was published by Ludwig et al., (1970) after Nafe and Drake, (1968) and is an empirically derived velocity-density relationship that provides a rough estimate of velocity if density is known (Sharma, 1997). The curve

itself describes the relationship of saturated marine sediments and igneous rocks from the ocean floor from measurements from numerous locations (cf. Nafe and Drake, 1968). It fits a wide range of sedimentary and crystalline rock types. Brocher (2005) outlined a polynomial regression fit, which enables the replication of the Nafe-Drake curve:

$$\rho = 1.6612Vp - 0.4721Vp^2 + 0.0671Vp^3 - 0.0043Vp^4 + 0.000106Vp^5 \qquad (6.3)$$

where ρ = density (g/cm^3), V_p = p wave velocity (m/s). Hyaloclastite samples from the HSDP phase II are a poor fit to this curve (Fig. 6.3). Additionally, the samples plot with a large variation in Vp values for a given density. This observation is not true of other igneous rock samples (e.g., Nafe and Drake, 1968).

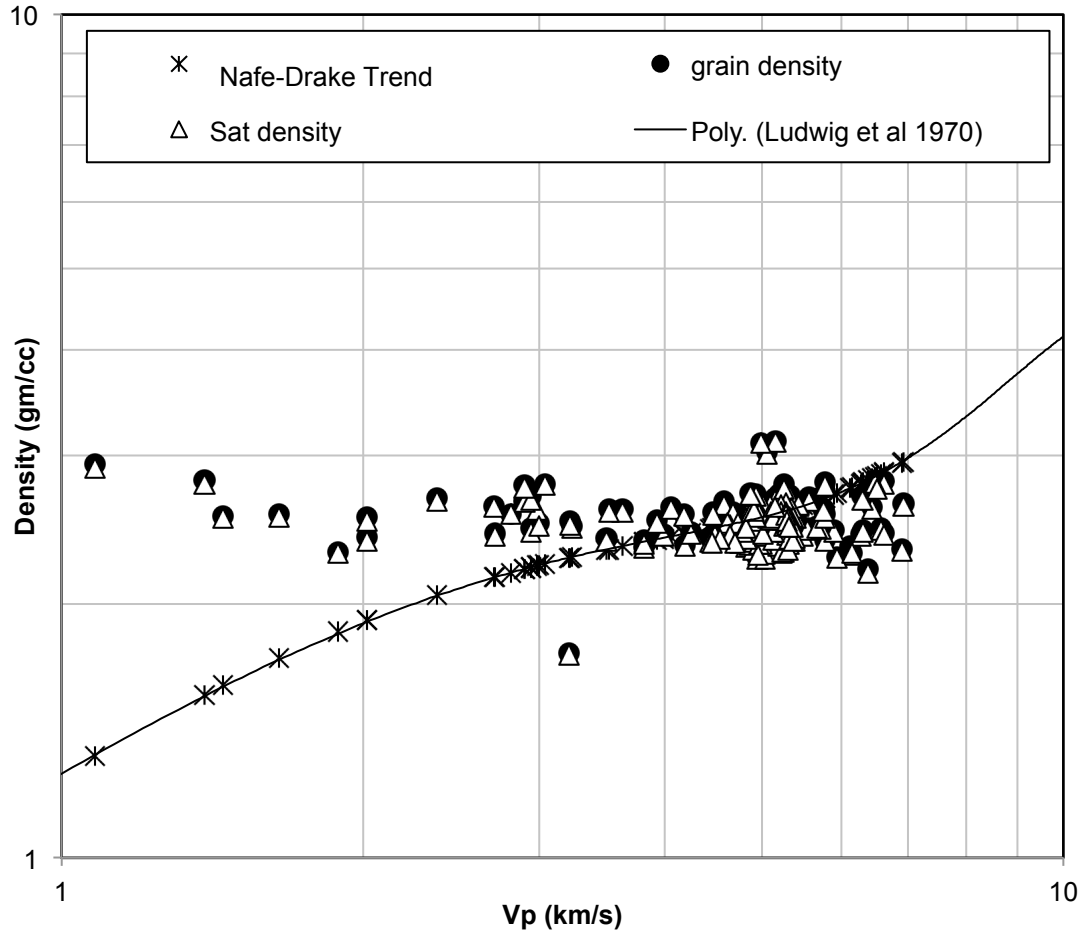

Figure 6.3. The Nafe-Drake equation (Brocher, 2005 from Ludwig et al. 1970, eq. 6.3) fitted to hyaloclastite data from HSDP II. (Moore 2001) density measurements on a log/log plot. The best fit line is a polynomial regression required to satisfy the equation as produced by the Excel best fit line tool. Samples do not fit the line especially at low and high Vp values.

6.2.2 Gardner Equation (Gardner et al., 1974)

The Gardner equation describes the result of series laboratory- and field-based experiments to describe saturated sedimentary rocks in terms of their Vp and density:

$$\rho = aV_p{}^b \tag{6.4}$$

where ρ = density (g/cm^3), V_p = p wave velocity (m/s or ft/s) and a and b are constants 0.31 (if Vp is m/s) or 0.23 (if Vp is ft/s) and 0.25 respectively. Most siliciclastic lithologies plot along or close to the line defined by this empirical trend—this means that Vp and density are linked and Vp can be used as a predictive tool for density determination (Fig. 6.5; Sheriff and Geldart, 1995; Potter and Stewart, 1998).

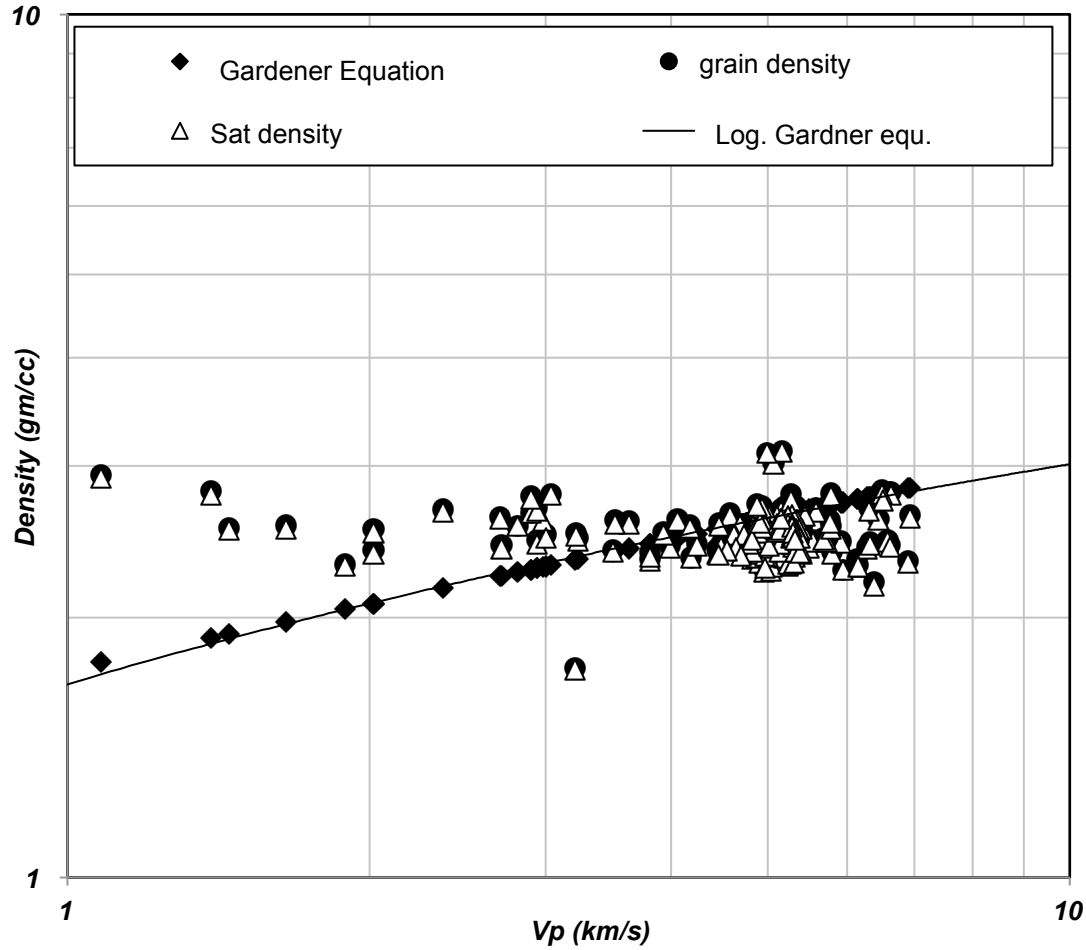

Figure 6.4. A log-log Density (g/cm^3) vs. P-wave velocity (km/s) for HSDP II data from Moore (2001) plotted against the Gardener equation (eq. 6.4). There is generally a poor fit to the hyaloclastite data at values <5 km/s and >8 km/s although upper limit of density is well constrained.

Hyaloclastite density data recorded from HSDP II are generally a poor fit for the trend line except for some values between 5–6 km/s (Fig. 6.4). This suggests that some hyaloclastite deposits may be considered analogous to some sedimentary rocks (specifically dolomite and limestone). However, for both high (>8 km/s) and low (<5 km/s) the Gardener equation cannot describe the variation in Vp response and as such other estimation methods are needed. The large spread in the dataset may suggest that there is a lithofacies control on Vp distribution.

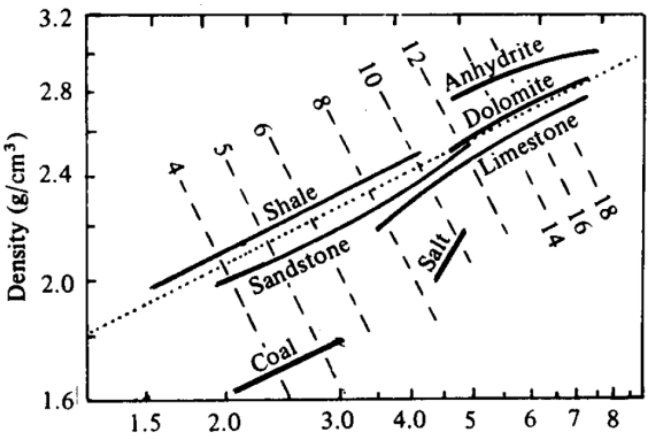

Figure. 6.5. A log-log Density (g/cm^3) vs. P-wave velocity (km/s) for varying siliciclastic lithologies. Empirical trend defined by the Garner equation is defined as a dashed line. (From Sheriff and Geldart, 1995).

6.2.3 Christensen and Mooney Model (Christensen and Mooney, 1995)

The model proposed by Christen and Mooney, (1995) is widely used for density prediction in crystalline rocks. Since hyaloclastite deposits contain mainly basalt fragments and generally have high velocities (>5 km/s) then:

$$\rho = 0.541 + 0.3601V_p \tag{6.5}$$

This model is used to predict density at ~10 km burial depth at velocities at between 5–7 km/s and for crystalline rocks but is used in a variety of datasets where a depth trend cannot be found (e.g. Brocher, 2005). However, as figure 6.6 shows, the fit with measured density values is extremely poor except for a small cluster of values between 5–6 km/s (see lithofacies analysis). This can be explained if hyaloclastite deposits are sediments that behave acoustically in a manner similar to altered basalts as most hyaloclastite deposits contain a high volume of clasts.

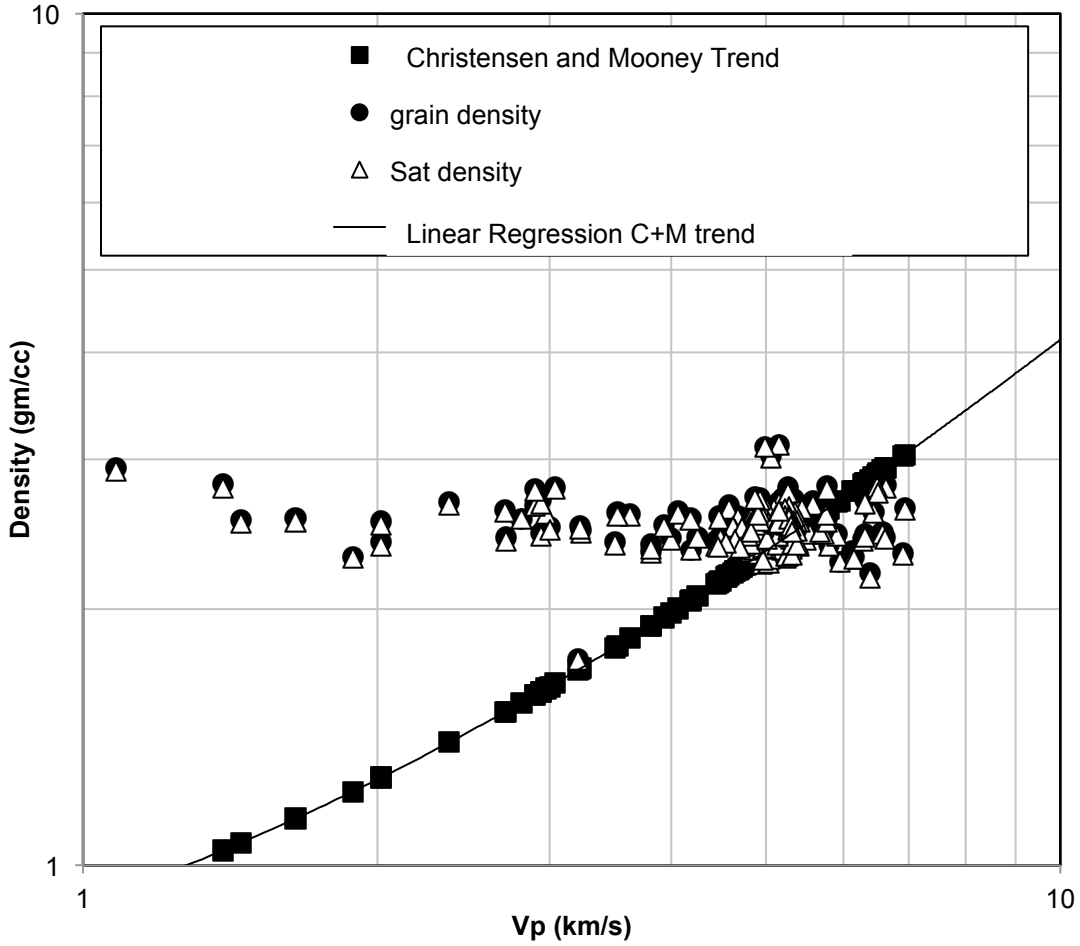

Figure. 6.6. A log-log Density (g/cm^3) vs. P-wave velocity (km/s) for HSDP II data from Moore (2001) plotted against eq. 6.5. This model is only valid between 5-7 km/s. There is generally a poor fit to the actual hyaloclastite data except for a small cluster of values at 5-6 km/s.

6.2.4 Godfrey Model (Godfrey et al., 1997)

Godfrey et al., (1997), upon investigation of the crustal structure of the North American continental margin, proposed a Vp vs. density relationship in volcanic rocks at depths of 5.9–8 km. The relation is based upon Christensen and Mooney's values of basalt, diabase and gabbro at 10 km depth and can be described as;

$$\rho = 2.2372 + 0.0761V_p \tag{6.6}$$

Brocher (2005) added to this equation and incorporated values of zeolite, greenschist and prehnite-pumpellyite to account for alteration giving the relation;

$$\rho = 2.2428 + 0.1052V_p \tag{6.7}$$

When both relationships are plotted together eq. 6.8 has slightly lower density values at velocities of 5.9–7.1 km/s (Brocher, 2005) (defined as Zeo C and M in Fig.6.7). Both equations are plotted because they represent the most common volcanic correlation methods even though HSDP II occur at burial depths shallower than 10 km. Samples generally plot on the same trend as recorded by both relationships albeit with higher density values for a given velocity except for a small cluster at 4.7-5.3 km/s.

Figure. 6.7. A log-log Density (g/cm3) vs. P-wave velocity (km/s) for HSDP II data from Moore (2001) plotted against eq. 6.6 and 6.7. These models are only valid between 5-8 km/s. There is

generally a poor fit to the actual hyaloclastite data which is due to the HSDP II samples occurring at shallower burial depths. Zeo C and M '95 refers to equation 6.7.

6.2.5 Lindseth Equation (Lindseth, 1979)

The Linseth equation is based upon the Gardener equation, where it is also possible to generate a empirical linear relationship between acoustic impedance (which is the product of density and velocity ρV – in g/ft/s) and velocity where (Fig. 9 a);

$$V_p = 0.308\rho V + 3460 \tag{6.8}$$

so where density data is not present the acoustic impedance can be calculated as;

$$\rho V = \frac{(V_p - 3460)}{0.308} \tag{6.9}$$

Therefore figure 6.8b plots acoustic impedance data, as calculated from direct saturated density measurements of Moore, (2001) (blue) and calculated acoustic impedance data from eq. 6.9, against the measured velocity from the sonic log (all velocity data converted to ft/s as required by equation 6.8).

Comparison of figures 6.8a and 6.8b indicate that although the general fit of the data are good HSDP II data overlap many different rock data fields. However, there seems to be a good fit to limestone values <10000 ft/s and sandstone values > 10000 ft/s. This relationship suggests that hyaloclastite deposits share similarities to both carbonate and siliciclastic deposits hence further analysis is needed which may relate to lithofacies (see section 6.2.7) or mineralisation (see section 6.6).

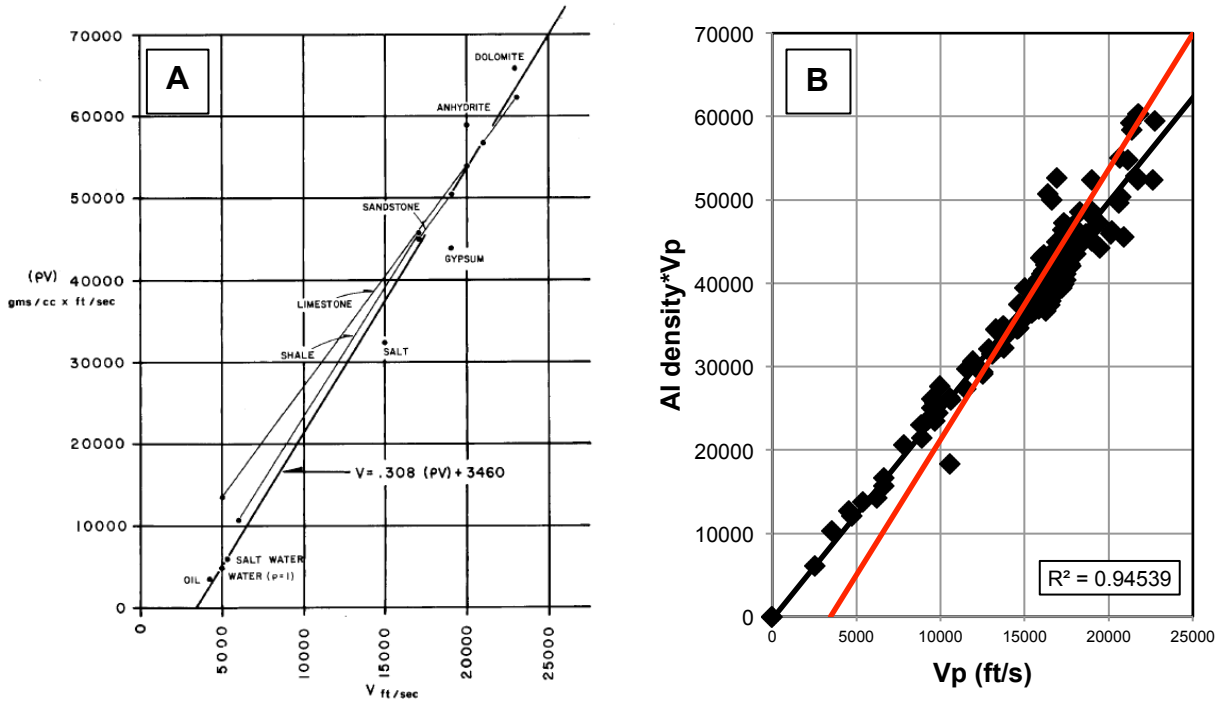

Figure 6.8. A and B are plots of acoustic impedance vs. Vp. A) Is taken from Lindseth 1979 and shows key trends of each lithofacies. B) Uses actual data density and acoustic impedance data calculated from HSDP II values and Vp derived values from eq 6.9. The red line is the line defined by the Lindseth equation, a good trend (r2=0.94539) fit hyaloclastite samples that lie off this trend but plot similar to limestone/dolomite values.

6.2.6 Summary of Existing Vp Based Density Models Applied to Hyaloclastite Deposits

A comparison of all density models is provided in figure 6.9. Observations can be summarized as:

- No density model fully predicts measured hyaloclastite values;
- Some density values of hyaloclastite samples are predicted well by different models although there is no coherent fit;
- Hyaloclastite deposits do not generally fit crystalline (siliciclastic) rock trends;
- Even though they are sediments they behave much like coherent volcanic rocks (lava) in the subsurface;
- Hyaloclastite deposits exhibit similar values as carbonate lithologies;

- Linear average fit of saturated density values shows a slight overall decrease in density with increasing Vp.

Potential variation from modelled datasets occur as some hyaloclastite deposits are more similar to sediments than others, meaning there is potentially lithofacies-specific variation that is not recorded when considering all samples as one rock type. A Nafe-Drake density-velocity relationship is not observed in hyaloclastite samples from the HSDP II dataset. Density is thought to remain almost constant because upon burial glass of high density is replaced by low density palagonite, however as porosity is rapidly reduced also by replacement e.g. if water filled porosity has a density of 1 g/cm^3 and replaced by palagonite with limited compaction a constant density is thought to exist (Moore 2001 also see section 6.5.2 and Fig. 6.13b).

Hyaloclastite deposits can contain up to 25 % zeolite in a 2D thin section (see Fig. 6.32). Zeolites share similarities to carbonates in their overall chemical make up. This may cause hyaloclastite deposits to plot near a limestone trend and is discussed further in section 6.3.3.

These observations form the basis of the investigation in the rest of the chapter. First, modelling based upon each hyaloclastite lithofacies analysis is considered then implications of these results are tested for simple 1D depth conversion and normal incidence reflectivity study aimed to better characterise hyaloclastite deposits and hyaloclastite lithofacies in the subsurface. Then using the wealth of core data available for the HSDP II specific causes of well log variation are considered via core logging, microscopic and spot geochemical analysis.

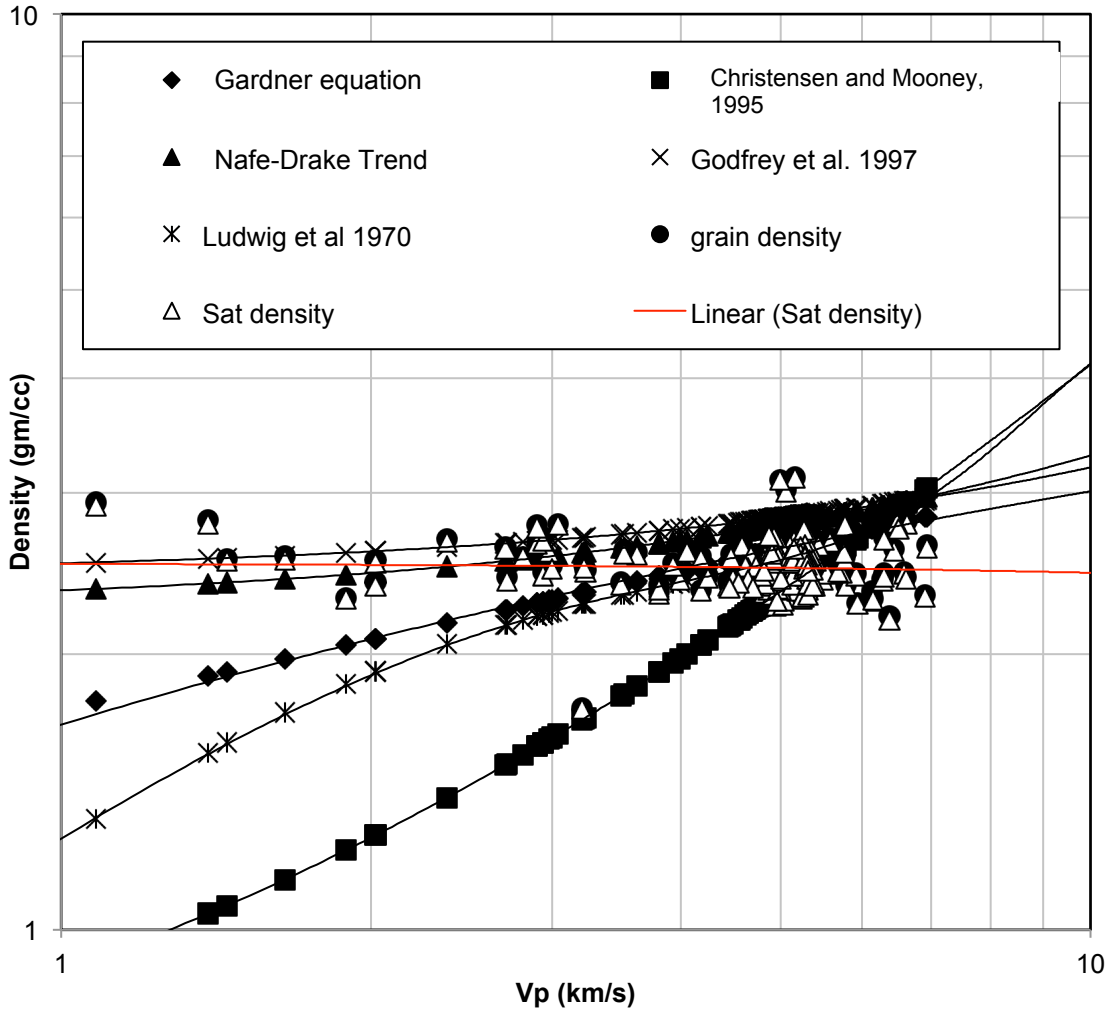

Figure. 6.9. A log-log Density (g/cm^3) vs. P-wave velocity (km/s) for HSDP II data from Moore (2001) plotted against eq. 6.3, 6.4,6.5, 6.6, 6.7. A linear average density for measured HSDP II values is provided in red. See text for details.

6.2.7 How do Vp Based Density Models Fair When Compared to Different Hyaloclastite Lithofacies?

Density measurements from Moore, (2001) have been augmented by unpublished lithofacies information for each sample that the author provided in a personal communication. (Table 6.1, see appendix for this chapter). With this information it is possible to re-plot all the modelled values of density against each lithofacies (Fig. 6.10 a and b). Some unique observations are possible once hyaloclastite samples have been grouped in to lithofacies.

- The model of Christensen and Mooney, (1995) predicts some Fh and h values indicating the similarity of well-sorted fine-grained hyaloclastite material to siliciclastic crystalline rocks.
- The Gardner et al., (1974) equation does well to predict the upper limit of ch values, which respond to dolomite lithologies in the Lindseth equation. However, there is still significant spread away from the Gardner trend. This suggests that some hyaloclastite and most ch samples contain a dolomite signature, which may be consistent with an increased zeolite component. Zeolites have high Mg and Ca values similar to dolomite (see section 6.6).
- The Ludwig et al., (1970) model is better at predicting fh at lower Vp values which suggests that some hyaloclastite sample are similar to siliciclastic rocks.
- Brocher's, (2005) modification of Christensen and Mooney's, (1995) and the Godfrey et al., (1997) equations are generally predict unrealistic density values and can be discounted due to the limited burial depth of the HSDP II samples.
- The Lindseth, (1979) equation has been plotted for each lithofacies and a linear trend has been plotted for each example. It shows that all hyaloclastite lithofacies plot on a different overall trend although they are similar to limestone values. Additionally, because all of the values plot as a large spread along the Lindseth trend (except for p_breccia and mh) this is indicates that variation in Vp is not just lithofacies dependant so other variables must also be considered such as, mineralogy or porosity.

Therefore, the data collected for each lithofacies can be averaged for each measurement and predicted density value (Table 6.2). Table 6.2 also includes averaged values from hyaloclastite deposits in the LOPRA 1/1A bore-hole summarized in section 6.3 and values for olivine rich and olivine poor hyaloclastite values from this study and Moore (2001) data (see 6.6.6).

Table 6.1

Code	Description
h	hyaloclastite (undifferentiated)
ch	coarse hyaloclastite breccia (>1-2 cm)
p_breccia	pillow breccia
mh	medium hyaloclastite (Coarse grade sand size)
fh	fine hyaloclastite (Medium grade sand size)

Table 6.1. Lithofacies as recorded by Moore unpublished data with grain-size description.

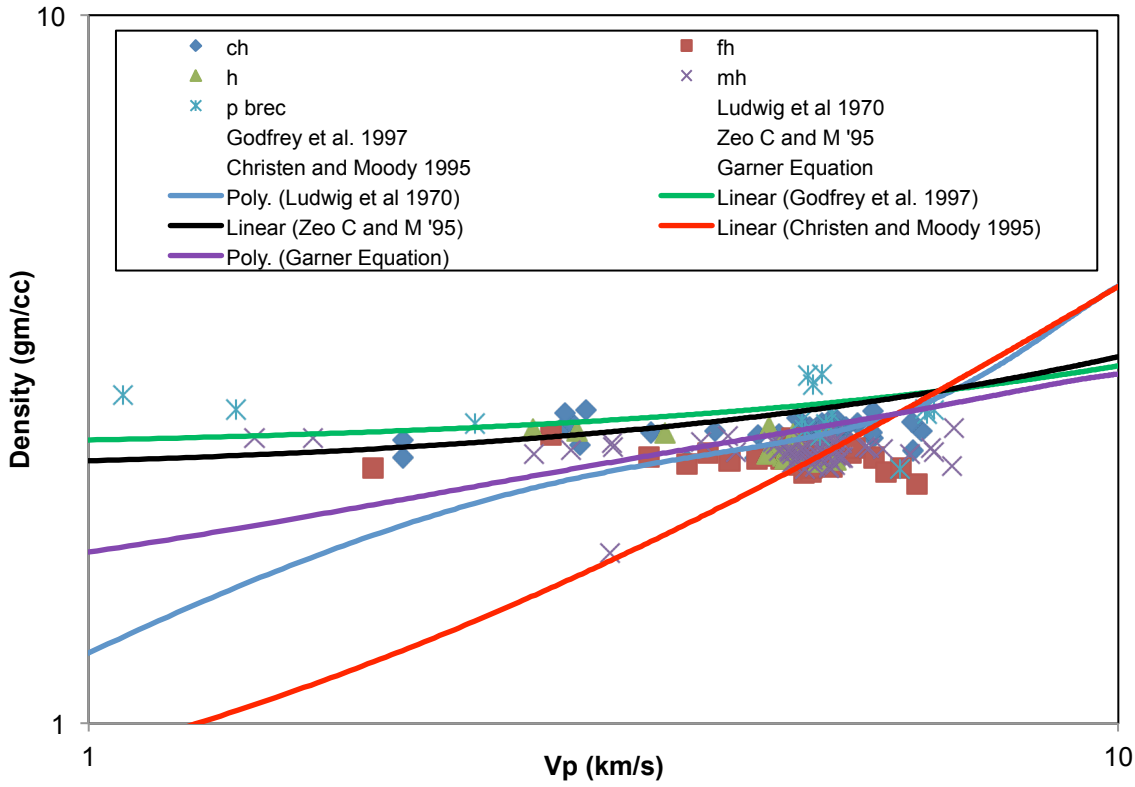

Figure. 6.10. a A log-log Density (g/cm^3) vs. P-wave velocity (km/s) for HSDP II data of lithofacies data from Moore (2001) plotted against eq. 6.3, 6.4,6.5, 6.6, 6.7. See text for details.

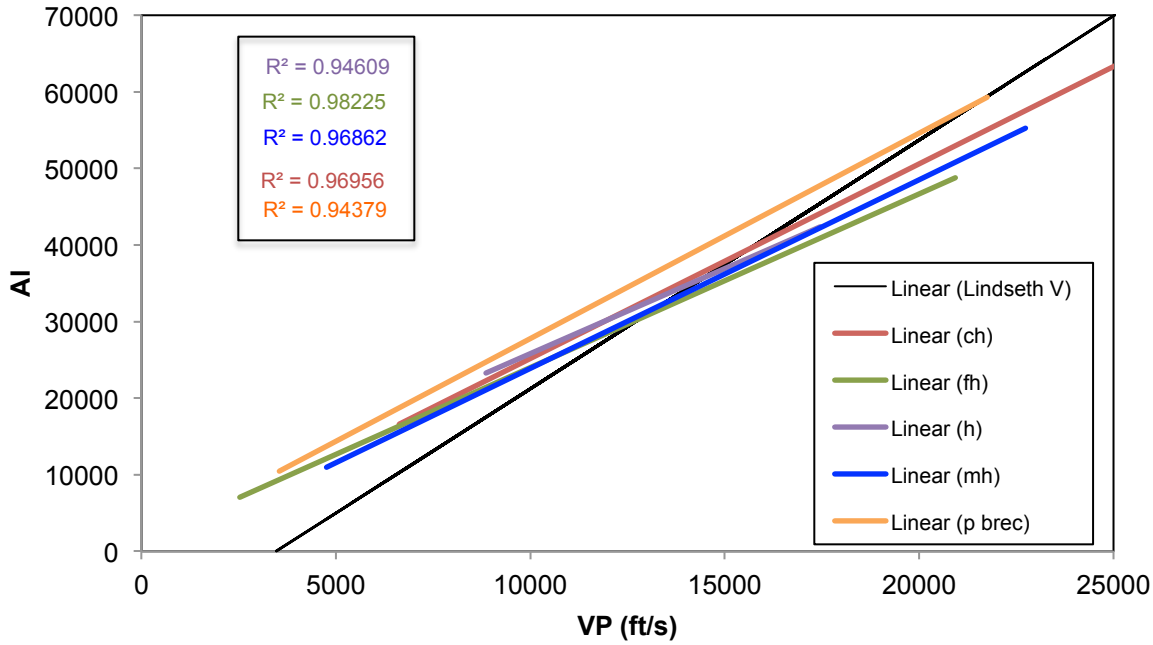

Figure. 6. 10b. Acoustic impedance vs. Vp. Each line represents the best fit of each hyaloclastite lithofacies indicating that hyaloclastite samples in general have a trend different to siliciclastic rocks. Impedance data calculated from HSDP II values and Vp derived values from eq. 6.9 provided in black.

Table 6.2

From Moore unpublished data and TJW Thesis	Velocity (km/s) from HSDP database	Measured Density (g/cm^3)		Log Density (g/cm^3)	Modelled Density (g/cm^3)				
Facies	Vp	Grain	Saturated	Gamma	Nafe-Drake (Lindseth et al. 1970)	Christensen and Moody 1995 - Normal	Christensen and Moody 1995 - Zeolite	Gardener et al. 1974	Godfrey et al. 1997
ch	5.02	2.548	2.527	X	2.538	2.399	2.77	2.607	2.819
h	4.556	2.491	2.481	X	2.446	2.182	2.722	2.547	2.784
fh	4.722	2.370	2.358	X	2.493	2.241	2.73	2.570	2.796
mh	4.901	2.433	2.416	X	2.519	2.306	2.758	2.593	2.812
P_breccia	4.754	2.7805	2.755	X	2.49	2.252	2.742	2.574	2.799
LOPRA_1/1a Average uniform hyaloclastite (2600-2800 m)	4.932	X	X	2.724	2.52	2.317	2.762	2.598	2.813
LOPRA_1/1a Interbedded lava average (2860-2890 m)	5.087	X	X	2.797	2.548	2.372	2.778	2.618	2.824
Olivine Rich Hyaloclastite HSDP	5.42	3.117	3.111	X	2.849	2.493	2.812	2.660	2.82
Olivine Poor Hyaloclastite HSDP	5.1	2.347	2.341	X	2.825	2.376	2.779	2.620	2.85

Table 6.2. Recorded averaged values of measured velocity and measured and modelled density from HSDP II and LOPRA 1/1A. Ch = coarse hyaloclastite, h = undifferentiated hyaloclastite, fh = fine hyaloclastite, mh = medium hyaloclastite, P_breccia = pillow breccias

6.3 HSDP II to LOPRA 1/1A Comparison

To assess the results of HSDP II comparison to another thick hyaloclastite succession is needed. LOPRA-1/1A penetrated ~3.5 km of Palaeocene volcanic rocks correlated in the upper parts of the well to rocks that outcrop on the Faroe Islands (Heinesen et al., 2006). The lower 1.1 km of the borehole comprises the Lopra Formation, which consists of hyaloclastite, intrusive basaltic sills and

volcaniclastic sandstones. The overlying, up to 3.5 km thick, Beinisvørð Formation is composed of laterally extensive basalt lava sheet flows (see Passey and Jolley, 2009), forming a classic tabular geometry (Jerram et al., 2009). The Lopra formation contains a c. 500 m thick section of hyaloclastite deposits (this is a minimum as the base of the unit is not penetrated), which have near uniform velocity and density values except where they become periodically interbedded with lava (Waagstien, 2006). Therefore, it is possible to create two LOPRA 1/1A average values from the uniform part of the core (2600–2800 m depth) and from the interbedded areas (2860–2890 m depth). All velocity and density data taken are from Waagstien (2006) and Nelson (2010, see also Boldreel, 2006; Nelson et al., 2009).

6.3.1 Simple 1D Depth Conversion of Hyaloclastite Lithofacies

LOPRA 1/1A velocity results suggest that hyaloclastite deposits have a tight density distribution that clusters at 5.087 or 4.932 (table 6.3). HSDP II values show a large variation in Vp that is dependant on lithofacies. This will influence the travel time taken to get through the hyaloclastite sequence leading to different thickness estimates. Considered here are the outcomes of these observations that could influence decisions such as drilling depth estimates in petroleum applications.

Methodology

Each hyaloclastite lithofacies has a different recorded velocity. Therefore, by using data from HSDP II vs. LOPRA 1/1A it is possible to compare datasets to measure the simple difference from depth-converting a 1-dimensional (1D) 0.5s two-way time (twt) interval (simple layer-cake depth conversion). A value of 0.5 seconds has been selected at it represents the upper limit of the interval recorded in offshore seismic surveys of hyaloclastite piles (e.g. Planke et al., 2000; Thomson, 2005; Wright et al., 2012). Therefore, the thickness in km of a time-converted (d) section is:

$$d = \frac{st}{2} \tag{6.10}$$

where s = Vp in km/s and t = time in seconds and for each lithofacies which is given in table 6.3 column 3 and figure 6.13. Additionally, it is possible to substitute 25 and 50 % fh (to represented hyaloclastite lithofacies variation) into the interval by substituting 0.125 and 0.25 s intervals of fh (Table 6.3, columns 4 and 5). Values of fh have been added as they are the lowest Vp values and therefore represent lithofacies variation in the hyaloclastite pile. Now it is possible to compare HSDP II and LOPRA 1/1a results where the difference between a 0.5 s average uniform LOPRA 1/1a interval is deducted from each lithofacies (Fig. 6.14). The LOPRA 1/1a average value is assumed to best represent hyaloclastite values in wells in the Faroe-Shetland Basin (Nelson et al., 2009).

Table 6.3

From Moore unpublished data and TJW Thesis	Velocity (km/s) from HSDP database	Thickness for 0.5 s section twt	25 % fh twt	50% fh twt	Difference from Lopra values 100%	Difference from 100% Lopra 25 % fh	Difference from 100% Lopra 50 % fh
Facies	Vp	km	km	km	km	km	km
ch	5.02	1.255	1.236375	1.21775	0.022	0.003375	-0.01525
h	4.556	1.139	1.149375	1.15975	-0.094	-0.083625	-0.07325
fh	4.722	1.1805	1.1805	1.1805	-0.0525	-0.0525	-0.0525

mh	4.901	1.22525	1.2140625	1.202875	-0.00775	-0.0189375	-0.030125
P_breccia	4.754	1.1885	1.1865	1.1845	-0.0445	-0.0465	-0.0485
LOPRA_1/1a Average uniform hyaloclastite	4.932	1.233	1.219875	1.20675	0	-0.013125	-0.02625
LOPRA_1/1a Interbedded lava average	5.087	1.27175	1.2489375	1.226125	0.03875	0.0159375	-0.006875
Olivine Rich Hyaloclastite HSDP	5.42	1.355	1.311375	1.26775	0.122	0.078375	0.03475
Olivine Poor Hyaloclastite HSDP	5.1	1.275	1.251375	1.22775	0.042	0.018375	-0.00525

Table 6.3. Results from simple 1D depth conversion of a hyaloclastite pile incorporating different amounts of fh.

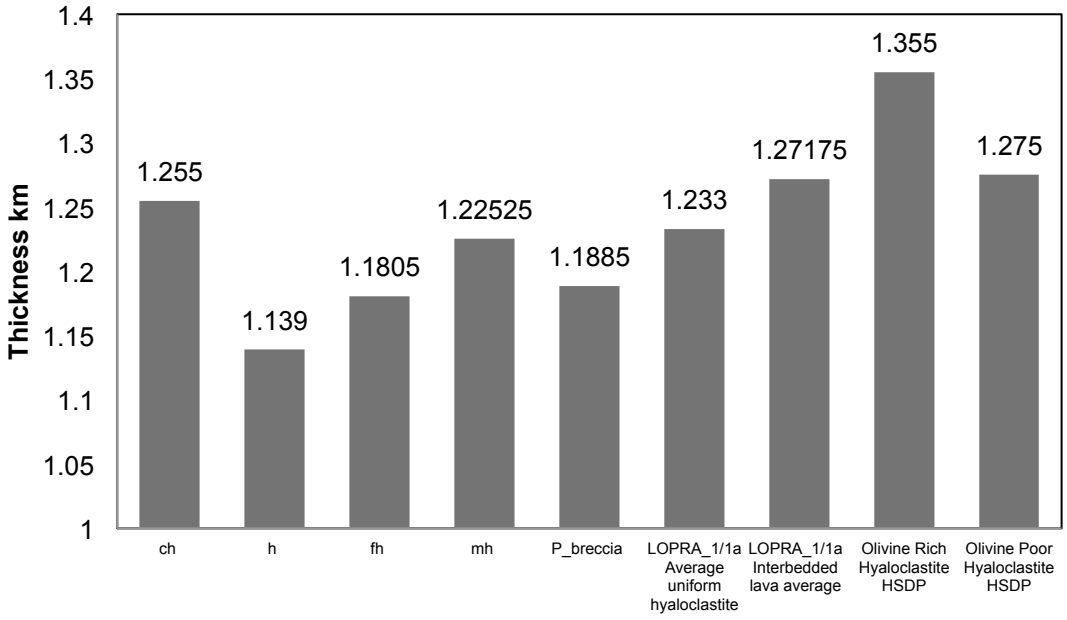

Figure 6.13. Thickness variation of a depth converted 0.5s hyaloclastite pile of uniform velocity. Using velocities from HSDP II and LOPRA 1/1A.

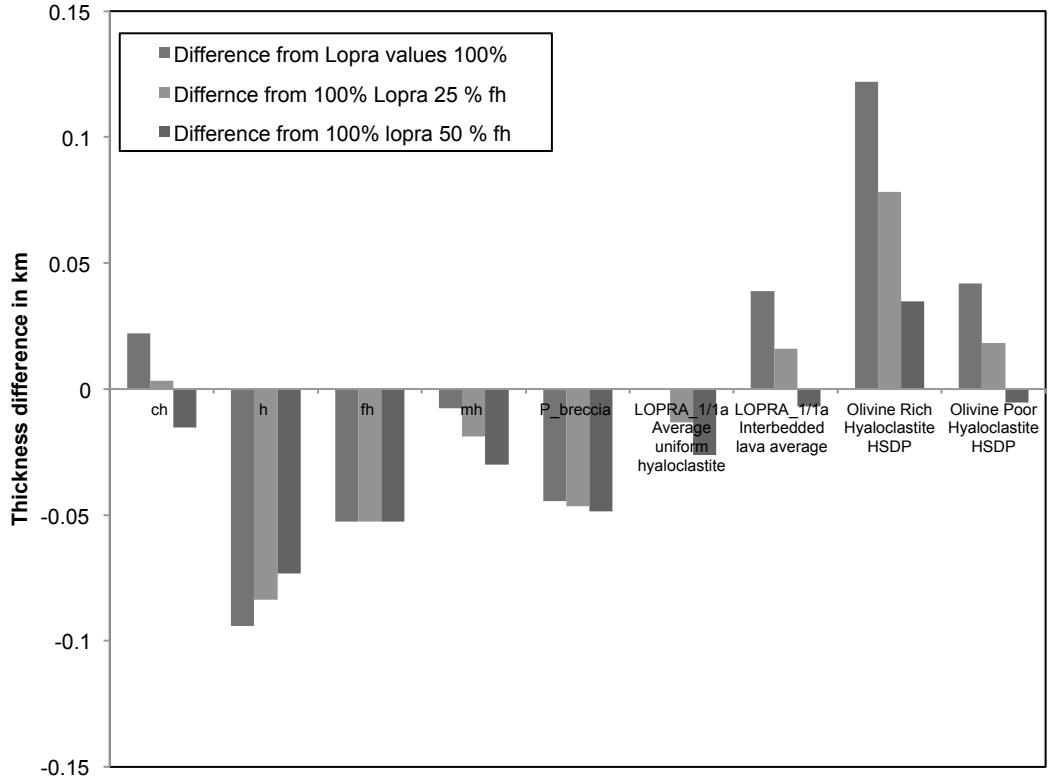

Figure. 6.14. Simple 1 D depth conversion difference between average LOPRA 1/1A and each lithofacies with increasing fh as a total amount. See text for details.

Results

The LOPRA 1/1A pile is relativity homogeneous in both its log response and overall clast componentry (Boldreel, 2006; Waagstein, 2006); although in thin c. 30 m intervals it is interbedded with lavas. In the uniform LOPRA 1/1A case the depth-converted section best matches coarse hyaloclastite breccia (ch) from HSDP II. Undifferentiated hyaloclastite (h), fine hyaloclastite (fh) and pillow breccia (P_breccia) all have lower predicted thicknesses than average LOPRA 1/1A values, whereas olivine-poor samples compare well with the LOPRA 1/1A interbedded results. Olivine-rich samples have significantly greater depth values (122 m) than the average LOPRA 1/1A samples. The addition of 25 and 50 % fh values respectively reduces the difference from LOPRA 1/1A values. This occurs when lower velocity material is added to higher velocity (e.g. olivine-rich hyaloclastite) producing an average value similar to LOPRA 1/1A results.

Interpretation

The implications of these results can be summarised as:

- 1D depth conversions highlight the importance of initial lava composition. Olivine rich hyaloclastite has faster velocities due to the density of olivine (3.0 g/cm^3, see section 6.6.6). However, if only a time interval is known (and compositional information is unknown) then large errors could occur in depth-converted sections (up to 122 m).
- As higher percentages of fh are added to each lithofacies the divergence from LOPRA 1/1A decreases.
- Up to 122 m difference between lithofacies is important for drilling e.g. predicting depth to base volcanics and influence the burial depth of sub-basalt petroleum plays that could interfere with hydrocarbon maturation.

6.3.2 What Causes Reflections in Hyaloclastite Deposits?

The reflection coefficient (RC) describes the ratio of amplitude of the reflected wave to the incident wave, or how much energy is reflected at each layer boundary. Therefore the larger the RC at a layer boundary dictates the higher the intensity of the reflector produced at the layer boundary. The reflection coefficient is calculated using the acoustic impedance contrast between two layers.

Acoustic Impedance (AI) can be calculated for each hyaloclastite lithofacies for real and modelled density values (Table 6.4; Fig. 6.15a). There is a huge variety in AI values across all lithofacies types. Figure 15b highlights the difference between measured and predicted AI values for HSDP II and LOPRA 1/1A samples. P_breccia and LOPRA 1/1A can be predicted well using both the Christensen and Mooney (1995) and Godfrey et al., (1997) average values, however, in general, the HSDP II deposits are not predicted well by these models. HSDP II samples best fit with the average values of the Nafe-Drake Curve. These results indicate that lithofacies in LOPRA 1/1A are more uniform and have been buried to greater depths than the HSDP II core.

As hyaloclastite deposits display a large degree of lithofacies heterogeneity it may be possible that RC's can be generated by this variation. Field studies of hyaloclastite deposits in this thesis have yielded three main sequences of hyaloclastite deposits (Table 6.5, Chapter 4 and appendix for this chapter):

1. ***Complex Hyaloclastite Deposits (CHD)*** that consist of numerous associated lithofacies, for example, repeated sequences of fine-grained sand grade to coarse breccias deposits (for this example I use log III from the Stóri-Núpur hyaloclastite deposit (see chapter 4 and appendix for chapter 4). This shall be labelled a Log 1 in the following section (see table 6.5)
2. ***Prograding Pillow Complexes (PPC)*** are common where water levels are limited or in lacustrine settings (see Fuller, 1931a, and Chapter 3). Used here is a log based on field observations from the Snake River Plain (log provided in the appendix for this chapter). This shall be labelled a Log 2 in the following section (see table 6.5)
3. ***Reworked Hyaloclastite Deposits (RHD)*** are formed through the reworking of hyaloclastite material, are fairly homogenous and clast supported (the Hjörleifshöfði sequence was used for simplicity, which consists of three lava flows, a pillow lava sequence and a reworked hyaloclastite interval). This shall be labelled a Log 3 in the following section (see table 6.5)

Provided in table 6.5 are the lithofacies and lithofacies codes that correspond to chapter 4. Each lithofacies has been associated with an equivalent remote example from either HSDP II and LOPRA 1/1A examples.

Table 6.4

	AI							Predicted minus actual				
Facies	**Nafe-Drake (Lindseth et al. 1970)**	**Christensen and Moody 1995 - Normal**	**Christensen and Moody 1995 - Zeolite**	**Gardener et al. 1974**	**Godfrey et al. 1997**	**Actual AI HSDP**	**Actual AI lopra**	**Nafe-Drake (Lindseth et al. 1970)**	**Christensen and Moody 1995 - Normal**	**Christensen and Moody 1995 - Zeolite**	**Gardener et al. 1974**	**Godfrey et al. 1997**
ch	12.74076	12.04298	13.9054	13.08714	14.15138	12.6854	X	0.05522	-0.64256	1.21986	0.4016	1.46584
h	11.143976	9.941192	12.401432	11.604132	12.683904	11.303436	X	-0.15946	-1.362244	1.097996	0.300696	1.380468
fh	11.771946	10.582002	12.89106	12.13554	13.202712	11.134476	X	0.63747	-0.552474	1.756584	1.001064	2.068236
mh	12.345619	11.301706	13.516958	12.708293	13.781612	11.8408	X	0.504803	-0.53911	1.676142	0.867477	1.940796

						16							
P_brec						13.0						-	
cia		10.7060		12.23	13.30	972						0.860	0.20
	11.83746	08	13.035468	6796	6446	7	X	-1.25981	-2.391262	-0.061802		474	9176
LOPRA							13.4					-	
_1/1a		11.4274		12.81	13.87		347					0.621	0.43
AVG	12.42864	44	13.622184	3336	3716	X	68	-1.006128	-2.007324	0.187416		432	8948
LOPRA													
_1/1a							14.2					-	
Interbe	12.96167	12.0663		13.31	14.36		283					0.910	0.13
dded	6	64	14.131686	7766	5688	X	39	-1.266663	-2.161975	-0.096653		573	7349
Olivine													
Rich						16.8						-	-
Hyalocl		13.5120		14.41	15.28	616						2.444	1.57
astite	15.44158	6	15.24104	72	44	2	X	-1.42004	-3.34956	-1.62058		42	722
Olivine													
Poor													
Hyalocl				13.36	14.53	11.9						1.422	2.59
astite	14.4075	12.1176	14.1729	2	5	391	X	2.4684	0.1785	2.2338		9	59

Table 6.4. Recorded Acoustic Impedance Values vs. modelled values based upon density estimates. Lava crust and core relationships use average values as recorded by Nelson (2010)

Table 6.5

Log 1
CHD

Recorded Log Facies	Equivalent facies		km Interval thickness
	Lopra	HSDP	
cL	LAVA CORE	LAVA CORE	0.0184
CBH	Hyalocl astite	ch	0.0092
Fhc-Hsc	Hyalocl astite	fh	0.00184
CBH	Hyalocl astite	ch	0.00883 2
Fhc-Hsc	Hyalocl astite	fh	0.00588
hP	Mixed	p_brec cia	0.00736

Log 2
PPC

Recorded Log Facies	Equivalent facies		km Interval thickness
	Lopra	HSDP	
ftL	LAVA CRUST	LAVA CRUST	0.005
cL	LAVA CORE	LAVA CORE	0.00336
ftL	LAVA CRUST	LAVA CRUST	0.001
pH	Mixed	p_brec cia	0.0015
cH	Hyalocl astite	ch	0.003
pillow	LAVA CRUST	LAVA CRUST	0.0007

Log 3
RHD

Recorded Log Facies	Equivalent facies		km Interval thickness
	Lopra	HSDP	
ftL	FLOW CRUST	FLOW CRUST	0.004
cL	FLOW CORE	FLOW CORE	0.005
ftL	FLOW CRUST	FLOW CRUST	0.001
ftL	FLOW CRUST	FLOW CRUST	0.003
cL	FLOW CORE	FLOW CORE	0.004
ftL	FLOW CRUST	FLOW CRUST	0.001

CBH	Hyalocl astite	ch	0.009568	cH	Mixed	p_brec cia	0.002	ftL	FLOW CRUST	FLOW CRUST	0.004
CBH	Hyalocl astite	ch	0.00736	pillow	LAVA CRUST	LAVA CRUST	0.001	cL	FLOW CORE	FLOW CORE	0.005
fTl	LAVA CRUST	LAVA CRUST	0.01472	ibH	hyalocl astite	mh	0.005	ftL	FLOW CRUST	FLOW CRUST	0.001
								pH	mixed	P_brec cia	0.01
								ipH	hyalocl astite	h	0.06

Table 6.5. Logged thickness and lithofacies for field hyaloclastite examples of Complex Hyaloclastite Deposits (CHD), Prograding Pillow Complexes (PPC) and Reworked Hyaloclastite Deposits (RHD). See section 6.3.2 for details.

Once the thickness and lithofacies type of each unit is known, then Vp and density can be attributed. In this case one set of values represents hyaloclastite lithofacies values from HSDP II and one set represents those observed in LOPRA 1/1A. It is then possible to generate a dataset that allow the calculation of the reflection coefficient and travel time between each interval in order to investigate what the influence an only LOPRA 1/1A assumption would have on field logs. At normal incidence the reflection coefficient (RC) between each layer can be calculated as;

$$RC = \frac{(\rho_2 V_2 - \rho_1 V_1)}{(\rho_2 V_2 + \rho_1 V_1)} \tag{6.11}$$

And interval time (t) as;

$$t = \frac{interval\ time}{Velocity\ of\ attribted\ facies} \tag{6.12}$$

where $\rho_1 V_1$ is the acoustic impedance of layer 1 and $\rho_2 V_2$ is the acoustic impedance of layer 2. Typical values of R are approximately -1 from water to air, meaning that nearly 100 % of the energy is reflected and none is transmitted; ~ 0.5 from water to rock; and ~ 0.2 for shale to sand (Schlumberger website [www.glossary.oilfield.slb.com/en/Terms.aspx?LookIn=term%20name&filter=reflec

tion%20coefficient]). All reflection coefficients and travel time values are provided in the appendix for each log for LOPRA 1/1A and HSDP II values as well as predicted values based upon Vp/density modelling. These calculations assume all energy is transferred at the layer boundary that does not occur, as the uppermost lava flow will reflect most of the energy. However for this application our interest is to investigate boundary effects between different hyaloclastite lithofacies and hence can be ignored.

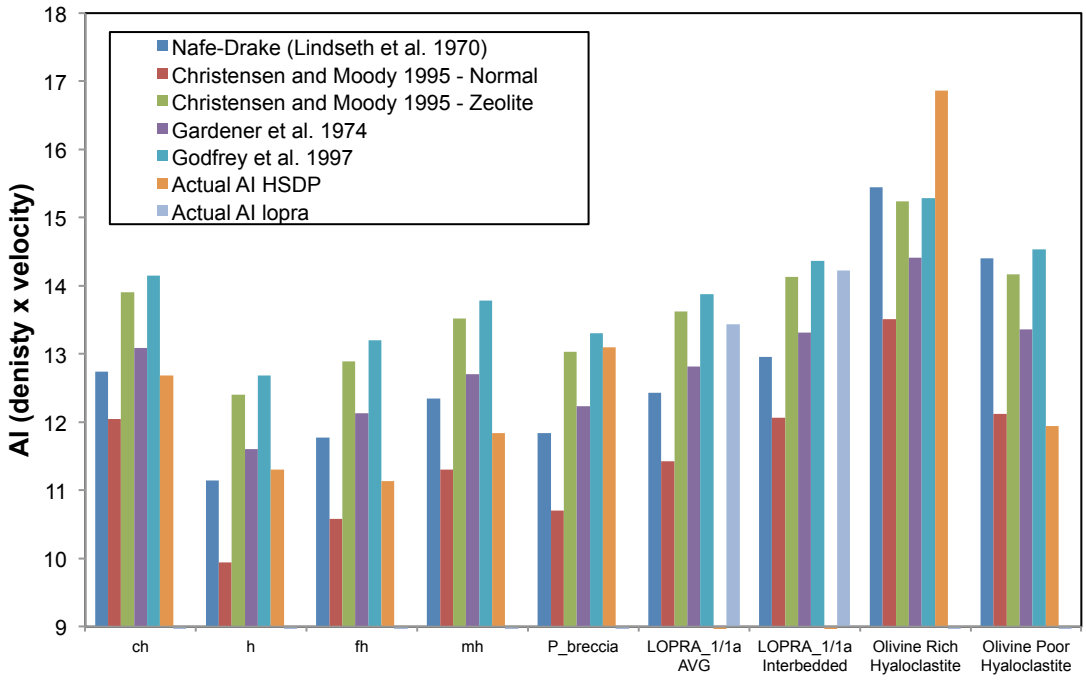

Figure 6.15 a. A comparison of AI values for each lithofacies vs. modelled values in each case. See text for details.

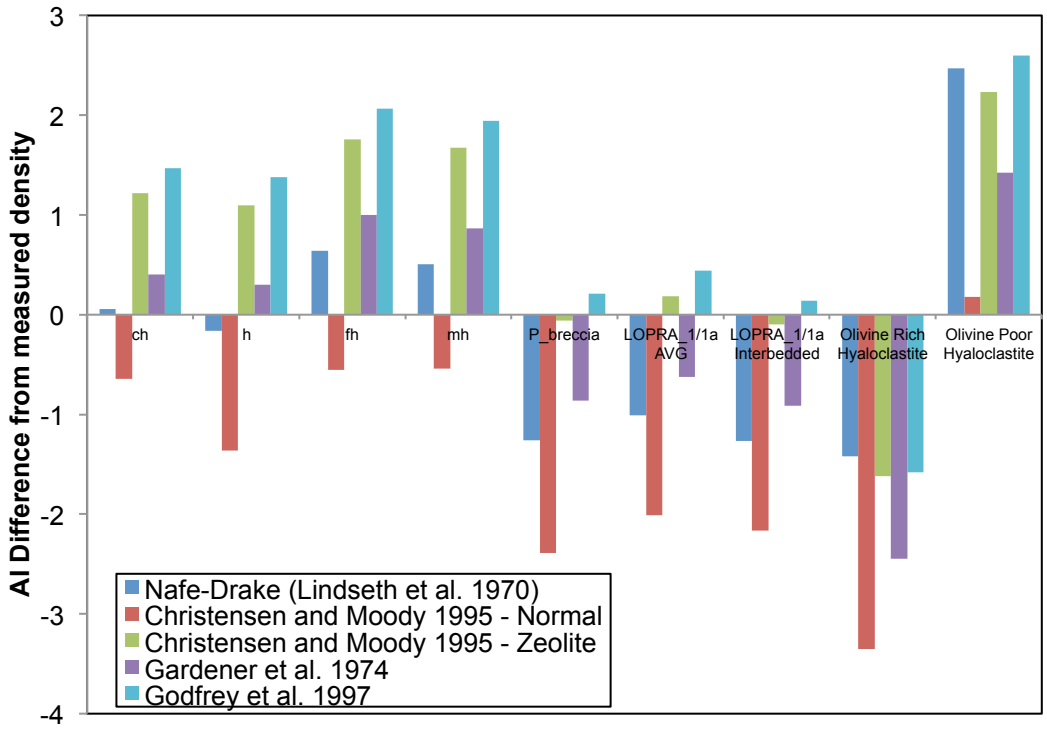

Figure. 15 b. AI difference (modelled prediction minus LOPRA 1/1A and HSDP II values) for each respective lithofacies (see text for details).

Observations

Log 1 plots the RC values of a complex hyaloclastite sequence with a high degree of lithofacies variation (Fig. 6.16). The upper lava flow-to-hyaloclastite contact has a small (-0.05) RC in the LOPRA 1/1A values. However in the HSDP II values the RC from the lava core to ch and from ch to fh show are both larger (c. -0.1) which would produce one strong negative reflector. The LOPRA 1/1A example shows little or no deviation from averaged flow cores, and little deviation between each lithofacies in the hyaloclastite breccias. This is in part due to the uniform Vp and density of the deposit. In contrast, the HSDP II example shows significant RC production between fh and ch lithofacies that reflects significant Vp and density variation. The HSDP II result would therefore produce a complex waveform. In both cases the return to lava flow core produces a strong negative RC values (c. -0.2) and would produce a strong negative reflector.

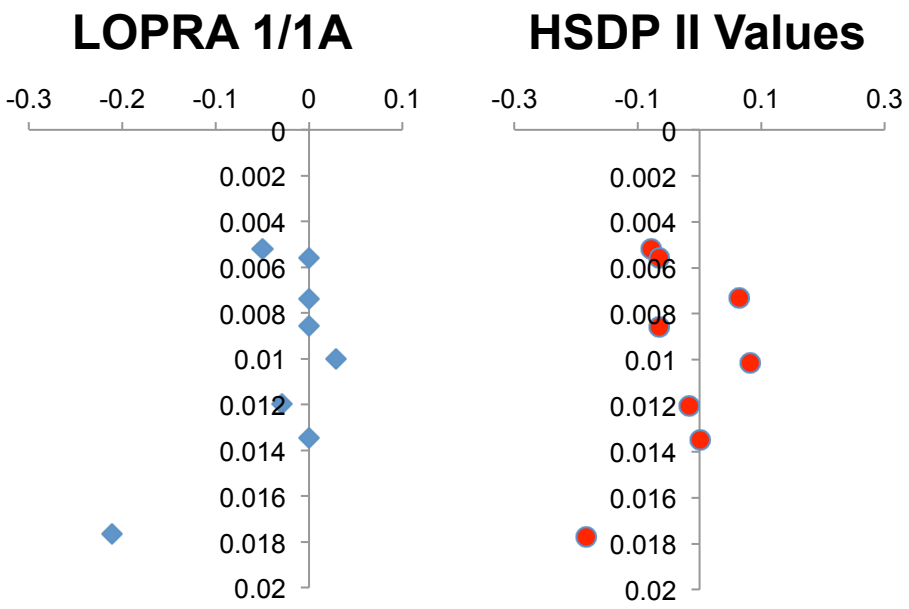

Figure 6.16. Reflection coefficient vs. time log of Log 1 CHD sequence. See text for details.

Log 2 plots RC values from a relatively thin pillow lava-dominated hyaloclastite sequence. If this sequence were for example, intersected in core it would be formed of a capping lava flow sequence underlain by alternating hyaloclastite breccia and pillow lavas (Fig. 6.17). At first glance, both sequences look the same. Initially, a large positive-negative kick is produced, which is the boundary between flow crust and core. In reality this does not happen because Vp and density "grade" from lower to higher values (see Nelson et al., 2009). Both sequences show no RC development between lava crust and pillow breccias and subsequently show large (up to 0.3) RC development between hyaloclastite and pillow lavas (in this case assumed to have the same affinity as plot crust). Not immediately obvious is the slightly lower (c. +0.1) positive RC's n the HSDP II core which reflectors the use of a true pillow breccia value instead of a generic hyaloclastite value like in LOPRA 1/1A.

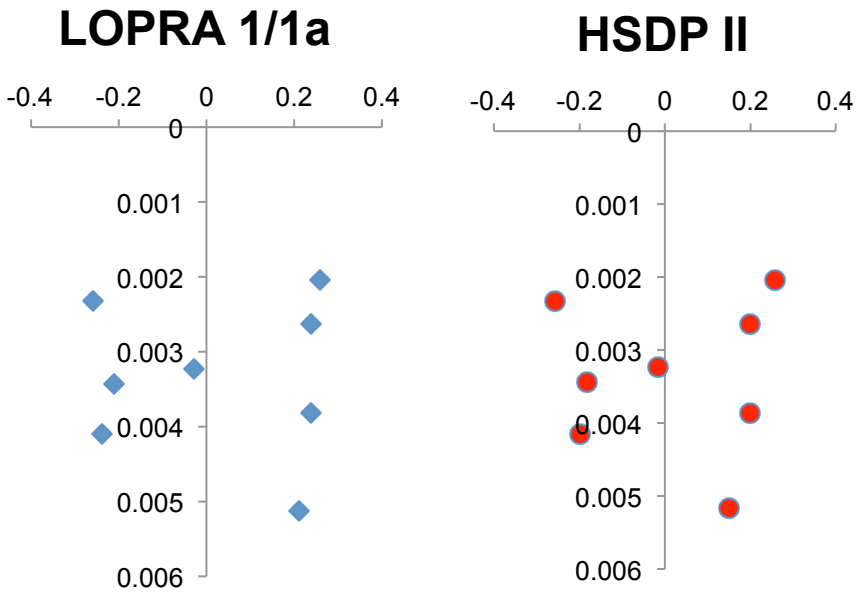

Figure 6.17. Reflection coefficient vs. time log of Log 2 PPC sequence. See text for details.

Log 3 plots RC values from a reworked hyaloclastite sequence that contains a set of capping lava flows then a gradual transition from overlying pillow lava to underlying reworked generally homogenous hyaloclastite producing a spike at 0.02125 seconds (Fig. 6.18). There is again is a false representation of each lava flow core/crust package. In this sequence both examples show strong (+0.2) RC's from lava to pillow breccia. However in LOPRA 1/1A the transition from pillow to reworked breccia has no RC whereas in HSDP II a slightly stronger negative event (c. -0.7) RC is produced.

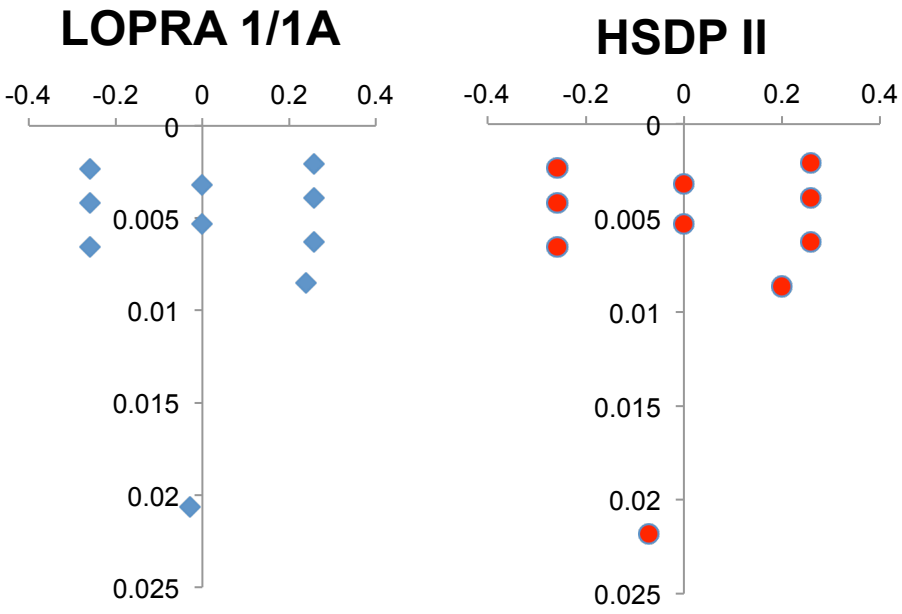

Figure 6.18. Reflection coefficient vs. time log of CHD sequence. See text for details.

Comparison to Vp-based Density Models

RC vs. time plots of field logs 1-3 can be also plotted using modelled density values (Fig. 6.19, 6.20, 6.21). The results of this section are interesting as if, for example each lithofacies stacking pattern was prior to analysis assumed then could modelled densities taken from Vp predict why reflections occur? RC vs. time value tables are provided for the appendix for this chapter.

Log 1 – Complex Hyaloclastite Deposits (CHD)

Predicted density measurements for LOPRA 1/1A produced very similar RC's. An exception occurs in the transition from flow core to crust in the Christensen and Mooney, (1995) model. This can be discounted as the predicted density is in excess of any known density values for lava flows. However, although the HSDP II predicted density results are all similar they are significantly different from the measured Vp and density values. This variation can be explained by the presence of fh and P_breccias, which has a high velocity for relatively low density values.

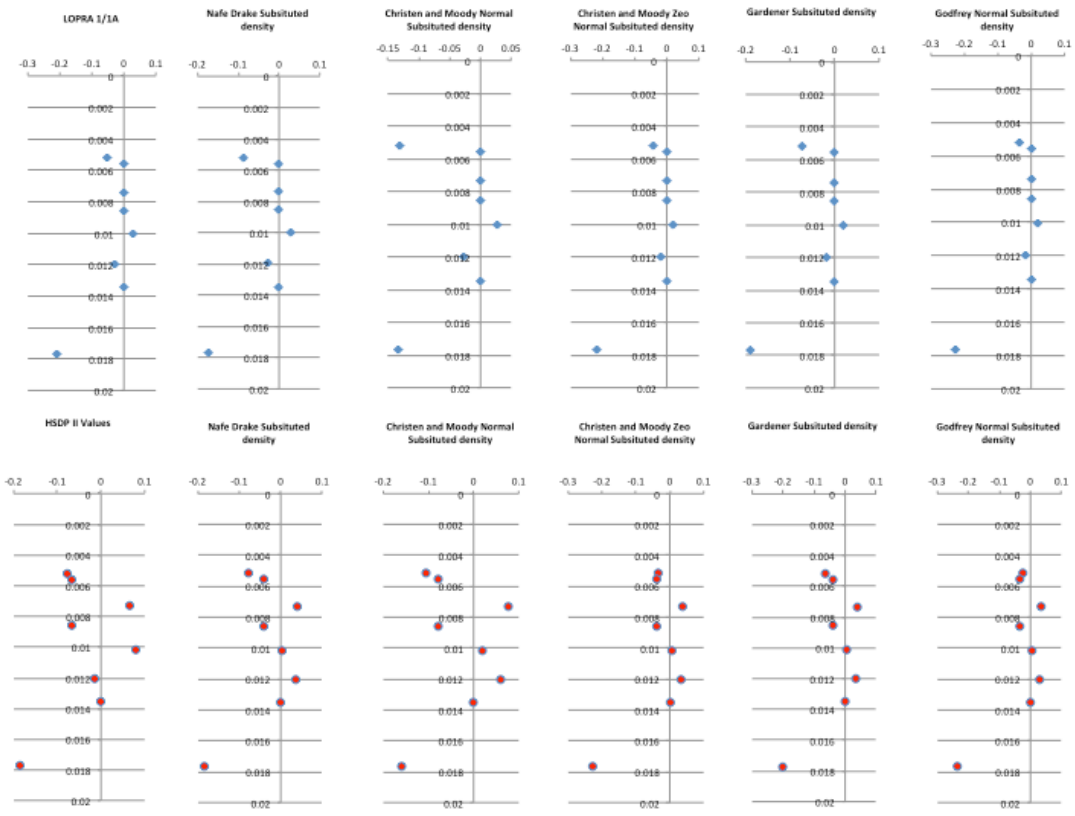

Figure 6.19 . Reflection Coefficient vs. time for modelled density values from table 6.4 for CHD (Log 1). LOPRA 1/1A values are represented by blue labels whereas HSDP II values are red. For each example (HSDP II or LOPRA 1/1A) the original RC vs. time log is also given on the far left of the diagram.

Log 2 – Prograding Pillow Complexes (PPC)

Modelled density values are a good match for the pattern of RC's in both LOPRA 1/1A and HSDP II examples with no significant variation except in the Christen and Mooney model that predicts anomalously high density values. However in HSDP II the Nafe-Drake and Christensen and Mooney equations predict lower (c. 0.05-0.1) RC's than the actual values, which, would produce a much less distinct waveform.

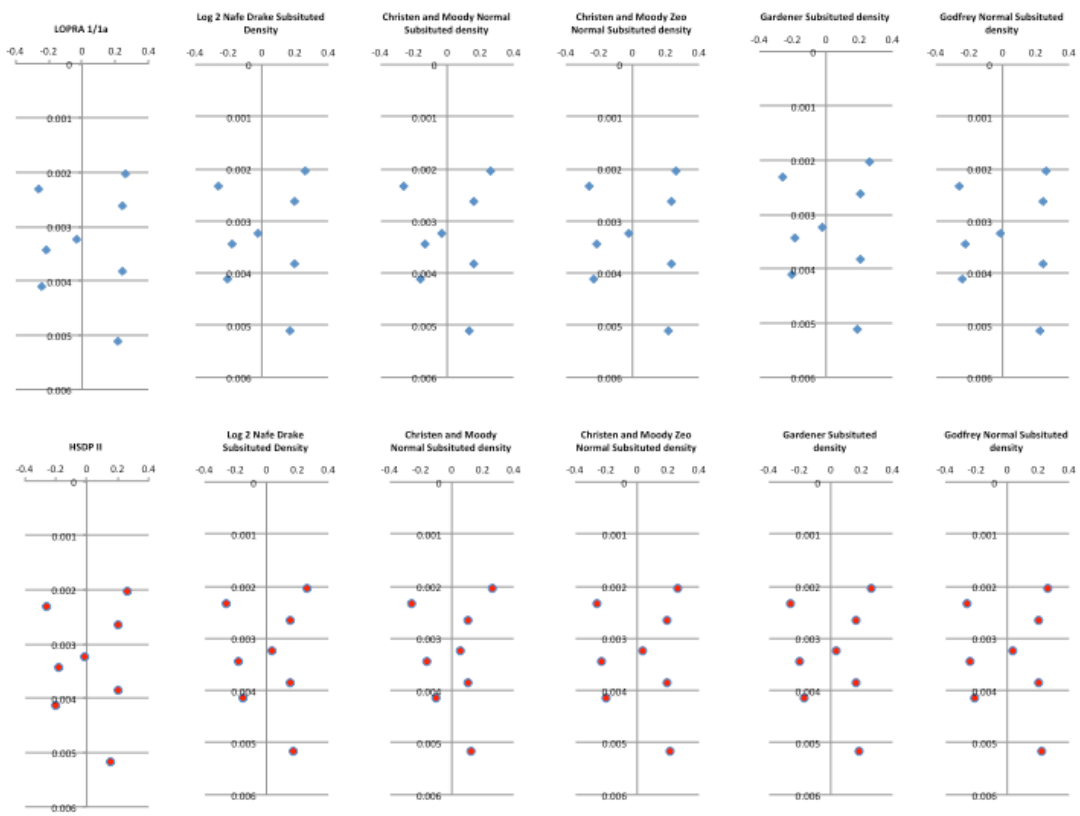

Figure. 6.20. Reflection Coefficient vs. time for modelled density values from table 6.4 for PPC (Log 2). LOPRA 1/1A values are represented by blue labels whereas HSDP II values are red. For each example (HSDP II or LOPRA 1/1A) the original RC vs. time log is also given on the far left of the diagram.

Log 3- Reworked Hyaloclastite Deposits (RHD)

Modelled density values are a good match for the LOPRA 1/1A values for all RC's. However, in HSDP II, modelled density values cannot predict the RC between pillow lavas and reworked hyaloclastite deposits. In reality the difference in mh and pillow density measures is high (c 0.3 g/cm3) although their Vp is similar. Therefore modelled density values do not account for this change meaning that there is little different between the two AI values leading to no RC.

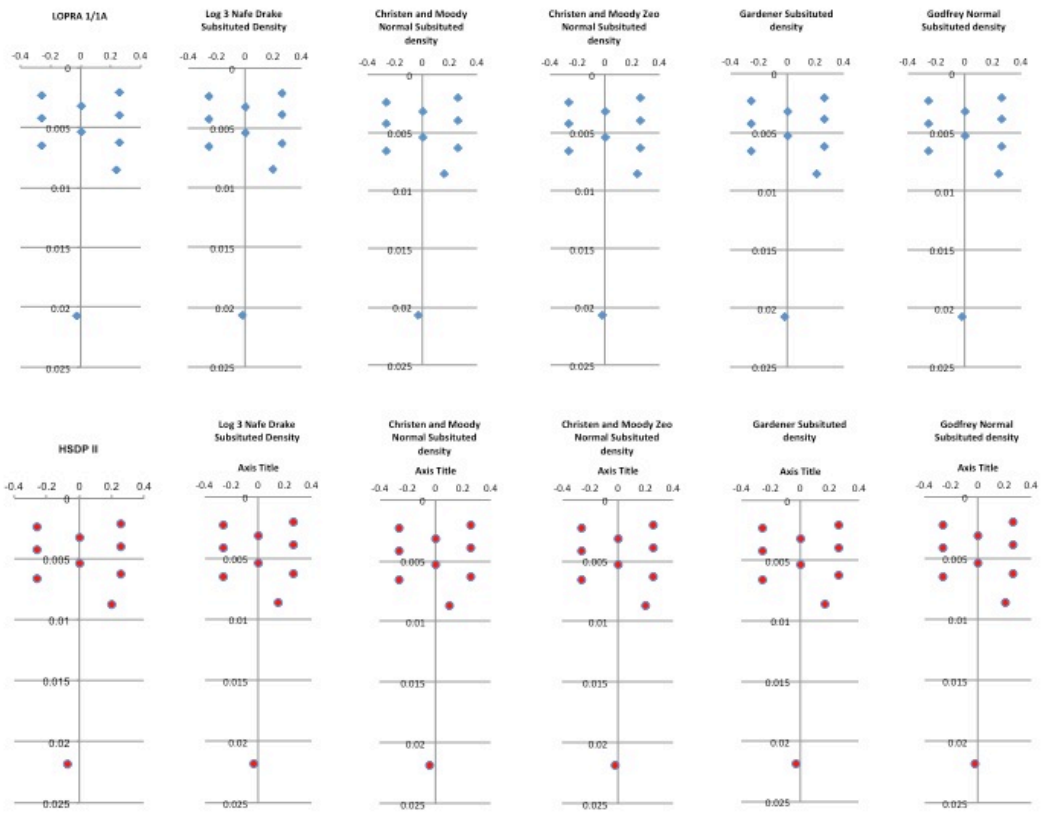

Figure. 6.21. Reflection Coefficient vs. time for modelled density values from table 6.4 for RHD (Log 3). LOPRA 1/1A values are represented by blue labels whereas HSDP II values are red. For each example (HSDP II or LOPRA 1/1A) the original RC vs. time log is also given on the far left of the diagram.

Results and Discussion

In LOPRA 1/1A hyaloclastite deposits have near uniform velocity and density (Boldreel, 2006; Nelson et al., 2009), however some deviation is seen especially where they are mixed with basalt intervals (e.g. Waagstien, 2006). The reflector coefficients between hyaloclastite intervals in the LOPRA 1/1A examples show small or no RC's, yet reflectors are seen in subsurface examples of lava deltas that have coherent prograding reflectors (see Jerram et al., 2009; Wright et al., 2012 and Fig. 3.2). This suggests that the lava delta hyaloclastite lithofacies seen as prograding reflectors in offshore sequences and in observations of outcrop examples of prograding deltas (e.g. Watton et al., 2013) require significant heterogeneity in rock properties to help explain why seismic reflectors exist.

HSDP II results (Field Log 1, Table 6.5, Fig. 6.19) show that fine- to coarse-grained hyaloclastite packages can produce strong (0.13) total differences in RC values. Likewise, transitions from pillow-dominated breccias to clast-supported hyaloclastite deposits can also produce a strong reflector (RC = - 0.07; Field Log 3, Fig. 6.21). Both these differences are not predicted by modelled density values because different hyaloclastite lithofacies have different density values for a given Vp. There is no easy explanation for this observation and it is probably due to a number of factors such as mineralogy, diagenesis, and burial compaction (assessed in section 6.6). Finally, a pillow-to hyaloclastite transition (Field Log 2, Fig. 6.20) could also give a strong reflector coefficient (RC = 0.19), which is also observed in the LOPRA 1/1A log. The LOPRA 1/1A data set also shows smaller RC changes from lava core to hyaloclastite deposits.

Another possible mechanism to generate RC's is the change between hyaloclastite deposits that contain palagonite in their matrix and those that do not (indurated and non-indurated respectively). Density data from Le Masurier et al., (2002) can be compared indurated sample from HSDP II where velocity is fixed (representative of Moore, 2001, h samples). Significant (up to -0.11 in this case) reflection coefficients can be generated between hyaloclastite and pillow lava boundaries (Fig. 6.22a and in appendices to this chapter).

Variations in induration occurs in PPC's from the Columbia River Flood Basalt inter lava sequences (e.g. Fig. 6.22b). However in most cases, in actively subsiding basins, with high degrees of hydrothermal fluid circulation or increased burial depth, induration is usually rapid and pervasive through the entire deposit (e.g. section 6.5 and Figure 6.1) and therefore is unlikely occur in thick, buried offshore hyaloclastite deposits.

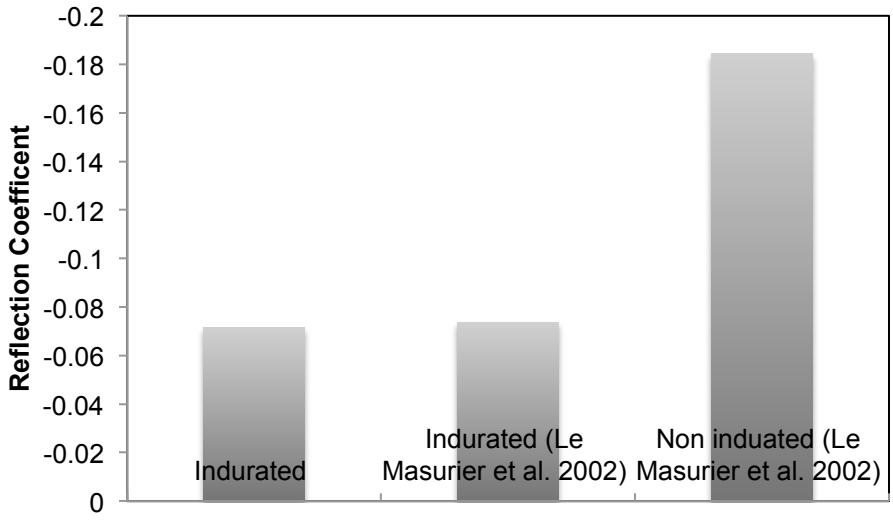

Figure. 6.22a Reflection coefficient vs. degree of induration at the interface between a pillow lava and hyaloclastite. See text for details. Density data from Le Masurier, 2002 and provided in the appendix for this chapter.

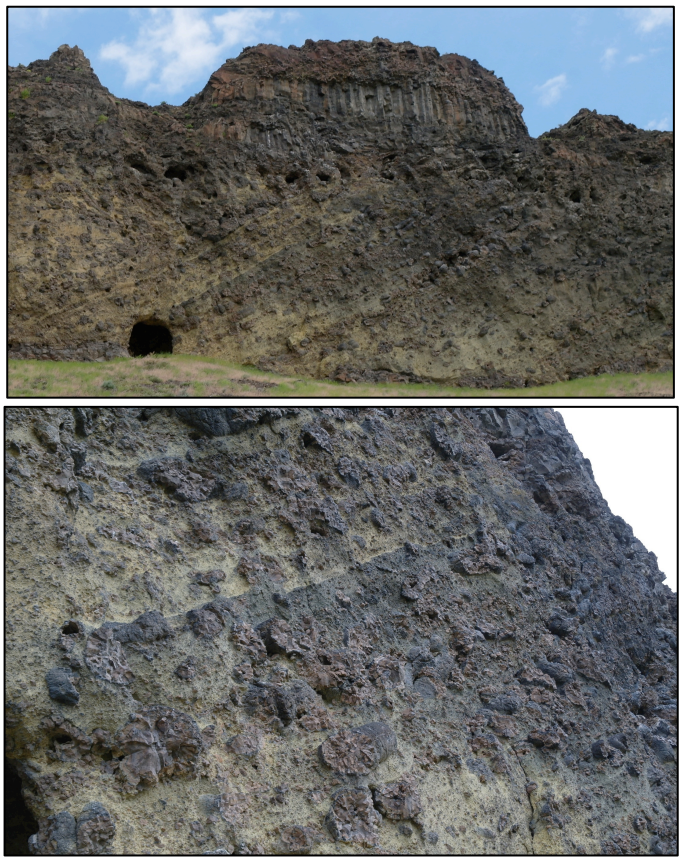

Figure. 6.22b Changes in the degree of induration in a pillow lava succession from the Columbia River Flood Basalt. Locality from Cresent Bar (UTM Grid 10 T 0722047, 5236170). Note the sharp contacts between light (palagonite filled; indurated) and dark (non-indurated) hyaloclastite breccia between each pillow lava. RC calculations suggests that this could give rise to a significant RC if seen in the subsurface.

Table 6.6

Reflection Coefficient Value	Roughness/Contact type	Boundary Type
0.3	Low/Sharp-Gradational	Fh-Ch couplets, sedimentary origin
	Low/Sharp	Slump Scarp Collapses, listric detachment surfaces
0.1	High/Sharp	Passage zone contact between lava supplying and hyaloclastite
0.18	Low?/ Sharp	Diagenetic boundaries within units
0.2	High/Gradational	Contact between pillow lava and hyaloclastite

Table 6.6. A Summary table representing the potential causes of reflection coefficients in hyaloclastite deposits.

Table 6.6 summarizes the possible causes of reflection coefficients in hyaloclastite deposits based upon common boundaries described in this and the previous chapters. The transition between Fh-Ch couplets, pillow lava and hyaloclastite and diagenetic boundaries has already been discussed. Other possible causes of reflection coefficients are slump scarps common in hyaloclastite deposits onshore (e.g. Skilling, 2002). Slump scarps can form listric planar geometries. Large fault scarps on Hjörleifshöfði (chapter 4 and 5) suggest that different damage zones can occur. The type and width of the damage zone and its associated sediment fill is likely to dictate whether a reflection coefficient is generated. Finally, the passage zone transition itself will and is known to generate strong reflection coefficients and is not discussed here but the author suggests reading Planke et al., (2000) and Wright et al., (2012).

Therefore all of the boundaries outlined above could give rise to coherent prograding reflectors but, as shown by results from the LOPRA 1/1A well, thick hyaloclastite deposits (~1 km-thick packages) tend to be dominated by hyaloclastite rather than pillow lavas or lava flows. These results suggest that at least some reflectors in hyaloclastite sequences are probably a result of fine- to coarse-grained hyaloclastite interbeds. This supports the hypothesis that strong prograding reflectors could represent hiatuses between eruptive events (as inferred from field examples, e.g., Watton et al., 2013).

6.3.3 The S-wave (Vs) Problem

S-wave (Vs) values in the HSDP core have no correlation to known Vp vs. trends for siliclastic rocks (Fig. 6.23), e.g., the mudrock line defined by Castagna et al., (1985) where:

$$V_p = 1.16V_s + 1.36 \quad (6.13)$$

However, within one logged core interval (1830–1870m; section 6.6, Fig. 6.35) there are significant deviations in Vs that do not correspond to Vp increases. The Vs log can be tidied-up using a simple replacement of velocity values (from 3-2 km/s and 4-3 km/s) in order to minimise jumps in the data and so that increasing Vp matches increasing Vs velocities (Fig. 6.24). No significant changes in the core in terms of clast content or mineralogy were observed at the Vs deviations. Once corrected the recorded trend shows a similar gradient to that of the Castagna equation (6.10) that defines the mudrock line, but, on average, values are 0.4 km/s lower than predicted. This could be attributed to tool error or to the hyaloclastite deposits having much lower s-wave values than saturated mudstone/sandstone. Given the extent of the correction applied to these logs I am unsure if any firm conclusions can be made regarding Vs data in the HSDP II core and hence this does not receive any further discussion. This is compounded when all Vp/Vs data from LOPRA 1/1A data is plotted showing a general cluster around the mudrock line.

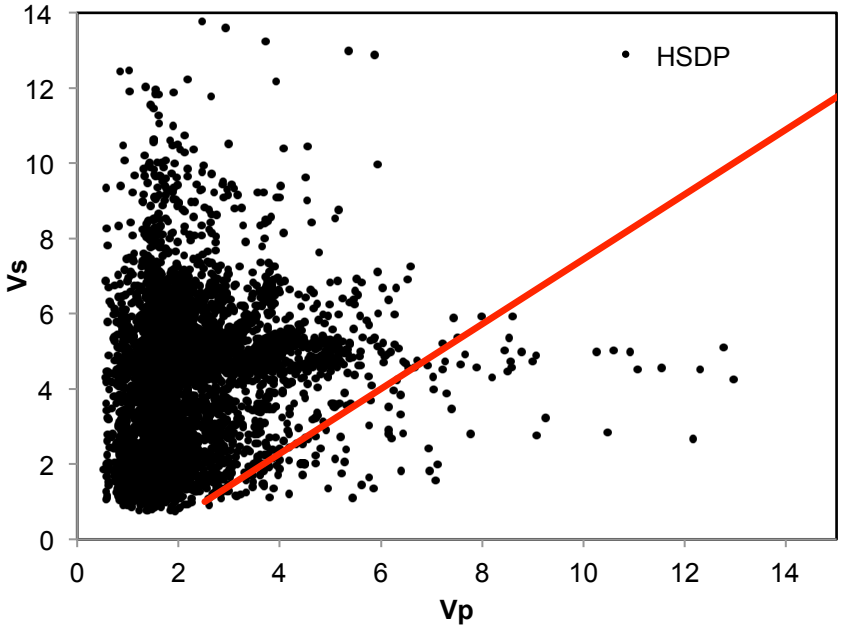

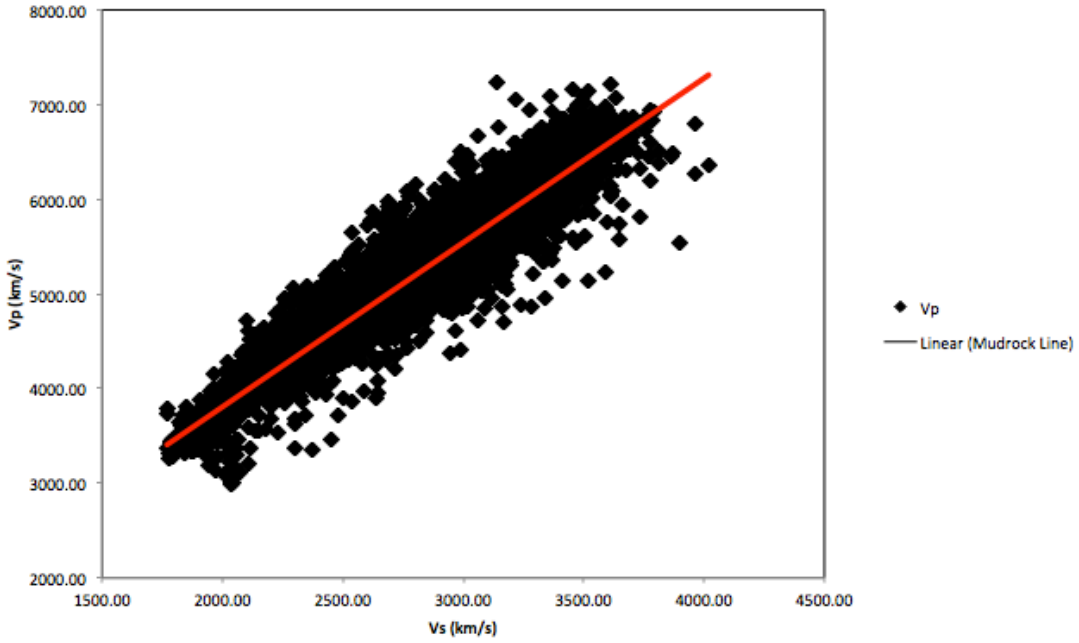

Figure. 6.23. Plot of Vp vs. Vs for the whole HSDP II well. The mudrock line is plotted in red. None of the samples lie on this trend but there is no correlation of any data suggesting that Vs data is unreliable. In contrast the Lower figure shows Vp and Vs data from LOPRA 1/1A which generally follows a mudrock trend. (Data presented as km/s and m/s)

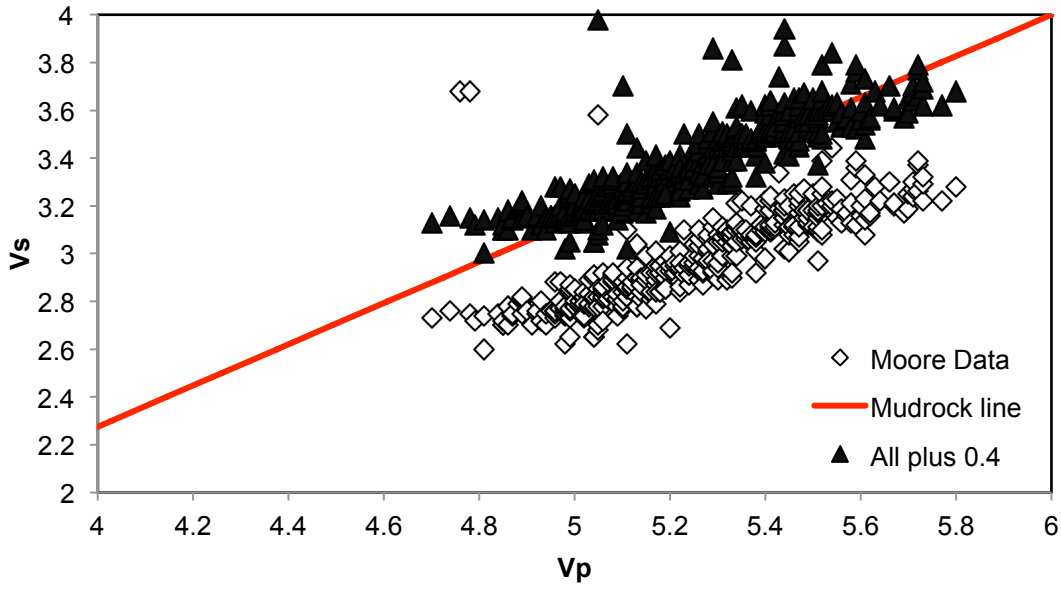

Figure. 6.24. Corrected Vs values for 1830-1870 m (see section 6.6; section was logged in detail see Fig. 6.29). Corrections applied shows that hyaloclastite samples can generally follow a mud rock trend however the corrections will be non-uniform for the entire core indicating the data is unreliable. (Data presented as km/s).

Klarner and Klarner, (2012) using examples from the Stantos Basin, offshore Brazil, the Sirte Basin, Lybia and the Central North Sea suggest that Vp and Vs relationships in volcanic rocks can be defined by a linear regression;

$$Vs = 0.51Vp + 148 \tag{6.14}$$

This trend closely follows the Castagna et al., (1993) defined from limestone values;

$$Vs = 0.583Vp^2 + 1.017\,Vp - 1.031 \tag{6.15}$$

As Vs in the HSDP II dataset cannot be used due to anomalous readings, data from LOPRA 1/1A hyaloclastite interval (2530-2800 m) can be compared to the linear trend defined by Castangna et al., (1993) and Klarner and Klarner, (2012) (Fig. 6.25). Hyaloclastite Vp/Vs data from LOPRA 1/1A closely matches both trends

implying hyaloclastite physical rock properties may be analogous to carbonate rocks (discussed below). However, LOPRA 1/1A samples show a high degree of density variation is concordant with no density/velocity relationships similar to HSDP II results (Fig. 6.26).

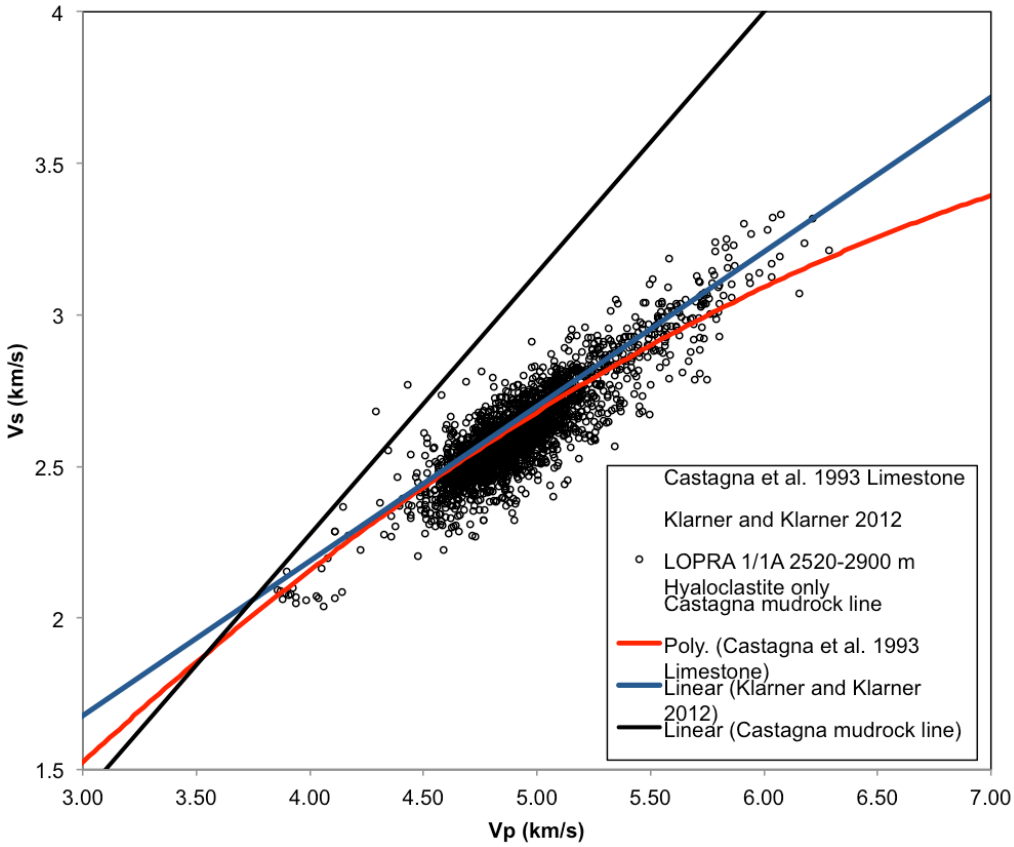

Figure. 6.25 Vs vs. Vp in the LOPRA 1/1A hyaloclastite interal (2530-2900 m). The mudrock line is plotted in black. Hyaloclastite deposits align along the trends for volcanic and carbonate rocks defined by Castagna et al., (1993) and Klarner and Klarner, 2012. Reasons behind this relationship are discussed in section 6.3.3. Data provided in the appendix for this chapter.

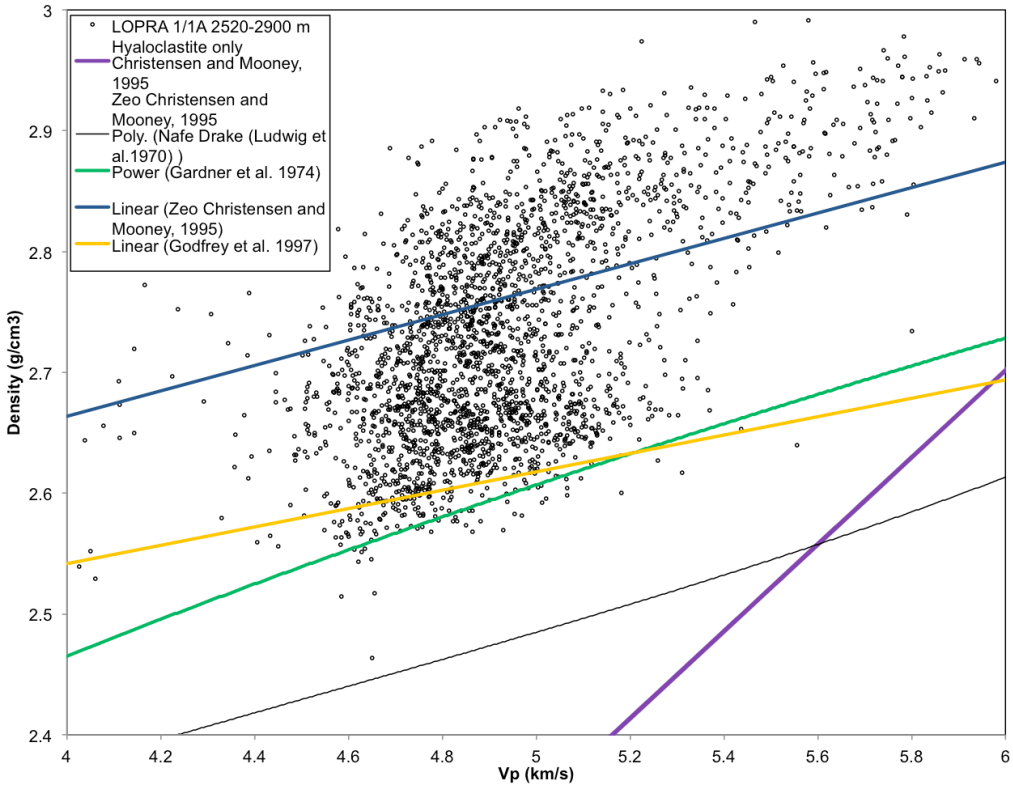

Figure. 6. 26 Vp vs. Density for the LOPRA 1/1A hyaloclastite interval (2530-2900 m). The spread in values is much less than HSDP II results however the samples fit no known trend. However, at density values of .2.75 g/cm^3 the LOPRA 1/1A data points divert and begin to follow the line of altered volcanic rocks as defined by Chirstensen and Mooney, (1995) and Brocher, (2005). Data provided in the appendix for this chapter.

Implications of Vs Results

LOPRA 1/1A and HSDP II density/velocity comparisons suggest hyaloclastite deposits in general do not plot along a Nafe-Drake Trend. However, LOPRA 1/1A hyaloclastite deposits plot along well-defined Vp/Vs trends that include a variety of volcanic rocks and limestones from different basins worldwide (Castagna et al., 1993; Klarner and Klarner, 2012). This observation implies that hyaloclastite deposits have a much higher Vp/Vs separation than siliciclastic rock types and may share physical characteristics to carbonates (Fig. 6.27).

No systematic study has compared Vp/Vs values and determined the reasons behind high Vp/Vs separation in volcanic rocks. Klarner and Klarner, (2012) suggest that textures in volcanic rocks such as their pore structure and clay alteration are similar to carbonate textures. However, Vp/Vs separation studies on carbonates suggest a number of causes (e.g. Kupier et al., 1959; Rafavich et al., 1984; Wilkens

et al., 1984; Miller, 1992). In chemically pure carbonate rocks Vp and the poissons ratio (the degree of expansion or contraction of a sample due to strain) are both strongly linked to density (Kupier et al., 1959). Additionally, porosity, pore shape and density are also thought to control both Vp and Vs, although compositional effects (such as increasing silica content) could be more dominant (Tatham, 1982; Wilkens, 1984). Laboratory Vp/Vs studies have concluded that density and porosity in carbonates generally controls Vp/Vs ratios (Rafavich et al., 1984).

Hyaloclastite deposits in the LOPRA 1/1A borehole have a high Vp/Vs separation similar to that of limestones (Fig. 6.27). X-ray CT scans of a hyaloclastite sample (chapter 2, Fig. 2.7 a, b, c.) show porosity but limited connectivity. Mechanisms of hyaloclastite compaction are covered in section 6.5 however; high basalt clast content possible resists compaction (see Fig. 6.31) leading to high Vp results. Vs is likely to remain low due to the presence of abundant palagonite at grain boundaries which is lower density and can be gel like (see chapter 3) meaning shear stress is transferred less effectively. Furthermore, hyaloclastite deposits can contain large percentages of zeolites and calcite in pore space. Zeolites create similar textures to carbonate rocks in terms of porosity and pore structure that also may contribute to similar Vp/Vs responses. Therefore in hyaloclastite deposits Vp/Vs ratios are likely to be a texture control but could be lithofacies dependant indicating further study is needed.

The recognition of a high Vp/Vs ratio is primarily important in hydrocarbon exploration. Amplitude vs. Offset (AVO) (e.g. amplitude changes with offset as seismic energy is reduced) analysis is used to find potential hydrocarbon targets that, due to low Vp/Vs ratios when within a host reservoir rock show as soft, dim reflection due to a dispersal of wave energy. Hyaloclastite deposits also have a high Vp/Vs ratios like many volcanic rocks which leads to an increase in amplitude with distance from source (Klarner and Klarner, 2012). If volcanic rocks are interbedded, for example, with carbonates similar AVO responses to charged reservoirs can be observed.

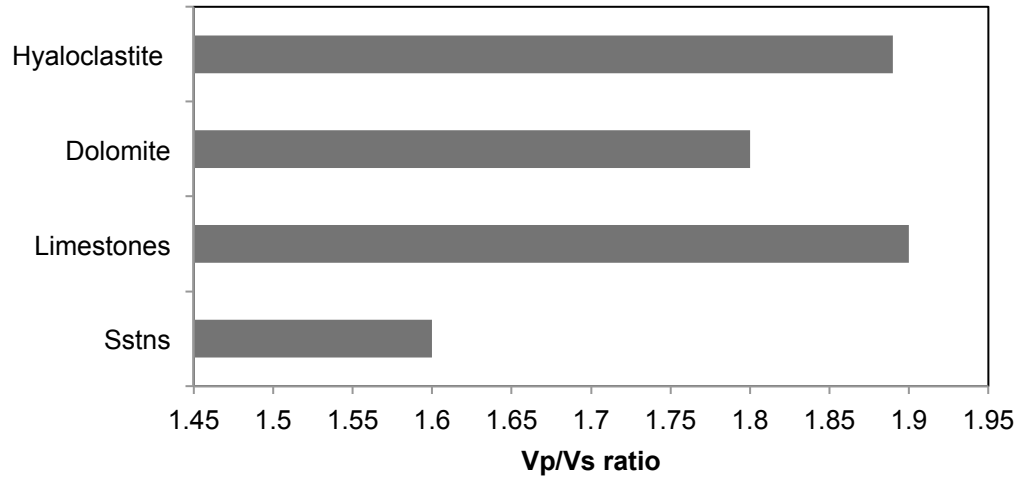

Figure. 6.27. Typical values of Vp vs Vs separation in siliciclastic (sandstones = sstn), carbonate and hyaloclastite deposits. (Data from Miller, 1992 and this study).

6.4 Summary of Vp Analysis

Vp-to-density modelling of hyaloclastite deposits cannot accurately predict the variation in density of hyaloclastite deposits or separate hyaloclastite lithofacies. Although the values of different hyaloclastite lithofacies can be averaged and used in 1D depth conversions or RC calculations there is still a large spread in the velocity and density values for each lithofacies. Therefore results presented above are the best estimate based upon the lithofacies separation (grain size) conducted by Moore (2001). A better understanding of hyaloclastite deposits from direct core to well log observations is needed to constrain the variation in Vp and density, amongst other parameters, in the HSDP II core (see section 6.6). If additional data is available alongside Vp, such as down bore hole images (see chapter 7), through a well section intersecting hyaloclastite deposits, then it may be possible to better constrain the lithofacies and therefore understand the causes for RC's using the processes outlined above.

6.5 Porosity Modelling in HSDP II

Following on from section 6.2, Moore (2001) measured porosity in 1600 samples taken from 889 to 3097 m depth. At depths greater than ~1800 m, palagonite and authigenic minerals infill the pore spaces and both porosity and permeability are

reduced to negligible levels. Using this dataset for where palagonite formation begins we can envisage how porosity reduction occurs with progressive burial on the flank of a geologically young, subsiding emergent volcano (excluding certain parameters such as variations in fluid composition and circulation for which data are lacking). This can potentially be used as a proxy for the type of burial diagenesis that we may expect in hyaloclastite deposits with similar lithofacies distributions although the separation of chemical vs. physical compaction effects are hard to quantify.

6.5.1 Initial Modelling (Using Standard Compaction Trends)

The modelling indicates that, using a normal compaction trend with limited palagonite growth and an initial porosity of 36% (e.g. Hay and Iijma, 1974), the effective porosity at 1000 m is 26% and is consistent with a best fit for the Moore (2001) dataset. This follows the Athy equation (Athy, 1930) for sandstone examples. Therefore, until the palgonitization process starts porosity loss is assumed to be similar to that of sandstone with variation like likely to be lithofacies dependent.

From the Moore (2001) data set a minimum porosity (%) can be calculated as:

$$\emptyset = 1 - \frac{Dry\ Denisty}{Grain\ Density} \tag{6.16}$$

Since there is a rapid effective porosity decrease between 1000 and 1800m from 26 % to 1-2 % we can simply envisage the percentage of pore throats infilled with palagonite within the palagonite zone (on the assumption that no palagonite precipitates before this point) and modify the Athy equation. This can be expressed as:

$$\emptyset = \emptyset_{pz} e^{\left(-td_p\left(\frac{c}{\alpha}\right)\right)d} \tag{6.17}$$

where $\emptyset_{pz}$ is the porosity of the material as it enters the palagonite zone, td_p is the total depth of the palagonite zone, c is the constant (0.27/km) compaction value for a sandstone defined by Sclater and Christie, (1980), α is the fraction of pore throats free of palagonite as a percentage and d is the depth. Figure 6.28 shows curves

calculated for a variety of α values simulating different degrees of pore throat filling. For example in the case of 99 % pore throat reduction the porosity rapidly descends to very low levels once the sample enters the palagonite zone. The data points from the HSDP II samples occur between the 0.03 (97% pore throat reduction due to palagonite formation) and 0.2 (80% pore throat reduction) curves.

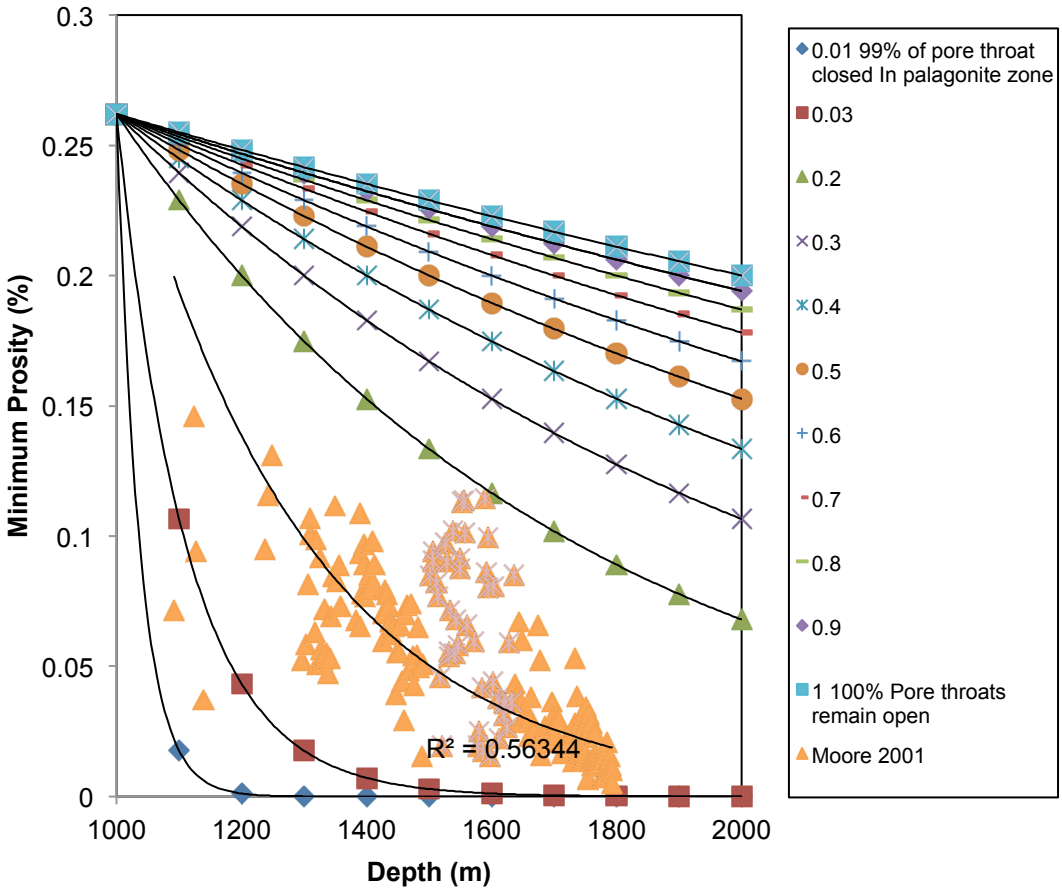

Figure 6.28. Depth vs. Minimum porosity plotted for the HSDP II samples using a (c) value of 0.27 km. This model suggests that most pore spaces are shut during burial and hence can predict where porous hyaloclastite will occur if the depth and thickness of the palagonite zone is known.

6.5.2 Hyaloclastite Compaction

The compaction trend for hyaloclastite deposits is generally unknown. If we discount the palagonite process, which is unrealistic, then reduction in sample porosity can be used to calculate total sample % as;

$$total\ sample\ \% = 100 - \emptyset\% \qquad (6.18)$$

Therefore we can plot this vs. depth to calculate a compaction value based upon a linear best-fit line (Fig. 6.29). The fit is generally poor and from density data we know that it remains constant throughout the core, therefore palagonite replacement is probably the cause of porosity loss and increased total sample %. Although the fit is not very good (R^2 only 0.52653) a compaction value (c) of roughly 0.1125 km can be calculated.

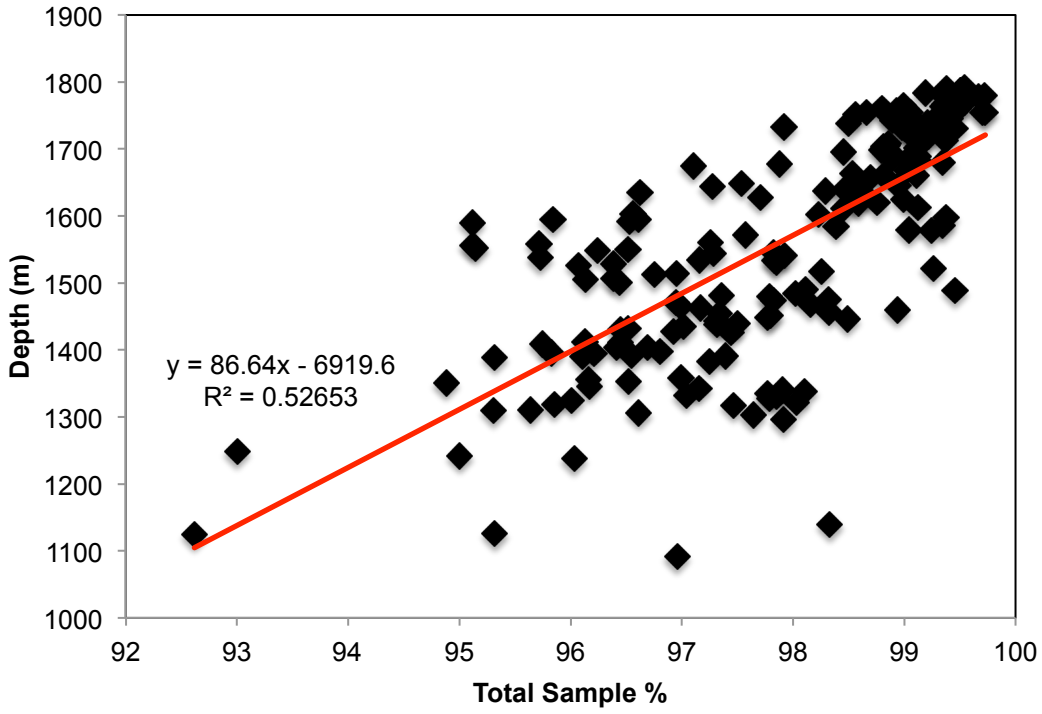

Figure. 6.29 Depth vs. Total sample percentage. The gradient Linear best fit line could can be used to calculate c (roughly 0.1125 / km). However this is generally unrealistic due to palagonite formation and a rapid decrease post 1800 to a constant reduced porosity. However other factors may lead to hyaloclastite deposits resisting compaction.

The compaction of hyaloclastite deposits is unlike that of sandstones even before the palagonite process becomes dominant. During the initial packing process irregular grains will tend to have high coordination numbers (number of contact

points with other grains) (Fig. 6.30, after Alberts, 2005) due to their angular shapes. Porosity is increased by angular separation, which occurs due to bridging between grains, and this reduces the coordination number. However, quench fragmentation processes can result in jigsaw- fit textures (e.g. McPhie et al., 1993), which act to reduce angular separation and increase the coordination number. This helps inhibit compaction, lower porosity and limit the amount of pore throats. This style of packing also promotes pore throat reduction when concentric growth of clay minerals starts. It is also not clear how the physical properties of unstable glass will change as it starts to degrade to clays, and therefore the potential difficulties of using a compaction curve for sands, or that for clays, to model the behaviour of a medium which will be varying relative proportions of its mineral species as it compacts.

Reworking in hyaloclastite deposits can reduce grain angularity. Sharp edges develop from vesiculation and bubble bursting on quench contact (e.g. Fisher and Schmincke, 1984). Reducing the grain size means angular separation is reduced. However there is also the potential to add a new lithic component via reworking, which may enhance separation through facilitating multiple grain sizes.

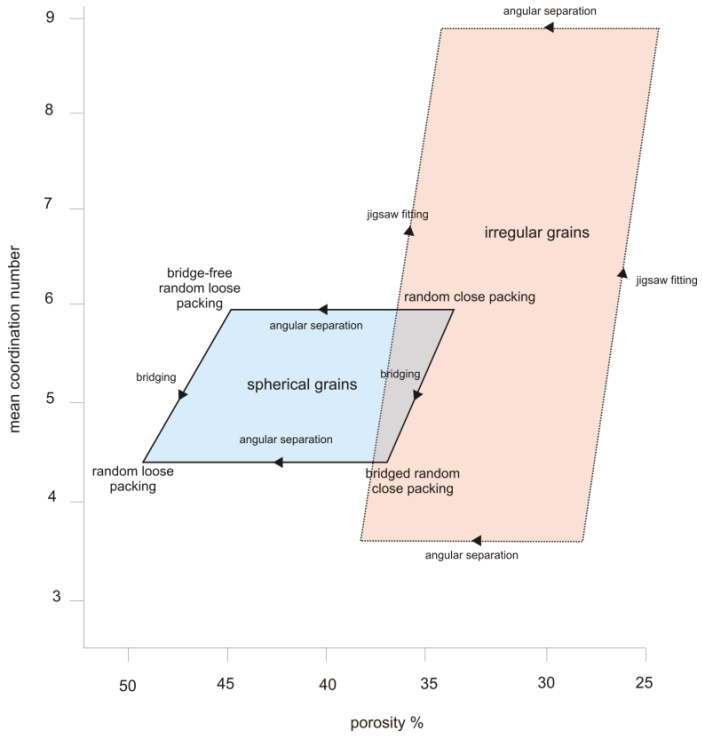

Figure. 6.30 Porosity as a function of mean coordination number. Irregular grains are typified by lower porosity estimates however angular separation can act not only to increase porosity

but decrease coordination number. Jigsaw fitting is likely not only to increase grain contacts but also limit porosity and connectivity. (After Alberts, 2005)

The nature of grain packing has a strong control on pore throat diameter. Where packing facilitates multiple grain contacts due to multiple grain sizes then pore throats will become restricted for idealised spherical grains. This is true in random packing fashions (e.g. Finney, 1970; Jerram, 2001). The distribution of pore throats becomes irregular (Wardlaw et al., 1987) and as such pore throat distribution becomes non-uniform and connectivity is reduced. The nature of grain packing in hyaloclastite deposits is more complex than simple spherical models predict due to the irregular grain shapes as well as the presence of crystals (e.g., plagioclase) or clast-on-clast contacts that can hold open the pore space and reduce compaction (Fig. 6.31a).

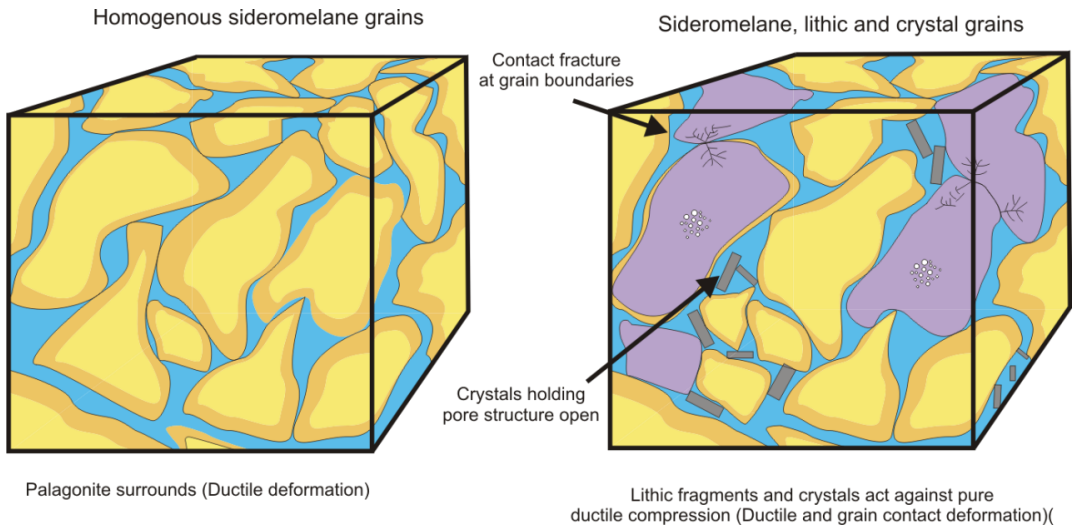

Figure. 6.31a. Compaction processes operating on a homogenous glassy hyaloclastite and a crystal and lithic rich hyaloclastite deposit. Crystals within the hyaloclastite structure are less prone to alteration and hence help maintain pore throat diameters. Basaltic lithic fragments may develop a thin palagonite rind but this will not be as thick as sideromelane shards. Often lithic fragments show no alteration on the grain edges. Both crystals and basalt clasts act to hold open pore structure and help inhibit compaction.

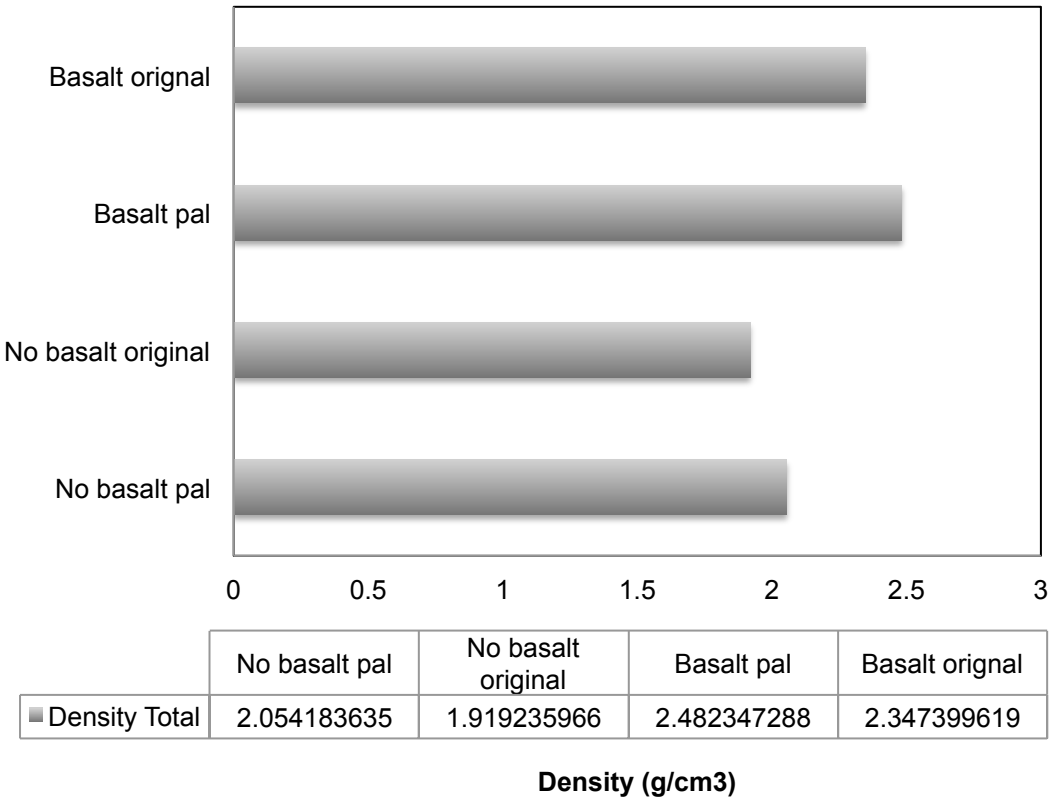

	No basalt pal	No basalt original	Basalt pal	Basalt orignal
Density Total	2.054183635	1.919235966	2.482347288	2.347399619

Figure. 6.31b Calculated replacement effect based upon image analysis of thin section X1 (see figure 6.35 for location). Image analysis outline in chapter 2 can determine the amount of palagonite, zeolite, olivine, glass and porosity of the sample. If palagonite and zeolite are removed, then the original porosity of the sample can be calculated (in this case 22%). If the density of palagonite (1.67 g/cm^3), zeolite (c. 2 g/cm^3), porosity (water filled, c. 1 g/cm^3), and sideromelane glass (2.1 g/cm^3), olivine (3.25 g/cm^3) (Hay and Iijima, 1968; Staudigel and Hart, 1983; Stroncik and Schmincke, 2002) and the percentage are known then the density of the entire sample can be calculated. As this is a matrix value, 50% of the glass can be substituted basalt (3 g/cm^3). These give two results no basalt/basalt original that contains 22% porosity and no palagonite or zeolite and no basalt pal/Basalt pal that contain palagonite and zeolite. There is only a negligible difference between the palagonite replaced and original samples.

The grain size distribution of a deposit can also affect compaction. Smaller grains fill the spaces between larger grains and increase packing density. The pore throats become smaller but have a higher width to height ratio (Yang et al., 2003; based upon computer generated models). In well-sorted sandstones where the grain sizes are relatively homogenous the pore throat size will be restricted and the size distribution will be narrow. Additionally, compaction is likely to be less due to basalt

clasts, lithic fragments and loose crystals allowing the structure to be kept open which are more likely to resist the palagonitization process (Fig. 6.31a).

These observations support why a Nafe-Drake density relationship is generally not followed. First compaction is resisted by basalt-basalt contacts or crystals propping open the pore structure resisting compaction and maintaining a open pore structure which facilitates rapid palagonite formation as grain remained exposed. Secondly the replacement of porosity with denser palagonite means that overall density only increases by a small amount meaning a Nafe-Drake relationship is not observed and supporting why additional models of Vp vs. density need to be conducted (Fig. 6.31b).

6.5.3 Revised Model (Using New Estimates of Hyaloclastite Compaction)

If a compaction value of 0.1125 / km is substituted into equation 2 the exponential best-fit line of measured HSDP II values fits the calculated trend of 0.03 % of pore throats that remain open once the palagonite depth is reached. The residual porosity is roughly 1 % (Fig. 6.32). This value corresponds well to image analysis of porosity in thin-sections from samples taken between 1830–1870 m (1-4 %, see section 6.6.4).

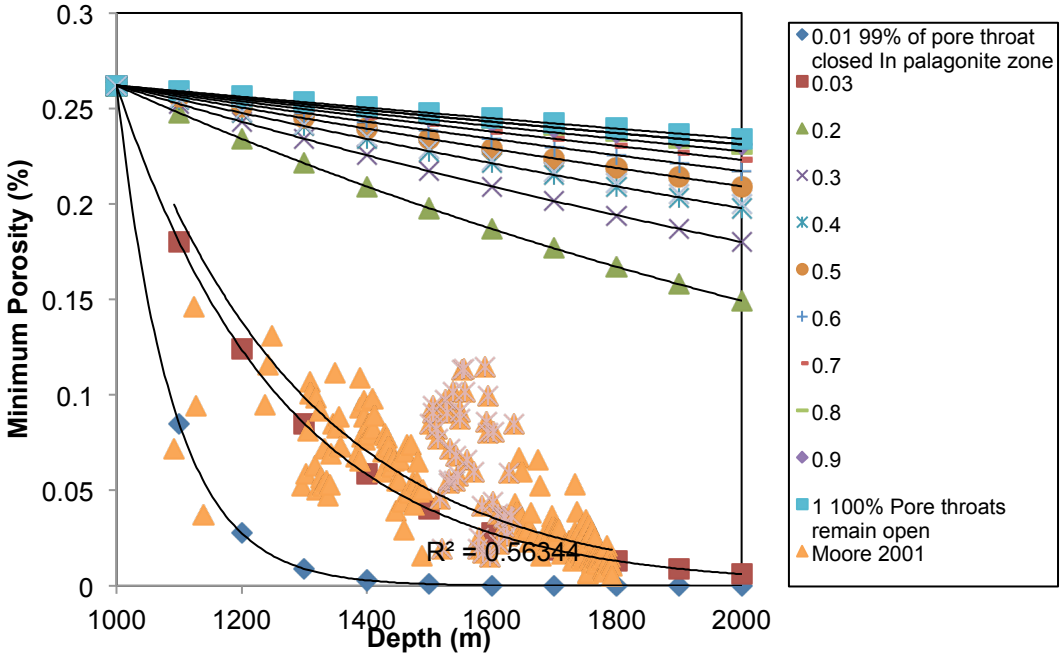

Figure. 6.32. Porosity vs. depth for model values using a compaction value of 0.1125 / km and a initial porosity of 26.2 %.

However, compaction is likely to be resisted before the palagonite process occurs and the starting porosity of the sample can be calculated by also using c in the initial Athy equation. This gives a starting porosity in the palagonite zone of 32.1 % (Fig. 6.33). The results of this model are similar to figure 6.26 although the fit is generally better (except for values at very shallow depths).

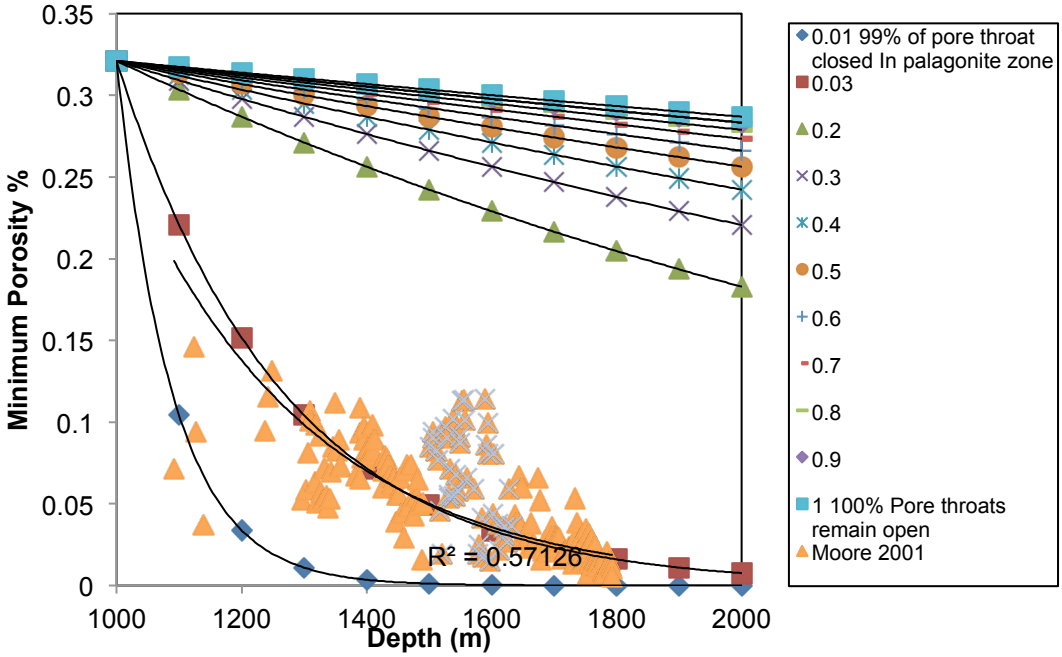

Figure. 6.33 Porosity vs. depth for model values using a compaction value of 0.1125 / km and a initial porosity of 32.1 %.

6.5.4 Discussion

Bulk compositional geochemical data for samples over this interval (1000-2000 m) from a study by Rhodes and Vollinger, (2004) are freely available on the ICDP, HSDP II website (Fig. 6.34). Interestingly, some samples have higher than average porosity for their given depth (denoted by stars in Fig. 6.28). Discounting these from the model leads to an increase of ~0.12 in the R^2 correlation factor for an exponent best-fit line. Samples with increased porosity may represent a slight bulk compositional change (e.g. increase SiO_2 and decreased MgO within a well defined geochemical group), a change in grain density (values 1σ above the mean value) or changes in lithofacies type (higher porosity zones are closely associated with thin

olivine-phyric basalt flows that potentially shielding them from compaction) each support observations from image analysis, section 6.3.3. Therefore all these factors must be considered as potential factors in modifying the rock properties in hyaloclastite deposits and controlling the initial porosity value used in the models presented above.

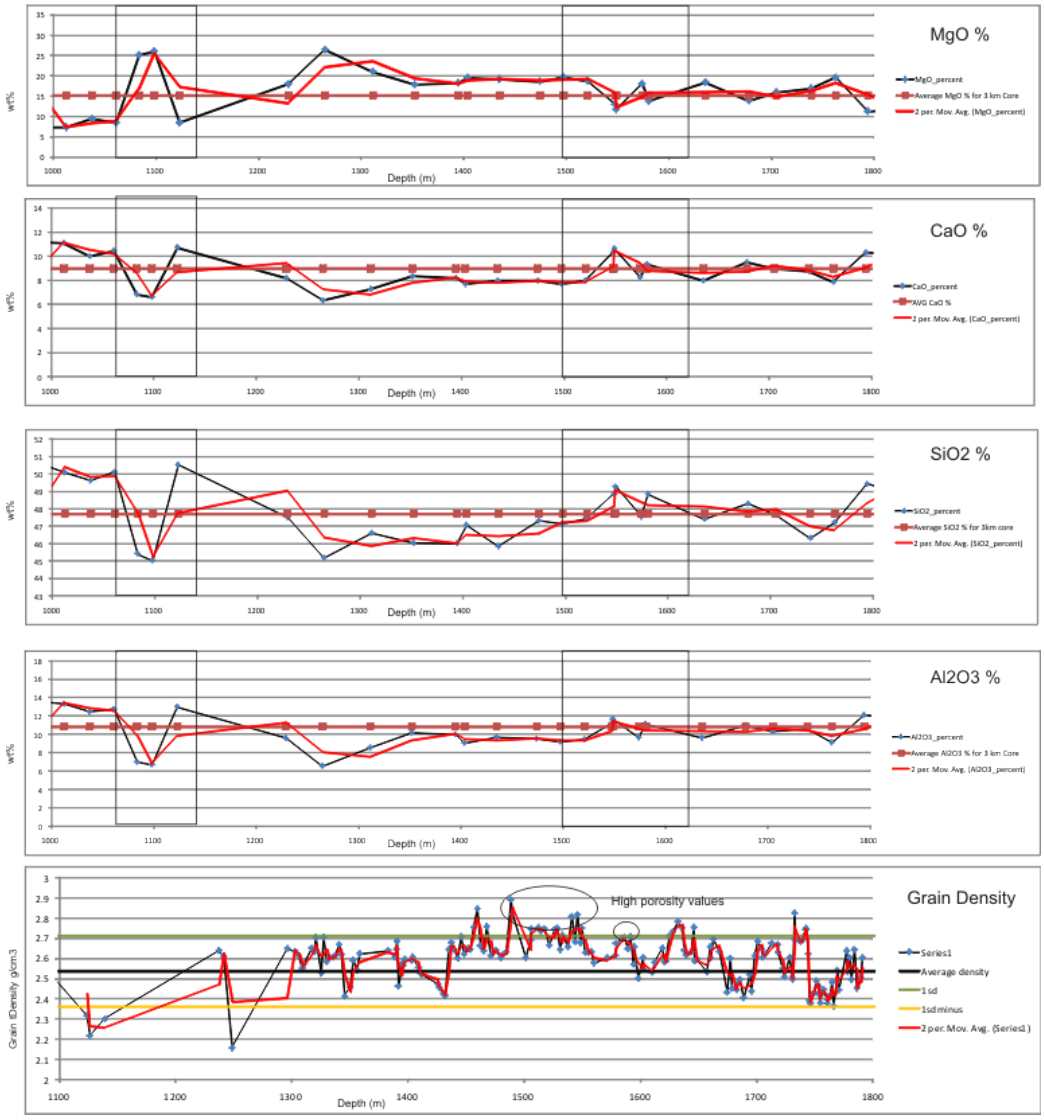

Figure. 6.34. Wt % major element and variation across the interval. Box between 1500-1620 m indicates the zone of enhanced porosity, which corresponds with increases in the average wt. SiO_2 and grain density of the sample.

6.6 Well Log to Core Comparison HSDP II

It is apparent from the results of sections 6.2-6.5 that there is a need for a characterisation of cored hyaloclastite material to be compared to petrophysical log

data. The next section undertakes such a study using samples from the HSDP II core based upon logging and sampling of the core in the store of the Natural History Museum of New York under the supervision of Mike DaSilva.

Two sections of core—section A (1831–1870 m) and section B (2530–2597 m)—were selected for this study based upon initial well site logging. An effort was made to identify comparable rock sequences at different depth intervals. The two selected sections occur within log unit 4 and 8 of Pechnig et al., (2000). Both sections represent thick hyaloclastite intervals that show downhole petrophysical differences in terms of GR and RES response. Each core was logged at a centimetre scale and 28 samples from both sections were taken for petrographic study. The aim was to characterise the difference in lithofacies variation and the effect of mineralogy on wire-line log response that has been highlighted in sections 6.2-6.5.

The wire-line log data used in this study were collected by HSDP scientists for the interval below 1820 m using a Dual Laterlog DLL, Spectral Gamma Ray Tool SGR (with GR, K%, Th ppm and U ppm) and a Compensated Sonic Tool BCS. Hole deviation was controlled by a Sandia Core Tube Logger (CTDL). No density log measurements were taken. All logs have been depth-corrected by GFZ Potsdam and were acquired by us from the public data release on the ICDP website. An example of the calibrated core logs, petrophysical logs and major mineral phases are provided in figure 6.29 for section A.

Polished thin sections were made from each sample. All samples were impregnated with blue resin to highlight porosity. Each thin section was photographed optically, and then scanned at 1000 dpi. Porosity, and palagonite, zeolite and olivine percentages were calculated from these images using Image analysis software (ImageJ, Rasband, 2012 and JPor, Grove and Jerram, 2011) (See chapter 2) for the A section. Ten representative samples from both core runs were analysed using a scanning electron microscope at the Durham University Scanning Electron Microscope Facility (Hitachi SU-70 FEG SEM). Calibrated EDX (Oxford Instruments INCA x-act LN_2-free analytical Silicon Drift Detector) major elemental analysis was conducted on 42 sites. In total 400 EDX mineral analyses were collected and provided in the appendix.

6.6.1 Key Petrophysical and Petrological Observations

Figure 6.35 shows a simplified log of sections A and B that illustrates variations in rock texture, clast shape and interstitial minerals that have been calculated using a combination of log (observational), petrographic and EDX analyses. A comparison is made to figure 6.36, which shows core images of the hyaloclastite components, recorded from each of the interbedded clast-supported and matrix-supported units. This contribution has broken down the key observations and interpretations for each lithofacies into mineralogical response, velocity response, and Spectral Gamma Ray (SGR) response over the studied core intervals.

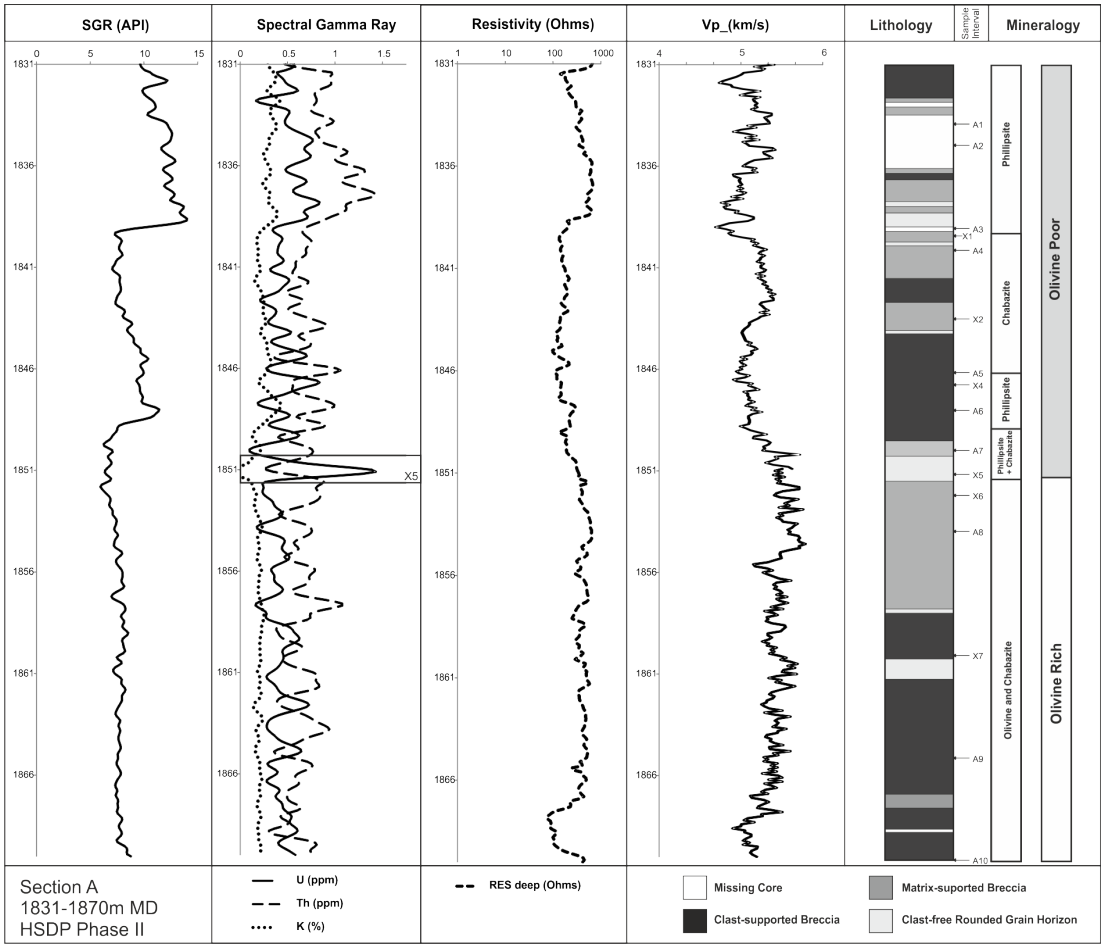

Figure 6.35. Composite log, sample intervals and mineralogical observations from core section A and B. In section B the velocity data past 2545 spikes erratically therefore a 20-point average curve has been used for future reference to this section and coloured red in the figure. There is limited olivine present in the b section. Density data was not recorded for the HSDP II wire-line log dataset.

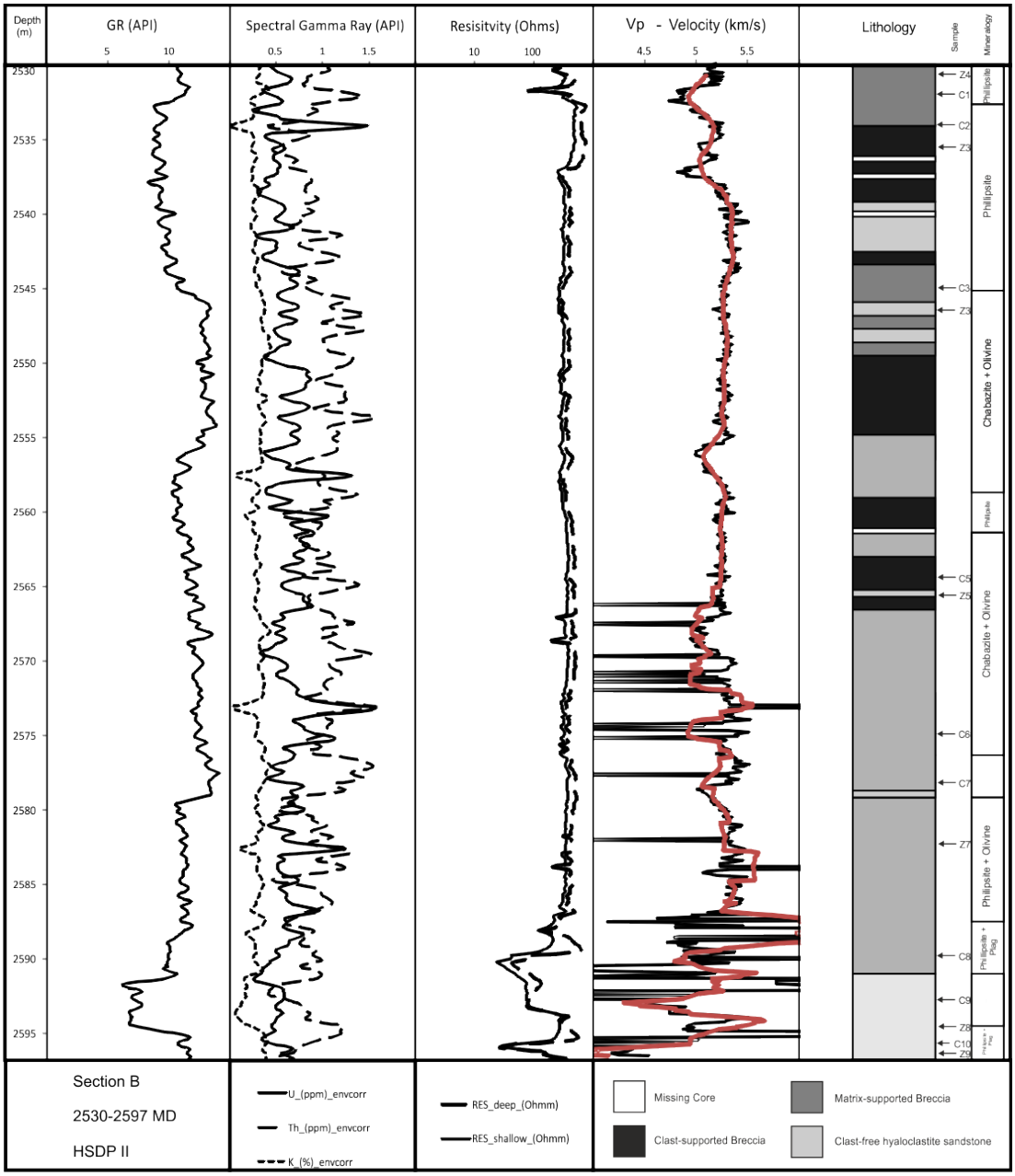

Figure 6.35 Composite log, sample intervals and mineralogical observations from core section A and B. In section B the velocity data past 2545 spikes erratically therefore a 20-point average curve has been used for future reference to this section and coloured red in the figure. There is limited olivine present in the b section. Density data was not recorded for the HSDPP wire-line log dataset.

6.6.2 Lithofacies Variation

Observations - The hyaloclastite deposits can be divided into matrix-supported hyaloclastite breccia, clast-supported hyaloclastite breccia, and fine-grained hyaloclastite sandstones (forming interlayers). Clast-supported hyaloclastite breccias are characterized by inter-locking jigsaw-fit angular basalt clasts in a coarse-grained, ungraded, sideromelane and palagonite matrix (Fig. 6.36c). Clast size is highly variable (max > 10 cm). Fractured closely-spaced jigsaw-fit breccias occur in the olivine-phyric lavas (Fig. 6.36b and Fig. 6.37B). Matrix-supported breccias do not display jigsaw-fit textures and have a coarse- to medium-grained normally-graded matrix composed of sand-grade sideromelane glass and sub-angular basalt clasts (<6 cm in diameter on average). Fine-grained hyaloclastite sandstones are c. 0.3–3 m thick are finely laminated and contain fine-grained (<0.42 mm) basalt fragments and variable quantities of liberated phenocrysts (Fig. 6.36a). There is no correlation between log responses and lithofacies in both logged examples except for increases in uranium log responses within clast-free zones (see section 6.6.7).

Interpretation - Interlocking clast-supported hyaloclastite breccias are typical of in-situ lava fragmentation with limited remobilization of fragments (cf. McPhie et al., 1993). Olivine-phyric intervals have closely spaced jig-saw fit textures and may therefore represent periods of limited remobilization. Destabilisation of hyaloclastite deposits on the flanks of submarine volcanic edifices can lead to downslope reworking and the creation of matrix-supported hyaloclastite deposits (cf. Watton et al., 2013). Two types of remobilized hyaloclastite deposits occur in the studied core. Clast supported breccias occur due to remobilization of a hyaloclastite pile downslope. Fine-grained hyaloclastite sandstones represent pauses in the supply of hyaloclastite material to the system. These may result from the settling of fine-grained suspended particles following pauses in or the cessation of volcanic activity or from fine-grained sediment from plumes generated by a major mass movement remobilization event. Changes in the composition of the erupted lava through time are recorded by changes in olivine abundance.

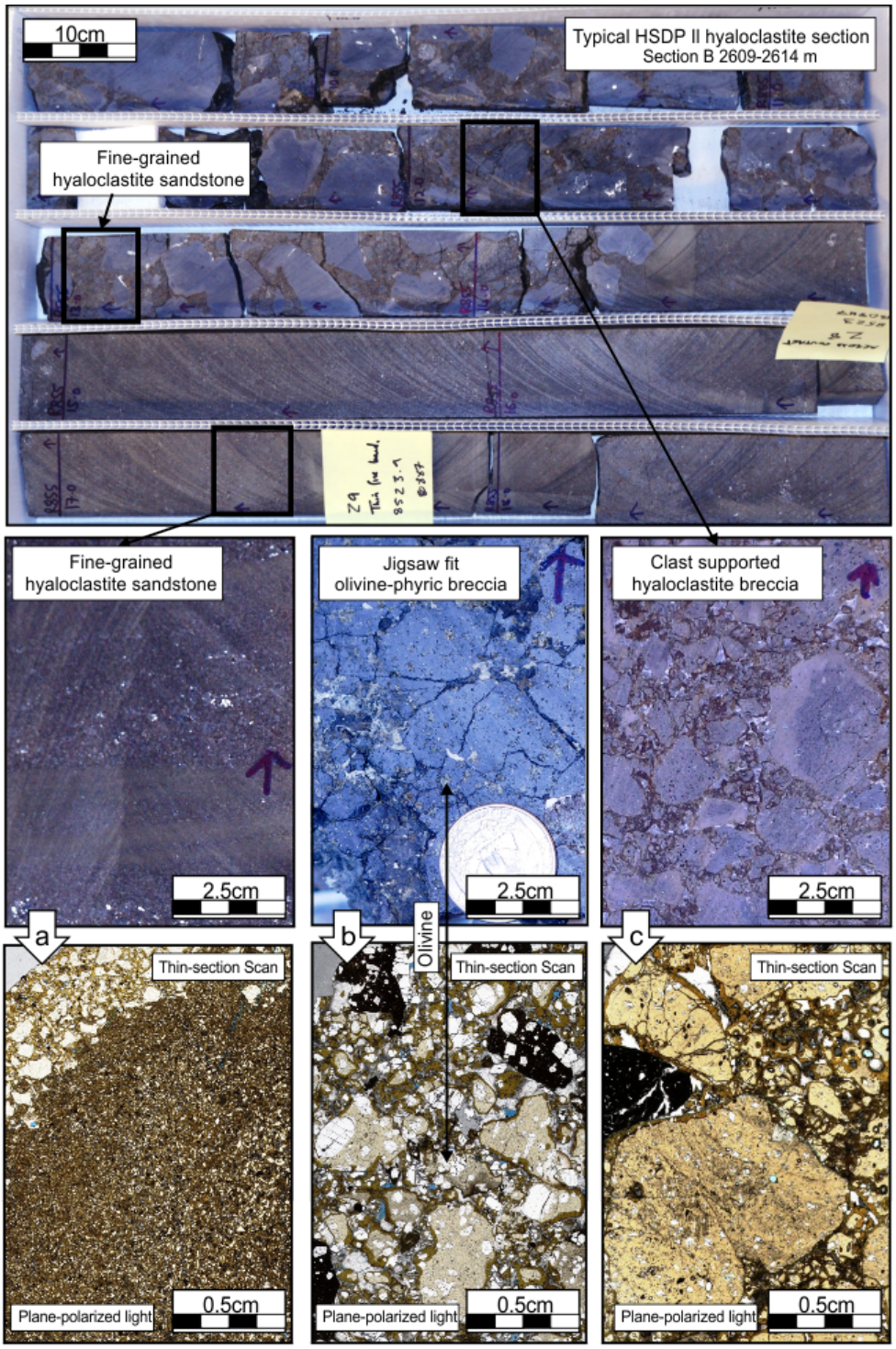

Figure. 6.36. A typical core box from the HSDP II core. Highlighted are A) a clast-free fine grained hyaloclastite sandstone interlayer with fine laminations, B) an olivine-phyric breccia, c) a clast-supported hyaloclastite breccia. Note the grain-size and phenocryst variations between samples.

6.6.3 Thin Section Observations – Summary of Mineralogy

This section summarises characterises thins section observations from the HSDP II core examples. Hyaloclastite samples in the HSDP II core are dominated by sideromelane glass (light brown in Fig. 6.37), which are surrounded by a palagonite rind (dark brown). Sideromelane grains are generally vesicle poor although occasional vesicles do occur and can be filled with zeolites (Fig. 6.37 C). Studies based on the quench rate or sideromelane glass in the HSDP II core have suggested generation from passive water quenching (Nichols et al., 2009). Within sideromelane grains or even loose in the matrix of hyaloclastite deposits olivine phenocrysts can form up to 16% of the sample (section 6.6.7, Fig. 6.36 b, Fig. 6.37 B). The presence of olivine reflects changing composition of source magma supplying material for fragmentation (Rhodes and Vollinger, 2004). Olivine-rich hyaloclastite therefore occurs due to the fragmentation of olivine phyric lava flows. Some olivine phenocrysts have skeletal textures (Fig. 6.30 B), which is indicative of olivine saturation in the parent melt and super-cooling of the phenocrysts both concordant with HSDP II geochemical observations (Donaldson, 1976).

Palagonite forms as a replacement process of sideromelane glass through hydration and element exchange processes (Stronick and Schimncke, 2002; Walton et al., 2005). Commonly in the HSDP II samples palagonite formation is associated with pore lining smectite alteration (Fig. 6.37 D). Palagonite forms rims of various thicknesses (0.01-1 mm) which is dependant on the amount of zeolite in the sample and the grain size of the sideromelane glass. Fine-grained hyaloclastite deposits contain a higher proportion of small grains, which are all in turn surrounded by palagonite meaning they have a higher overall palagonite amount in a 2D section. Palagonite alteration is likely to significantly reduce the density of fine-grained hyaloclastite intervals. Palagonite (1.67 g/cm^3) has a significantly lower density then significantly lower than fresh sideromelane glass (1.90-2.10 g/cm^3) (Hay and Iijima, 1968; Staudigel and Hart, 1983).

Zeolite mineralisation is thought to occur contemporaneously with palagonite formation (Walton et al., 2005). The HSDP II sections in this study contain two dominant zeolite types philipsite and chabazite they are defined by their morphology (see section 6.6.8) and chemistry (section 6.6.7) and have also been identified by

Walton and Schiffman (2003) (Fig. 6.37 A). Zeolite mineralisation forms in in pore spaces left between glass grains or within vesicles in the glass. For the A section there is no correlation between porosity and % component in any case, which is supported by Walton and Shiffman's (2003) observations (Fig. 6.38).

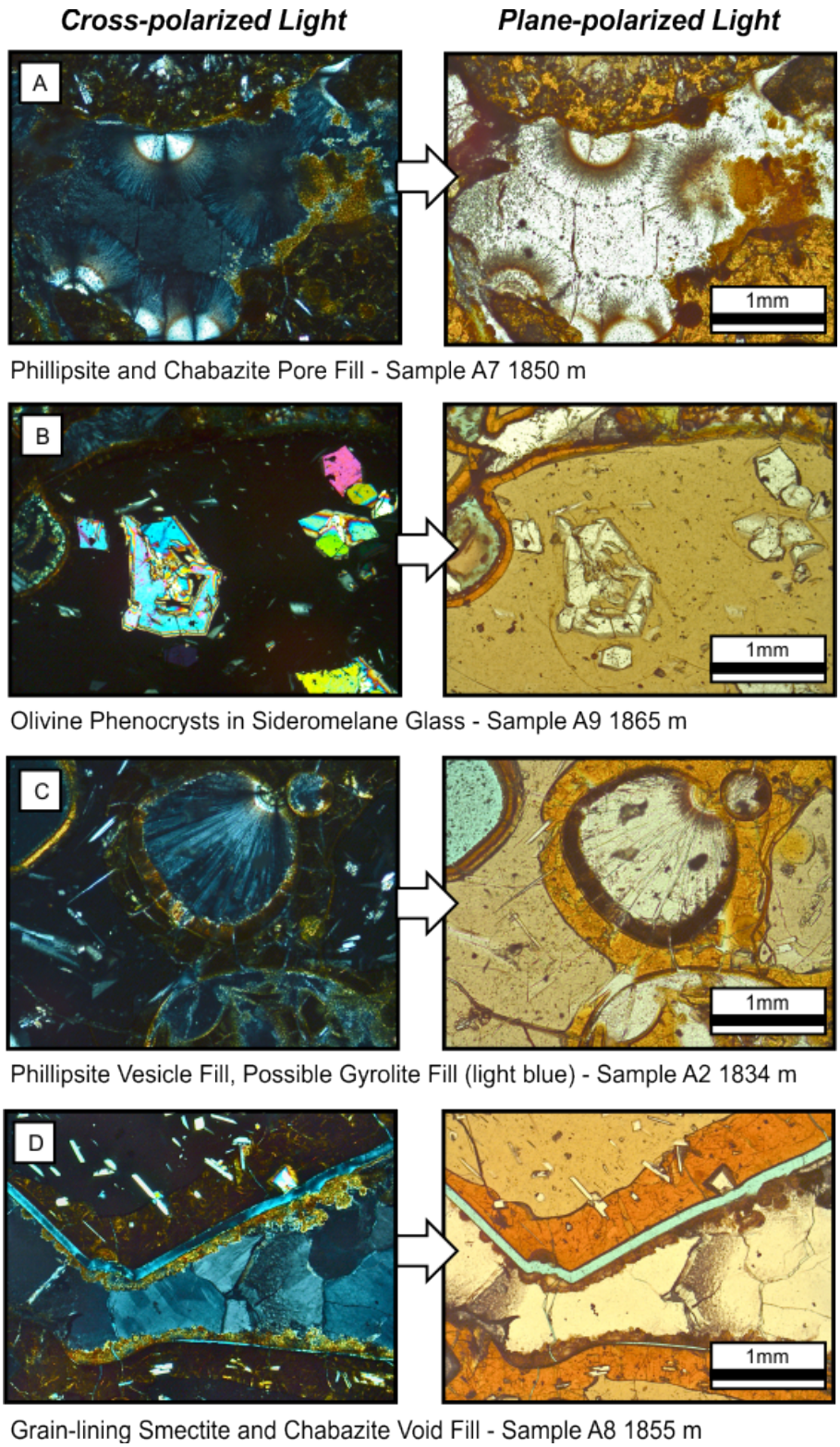

Figure. 6.37 . Photomicrographs of key pore-filling cements in hyaloclastite units from HSDP phase II. A) Phillipsite radial crystal growths and chabazite more massive within a void space between sideromelane glass grains altered to palagonite (brown). B) Olivine phenocrysts in sideromelane glass grains in the olivine-phyric breccia zone. C) Radial phillipsite growths in

vesicles in sideromelane glass grains. D) Grain lining smectite (darkest brown) with chabazite fracture fill between grains.

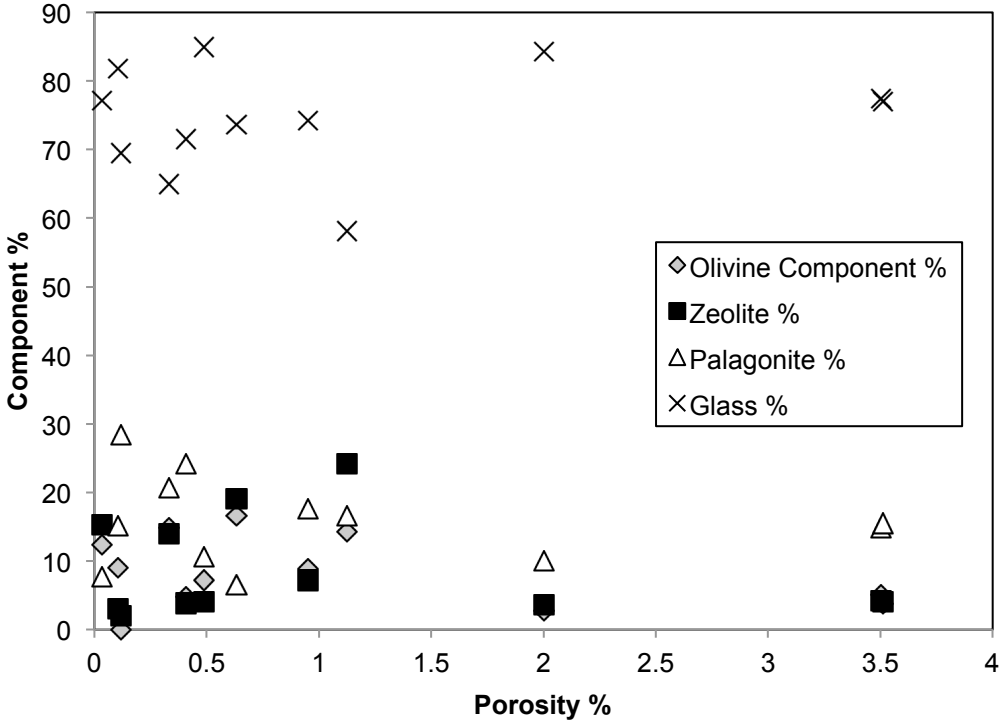

Figure 6.38. Component percentage of section A sample plotted against porosity. There is no correlation between the amount of any one component and the porosity of the sample. (Data in the appendix for this chapter).

6.6.4 Mineralogical Response (GR and Deep_RES)

Observations - In both logs there are stepwise changes in the GR and RES log responses. Cross-plotting these parameters for the hyaloclastite intervals reveals groupings between common interstitial (phillipsite and chabazite) and bulk (olivine phenocryst) components (Fig. 6.39). Phillipsite and chabazite are low temperature zeolites formed from hydrothermal circulation and from shallow burial diagenesis (c. 60–80^{o}C; Jørgensen, 2005). Olivine phenocryst-rich layers have lower GR values. The separation of zeolites is based upon Deep RES values that reflect variations in porosity between phillipsite- and chabazite-dominated void spaces. The clast-free fine-grained hyaloclastite sandstone intervals show large variations in both GR and RES values.

Interpretation - Thin section observations indicate the increased component of phillipsite in the phillipsite zone leads to a decrease in RES values in well logs. Image analysis of thin sections reveals higher porosities in the phillipsite zones than in other zeolite zones, which may account for a decrease in RES values. Image analysis also shows the dominant phenocryst phase can reduce the GR response. Higher percentages of mafic minerals in a sample (in this case olivine phenocyrsts) correspond to lower GR values. Large point clouds occur in the fine-grained interval arrays due to changes in dominant phenocryst or zeolite abundance. However sampling density was not high enough to sufficiently characterise the phenocryst component of these fine-grained groupings. Down hole variation in type of abundant zeolite occurs due to the fluid mobility of zeolite forming ions released in the palagonite forming process (see chapter 2).

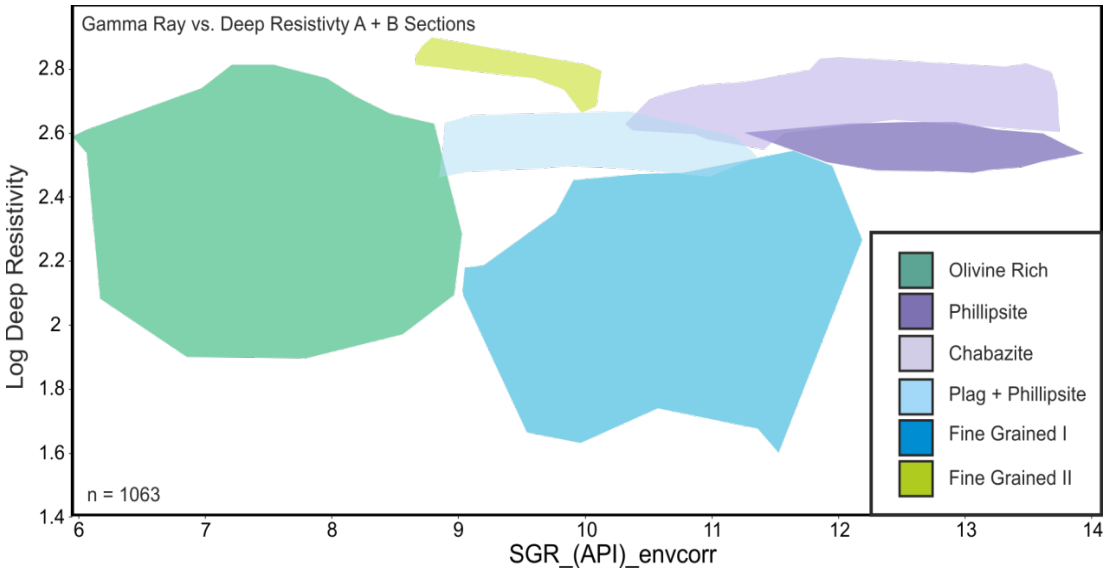

Figure. 6.39. GR responses in both A and B sections with mineral separation from thin section and EDX analysis.

6.6.5 Velocity (Vp) Response

Observations – A long-wave down-interval increase in p-wave velocity (Vp) from ~5.1–5.5 km/s is observed in both log sections. In section A, two zones are recognised: an olivine-rich zone (below 1851.2 m) and an olivine-poor zone (above). These variations do not reflect dominant matrix- or clast-supported breccia intervals. A Vp histogram shows the variation in mean p-sonic values (Fig. 6.40). A

Kolmogorov-Smirnov test suggests that the likelihood that the data sets are the same is $p = 1.275e^{-44}$. This very low probability suggests that both populations are unique. It is important to note that this is a worst-case scenario because the olivine-rich zone has thin hyaloclastite sandstone interlayers, which are olivine-poor—this skews the data to negative values creating accessory peaks at 5.1 km/s. There is a general increase of Vp with increasing modal olivine percentage, however this is only true at higher olivine concentrations (Fig. 6.40 lower).

Interpretation – Long-wave variations in Vp response generally correspond increases in olivine phenocryst abundance in the hyaloclastite matrix (see Fig. 6.36b). Olivine has a higher density (3.25 g/cm^3) than average basalt (~3.0 3.25 g/cm^3) or sideromelane glass (2.1 g/cm^3; Stronick and Schimincke, 2002). Greater abundances of olivine result in increases in Vp propagation. These olivine/Vp relationships are at smaller scales than sampled by previous density studies and have not been noted before.

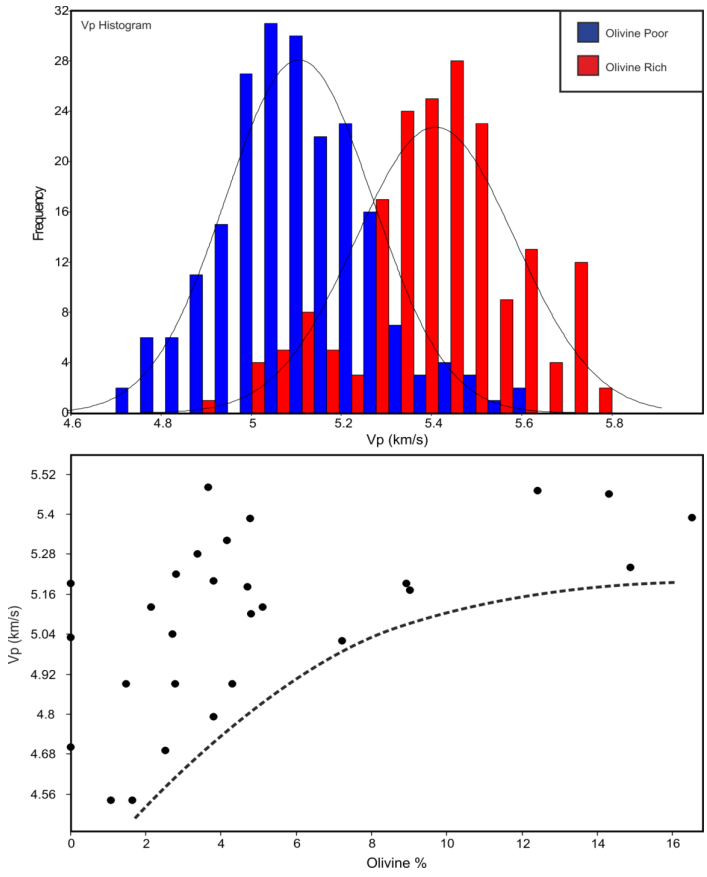

Figure. 6.40. A histogram of section A Vp responses. The bimodal peak reflects the presence or absence of olivine. In the olivine-rich array there is a small peak skewed to lower (olivine-poor) values. This represents the presence of olivine-poor interbeds within the olivine-rich zone. Below, Vp vs. Olivine % from thin section image analysis. At low olivine percentages there is no correlation to Vp. At higher values a poor positive correlation can be realized.

6.6.6 Spectral Gamma Ray Response (Secondary Mineralisation)

Observations - EDX analyses and optical petrography show that four main interstitial minerals are present in the hyaloclastite sections (Fig. 6.37 and Fig. 6.41). These are chabazite, phillipsite, hydroxi-apatite and calcite (calcite is only observed as a late stage residual pore fill in SEM backscatter images, Fig. 6.42). Detailed examination of the textures of these minerals is considered in section 6.6.8. Both chabazite and phillipsite have similar EDX responses although phillipsite contains more wt % potassium. They are easily distinguished optically—chabazite is more massive and has high-relief random fractures whereas phillipsite exhibits radial growth forms (Fig. 8A, C, D). Dendritic hydroxi-apatite (phosphorous-rich) growths are commonly associated with the chabazite zones. Late-stage calcite fills are present but are very rare (only visible in SEM images).

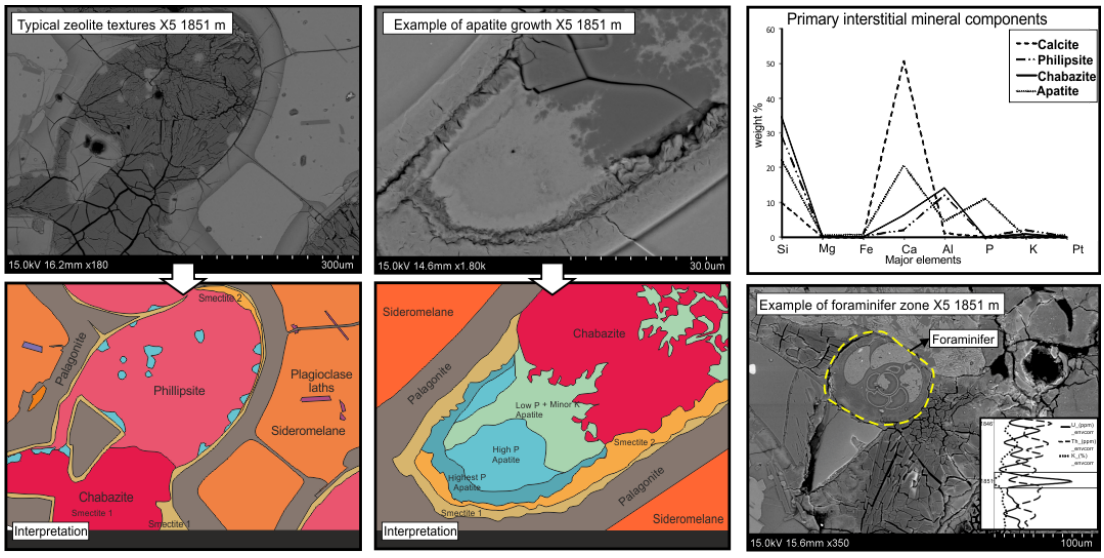

Figure. 6.41. Electron backscatter (YAGBSE) images of interstitial minerals show differences between chabazite (massive with fracture), phillipsite (radial crystals) and phosphourous-rich apatite minerals (light white, branching forms). A YAGBSE image of sample X5 reveals a foraminifera fossil leaching phosphorous to the HSDP zeolites. The occurrence of foraminifera coincides with increases hydroxi-apatite growth and uranium spectral gamma ray log spikes.

Spot EDX weight and mole percentage values can be plotted for common elements in phosphate –enriched suspected hydro-apatite zones (fig. 6.42 a, b c). There is a linear increase in both the mole and weight percentage of Ca/P for all suspected hydroxi-apatite samples. Hydro-apatite can form via bioclast replacement (Baker et al., 1998). In the HSDP II logged sections (A and B) foraminifera are found within the fine grained hyaloclastite horizons associated with hydroxi-apatite growth. Foraminifera test and carapace values for Ca and P are low however P is still present suggesting P has been leached after bioclast replacement has occurred (Fig. 6.42 a). In figure 36 the highest concentration of P occurs at the rim with the alteration front pervasive through the sample gradually replacing the chabazite structure (Fig. 6.41). Therefore the gradient of the mole concentration linear trend characterises the alteration from chabazite to hydroxi-apatite. Therefore at a set P value e.g. 0.2. Ca values equal 0.3. Then the calculated gradient of c. 0.6 suggests for every 10 Ca molecules there are 6 P molecules, so given the common hydroxi-apatite structure ($C_{10}(PO_4)_6(OH)_2$) this suggests that the P-enriched zone are in fact hydroxi-apatite.

Other P relationships are not as clear. Both Fe and Al are reduced with increases P that suggests a replacement process. Two trends exist in each of the data sets, for Fe there is a low wt % trend from foraminifera carapaces and a high wt % trend from foraminifera tests (Fig. 6.42b). This may suggest differential rates of replacement to P rich hydroxi-apatite depending on the type of bioclast undergoing replacement. The Al trend reflects either a replacement in the original foraminifera bioclast or subsequent alteration of the chabazite structure (removing Al). This gives rise to two trends, a rapid decrease in Al, which is removed from the chabazite structure and a constant low Al value, which is already low in the foraminifera test. Both of these trends are also reflected in the mole % of each sample (6.42c).

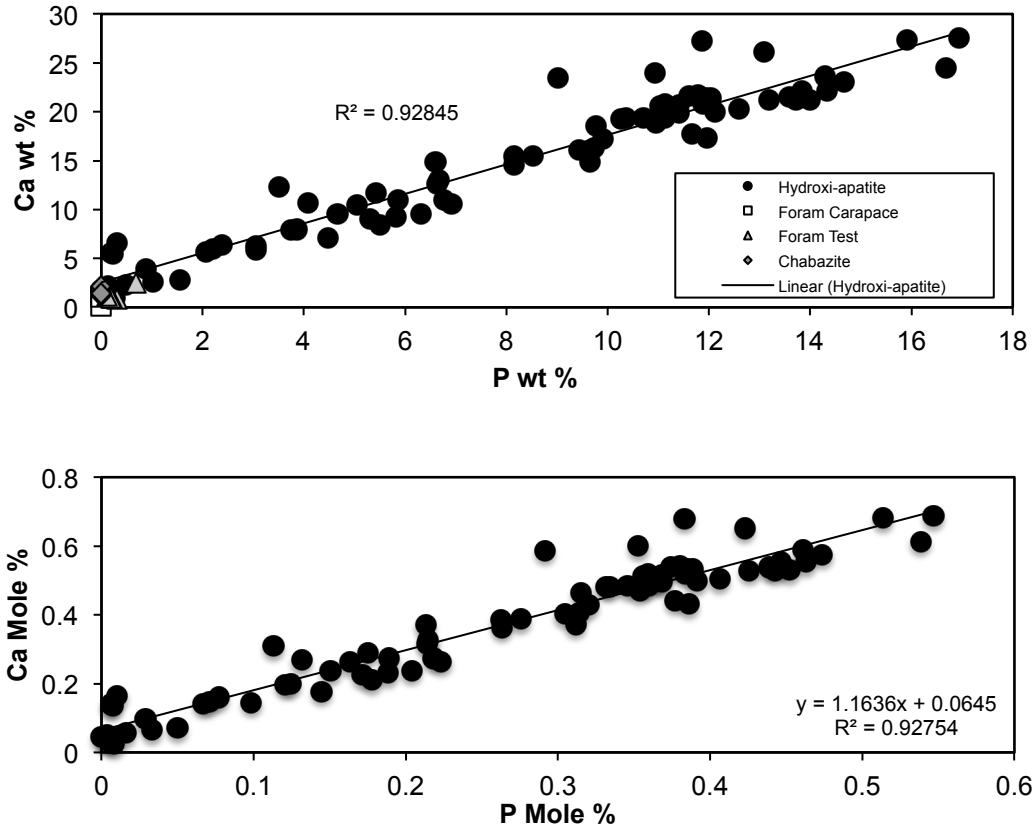

Figure 6.42 a. Ca wt. and Mole % vs. P wt. and Mole % for suspected hydroxi-apatite samples. A good linear trend is observed in both cases which indicates the formation of Ca and P are mutually beneficial and the gradient of the line suggesting hydro-apatite growth. See text for details.

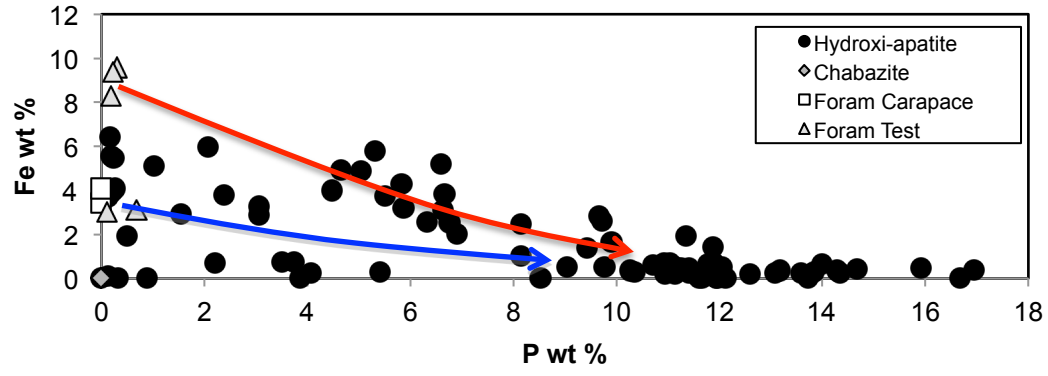

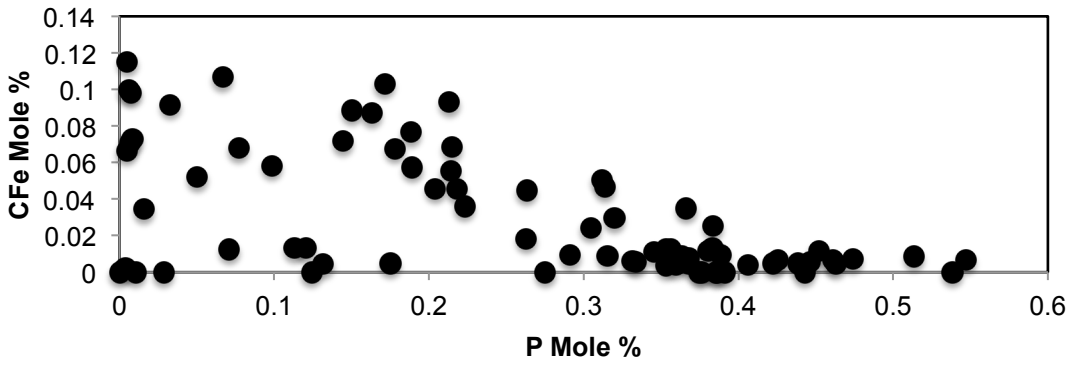

Figure 6.42 b. Fe wt. and Mole % vs. P wt. and Mole % for suspected hydroxi-apatite samples. Two trends are observed one from high Fe values reflecting chabazite replacement and one from low Fe values reflecting bioclast replacement.

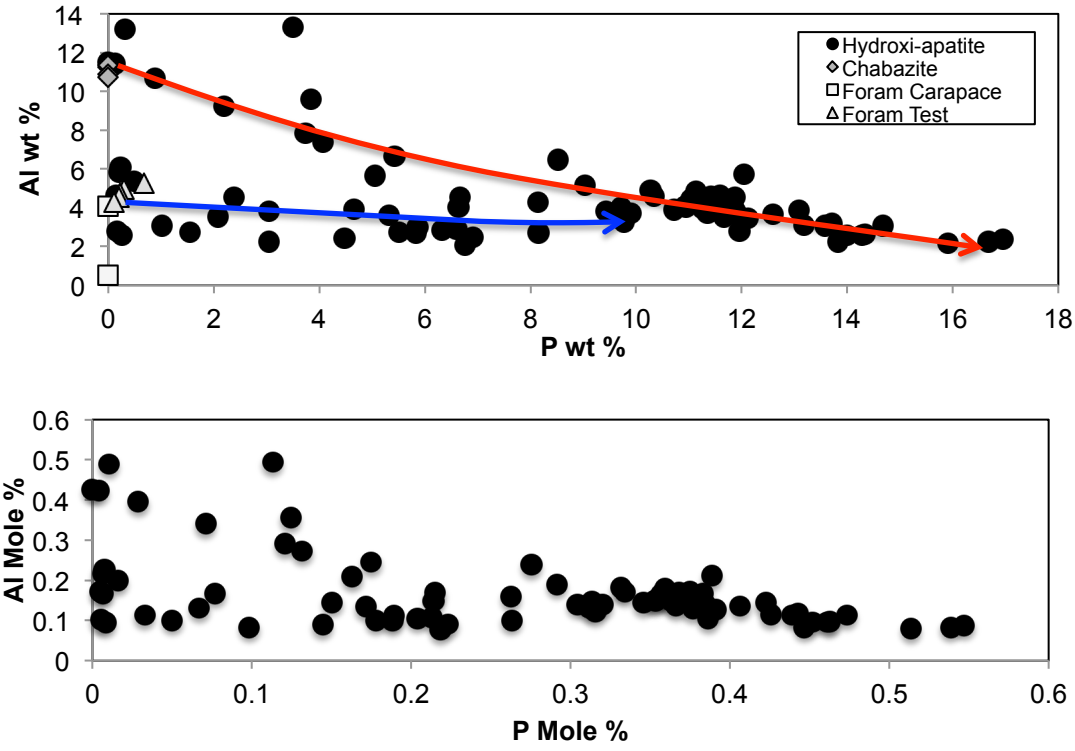

Figure 6.42 c. Al wt. and Mole % vs. P wt. and Mole % for suspected hydroxi-apatite samples. A good linear trend is observed in both cases. Two trend are seen one from Chabazite samples loosing Al and one constant value from bioclasts which had already low Al.

Interpretation - Chabazite and phillipsite are common pore-filling and pore-lining zeolites in hyaloclastite deposits. Hydroxi-apatite growth can occur when phosphorous is added to the zeolite ring structure (Karapinar, 2009). Hydroxi-apatite

can occur as a common grain coating from bioclast replacement (Baker et al., 1998). In the HSDP Phase II core, fragments of foraminifera skeletons (bioclasts) have been replaced by hydroxi-apatite in void-filling zeolites (recognized by light spots in electron backscatter images)**.** This allows the recognition of alteration trends, which reflect the replacement of bioclast components or chabazite. Phosphate minerals preferentially absorb radioactive elements, which could result in uranium spikes on spectral gamma ray logs. Where foraminifer bioclasts occur in abundance uranium log spikes are recorded (e.g. Fig. 6.41. Sample X5). Future work could micro sample hydroxi-apatite alteration fronts to test for Uranium.

6.6.7 Diagenetic Summary - Microtextures in HSDP II Thin sections

Although the main objective of the this chapter was to enable better characterisation of hyaloclastite deposit in wire-line logs and not assess the diagenesis of the HSDP II core, due to the numerous sites analysed several new observations can be made. For our sections a purely relative step-by-step diagenetic history can then be built which summarizes our observations (Fig. 6.43). This section then characterizes the variation in diagenesis in our hyaloclastite deposits providing SEM photomicrographs for each (further examples of each stage and additional EDX geochemical analysis are provided in the appendix for this chapter in folders for each studied section). A detailed of assessment of the initial diagenesis processes especially the palagonite and smectite forming processes (Stage A) within the entire HSDP II core has already been conducted by Walton and Schiffman, (2003) and Walton et al., (2005). Therefore presented here is only a summary of the SEM textures specifically referring to zeolite growth and replacement with hydroxi-apatite (see section 6.6.7). HSDP II samples in this study can be divided into four main stages with observations from stages B, C and D are provided here as zeolite type and replacements control the overall GR response of a hyaloclastite unit. Each image corresponds to a section (A or B (B = C)) and site, which contains supporting EDX data and can be found in the appendix.

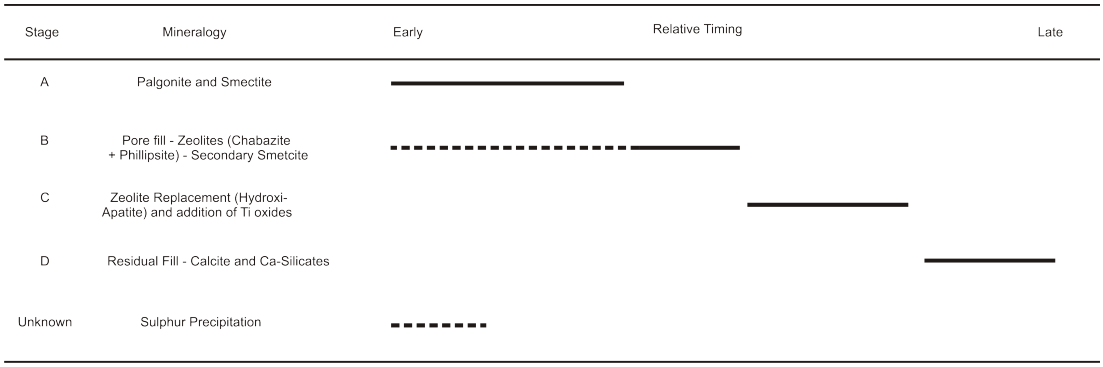

Figure. 6.43. Relative timing of diagenesis and key mineralogy involved in each stage. The actual timescale of diagenesis in hyaloclastite systems is relative rapid (see chapter 3).

Stage B – Pore fill – Zeolites – Secondary Smectite

The identification of zeolites in the HSDP II core is covered in section 6.62 and 6.6.7. There are two main textures, pore filling where zeolites occur where philipsite and chabazite growth together to infill void spaces left by interlocking sideromelane grains (Fig. 6.44) and vesicle filling zeolites which occur within bubbles in sideromelane glass (Fig. 6.45). Usually radial philipsite crystals nucleate at the margins to the void space. Chabazite infills the residual cavity. Figure 6.44 also shows sideromelane (lightest grey) with lath shaped plagioclase phenocrysts trapped in the glass. Palagonite surrounds each glass grain with a thin veneer of smectite (which produces and irregular margin) before either philipsite or chabazite occur. The second type of zeolite growth occurs in vesicles within sideromelane grains. The growths are often circular and almost entirely composed of phillipsite (Fig. 6.45). The formation of chabazite and philipsite is thought to occur at temperatures between 50-100 ^{o}C (Jørgensen, 2006). Walton et al., (2005) suggested that during the palagonite process chabazite is formed at the same time, however it is also fluid mobile allowing to migrate through the pore network before precipitation and hence occurs a different concentrations along the core.

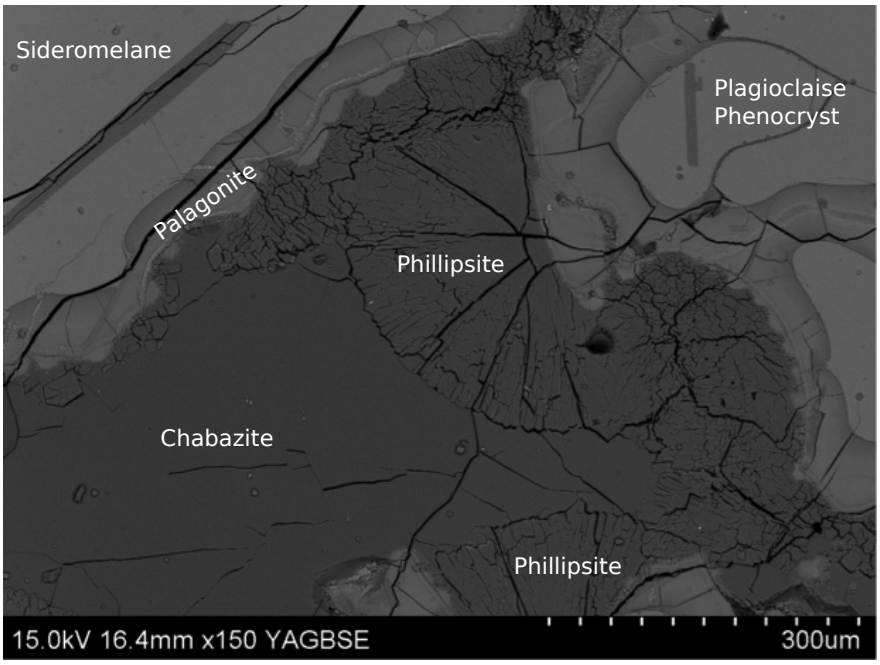

Figure. 6.44. C1 site 4. x150 mag. YAGBSE (Backscatter) image showing differences between chabazite (massive with occasional fracture) and philipsite (radial growths). See text for additional details.

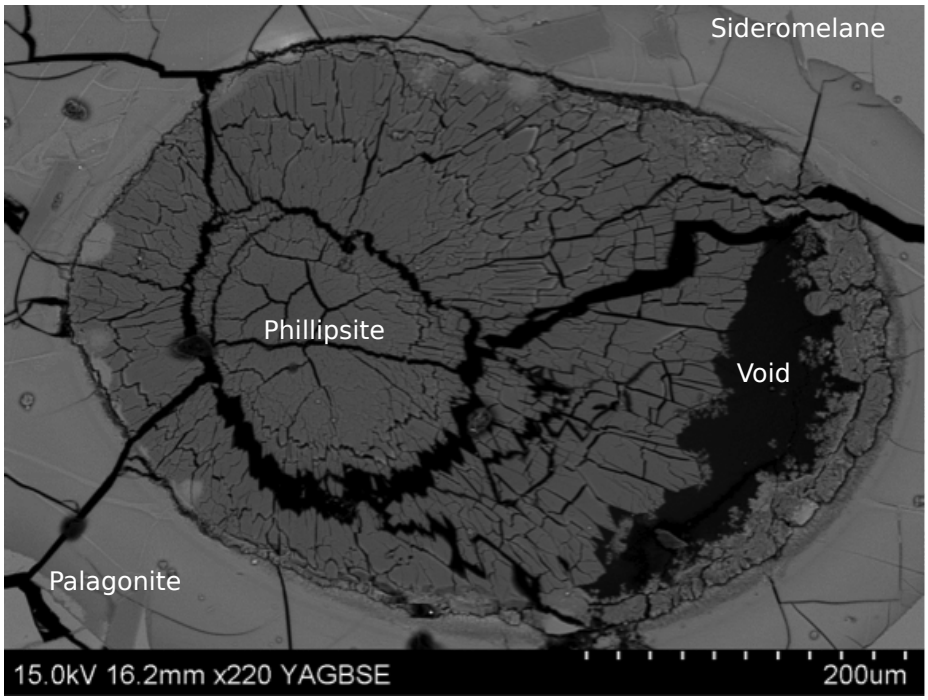

Figure. 6.45. C1 site 1. x220 mag. YAGBSE (Backscatter) image showing Philipsite vesicle fill in glass shard (fractured from sectioning process)

Stage C – Zeolite Replacement

Replacement of zeolite for phosphor rich hydroxi-apatite occurs in proximity to foraminifera tests. At 800 times magnification it is possible resolve the textures between apatite (lightest colour) and chabazite (darkest colour) (Fig. 6.46). Figure 6.35 showed a gradual increase in phosphorus away from the margin if a void. At this resolution dendritic "fingers" of hydroxi-apatite spread into the sample and then join. This produces small "transitional" (share EDX characteristics of chabazite and hydroxi-apatite) blobs with irregular margins, which form the Al and Fe trends in figures 6.42 b and c. The alteration front in all samples does not follow a fracture plane in the chabazite structure. Ti-oxides were not observed in this study although are a common accessory mineral which occurs with zeolites (Walton and Schiffman 2003).

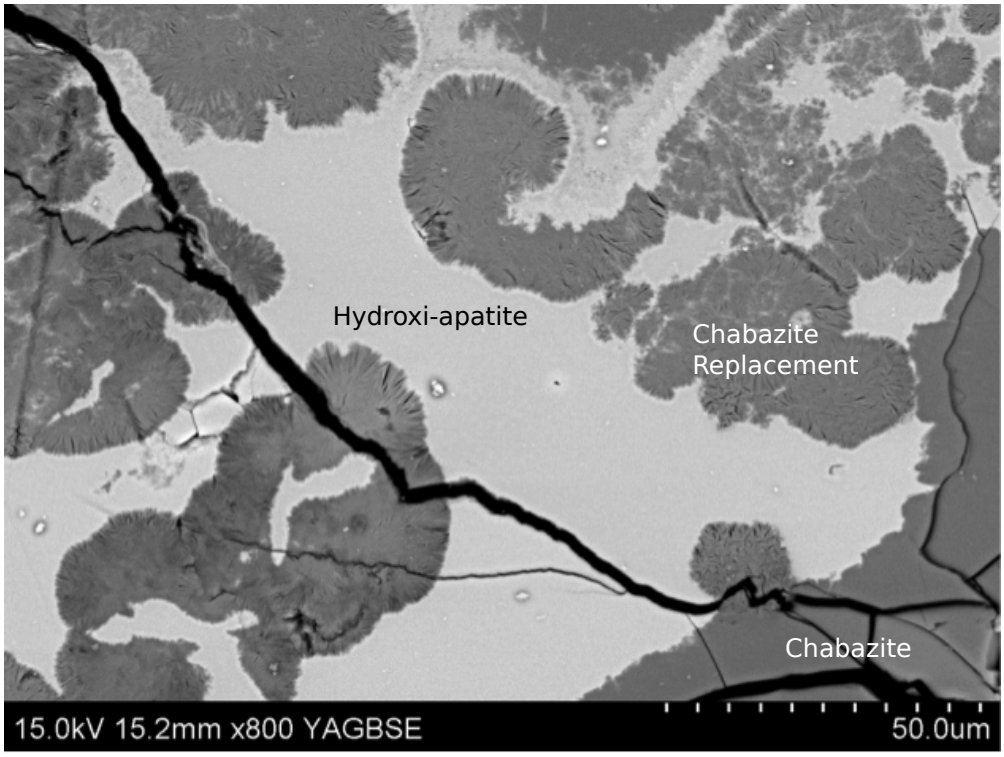

Figure. 6.46. C7 site 5a –x800 mag. YAGBSE (Backscatter) image showing a highly magnified image of phosphor rich hydroxi-apatite intergrowths (white). Residual chabazite enclosed as darker blobs.

Stage D – Residual Fill – Calcite and Phylosilicates

Occurring in vesicle alongside philipsite are unknown Ca-silicate minerals. They appear as concentric multi-component fragments usually in the centre of the vesicle surrounded by crystalline phillipsite (Fig. 6.47). Some of these Ca-Si rich fragments have been identified as gyrolite (Walton and Schiffman, 2003). Gyrolite is an uncommon phylosilicate, which dominantly occurs in vesicles in basalt volcanic glass (Merlino, 1988). This study does not challenge this interpretation.

This study has also revealed a previously unrecognised later stage calcite stage. Calcite forms as a thin pore lining film of small cubic crystals (Fig. 6.48). The precipitation of calcite always occurs in pore spaces where there is still porosity (black) present, which suggests that it was a late stage to precipitate.

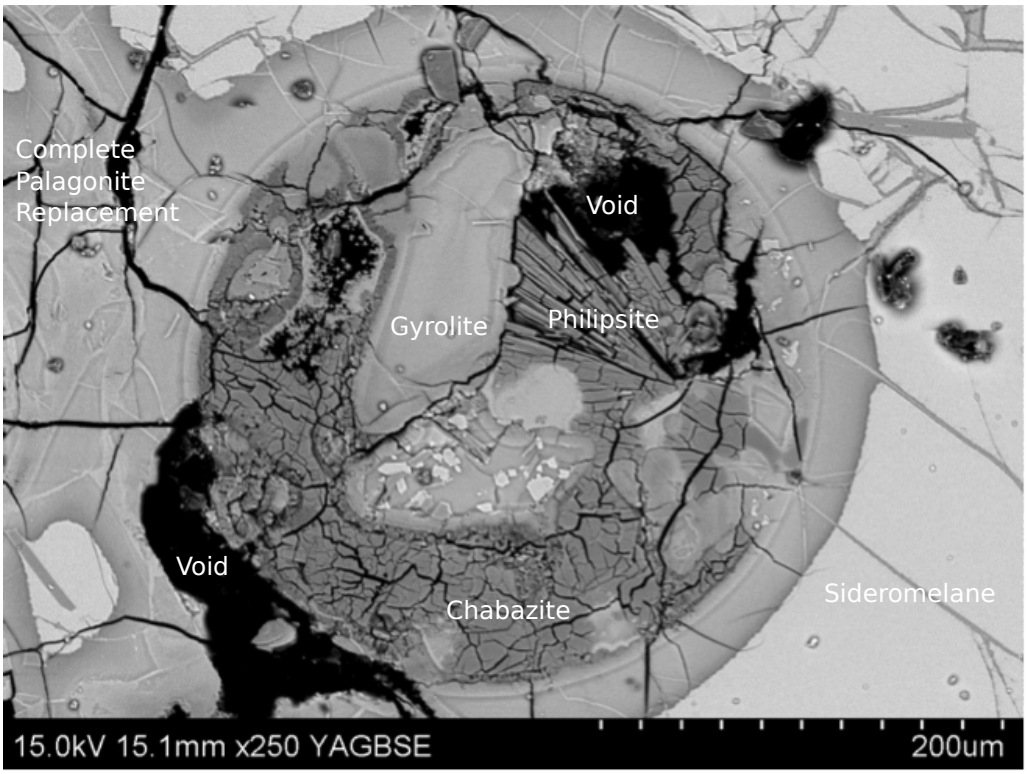

Figure. 6.47. C2 site 4. x250 mag. YAGBSE (Backscatter) image of Gyrolite and other minerals in vesicles

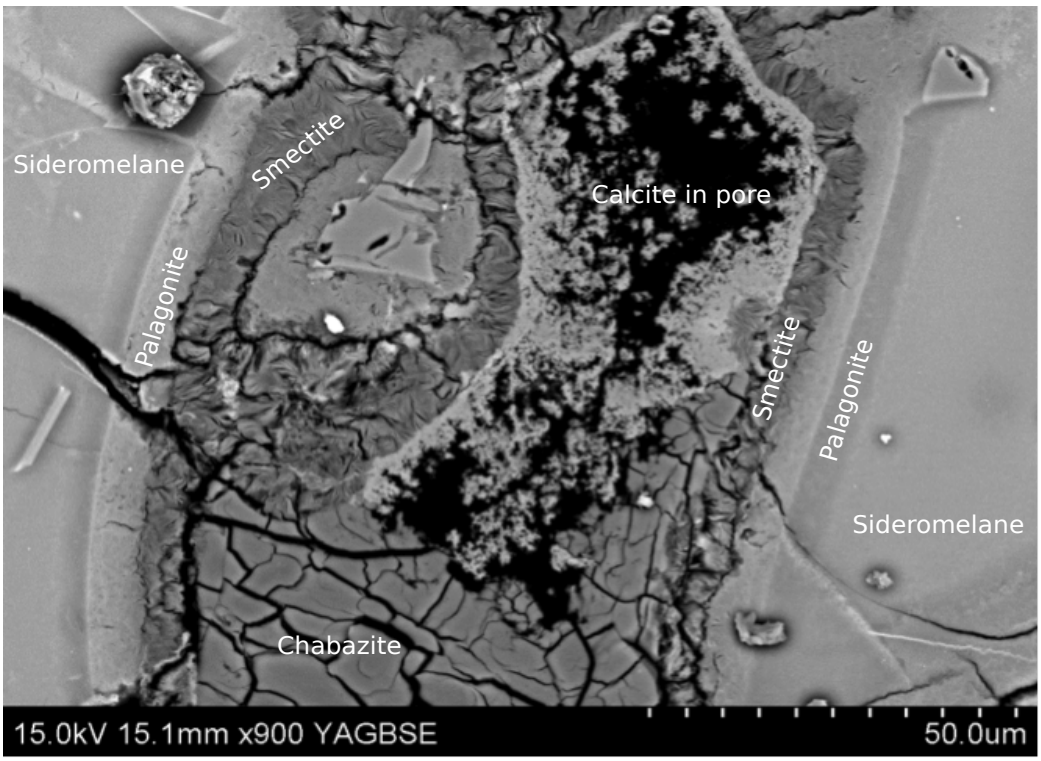

Figure. 6.48. C2 site 4b x 900 mag. YAGBSE (Backscatter) image of late stage calcite pore fill in residual void space.

Stage Unknown – Sulphide precipitation (probably early)

Some vesicles, which are filled, in this case with clay (probably smectite) are surrounded by sulphur rich inclusions (Fig. 6.49). Sulphide growths on the margins of vesicles have been recognised in previous studies of submarine volcanic glass from Hawaii (e.g. Davis and Clague, 2005). They are thought to occur due during degassing when sulphur interacts with Fe in the glass.

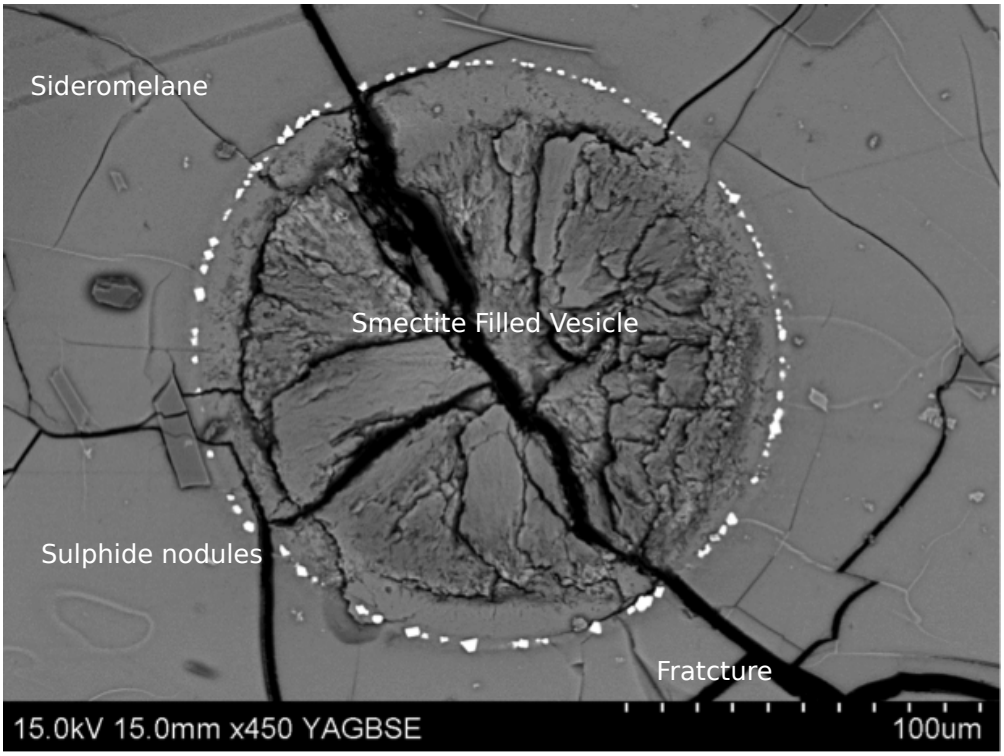

Figure. 6.49. C10 site 5 x 450 mag. YAGBSE (Backscatter) image of sulphide crystals surrounds to clay filled vesicle probably and early stage quench feature.

6.7 Conclusions

The implications of this chapter are discussed in chapter 8 where these results are combined with field data to assess hyaloclastite deposits more fully. From the observations and interpretations presented in the preceding sections a number of conclusion can be made about hyaloclastite deposits in well logs:

- Modelling of hyaloclastite deposits is difficult due to diagenetic processes and lithofacies variation. Certain hyaloclastite lithofacies share similarities in rock properties to either carbonate or siliciclastic rocks, therefore accurate lithofacies characterisation is needed before modelling can be used. However generally hyaloclastite deposits lie on their own trend that is independent of existing models.

- Characterisation of the Vp for each lithofacies has shown that a simple 1D depth conversion of a 0.5 s hyaloclastite pile can yield up to 200 m variation

with could significantly affect basin reconstruction (e.g. base basalt estimation, an important target for drilling considerations).

- The density of hyaloclastite deposits is likely to remain constant with increasing velocity due to pore-space replacement with palagonite, which in part explains why modelling, is difficult. Calculation of acoustic impedance and reflection coefficients mean that fine-grained hyaloclastite deposits can produce a seismic reflector. This is not predicted if modelled values are used.

- Hyaloclastite deposits have high Vp/Vs separation similar to carbonate rocks. This is in part due to the texture of hyaloclastite deposits that resist compaction forming a basalt framework leading to high Vp but hydrous clay surrounding many grains leading to limited transmission on shear stress and hence lower Vs.

- Porosity modelling indicates that pore spaces are rapidly shut off once hyaloclastite deposits are in the palagonite zone. However before entering the palagonite zone hyaloclastite deposits are likely to resist compaction due to high coordination numbers in particles and basalt clasts supporting the structure.

- The dominant interstitial secondary minerals and phenocryst components (in this case olivine). P-wave velocity is closely linked to olivine phenocryst abundance within hyaloclastite. This produces a significant variation in Vp response (c. 0.3 km/s).

- Zeolite components control the remaining overall porosity of the sample once the palagonite process has finished and thus the RES values.

- Early precipitation of carbonates/zeolites into the pore space can arrest the formation or palagonite and produce enhanced porosity with depth if subsequently dissolved by later fluids.

- The chemical structure and properties of zeolite minerals the leaching of phosphorus from dead marine micro-organisms can lead to hydroxi-apatite growth. These intervals are visible as spikes in the uranium log.

- On seismic scales the variation in hyaloclastite deposits is generally not resolved (chapter 4), though reflector images of prograding foresets can be resolved. This study suggests that reflectors can be either caused by fine-coarse grained hyaloclastite couplets or pillow lava. This point is expanded on in the discussion chapter (8).

d5

7

7. USING FORMATION MICRO IMAGING (FMI), WIRELINE LOGS AND ONSHORE ANALOGUES TO DISTINGUISH VOLCANIC LITHOFACIES IN BOREHOLES 265

CHAPTER FIGURES AND TABLES

7. Using Formation Micro imaging (FMI), Wireline Logs and onshore Analogues to Distinguish Volcanic Lithofacies in Boreholes

Chapter Summary

Formation Micro Imaging (FMI) is a tool that produces micro resistivity images of the sidewall of the well bore. FMI logging used in conjunction with conventional well logging techniques (e.g. GR/RES/DEN/NPHI/SONIC tools) allows unrivalled analysis of volcanic lithofacies variation and allows a robust interpretation of volcanic sequences. This methodology is of particular use where rock core data is limited or not present. Examples are presented from the Rosebank Field in the Faroe-Shetland Basin (FSB, West of Shetland, UKCS) where the re-establishment of fluvial activity between phases of effusive volcanism resulted in a complex sequence of siliciclastic sedimentary rocks and basaltic lavas. We demonstrate how high-resolution FMI images through this sequence can differentiate internal basalt lava flow features, such as vesicular zones, brecciated horizons, sediment-lava contact relationships and joint/fracture networks. If FMI data exists through volcanic packages and if assessed and calibrated properly via core, side-wall core and field analogue comparisons, it can provide additional constraints on the interpretation and classification of reservoir (siliciclastic) and non-reservoir (volcanic) rocks.

7.1 Introduction

Volcanic and igneous rocks occur in many hydrocarbon-bearing sedimentary basins worldwide and pose considerable challenges in the identification and assessment of potential hydrocarbon reserves. They can reach kilometres in thickness and can overlie and mask potential reservoirs (the 'sub-basalt' problem, e.g. White et al.,, 2003; Changzhi et al.,, 2006). Volcanic rocks can be intimately interlayered with siliciclastic reservoir rocks (e.g. the Rosebank discovery, Helland-Hansen et al., 2009), which complicates the construction of accurate reservoir models Successful petroleum exploration in such settings requires a comprehensive understanding of the

emplacement mechanisms, geometries, geophysical and petrophysical properties of the volcanic and igneous components.

The petrophysical responses of volcanic rocks encountered in boreholes have received little attention in the past—most research has been undertaken by the International Ocean Drilling Project (IODP, Planke, 1994; Delius et al., 1995; Delius et al., 1998; Bücker et al., 1998; Planke and Cambray, 1998; Brewer et al., 1999; Delius et al., 2003; Bartetzko et al., 2005). In the FSB, well log identification of volcanic deposits has evolved significantly since the completion of the LOPRA-1/1A well (Faroes Islands, 1996). LOPRA-1/1A penetrated ~3.5 km of Palaeogene volcanic rock that also outcrops on the Faroe Islands (Heinesen et al., 2006). The lower 1.1 km of the borehole comprises the Lopra Formation, which consists of hyaloclastite, intrusive basaltic sills and volcaniclastic sandstones. The overlying 3.5 km thick Beinisvørð Formation is composed of laterally extensive basalt sheet lobes (see Passey and Jolley, 2009). Studies of the seismic attributes of the LOPRA-1/1A rocks have illustrated how internal lithological variations within lava flows have varying petrophysical properties (Christie et al., 2006; Boldreel, 2006; Andersen et al., 2009; Nelson et al., 2009). Studies elsewhere, for example in the Daqing oil field, China, have proved the effectiveness of using wire-line and Formation Micro Image (FMI) data for interpreting felsic volcanic rocks in boreholes (Dezhi et al., 1991; Ning et al., 2009; Wang et al., 2009). Other studies have shown how low-resolution data from Formation Micro Scanner (FMS) tools can be useful in interpreting mafic volcanic rocks (e.g. Delius et al., 1998; Brewer et al., 1999; Waagstein 2000).

Exploration in frontier volcanic margins settings is becoming more common, and some hydrocarbon fields in volcanic-affected basins are moving into development phases. Thus, there is a pressing need for new, updated methodologies for interpreting sub-surface data gathered on volcanic and igneous rocks. In this paper we examine the Palaeocene rocks of the Faroe-Shetland Basin (FSB, Faroe Islands and UKCS) that were laid down in a volcanic margin setting and are the subject of sustained petroleum exploration. They comprise a complex sequence of siliciclastic sedimentary rocks, volcaniclastic rocks (including hyaloclastite and pyroclastic rocks) and basaltic lava flows (e.g. Passey and Bell 2007; Jerram et al., 2009; Helland-Hansen et al., 2009) associated with the opening of the Atlantic Ocean. We present new high-resolution FMI image data for volcanic rocks encountered in

boreholes in the Rosebank field in the FSB. We first calibrate the FMI datasets against a number of other datasets and the then compare lithofacies recognised in the FMI dataset to surface outcrop examples in Iceland and Namibia. Our aim is to illustrate how volcanic lithofacies can be accurately recognised in FMI logs. We show how powerful FMI data can be for interpreting volcanic rocks when drill core is unavailable or when analyses of composite log data are ambiguous.

7.2 Uses of FMI^{TM} in downhole well analysis of volcanic rocks

The Formation Micro Imager^{TM} (FMI) is a qualitative, high-resolution, resistivity tool designed by Schlumberger, which produces comparative images of the side walls of a well bore (Ekstrom et al., 1987 and chapter 2). Its precursor tool, the Formation Micro Scanner (FMS), was used extensively by IODP scientists over the last 20 years for interpreting volcanic stratigraphy. The FMS tool had only 4 detector pads and a lower spatial resolution than FMI. Brewer et al., (1999) showed how FMS image log evaluation could lead to the recognition of different volcanic rocks where core recovery was poor. FMS images were subjected to detailed core-log integration in order to justify their effectiveness as a formation analysis tool.

The FMI tool obtains resistivity measurements from eight sensor pads placed upon four orthogonally positioned caliper arms that run along the borehole walls (Siddiqui et al., 2004). The data coverage is dependent on the pad spacing—typically 80–100 % of the hole is covered at resolutions of 5 mm or less. Processing of the FMI image yields a high-resolution vertical image of the borehole that is colour-coded for resistivity values. Static and dynamic images can be produced depending on methods used to average the downhole resistivity values—static images are produced for the entire well, whereas dynamic images are averaged every 2 m. FMI is commonly applied to the mapping of sedimentary lithofacies in boreholes (Ekstrom et al., 1987 and references therein), however, it has had only limited application to volcanic sequences (Wang et al., 2009; Ning et al., 2009). The high-resolution images obtained by FMI reveal previously unrecognised diagnostic volcanic features, such as clast sizes and shapes, contacts, fractures and vesicles, which can greatly improve the accuracy of volcanic lithofacies interpretation. We detail these features below.

7.3 Study Area and Stratigraphy

The Rosebank Field in the FSB is situated between the Faroe Islands and the Shetland Islands in the North Atlantic Ocean (Fig. 7. 7. 1) in licence blocks 205/1, 213/26 and 213/27. It lies above the Corona ridge—a broad, basement-controlled anticline. The Palaeogene volcanic rocks in this study were erupted in response to the break-up of the NE Atlantic and the development of the North Atlantic Igneous Province. The stratigraphy of the Rosebank field can be simplified into reservoir units (Colsay units—siliciclastic sandstones and mudstones) and non-reservoir units (lavas, volcaniclastic siltstone, breccias and sandstones, Fig. 7. 7.2). In this paper we focus on the volcanic non-reservoir units of the Rosebank Field with specific reference to well 213/27-2 that drilled through a significant thickness of volcaniclastic rocks that accumulated as an age equivalent to the uppermost Colsay unit.

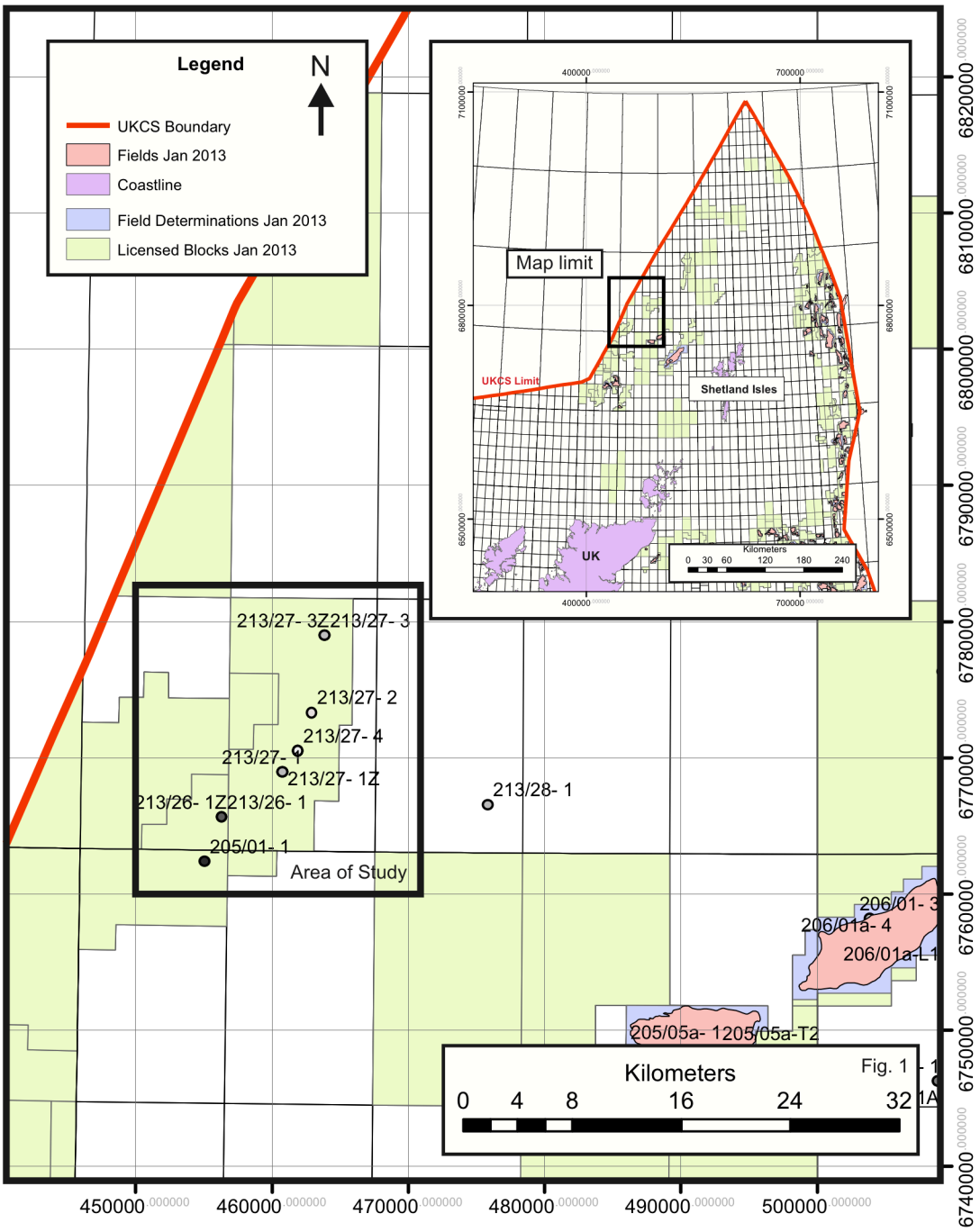

Figure 7. 1. Location of study areas and wells within the Faroe-Shetland Basin, UCKS. All data is in the public domain and was acquired from the UK Department of Energy and Climate Change (DECC) website. The Rosebank prospect is still not considered a field as of Jan 2013 by the UK government even though it is entering the development phase.

7.4 Methodology

Data has been taken from four wells (Fig. 7.2 and Table 7.1). The aim of this chapter, due to confidentially agreements, is to document the volcanic textures and methods of calibrating FMI data where extensive core is not present. As the data project is held within DONG Energy E and P, UK, Ltd. the appendix provides a correlation panel for wells interpreted in the project. Petrophysical identification of individual volcanic lithofacies was initially determined using composite well logs (Gamma Ray – GR - API, P-wave Velocity – Vp - ft/ms, Shear Wave Velocity – Vs - ft/ms, Density – Rhob_B - gm/cc, Resistivity - Ohms and Photoelectric effect – PEF - Barnes) based upon methodologies outlined by Planke, (1994), Brewer et al., (1999), Delius et al., (2003), Boldreel, (2006), Andersen et al., (2009) and Nelson et al., (2009). In order to validate the lithofacies interpretations, FMI log data was calibrated using proven techniques for the remote identification of volcanic rocks from rock core, sidewall core, Vp analysis and analogue examples. Table 7. 2 outlines the perceived usefulness and accuracy of these techniques. Where possible all techniques should be used in conjunction with interpreted wire-line log data to give the most accurate interpretation of available FMI data. FMI logs once calibrated were loaded into Petrel^{TM} and tied to the other well logs at known recovery depths. This allows a side-by-side comparison of well logs and FMI logs and the production of a revised stratigraphy (methodology is outlined in Fig. 7. 7. 3). The FMI tool was run in an 8.5 and 12.5-inch borehole diameters. All well log and FMI data was sourced from the Rosebank discovery and has been kindly supplied by the Rosebank partnership (Operator - Chevron North Sea Limited (U.K) Ltd., Statoil (U.K) Ltd., OMV (U.K) Ltd. and DONG (E and P, UK Ltd.).

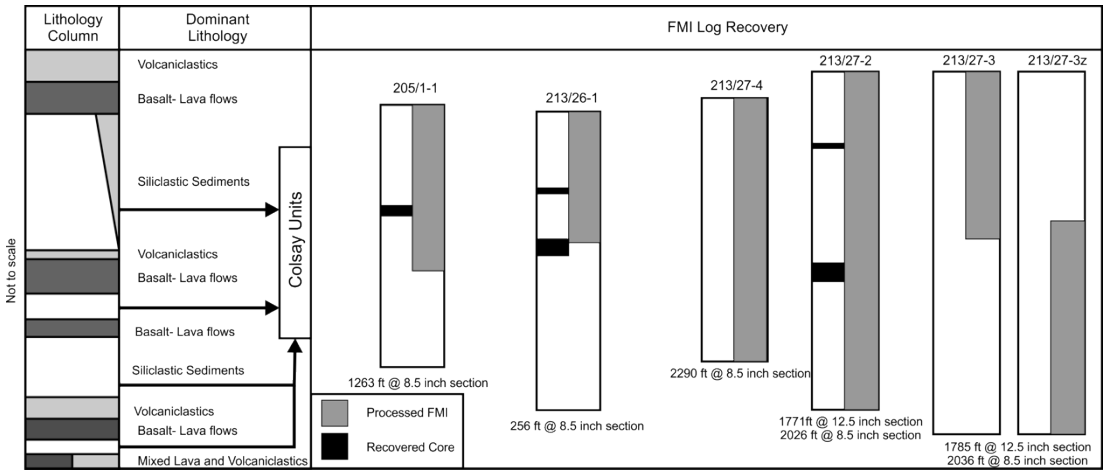

Figure 7. 2. A generalized stratigraphy for the Rosebank field comprising four siliciclastic packages and five volcanic packages. Processed FMI and Core recovery for each well is highlighted in the figure. The author only had access to well 213/27-4, 205/1-1, partial recovery of 213/27-2 (only uppermost Colsay unit provided c. 2760-2822 m MD) and 204/10-A-3 (which is an off structure well situated just south of the Rosebank field) and summarized in Table 7. 1. Therefore fully interpretation is only provided of three wells based upon FMI, 231/27-4 , 205/1-1 and 231/27-2. Image log of 213/26-1 contains no volcanic material. The lithology column, dark grey = dominantly volcaniclastic , darkest colours = dominantly volcanic, white = siliclastic modified from Helland-Hansen, 2009.

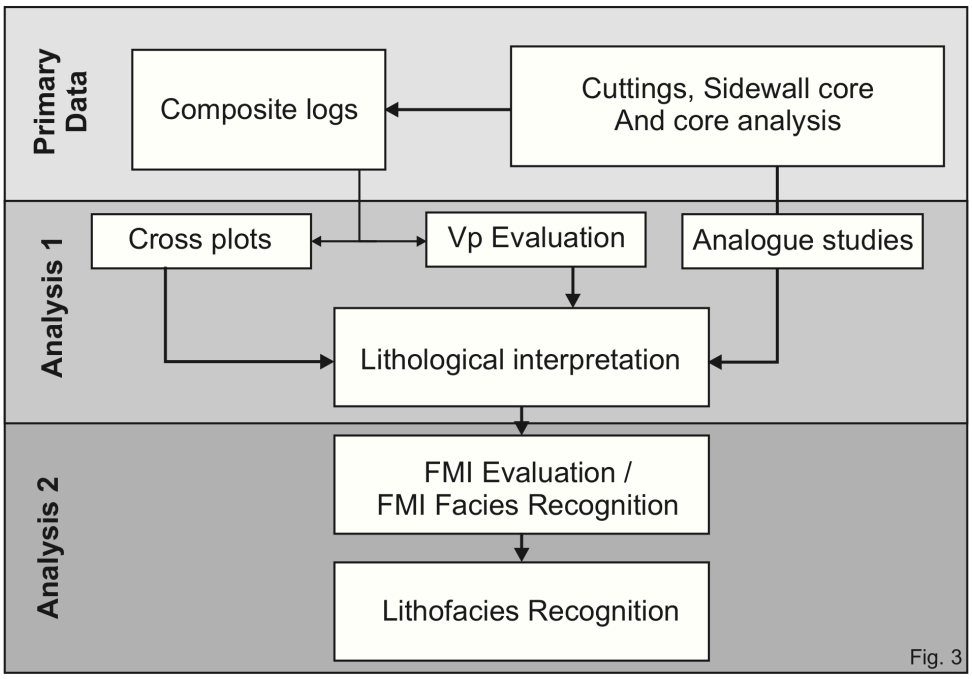

Figure 7. 3. A flow chart methodology of FMI-based log evaluation to determine volcanic lithofacies in the Rosebank field.

Table 7. 1

Well Header	Core Recovery (intervals)	FMI Total Recovery ft
213/27-2	2	206
213/27-4	0	2290
205/10A-3	0	185
205/1-1	1	1263

Table 7. 1. Well header and Recovered FMI log lengths and core for each well used in the study.

7.5 Well Top Determination in the Rosebank Fields

Well log data was used to create well tops of key time equivalent sequences within the Rosebank field to aid the determination of FMI logs (FMI logs are only sourced from the Rosebank field). Essentially detailed correlation of the stratigraphy is needed before any FMI analysis can be performed (a correlation panel is provided in the appendix for this chapter). All of the well tops have been created with reference to the biostratigraphic data available on the DONG internal database for the wells in Table 7. 2. Well top interpretation for the Rosebank field are provided in Table 7. 3. Data that has been FMI "enhanced" refers to well tops have been modified based upon FMI data where good data has been available. Data here provided accurate information for the determination of well tops in MD (measured depth) values.

Table 7.2

Well Header	Field
204/10A-3	N/A
205/01-1	Rosebank
213/23-1	Rosebank
213/26-1	Rosebank
213/27-1	Rosebank
213/27-2	Rosebank
213/27-3	Rosebank
213/27-4	Rosebank

Table 7. 2 Well used for Volcanic Correlation

Table 7. 3

Well top	Characteristic Log response	Example	FMI Enhanced
Top Colsay 0.5 /0.7	• Thin sand and shale units interbedded within the upper volcanic sequence • Display characteristic high gamma ray responses in contrast to the surrounding volcanic and volcaniclastic material • This is often accompanied by a decrease in the density log response	**213/26-1z** 2664.26m MD **213/27-2** 2757.42m MD	***No*** FMI recovered over this interval with the data available at DONG Energy at this current time
Top Rosebank Upper Basalts (UVS)	• Jump in both gamma-ray and resistivity values. Highest resistivity denote basalt core and columnar jointing • A sharp jump in neutron porosity values denotes the change to the uppermost volcaniclastic unit. This is due to formation bound water.	**213/27-2** 2660m MD	***Yes*** where parts of the Colsay 1 interval can be brecciated. This is not obvious in the log response
Colsay 1	• Very large drop off in density values from overlying basalts to 2.4g/cm^3 average. • Jump in the gamma ray response to >100 API. • Clear increase in permeability values and a drop in PEF/Den values to less than 1.5 barns/cm3	**205/01-1** 2869.69m MD	***Yes*** where parts of the Colsay 1 interval can be breccias. This is not obvious in the log response
Top Rosebank Middle Volcanics (MVS)	• Very high density contrast between Colsay 1 • Initial rapid decrease in P-sonic values • Both Neutron and gamma ray responses drop to low values • Clear increase in the PEF /Den values	**205/01-1** 2925.03m MD	***No*** the log response produces a very clear boundary.
Top Colsay 2	• Very drop off in density values from overlying basalts to 2.5g/cm^3 average. • Jump in the gamma ray response to >100 API. • Clear drop in PEF/Den values to less than 1.5 barns/cm3	**213/26-1** 2868.63m MD	***Yes*** in 205/01-1 where the flow base of the basalt is clearly visible in the FMI but absent in the well logs
Top lower Middle Volcanics (LVS)	• Not as distinct as top MVS as initially a volcaniclastic sequence in some wells • Identified best as a jump in resistivity from a generally low resistivity Colsay 2 unit • Drop in gamma ray values but not a significant as other volcanic units (still often >50 API) • Easily recognised as a jump in the PEF/Density to values over 5 barns/cm^3	**213/27-4** 3199.43m MD	**Yes** assessment of the FMI data has lead to an additional 6m in Colsay 2 213/27-4. Due to the log response and well defined bedding the boundary for this unit has been redefined
Top Colsay 3	• Base is potentially volcaniclastic hence best identified by a jump in the PEF/Den value from greater than 2 to less than 1.3 barns/cm^3 • P-sonic values jump to >100 ft/s^{-1} • Distinct increase in permeability and gamma ray values >100 API.	**213/27-4** 3007.64m MD	***Yes*** higher bedded resistivity values coupled with PEF/Den logs show that the base part of 213/27-4 Colsay 3 may be volcaniclastic
Top Lower Rosebank Volcanic	• A thick tabular flow often caps the sequence • Characteristic "half loaf" p-sonic log response. Classic positively skewed velocity histogram (Nelson *et al.,,* 2008)	**213/26-1** 2912.52m	***Yes*** distinct bedding in FMI would mean Colsay 3 is thicker in some cases as

Sequence	• Very High resistivity response accompanied by a very low gamma ray response in comparison to the overlying Colsay 3 interval • Where initially volcaniclastic distinct change in density over the boundary coupled with a distinct gamma ray drop. e.g. 213/27-4	MD	underlying basalts are easily recognisable this material is likely to be volcaniclastic due to its log response. However adds 2m to the Colsay 3 interval.
Top Colsay 4	• Identified in all wells except 205/01-1 • Distinct siliciclastic sequence with high gamma ray and neutron responses (unlike basalt) • Jump in PEF signature above Cretaceous • Noticeable drop in resistivity from overlying basaltic sequence	**27/26-1z** 3113.3m MD	***Yes*** in 213/27-4 small siliciclastic sand may be determined where previously overlooked. It may be part of Colsay 4 and occurs above the lower volcaniclastic unit
Top Lower Volcaniclastic	• Specific interval to 213/27-4, 213/27-2 and 213/27-3. Changes nature towards the North • Initially recognised by a jump in the neutron repose indicative of more formation bound water • Highly variable but averagely high p-sonic values >100 ft/s^{-1} suggest non sediment origin • Possible changes to volcaniclastic debris flows away from 213/27-4 with flow low gamma ray responses	**213/27-4** 3359.85m MD	***Yes*** very difficult to identify in well logs only apparent where FMI data was available in 213/27-4
Palaeocene Sequence	• Change in seismic response over this interval • Only identified by biostrat interpretation • Possible increase in Gamma and decrease in Neutron porosity however the change is less pronounced than the cretaceous interval	**213/27-3** 3132.52m MD	***No*** not seen in any well that FMI is currently available for
Top Cretaceous	• Jump in the Gamma ray response to average 130 from volcanic and Palaeocene • Decrease in Neutron Porosity to 0.24 compared to volcaniclastics	**213/27-2** 3074.60m MD	***Yes*** in 213/27-4 below volcanic breccia layer revised to 3434.19m MD

Table 7.3 Rosebank and Cambo Well Top Justifications

7.6 Methods of FMI Calibration

Calibration of FMI logs is essential for understanding the final processed image. Errors recorded from the FMI logs in the Rosebank field are minimal and are covered in chapter 2. Table 7. 4 summarized the usefulness and accuracy of different calibration techniques used within this project in order to justify FMI interpretation.

Table 7. 4.

Technique	***Usefulness***	***Accuracy***
Vp Comparison	The velocity histogram technique from Nelson et al., (2009) allows the calibration of the internal structure of lava flows to FMI images where core is not present. Can help aid the identification of lava breccia deposits in FMI logs due to their tightly distributed Vp values.	When FMI logs are compared to histogram distributions there is good correlation between observed Vp response and tabular vs. compound lava flows .
Core Analysis	The most direct and accurate comparison that allows direct lithological observations to be linked to FMI logs.	Usefulness is limited where core recovery is low or core is prohibitively expensive to acquire.

		Comparison of FMI log images to FMS logs from older studies (with extensive core recovery) yield more consistent results (cf. Brewer et al., 1999)
Sidewall Core / Cuttings	Sidewall core can aid identification of lithologcial changes observed in FMI logs. Cuttings aid the separation of silicilastic and volcaniclastic rocks which can have similar visual characteristics on FMI logs.	Sidewall cores provide a more cost effective solution than using rock core core data to aid FMI calibration; need closely spaced to capture changes in lithology. Cuttings greatly aid the interpretation of FMI log responses when accurate depths of recovery are recorded.
Field Based Acquisition	Field-based acquisition of well log responses such as spectral gamma ray can help accurate interpretation of traditional composite log data. FMI images can be more accurately compared to this data.	Field based acquisition is especially useful in aiding the interpretation of mixed silicilastic and volcaniclastic sequences where the understanding of composite log changes is limited.

Table 7.4. A summary of FMI calibration techniques used to validate volcanic lithofacies identification.

7.6.1 Recognition of Individual Lava Flows using Vp – P Wave Velocity Comparisons

The first stage in interpreting volcanic lithofacies in well logs is to distinguish lithological contacts and recognise individual lava flows. This can help determine if the lavas were emplaced in a subaerial or subaqueous environment and determine the morphology of the lava flows, e.g., whether tabular or compound/braided pāhoehoe lava flows (e.g. Jerram, 2002; Nelson et al., 2009). Morphologically, tabular pāhoehoe lava flows consist of individual sheet lobes that are up to 100 m thick and 10's to 100's of metres (> 1 km in some cases) in lateral extent (Walker, 1971). Compound braided pāhoehoe lava flows are typically much thinner (a few meters) and are composed of a series of thin stacked lobes, each up to several metres thick. Compound pāhoehoe lava flows are thought to represent small breakouts of lava either at the margin of a flow field or as volcanic activity wanes (Jerram, 2002). Both tabular and compound pāhoehoe lava flows are common in the FSB (Passey and Bell, 2007; Jerram et al., 2009).

Several studies have shown that Vp velocity profiles can be used to distinguish between different types of basaltic lava flow packages (Planke, 1994; Boldreel, 2006; Nelson et al., 2009). FMI data can also pick up important characteristics that are indicative of the different lava flow types. Figure 7. 4 shows two 20 m intervals that display characteristic Vp response profiles for tabular lavas and for compound braided lavas. Each histogram profile matches the Vp distribution models proposed by Nelson et al., (2009) and the FMI log interpretation matches the predicted Vp distributions. In FMI logs, tabular pāhoehoe lava flows are

characterized by a high conductivity and a clear differentiation between lava core, crust and base. In comparison, compound pāhoehoe lava flows exhibit a distinct bimodal resistivity response reflecting alternating core-crust relationships over much shorter intervals. This is a very useful technique for calibrating FMI images to lava flows where no core has been recovered and is a more accurate method for picking flow-on-flow contacts (as compared to using conventional wire line log data such as Vp or GR).

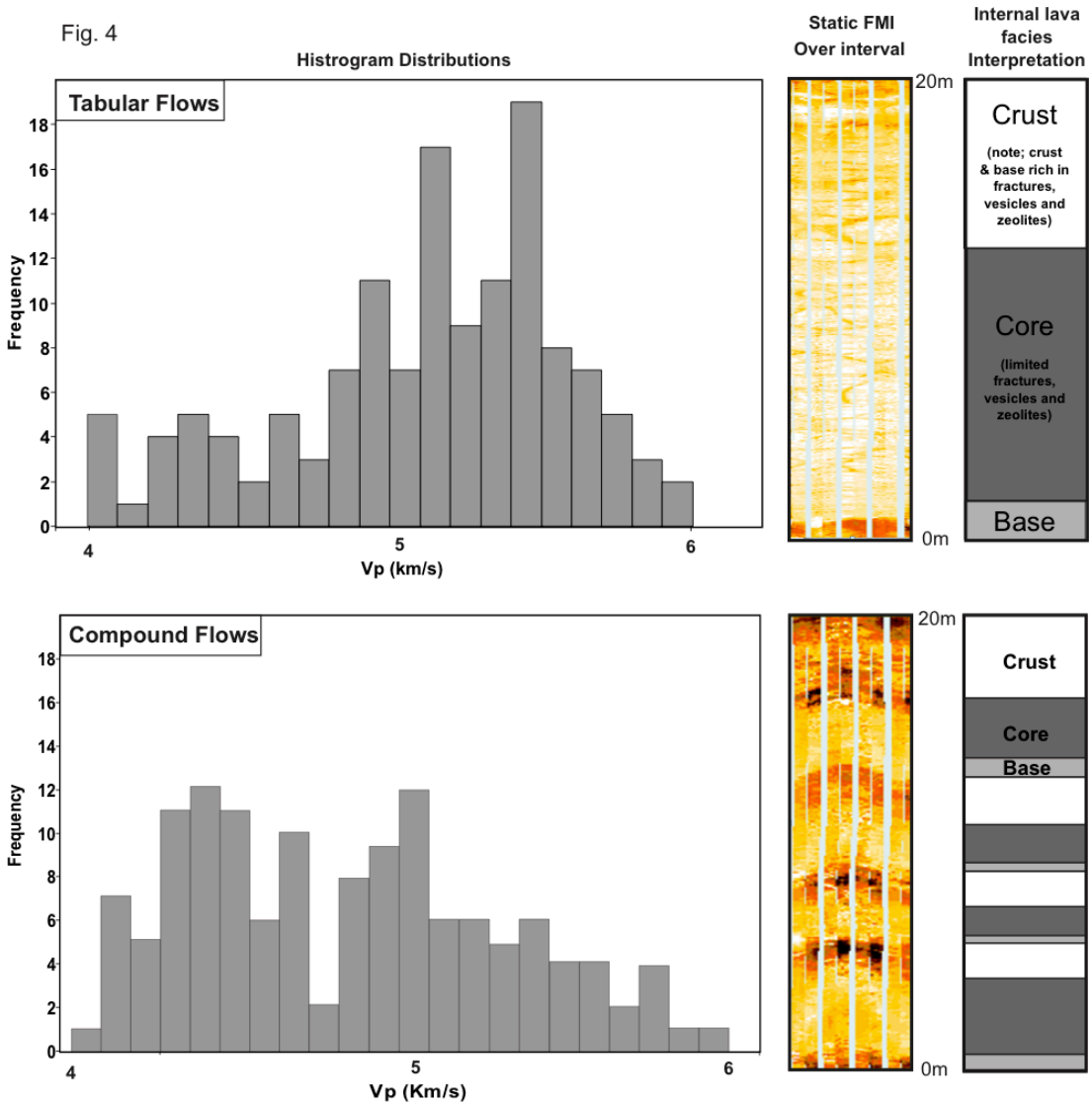

Figure 7. 4. An example of FMI logs from 213/27-4. Tabular flows 2890-2910 m, Compound Flows, 2360-2380 m Histogram distributions (left) have been calculated for each of the packages from Vp response using the methodology of Nelson et al., (2009). FMI log examples (right) show bi-modal responses between resistive (dark) and conductive (light) responses. The interpretation represents core and crust relationships in a lava flow (see section 7.7).

7.6.2 Core Analysis and Analogue Study

The most powerful FMI calibration technique is tying logs to cored intervals. Figure 7. 5 shows two volcanic cores linked to their FMI log responses (including dynamic FMI images with resistivity values averaged every 2 m, and static FMI logs with resistivity values averaged over the entire well). The lava in the upper core shows a high degree of fracturing and has a high vesicularity. The latter feature is picked up in the FMI image as a distinct mottled appearance. Unfortunately core is missing at the contact with the planar laminated unit observed in the dynamic FMI log. From core data we recognise this interval as a vesiculated upper crust of a tabular pāhoehoe lava flow (Fig. 7. 5A). The second core image is less fractured, more homogenous and is less vesicular (Fig. 7. 5B). The distinct ~ 45° fracture in the core has been highlighted in blue on the FMI image. Labelled in green are horizontal striations of higher resistivity that are evenly spaced and are not present in core. This suggests that they are drilling-induced features. Core observations suggest that this interval represents the dense core of a tabular basalt lava flow. Where core data is unavailable, for example, through the conductive clast or conductive bulbous type FMI facies (Table 7. 3) then remote data can instead be used to aid interpretation and to calibrate the FMI log. In such cases we have used observations from Brewer et al., (1999) to positively identify and interpret such features in Rosebank FMI logs.

Fig. 5

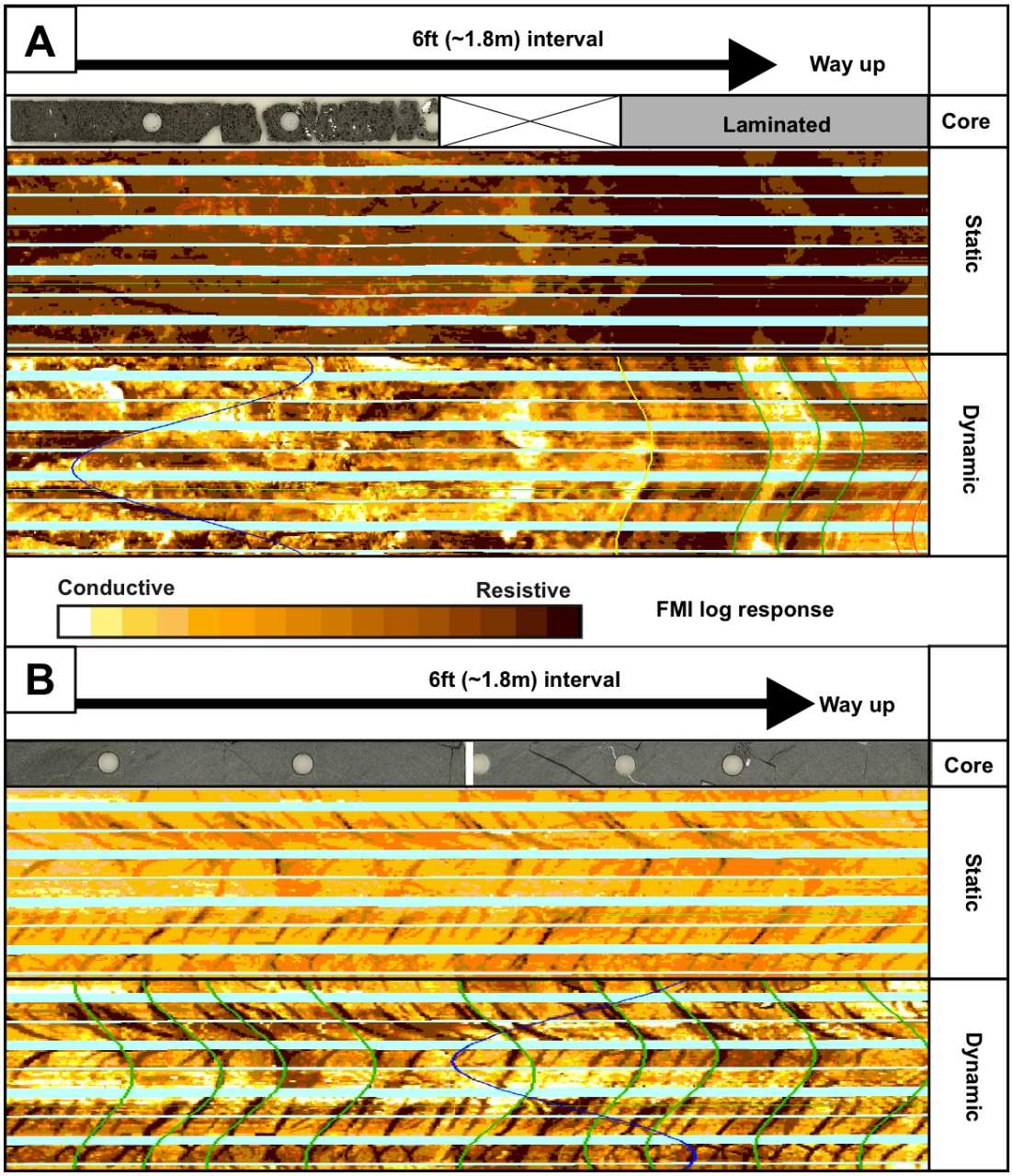

Figure 7. 7. 5. A) Core example from 205/01-1 showing a highly vesicular basaltic flow top. In the FMI log we can see a distinct mottled appearance to the flow core reflecting the presence of vesicles and or amygdales. B) Core show a homogenous dense (non-vesicular) basalt with small fractures interpreted to be a flow core. FMI response is of uniform high conductivity. Horizontal fractures (green lines) are evenly spaced and probably relate to the drilling technique as they are not reflected as a volcanic feature in the recovered core. Laminations are marked with a yellow line, blue lines represented high angle fractures.

7.6.3 Sidewall Core Analysis

Sidewall cores provide another useful calibration dataset for FMI logs. For the purposes of this study three cores were selected from the uppermost Colsay unit of 213/27-2. Detailed analyses of the components of each core are shown in Figure 7. 6. All of the cores show an increased abundance of basaltic lithic clasts relative to typical Colsay sandstone, which does not contain volcanic material. Graphs showing GR plotted against Vp for the selected interval reveal significant deviation from that of the average Colsay sandstone in 213/27-2 (Fig. 7. 6 A). Values that trend towards the average basalt are inferred to be enriched in volcaniclastic components. The FMI log reveals a conductive highly fractured zone; a coarse-grained clastic zone composed of conductive clasts and a zone of horizontal laminations (see Fig. 7. 8). Each zone has been plotted as a point cloud in order to group FMI observations. The conductive fractured zone contains the greatest abundance of basalt lithic clasts. The basaltic component decreases as the siliciclastic component increases into the laminated zone volcaniclastic sandstone. Thus, sidewall cores can be used in conjunction with FMI logs to help identify zones that contain varying abundances of basaltic lithic fragments.

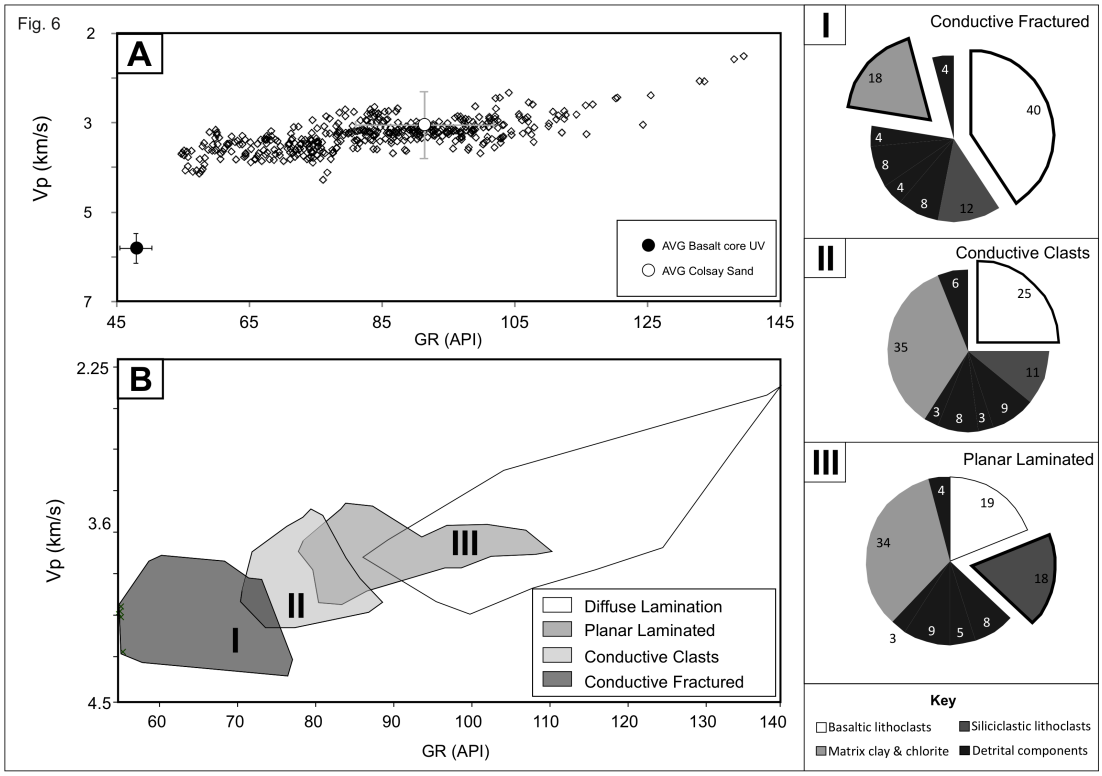

Figure 7. 6. A) Vp vs. GR cross plots of the uppermost Colsay succession in 213/27-2 (diamonds represent actual values for the formation. A) Average values for basalt core and Colsay sandstone are plotted with error bars. Data points from 213/27-2 are plotted as diamonds showing a spread between two end members. B) FMI facies as point clouds (see Fig. 7. 8 for examples). I, II, III are pie charts of sidewall core components with a percentage provided in each sector.

7.6.4 Field-based Acquisition

Outcrops of mixed volcaniclastic and siliciclastic sequences on the Earth's surface can provide additional constraints for FMI log calibration. Using data acquired from the Huab outliers, Namibia, we compare the Spectral Gamma Ray (SGR) signature of a mixed siliciclastic and volcanic succession. The Huab outliers are composed of aeolian sandstone dunes encased within basalt and basaltic andesite pāhoehoe lava flows that were emplaced during the formation of the 133–132 Ma Etendeka flood basalt province (Jerram et al., 1999; Jerram et al., 2000). In the upper part of the Huab sequence thin sandstone intervals alternate with very fine-grained volcaniclastic rocks interbedded within lava flows with dense cores and brecciated or fractured tops. This provides an excellent opportunity to examine the transitions from lava to sediments and from clean sandstone to volcaniclastic sandstone. Spectral Gamma Ray data on the rocks were acquired using a Radiation Inc. RS-230 BGO Super-Spec handheld device at either a ~30 cm spacing or at intervals determined by exposure. The device uses a Bismuth Germanate source to record SGR components (as U ppm, Th ppm, and K %) with high precision**.** This data can be combined with a lithological log (Fig. 7. 7). SGR values in the sandstone are low and increase up into the volcaniclastic sandstone, which has similar SGR values to the basalt lava flows. The lava flow values were taken four times to validate this observation.

The Rosebank well logs show similar SGR profiles to the Namibian examples. SGR component values of the Rosebank well logs (the upper most Colsay unit in well 213/27-2; Fig. 7. 8) can be compared with the field logs (Fig. 7. 7). The highest SGR values occur in the laminated zones (e.g. top of FMI section in Fig. 7.8 C) and are comparable to sandstone in the Namibian examples. Highly fractured intervals (Fig. 7. 8 B) have values that are similar to the fractured basalt flow tops in Namibia. In well 213/27-2 the conductive clast zones show a slightly elevated K % (Fig. 7. 8 A). This is similar to the trends seen in brecciated horizons in Namibia.

The SGR trends in the Namibian and Rosebank rocks are similar due to similarities in bulk mineralogy rather than geochemical composition. Core (Fig. 7.8 D) helps constrain values of volcaniclastic material present here as a fracture in the top of a basalt flow crust.

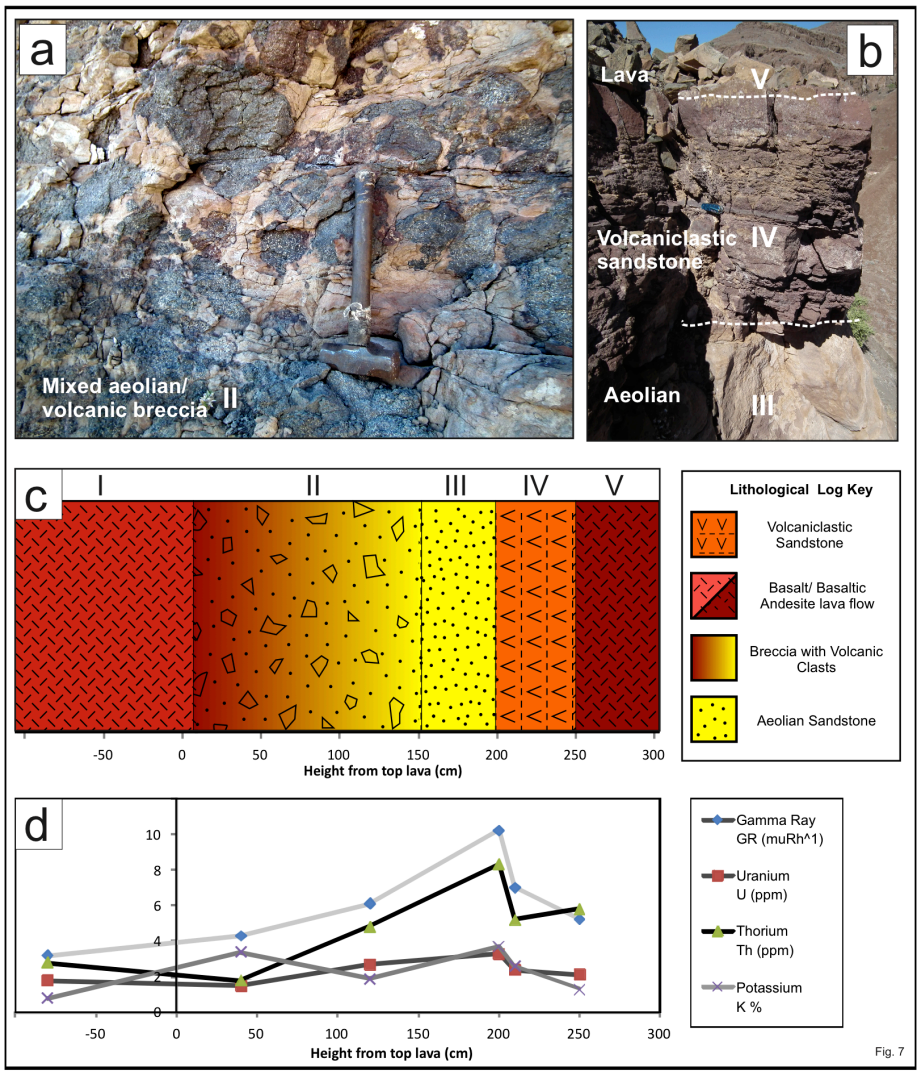

Figure 7. 7. A logged section with recorded SGR points along its profile. Section shows a contaminated sandstone/basalt/basaltic andesite contact from the Huab Outliers, Namibia. A) Lava top breccias containing vesicular basalt clasts within an aeolian sandstone matrix, lithofacies II in schematic log C. B) Photo highlighting the transition from clean aeolian sandstone to volcaniclastic sandstone and basaltic-andesite lava top, lithofacies III-V of the study section. C) Schematic log highlighting the volcanic and sedimentary lithofacies distribution (labelled I-V) in the studied section, with measured thicknesses taken from the top of the lower lava. D) The recorded SGR data across the study section (Uranium, Thorium and potassium plotted).-. See section 7.6.4 for details.

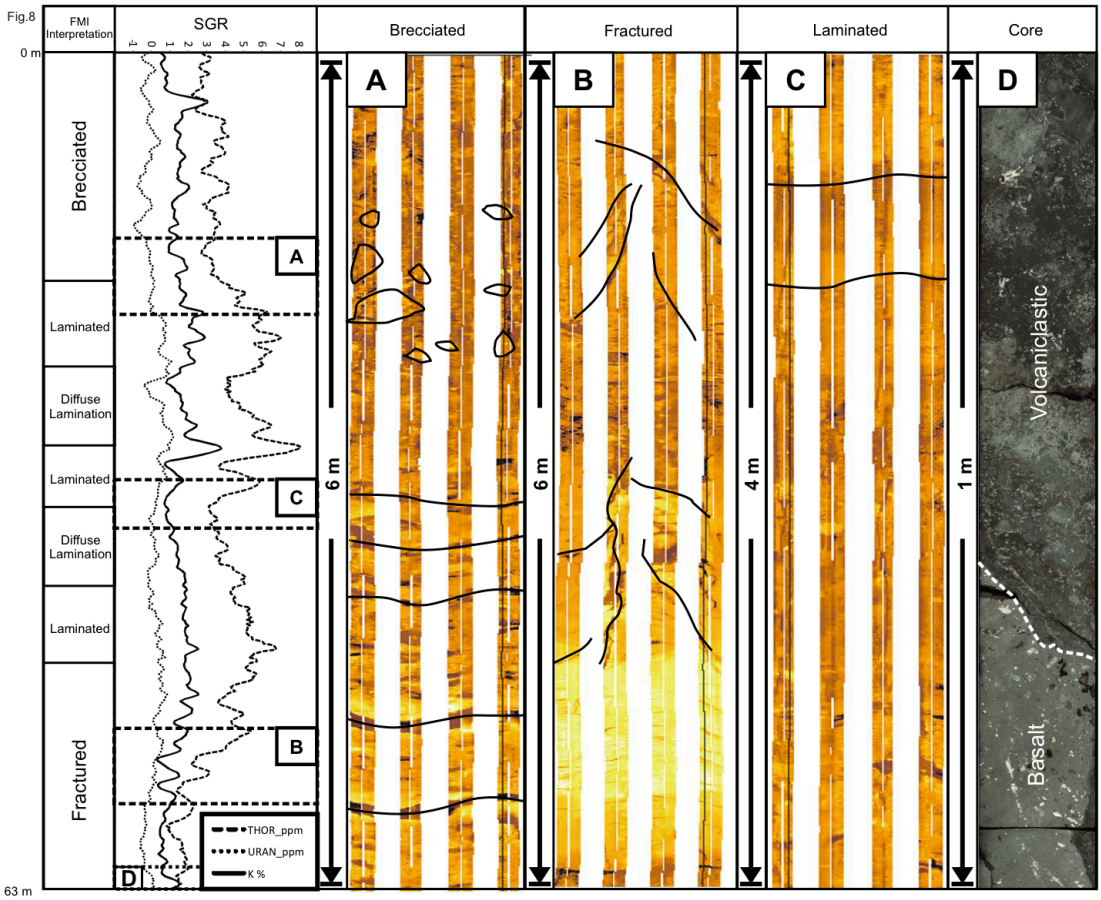

Figure 7. 8. Examples of FMI log responses from the uppermost Colsay interval 213/27-2. A SGR log has been provided for comparison with remotely recorded examples. A) Conductive breccia interval above a laminated interval B) Fractured conductive log response C) Diffuse-laminated and laminated zones. Laminated zones are inferred to be bedding within sedimentary rocks D) Cored interval showing a mix of volcanic and basalt components. FMI Log recovery has a limited pad number through this interval due to technical failure.

7.7 Volcanic Lithofacies Identification Using FMI

This study provides the opportunity to outline some of the main volcanic facies that can be identified using FMI, combined with well log data and outcrop analogues, and provides a working template for future FMI interpretations in volcanic lithologies. Table 7.5 outlines the volcanic lithofacies that have been identified according to their FMI data from wells in the Rosebank field. Each of the FMI facies (interpreted from FMI log alone) includes examples of both static and dynamic FMI log images. The FMI facies have been designed to be non-genetic.

Diagnostic FMI characteristics and well log parameters are provided for each FMI facies and these are discussed in the text. Field examples from Iceland of the various interpreted volcanic facies are linked with each FMI facies providing a lithofacies interpretation and placing them in the context of their volcanic setting (for further information on the Icelandic examples see Watton et al., 2013).

7.7.1 Mottled Upper/Lower to Homogeneously Highly Conductive Units

Observation- Zones exhibiting either a mottled-appearance or an almost homogeneously high conductivity are the most common FMI facies in the Rosebank field (205/1-1, 204/10-A-3 and 213/27-4) (>60 % of total facies volume). These zones are generally 4–8 m thick but can reach 20 m thick. Mottled facies make up ~ 60% of this facies group. The mottling is defined by circular patches c. 2–4 mm diameter of either higher or lower conductivity than the background. Mottled and homogeneously conductive units form packages separated by contact facies. Upper and lower mottled units sandwich homogeneously conductive facies. Upper mottled units compose up to 60% of each up to 20 m thick package that is analogous to pāhoehoe lava flows. Homogeneous zones are areas of constant conductivity that are devoid of other features except for rare randomly-orientated fractures or joints (see section 7). The petrophysical responses of the mottled facies show significant variation in GR (15 API), Vp (1.5 km/s) and Rhob D (0.3 gm/cc) values in comparison with the homogenously conductive facies, although the photoelectric factor (PEF) in both remains the same.

Context **–**Rock core (Fig. 7.5) and petrophysical characteristics of the mottled and homogenously conductive units are consistent with basalt lava flows (Planke 1994; Boldreel 2006; Nelson et al., 2009). Mottled features are interpreted as vesicular upper crusts (the small patches are vesicles or amygdales), while homogenous zones represent dense lava cores. Combined, One lava flow is composed of a thin lower mottled unit, a homogeneously conductive unit and a thick upper a mottled unit. This observation is consistent with the upper mottled facies (vesicular upper crust) comprising ~60% of the total lava flow thickness (Nelson et al., 2009). Most basaltic lava flow fields in the FSB are pāhoehoe lavas (Passey and Jolley, 2009, and references therein).

The characteristic tri-partite internal structure of pāhoehoe lavas (lower crust, core, upper crust) results from endogenous growth during emplacement. They are emplaced slowly and advance as a series of thin, small breakout lobes. Solid crusts form quickly on these cooling lobes. The lava flow thickens through a process termed inflation whereby magma is transported to the advancing margin of the flow and accretes to the base of the upper crust (e.g., Roland and Walker 1990; Hon et al., 1994). As the lava flows, gas bubbles rise upwards and the lava that accretes to the base of the crust is typically vesicular. The upper crust thickens at a faster rate than the lower crust and can grow many metres thick (typically <60% of the flow thickness) above the flowing lava (Self et al., 1998). As the lava flow field matures, preferential pathways (lava tubes) form a distributary network channelling lava to the flow front (e.g., Keszthelyi, 1995; Thordarson and Self, 1998). When the lava flow ceases, stagnant lava cools to form the lava core—typically formed of degassed, dense lava. Each part (lower crust, core, upper crust) has distinctive petrophysical properties (cf. Nelson et al., 2009). The lower crust is typically thin (< 10 cm) and may be poorly vesicular, the core is often non-vesicular and may exhibit widely spaced (50–100 cm) columnar joints. The upper crust is often characterised by diffuse layers of varying vesicularity that are visible in FMI images as highly conductive spots (mottling). Large cavities may be present between accreted layers in the upper crust. The upper crust may additionally become fragmented into blocks and rubble during flow.

Pāhoehoe lava is distinct from other types of basaltic lava, such as a'ā lavas, which are characterised by basal and upper clinker breccias surrounding a dense lava core (e.g., MacDonald, 1953). A'ā lavas may develop due to changes in the crystal content, viscosity, volumetric flow rate and volatile component (Roland and Walker 1990; Cashman et al., 1999; Kilburn, 2004). In FMI logs a'ā lava flows may be recognised by a two layers of breccia that sandwich a highly conductive dense lava core.

7.7.2 Random and Systematic Fracture

Observation **–** Both random joints and systematic joints are present in > 50 % of the mottled and homogenously conductive FMI facies (in 205/1-1, 204/10-A-3 and 213/27-4). Random fractures are closely-spaced and display high resistivity values.

Generally, fracture density increases towards the top of the upper mottled facies. Dynamic FMI often needs to be used in collaboration with static FMI logs to determine fracture vs. noise. Systematic fractures occur in the homogeneously conductive facies and form crude 5–8 sided polygons. The fracture density is commonly regular (from 0.2 –15 cm). There is a substantial difference in the petrophysical properties of the systematic joints and the random fractures—although GR values remain similar, RES values (>80 ohms) and Vp are 1.3 km/s lower) respectively.

Context **–** We interpret the random fractures as hackly (jagged) fractures in basalt flow tops and the systematic fractures as columnar cooling joints in the basalt flow core. Columnar jointing varies with height in lava flows due to their layered nature and heterogeneous cooling times. Regularly spaced columnar joints develop in the stagnant flow cores. This interpretation is supported from FMI log observations — columnar joints are only present in homogeneously conductive units. Random fractures are differentiated from columnar joints on the basis of having no systematic pattern between resistive cuts in the FMI log. Hackly or random fracturing can develop in the flow crust when surface water percolates down into the lava flow (e.g., when the upper surface of a lava is flooded). This interpretation is supported by the random fractures being confined to the upper mottled facies. Columnar joints in basalt lavas result from thermal contraction during cooling. Columnar joints propagate perpendicular to the cooling front and form more-or-less regularly spaced 5- and 6-sided columns (Hetényi et al., 2012). Joint growth is controlled by crack propagation creating plumose structures perpendicular to column faces (Degraff and Aydin, 1987). Water infiltration at the top of the flow can lead to radial joints sets the isotherms in the flow core are deflected leading to curved columnar joints shown in Table 7. 3. The presence of radial joints means joint sets cannot be used as palaeo-dip indicators. Joint orientation is modified by flooding by water (Saemundsson, 1970; Long and Wood 1986). Hackly fracture (Entablature) and Kubberberg (cube) jointing develop due to vastly increased water interaction at the top of the flow soon after emplacement (Saemundsson, 1970).

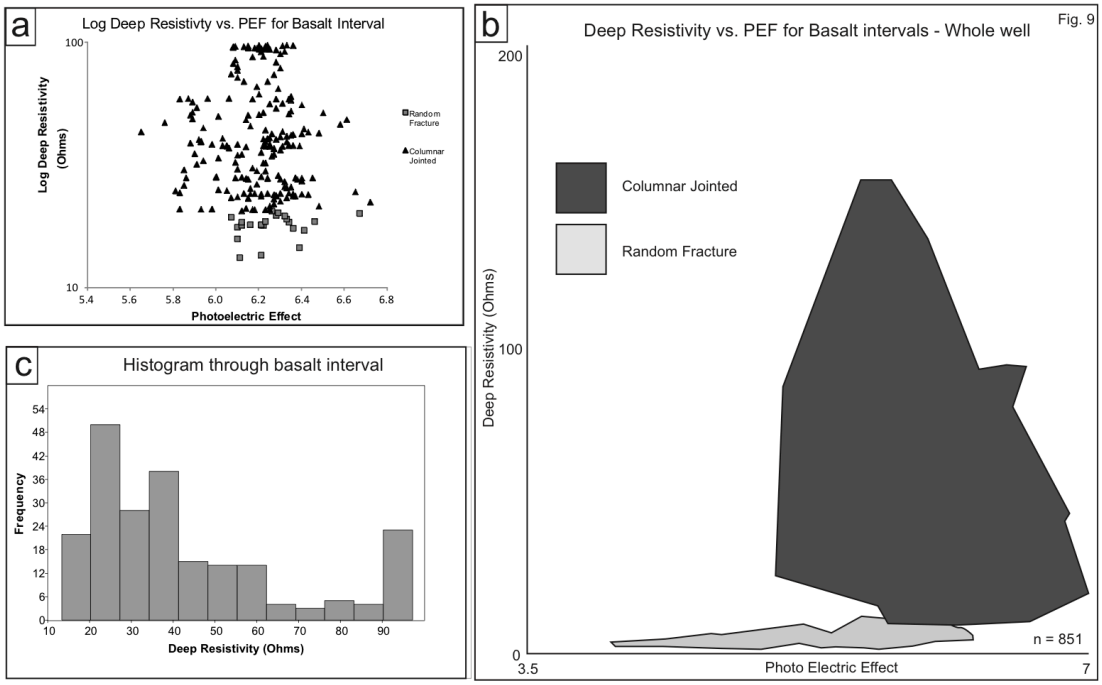

Figure 7. 9. PEF vs. RES cross plots for A) one lava flow and B) all lavas in well 213/27-4 C) histogram of resistivity results through the basalt interval. Results are discussed in section 7.8. The spread and average resistivity values are higher in columnar (systematic) joint sets than in those that display random fracture.

7.7.3 Bulbous Conductive FMI Lithofacies

Observation - The bulbous conductive lithofacies occurs in one well (213/27-4) as discrete packages within the lowermost volcanic unit. It is associated with conductive breccia facies. It is characterised by highly conductive bulbous or oval features (> 20 cm) within a higher resistivity matrix. The conductive features display < 2 mm thin fractures on their surfaces that are parallel to the outer margins. In some places in the matrix cuspate clasts (up to 4 cm) occur in association with the bulbous shapes. Generally the petrophysical response of this lithofacies is similar to that of uniform conductive facies and lithofacies is recognised based on the FMI image rather than the composite log.

Context – This FMI facies is interpreted as pillow lavas (e.g., Brewer et al., 1999). Pillow lavas form from when lava flows into water and reacts with it in a non-explosive manner. Pillow lavas advance in a manner similar to pāhoehoe lavas, with the lobe shape modified by the increased density of water. They typically have lower aspect ratios than subaerial pāhoehoe break-out lobes, and grow by endogenous

growth of the crust that causes the stretching and fracturing of each lobe (Moore, 1975). Pillows have bulbous forms in cross-section, but are tube-like in three dimensions (Walker, 1992).

7.7.4 Conductive Breccias (Clast-supported, Matrix Supported)

Observation – Clast-supported conductive breccia horizons occur in a number of wells (205/1-1, 213/27-2, 204/10-A-3 and 213/27-4). They comprise ~10% of the entire volcanic sequence. Clasts range in size from 2–15 cm in diameter. Two types of conductive breccia lithofacies are recognised. Type 1 breccias (Fig. 7. 8) are associated with the mottled and homogenous conductivity facies, whereas type 2 breccias are associated with the conductive bulbous facies (Table 7. 3). They can be distinguished by variations in the matrix conductivity (high in type I and low in type II) and by their overall RES values (30–50 Ohms difference).

Context - Volcanic breccias can form in a number of ways, e.g., from pyroclastic activity, during the emplacement of subaerial lavas (flow top breccias, ‘a‘ā lava flows), by quenching of lava upon water entry (hyaloclastite) or by sedimentary processes. Discrimination between these processes is difficult as lateral facies variations are often required. In a one-dimensional borehole FMI interpretation is reliant on up- or down-section relationships to determine lithofacies type. Type 1 conductive breccia facies occur adjacent to upper and lower mottled facies suggesting they are associated with lava flows. We interpret these as the brecciated upper crusts of pāhoehoe lavas. The formation of cooling joints in crusts and fracturing associated with differential inflation of a lava lobe can result in rubbly flow tops. These can be of local extent (metres to tens-of metres wide) or cover the entire flow field. They can be up to several metres thick and can have metre-scale relief.

Type 2 conductive breccias are associated with the conductive bulbous facies (pillow lavas). Breccias associated with pillow lavas are formed by the quenching and primary fragmentation of lava upon water contact and are termed hyaloclastite deposits (Carlisle, 1963; Moore et al., 1973; Kokelaar, 1984; Tribble, 1991, Mattox and Mangan 1997; Umino et al., 2006). Hyaloclastite deposits can modified by syn-eruptive resedimentation and reworking of hyaloclastite material (Watton et al.,

2013). In this case type II breccias are closely related to pillow lavas suggesting that they are hyaloclastite deposits derived from primary fragmentation processes. Whether this fragmentation was in a fluvial, marine or lacustrine environment is unclear.

7.7.5 Undulose and Resistive Contact Facies

Observation – Two types of contacts are observed in the FMI data (205/1-1, 213/27-2, 204/10-A-3 and 213/27-4); contacts between mottled facies units and sediments (undulose contacts) and contacts between units of the mottled facies (resistive contacts). Undulose contacts are complex and have high conductivity and high resistivity components. The material in areas of high resistivity is brecciated or forms rounded blebs that typically range in size from 2–10 cm, but can reach 1 m in diameter. This material can be incorporated into the overlying homogeneously conductive facies. Undulose contact facies always occur at the base of lower mottled facies and Colsay units. Whereas resistive contacts are associated with the upper mottled facies and occur always on the upper most flow in the lava package in each volcanic sequence. Resistive contacts are mottled but the mottling is more diffuse, does not form coherent blobs, occurs in thinner zones (<1 m) and generally has higher resistivity values. The petrophysical characteristics of the resistive contact facies are significantly different (RES (40 Ohms), and Vp (2 km/s).

Context – The undulose contact facies marks the contacts between lava and sedimentary rocks of fluvial or marine in origin. In FMI logs peperite horizons have been interpreted where rocks show mixed siliciclastic/volcanic log responses (higher GR and lower Vp responses), exhibit fluidal rounded textures (unlike type 1 or 2 breccias) and have clast sizes that are analogous to field observations. The distribution of conductive vs. resistive material is more diffuse (unlike the sharp contacts seen in brecciated horizons). This is also consistent with vertical facies associations where proposed peperitic contacts always occur at the base of lava flow packets in contact with sedimentary deposits. Peperites form when lava or intruding magma interacts with unconsolidated, usually saturated sediments (e.g. Jerram & Stolhofen 2002; Skilling et al., 2002; Brown and Bell 2007; Waichel et al., 2007). They comprise an intimate mixture of lava or magma fragments and host sediment.

Peperites can exhibit a range of textures (see McPhie et al., 1993) dependent on host lithology, degree of lithification, lava flow viscosity, cooling rates, magma fragmentation, density contrasts and hydromagmatic activity. They can form quenched glassy layers that may be highly impermeable thus limiting fluid transfer between the sediment and the lava.

We interpret the resistive contacts as palaeosols developed on the tops of lava flows. The development of both laterite (iron-rich) and bole (kaolinite-rich) soil horizons on basalt flows has been documented throughout Palaeogene volcanic successions in the UK and the Faroes (Hill et al., 2001; Passey and Bell, 2007). Laterite, bole and thin inter-basalt sediment horizons indicate pauses in volcanic activity and can be useful in the interpretation of palaeo-climates and palaeo-environments and can be used to subdivide thick sequences of stacked lavas (Jolley et al., 2005; Passey and Jolley, 2009). The recognition of laterite or bole horizons again relies on the facies association with upper mottled facies (i.e., overlying a vesicular upper crust of a pāhoehoe lava flows). The occurrence of palaeosols can be indicative of a significant time gap between lava flow emplacement (c. 0.3 m / Ma, Pillans, 1997) suggesting time gaps between lava emplacement in the Rosebank field could be up to 1.5 Ma.

7.8 Interpreting Jointing and Fracture Systems in FMI

The FMI tool allows us to recognise basalt intervals characterised by different joint types (regular or random) and therefore to investigate the effects of jointing patterns on the petrophysical response. Using the FMI log it is possible to select flow basalt intervals with either regular columnar jointing or random fractures (Fig. 7. 9). If we plot the photoelectric factor values for these intervals (PEF) against deep resistivity, which does not change between basalt core and crust, we can make the data spread a function of deep resistivity values and joint/fracture set characteristics. This indicates that the basalt lava cores with columnar joints have higher resistivity values than basalt with high fracture densities within any one flow unit (Fig. 7. 9A). This is supported by a bimodal spread in the histogram distribution. The same holds true for all basalt flows within an entire well (Fig. 7. 9B). The regular-spaced columnar joint intervals have mean resistivity values that are almost an order of

magnitude greater than those of the randomly fractured intervals. This indicates that there are significant differences in the fluid flow potential of the different joint systems, which may relate to how different orientations of joints close in response to confining pressure.

7.9 Lithological Separation Using FMI Data

Detailed analysis of FMI images that have been calibrated to core and wireline logs can help distinguish contact lithofacies (such as peperites) between siliciclastic and volcaniclastic rock types and give increased confidence to well log interpretations (Fig. 7. 10). This cross-plot simply represents positively identified volcanic and siliciclastic rocks as well as volcanic spread of undetermined values before analysis of the FMI logs. Using FMI in well 213/27-4 it is possible to constrain the volcanic spread using Table 7.3a, b, c and accurately separate volcanic from siliciclastic rocks resulting in significantly less overlap in interpretation and thus a more accurate characterisation of the reservoir intervals. Accurately classifying contacts and calibrating FMI logs using multiple techniques can also improve the understanding of mixed volcanic and siliciclastic successions. Combining field-based data collection and interpretation with wire line logging and side wall core recovery has led to an improved understanding of contaminated siliciclastic units (e.g. 213/27-2). These observations can be fed back into lithofacies interpretation increasing confidence in the determination of reservoir and non-reservoir units. We recommend developing the use of FMI logs in combination with downhole geochemical proxies (such as Electron Capture Spectroscopy and geochemical typing of lava flow packages) in order to provide additional constraints on the evolution and architecture of volcanic sequences.

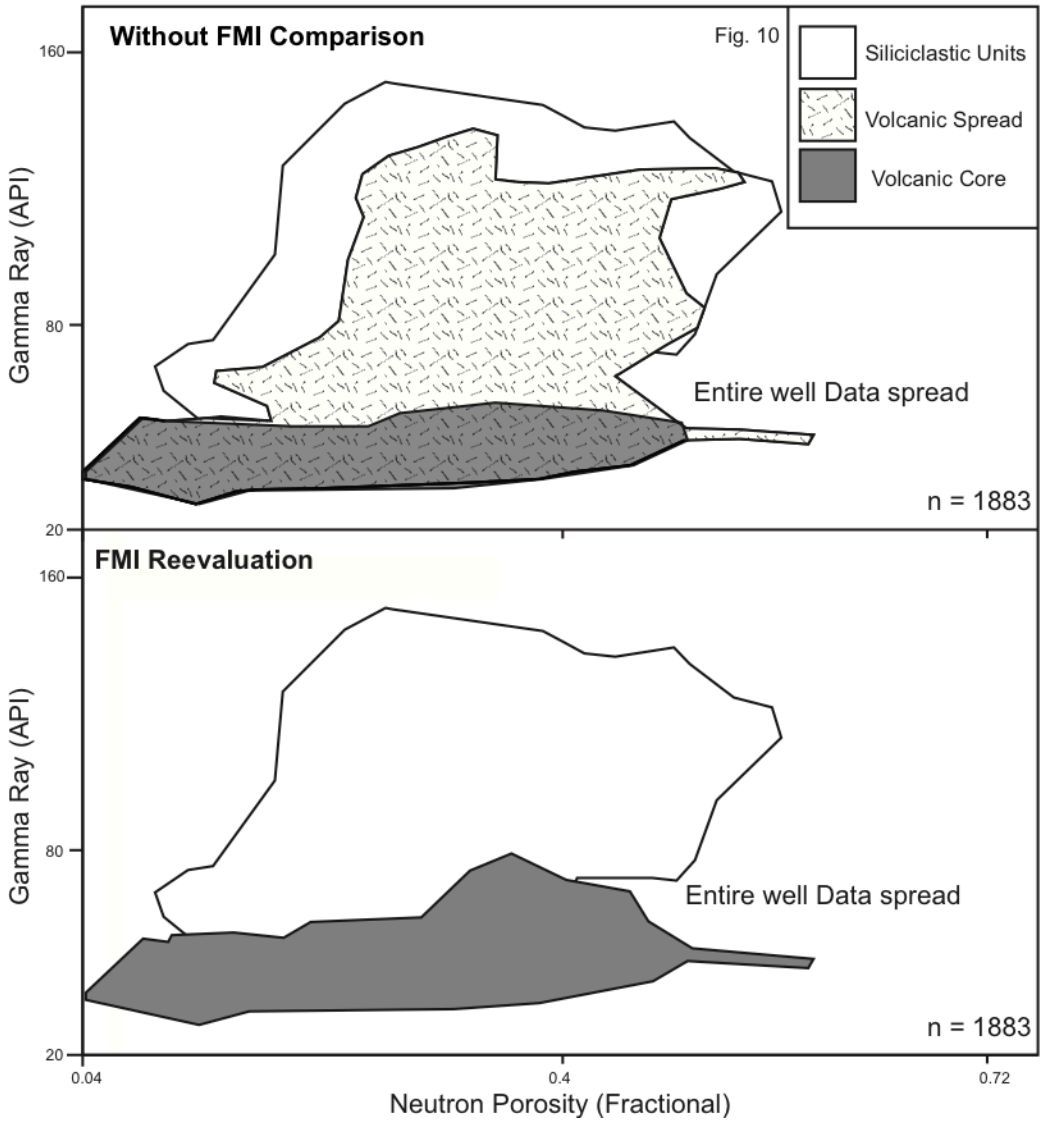

Figure 7. 10. GR vs. Neutron Porosity (Fractional) crossplots for 213/27-4. Results have been sorted into point clouds and discussed in section 7.9.

7.10 Conclusions

FMI log analysis of mixed volcanic and volcaniclastic rocks in the Rosebank field, FSB, has allowed the accurate characterisation of distinct volcanic lithofacies. We have outlined four methods for calibrating FMI logs (P-wave velocity comparisons, wire-line log collection of field based analogues and wire-line log vs. sidewall core analysis), three of which can be conducted in the absence of rock core. Internal lava flow features, contact relationships and joint networks can be readily identified. Such a tool is extremely useful in identifying potential migration

pathways, seals and reservoirs in hydrocarbon-bearing basins containing volcanic and siliciclastic rocks. Integration of FMI-derived lithological interpretations with seismic data should substantially increase the accuracy of interpretations of subsurface geology.

FMI facies	FMI Identification	Composite log Attributes	Interpretation Volcanic lithofacies	FMI Image (Conductive – Resistive) Scale / Static / Dynamic / Interpretation	Field analogue
Mottled Upper	High conductivity in comparison to flow core. Resistive "spots" pepper the interval. Often overall grading to higher resistivity values in both static and dynamic logs at the top of the unit. Higher fracture abundance can differentiate interval from the core where gradational changes are lost. Flow top, Core and Base have been identified by Vp distribution see Fig. 2.	• Low GR API <30 • Lower Resistivity (deep) than flow core (10-80 Ohms) • Vp decrease (4-6km/s) • Density decrease (2.5-3gm/cc) • PEF remains constant (5-6.5)	**Flow Crust.** Higher conductivity "spots" represent vesicles which can be banded. Once buried these vesicles can be filled with calcite and zeolite to form amygdales .These features have been confirmed when the FMI logs have been compared to core data. Sharp relationships mark the transitions between flows.	2m / 0m Crust / Core	Highly vesicular flow tops grade into glassy chilled contacts indicated by a change in resistivity values.
Uniform Conductive	High conductivity overall, some vertical fractures which are drilling induced. Near constant resistivity values on static FMI. Noticeable lack of features separates the unit from the flow top. . Flow top, Core and Base have been identified by Vp distribution see Fig. 2.	• Low GR API <15 • Higher Resistivity (deep) >100 Ohms • Vp increase (5-6.5 km/s) • Density decrease (2.7-3.3gm/cc) • PEF remains constant (5-6.5)	**Flow Core** Finely crystalline vesicle poor central segment of a lava flow. Can be fractured or jointed but often absent of any features hence uniform appearance in the image log. Flow cores are formed as magma cools more slowly as insulated by the crust.	4m / 0m Core	Basalt flow core absent in vesicles. In this example the core is much thicker than the surrounding crust.
Mottled Lower	Similar to flow tops with a resistive base and increasing in conductivity towards the core. Small resistive spot are again visible but can be elongate perpendicular to the flow base. The basal contact can be locally irregular. Flow top, Core and Base have been identified by Vp distribution see Fig. 2.	• Low GR API <30 • Lower Resistivity (deep) than flow core. (10-80 Ohms) • Vp decrease (4-6km/s) • Density decrease (2.5-3gm/cc) • PEF remains constant (5-6.5)	**Flow Crust (Base).** At the flow base vesicles or occasionally in-filled amygdales occur. They originate from cooling and volatile release. Segregation of a more silica rich component can lead to the formation of elongate vesicles at the flow base. Vesiculation can be partially laminated upon ductile deformation of the flow during cooling.	2m / 0m Core / Base	Flow bases can be highly vesicular and fractured (as above) especially in contact with a water saturated sediment or soil.
Resistive contact	Resistive contact in FMI image between two flows. Mottled, diffuse appearance with patches of higher and lower resistivity. The contact changes are gradation with no sharp contacts. Usually only 0.2-0.7m thickness. Where present flow to facies can be difficult to determine.	• High GR API >40 • Higher Resistivity (deep) than flow top (40-80 ohms) • Vp decrease (2.5-3km/s) • Density decrease (2.3-2.7gm/cc) • PEF decrease to lower values (2-4)	**Palaeosol or laterite** derived from the weathering and leaching of basalt flow tops. In outcrop they often have a reddened appearance due to oxidising iron. Palaeosols are important as they marks breaks in activity in volcanism and can provide useful stratigraphic markers. Recognition of palaeosols in image logs can be difficult.	1m / 0m Base / Laterite / Crust	Reddened laterite horizon. note the leaching (yellow) surrounding the reddened interval.

Table 7.5 Volcanic lithofacies identified according FMI data. Each of the FMI facies (interpreted from FMI log alone) includes examples of both static and dynamic FMI log images. The FMI facies have been designed to be non-genetic.

FMI facies	FMI Identification	Composite log Attributes	Interpretation Volcanic lithofacies	FMI Image (Conductive – Resistive)	Field analogue
Rounded Resistive	Rare elliptical structures too large to be bulbous facies. Have radial fracture and are more resistive than the flow core. They can also appear as highly resistive 2-3 m “holes” in the FMI image. Overall they are very rare in entire FMI image.	• Low GR API <10 • Lower Resistivity (deep) than flow core • Vp as flow core • Density as flow core • PEF remains constant	**Lava Tubes** develop through internal flow localisation of lava upon cooling. They are very common in Hawaii where the underlying angle of slope is high. The chances of intersection of these features is low some however can be filled like this example but others can be empty and look like very large (metre scale) high resistive features in the image log.	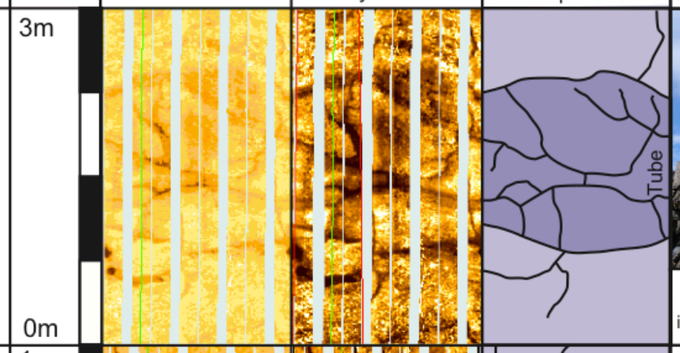	 A n in filled lava tube within a pahoehoe flow Above lava tube tumuli develop due to tube inflation exceeding crustal strength of the flow.
Laminated Conductive	Occasionally at the very surface of the flow top discontinuous laminations can be observed. The laminations appear as combination of conductive and resistive bands.The intervals are very thin and best observed in the static FMI log.	• As flow top	**Flow Textures (Pahoehoe).** Upon cooling low viscosity basalt lava will produce a ductile skin. This can be deformed and folded back on its self commonly known as pahoehoe or rope like textures. In cross section at the top of a lava flow pahoehoe textures look akin to discontinuous laminations. Conductive and resistive variation in lamination is likely to represent a undulating surface.	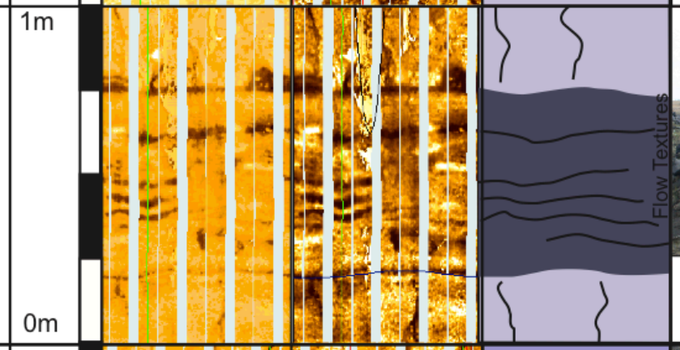	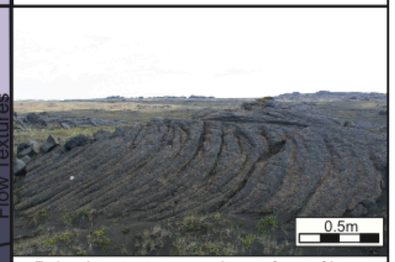 Pahoehoe textures on the surface of lava flow. Not the rope like textured formed by cooling and ductile deformation of the lava skin.
Undulose contact	Complex undulose texture between conductive and highly resistive layers. In this case the resistive interval has been identified from composite log data and drill cuttings to represent a siliciclastic sediment. In this case the image log has just imaged the contact between the two lithologies. Note the chaotic mixing of both the intervals.	• Contact relationship	**Peperite** forms where lava meets water saturated non-lithified sediment. Complex quenching, loading and mineral replacement occurs in the sediment and the lava to create usual textures. The identification of a contact like this may help determine timing of lava emplacement.	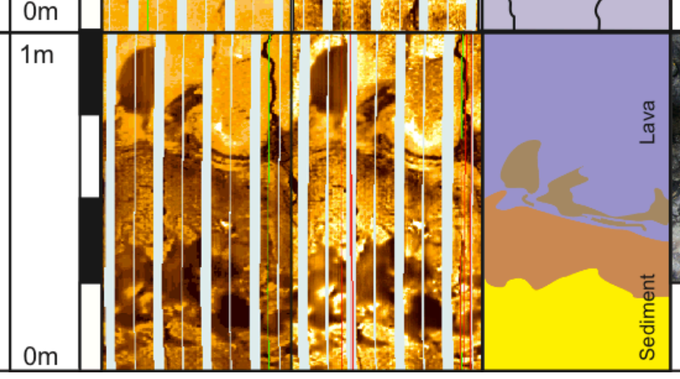	 Peperitic contact between a lava and a wet siliciclastic sediment. Complex replacement of minerals and glass formation has produced an impermeable layer.

Table 7.5 Volcanic lithofacies identified according FMI data. Each of the FMI facies (interpreted from FMI log alone) includes examples of both static and dynamic FMI log images. The FMI facies have been designed to be non-genetic.

FMI facies	FMI Identification	Composite log Attributes	Interpretation Volcanic lithofacies	FMI Image (Conductive — Resistive)	Field analogue
				Scale · Static · Dynamic · Interpretation	
Conductive clast	Angular patches of conductive material situation within a resistive matrix. Contacts are often transitional from a flow core or top. Some fragments can be highly angular others more rounded. Often highly fractured by drilling.	• Low GR API <12 • Low Resistivity (deep) type I 20-40, type II 10-20 Ohms • Vp uniform (5.5-6km/s) • Density (2.7-3.3 gm/cc) • PEF (2-5)	**Volcanic Breccia (hyaloclastite)** Difficult to distinguish from a primary volcanic breccia such as that at the base of an a'a flow. However potentially a hyaloclastite breccia due to jigsaw fit clasts and very high neutron porosity values which are indicative of water bound clays. High resistivity values between clasts are also consistent with extensive fracturing of hyaloclastite deposits.	2m … 0m; Breccia / Crust	An example of a hyaloclastite breccia. Note the highly angular clasts and brown altered matrix of palagonite clays and quenched glass.
Conductive Bulbous	Rounded to sub-rounded characteristic conductive bulb shapes occasionally ajoined but often split with a resistive layer. Potentially radial fracture in some examples are large cavities at the centre of bulbs although FMI resolution poor in this interval. Drilling through pillow lava secessions can create large cavities in the bore hole wall smearing the image log.	• Low GR API <20 • Lower Resistivity (deep) than hyaloclastite deposits (<10 ohms) • Vp (5.5-6km/s) • Density (2.7-3.3 gm/cc) • PEF remains (2-6)	**Pillow lava** forms bulb like forms in cross section but are actually networks of small elongate lobes. Pillow lava usually have a quenched rim and radial joints developed from cooling contraction. Some pillow lava can have large cavities in the centre where volatiles have concentrated. The resistive matrix is likely to be spalled fragments of pillow lava and associated clays analogous to hyaloclastite breccias.	4m … 0m; Pillows	Pillow lava example showing bulb like pillow structure in cross section. Small fragments spalled pillow lava rim make up the matrix.
Systematic Fracture	Regular spaced hexagonal or 8 sided fractures within the flow core. Can appear as 15m thick intervals. Fractures are highly resistive. Note the regularly spaced resistive striations in this example.Striations have been image analyzed and occur at even 20cm intervals. These features are caused by aggressive drill bits used to drill basal.	• Low GR API <12 • High Resistivity (deep) relative to random fracture (>90 Ohms) • Vp increase (>5-6 km/s) • Density increase (2.9-3.2 gm/cc) • PEF as flow	**Columnar jointing** forms upon water enhanced cooling of the basalt core. Joint propagate perpendicular to the cooling surface. Regularly spaced hexagonal joint patterns can develop as in this example. However as cooling is water enhanced columnar joints are often not vertical but curved (see field example) hence they cannot be used to determine dip angles of lava flows.	2m … 0m	Curvy-columnar joints. Note the regular space between each column but the highly variable direction of joint propagation.
Random fracture	Highly fractured restive features in random orientations. Easier to observe on the dynamic FMI log. Secondary sub-vertical fractures are probably drilling induced.	• Low GR API <16 • Lower Resistivity (deep) than systematic fracture (10-90 ohms) • Vp decrease (4.7-5.5 km/s) • Density decrease (2.7-3 gm/cc) • PEF as flow	**Fractured flow top (Hackley fracture)**develops due to rapid cooling which is usually water enhanced from the top of the flow. Systematic fracture is abandoned a dense fracture network is produced. Interestingly there is a significant variation in resistivity values from columnar jointed examples.	1m … 0m	Highly fractured flow core developed when fluvial activity reestablished itself over the top of a cooling basalt flow.

Table 7.5 Volcanic lithofacies identified according FMI data. Each of the FMI facies (interpreted from FMI log alone) includes examples of both static and dynamic FMI log images. The FMI facies have been designed to be non-genetic.

8

CHAPTER FIGURES AND TABLES

8. Discussion, Conclusions and Future Work

Chapter Summary

This thesis has combined a variety of different field, core, wire-line logs datasets to investigate the formation and physical properties of hyaloclastite and volcaniclastic deposits. This chapter discusses the implications of work presented in this thesis on the interpretation of hyaloclastite deposits in wire-line and seismic data, provides some general conclusions, and then outlines potential future research.

8.1 Hyaloclastite Wire-line Response and Seismic Implications

Hyaloclastite deposits in volcanic margin settings can reach ~1 km in thickness (e.g. Jerram et al., 2009; Wright et al., 2012), and are commonly 10's to 100's of meters thick. Understanding the roles that hyaloclastite deposits play in such settings (such as the Faroe Shetland Basin, and the South Atlantic Margins) is a fundamental problem for petroleum exploration. The recognition of variations in hyaloclastite well-log responses in this study and the linking of these to well-preserved drill core is an important step in understanding hyaloclastite deposits in the subsurface.

Drill core through hyaloclastite deposits has additionally revealed important information about the palaeo-environment (Chapter 6). Watton et al., (2013) highlighted various transitions from primary to re-worked hyaloclastite lithofacies in two onshore examples in Iceland. In HSDP core section A the presence of inter-bedded clast-supported hyaloclastite breccias, matrix-supported hyaloclastite breccias and fine-grained hyaloclastite sandstone suggests that substantial reworking of hyaloclastite deposits occurred on the submarine flanks of Hawaii.

Comparison of Vp, Vs and density in hyaloclastite deposits has revealed important information on the physical rock properties in hyaloclastite deposits and the causes of seismic reflectors, which are either sedimentary (i.e. contacts between hyaloclastite lithofacies), volcanic (contacts between lava flows and hyaloclastite), diagenetic (contacts between palagonite and not palagonitized hyaloclastite deposits) or structural (i.e. fault scarps). Additionally hyaloclastite Vp/Vs response and spread

in the data is similar to other volcanic rocks meaning separation of volcanic units that include hyaloclastite deposits in seismic datasets is difficult. Therefore a fundamental problem arises when comparing hyaloclastite deposits in seismic data. Are seismic reflectors a manifestation of gravitational collapses, pillow lava/lava flows down the delta front or hiatuses in effusive activity? This section considers these possibilities with reference to the Hreppar Formation (where Stóri-Núpur is located).

8.1.1 Scaling Issues

Reflection seismic surveys have revealed buried offshore hyaloclastite deposits (Symonds et al., 1998; Kiørboe, 1999; Planke et al., 2000; Berndt et al., 2001; Thomson, 2005; Calves et al., 2011; Wright et al., 2012; Holford et al., 2012). These hyaloclastite deposits are termed lava deltas and are characterised by low amplitude prograding foreset units either surrounded or capped by high amplitude reflectors (lava flows). Lava deltas in such settings have been interpreted to react to fluctuations in sea level in a manner analogous to Jones and Nelson's (1970) model (Kiørboe, 1999; Thomson, 2005; Wright et al., 2012). However, the scale of hyaloclastite deposits in the subsurface (2D seismic sections) ranges from 2-20 km lenght and up to 2 km thickness (Kiørboe, 1999) with foreset dips much lower angles of repose (c. 4-5° although confidence in these values is low due to inherent problems with depth conversion) (Wright et al., 2012). This is unlike many hyaloclastite systems exposed or forming at the present day generally that have a foreset angle of 25-30° (Tribble, 1991; Skilling, 2002). Therefore, packages of similar scales to offshore examples need to be considered if these subsurface hyaloclastite deposits are to be fully understood.

Previous field-based models of hyaloclastite delta formation have considered the overlying lava flow package and its contribution to the hyaloclastite delta system (e.g. Porębski and Gradziński, 1990; Schmincke et al., 1997; Skilling, 2002). Observations of exposed onshore examples have been scaled into offshore seismic reflection studies of large (>1 km) hyaloclastite sequences in the Rockall Trough / Norwegian Margin (Planke et al., 2000; Berndt et al., 2001; Thomson, 2005) and the Faroe Shetland Basin, UK and Faroe Islands (Kiørboe, 1999; Spitzer et al., 2008; Jerram et al., 2009; Wright et al., 2012). Only limited attempts have been made to incorporate hyaloclastite deposits into a regional lithostratigraphic framework at

seismic scales, which encompasses the offshore hyaloclastite delta sequence, the fore-delta lava supply and original drainage networks in non-subglacial environments. Interestingly, the best onshore analogues for such deposits are found in Greenland, but form large c. 600 m cliff sections (e.g. Jerram et al., 2009), which pose clear sampling and logging problems.

Previous interpretations of lava deltas have summarized these sequences as packages of genetically linked lava flows overlying hyaloclastite deposits however, most known examples of large hyaloclastite systems are sourced in lacustrine settings and are usually 250 m and no more than 600 m high (Pedersen, 1998; Skilling, 2002; Smellie, 2006, 2008). These studies reveal a complex relationship between subsidence and lithofacies stacking patterns in association with lacustrine sediments (Pedersen et al., 1998) or overlying lava flows (Skilling, 2002) Recent studies have attempted to characterise the submarine portion of proximal volcanic systems, which show high degrees of lithofacies variation (Saint-Ange et al., 2013). Therefore there is a need to understand lithofacies variation and stacking patterns in 2D sequences of the scale of seismic examples (~20 x 2 km) that contain hyaloclastite deposits in order to accurately characterise offshore sequences. This is attempted in the following sections using examples from Iceland (the Hreppar formation, which contains the Stóri-Núpur hyaloclastite sequence, see chapter 4). Each study locality is shown in figure 8.1 with additional data provided in table 8.1 and the appendix to this chapter.

8.1.2 The Hreppar Formation

To approach the scale of hyaloclastite deposits in the subsurface the Hreppar formation that contains the Stóri-Núpur hyaloclastite delta (described in chapter 1 and 4) can be used to investigate the gross regional scale variation of a hyaloclastite system with allows study of the supplying lava flow field in a marine setting.

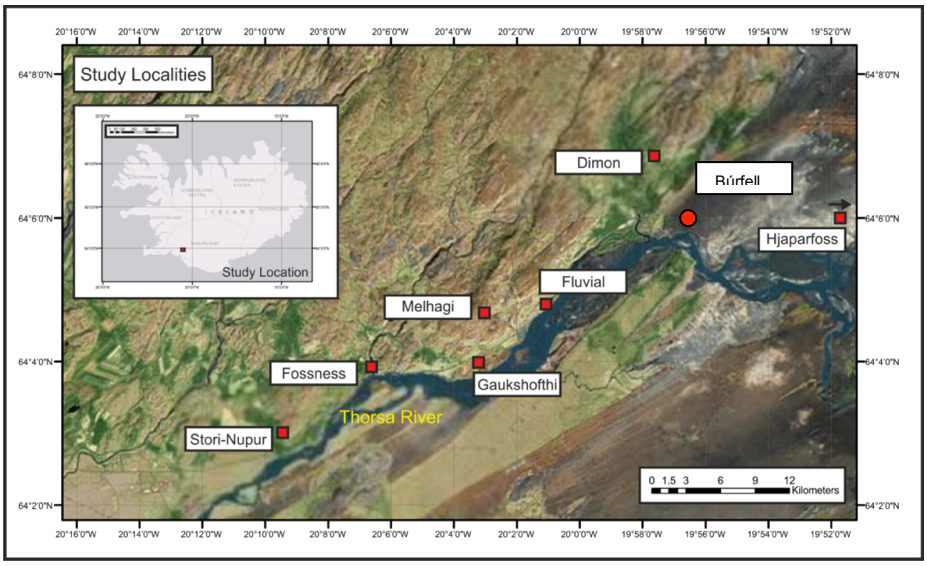

Figure. 8.1 Log and photo localities from the southern portion of the Hreppar Formation in the Árnes region of South-Central Iceland containing the Stori-Nupur hyaloclastite sequence discussed in chapter 4. Logs and photos for each area are provided in the appendix for this chapter.

The localities presented in this section represent outcrop exposure generally south of Búfell where unit geochronology is less constrained. Each locality in this study has been linked to its closest K/Ar date and the gross lithostratigraphy has been outlined in figure 8.2. The study area is a stacked up dip vertical succession lying on the western limb of a regional anticline outlined in chapter 1.

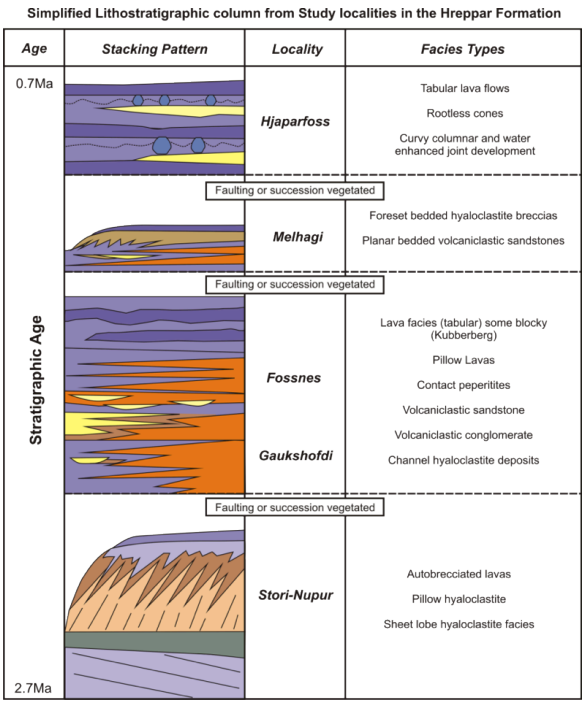

Figure 8.2 Summary stratigraphic section of the southern Hreppar Formation containing the key study localities, lithofacies and K/Ar dates in each case.

8.1.3 Lithofacies Variation in the Hreppar formation

The gross lithological variation in the Hreppar formation is summarized in figure 8.2 and Table 8.1. The aim is to summarise the regional development of a large hyaloclastite pile at the same scale as an offshore hyaloclastite sequence Supporting logs and figures to the interpretations made in this section are (including captions) provided in the appendix to this chapter.

Table 8.1

Locality	Setting	Lithology Description	Lithofacies Interpretation	Appendix Log / Diagram
Stori-Nupur	Hyaloclastite delta	200 m thick volcanic breccia sequence and lava flows.	Hyaloclastite sequence formed in a shallow enclosed bay (see chapter 4 for details)	(Chapter 4)
Gaukshofdi	Mixed Fluvial and Hyaloclastite, pillow lava and lava flows	30 m logged interval of interbedded volcanic breccia, cross bedded lenticular volcaniclastic sandstone and tabular lava flows with occasion fine grained horizons of quenched hyaloclastite glass. Pillow lavas occur above volcaniclastic sedimentary layers	Fluvially derived sediments with localised lava lobes fragmented to hyaloclastite. Fine hyaloclastite material may have been formed from remobilisation and distal reworking of the material in a fluvial system (e.g. Tolan and Beeson, 1984)	Chapter 6 Log 1 and Fig. 1.
Fossness	Fluvial, and lava flows	c. 200 m thick sequence of volcaniclastic sandstones, conglomerates and breccia. Quenched glasts in breccia horsizons.	Fluvial volcaniclastic sandstones and conglomerates mixed with hyaloclastite potentially forming dams lava flows. Lava flows	Chapter 6 Logs 2-7.

		Peperite development at the base of lava flows. Thick (upto 4 m) tabular lava flows with two tiered columnar joint sets.	are emplaced on wet sediment as peperitic contact are present between lava flows and sediment (Brown and Bell, 2007; Waichel et al., 2007).	
Melhagi	Perched hyaloclastite delta	20 m thick sequence of prograding low angle breccias quenched fragments overlying a planar bedded volcaniclastic sandstone.	Backstepped hyaloclastite delta system after period sea level rise (e.g. Jone and Nelson 1970 or Wright et al. 2012).	Chapter 6 Fig. 2
Fluvial	Fluvial Volcaniclastic sandstones	10 m thick sequence of trough cross bedded volcaniclastic sandstone and conglomerate with overlying lava flow.	Well developed trough cross bedded volcaniclastic sandstones and conglomerates indicating the re-establishment of a fluvial system post-lava emplacement.	Chapter 6 Fig. 3 and Log 8.
Hjalparfoss	Rootless cones and Lava flow field	20-40 m thick sequence of curvi-columnar jointed lava flows overlying volcaniclastic sandstones. Abundant rootless cone development in lava flows.	Rootless cones form as the result of explosive interaction between lava and water bearing substrates. As lava is emplaced onto saturated sediments they become compressed or compacted leading to flexure in a lavas basal crust. Tensile failure of the basalt crust allows MCFI (Moltern-Fluid Coolant Interaction Processes) to occur between the lava and sediment (Hamilton et al., 2010 and references therein). Rootless cones usually occur in areas of water logged sediment such as in shallow lakes, wetlands or outwash plains (Fagents and Thordarson, 2007).	Chapter 6 Fig. 4, 5.

Table 8.1 Localities in the Hreppar formation with descriptions and interpretations of each.Supporting logs and photos are provided in the appendix to this chapter.

The Hreppar formation is lithologically diverse in terms of the type and origin its different volcanic different components. Rocks deposited in sub aerial settings include thick lava flows and fluvial sandstones that contain highly localized hyaloclastite deposits and products of lava-water interaction (such as peperites and rootless cones) (Table 8.1).

8.1.4 Hreppar Formation Interpretation

The general development of the hyaloclastite system in the Hreppar formation is summarized in figure 8.3. Initially a fluvial system supplies sedimentary material to the basin through bedload transport. Cones of volcanogenic alluvial sediment develop in a marine setting (Stage 1). Subsequent volcanic activity means the lowest point in the topography (flood plain) becomes enveloped by lava flows which interact with saturated ground (forming rootless cones e.g. Hamilton et al., 2010) or within river systems themselves (forming hyaloclastite dams e.g. Hamblin, 1994 which can be breached and reworked into a fluvial system e.g. Tolan and Beeson, 1984; Fenton et al., 2006). Interaction with unlithified sediment also leads to the formation of peperite (mixing of hot lava and sediment e.g. White et al., 2000) as

has been documented palageogene volcanic sequences of Mull, Scotland (Brown and Bell, (2007), which occurs at the base of lava flows in the Fossness locality.

Once lava envelops the fluvial sequence and reaches the basin margin lava enters the sea causing hydromagmatic fragmentation processes. Depending on the degree of wave interaction, slope angle, fragmentation efficiency, lava flow morphology, hyaloclastite material can be sorted into complex lithofacies arrangements (such as Stóri-Núpur, chapter 4) or can form homogenous prograding sets which may be a function of environment (e.g. these deposits are characteristic of lacustrine settings, Pedersen et al., 1998; Skilling, 2002). In the case of Stóri-Núpur, initial fragmentation causes sheet-like deposits to enter the basin that act as a surface for hyaloclastite accumulation (Stage 3). The hyaloclastite deposit can then either prograde simply (forming clinoforms) into the basin or form a more complex system (with chaotic lithofacies arrangements). At this point fine sediment plumes can mobilise as concentrated density currents (Tribble, 1991; Sansone et al., 1991), which develop into toe-set units (Porębski and Gradzinski, 1990) (Stage 4) and may be imaged in seismic as bottom sets (Planke et al., 2000).

Periodically sea level rises, e.g., during interglacial periods or via large-scale delta subsidence produces backstepping hyaloclastite systems (Jones and Nelson, 1970; Schmincke et al., 1997; Wright et al., 2012) (Stage 5). Importantly, backstepping of the system moves the point of lava water entry and any fluvial system that could potentially develop during periods of volcanic quiescence. Slumping at the front of the delta adds further complexity to the hyaloclastite system (Chapter 4 and Skilling, 2002). This potentially juxtaposes different lithofacies types during pauses in delta progradation (Sansone and Smith, 2006).

If the stages above are placed conceptually into a depth-equivalent framework then a regional-scale deposit contains a high degree of lithofacies heterogeneity (Fig. 8.3, lower). As such intersection of the sequence at any one of the 5 localities shown in figure 8.1 would intersect not only lava and hyaloclastite (e.g. Fig. 8.1 - 1) but also a mixture of all lithofacies in table 6.

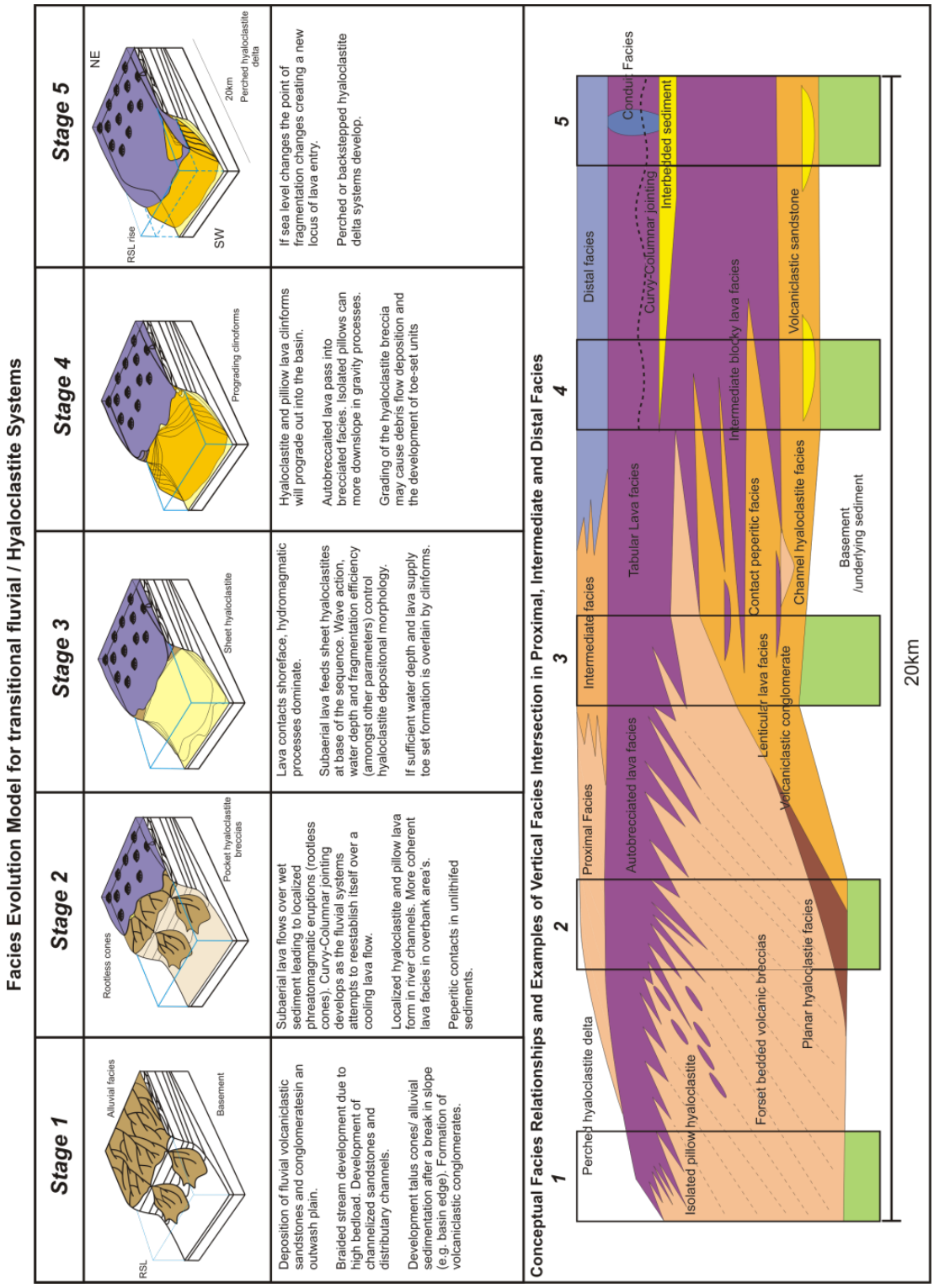

Figure. 8.3 Lithofacies evolution model for the transition from hyaloclastite to fluvial volcanic systems. See text for details.

8.1.5 Implications for Seismic Study

The density and Vp variations in hyaloclastite deposits illustrated in chapter 6 allow the calculation of the reflection coefficients for different lithofacies from hyaloclastite sequences logged from field studies. This study showed that coherent reflectors could be generated between, for example, sedimentary contacts (i.e. between hyaloclastite lithofacies), volcanic contacts (i.e. between lava flows and hyaloclastite), diagenetic contacts (between palagonite and not palagonitized hyaloclastite deposits) or structural contacts (i.e. fault scarps), which when combined with the large-scale heterogeneity of sequences (section 8.1.4) containing hyaloclastite deposits at seismic scales questions whether models of hyaloclastite systems at smaller scales (e.g. Jones and Nelson, 1970; Moore et al., 1973) can be scaled-up for use in the subsurface at the scale of lava deltas in the Faroe-Shetland Basin, for example. Current models for the generation of hyaloclastite deposits in the FSB suggest that the high amplitude reflectors represent individual lava flows (Wright et al. 2012). However, chapter 7 suggests that seismic reflectors mask a complex volcanic stratigraphy (also, Fig. 8.4) and from chapter 4 it is known that hyaloclastite deposits in different settings create complex lithofacies stacking patterns. Therefore, these models may be missing a lot of internal variation in hyaloclastite deposits.

Chapter 6 (Section 6.4.2) shows that significant Reflection Coefficients can be generated from variations in hyaloclastite lithofacies (at normal incidence). However, volcanic contacts such lava flows or pillow lavas, due to the scattering properties of basalt layers, and the difficulties of seismic imaging below thick basalt sequences (Maresh and White, 2005; Jergen et al., 2009) can mask heterogeneity in hyaloclastite deposits and produce generally low amplitude events. An example of this is shown in figure 8.4 where the seismic section for well 213/27-4 in the Rosebank Field masks variation seen in the FMI log distribution of volcanic lithologies (West of Shetland Basin, UCKS see Chapter 7). In this case, a combination of a ~ 200m thick succession of basalt lava flows, volcanic breccias, volcaniclastic and siliciclastic rocks from the Rosebank Upper Volcanic Sequence (UVS) produces only one coherent reflector and therefore masks volcanic heterogeneity.

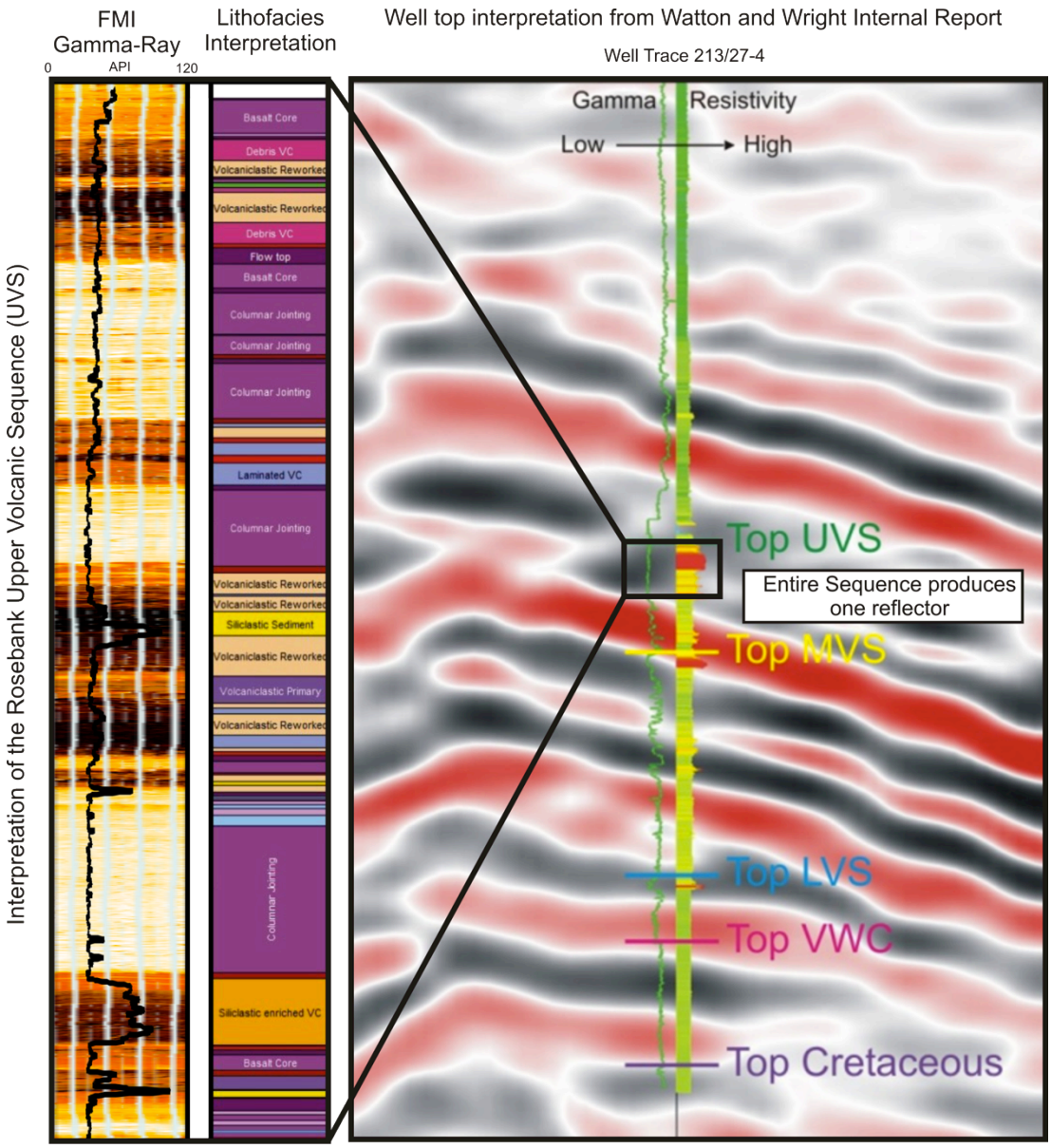

Figure. 8.4. A comparison of lithofacies recorded from bore-hole imaging 9see chapter 7) vs. the seismic resolution over that interval. One reflector characterizes all lithologies. Seismic section from Watton and Wright 2010 internal DONG Report. Logged section c. 200 ft.

In addition to lithofacies variation and the sub-basalt problem surface roughness can also degrade the seismic image. Surface roughness is calculated from x, y, z coordinate data. Roughness, defined by the Hurst number, quantifies the fractal properties of the media (Saupe, 1988). Attempts to characterise the scattering effect of the surface of basalt lava flows based upon surface roughness have

identified that the surfaces have a fractal nature (Nelson, 2010). In the case of the passage zone (lava-water contact) it is not known whether a morphological fractal pattern exists in terms of x, y, z parameter space. However, at small scales the transition between subaerial lava flows and hyaloclastite can be highly irregular. Even when scaled in 2D the passage zone still displays irregularity (e.g. Smellie, 2008; Watton et al., 2013) that is likely to be much greater than the variation seen at the surface of a lava flow. This observation suggests the waveform would be scattered and hence the transition from basalt to hyaloclastite will be ill-defined in a seismic image. Conversely, contacts between two packages of different hyaloclastite lithofacies or diagenetic boundary can be sharp. If a relatively planar contact between units is created the scattering effect is reduced leading to a well-defined, more coherent reflector development.

An exception to this is where seismic imaging is capable of resolving individual lava flows (Holford et al., 2012). This is case the interpreted hyaloclastite deposit is probably represent lava deltas analogues field examples (e.g. Skilling, 2002). However, even without the effect of basaltic overburden scattering the wave-field, the resolution of recorded lava flows is still an order of magnitude greater than flow diversion features observed in the Nesjahraun which are thought to in part give rise to hyaloclastite lithofacies heterogeneity (see Chapter 4) (Fig. 8.5).

Therefore, as the scale of the lateral extent of the Hreppar formation approaches that of recorded seismic reflection surveys, and it is known that heterogeneities can be masked in mixed hyaloclastite and basalt sequence, it implies that high amplitude reflections in the subsurface may not only represent single lava flows (e.g. Wright et al. 2012), but rather packages of lava flows linked to eruptive events with interbedded fluvial deposits which re-established during inter-eruption hiatus periods (e.g. Watton et al. 2013). Seismic reflection studies also suggest that prograding reflectors do not need to be formed from "pods" of volcanic material (e.g. Kiørboe, 1999), but are just as likely to be contacts between different hyaloclastite/lava lithofacies, diagenetic boundaries or slump-induced faults. In addition, a lava delta system in an active basin will incorporate a variety of lava flow morphologies, rootless cones, fluvial deposits and hyaloclastite deposits formed in both the marine and fluvial environments. Therefore, the fore-delta system is complex and cannot be simply interpreted as an individual lava flow.

In active flood basalt provinces the establishment of rivers on the lava surface may be quite different to that of Iceland today. The formation of rivers may be inhibited and instead may favour relatively homogenous lava and hyaloclastite sequences. However, significant fluvial deposits can be generated in such settings especially at the margins of the flow field, which suggest that observations in Iceland may be at least partially representative of these systems (e.g. FSB – Chapter 7, Ellis et al., 2002; or the Columbia River Flood Basalt Group, Reidel, 1998). Moreover, fluvial system establishment is also dependant on the proximity to the eruption site controlling the volume of lava supply (unknown for the FSB). For this reason seismic observations need to be tied with well log data and FMI data where available in order to more accurately determine seismic reflectors and aid interpretations.

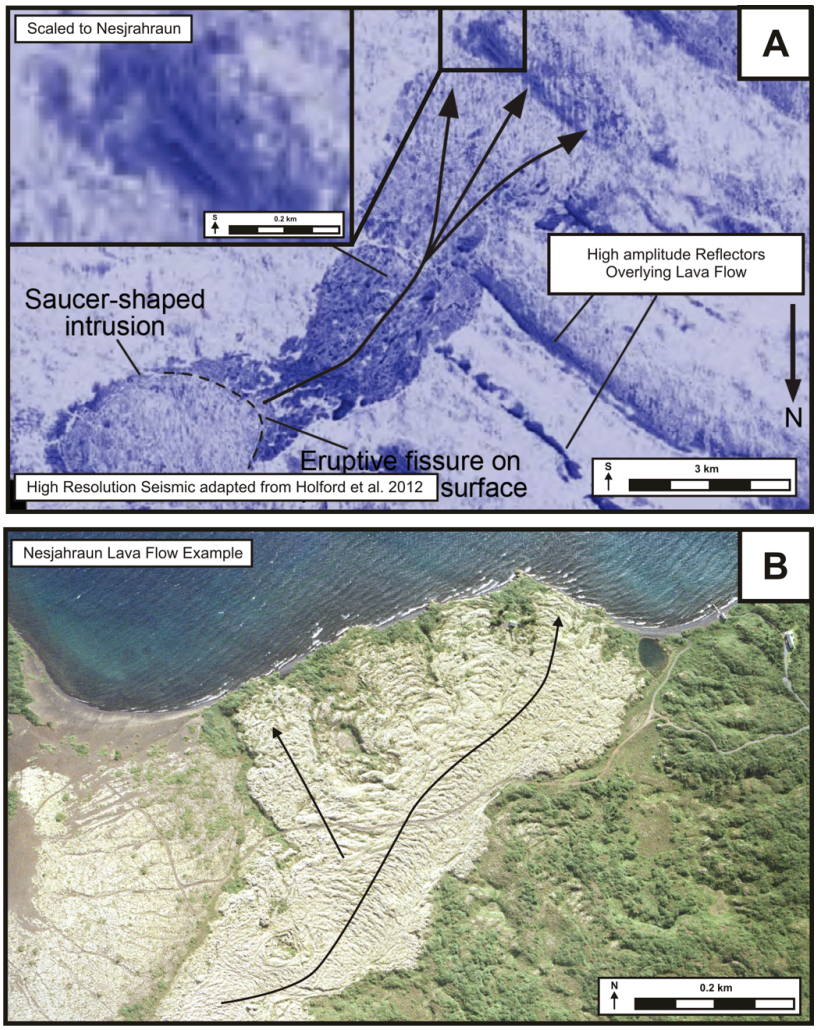

Figure. 8.5. A) High-resolution seismic imaging of a top lava flow with limited overburden (adapted from Holford et al., 2012) vs. B) A high-resolution aerial photo from the Nesjahraun (NERC Aerial Survey IPY 7-02 [http://arsf.nerc.ac.uk/data/archive.asp]). Inset in A) is the seismic image at the scale of B) showing the limited resolution of seismic imaging.

8.1.6 Hyaloclastite Deposits in Petroleum Systems

Although hyaloclastite delta systems may form an unlikely target for petroleum exploration they can cover, or be in present in, active petroleum systems. Understanding them can help with depth conversion or characterisation of the seismic pile (Chapter 6 and section 8.1.5). Significant (~ 1 Tcf) silicic petroleum reservoirs exist within hyaloclastite-pillow dome complexes occur offshore Japan (Yamada and Okana, 2005, 2007). The connectivity of these reservoirs is primarily determined by fractures and clay formation (following devitrification of volcanic glass, Yamada and Okana, 2007). This, and other fractured volcanic reservoirs, highlights the potential importance of volcanic hosted reservoirs.

In basaltic hyaloclastite systems the rate of palagonite formation either with depth (Moore, 2001), or with time and temperature (Jakobsson and Moore, 1986; Stroncik and Schmincke, 2002), is much greater than in non-quenched volcanic rocks, meaning that the connectivity of the pore throats can be drastically reduced soon after burial. However, if alteration does not occur, then significant aquifers can develop in basaltic pillow lava hyaloclastite systems (e.g., the Columbia River Basalt Group U.S.A., Tolan pers. comm. see chapter appendix). Characterising lateral lithofacies variations in hyaloclastite systems is important in understanding potential fluid migration pathways or to assess their regional potential as a seal rock.

Scutter, (2003) and Roger et al., (2006) show examples of petroleum systems within complex volcanic successions. Both studies indicate that hot fluid circulation can result in secondary porosity (through removal of calcite and zeolite phases) especially when the fluid is CO_2 charged (Rogers et al., 2006). The early precipitation of calcite and zeolite phases acts to maintain the minus cement porosity (porosity now filled with zeolite) in hyaloclastite deposits (Walton and Schiffman, 2003). Therefore, secondary dissolution of the calcite/zeolite phase could greatly enhance porosity. Knowledge about key basin-wide parameters, such as the ambient geothermal gradient and burial or uplift rates, and rock-specific properties such as the original lava geochemistry and burial porosity, makes it possible to understand how

hyaloclastite deposits may act in a volcanic-affected petroleum basin (Fig. 6.50). Depending on the nature of the hyaloclastite rocks and specific hyaloclastite properties (such as glass or zeolite mineralogy) the deposit may act to halt migration by forming a seal and a stratigraphic trap (as in Fig. 8.6), act as a reservoir, or have no effect at all.

Therefore the identification of zeolite mineral types and their distribution with depth may help determine the temperature of fluids at the time of deposition and explain porosity variations. Such information is highly useful in determining the timings and pathways for hydrocarbons in the subsurface. Recognition of marine microfossils either directly in drill cuttings or by proxy in SGR logs may also help the basin-wide correlation of sequences containing hyaloclastite deposits.

Furthermore hyaloclastite deposits, like many volcanic rocks, have been proven in this thesis to have high Vp/Vs separation (chapter 6). Klarner and Klaner, (2012) have shown that high Vp/Vs ratios in volcanic rocks when present in a interbedded volcanic sequence lead to AVO (amplitude vs. offset) anomalies that can be confused with similar anomalies produced when gas or oil is charging a reservoir. Therefore, understanding key hyaloclastite rock physics is potentially important in hydrocarbon exploration.

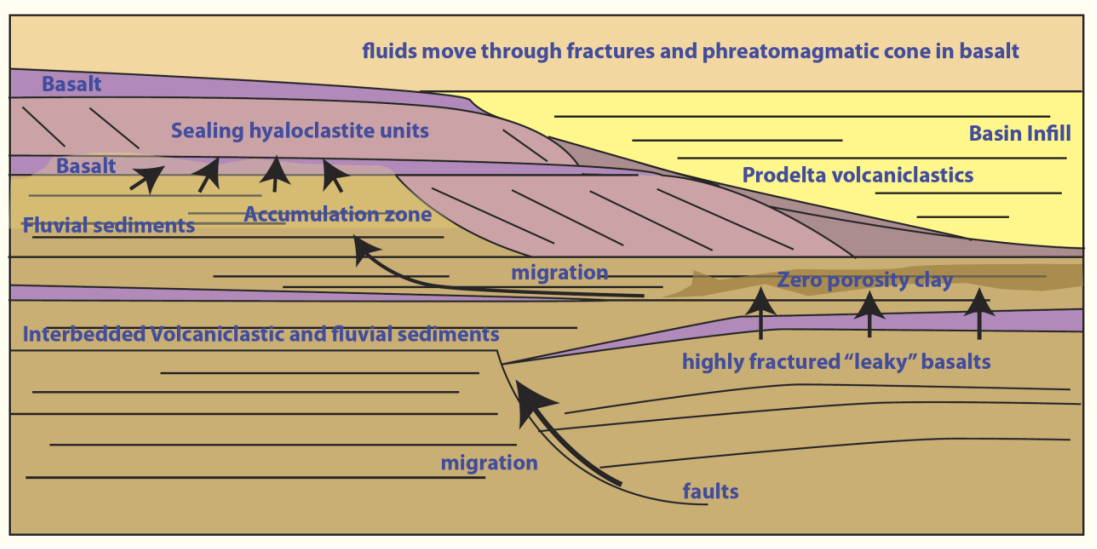

Figure. 8.6. A conceptual model of hyaloclastite deposits in petroleum systems acting as a seal presenting hydrocarbon migration. See section 6.7.5 for details.

8.2 Conclusions

8.2.1 Hyaloclastite Deposits and Lava Delta Formation

Field data from Stóri-Núpur and Hjörleifshöfði (Chapter 4) provides additional constraints on lava delta formation in basaltic systems. Both examples show distinct hyaloclastite depositional profiles reflecting localised extrusion pathways and syn-sediment reworking that controlled the 3D lithofacies architecture. Small lava breakouts, variations in lava flow morphology and lava tubes act to produce complex 3D lithofacies heterogeneities unless the lava flux is sufficiently high, in which case, pāhoehoe in large inflated sheets promotes fragmentation of a wide area and promotes clinoform development. Conversely, if lava flux is high, yet the available accommodation space is limited, then more sheet-like flows will develop. In Surtseyan settings, reworking is promoted due to the inherent instability of the steep volcano flank leading to mass movement and slump structures. This thesis highlights that distinctions should be made between hyaloclastite deposits of syn-sedimentary deposition and those dominated by primary fragmentation and near-shore deposition.

8.2.2 Hjörleifshöfði – A Unique example of Surtseyan Volcanism

Hjörleifshöfði is a well exposed partially preserved Surtseyan edifice in southern Iceland (Chapter 5). The evolution of Hjörleifshöfði can be split into five phases charting the submarine to emergent construction of the edifice. It is unique, as it records a phase of silicic volcanism attributed to the neighbouring Katla volcanic system. Major and Trace element geochemistry has proved that silicic volcanism relates to the Sólheimar Ignimbrite meaning that late stage effusive volcanism on Hjörleifshöfði occurred no earlier than 12,383 C14 years BP (during the last late glacial maximum, when sea level was at its highest). The extensive cross-sectional exposure of Hjörleifshöfði allows a comparison to be made to 2D seismic surveys revealing how hyaloclastite deposits associated with surtseyan edifices may be interpreted.

8.2.3 Tying Hyaloclastite Deposits to Wire-Line Logs datasets

Velocity/density modelling of hyaloclastite deposits is difficult due to diagenetic processes and lithofacies variation. Certain hyaloclastite lithofacies share similarities with some carbonate and siliciclastic rocks, and therefore accurate lithofacies characterisation from remote data is needed before modelling can be used. However, in general hyaloclastite deposits lie on their own trend that is independent of existing velocity /density models which has implications for both depth conversion and the calculation of reflection coefficients that govern the reasons behind prograding foresets. The density of hyaloclastite deposits is likely to remain constant with increasing velocity due to pore-space replacement with palagonite and hyaloclastite deposits do not follow a Nafe-Drake trend. Porosity modelling indicates that pore spaces are rapidly shut off once hyaloclastite deposits are in the palagonite zone.

However, before entering the palagonite zone hyaloclastite deposits are likely to resist compaction due to high coordination numbers in particles and basalt clasts that support the structure. Hyaloclastite deposits also show high Vp/Vs separation, like other volcanic rocks, which is important in hydrocarbon exploration as it can cause AVO anomalies (see section 8.1.6). Wire-line log responses are closely linked to the dominant interstitial secondary minerals and phenocryst components (in this case olivine). P-wave velocity is closely linked to olivine phenocryst abundance within hyaloclastite producing a significant variation in Vp response (c. 0.3 km/s).

Hyaloclastite deposits form part of the sedimentary rock record and therefore can contain fossils. The chemical structure and properties of zeolite minerals that leach phosphorus from dead marine micro-organisms can lead to hydroxi-apatite growth.

8.2.4 FMI use in Volcanic Sequences

FMI log analysis of mixed volcanic and volcaniclastic rocks in the Rosebank field, Faroe-Shetland Basin, has allowed an accurate characterisation of distinct volcanic lithofacies and the discrimination of siliciclastic rocks. Internal lava flow features, contact relationships and joint networks can be readily identified. Such a

tool is extremely useful in identifying potential migration pathways, seals and reservoirs in hydrocarbon-bearing basins containing volcanic and siliciclastic rocks. FMI has also proved useful in characterising complex volcanic packages, which can either aid the interpretation of seismic data or highlight the limitations of seismic resolution in volcanic settings.

8.2.5 Implications for Hyaloclastite Deposits in Seismic Surveys

The variation in hyaloclastite deposits cannot be resolved on seismic scales. Field observations of complex hyaloclastite and fluvial systems from Iceland indicate high degrees of lithofacies heterogeneity, which are masked in seismic surveys by lava flows due to attenuation and scattering. Furthermore, this study raises questions as tow whether models of hyaloclastite systems developed in the field can be accurately scaled into the subsurface if lithofacies variations and the original scale of the system are not known.

8.3 Future Work

General future work in this field should include:

1. Assessment of large scale (up to 1 km) hyaloclastite deposits (e.g. those in Greenland) in the light of new models presented in Chapter 4 to better constrain depositional mechanisms in hyaloclastite deposits.
2. Measure additional core material to further add to a hyaloclastite density database allowing clarification of the velocity density trends in Chapter 6. This could be developed into a useful predictive tool that could aid hydrocarbon exploration.
3. Understand the microtextural causes behind the high Vp/Vs separation in hyaloclastite deposits and other volcaniclastic rocks.
4. Explore the relation between FMI image logs and core data more fully where core data would allow. This project was constrained to good quality FMI data from the Rosebank field however other volcanic systems in the future could yield important information that would expand on the textural data base. Comparing Electron-capture (Major element proxy) data to FMI would yield positive results in the accurate assessment of volcaniclastic deposits.

5. Seismic modelling of hyaloclastite deposits to produce 2D reflection lines and the depth conversions of actual hyaloclastite seismic data to accurately compare the depositional profile of hyaloclastite deposits from field examples to seismic datasets.
6. Dimensional analysis of the passage zone to determine surface roughness and scaling relationships (if any). This would allow for more accurate interpretations of the top surface of a hyaloclastite interval in the subsurface.

8.3.1 Rock Property Analysis

During the thesis rock property analysis (porosity and permeability) was to be carried out on hyaloclastite samples recovered from Iceland. However, as mentioned in Chapter 2 drilling of the samples proved difficult. X-ray CT analysis proved that even in good recovered core pervasive drilling-induced fractures and clast movement caused by drill bit torque invalidate any results. Although these concerns were raised testing of several core samples at University College London was performed in 2012. These measurements were to test effective permeability a different effective stresses to simulate confining pore pressures. None of the samples created from c. 300 kg for rock samples produced a reliable result, and many samples were aborted due to water-soluble clays becoming mobilized under pressure. Recommendations for future attempts to core and test hyaloclastite samples are:

1. Characterise the clay phase to assess whether water is a suitable for simulating pore pressure effects.
2. Scan the sample using X-ray CT, which is a non-destructive process and there is potential to model permeability based upon calibrated results. This helps quantify unknowns if high permeability values are recorded.
3. Use a gas system to measure permeability because fluid systems can dislodge matrix material. This is problematic if effective stress measurements are needed.

8.3.2 Correlation of Volcanic Units

PEF or the photoelectric effect is a wire-line log of the photoelectric absorption properties of a formation (see chapter 2). Fluids have very little effect of the PEF log and therefore it is a measure of the rocks matrix properties. This makes it

particularly useful for volcanic and volcaniclastic rocks because most volcaniclastic rocks have higher PEF values than siliciclastic counterparts. The PEF log is particularly susceptible to clay, and magnesium- and iron-bearing minerals (Rider, 1996; Helm-Clark et al., 2004), all of which are abundant in volcaniclastic rocks. In this section we describe how these preliminary observations could help develop a new volcanic stratigraphy for the Rosebank Field when used in conjunction with recovered FMI datasets.

Volumetric Cross-Section

The volumetric cross-section is calculated from the photoelectric factor (PEF) and the density to give photoelectric absorption in barns/cm^3. Figure 8.7 shows how this may be applied to large volcaniclastic sequences within a variety of wells that show distinct jumps in the PEF response. This technique can be applied to all well data to differentiate between units. The largest separation in PEF values is observed in the basalt units. It is possible to subdivide the upper middle and lower volcanic sequences in the Rosebank (chapter 7) into nine events based upon PEF value and geographical position in the field.

Table 8.2

Acronym	Name	Characteristic PEF Value (barns/cm^3)
LVC	Lower Volcanic Sequence	4
LLVS	Lower Lower Volcanic Sequence	4.2-5
ULVS	Upper Volcanic Sequence	5.5-6
MVSN	Middle Volcanic Sequence North	5.5
LMVS	Lower Middle Volcanic Sequence	5-5.5
UMVS	Upper Middle Volcanic Sequence,	4-4.5
LUVS	Lower Upper volcanic Sequence	5-5.2
UVS	Upper Volcanic Sequence	5.2-5.5
UUVS	Upper Upper Volcanic Sequence	6-6.5

Table 8.2. Abbreviations used and characteristic PEF values used in the correlation of volcanic units over the Rosebank Field.

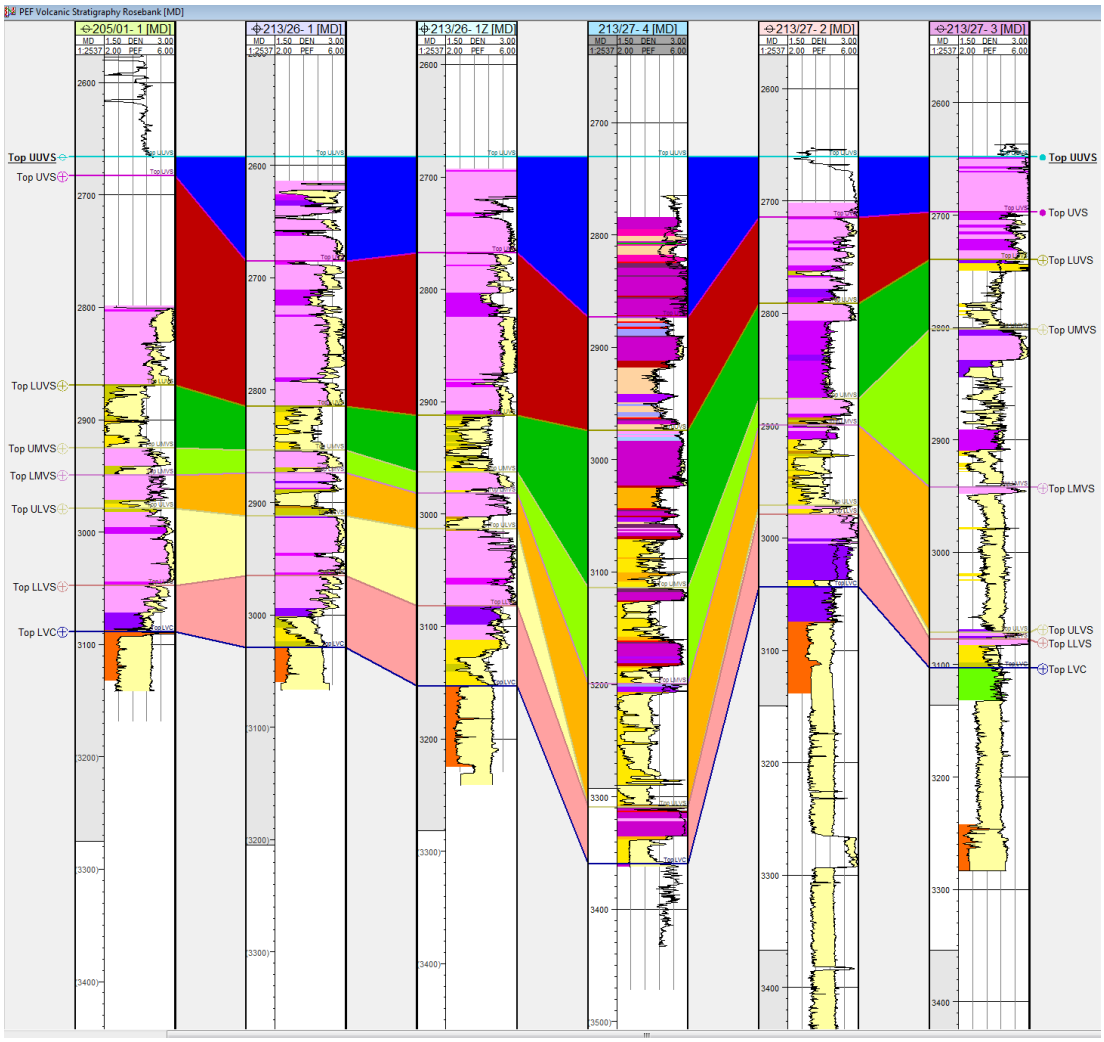

Figure. 8.7 PEF correlation with well tops modified from chapter 7. Note that the PEF log now jumps in the lower volcanic sequence to higher values. This does not reflect a casing jump. Logs flattened to top UUVS.

8.3.3 The PEF Log as a Technique for Stratigraphic Correlation

In the case of volcaniclastic rocks water-bound clay is a common occurrence due to devitrification of volcanic glass. However, if only basalt flows are considered then distinct PEF populations exist and are traceable across the Rosebank field (Fig. 8.7 and Table, 8.2). Therefore, the well tops defined in chapter 7 outlining the volcanic stratigraphy are disregarded and a new section based upon the PEF can be created. Internally within DONG Energy it is possible to cross-check this data with chemostratigraphic downhole analysis of the volcanic units, however permissions do

not allow this to be shown in the thesis and hence this section is provided in the work section. It is important to note that no casing changes are seen over jumps in the PEF logs. The tool has not been reset at PEF "jumps" and there is no simple down-hole decay of PEF values. This means that these are most likely formation-induced changes that reflect variable mineralogy.

Figure 8.8 describes a new volcanic stratigraphy for the Rosebank field (see caption). This is a revised stratigraphy based upon PEF and chemostratigraphic changes in conjunction with wire-line logs and FMI data sets (Chapter 7). The LVC consists of mainly breccia and pillow lavas and is capped with small compound flows. It has a separate chemostratigraphic signature and may represent volcanic products from a separate source. When linked with seismic data the LVS has a semi-regional extent although it source is unclear. The Middle Volcanic Sequence is best divided into two events. Both have separate PEF markers. The upper volcanic sequence can be sub divided into three field wide PEF events. Future work needs to confirm the correlation between geochemistry and PEF response.

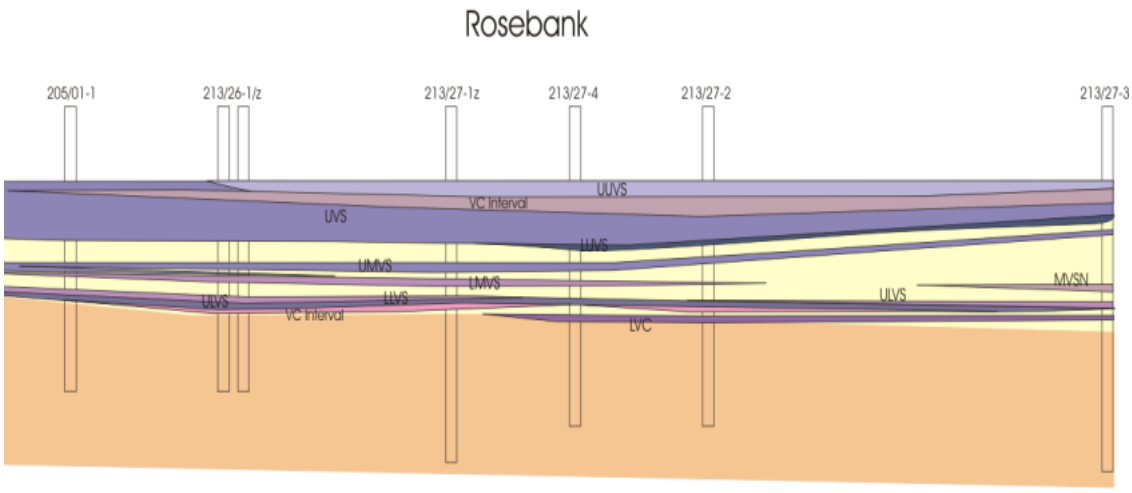

Figure. 8.8 A summary diagram indicating the volcanic stratigraphy from the Rosebank field. This is a much more accurate representation than the Petrel PEF correlation panel presented earlier. Two major volcaniclastic intervals are also shown. The MVSN refers to the middle volcanic sequence equivalent observed in 213/27-3 which has a different signature than the general middle volcanic sequence response. LVC = Lower Volcanic Sequence, LLVS = Lower Volcanic Sequence, ULVS = Upper Volcanic Sequence, MVSN = Middle Volcanic Sequence North, LMVS = Lower Middle Volcanic Sequence, UMVS = Upper Middle Volcanic Sequence, LUVS = Lower Upper volcanic Sequence, UVS = Upper Volcanic Sequence and UUVS = Upper

Upper Volcanic Sequence. The centre panel describes volcanic sourcing with the lower and middle volcanics been locally sourced albeit field wide. The Middle Volcanic Sequence has a separate source direction than the Upper and Lower Volcanic Sequences. The Upper Volcanic Sequence is a regional event which can be correlated back to the Faroes shelf.

Once a PEF (chemical) stratigraphy has been constructed it can be linked to FMI changes in a field wide context (Fig. 8.9). Therefore, it is possible to link PEF with flow package morphology in the two long FMI intervals (213/27-4 and 205/1-1). Even though a simple tripartite stratigraphy is still realised now PEF variation also corresponds to variations in lava flow morphology (compound vs. tabular), especially at the boundary between the LLVS – ULVS and the LUVS – UVS. Future work could link the variation in lava flow morphology to seismic data in order to assess the extent of the different flow fields across the Rosebank field.

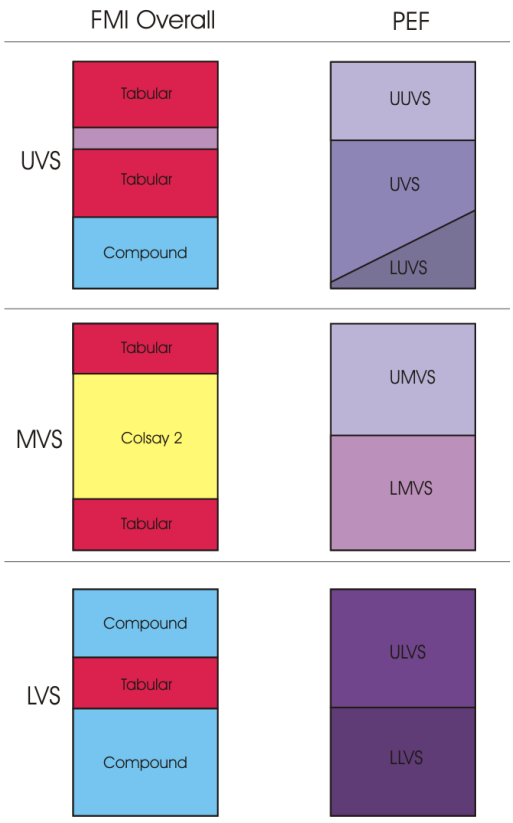

Figure. 8.9. An overall summary of well log integration using FMI analysis to show volcanic and volcaniclastic distribution

8.3.4 Assessing Hyaloclastite Foreset Geometry

Fieldwork carried out in the U.S.A involved detailed pillow lava measurements from road cuts from a number of sites (see table 8.3). Preliminary analysis of the data acquired from this fieldwork is presented here although the implications of it are not fully investigated. The aim of this work was to better understand the reasons behind the causes of clinoform development in hyaloclastite deposits and to see first-hand some of the first documented hyaloclastite deposits (e.g. Fuller, 1931a). Pillow numbers and details were recorded in tabulated sheets, explained below is how each measurement was recorded, the reader is also asked to refer to figure 8.10:

- **Pillow long axis:** Only pillows where the pillow long axis (indicating transport direction) were recorded. This data was recorded as a dip and dip direction.
- **Height vs. Width:** Pillow height and width were recorded once the transport direction is known so that measurements are made at 90°to this angle. This removes the section effect where pillows can appear wider or taller dependant on the angle they were cut.
- **Spalled Pillow Lava:** The identification of spalled pillow lavas in outcrop is often difficult due to the 3D nature of the pillow lava network. Spalled pillows were counted where the crust of the pillow was partially disturbed indicating in-situ fragmentation potentially indicating rolling, a 1:1 width to height ratio and on all sides surrounded only by hyaloclastite material.
- **Clinform Angle:** Elongate pillow lava lobes or spalling of material means that the angle of repose for pillow lava systems is reached. Recorded in these locations are the clinform angle or the general dip and dip direction of the formation at any given point. Due to the large variation in pillow lava dip and dip direction this measurement is inherently less accurate.

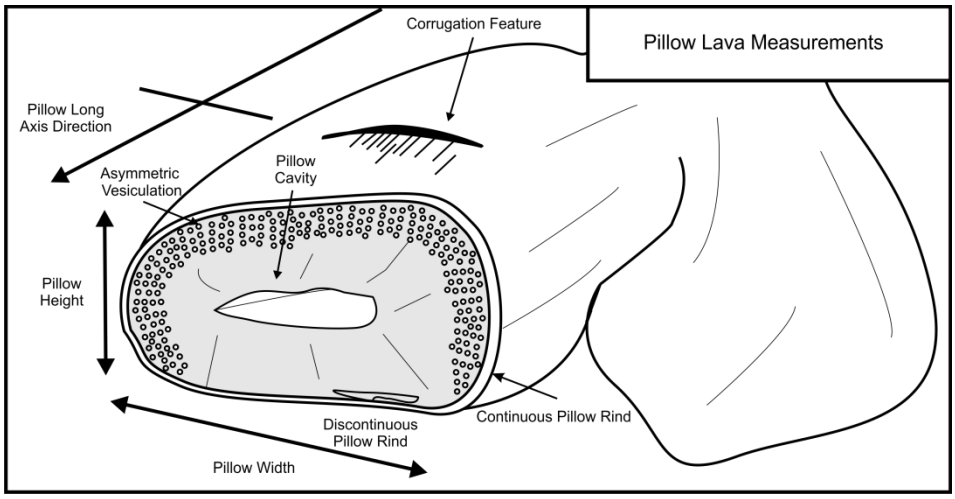

Figure 8.10. A schematic sketch of pillow lavas showing the main measurement criteria used to create pillow lava data tables

Spalled pillow lavas occur due to ductile pinching as lava flows down a steep slope close to the angle of repose (Skilling, 2002). Therefore, the total percentage of spalled pillows as function of the total amount of pillows recorded can give an accurate proxy on the extent of remobilisation and reworking. Table 8.2 plots the water depth, which is the height of the pillow lava pile from the base contact to the transition into coherent lava flows (dashed red on Fig. 8.11a), the number of spalled pillow and the number of pillows recorded in each locality.

Figure 8.11a links spalled pillow percentage, water depth and clinoform geometry together. Results suggest that there is a linear trend ($r^2 = 0.969$) between water depth and the percentage of spalled pillows. Each photograph shows the end members of water depth for measured examples showing the curvature of the clinoform angle. Therefore as spalling increases this enhances downslope mobilisation leading to more listric (tangential) clinoform geometry. If spalling is limited, clinoforms are poorly defined which reflects limited water depth. These studies are conducted where pillow lavas are forming on flat lake beds with limited breaks in slope and minimal wave action meaning that water depth is thought to be the primary control on slope angle. Therefore listric geometries develop when > 12% total spalled pillows are recorded which reflects water depths of greater than 10 m. However future studies of these deposits could constrain this trend by incorporating

more examples and more pillow lavas in addition to documenting the variety of pillow lava morphologies that exist in such systems that may act to also control progradation. Interestingly, the geometry of deep-water lacustrine examples in this study share similarities to c. 200 m thick hyaloclastite sequences from Greenland (Fig. 8.11b, Pedersen et al., 1998). This observation suggests that hyaloclastite deposits in these settings are controlled by downslope reworking possibly with limited wave interaction.

Table 8.3

Example	Basalt Province/Flow Unit	Grid Reference (UTM)	Water_Depth	Number_of_ Spalled_Pillo ws	Total_Rec orded_Pill ows	Spalled_Pillows _%
Dalles	CRBG/Preist Rapids	10T 0645475, 5051531	4	2	83	2.409638554
Strike_Ri ver_Dam	Snake River Plain	11T 0583754, 4710200	8	9	138	6.52173913
Lewiston _Grade	CRBG/Rosa	11 T 0494207, 5133453	3	0	17	0
Crescent _Bar	CRBG/Grand Rhonde	10 T 0722047, 5236170	13	22	131	16.79389313
Sunland_ Estates	CRBG/Grand Rhonde	10T 0725902, 5217222	8	6	60	10
Vantage_ 26	CRBG/Ginkgo	11T 0275317, 5201615	9	11	86	12.79069767

Table 8.3 Location of pillow lava deltas from USA examples used in the preliminary study of spalled pillow abundance data to determine degree of reworking.

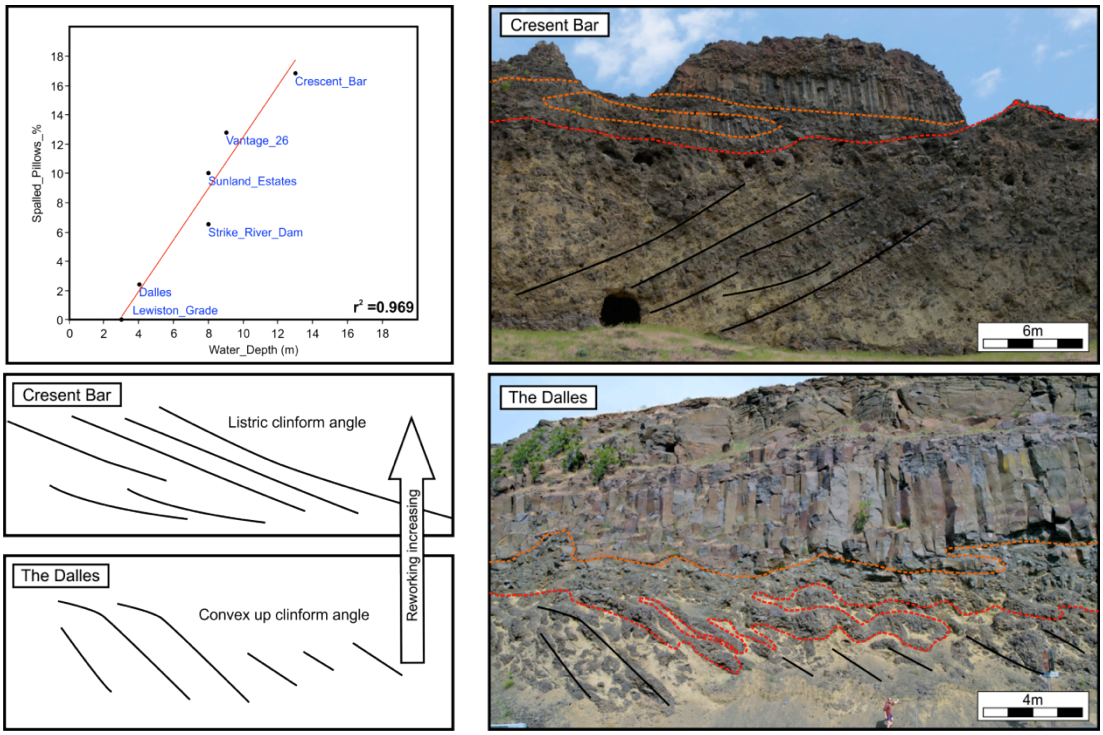

Figure. 8.11a. % of spalled pillows vs. water depth showing a linear relationship indicating increasing reworking in absence of other factors such as wave action. Two end members Crescent Bar (deep water) and The Dalles (shallow water) show either listric (tangential) or convex up clinform geometries respectively.

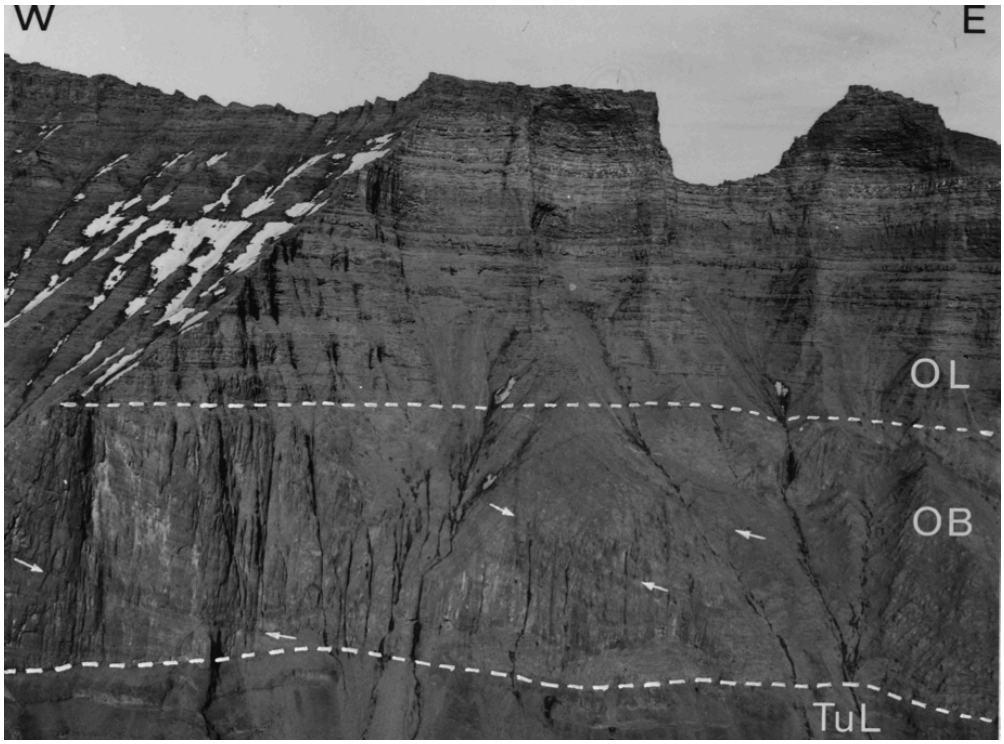

Figure. 8.11b Clinoform development in hyaloclastite deposits in Greenland. Not the similarity to the Crescent Bar (deep water) example from this study. (from Pedersen et al., 1998)

REFERENCES

Aalto, K.R., 1986. Depositional sequence of argillite, diamictite, hyaloclastite, and lava flows within the Franciscan Complex, northern California. The Journal of Geology 744–752.

Alberti, A., Armbruster, T., Artioli, G., Colella, C., Galli, E., Grice, J.D., Liebau, F., Minato, H., Nickel, E.H., Passaglia, E., 1997. Recommended nomenclature for zeolite minerals: Report of the subcommittee on zeolites of the International Mineralogical Association, Commission on New Minerals and Mineral Names. The Canadian Mineralogist 35, 1571–1606.

Alberts, L.J.H., 2005. Initial porosity of random packing: computer simulation of grain rearrangement. PhD Thesis, Deft University of Technology.

Andersen, M., S., Boldreel, L.O., SeiFaBa Group, 2009. Log responses in basalt successions in 8 wells from the Faroe-Shetland Channel - a classification scheme for interpretation of geophysical logs and case studies. In: Varming, T., Ziska, H., (ed.) Faroe Islands Exploration Conference: Proceedings of the 2nd Conference. Annales Societatis Scientiarum Færoensis 50, 364–391.

Andrews, B., 2003. Eruptive and depositional mechanisms of an Eocene shallow submarine volcano, Moeraki Peninsula, New Zealand. Geophysical Monograph Series 140, 179–188.

Archer, S.G., Bergman, S.C., Iliffe, J., Murphy, C.M., Thornton, M., 2005. Palaeogene igneous rocks reveal new insights into the geodynamic evolution and petroleum potential of the Rockall Trough, NE Atlantic Margin. Basin Research 17, 171–201.

Athy, L.F., 1930. Density, porosity, and compaction of sedimentary rocks. AAPG Bulletin 14, 1–24.

Baker, J.C., Jell, J.S., Hacker, J.L., Baublys, K.A., 1998. Origin of Recent Insular Phosphate Rock on a Coral Cay–Raine Island, Northern Great Barrier Reef, Australia. Journal of Sedimentary Research 68, 5, 1001-1008.

Bartetzko, A., Delius, H., Pechnig, R., 2005. Effect of compositional and structural

variations on log responses of igneous and metamorphic rocks. I: mafic rocks. In: Harvey, P.K., Brewer, T.S., Pezard, P.A., Petrov, V.A., (ed.) Petrophysical Properties of Crystalline Rocks. Geological Society, London, Special Publications 240, 255–278.

Batiza, R., White, J.D., 2000. Submarine lavas and hyaloclastite. In: Sigurdsson, H., Encyclopedia of Volcanoes, 361–381.

Bear, A.N., Cas, R.A.F., 2007. The complex facies architecture and emplacement sequence of a Miocene submarine mega-pillow lava flow system, Muriwai, North Island, New Zealand. Journal of Volcanology and Geothermal Research 160, 1–22.

Befus, K.S., Hanson, R.E., Lehman, T.M., Griffin, W.R., 2008. Cretaceous basaltic phreatomagmatic volcanism in west Texas: maar complex at Pena Mountain, Big Bend National park. Journal of Volcanology and Geothermal Research 173, 245–264.

Behncke, B., 2004. Late Pliocene volcanic island growth and flood basalt-like lava emplacement in the Hyblean Mountains (SE Sicily). Journal of Geophysical Research: Solid Earth (1978–2012) 109, B09201, 1-20.

Bergh, S.G., Sigvaldason, G.E., 1991. Pleistocene mass-flow deposits of basaltic hyaloclastite on a shallow submarine shelf, South Iceland. Bulletin of Volcanology 53, 597–611.

Berndt, C., Planke, S., Alvestad, E., Tsikalas, F., Rasmussen, T., 2001. Seismic volcanostratigraphy of the Norwegian Margin: constraints on tectonomagmatic break-up processes. Journal of the Geological Society 158, 413–426.

Birks, H.H., Gulliksen, S., Haflidason, H., Mangerud, J., Possnert, G., 1996. New radiocarbon dates for the Vedde Ash and the Saksunarvatn Ash from western Norway. Quaternary Research 45, 119–127.

Bishop, P., 1985. Early Miocene flow-foot breccia from the Upper Lachlan Valley, New South Wales: Characteristics and significance. Australian Journal of Earth Sciences 32, 107–113.

Björnsson, A., 1985. Dynamics of crustal rifting in NE Iceland. Journal of Geophysical Research 90, 10151–10.

Björnsson, H., 2003. Subglacial lakes and jökulhlaups in Iceland. Global and Planetary Change 35, 255–271.

Blackbourn, G., 1990. Cores and Core Logging for Geologists. Whittles Publisher, Caithness.128 pp.

Bluck, B.J., 1982. Hyalotuff deltaic deposits in the Ballantrae ophiolite of SW Scotland: evidence for crustal position of the lava sequence. Transactions of the Royal Society of Edinburgh Earth Sciences 72, 217–28.

Boldreel, L.O., 2006. Wire-line log-based stratigraphy of flood basalts from the Lopra-1/1A well, Faroe Islands. In: Chalmers J. A., Waagstein R., (ed.) Scientific Results from the Deepened Lopra-1 Borehole, Faroe Islands. Geological Survey of Denmark and Greenland Bulletin 9, 7–22.

Bonatti, E., Harrison, C.G.A., 1988. Eruption styles of basalt in oceanic spreading ridges and seamounts: Effect of magma temperature and viscosity. Journal of Geophysical Research: Solid Earth (1978–2012) 93, 2967–2980.

Bonforte, A., Bonaccorso, A., Guglielmino, F., Palano, M., Puglisi, G., 2008. Feeding system and magma storage beneath Mt. Etna as revealed by recent inflation/deflation cycles. Journal of Geophysical Research: Solid Earth (1978–2012) 113, B5, 2156-2202.

Boyle, J.F., Robertson, A.H.F., 1984. Evolving metallogenesis at the Troodos spreading axis. In: Gass, I.G., Lippard, S.J., Shelton, A.W., Ophiolites and Oceanic Lithosphere. Geological Society, London, Special Publications 13, 169–181.

Brand, B.D., White, C.M., 2007. Origin and stratigraphy of phreatomagmatic deposits at the Pleistocene Sinker Butte volcano, western Snake River Plain, Idaho. Journal of Volcanology and Geothermal Research 160, 319–339.

Branney, M.J., Kokelaar, B.P., 2002. Pyroclastic density currents and the sedimentation of ignimbrites. Geological Society, London, Memoirs 27, 152 pp.

Brewer, T.S., Harvey, P.K., Haggas, S., Pezard, P.A., Goldberg, D., 1999. Borehole images of the ocean crust: case histories from the Ocean Drilling Program. In: Lovell, M., Williamson, G., Harvey, P., Borehole Imaging: Applications and Case Histories. Geological Society, London, Special Publications 159, 283–294.

Brocher, T.M., 2005a. Empirical relations between elastic wavespeeds and density in the

Earth's crust. Bulletin of the Seismological Society of America 95, 2081–2092.

Brocher, T.M., 2005b. Compressional and shear wave velocity versus depth in the San Francisco Bay Area, California: rules for USGS Bay Area Velocity Model 05.0.0. US Geological Survey, Open-file Report, 2005-1317. [http://pubs.usgs.gov/of/2005/1317/]

Brossy, C.C., 2006. Fluvial response to intra-canyon lava flows, Owyhee River, southeastern Oregon. Masters Thesis, Central Washington University.

Brown, D.J., Bell, B.R., 2007. How do you grade peperites? Journal of Volcanology and Geothermal Research 159, 409–420.

Bücker, C.J., Delius, H., Wohlenberg, J., 1998. Physical signature of basaltic volcanics drilled on the northeast Atlantic volcanic rifted margins. In: Harvey, P.K., Lovell, M.A., Core-Log Integration. Geological Society, London, Special Publications 136, 363–374.

Busby-Spera, C.J., White, J.D., 1987. Variation in peperite textures associated with differing host-sediment properties. Bulletin of Volcanology 49, 765–776.

Buysch, A., Pechnig, R., Harms, U., 2000. Geophysical downhole measurements in the scientific drillhole HSDP Hilo/Hawaii: Core-log integration to characterize effects of alteration and structures. Eos Transactions 81, F1349.

Caine, J.S., Evans, J.P., Forster, C.B., 1996. Fault zone architecture and permeability structure. Geology 24, 1025–1028.

Calvès, G., Schwab, A.M., Huuse, M., Clift, P.D., Gaina, C., Jolley, D., Tabrez, A.R., Inam, A., 2011. Seismic volcanostratigraphy of the western Indian rifted margin: The pre-Deccan igneous province. Journal of Geophysical Research: Solid Earth (1978–2012) 116, B1, [DOI: 10.1029/2010JB000862].

Carlisle, D., 1963. Pillow breccias and their aquagene tuffs, Quadra Island, British Columbia. The Journal of Geology 71, 48–71.

Carr, P.F., Jones, B.G., 2001. The influence of palaeoenvironment and lava flux on the emplacement of submarine, near-shore Late Permian basalt lavas, Sydney Basin (Australia). Journal of Volcanology and Geothermal Research 112, 247–266.

Cas, R.A., Wright, J.V., 1991. Subaqueous pyroclastic flows and ignimbrites: an assessment. Bulletin of Volcanology 53, 357–380.

Cas, R.A.F., 1992. Submarine volcanism; eruption styles, products, and relevance to understanding the host-rock successions to volcanic-hosted massive sulfide deposits. Economic Geology 87, 511–541.

Casaing, R., 1951. Application of Electron Probes to Local Chemical and Crystallographic Analysis. University of Paris.

Cashman, K.V., Thornber, C., Kauahikaua, J.P., 1999. Cooling and crystallization of lava in open channels, and the transition of Pāhoehoe Lava to'A'ā. Bulletin of Volcanology 61, 306–323.

Castagna, J.P., Batzle, M.L., Eastwood, R.L., 1985. Relationships between compressional-wave and shear-wave velocities in clastic silicate rocks. Geophysics 50, 571–581.

Castagna, J.P., Batzle, M.L., Kan, T.K., 1993. Rock Physics – The link between rock properties and AVO response. In: Castagna, J.P., Backus, M., (ed.), Offset-dependent reflectivity – theory and practice of AVO analysis: Investigations in Geophysics 8, 135-171.

Chadwick, W.W., Dziak, R.P., Haxel, J.H., Embley, R.W., Matsumoto, H., 2012. Submarine landslide triggered by volcanic eruption recorded by in situ hydrophone. Geology 40, 51–54.

Chen, Z., Yan, H., Li, J., Zhang, G., Zhang, Z., Liu, B., 1999. Relationship between Tertiary volcanic rocks and hydrocarbons in the Liaohe basin, People's Republic of China. AAPG bulletin 83, 1004–1014.

Cheung, P.S., 1999. Microresistivity and ultrasonic imagers: tool operations and processing principles with reference to commonly encountered image artifacts. In: Lovell, M., Williamson, G., Harvey, P., Borehole Imaging: Applications and Case Histories. Geological Society, London, Special Publications 159, 45–57.

Christensen, N.I., Mooney, W.D., 1995. Seismic velocity structure and composition of the continental crust: A global view. Journal of Geophysical Research: Solid Earth (1978–2012) 100, 9761–9788.

Christie, P., Gollifer, I., Cowper, D., 2006. Borehole seismic studies of a volcanic succession from the Lopra-1/1A borehole in the Faroe Islands, northern North Atlantic. In: Chalmers J. A., Waagstein R., (ed.) Scientific Results from the

Deepened Lopra-1 Borehole, Faroe Islands. Geological Survey of Denmark and Greenland Bulletin 9, 23–40.

Clague, D.A., Jarrard, R.D., 1973. Tertiary Pacific plate motion deduced from the Hawaiian-Emperor chain. Geological Society of America Bulletin 84, 1135–1154.

Clague, D.A., Moore, J.G., Davis, A.S., 2002. Volcanic breccia and hyaloclastite in blocks from the Nuuanu and Wailau landslides, Hawaii. Geophysical Monograph Series 128, 279–296.

Clark, G.A., Alvárez-Fernández, E., 2004. The Mesolithic of the Atlantic façade: proceedings of the Santander symposium. Arizona State University Anthropological Research Papers 55. 262 pp.

Cole, P.D., Guest, J.E., Duncan, A.M., Pacheco, J.-M., 2001. Capelinhos 1957–1958, Faial, Azores: deposits formed by an emergent surtseyan eruption. Bulletin of Volcanology 63, 204–220.

Crovisier, J.L., Advocat, T., Dussossoy, J.L., 2003. Nature and role of natural alteration gels formed on the surface of ancient volcanic glasses (Natural analogs of waste containment glasses). Journal of Nuclear Materials 321, 91–109.

Crowe, B.M., Fisher, R.V., 1973. Sedimentary structures in base-surge deposits with special reference to cross-bedding, Ubehebe Craters, Death Valley, California. Geological Society of America Bulletin 84, 663–682.

Davis, A.S., Clague, D.A., 2006. Volcaniclastic deposits from the North Arch volcanic field, Hawaii: explosive fragmentation of alkalic lava at abyssal depths. Bulletin of Volcanology 68, 294–307.

Davison, I., Stasiuk, S., Nuttall, P., Keane, P., 2010. Sub-basalt hydrocarbon prospectivity in the Rockall, Faroe–Shetland and Møre basins, NE Atlantic. Geological Society, London, Petroleum Geology Conference Series. pp. 1025–1032.

Dean, K., McLachlan, K., Chambers, A., 1999. Rifting and the development of the Faeroe-Shetland Basin. Geological Society, London, Petroleum Geology Conference Series. pp. 533–544.

DeGraff, J.M., Aydin, A., 1987. Surface morphology of columnar joints and its

significance to mechanics and direction of joint growth. Geological Society of America Bulletin 99, 605–617.

Delius, H., Brewer, T.S., Harvey, P.K., 2003. Evidence for textural and alteration changes in basaltic lava flows using variations in rock magnetic properties (ODP Leg 183). Tectonophysics 371, 111–140.

Delius, H., Bücker, C., Wohlenberg, J., 1998. Determination and characterization of volcaniclastic sediments by wireline logs: Sites 953, 955, and 956, Canary Islands. Proceedings of the Ocean Drilling, Scientific Results 157, 29–37.

Delius, H., Buecker, C., Wohlenberg, J., 1995. Significant log responses of basaltic lava flows and volcaniclastic sediments in ODP Hole 642E. Scientific Drilling 5, 217–226.

DePaolo, D.J., Stolper, E.M., 1996. Models of Hawaiian volcano growth and plume structure: Implications of results from the Hawaii Scientific Drilling Project. Journal of Geophysical Research: Solid Earth (1978–2012) 101, 11643–11654.

Desbrands, R., 1985. Encyclopedia of Well Logging. Technip Editions, Blackwell Publishing Ltd Oxford, 585 pp.

Dezhi, B., Zigang, Q., Minggao, L., 1991. Method and application effects of the identifying igneous lithology based on fuzzy mathematics: Geological application of the well logging data. Petroleum Industry Press.

Dick, H.J., Tivey, M.A., Tucholke, B.E., 2008. Plutonic foundation of a slow-spreading ridge segment: Oceanic core complex at Kane Megamullion, 23 30′ N, 45 20′ W. Geochemistry, Geophysics, Geosystems 9, [DOI: 10.1029/2007GC001645].

Dickinson, J.A., Harb, N., Portner, R.A., Daczko, N.R., 2009. Glassy fragmental rocks of Macquarie Island (Southern Ocean): Mechanism of formation and deposition. Sedimentary Geology 216, 91–103.

Dixon, J.E., Filiberto, J.R., Moore, J.G., Hickson, C.J., 2002. Volatiles in basaltic glasses from a subglacial volcano in northern British Columbia (Canada): implications for ice sheet thickness and mantle volatiles. In: Smellie, J.L., Chapman, M.G., (ed.) Volcano-Ice Interaction on Earth and Mars. Geological Society, London, Special Publications 202, 255–271.

Donaldson, C.H., 1976. An experimental investigation of olivine morphology.

Contributions to Mineralogy and Petrology 57, 187–213.

Doré, A.G., Lundin, E.R., Jensen, L.N., Birkeland, Ø., Eliassen, P.E., Fichler, C., 1999. Principal tectonic events in the evolution of the northwest European Atlantic margin. Geological Society, London, Petroleum Geology Conference Series. pp. 41–61.

Doyle, M.G., McPhie, J., 2000. Facies architecture of a silicic intrusion-dominated volcanic centre at Highway–Reward, Queensland, Australia. Journal of Volcanology and Geothermal Research 99, 79–96.

Einarsson, T., 1967. The Icelandic fracture system and the inferred causal stress field. Iceland and Mid-Ocean Ridges. Societae Scientiarum Islandica 38, 128–139.

Ekstrom, M.P., Dahan, C.A., Chen, M.Y., Lloyd, P.M., Rossi, D.J., 1987. Formation imaging with microelectrical scanning arrays. Log Analyst 28, 294–306.

Ellefsen, M., Boldreel, L.O., Larsen, M., 2010. Intra-basalt units and base of the volcanic succession east of the Faroe Islands exemplified by interpretation of offshore 3D seismic data, in: Geological Society, London, Petroleum Geology Conference Series. pp. 1033–1042.

Ellis, D., Bell, B.R., Jolley, D.W., O'Callaghan, M., 2002. The stratigraphy, environment of eruption and age of the Faroes Lava Group, NE Atlantic Ocean. In: Jolley, D.W., Bell, B.R., The North Atlantic Igneous Province: Stratigraphy, Tectonic, Volcanic and Magmatic Processes. Geological Society, London, Special Publications 197, 253–269.

Emeleus, C.H., Gyopari, M.C., 1993. Isle of Mull, In: British Tertiary Volcanic Province, Geological Conservation Review, Chapman and Hall, London, pp. 143–183.

England, R.W., McBride, J.H., Hobbs, R.W., 2005. The role of Mesozoic rifting in the opening of the NE Atlantic: evidence from deep seismic profiling across the Faroe–Shetland Trough. Journal of the Geological Society 162, 661–673.

Fagents, S.A., Thordarson, T., 2007. Rootless volcanic cones in Iceland and on Mars. In: Chapman, M.G., The Geology of Mars: Evidence from Earth-Based Analog. Cambridge University Press, Cambridge, 151 pp.

Fenton, C.R., Cerling, T.E., Nash, B.P., Webb, R.H., Poreda, R.J., 2002. Cosmogenic

3He ages and geochemical discrimination of lava-dam outburst-flood deposits in western Grand Canyon, Arizona. Water Science and Application 5, 191–215.

Fenton, C.R., Webb, R.H., Cerling, T.E., 2006. Peak discharge of a Pleistocene lava-dam outburst flood in Grand Canyon, Arizona, USA. Quaternary Research 65, 324–335.

Finamore, S.M., Gibson, H.L., Thurston, P.C., 2008. Archean synvolcanic intrusions and volcanogenic massive sulfide at the Genex Mine, Kamiskotia Area, Timmins, Ontario. Economic Geology 103, 1203–1218.

Finney, J.L., 1970. Random packings and the structure of simple liquids. I. The geometry of random close packing. Proceedings of the Royal Society of London. A. Mathematical and Physical Sciences 319, 479–493.

Fisher, R.V., Schmincke, H.-U., 1984. Pyroclastic Rocks. Springer-Verlag, Berlin. 472 pp.

Fisher, R.V., Waters, A.C., 1970. Base surge bed forms in maar volcanoes. American Journal of Science 268, 157–180.

Fornari, D.J., Peterson, D.W., Lockwood, J.P., Malahoff, A., Heezen, B.C., 1979. Submarine extension of the southwest rift zone of Mauna Loa Volcano, Hawaii: visual observations from US Navy deep submergence vehicle DSV Sea Cliff. Geological Society of America Bulletin 90, 435–443.

Freundt, A., 1999. Formation of high-grade ignimbrites Part II. A pyroclastic suspension current model with implications also for low-grade ignimbrites. Bulletin of volcanology 60, 545–567.

Fridleifsson, I.B., 1977. Distribution of large basaltic intrusions in the Icelandic crust and the nature of the layer 2–layer 3 boundary. Geological Society of America Bulletin 88, 1689–1693.

Fuller, R.E., 1931a. The aqueous chilling of basaltic lava on the Columbia River Plateau. American Journal of Science 5, 281.

Fuller, R.E., 1931b. The geomorphology and volcanic sequence of Steens Mountain in southeastern Oregon. University of Washington Press.

Furnes, H., 1978. Element mobility during palagonitization of a subglacial hyaloclastite in Iceland. Chemical Geology 22, 249–264.

Furnes, H., Fridleifsson, I.B., 1974. Tidal effects on the formation of pillow lava/hyaloclastite deltas. Geology 2, 381–384.

Furnes, H., Fridleifsson, I.B., Atkins, F.B., 1980. Subglacial volcanics—on the formation of acid hyaloclastites. Journal of Volcanology and Geothermal Research 8, 95–110.

Furnes, H., Sturt, B.A., 1976. Beach/shallow marine hyaloclastite deposits and their geological significance: an example from Gran Canaria. The Journal of Geology 439–453.

Garcia, M.O., Haskins, E.H., Stolper, E.M., Baker, M., 2007. Stratigraphy of the Hawaii Scientific Drilling Project core (HSDP2): Anatomy of a Hawaiian shield volcano. Geochemistry, Geophysics, Geosystems 8, DOI: 2006GC001379.

Gardner, G.H.F., Gardner, L.W., Gregory, A.R., 1974. Formation velocity and density-the diagnostic basics for stratigraphic traps. Geophysics 39, 770–780.

Geirsdóttir, A., Thordarson, T., Kristjansson, L., 1993. The interactive impact of climate deteriorations and volcanic activity in facies assemblages in late Pliocene to early Pleistocene strata of the Hreppar Formation, South Central Iceland. Eos Transactions 74, 131.

Gilbert, J.S., Lane, S.J., 1994. The origin of accretionary lapilli. Bulletin of Volcanology 56, 398–411.

Gloppen, T.G., Steel, R.J., 1981. The deposits, internal structure and geometry in six alluvial fan—fan delta bodies (Devonian-Norway)—a study in the significance of bedding sequence in conglomerates. In: Ethridge, F.G., Flores, R., Recent and Ancient Nonmarine Depostional Environments; Models for Exploration, Special Publications of the SEPM 31, 49-69.

Gluyas, J., Swarbrick, R., 2004. Petroleum geoscience. Wiley-Blackwell, London, 376 pp.

Godchaux, M.M., Bonnichsen, B., 2002. Syneruptive magma-water and posteruptive lava-water interactions in the Western Snake River Plain, Idaho, during the past 12 million years. Tectonic and magmatic evolution of the Snake River Plain Volcanic Province. Idaho Geological Survey Bulletin 30, 387–434.

Godfrey, N.J., Beaudoin, B.C., Klemperer, S.L., 1997. Ophiolitic basement to the Great

Valley forearc basin, California, from seismic and gravity data: Implications for crustal growth at the North American continental margin. Geological Society of America Bulletin 109, 1536–1562.

Goehring, L., Morris, S.W., 2005. Order and disorder in columnar joints. EPL (Europhysics Letters) 69, 739.

Govindaraju, K., 1994. 1994 compilation of working values and sample description for 383 geostandards. Geostandards Newsletter 18, 1–158.

Greene, A.R., Scoates, J.S., Weis, D., Katvala, E.C., Israel, S., Nixon, G.T., 2010. The architecture of oceanic plateaus revealed by the volcanic stratigraphy of the accreted Wrangellia oceanic plateau. Geosphere 6, 47–73.

Grove, C., Jerram, D.A., 2011. jPOR: An ImageJ macro to quantify total optical porosity from blue-stained thin sections. Computers & Geosciences 37, 1850–1859.

Gudmundsson, A., 1995. Infrastructure and mechanics of volcanic systems in Iceland. Journal of Volcanology and Geothermal Research 64, 1–22.

Gudmundsson, A., 2000. Dynamics of volcanic systems in Iceland: example of tectonism and volcanism at juxtaposed hot spot and mid-ocean ridge systems. Annual Review of Earth and Planetary Sciences 28, 107–140.

Gudmundsson, M.T., Sigmundsson, F., Björnsson, H., 1997. Ice–volcano interaction of the 1996 Gjálp subglacial eruption, Vatnajökull, Iceland. Nature 389, 954–957.

Gudmundsson, M.T., Sigmundsson, F., Björnsson, H., Högnadóttir, T., 2004. The 1996 eruption at Gjálp, Vatnajökull ice cap, Iceland: efficiency of heat transfer, ice deformation and subglacial water pressure. Bulletin of Volcanology 66, 46–65.

Guilbaud, M., Self, S., Thordarson, T., Blake, S., 2005. Morphology, surface structures, and emplacement of lavas produced by Laki, AD 1783-1784. Special Papers of the Geological Society of America 396, 81.

Gutiérrez, M., Casillas, R., Fernández, C., Balogh, K., Ahijado, A., Castillo, C., Colmenero, J.R., García-Navarro, E., 2006. The submarine volcanic succession of the basal complex of Fuerteventura, Canary Islands: A model of submarine growth and emergence of tectonic volcanic islands. Geological Society of America Bulletin 118, 785–804.

Hackman, M.C., King, G.C., Bilham, R., 1990. The mechanics of the south Iceland

seismic zone. Journal of Geophysical Research: Solid Earth (1978–2012) 95, 17339–17351.

Hamblin, W.K., 1994. Late Cenozoic lava dams in the western Grand Canyon. Memoirs of the Geological Society of America 183, 183 pp.

Hamilton, C.W., Thordarson, T., Fagents, S.A., 2010. Explosive lava–water interactions I: architecture and emplacement chronology of volcanic rootless cone groups in the 1783–1784 Laki lava flow, Iceland. Bulletin of Volcanology 72, 449–467.

Hansen, J., Jerram, D.A., McCaffrey, K., Passey, S.R., 2009. The onset of the North Atlantic Igneous Province in a rifting perspective. Geological Magazine 146, 309.

Hansen, J., Jerram, D.A., McCaffrey, K., Passey, S.R., 2011. Early Cenozoic saucer-shaped sills of the Faroe Islands: an example of intrusive styles in basaltic lava piles. Journal of the Geological Society 168, 159–178.

Hanson, R.E., Schweickert, R.A., 1982. Chilling and brecciation of a Devonian rhyolite sill intruded into wet sediments, northern Sierra Nevada, California. The Journal of Geology 717–724.

Hathway, B., Hudak, G., Hamilton, M.A., 2008. Geologic setting of volcanic-associated massive sulfide deposits in the Kamiskotia area, Abitibi subprovince, Canada. Economic Geology 103, 1185–1202.

Hay, R.L., Iijima, A., 1968. Nature and origin of palagonite tuffs of the Honolulu Group on Oahu, Hawaii. Memoirs of the Geological Society of America 116, 331–376.

Head III, J.W., Wilson, L., 1989. Basaltic pyroclastic eruptions: influence of gas-release patterns and volume fluxes on fountain structure, and the formation of cinder cones, spatter cones, rootless flows, lava ponds and lava flows. Journal of Volcanology and Geothermal Research 37, 261–271.

Head, J.W., Wilson, L., 2003. Deep submarine pyroclastic eruptions: theory and predicted landforms and deposits. Journal of Volcanology and Geothermal Research 121, 155–193.

Hearst, J.R., Carlson, R.C., 1969. The RIDS: A density logger for rough holes. Geophysics 34, 222–234.

Hearst, J.R., Nelson, P.H., 1985. Well logging for physical properties. McGraw-Hill,

University of Michigan 571 pp.

Heath, R.L.V., 1964. Scintillation spectrometry: gamma-ray catalogue. Phillips Petroleum Company, Atomic Energy Division, National Reactor Testing Station, Idaho.[http://babel.hathitrust.org/cgi/pt?id=mdp.39015086567198;view=1up;seq=1]

Heinesen, M.V., Rosenkrands, L., Sørensen, K., 2006. Introduction. In: Chalmers, J. A., Waagstein, R. (ed.) Scientific Results from the Deepened Lopra-1 Borehole, Faroe Islands. Geological Survey of Denmark and Greenland Bulletin 9, 1–6.

Hekinian, R., Hoffert, M., 1975. Rate of palagonitization and manganese coating on basaltic rocks from the rift valley in the Atlantic Ocean near 36 50′ N. Marine Geology 19, 91–109.

Helgason, J., Duncan, R.A., 2001. Glacial-interglacial history of the Skaftafell region, southeast Iceland, 0–5 Ma. Geology 29, 179–182.

Helland-Hansen, D., 2009. Rosebank – challenges to development from a subsurface perspective. In: Varming, T., Ziska, H. (ed.) Faroe Islands Exploration Conference: Proceedings of the 2nd Conference. Annales Societatis Scientarium Faeroensis, Supplementum 50, 241–245.

Helm-Clark, C.M., Rodgers, D.W., Smith, R.P., 2004. Borehole geophysical techniques to define stratigraphy, alteration and aquifers in basalt. Journal of Applied Geophysics 55, 3–38.

Hetényi, G., Taisne, B., Garel, F., Médard, É., Bosshard, S., Mattsson, H.B., 2012. Scales of columnar jointing in igneous rocks: field measurements and controlling factors. Bulletin of Volcanology 74, 457–482.

Hill, I.G., Worden, R.H., Meighan, I.G., 2001. Formation of interbasaltic laterite horizons in NE Ireland by early Tertiary weathering processes. Proceedings of the Geologists' Association 112, 339–348.

Hjaltadóttir, S., Vogfjörð, K.S., Slunga, R., 2009. Seismic signs of magma pathways through the crust in the Eyjafjallajökull volcano, south Iceland Report VI 13, 33 pp.[http://www.vedur.is/media/vedurstofan/utgafa/skyrslur/2009/VI_2009_013.pdf]

Holcomb, R.T., Moore, J.G., Lipman, P.W., Belderson, R.H., 1988. Voluminous

submarine lava flows from Hawaiian volcanoes. Geology 16, 400–404.

Holford, S.P., Schofield, N., MacDonald, J.D., Duddy, I.R., Green, P.F., 2012. Seismic Analysis of Igneous Systems in Sedimentary Basins and their Impacts on Hydrocarbon Prospectivity: Examples from the Southern Australian Margin. APPEA Journal, 229-252.

Hon, K., Kauahikaua, J., Denlinger, R., Mackay, K., 1994. Emplacement and inflation of pahoehoe sheet flows: Observations and measurements of active lava flows on Kilauea Volcano, Hawaii. Geological Society of America Bulletin 106, 351–370.

Honnorez, J., Kirst, P., 1975. Submarine basaltic volcanism: morphometric parameters for discriminating hyaloclastites from hyalotuffs. Bulletin Volcanologique 39, 441–465.

Hooten, J.A., Ort, M.H., 2002. Peperite as a record of early-stage phreatomagmatic fragmentation processes: an example from the Hopi Buttes volcanic field, Navajo Nation, Arizona, USA. Journal of Volcanology and Geothermal Research 114, 95–106.

Höskuldsson, A., Sparks, R.S.J., 1997. Thermodynamics and fluid dynamics of effusive subglacial eruptions. Bulletin of Volcanology 59, 219–230.

Houghton, B.F., Schmincke, H.U., 1989. Rothenberg scoria cone, East Eifel: a complex Strombolian and phreatomagmatic volcano. Bulletin of Volcanology 52, 28–48.

Jakobsdóttir, S.S., 2008. Seismicity in Iceland: 1994–2007. Jökull 58, 75–100.

Jakobsson, S.P., Moore, J.G., 1986. Hydrothermal minerals and alteration rates at Surtsey volcano, Iceland. Geological Society of America Bulletin 97, 648–659.

Jakobsson, S.P., Thors, K., Vesteinsson, A.TH., Asbjornsdottir, L. 2009. Some aspects of the seafloor morphology at Surtsey volcano: The new multibeam bathymetric survey of 2007. Surtsey Research 12, 9-20.

Jegen, M.D., Hobbs, R.W., Tarits, P., Chave, A., 2009. Joint inversion of marine magnetotelluric and gravity data incorporating seismic constraints: Preliminary results of sub-basalt imaging off the Faroe Shelf. Earth and Planetary Science Letters 282, 47–55.

Jerram, D., Mountney, N., Holzförster, F., Stollhofen, H., 1999. Internal stratigraphic relationships in the Etendeka Group in the Huab Basin, NW Namibia:

understanding the onset of flood volcanism. Journal of Geodynamics 28, 393–418.

Jerram, D., Petford, N., 2011. The field description of igneous rocks. Wiley-Blackwell, London, 256 pp.

Jerram, D.A., 2002. Volcanology and facies architecture of flood basalts. Volcanic Rifted Margins. GSA Special Publications 362, 119-132.

Jerram, D.A., Higgins, M.D., 2007. 3D analysis of rock textures: quantifying igneous microstructures. Elements 3, 239–245.

Jerram, D.A., Mock, A., Davis, G.R., Field, M., Brown, R.J., 2009. 3D crystal size distributions: A case study on quantifying olivine populations in kimberlites. Lithos 112, 223–235.

Jerram, D.A., Mountney, N.P., Howell, J.A., Long, D., Stollhofen, H., 2000. Death of a sand sea: an active aeolian erg systematically buried by the Etendeka flood basalts of NW Namibia. Journal of the Geological Society 157, 513–516.

Jerram, D.A., Robbe, O., 2001. Building a 3-D model of a flood basalt: an example from the Etendeka, NW Namibia. Visual Geosciences 6, 1–8.

Jerram, D.A., Single, R.T., Hobbs, R.W., Nelson, C.E., 2009. Understanding the offshore flood basalt sequence using onshore volcanic facies analogues: an example from the Faroe–Shetland basin. Geological Magazine 146, 353–367.

Jerram, D.A., Stollhofen, H., 2002. Lava–sediment interaction in desert settings; are all peperite-like textures the result of magma–water interaction? Journal of Volcanology and Geothermal Research 114, 231–249.

Jerram, D.A., Widdowson, M., 2005. The anatomy of Continental Flood Basalt Provinces: geological constraints on the processes and products of flood volcanism. Lithos 79, 385–405.

Johnson, J.S., Smellie, J.L., 2007. Zeolite compositions as proxies for eruptive paleoenvironment. Geochemistry, Geophysics, Geosystems 8, [DOI: 10.1029/2006GC001450].

Jolley, D.W., Morton, A., Prince, I., 2005. Volcanogenic impact on phytogeography and sediment dispersal patterns in the NE Atlantic. Geological Society, London, Petroleum Geology Conference Series. pp. 969–975.

Jónasson, K., 2007. Silicic volcanism in Iceland: Composition and distribution within the active volcanic zones. Journal of Geodynamics 43, 101–117.

Jones, J.G., 1970. Intraglacial volcanoes of the Laugarvatn region, southwest Iceland, II. The Journal of Geology 78, 127–140.

Jones, J.G., Nelson, P.H.H., 1970. The flow of basalt lava from air into water–its structural expression and stratigraphic significance. Geological Magazine 107, 13–19.

Jørgensen, O., 2006. The regional distribution of zeolites in the basalts of the Faroe Islands and the significance of zeolites as palaeotemperature indicators. In: Chalmers J. A., Waagstein R., (ed.) Scientific Results from the Deepened Lopra-1 Borehole, Faroe Islands. Geological Survey of Denmark and Greenland Bulletin 9, 123–156.

Jurado-Chichay, Z., Rowland, S.K., 1995. Channel overflows of the Pōhue Bay flow, Mauna Loa, Hawai'i: examples of the contrast between surface and interior lava. Bulletin of Volcanology 57, 117–126.

Jurado-Chichay, Z., Rowland, S.K., Walker, G.P., 1995. The formation of circular littoral cones from tube-fed pāhoehoe: Mauna Loa, Hawai'i. Bulletin of Volcanology 57, 471–482.

Karapınar, N., 2009. Application of natural zeolite for phosphorus and ammonium removal from aqueous solutions. Journal of Hazardous Materials 170, 1186–1191.

Katz, M.G., Cashman, K.V., 2003. Hawaiian lava flows in the third dimension: Identification and interpretation of pahoehoe and′ a′ a distribution in the KP-1 and SOH-4 cores. Geochemistry, Geophysics, Geosystems 4, [DOI: 10.1029/2001GC000209]

Kauahikaua, J., Cashman, K.V., Mattox, T.N., Heliker, C.C., Hon, K.A., Mangan, M.T., Thornber, C.R., 1998. Observations on basaltic lava streams in tubes from Kilauea Volcano, island of Hawaii. Journal of Geophysical Research 103, 27303–27323.

Keating, G.N., Valentine, G.A., Krier, D.J., Perry, F.V., 2008. Shallow plumbing systems for small-volume basaltic volcanoes. Bulletin of Volcanology 70, 563–

582.

Keszthelyi, L., 1995. A preliminary thermal budget for lava tubes on the Earth and planets. Journal of Geophysical Research: Solid Earth (1978–2012) 100, 20411–20420.

Kilburn, C.R., 2004. Fracturing as a quantitative indicator of lava flow dynamics. Journal of Volcanology and Geothermal Research 132, 209–224.

Kiørboe, L., 1999. Stratigraphic relationships of the Lower Tertiary of the Faeroe basalt plateau and the Faeroe–Shetland Basin. Geological Society, London, Petroleum Geology Conference Series. pp. 559–571.

Klarner, S., Klarner, O., 2012. Identification of Paleo-Volcanic Rocks on Seismic Data. In: Stoppa, F., (ed.) A Comprehensive Approach to Volcanological Problems. [http://cdn.intechopen.com/pdfs/25987/InTech-Identification_of_paleo_volcanic_rocks_on_seismic_data.pdf]

Kokelaar, B.P., 1983. The mechanism of Surtseyan volcanism. Journal of the Geological Society 140, 939–944.

Kokelaar, B.P., Durant, G.P., 1983. The submarine eruption and erosion of Surtla (Surtsey), Iceland. Journal of Volcanology and Geothermal Research 19, 239–246.

Kokelaar, P., 1986. Magma-water interactions in subaqueous and emergent basaltic. Bulletin of Volcanology 48, 275–289.

Kralj, P., 2012. Facies architecture of the Upper Oligocene submarine Smrekovec stratovolcano, Northern Slovenia. Journal of Volcanology and Geothermal Research 247-248, 122-138.

Kristjansson, L., 1985. Some statistical properties of palaeomagnetic directions in Icelandic lava flows. Geophysical Journal of the Royal Astronomical Society 80, 57–71.

Kristjánsson, L., Duncan, R.A., Guðmundsson, Á., 1998. Stratigraphy, palaeomagnetism and age of volcanics in the upper regions of ÞJórsárdalur valley, central southern Iceland. Boreas 27, 1–13.

Kruber, C., Thorseth, I.H., Pedersen, R.B., 2008. Seafloor alteration of basaltic glass: Textures, geochemistry, and endolithic microorganisms. Geochemistry,

Geophysics, Geosystems 9, [DOI: 10.1029/2008GC002119].

Kuiper, J., Ryen, W.M.L., Koefoed, O., 1959. Laboratory determinations of elastic properties of some limestones. Geophysical Prospecting 7, 38–44.

Lacasse, C., Sigurdsson, H., Carey, S.N., Jóhannesson, H., Thomas, L.E., Rogers, N.W., 2007. Bimodal volcanism at the Katla subglacial caldera, Iceland: insight into the geochemistry and petrogenesis of rhyolitic magmas. Bulletin of Volcanology 69, 373–399.

Larsen, M., Pedersen, A.K., n.d. Volcanic marker horizons in the Maligât Formation on Disko and Nûgssuaq, and implications for the development of the southern part of the West Greenland basin in the early Tertiary. Rapport Grønlands geologiske Undersøgelse 148, 65–73.

Le Maitre, R.W., 1984. A proposal by the IUGS Subcommission on the Systematics of Igneous Rocks for a chemical classification of volcanic rocks based on the total alkali silica (TAS) diagram: (on behalf of the IUGS Subcommission on the Systematics of Igneous Rocks). Australian Journal of Earth Sciences 31, 243–255.

Lescinsky, D.T., Fink, J.H., 2000. Lava and ice interaction at stratovolcanoes: use of characteristic features to determine past glacial extents and future volcanic hazards. Journal of Geophysical Research: Solid Earth (1978–2012) 105, 23711–23726.

Lindseth, R.O., 1979. Synthetic sonic logs-a process for stratigraphic interpretation. Geophysics 44, 3–26.

Lipman, P.W., Moore, J.G., 1996. Mauna Loa lava accumulation rates at the Hilo drill site: Formation of lava deltas during a period of declining overall volcanic growth. Journal of Geophysical Research 101, 11631–11641.

Lodge, R.W., Lescinsky, D.T., 2009. Anisotropic stress accumulation in cooling lava flows and resulting fracture patterns: Insights from starch-water desiccation experiments. Journal of Volcanology and Geothermal Research 185, 323–336.

Lofts, J.C., Bourke, L.T., 1999. The recognition of artefacts from acoustic and resistivity borehole imaging devices. In: Lovell, M., Williamson, G., Harvey, P., Borehole Imaging: Applications and Case Histories.Geological Society, London, Special

Publications 159, 59–76.

Long, P.E., Wood, B.J., 1986. Structures, textures, and cooling histories of Columbia River basalt flows. Geological Society of America Bulletin 97, 1144–1155.

Lonsdale, P., Batiza, R., 1980. Hyaloclastite and lava flows on young seamounts examined with a submersible. Geological Society of America Bulletin 91, 545–554.

Loughlin, S.C., 2002. Facies analysis of proximal subglacial and proglacial volcaniclastic successions at the Eyjafjallajökull central volcano, southern Iceland. In: Smellie, J.L., Chapman, M.G., (ed.) Volcano-Ice Interaction on Earth and Mars. Geological Society, London, Special Publications 202, 149–178.

Ludwig, W.J., Nafe, J.E., Drake, C.L., 1970. Seismic refraction. In: Maxwell, A.E., The Sea, Wiley, New York 4, 53–84.

Macdonald, G.A., 1953. Pahoehoe, aa, and block lava. American Journal of Science 251, 169–191.

MacGeehan, P.J., MacLean, W.H., 1980. Tholeiitic basalt-rhyolite magmatism and massive sulphide deposits at Matagami, Quebec. Nature 283, 153–157.

Maeno, F., Taniguchi, H., 2006. Silicic lava dome growth in the 1934–1935 Showa Iwo-jima eruption, Kikai caldera, south of Kyushu, Japan. Bulletin of volcanology 68, 673–688.

Mahood, G.A., Hildreth, W., 1986. Geology of the peralkaline volcano at Pantelleria, Strait of Sicily. Bulletin of Volcanology 48, 143–172.

Maicher, D., 2003. A cluster of surtseyan volcanoes at Lookout Bluff, North Otago, New Zealand: Aspects of edifice spacing and time. Geophysical MONOGRAPH-American Geophysical Union 140, 167–178.

Maicher, D., White, J.D., Batiza, R., 2000. Sheet hyaloclastite: density-current deposits of quench and bubble-burst fragments from thin, glassy sheet lava flows, Seamount Six, Eastern Pacific Ocean. Marine Geology 171, 75–94.

Manville, V., Németh, K., Kano, K., 2009. Source to sink: A review of three decades of progress in the understanding of volcaniclastic processes, deposits, and hazards. Sedimentary Geology 220, 136–161.

Maresh, J., White, R.S., 2005. Seeing through a glass darkly: strategies for imaging

through basalt. First Break 23, 3–9.

Martin, E., Sigmarsson, O., 2010. Thirteen million years of silicic magma production in Iceland: Links between petrogenesis and tectonic settings. Lithos 116, 129–144.

Mastin, L.G., Guffanti, M., Servranckx, R., Webley, P., Barsotti, S., Dean, K., Durant, A., Ewert, J.W., Neri, A., Rose, W.I., 2009. A multidisciplinary effort to assign realistic source parameters to models of volcanic ash-cloud transport and dispersion during eruptions. Journal of Volcanology and Geothermal Research 186, 10–21.

Mattox, T.N., Mangan, M.T., 1997. Littoral hydrovolcanic explosions: a case study of lava-seawater interaction at Kilauea volcano. Journal of Volcanology and Geothermal Research 75, 1–17.

Mattsson, H.B., 2010. Textural variation in juvenile pyroclasts from an emergent, Surtseyan-type, volcanic eruption: The Capelas tuff cone, São Miguel (Azores). Journal of Volcanology and Geothermal Research 189, 81–91.

Mattsson, H.B., Höskuldsson, Á., Hand, S., 2005. Crustal xenoliths in the 6220 BP Sæfell tuff-cone, south Iceland: Evidence for a deep, diatreme-forming, Surtseyan eruption. Journal of Volcanology and Geothermal Research 145, 234–248.

McGarvie, D.W., Stevenson, J.A., Burgess, R., Tuffen, H., Tindle, A.G., 2007. Volcano ice interactions at Prestahnukur, Iceland: rhyolite eruption during the last interglacialglacial transition. Annals of Glaciology 45, 38–47.

McPhie, J., Doyle, M., Allen, R., Allen, R.L., 1993. Volcanic textures: a guide to the interpretation of textures in volcanic rocks. CODES-University of Tasmania, 198 pp.

Merlino, S., 1988. Gyrolite: its crystal structure and crystal chemistry. Mineralogical Magazine 52, 377–387.

Miller, S.L.M., 1992. Well log analysis of Vp and Vs in carbonates. CREWES Research Report 4, 12, 1-11.

Mills, A.A., 1984. Pillow lavas and the Leidenfrost effect. Journal of the Geological Society 141, 183–186.

Mitchell, N.C., 2001. Transition from circular to stellate forms of submarine volcanoes.

Journal of Geophysical Research 106, 1987–2003.

Mitchell, N.C., Beier, C., Rosin, P.L., Quartau, R., Tempera, F., 2008. Lava penetrating water: submarine lava flows around the coasts of Pico Island, Azores. Geochemistry Geophysics Geosystems 9, Q03024, [DOI: 10.1029/2007GC001725]

Mitchell, N.C., Masson, D.G., Watts, A.B., Gee, M.J., Urgeles, R., 2002. The morphology of the submarine flanks of volcanic ocean islands: A comparative study of the Canary and Hawaiian hotspot islands. Journal of Volcanology and Geothermal Research 115, 83–107.

Mitchell, N.C., Quartau, R., Madeira, J., 2012. Assessing landslide movements in volcanic islands using near-shore marine geophysical data: south Pico island, Azores. Bulletin of Volcanology 74, 483–496.

Moorbath, S., Sigurdsson, H., Goodwin, R., 1968. KAr ages of the oldest exposed rocks in Iceland. Earth and Planetary Science Letters 4, 197–205.

Moore, J.G., 1966. Rate of palagonitization of submarine basalt adjacent to Hawaii. US Geological Surey Professional Paper 550, 163–171.

Moore, J.G., 1967. Base surge in recent volcanic eruptions. Bulletin Volcanologique 30, 337–363.

Moore, J.G., 1975. Mechanism of Formation of Pillow Lava: Pillow lava, produced as fluid lava cools underwater, is the most abundant volcanic rock on earth, but only recently have divers observed it forming. American Scientist 63, 269–277.

Moore, J.G., 1985. Structure and eruptive mechanisms at Surtsey Volcano, Iceland. Geological Magazine 122, 649–661.

Moore, J.G., 2001. Density of basalt core from Hilo drill hole, Hawaii. Journal of Volcanology and Geothermal Research 112, 221–230.

Moore, J.G., Clague, D.A., 1992. Volcano growth and evolution of the island of Hawaii. Geological Society of America Bulletin 104, 1471–1484.

Moore, J.G., Jakobsson, S.P., Norrman, J.O., 1986. Investigation of Surtsey Volcano. Eos, Transactions American Geophysical Union 67, 74–74.

Moore, J.G., Phillips, R.L., Grigg, R.W., Peterson, D.W., Swanson, D.A., 1973. Flow of lava into the sea, 1969–1971, Kilauea Volcano, Hawaii. Geological Society of

America Bulletin 84, 537–546.

Morrissey, M., Gisler, G., Weaver, R., Gittings, M., 2010. Numerical model of crater lake eruptions. Bulletin of Volcanology 72, 1169–1178.

Mountney, N.P., Russell, A.J., 2009. Aeolian dune-field development in a water table-controlled system: Skeiðarársandur, Southern Iceland. Sedimentology 56, 2107–2131.

Moy, D.J., Imber, J., 2009. A critical analysis of the structure and tectonic significance of rift-oblique lineaments ("transfer zones") in the Mesozoic–Cenozoic succession of the Faroe–Shetland Basin, NE Atlantic margin. Journal of the Geological Society 166, 831–844.

Mueller, W.U., Garde, A.A., Stendal, H., 2000. Shallow-water, eruption-fed, mafic pyroclastic deposits along a Paleoproterozoic coastline: Kangerluluk volcano-sedimentary sequence, southeast Greenland. Precambrian Research 101, 163–192.

Murphy, B., Corcoran, P.L., Moore, L.N., 2008. Subaqueous eruption and shallow-water reworking of a small-volume Surtseyan edifice at Kakanui, New Zealand. Canadian Journal of Earth Sciences 45, 1469–1485.

Murtagh, R.M., White, J.D., Sohn, Y.K., 2011. Pyroclast textures of the Ilchulbong "wet"tuff cone, Jeju Island, South Korea. Journal of Volcanology and Geothermal Research 201, 385–396.

Nafe, J.E., Drake, C.L., 1968. Physical properties of rocks of basaltic composition. In: Hess, H.H., (ed.) Basalts, The Poldervaart Treatise on Rocks of Basaltic Composition 2, New York, 483.

Nelson, C., 2010. Methods for constructing 3D geological and geophysical models of flood basalt provinces. PhD Thesis, Durham University.

Nelson, C.E., Jerram, D.A., Hobbs, R.W., 2009. Flood basalt facies from borehole data: implications for prospectivity and volcanology in volcanic rifted margins. Petroleum Geoscience 15, 313–324.

Németh, K., Cronin, S.J., Charley, D.T., Harrison, M.J., Garae, E., 2006. Exploding lakes in Vanuatu-" Surtseyan-style" eruptions witnessed on Ambae Island. Episodes 29, 87-92.

Németh, K., Pécskay, Z., Martin, U., Gméling, K., Molnár, F., Cronin, S.J., 2008. Hyaloclastites, peperites and soft-sediment deformation textures of a shallow subaqueous Miocene rhyolitic dome-cryptodome complex, Pálháza, Hungary. In: Thomson, K., Petford, N., (ed.) Structure and Emplacement of High-Level Magmatic Systems. Geological Society, London, Special Publications 302, 63–86.

Newcomb, R.C., 1961. Storage of ground water behind subsurface dams in the Columbia River Basalt, Washington, Oregon, and Idaho. US Government Printing Office, 19 pp, [http://pubs.usgs.gov/pp/0383a/report.pdf].

Nichols, A.R.L., Potuzak, M., Dingwell, D.B., 2009. Cooling rates of basaltic hyaloclastites and pillow lava glasses from the HSDP2 drill core. Geochimica et Cosmochimica Acta 73, 1052–1066.

Ning, L., Dexing, Q., Qingfeng, L., Hongliang, W., Youshen, F., Lixin, D., Qingfu, F., Kewen, W., 2009. Theory on logging interpretation of igneous rocks and its application. Petroleum Exploration and Development 36, 683–692.

Norrish, K., Hutton, J.T., 1969. An accurate X-ray spectrographic method for the analysis of a wide range of geological samples. Geochimica et Cosmochimica Acta 33, 431–453.

Ollier, G., Cochonat, P., Lenat, J.F., Labazuy, P., 1998. Deep-sea volcaniclastic sedimentary systems: an example from La Fournaise volcano, Reunion Island, Indian Ocean. Sedimentology 45, 293–330.

Orton, H., Fritz, B., 1990. Excursion F: Cwn Eigiau, Pitts Head Tuff, Lower Rhyolitic Tuff and Bedded Pyroclastic Formations-shallow marine volcaniclastic sedimentation in about primary extrusive volcanic rocks, Cwn Bochlwyd-Cwn Cneifion-Cwn Idwal, in: Volcanic Sedimentation in Ancient Terrains, Field Guide II. IAVCEI/IAS Field Workshop, pp. 89–98.

Owen, J., Tuffen, H., McGarvie, D.W., 2012. Using dissolved H2O in rhyolitic glasses to estimate palaeo-ice thickness during a subglacial eruption at Bláhnúkur (Torfajökull, Iceland). Bulletin of Volcanology 74, 1355–1378.

Palinkas, L., Kolar-Jurkovsek, T., Borojević, S., Bermanec, V., 2000. Triassic rifting magmatism within Zagorje-Mid-Transdanubian zone, examplified by pillow

lavas of Hru\vskovec, Mt. Kalnik, N Croatia. PANCARDI, Dubrovnik, Croatia 37, 98-99.

Passey, S.R., 2004. The volcanic and sedimentary evolution of the Faeroe plateau lava group, Faeroe Islands and Faeroe-Shetland Basin, NE Atlantic. PhD Thesis, University of Glasgow.

Passey, S.R., Bell, B.R., 2007. Morphologies and emplacement mechanisms of the lava flows of the Faroe Islands Basalt Group, Faroe Islands, NE Atlantic Ocean. Bulletin of Volcanology 70, 139–156.

Passey, S.R., Jolley, D.W., 2008. A revised lithostratigraphic nomenclature for the Palaeogene Faroe Islands Basalt group, NE Atlantic Ocean. Earth and Environmental Science Transactions of the Royal Society of Edinburgh 99, 127–158.

Pearce, J.A., 1976. Statistical analysis of major element patterns in basalts. Journal of Petrology 17, 15–43.

Peate, I., Larsen, M., Lesher, C., 2003. The transition from sedimentation to flood volcanism in the Kangerlussuaq Basin, East Greenland: basaltic pyroclastic volcanism during initial Palaeogene continental break-up. Journal of the Geological Society 160, 759–772.

Pechnig, R., Kueck, J., Harms, U., Buysch, A., Wohlenberg, J., 2000. Geophysical Downhole Measurements in the Scientific Drillhole HSDP Hilo/Hawaii: Logging Program and Results of Interpretation, in: Eos, Transactions, AGU 2000 Fall Meeting. p. F1350.

Pedersen, A.K., Larsen, L.M., Riisager, P., Dueholm, K.S., 2002. Rates of volcanic deposition, facies changes and movements in a dynamic basin: The Nuussuaq Basin, West Greenland, around the C27n-C26r transition. In: Jolley, D.W., Bell, B.R., The North Atlantic Igneous Province: Stratigraphy, Tectonic, Volcanic and Magmatic Processes. Geological Society, London, Special Publications 197, 157–181.

Pedersen, G.K., Larsen, L.M., Pedersen, A.K., Hjortkjær, B.F., 1998. The syn-volcanic Naajaat lake, Paleocene of West Greenland. Palaeogeography, Palaeoclimatology, Palaeoecology 140, 271–287.

Petry, K., Jerram, D.A., de Almeida, D. del P.M., Zerfass, H., 2007. Volcanic-sedimentary features in the Serra Geral Fm., Paraná Basin, southern Brazil: Examples of dynamic lava-sediment interactions in an arid setting. Journal of Volcanology and Geothermal Research 159, 313–325.

Pichler, H., 1965. Acid hyaloclastites. Bulletin Volcanologique 28, 293–310.

Pillans, B., 1997. Soil development at snail's pace: evidence from a 6 Ma soil chronosequence on basalt in north Queensland, Australia. Geoderma 80, 117–128.

Planke, S., 1994. Geophysical response of flood basalts from analysis of wire line logs: Ocean Drilling Program Site 642, Vøring volcanic margin. Journal of Geophysical Research: Solid Earth (1978–2012) 99, 9279–9296.

Planke, S., Cambray, H., 1998. Seismic properties of flood basalts from hole 917a downhole data, southeast Greenland volcanic margin. In: Saunders, A.D., Larsen, H.C., Wise, S.W., Proceedings of the Ocean Drilling Program, Scientific Results 152, 453-462.

Planke, S., Symonds, P.A., Alvestad, E., Skogseid, J., 2000. Seismic volcanostratigraphy of large-volume basaltic extrusive complexes on rifted margins. Journal of Geophysical Research: Solid Earth (1978–2012) 105, 19335–19351.

Porębski, S.J., Gradziński, R., 1990. Lava-Fed Gilbert-Type Delta in the Polonez Cove Formation (Lower Oligocene), King George Island, West Antarctica. In: Colella, A., Prior, D. Coarse-Grained Deltas. Special Publication of the International Association of Sedimentologists 10, 333–351.

Portner, R.A., Daczko, N.R., Dickinson, J.A., 2010. Vitriclastic lithofacies from Macquarie Island (Southern Ocean): compositional influence on abyssal eruption explosivity in a dying Miocene spreading ridge. Bulletin of Volcanology 72, 165–183.

Postma, G., 1990. Depositional architecture and facies of river and fan deltas: a synthesis. In: Colella, A., Prior, D. Coarse-Grained Deltas. Special Publication of the International Association of Sedimentologists 10, 13–28.

Potter, C.C., Dey, A.K., Stewart, R.R., 1998. Density prediction using P-and S-wave sonic velocities. Geo-triad '98: Abstracts 320,

[http://www.crewes.org/ForOurSponsors/ConferenceAbstracts/1998/CSEG-1998/den_pred.pdf].

Prensky, S.E., 1999. Advances in borehole imaging technology and applications. In: Lovell, M., Williamson, G., Harvey, P., Borehole Imaging: Applications and Case Histories. Geological Society, London, Special Publications 159, 1–43.

Rafavich, F., Kendall, C.S.C., Todd, T.P., 1984. The relationship between acoustic properties and the petrographic character of carbonate rocks. Geophysics 49, 1622–1636.

Rasband, W.S., 2012. ImageJ: Image processing and analysis in Java. Astrophysics Source Code Library 1, 06013, [http://rsbweb.nih.gov/ij/].

Reed, S.J.B., 2005. Electron microprobe analysis and scanning electron microscopy in geology. Cambridge University Press, Cambridge, 212 pp.

Reedman, A.J., Park, K.H., Merriman, R.J., Kim, S.E., 1987. Welded tuff infilling a volcanic vent at Weolseong, Republic of Korea. Bulletin of Volcanology 49, 541–546.

Reidel, S.P., 1998. Emplacement of Columbia River flood basalt. Journal of Geophysical Research: Solid Earth (1978–2012) 103, 27393–27410.

Rhodes, J.M., Vollinger, M.J., 2004. Composition of basaltic lavas sampled by phase-2 of the Hawaii Scientific Drilling Project: Geochemical stratigraphy and magma types. Geochemistry, Geophysics, Geosystems 5, [DOI: 10.1029/2002GC000434].

Rider, M.H., 1996. The geological interpretation of well logs, Rider-Franch Limited, 440 pp.

Ritchie, J.D., Hitchen, K., 1996. Early Paleogene offshore igneous activity to the northwest of the UK and its relationship to the North Atlantic Igneous Province. In: Knox, R.B.O'B., Corfield, R.M, Dunay, R.E., Corelation of the Early Paleogene in Northwest Europe. Geological Society, London, Special Publications 101, 63–78.

Rogers, K.L., Neuhoff, P.S., Pedersen, A.K., Bird, D.K., 2006. CO_2 metasomatism in a basalt-hosted petroleum reservoir, Nuussuaq, West Greenland. Lithos 92, 55–82.

Rollinson, H.R., 1993. Using geochemical data: evaluation, presentation, interpretation.

Longman Scientific & Technical, Essex, 352 pp.

Ross, P.-S., Ukstins Peate, I., McClintock, M.K., Xu, Y.G., Skilling, I.P., White, J.D.L., Houghton, B.F., 2005. Mafic volcaniclastic deposits in flood basalt provinces: a review. Journal of Volcanology and Geothermal Research 145, 281–314.

Rowland, S.K., Walker, G.P., 1990. Pahoehoe and aa in Hawaii: volumetric flow rate controls the lava structure. Bulletin of Volcanology 52, 615–628.

Russell, A.J., Duller, R., Mountney, N.P., 2010. 11 Volcanogenic Jökulhlaups (Glacier Outburst Floods) from Mỳrdalsjökull: Impacts on Proglacial Environments. Developments in Quaternary Sciences 13, 181–207.

Russell, I.C., 1902. Geology and water resources of the Snake River Plains of Idaho. USGS Bulletin 199, 192 pp.

Sæmundsson, K., 1967. Outline of the structure of SW-Iceland. Visindafelag Islendinga 38, 151-161

Saemundsson, K., 1978. Fissure swarms and central volcanoes of the neovolcanic zones of Iceland. In Bowes, D.R., Leake, B.E., Crustal evolution in northwest Britian and adjacent regions. Geol. J. Spec. Issue 10, 415–432.

Saemundsson, K., n.d. Interglacial lava flows in the lowlands of southern Iceland and the problem of two-tiered columnar jointing. Jökull. 20, 62–77.

Saint-Ange, F., Bachèlery, P., Babonneau, N., Michon, L., Jorry, S.J., 2013. Volcaniclastic sedimentation on the submarine slopes of a basaltic hotspot volcano: Piton de la Fournaise volcano (La Réunion Island, Indian Ocean). Marine Geology, In press, corrected proof.

Sansone, F.J., Resing, J.A., Tribble, G.W., Sedwick, P.N., Kelly, K.M., Hon, K., 1991. Lava-seawater interactions at shallow-water submarine lava flows. Geophysical Research Letters 18, 1731–1734.

Sansone, F.J., Smith, J.R., 2006. Rapid mass wasting following nearshore submarine volcanism on Kilauea volcano, Hawaii. Journal of volcanology and geothermal research 151, 133–139.

Saunders, A.D., Fitton, J.G., Kerr, A.C., Norry, M.J., Kent, R.W., 1997. The north Atlantic igneous province. Geophysical Monograph-American Geophysical Union 100, 45–94.

Saupe, D., 1988. Algorithms for random fractals, in: The Science of Fractal Images. Springer, pp. 71–136.

Schiffman, P., Watters, R.J., Thompson, N., Walton, A.W., 2006. Hyaloclastites and the slope stability of Hawaiian volcanoes: Insights from the Hawaiian Scientific Drilling Project's 3-km drill core. Journal of Volcanology and Geothermal Research 151, 217–228.

Schmidt, R., Schmincke, H.-U., 2002. From seamount to oceanic island, Porto Santo, central East-Atlantic. International Journal of Earth Sciences 91, 594–614.

Schmincke, H.-U., 1967. Cone sheet swarm, resurgence of Tejeda caldera, and the early geologic history of Gran Canaria. Bulletin Volcanologique 31, 153–162.

Schmincke, H.-U., Behncke, B., Grasso, M., Raffi, S., 1997. Evolution of the northwestern Iblean Mountains, Sicily: uplift, Plicocene/Pleistocene sea-level changes, paleoenvironment, and volcanism. Geologische Rundschau 86, 637–669.

Schmincke, H.U., Von Rad, U., 1979. Neogene evolution of Canary Island volcanism inferred from ash layers and volcaniclastic sandstones of DSDP Site 397 (Leg 47A). Init. Rep. Deep Sea Drilling Project 47, 703–725.

Schopka, H.H., Gudmundsson, M.T., Tuffen, H., 2006. The formation of Helgafell, southwest Iceland, a monogenetic subglacial hyaloclastite ridge: sedimentology, hydrology and volcano–ice interaction. Journal of Volcanology and Geothermal Research 152, 359–377.

Schutter, S.R., 2003. Hydrocarbon occurrence and exploration in and around igneous rocks. In: Petford, N. McCaffrey, K.J.W., Hydrocarbons in crytalline rocks. Geological Society, London, Special Publications 214, 7–33.

Sclater, J.G., Christie, Paf., 1980. Continental stretching: An explanation of the post-Mid-Cretaceous subsidence of the central North Sea Basin. Journal of Geophysical Research: Solid Earth (1978–2012) 85, 3711–3739.

Scutter, C., Moore, C.L., Cas, R.A.F., 1998. Facies architecture and origin of a submarine rhyolitic lava flow–dome complex, Ponza, Italy. Journal of Geophysical Research 103 (b11), 27551–27566.

Seaman, C., Sherman, S.B., Garcia, M.O., Baker, M.B., Balta, B., Stolper, E., 2004.

Volatiles in glasses from the HSDP2 drill core. Geochemistry, Geophysics, Geosystems 5, [DOI 2003GC000596].

Seaman, C.A., Sherman, S.B., Garcia, M.O., Baker, M.B., Stolper, E.M., 2001. H2O and CO2 contents of basaltic glasses from Mauna Kea volcano, Hawaii. AGU Fall Meeting Abstracts. p. 1021.

Self, S., Keszthelyi, L., Thordarson, T., 1998. The importance of pahoehoe. Annual Review of Earth and Planetary Sciences 26, 81–110.

Self, S., Rampino, M.R., Newton, M.S., Wolff, J.A., 1984. Volcanological study of the great Tambora eruption of 1815. Geology 12, 659–663.

Self, S., Thordarson, T., Keszthelyi, L., Walker, G.P.L., Hon, K., Murphy, M.T., Long, P., Finnemore, S., 1996. A new model for the emplacement of Columbia River basalts as large, inflated pahoehoe lava flow fields. Geophysical Research Letters 23, 2689–2692.

Serra, O., Baldwin, J., Quirein, J., 1980. Theory, interpretation and practical applications of natural gamma ray spectroscopy. Transactions of the Society of Petrophysists and Well Log Analysts, 21st Annual. Logging Symposium. pp. Q1–Q30.

Sharma, P.V., 1997. Environmental and engineering geophysics. Cambridge University Press. Cambridge, 500 pp.

Sharp, W.D., Clague, D.A., 2006. 50-Ma initiation of Hawaiian-Emperor bend records major change in Pacific plate motion. Science 313, 1281–1284.

Sheridan, M.F., Wohletz, K.H., 1983. Hydrovolcanism: basic considerations and review. Journal of Volcanology and Geothermal Research 17, 1–29.

Sheriff, R.E., Geldart, L.P., 1995. Exploration seismology. Cambridge University Press, Cambridge, 628 pp.

Shervais, J.W., Kauffman, J.D., Gillerman, V.S., Othberg, K.L., Vetter, S.K., Hobson, V.R., Zarnetske, M., Cooke, M.F., Mathews, S.H., Hanan, B.B., 2005. Basaltic volcanism of the central and western Snake River Plain: a guide to field relations between Twin Falls and Mountain Home, Idaho. In: Pederson, J., Dehler, C.M. (Eds.), Interior Western United States. Geological Society of America Field Guide 6, 26.

Siddiqui, S., Hughes, G., Sadler, K.R., 2004. Density-Based Imaging to Supplement

FMI images for Sedimentary Facies Modelling. Saudi Aramco Journal of Technology Spring, 60–68.

Sigurdsson, H., Carey, S., Mandeville, C., Bronto, S., 1991. Pyroclastic flows of the 1883 Krakatau eruption. Eos, Transactions American Geophysical Union 72, 377–381.

Silvestri, S.C., 1963. Proposal for a genetic classification of hyaloclastites. Bulletin of Volcanology 25, 315–321.

Single, R.T., 2004. The facies architecture of large igneous provinces: an integrated geological and geophysical approach to the characterisation of volcanic successions in 3-D. PhD thesis, Durham University.

Single, R.T., Jerram, D.A., 2004. The 3D facies architecture of flood basalt provinces and their internal heterogeneity: examples from the Palaeogene Skye Lava Field. Journal of the Geological Society 161, 911–926.

Sinton, J., Grönvold, K., Sæmundsson, K., 2005. Postglacial eruptive history of the western volcanic zone, Iceland. Geochemistry, Geophysics, Geosystems 6.

Skilling, I.P., 1994. Evolution of an englacial volcano: Brown Bluff, Antarctica. Bulletin of Volcanology 56, 573–591.

Skilling, I.P., 2002. Basaltic pahoehoe lava-fed deltas: large-scale characteristics, clast generation, emplacement processes and environmental discrimination. Geological Society, London, Special Publications 202, 91–113.

Skilling, I.P., 2009. Subglacial to emergent basaltic volcanism at Hlöðufell, south-west Iceland: A history of ice-confinement. In: Smellie, J.L., Chapman, M.G., (ed.) Volcano-Ice Interaction on Earth and Mars. Journal of Volcanology and Geothermal Research 185, 276–289.

Skilling, I.P., White, J.D.L., McPhie, J., 2002. Peperite: a review of magma–sediment mingling. Journal of Volcanology and Geothermal Research 114, 1–17.

Smellie, J.L., 2001. Lithostratigraphy and volcanic evolution of Deception Island, South Shetland Islands. Antarctic Science 13, 188–209.

Smellie, J.L., 2006. The relative importance of supraglacial versus subglacial meltwater escape in basaltic subglacial tuya eruptions: An important unresolved conundrum. Earth-Science Reviews 74, 241–268.

Smellie, J.L., 2008. Basaltic subglacial sheet-like sequences: evidence for two types with different implications for the inferred thickness of associated ice. Earth-Science Reviews 88, 60–88.

Smellie, J.L., Hole, M.J., 1997. Products and processes in Pliocene–Recent, subaqueous to emergent volcanism in the Antarctic Peninsula: examples of englacial Surtseyan volcano construction. Bulletin of Volcanology 58, 628–646.

Smellie, J.L., Rocchi, S., Armienti, P., 2011. Late Miocene volcanic sequences in northern Victoria Land, Antarctica: products of glaciovolcanic eruptions under different thermal regimes. Bulletin of Volcanology 73, 1–25.

Smellie, J.L., Skilling, I.P., 1994. Products of subglacial volcanic eruptions under different ice thicknesses: two examples from Antarctica. Sedimentary Geology 91, 115–129.

Smellie, J.L., Wilch, T.I., Rocchi, S., 2013. ‘A ‘ā lava-fed deltas: A new reference tool in paleoenvironmental studies. Geology 41, 403–406.

Smith, D.K., 1988. Shape analysis of Pacific seamounts. Earth and Planetary Science Letters 90, 457–466.

Sohn, Y.K., 1995. Geology of Tok Island, Korea: eruptive and depositional processes of a shoaling to emergent island volcano. Bulletin of volcanology 56, 660–674.

Sohn, Y.K., Chough, S.K., 1989. Depositional processes of the Suwolbong tuff ring, Cheju Island (Korea). Sedimentology 36, 837–855.

Sohn, Y.K., Chough, S.K., 1992. The Ilchulbong tuff cone, Cheju Island, South Korea. Sedimentology 39, 523–544.

Sohn, Y.K., Chough, S.K., 1993. The Udo tuff cone, Cheju Island, South Korea: transformation of pyroclastic fall into debris fall and grain flow on a steep volcanic cone slope. Sedimentology 40, 769–786.

Sohn, Y.K., Cronin, S.J., Brenna, M., Smith, I.E.M., Németh, K., White, J.D.L., Murtagh, R.M., Jeon, Y.M., Kwon, C.W., 2012. Ilchulbong tuff cone, Jeju Island, Korea, revisited: A compound monogenetic volcano involving multiple magma pulses, shifting vents, and discrete eruptive phases. Geological Society of America Bulletin 124, 259–274.

Sohn, Y.K., Park, K.H., 2005. Composite tuff ring/cone complexes in Jeju Island,

Korea: possible consequences of substrate collapse and vent migration. Journal of Volcanology and Geothermal Research 141, 157–175.

Sohn, Y.K., Park, K.H., YOON, S.-H., 2008. Primary versus secondary and subaerial versus submarine hydrovolcanic deposits in the subsurface of Jeju Island, Korea. Sedimentology 55, 899–924.

Solgevik, H., Mattsson, H.B., Hermelin, O., 2007. Growth of an emergent tuff cone: Fragmentation and depositional processes recorded in the Capelas tuff cone, São Miguel, Azores. Journal of Volcanology and Geothermal Research 159, 246–266.

Sørensen, A.B., 2003. Cenozoic basin development and stratigraphy of the Faroes area. Petroleum Geoscience 9, 189–207.

Sorrentino, L., Cas, R.A., Stilwell, J.D., 2011. Evolution and facies architecture of Paleogene Surtseyan volcanoes on Chatham Islands, New Zealand, Southwest Pacific Ocean. Journal of Volcanology and Geothermal Research 202, 1–21.

Sparks, R.S.J., Sigurdsson, H., Carey, S.N., 1980. The entrance of pyroclastic flows into the sea I. oceanographic and geologic evidence from dominica, lesser antilles. Journal of Volcanology and Geothermal Research 7, 87–96.

Spitzer, R., White, R.S., Christie, P.A., 2008. Seismic characterization of basalt flows from the Faroes margin and the Faroe-Shetland basin. Geophysical Prospecting 56, 21–31.

Staudigel, H., Hart, S.R., 1983. Alteration of basaltic glass: Mechanisms and significance for the oceanic crust-seawater budget. Geochimica et Cosmochimica Acta 47, 337–350.

Staudigel, H., Schmincke, H.-U., 1984. The Pliocene seamount series of La Palma/Canary Islands. Journal of Geophysical Research: Solid Earth (1978–2012) 89, 11195–11215.

Stevenson, J.A., Mitchell, N.C., Cassidy, M., Pinkerton, H., 2012. Widespread inflation and drainage of a pāhoehoe flow field: the Nesjahraun, Þingvellir, Iceland. Bulletin of Volcanology 74, 15–31.

Stewart, A.L., McPhie, J., 2006. Facies architecture and Late Pliocene–Pleistocene evolution of a felsic volcanic island, Milos, Greece. Bulletin of Volcanology 68,

703–726.

Stix, J., 1991. Subaqueous, intermediate to silicic-composition explosive volcanism: a review. Earth-Science Reviews 31, 21–53.

Stolper, E., Sherman, S., Garcia, M., Baker, M., Seaman, C., 2004. Glass in the submarine section of the HSDP2 drill core, Hilo, Hawaii. Geochemistry, Geophysics, Geosystems 5, [DOI: 10.1029/2003GC000553].

Stolper, E.M., DePaolo, D.J., Thomas, D.M., 2009. Deep drilling into a mantle plume volcano: The Hawaii Scientific Drilling Project. Scientific Drilling 7, 4–14.

Stroncik, N.A., Schmincke, H.-U., 2001. Evolution of palagonite: Crystallization, chemical changes, and element budget. Geochemistry, Geophysics, Geosystems 2, [DOI: 10.1029/2000GC000102].

Stroncik, N.A., Schmincke, H.-U., 2002. Palagonite–a review. International Journal of Earth Sciences 91, 680–697.

Symonds, P.A., Planke, S., Frey, O., Skogseid, J., 1998. Volcanic evolution of the Western Australian continental margin and its implications for basin development. The Sedimentary Basins of Western Australia 2, 33–54.

Tanner, L.H., Calvari, S., 1999. Facies analysis and depositional mechanisms of hydroclastite breccias, Acicastello, eastern Sicily. Sedimentary Geology 129, 127–141.

Tatham, R.H., 1982. V p/V s and lithology. Geophysics 47, 336–344.

Thomas, D.M., Paillet, F.L., Conrad, M.E., 1996. Hydrogeology of the Hawaii Scientific Drilling Project borehole KP-1: 2. Groundwater geochemistry and regional flow patterns. Journal of Geophysical Research: Solid Earth (1978–2012) 101, 11683–11694.

Thompson, N., Watters, R.J., Schiffman, P., 2005. Hawaiian Volcano Flank Stability Appraised From Strength Testing the Hawaiian Scientific Drilling Project's (HSDP) 3.1-km Drill Core, in: AGU Fall Meeting Abstracts. p. 0604.

Thompson, N., Watters, R.J., Schiffman, P., 2008. Stability analysis of Hawaiian Island flanks using insight gained from strength testing of the HSDP core. Journal of Volcanology and Geothermal Research 171, 163–177.

Thomson, K., 2005. Volcanic features of the North Rockall Trough: application of

visualisation techniques on 3D seismic reflection data. Bulletin of Volcanology 67, 116–128.

Thomson, K., Schofield, N., 2008. Lithological and structural controls on the emplacement and morphology of sills in sedimentary basins. In: Thomson, K., Petford, N., (ed.) Structure and Emplacement of High-Level Magmatic Systems. Geological Society, London, Special Publications 302, 31–44.

Thorarinsson, S., 1966. The Surtsey Eruption Course of Events and the Development of the New Island. Surtsey Research Publication, Iceland, 9 pp.

Thorarinsson, S., 1968. On the rate of lava-and tephra production and the upward migration of magma in four Icelandic eruptions. Geologische Rundschau 57, 705–718.

Thorarinsson, S., Einarsson, T., Sigvaldason, G., Elisson, G., 1964. The submarine eruption off the Vestmann Islands 1963–64. Bulletin Volcanologique 27, 435–445.

Thordarson, T., 2004. Accretionary-lapilli-bearing pyroclastic rocks at ODP Leg 192 Site 1184: a record of subaerial phreatomagmatic eruptions on the Ontong Java Plateau. In: Fitton, J.G, Mahoney, J,J., Wallace, P.J., Saunders, A.D., (ed.), Origin and evolution of the Ontong Java Plateau Geological Society, London, Special Publications 229, 275–306.

Thordarson, T., Höskuldsson, Á., 2008. Postglacial volcanism in Iceland. Jökull 58, 197–228.

Thordarson, T., Larsen, G., 2007. Volcanism in Iceland in historical time: Volcano types, eruption styles and eruptive history. Journal of Geodynamics 43, 118–152.

Thordarson, T., Larsen, G., Hamilton, C. 2008. Historical Flood Lava Eruptions The 1783-84 Laki and 934-40 Eldgjá events August 14-17 2008. IAVCEI General Assembly 2008 Conference Field Excursions Excursion 1, 40 pp.

Thordarson, T., Self, S., 1998. The Roza Member, Columbia River Basalt Group: A gigantic pahoehoe lava flow field formed by endogenous processes? Journal of Geophysical Research 103, 27411–27.

Thors, K., Jakousson, S.P., 1982. Two seismic reflection profiles from the vicinity of Surtsey, Iceland. Surtsey Research Progress Report 9, 149.

Thorseth, I.H., Furnes, H., Tumyr, O., 1991. A textural and chemical study of Icelandic palagonite of varied composition and its bearing on the mechanism of the glass-palagonite transformation. Geochimica et Cosmochimica Acta 55, 731–749.

Tolan, T.L., Beeson, M.H., 1984. Intracanyon flows of the Columbia River Basalt Group in the lower Columbia River Gorge and their relationship to the Troutdale Formation. Geological Society of America Bulletin 95, 463–477.

Tomlinson, E.L., Thordarson, T., Lane, C.S., Smith, V.C., Manning, C.J., Müller, W., Menzies, M.A., 2012. Petrogenesis of the Sólheimar ignimbrite (Katla, Iceland): Implications for tephrostratigraphy. Geochimica et Cosmochimica Acta 86, 318–337.

Tribble, G.W., 1991. Underwater observations of active lava flows from Kilauea volcano, Hawaii. Geology 19, 633–636.

Troedson, A.L., Smellie, J.L., 2002. The Polonez Cove Formation of King George Island, Antarctica: stratigraphy, facies and implications for mid-Cenozoic cryosphere development. Sedimentology 49, 277–301.

Tucker, D.S., Scott, K.M., 2009. Structures and facies associated with the flow of subaerial basaltic lava into a deep freshwater lake: the Sulphur Creek lava flow, North Cascades, Washington. Journal of Volcanology and Geothermal Research 185, 311–322.

Tuffen, H., Castro, J.M., 2009. The emplacement of an obsidian dyke through thin ice: Hrafntinnuhryggur, Krafla Iceland. Journal of Volcanology and Geothermal Research 185, 352–366.

Tuffen, H., McGarvie, D.W., Gilbert, J.S., Pinkerton, H., 2002. Physical volcanology of a subglacial-to-emergent rhyolitic tuya at Rauðufossafjöll, Torfajökull, Iceland. In: Smellie, J.L., Chapman, M.G., (ed.) Volcano-Ice Interaction on Earth and Mars. Geological Society, London, Special Publications 202, 213–236.

Tuffen, H., Owen, J., Denton, J., 2010. Magma degassing during subglacial eruptions and its use to reconstruct palaeo-ice thicknesses. Earth-Science Reviews 99, 1–18.

Umino, S., Nonaka, M., Kauahikaua, J., 2006. Emplacement of subaerial pahoehoe lava sheet flows into water: 1990 Kūpaianaha flow of Kilauea volcano at Kaimū Bay,

Hawaii. Bulletin of Volcanology 69, 125–139.

Vaughan, R.G., Webley, P.W., 2010. Satellite observations of a surtseyan eruption: Hunga Ha'apai, Tonga. Journal of Volcanology and Geothermal Research 198, 177–186.

Verwoerd, W.J., Chevallier, L., 1987. Contrasting types of surtseyan tuff cones on Marion and Prince Edward islands, southwest Indian Ocean. Bulletin of Volcanology 49, 399–413.

Vink, G.E., 1984. A hotspot model for Iceland and the Vøring Plateau. Journal of Geophysical Research: Solid Earth (1978–2012) 89, 9949–9959.

Waagstien, R., 2000. Formation Micro-Scanner Image logging of a basalt lava - hyaloclastite sequence from the Lopra-1/1A well, Faroe Islands. Danmarks og Grønlands Undersogelse Rapport, 2000/78.

Waagstien, R., 2006. Composite log from the LOPRA-1/1A well, Faroes Islands. In: Chalmers J. A., Waagstein R., (ed.) Scientific Results from the Deepened Lopra-1 Borehole, Faroe Islands. Geological Survey of Denmark and Greenland Bulletin 9, online data [http://www.geus.dk/publications/bull/nr9/nr9_Composite_log.pdf]

Waichel, B.L., de Lima, E.F., Sommer, C.A., Lubachesky, R., 2007. Peperite formed by lava flows over sediments: An example from the central Paraná Continental Flood Basalts, Brazil. Journal of Volcanology and Geothermal Research 159, 343–354.

Walker, G.P., 1992. Morphometric study of pillow-size spectrum among pillow lavas. Bulletin of Volcanology 54, 459–474.

Walker, G.P.L., 1971. Compound and simple lava flows and flood basalts. Bulletin Volcanologique 35, 579–590.

Walton, A.W., Schiffman, P., 2003. Alteration of hyaloclastites in the HSDP 2 Phase 1 Drill Core 1. Description and paragenesis. Geochemistry, Geophysics, Geosystems 4.

Walton, A.W., Schiffman, P., Macpherson, G.L., 2005. Alteration of hyaloclastites in the HSDP 2 Phase 1 Drill Core: 2. Mass balance of the conversion of sideromelane to palagonite and chabazite. Geochemistry, Geophysics,

Geosystems 6, [DOI: 10.1029/2002GC000368].

Wang, Z., Jin, L., Guan, Q., Yang, L., Wu, J., 2009. Comprehensive Evaluation of Volcanic Reservoir Based Upon FMI and ECS. Journal of Southwest Petroleum University (Science & Technology Edition), 5–10.

Wardlaw, N.C., Li, Y., Forbes, D., 1987. Pore-throat size correlation from capillary pressure curves. Transport in Porous Media 2, 597–614.

Waters, A.C., Fisher, R.V., 1971. Base surges and their deposits: Capelinhos and Taal volcanoes. Journal of Geophysical Research 76, 5596–5614.

Watkins, N.D., Walker, G.P.L., 1977. Magnetostratigraphy of eastern Iceland. American Journal of Science 277, 513–584.

Watton, T.J., Jerram, D.A., Thordarson, T., Davies, R.J., 2013. Three-dimensional lithofacies variations in hyaloclastite deposits. Journal of Volcanology and Geothermal Research 250, 19–33.

Watton, T.J., Wright, K.A., 2010. Volcanic Rocks in the West of Shetland, UCKS. DONG Energy Internal Report, DONG E and P, UK. Ltd, 250 pp.

Wells, R.E., Niem, A.R., Evarts, R.C., Hagstrum, J.T., 2009. The Columbia River Basalt Group—From the gorge to the sea. GSA Field Guides 15, 737–774.

Wentworth, C.K., 1922. A scale of grade and class terms for clastic sediments. The Journal of Geology 30, 377–392.

Werner, R., Schmincke, H.-U., 1999. Englacial vs lacustrine origin of volcanic table mountains: evidence from Iceland. Bulletin of Volcanology 60, 335–354.

White, J.D., 1996. Pre-emergent construction of a lacustrine basaltic volcano, Pahvant Butte, Utah (USA). Bulletin of Volcanology 58, 249–262.

White, J.D.L., Houghton, B.F., 2006. Primary volcaniclastic rocks. Geology 34, 677–680.

White, R.S., Bown, J.W., Smallwood, J.R., 1995. The temperature of the Iceland plume and origin of outward-propagating V-shaped ridges. Journal of the Geological Society 152, 1039–1045.

White, R.S., Smallwood, J.R., Fliedner, M.M., Boslaugh, B., Maresh, J., Fruehn, J., 2003. Imaging and regional distribution of basalt flows in the Faeroe-Shetland Basin. Geophysical Prospecting 51, 215–231.

Wilding, M., Dingwell, D., Batiza, R., Wilson, L., 2000. Cooling rates of hyaloclastites: applications of relaxation geospeedometry to undersea volcanic deposits. Bulletin of Volcanology 61, 527–536.

Wilding, M.C., Webb, S.L., Dingwell, D.B., 1995. Evaluation of a relaxation geospeedometer for volcanic glasses. Chemical Geology 125, 137–148.

Wilkens, R., Simmons, G., Caruso, L., 1984. The ratio V p/V s as a discriminant of composition for siliceous limestones. Geophysics 49, 1850–1860.

Wohletz, K., 2002. Water/magma interaction: some theory and experiments on peperite formation. Journal of Volcanology and Geothermal Research 114, 19–35.

Wohletz, K.H., 1983. Mechanisms of hydrovolcanic pyroclast formation: grain-size, scanning electron microscopy, and experimental studies. Journal of Volcanology and Geothermal Research 17, 31–63.

Wohletz, K.H., 1986. Explosive magma-water interactions: Thermodynamics, explosion mechanisms, and field studies. Bulletin of Volcanology 48, 245–264.

Wolfe, C.J., Bjarnason, I.T., VanDecar, J.C., Solomon, S.C., 1997. Seismic structure of the Iceland mantle plume. Nature 385, 245–247.

Wood, R.D., Wichmann, P.A., Watt, H.B., 1974. Gamma ray-neutron log. Review 1, 1–19.

Wright, J.V., Smith, A.L., Self, S., 1980. A working terminology of pyroclastic deposits. Journal of Volcanology and Geothermal Research 8, 315–336.

Wright, K.A., Davies, R.J., Jerram, D.A., Morris, J., Fletcher, R., 2012. Application of seismic and sequence stratigraphic concepts to a lava-fed delta system in the Faroe-Shetland Basin, UK and Faroes. Basin Research 24, 91–106.

Wu, C., Gu, L., Zhang, Z., Ren, Z., Chen, Z., Li, W., 2006. Formation mechanisms of hydrocarbon reservoirs associated with volcanic and subvolcanic intrusive rocks: Examples in MesozoicCenozoic basins of eastern China. AAPG bulletin 90, 137–147.

Yamada, T., Okano, Y., 2006. Modeling and flow simulation of a volcanic reservoir: Application of multi-point geostatistics and probability perturbation theories to a real field. Journal of the Japanese Association for Petroleum Technology 71, 85–93.

Yamada, T., Okano, Y., 2007. A Volcanic Reservoir: Integrated Facies Distribution Modeling and History Matching of a Complex Pressure System. SPE Reservoir Evaluation & Engineering 10, 77–85.

Yamagishi, H., 1991. Morphological and sedimentological characteristics of the Neogene submarine coherent lavas and hyaloclastites in Southwest Hokkaido, Japan. Sedimentary Geology 74, 5–23.

Yamagishi, H., Dimroth, E., 1985. A comparison of Miocene and Archean rhyolite hyaloclastites: evidence for a hot and fluid rhyolite lava. Journal of Volcanology and Geothermal Research 23, 337–355.

Yamagishi, H., Dimroth, E., 1987. Studies on the Neogene subaqueous lavas and hyaloclastites in southwest Hokkaido. Report of the Geological Survey Hokkaido 59, 55–117.

Yang, R.Y., Zou, R.P., Yu, A.B., 2003. Numerical study of the packing of wet coarse uniform spheres. AIChE journal 49, 1656–1666.

Yokose, H., Lipman, P.W., 2004. Emplacement mechanisms of the South Kona slide complex, Hawaii Island: sampling and observations by remotely operated vehicle Kaiko. Bulletin of Volcanology 66, 569–584.

Zhao, D., 2001. Seismic structure and origin of hotspots and mantle plumes. Earth and Planetary Science Letters 192, 251–265.

Zierenberg, R.A., Schiffman, P., Jonasson, I.R., Tosdal, R., Pickthorn, W., McClain, J., 1995. Alteration of basalt hyaloclastite at the off-axis Sea Cliff hydrothermal field, Gorda Ridge. Chemical Geology 126, 77–99.

Zimanowski, B., Buttner, R., 2003. Phreatomagmatic explosions in subaqueous volcanism. Geophysical Monograph-American Geophysical Union 140, 51–60.

Zimanowski, B., Büttner, R., Lorenz, V., 1997. Premixing of magma and water in MFCI experiments. Bulletin of Volcanology 58, 491–495.

Appendices Readme

The Appendix for this PhD can be supplied on DVD by contacting the author at the following email addresses (timwa@statoil.com or timwatton311@hotmail.com) Provided in this in section is a read me file designed to compliment the DVD.

This document and DVD contains the supporting information pertaining to the thesis itself. Each chapter, for reference has an individual folder with separate readme files that points the reader to files in the folder tree. Provided here is a summary of appendix data sets for convenient reference. A copy of PAST freeware, referred to throughout the thesis is provided as a separate file on the root menu. A guide to operation is also supplied. This program is an .exe file, which can be opened on any windows computer and runs directly from the disk with no installation necessary as an executable .jar file (therefore double click and select run).

Chapter 1

- Excel spread sheet with well log information for figure 1.2.

Chapter 2

- Table of analytical errors for geochemical data provided by laboratory in University of Edinburgh
- Raw Xray-CT cube with processed stack and instructions to open

Chapter 4

- Logs completed in support of the thesis
- Published paper in support of the thesis

Chapter 5

- Formatted XRF databases and Sample information
- Data sets used in comparison
- Photomicrographs used in thesis.

Chapter 6

- False Coloured images and image analysis data base
- LOPRA 1/1A Data Base
- HSDP II Data base A) and B)
- HSDP II geo chemical database
- HSDP II porosity modeling results
- Scans of hand drawn logs from core visits
- EDX data base
- Phosphor only data base
- Modeling data base
- Depth conversion data base
- Reflectivity data base

Chapter 7

- FMI data files for wells
- FMI PAST well logs
- Hand held GR data base
- FMI master sheet

Chapter 8

- Hreppar formation Logs and Field photos

Chapter 1 Readme

This folder contains:

1. Excel Document –Density data from nelson thesis.xlsx. These are the values used in figure 1.2 to show the variation in well log response for volcaniclastic deposits.

Chapter 2 Readme

This folder contains:

2. Word Document – XRF Average Detection Limits.docx
3. Root folder – Xray Ct Raw and Process Data

1. XRF Average detection limits are provided from University of Edinburgh Geochemistry labs

2. Root folder contains two folders

- ***Raw unprocessed volume*** - Raw data file from Xray CT Facility which can be opened in ImageJ for processing (Raw Data Volume.vol, test.view)
- ***Tiff image slices*** – contains three multi layer tiff images which can be opened in any image viewer. There are three options
    1. Unprocessed Raw tiff all slices.tif – This contains all slices from the original raw volume unprocessed
    2. Initial process void and fracture Substack (90-444).tf – This is the raw stack processed to only show slices 90-444
    3. Final Process void and fracture Substack (90-444).tif – This file was used to create thresholded volumes in chapter 2 (using the process outlined in the text). This stack has been noise reduced using the standard filter in the imageJ → process stack → noise reduction.

Chapter 4 Readme

This folder contains three root folders and 1 file:

1. Full lithological logs provided from Hjörleifshöfði (consist of ..pdf documents which can be opened in an image viewer) – 1 file – 5 logs
2. Full lithological logs Stóri-Núpur (consist of .eps documents) - 11 files – 13 logs. Position of logs is provided in Figure 4.2.
3. Papers published in support of thesis – a copy of the final submitted article to the January issue of Journal of Volcanology and Geothermal research – 1 .pdf document
4. 4) Sample Catalogue for Project.xlsx – All samples collected for thesis for future reference.

Chapter 5 Readme

The appendix for chapter 5 contains data used in the processing of geochemical data. Files that appear with no file suffix or as unix executable files are designed to be opened with **PAST** freeware. PAST is freely available statistics software package. A copy of past.exe is provided on the DVD. It can be opened on all windows machines and will run locally, therefore requires no installation. If prompted to update links in excel (.xlsx) documents please press ignore.

There are 14 files and 1 root folder in this section (***within the folder titled Chapter 5 appendix***);

1. Total alkali/silica (TAS) plot data used to create part of Figure 5.16.
2. Normalized major and trace element data of silicic volcanic centers across Iceland in comparison to values from the Hjörleifshöfði outlier.
3. Raw Geo Chem Data Hjor(2).xlsx – Contains normalized major and trace element data with plots used to correlate volcanism to the Katla volcanic system (Fig. 5.16)
4. Abbreviations used in geochemical plots.docx – contains the abbreviations
5. HJ comparison to other silicic centres.xlsx – Raw major/trace element data used for the comparison of the HJ outlier.
6. (**PAST FILE**) Hj vs. Sol Correlation – data used to produce correlation plots. Note past does not preserve graphs (unlike excel). Grpahs in the thesis can be plotted via the menu bar -> modeling -> linear
7. (**PAST FILE**) Trace vs. Major elements. Data used to construct diagram 5.15
8. HJ Major Elements ex ignimbrite formatted for thesis.xlsx – Major element vs. SiO2 Harker diagrams used in the interpretation of geochemical data excluding high silica unit (for ease of reading)

9. HJ Major Elements formatted for thesis.xlsx – Major element vs. SiO2 Harker diagrams used in the interpretation of geochemical data including high silica unit (for ease of reading)
10. HJ Major Elements vs Mg formatted for thesis.xlsx - – Major element vs. MgO Harker diagrams used in the interpretation of geochemical data including high silica unit (for ease of reading)
11. HJ Major Elements vs Mg formatted minus pyroclasts for thesis.xlsx - – Major element vs. SiO2 Harker diagrams used in the interpretation of geochemical data excluding high silica unit (for ease of reading)
12. (**PAST File**)AFM Diagram Data – use to plot figure 5.17 – Data can be plotted using menu bar -> graph -> ternary
13. XFR Sample list.xlsx list of samples used in chapter 6 including grid references
14. 14) img095.jpg Aerial photo base field slip with interpreted boundaries
15. 15) root folder containing 32 .jpg files containing original thin section photomicrographs describes in figure 5.10-5.15. Sample numbers are provided in the file name. These refer to samples provided into the sample list 13) XRF Sample list.xlsx
16. 16) Identification of Alteration in Hjörleifshöfði samples .docx– Process by where alteration was recognized in samples so they could be discarded for correlation purposes.

Chapter 6 Readme

Chapter 6 contains 2 files and 5 root folders that refer to sections within the chapter subsections. The folders contain a combination of .tiff images, PAST files and Excel files. Files that appear with no file suffix or as unix executable files are designed to be opened with **PAST** freeware. PAST is freely available statistics software package. A copy of past.exe is providedon the DVD. I can be opened on all Windows machines and will run locally for the CD, therefore requires no installation. If prompted to update links in excel documents (.xlsx) please press ignore.

- BLTN13-029_1.pdf – Submission file for accepted AAPG Bulletin Paper
- BLTN13029.pdf – AAPG acceptance letter
- AMNH FORM.jpeg – Conformation of Sample Acquisition and permission for sample Shipping from the Natural History Museum of New York

- ***Root folder -> Section 6_2 Appendix Density Prediction and Modeling results***;
  1. All density models.xlsx – Contains all Vp to Density modeling results for samples information provided by Jim Moore in a personal communication. Lithofacies abbreviations are provided in the document. Information is provided on different sheets which can be switched on the bottom tab. Averages used in the construction of table 6.2 are provided on sheet 2.
  2. Lopra raw data.xlsx - Data used from the LOPRA1/1A bore hole. Data range used for Vp given in table 6.2 using interpretation of Waagstien, 2000 available on the GEUS website.
  3. Lopra vp vs vs.xlsx – Vp and Vs data used to construct Figure 6.11
  4. (**PAST** File) HSDP Histogram data -> Data used in construction Fig. 6.2a and b. Past does not save graphs but a histogram can plotted using the menu bar -> graph -> histogram

- ***Root folder -> Section 6_3_1 Appendix Depth conversion Results;***

1. 1d%20depth%20simples%20values.xlsx - Simple 1D depth conversion results used to construct figure 6.13
2. Simple 1d depth conversion of a hyaloclastite pile.xlsx – Simple 1D depth conversion minus LOPRA 1/1A results used to construct figure 6.14

- ***Root folder -.Section 6_3_2 Appendix Reflection Coefficient Data;***
    1. All AI measurements.xlsx – Acoustic impedance calculations for different hyaloclastite lithofacies used to construct Fig. 15 a and b
    2. Velocity models using field data.xlsx – Data used to construct reflection coefficient models in figures 6.16 -6.21. Data is presented as a number of sheets. Log number refers to Table 6.5 and are the example logs based upon field data provided in the chapter 4 appendix and file 3)
    3. img100.jpg – Field Log slip of a pillow dominated hyaloclastite breccia succession at Strike River Dam, Idaho, USA. Grid reference in document.
    4. 4) Denisty Induration comparison.xlsx Data from Le Masurier, 2002 to compare amount of induration experience in hyaloclastite deposits and the impact on reflection coefficients.

- S***ection 6_3_3 Appendix S wave Problem***
    1. 1) Lopra raw data work up hyaloclastite deposits.xlsx – Data used in the comparison of Vp and Vs for hyaloclastite deposits in the LOPRA 1/1A borehole.

1. Root folder - Section 6_5 Appendix Porosity Modeling;

1. HSDP porosity modeling data xlsx – Contains three sheets use to construct diagrams 6.22, 6.23, 6.26, 6.27. The reader is asked to see section 6.4 for details for the construction of this data.
2. Classified hsdp data for geo chem.xlsx – Classified Geochemical data used to construct fig. 6.28. Data freely available on the ICDP database. Results also presented in Rhodes and Vollinger, 2004.
3. percentage density.xlsx – Data from section A1, root folder 6_6, file 4. Used to show how palagonite replacement can maintain density see Fig. 6.26b

4. Jim Moore Personal Communication.docx -> Personal communication with Jim Moore to supply raw data from the Moore 2001 paper.

2. Root folder - Section 6_6 Appendix Core to well log;

1. 1830m raw data.xlsx – Raw plotted data used in the thesis for section A, fig. 6.29
2. Raw Well logs 2530m.xlsx - Raw plotted data used in the thesis for section A, fig. 6.29
3. HSDP hyaloclastite only (Autosaved).xlsx – Data used to construct Fig. 6.1 density and wt % water absorbed adapted from Moore personal communication.
4. Image analysis results a and b.xlsx – Image analysis results based upon images in folders 4-5) method outlined in Analytical techniques section of the thesis.
5. Folder - Thin Scans 1830 1870m – Scans of thin sections and false colored palleted images with image J pallets to create % olivine, zeolite, porosity based upon the methodology outlined in chapter 2 and in Grove and Jerram, 2011.
6. Folder - Thin section scans 2500 Scans of thin sections and false colored palleted images with image J pallets (.cpl) to create % olivine based upon the methodology outlined in chapter 2 and in Grove and Jerram, 2011.
7. Folder - SEM EDX results → contains EDX results in wt % used in thesis separated into folders and presented as word documents (.txt) and low resolution .tif. All images are replicated at high resolution for figure production (high resolution images). Samples used are both A and B (B=C) sections. Depths of samples provided in figure 6.29 and appendix file 4)
    - Folder ->High Resolution images -> 8 folders
    - Folder ->Sample A8 -> 24 files
    - Folder ->Sample C1 -> 33 files
    - Folder ->Sample C2 -> 32 files
    - Folder ->Sample C7 - > 33 files
    - Folder ->Sample C10 -> 32 files
    - Folder ->Sample X5 -> 32 files
    - Folder ->Sample Z3 -> 16 files

8. Example edx responses.xlsx representative EDX responses used in this thesis (Fig. 6.35)
9. Phoshpor occurances in HSDp II.xlsx → al phosphorous occurrences in HSDP II in reference to figure 6.36, a , b , c.
10. (**PAST** File) used in construction of figure 6.34
11. Logs for A section, raw lithology logs from core visit (headers and depths on sheet
    - Sheet no 1.jpg
    - Sheet no 2.jpg
    - Sheet no 3.jpg
    - Sheet no 4.jpg
    - Sheet no 5.jpg
    - Sheet no 6.jpg
    - Sheet no 7.jpg
    - Sheet no 8.jpg
    - Sheet no 9.jpg
    - Sheet no 10.jpg
    - Sheet no 11.jpg
    - Sheet no 12.jpg
    - Sheet no 13.jpg
    - Sheet no 14.jpg
12. Logs for A section, raw lithology logs from core visit (headers and depths on sheet
    - img110.jpg
    - img111.jpg
    - img112.jpg
    - img113.jpg
    - img114.jpg
    - img115.jpg
    - img116.jpg
    - Sheet no 1.jpg
    - Sheet no 2.jpg

- Sheet no 3.jpg
- Sheet no 4.jpg
- Sheet no 5.jpg
- Sheet no 6.jpg
- Sheet no 7.jpg
- Sheet no 8.jpg
- Sheet no 9.jpg

13. (**PAST File**) 14) Log 1830 1870m mineralization - Mineralogy data used to plot fig. 6.33 data from file 1 in this section.

Chapter 7 Readme

The appendix for chapter 7 always refers back to back to appendix file 1. File 1 in this chapter is the master correlation panel showing the FMI data in context as well as the whole Rosebank interpretation including the positions of all well tops from table 7.3. This data has been supplied by the Rosebank Partnership, Chevron, DONG, Statoil and OMV and replication of the outside the correlation panel was not allowed (Work was carried out in DONG offices in London, which still holds the master file contact Alywn Ross for details alwro@dongenergy.co.uk). The aim of this chapter is to reveal methods of image log calibration and provide field examples to interpreted images not is not designed to provide a concise downhole stratigraphy of the field.

The author strongly recommends that FMI images are opened in an image editing package such as Corel Photopaint or Adobe Photoshop. GIMP image freeware will also load these images [http://www.gimp.org/]. Alternatively freely available Schlumberger software will also work but is a steeper learning curve. {http://www.slb.com/services/characterization/software/data_utilities/blueview_log_image_software.aspx}

15 files are provided. ;

1. well correlation diagram..jpg – Master correlation panel with well log and FMI interpretation
2. final_image_205_01_1 FMI.tif - Raw processed image log both dynamic and static for well 205/1-1 see file 1) for interpretation
3. 3) 213-27-2_dynamic_9531.7-9732.2ft.tif Raw processed image log both dynamic flog (see chapter 2) or uppermost colsay interval 213/27-2 see Fig. 7.6, 7.8 and file 9 for interpretation
4. 4) 213-27-2_static_9531.7-9732.2ft.tif Raw processed image log both static log (see chapter 2)for uppermost colsay interval 213/27-2 see Fig. 7.6, 7.8 and file 9 for interpretation
5. 5) FMI 213_27_4 9120_10400.TIF - Raw processed image log both dynamic and static for well 213/27-4 9120_10400 ft MD see file 1) for interpretation

6. 6) FMI 213_27_4 10390_11410.TIF - Raw processed image log both dynamic and static for well 213/27-4 10390_11410 ft MD see file 1) for interpretation
7. 7) 205_10a_3 FMI.TIF Raw processed image log both dynamic and static for well 205/10a-3 see file 1) for interpretation
8. 8) Hyaloclastite FMI.jpg – Hyaloclastite well log FMI interval at base of 213/27-4 as used in table 7.3
9. 9) (PAST FILE) 213272 Colsay 1 equi interpreatation. – Interpretation used for the construction of Fig. 7.6
10. 10) 213272 SGR plot for paper.xlsx – Raw SGR data provided by DONG energy E and P, UK. Ltd for the upper most colsay interval used in Fig. 7.8
11. 11) (PAST FILE) Fracture Comparison – Raw dataset used to construct fig 7.9. As before a histogram can be created using menu tab ->. Plot -> histogram or menu graph -> x/y plot. Random fractures are coloured dark blue, systematic fractures in purple.
12. 12) Nambia GR Results.xlsx – Raw Gamma ray data (Spectral) used in figure 7.7
13. 13) P-sonic Fmi Justifications.pptx – Histograms and depths of 213/27-4 lava flow distributions used in figure 7.4 and 7.9.
14.) FMI paper Submission Geol Soc Special Publications.pdf → FMI paper submission to Geological Society of London Special Publications
15. 15) WoSh Submission conformation.docxSubmission conformation for FMI paper submission

Chapter 8 Readme

Chapter 8 contains 1 root folder -> Hreppar Formation Logs and photos and five files with are logs and photos to support interpretation of results provided for the Hreppar formation. The files are .docx and can be opened in word;

1. 1) Log 1 and Fig 1 – Gaukshofdi
2. 2) Fig 2 - Melhagi
3. 3) Fig 3 and Log 8 Fluvial
4. 4) Figure 4 and 5 – Hjaparfoss Rootless Cone
5. 5) Log 2 to 7 – Fossness
6. Terry Tolan person communication of ideas based upon well logs.